A Synthetic and Computational Approach to the Design of New Photoactive Organometallic Materials

This Thesis is Presented for the Degree of

Doctor of Philosophy

By

Anthony Coleman B.Sc.

Under the Supervision of Dr. Mary Pryce

and

Prof. Conor Long

at

Dublin City University

School of Chemical Sciences

July 2007

Declaration

I hereby certify that this thesis, which I now submit for assessment on the programme of study leading to the award of Doctor of Philosophy is entirely my own work and has not been taken from the work of others save and to the extent that such work has been cited and acknowledged within the text of my work.

Signed: _____ Student ID No.: 99087553

Date: 21/09/02

Table of Contents

Dedication

I would like to dedicate this work to my parents all the support they've shown me over the last few years and to Phil for supporting me in this right from the start and putting up with me being a poor student again.

Acknowledgements

I would like to thank my supervisors Dr. Mary Pryce and Prof. Conor Long for allowing me the opportunity to carry out my studies. I am grateful to have had the chance to work under such patient, knowledgeable and helpful supervisors. Thanks to Mary for your unlimited optimism!

Thanks to Dr. Wesley Browne of the University of Groningen for the advice and help over the last year of my work, particularly as regards my research trip to RAL. Thanks too to Dr. Kate Ronayne of Rutherford Appleton Laboratories for her assistance with the time resolved infrared studies.

A special thanks too goes to the many people I've worked with over the last number of years. Firstly, the X-246 researchers past and present – Nikki, Steph, Johnny, Claire, Mohammed, Gemma and Audrey. Big thanks also to our old lab mates from the Han Vos research group – Lynda, Bill, Rob, Laura, Yvonne, Cindy, Stefania, Noel, Fiona Lynch, Fiona Frehill and Zita. And also our new lab mates from Tia Keyes research group – Linda, Steven, Andrea, Nigel, Muath, Qiang and Reena.

Big thanks too to Elena (Caca Milis) Campagnoli, Alan, Michael, Colm. Also who can forget the old V269 gang - Dr. Barry, Teresa, Aoife and Kate. Thanks for keeping me sane over the last few months of writing up!

Finally, a huge thanks to all the technical staff – Mick, Vinnie, Ambrose, John, Damien, Maurice, Veronica, Mary, Ann and Teresa. I've very grateful for all the help you gave me during my few years in DCU.

Abbreviations

IC	:	Interconversion
ISC	:	Intersystem crossing
MO	:	Molecular Orbital
LUMO	:	Lowest unoccupied molecular orbital
HOMO	:	Highest occupied molecular orbital
LF	:	Ligand Field
LC	:	Ligand Centred
MLCT	:	Metal to Ligand charge transfer
LMCT	:	Ligand to metal charge transfer
LBCT	:	Ligand based charge transfer
MSCT	:	Metal to Solvent charge transfer
IL	:	Intraligand
Nd-YAG	:	Neodymium yttrium aluminium garnet
TRIR	:	Time resolved infrared spectroscopy
TRO	:	Time resolved optical spectroscopy
HF	:	Hartree-Fock
RHF	:	Restricted Hartree Fock
DFT	:	Density Functional Theory
TDDFT	:	Time-dependent Density Functional Theory
SCF	:	Self-Consistent Field
KS	:	Kohn-Sham approximation
PBE	:	Perdew-Burke-Enzerhof exchange model

LYP	:	Lee-Yang-Paar correlation functional
B3LYP	:	Beckes 3 parameter hybrid functional using the LYP correlation functional
FF	:	Force Field
MM	:	Molecular Mechanics
MD	:	Molecular Dynamics
DZ	:	Dunning-Huzinaga double-ζ basis functions
FWHM	:	Full-Width Half-maximum
EHMO	:	Extended Hückel Molecular Orbital
py	:	pyridine
F_5py	:	pentafluoropyridine
4-Fpy	:	4-fluoropyridine
3-Fpy	:	3-fluoropyridine
2,6-F_2py	:	2,6-difluoropyridine
3-Brpy	:	3-bromopyridine
4-acpy	:	4-acetylpyridine
4-CNpy	:	4-cyanopyridine
MCH	:	methylcyclohexane
PFMC	:	perfluoromethylcyclohexane
Me-THF	:	methyltetrahydrofuran
Me_2-THF	:	dimethyltetrahydrofuran
PPh_3	:	triphenylphosphine
$P(OMe)_3$	:	trimethoxyphosphine
PAH	:	polycyclic aromatic hydrocarbon
RAL	:	Rutherford Appleton Laboratory
CLF	:	Central Laser Facility

PIRATE	**:**	**Picosecond Infra-red and Transient Excitation**
DPPM	**:**	**1,2-bis diphenylphosphino methane**

Abstract

Chapter one serves as an introduction to organometallic chemistry, specifically metal carbonyl complexes. The principles of photophysics are also introduced. This is followed by an outline of the techniques of matrix isolation and time-resolved infra-red (TRIR) spectroscopy. The rapidly developing area of computational chemistry is then introduced. Specific emphasis is placed on the *ab-intio* and Density Functional Theory (DFT) levels of theory as well as the method of Time-dependent Density Functional Theory (TDDFT), used for predicting excited states.

Chapter two begins with an introduction to the properties of the carbon-fluorine bond and a short review of recent reports of C-F bond activation in the literature. This is followed by a literature survey, which focuses on photochemistry and computational studies of a number of metal carbonyl compounds. The photochemistry of a series of fluorinated metal carbonyls of the type $XMn(CO)_5$ (X = fluorinated substituent), was probed *via* matrix isolation studies at 20 K, using both IR and UV-vis as detection methods. Theoretical studies were performed, and compared to the experimental data.

Chapter three involves a review of the photochemistry of $M(CO)_5$ systems, where M = W, Cr, bound to pyridine or substituted pyridines. The photochemistry of systems of the type $FpyW(CO)_5$, was then investigated using matrix isolation at 20 K in a number of matrix gases. Spectroscopic changes were monitored via UV-Vis and IR spectroscopy. Theoretical studies using TDDFT were also preformed. These are compared to the experimental data observed in matrix isolation studies.

Chapter four begins with a review of the literature of *cis-trans/trans-cis* isomerisation, particularly in stilbene and butadiene type compounds. This is then followed by a literature review of the photochemistry of (arene)$M(CO)_3$ type compounds. For comparison a review of the photochemistry of a number of photoisomerisable $Re(CO)_3L$ complexes is also included, as these systems contain both isomerisable stilbene-like units and carbonyl units. .Predominantly the chapter centres on the photoinduced *cis-trans* isomerisation of *cis*-(η^6-1,2-diphenylethene)$Cr(CO)_3$. The photochemistry of these compounds is then examined using techniques such as, matrix isolation, time resolved infra red (TRIR) spectroscopy, and steady-state

photolysis. These results are then compared to theoretical results achieved using quantum chemical calculations. The electrochemistry of these metal carbonyl systems is then briefly examined.

Chapter five begins with a general introduction to Sonogashira-Hagihara type cross coupling reactions. This is then followed by a literature survey on the synthesis and photochemistry of luminescent organometallic dyad systems. The synthesis of these novel systems using the Sonogashira-Hagihara method is described. The photophysical properties are then examined using room and low temperature fluorescence and life-time studies. The photochemistry of the $Co_2(CO)_6$ complexes are examined by steady-state photolysis studies in the presence of a trapping ligand. Electrochemical data is also included.

Chapter six involves the study of organometallic pyrenyl-ferrocenyl dyad systems. This chapter begins with a brief review of the literature of organometallic ferrocene compounds as luminescent pyrenyl dyad systems are discussed in detail in chapter four. The effect, on the excited state, of the ferrocenyl moiety and the level of conjugation present is examined using fluorescence spectroscopy and electrochemistry. The results of photoinduced CO loss of the $Co_2(CO)_6$ complexes in the presence of the trapping ligand triphenylphisphine and are also discussed.

Appendix: Experimental details for a number of metal carbonyl complexes and cyclopentenone complexes formed by a photochemically induced Pauson-Khand reaction. Matrix isolation sample preparation and matrix isolation studies for (η^6-phenanthrene)$Cr(CO)_3$ are also discussed.

Chapter 1

Introduction

Chapter one serves as an introduction to organometallic chemistry, specifically metal carbonyl complexes and their electronic structure. The principles of photophysics are also introduced. This is followed by an outline of the techniques of matrix isolation, laser flash photolysis, and Time-resolved infra-red (TRIR) spectroscopy. The rapidly developing area of computational chemistry is then introduced, with specific emphasis placed on ab-intio calculations and Denisty Functional Theory (DFT) as well as the method of Time-dependent Density Functional Theory (TDDFT) used for predicting transition energies to excited states.

1.1. Introduction

Organometallic chemistry is essentially a branch of inorganic coordination chemistry. By definition an organometallic compound can de described as one which contains a bonding interaction, ionic or covalent, between a carbon atom of an organic group to a metal. This can be a main group, lanthanide, actinide or transition group metal, the latter type being the focus of this thesis. The first transition metal (TM) complex $Na[PtCl_3C_2H_4]$ was discovered in 1827 by Zeise[1], a Dutch pharmacist. Following this in 1868 the French chemist Paul Schützenberger[1] synthesised the first metal carbonyl complex $[Pt(CO)Cl_2]_2$. It was not until 1890 however that organometallic chemistry was used in industry, with Monds[2] discovery of $Ni(CO)_4$, in developing a new method for extracting nickel from its ores. In 1891 a second metal carbonyl $Fe(CO)_5$ was isolated by Mond and Langer[3]. In 1905 Dewar and Jones observed that on subjecting the previously discovered $Fe(CO)_5$[3] to sunlight, a new species $Fe_2(CO)_9$ was formed[4]. However, the first resolute examination into the photochemistry of metal carbonyls was undertaken by Strohmeier in the substitution reactions of the carbonyl ligands in initially $CpMn(CO)_3$ and then other Group 7 and Group 6 metal carbonyl species[4]. It was not however until the late 1950s and early 1960s that photochemistry itself became a synthetic tool for organometallic chemists, with the first article on photochemistry by Green and Stear in the Journal of Organometallic Chemistry in 1964.[5]

As previously mentioned the main focus of this study is transition metal complexes, specifically transition metal carbonyl complexes. Transition metals are the elements comprising groups 3-12 ranging from common and long known elements such as iron, copper and gold to recent arrivals such as technetium, which was only discovered in 1937[6]. Transition metals are of such interest because of their partially filled d orbitals, which allow complexation with neutral ligands such as carbon monoxide. This partially filled metal d orbital also imparts unusual properties onto transition metal complexes, such as bright colours and unusual variations in magnetic behaviour. Excitation of the electrons in these d orbitals can result in a range of different colours depending on the oxidation state of the metal.

1.2. Bonding in metal carbonyls

In organometallic complexes, especially those containing a transition metal, the metal ions are in a low positive oxidation state that results in partially occupied d orbitals. In these complexes the central metal atom or ion is bonded to a number of ligands by coordinate-covalent bonds, which stabilises the low oxidation state of the central metal.

Bonding in metal carbonyl complexes arises from a combination of both σ- and π-bonding and can be viewed in terms of donor-acceptor bond interactions. σ-donation from the carbon monoxide ligand to the transition metal results from overlap of the σ orbitals of the metal and the carbon monoxide ligand. This arises from electron donation from the weakly anti-bonding 5σ bonding configuration of the CO ligand to the empty or partially empty d_z^2 orbital of the transition metal, which is located along the same axis of symmetry and a reduction in electron density on the σ^*-orbital, thus forming both a bonding and anti-bonding orbital. The $d_{x^2-y^2}$ orbital of the transition metal will also overlap with four CO ligands along the x- and y-axis resulting in the formation of another bonding- and anti-bonding molecular orbital. This σ-donation from the CO ligand onto the metal centre results in an increase in the electron density on the metal. A second type of bond interaction now takes place from the metal to the donor ligand. In the case of CO, π-back donation or back-bonding results in delocalisation of electron density from the occupied or partially occupied π-type d orbitals of the transition metal to the two degenerate $2p\pi^*$ antibonding molecular orbitals of the same symmetry. The d orbitals of the transition metal which have their lobes between the arbitrary x, y, z axis (d_{xy}, d_{xz} and d_{yz}) will each form four bonding orbitals with the $2\pi^*$ anti-bonding ligand orbitals of the appropriate symmetry. For example, the d_{xz} orbital of the transition metal will bond with two $2p\pi^*$ antibonding ligand orbitals along the x-axis and two along the z-axis.[7] Quantum-chemical calculations[1] have shown that as a result of this, even a small interaction of the vacant ligand $2\pi^*$ orbitals in the M-CO bond can greatly reduce the internal CO ligand bond strength and reduce its bond order. This is observed in the infrared as a shift in the ν_{co} carbonyl stretching band to a lower frequency on complexation compared to the free CO ligand. Thus both overlap of the σ symmetry orbitals of the metal and donor ligand giving rise to strong σ-donation interactions and $\pi \rightarrow \pi^*$ (TM $\rightarrow$ CO)

delocalisation leading to π-back bonding are involved in bonding between the transition metal and the diatomic carbon monoxide ligand. Generally, strong π-back bonding is associated with lower valent metals[8] having a tendency to delocalise electron density into the ligand, in order to compensate for increased electron density in the metal following σ- overlap between the metal and CO. Thus as the σ-donation onto the metal from the carbonyl or other σ-donor ligand increases so too does the π-back bonding. Although often ignored π-donor interactions also take place with donation of electron density from the carbon monoxide donor ligand to the transition metal M(π) ← CO(1π).

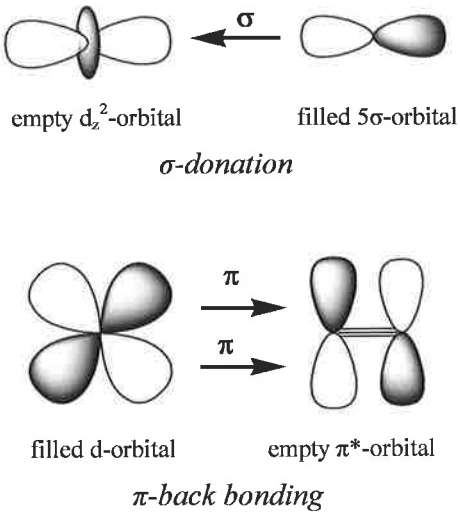

Figure 1 Schematic representation of the bonding involved between a transition metal and a carbon monoxide ligand demonstrating a (CO → TM) σ-bond and TM→ CO π-backbonding.

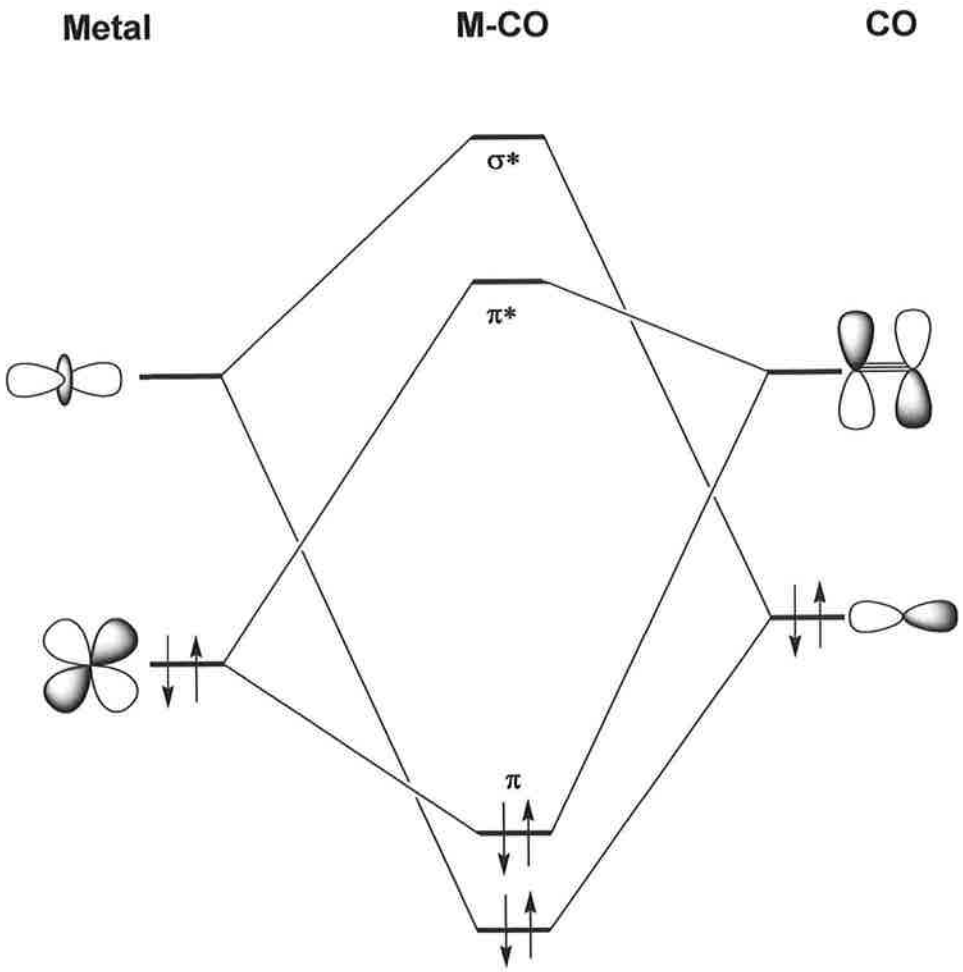

Figure 2 Rudimentary energy-level diagram illustrating the orbitals involved in bonding between the transition metal and the carbon monoxide ligand.

Both complexation and the bonding mode of the carbonyl moiety can exact a change on the characteristic vibrational frequency. Free CO exhibits a ν_{co} at approximately 2143 cm^{-1}, however on terminal complexation to a transition metal this decreases to 2120-1850 cm^{-1}.For μ^2-and μ^3-bound CO groups the ν_{co} band is observed at even lower frequencies, 1750-1850 cm^{-1} and 1620-1730 cm^{-1} for μ^2-and μ^3-bound CO groups respectively[1].

1.3. Principles of photophysics

The absorption of a photon of radiation (*hν*) by a molecule results in the formation of an electronically and vibrationally excited state of that particular species whereby an electron is promoted to an orbital of higher energy. (i.e $M \rightarrow M^*$). In organometallic chemistry, the transitions to an excited state can be characterised as either ligand field transitions whereby the orbitals in the ground state structure are predominantly metal based in character (d-d transitions) or alternatively charge transfer transitions. In the latter case the orbitals of the ground state structure contain both ligand and metal contributions.

The Born-Oppenheimer approximation states that on initial excitation following light absorption a electronic excited state is produced without changes in the position of nuclei of the molecule, as nuclei have a much larger mass than electrons. Nuclear motion occurs on a the longer timescale of $10^{-11} - 10^{-13}$ s compared to $< 10^{-15}$ s for electronic motion[9]. This excited state is known as a Franck-Condon excited state. Generation of these Franck-Condon excited states is predicted by the Born-Oppenheimer approximation, which states that the electronic motion is rapid compared to inter-nuclear motion. This results in an electronic transition, while the nuclei of the molecule retain their ground state coordinates. Following generation of the Franck-Condon excited state rapid vibrational and thermal relaxation to the lowest vibrational level of the electronic excited states occurs. These vibrationally and thermally equilibrated excited states, known as *'Thexi'* states, are generally created via loss of vibrational energy into the surrounding environment such as the solvent medium.

Such *'Thexi'* states have a definite chemical structure, chemical reactivity, absorption spectrum, molar energy, entropy and as such can be regarded as excited state isomers of the ground state structure. Following their generation there are a number of pathways by which *'Thexi'* states can return to the ground state. On formation of the high energy singlet (S_n) or 'Thexi' state rapid vibrational relaxation to the first singlet excited state (S_1) occurs. Non-radiative relaxation to a lower energy excited state can occur between two states of the same multiplicity ($S_2 \rightarrow S_1$, $S_1 \rightarrow S_0$). This is called

'interconversion' (IC). Non-radiative decay between two states of different multiplicity ($S_1 \rightarrow T_1$) is known as 'intersystem crossing' (ISC).

However, in contrast to non-radiative decay to the ground state, radiative decay can also occur. These radiative or emissive transitions occur when an excited state molecule loses its surplus energy in the form of a photon of light, which it emits as either fluorescence or phosphorescence. If the transition involved is between two states of the same multiplicity ($S_1 \rightarrow S_0$) this decay is called fluorescence whereas a transition between two states of different multiplicities ($T_1 \rightarrow S_0$) is known as phosphorescence. As polyatomic organic molecules usually have non-degenerate orbitals and a singlet ground state, radiative decay or emission occurs from either the lowest lying singlet state (fluorescence) or the lowest lying triplet state (phosphorescence). This is known as Kasha's rule[10]. The type of emission observed is dependent of the efficiency of IC or ISC from the first singlet excited state S_1. The Jablonski diagram shown in Figure 3 illustrates the various means by which relaxation, both radiative and non-radiative, from the excited state to the ground state can take place.

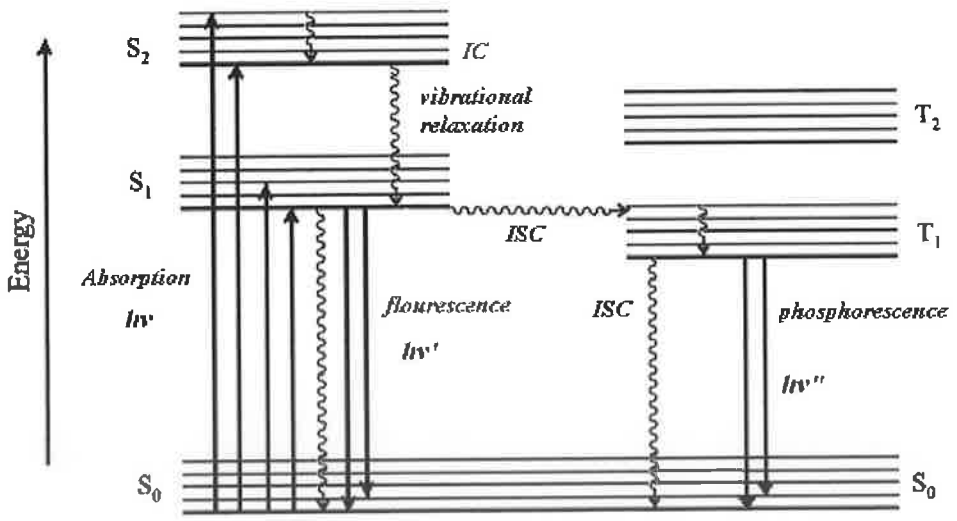

Figure 3 Jablonski diagram[11]

Fluorescence and phosphorescence can be easily distinguished from one another on the basis of the timescales on which they occur. Fluorescence involves a transition between two states of the same multiplicity and is thus spin-allowed while phosphorescence, involving transitions between two different multiplicities is spin-forbidden. The decay time of fluorescence and thus the lifetime of a singlet excited state is typically in the ns time range while that of phosphorescence is in the range 10^{-4} s – 10 s. Although IC and ISC are spin-forbidden they can occur where there is spin-orbit coupling, while ISC can occur where there is vibrational coupling between the singlet excited state and a triplet state. This spin-orbit coupling becomes more important in molecules containing heavy atoms. This '*heavy atom effect*' results in an increase in singlet-triplet mixing, which leads to an increase in absorption intensity as well as the phosphorescence rate constant. Following ISC vibrational relaxation to the lowest lying vibrational level of the triplet state occurs. The probability of non-radiative decay to the ground state is increased due to the fact that the energy gap between the lowest lying singlet excited state (S_1) and the triplet excited state (T_1) is less than that between S_1 and the ground state (S_0). However, more importantly due to the long life time of a triplet excited state the surplus excitation energy is usually lost or 'quenched' by collision transfer within the solution. Thus in order to observe emission from the triplet excited state or phosphorescence the molecule to be excited must be placed in a rigid medium. This is usually achieved by cooling the sample in a 4:1 EtOH: MeOH mix to 77 K.

Typically, a singlet excited state consists of an open shell where an unpaired electron occupies an antibonding and a bonding molecular orbital. Much more complex are triplet-excited states. These consist of three energetically similar or degenerate states or sublevels, which are thermally equilibrated at room temperature. This equilibrium becomes much slower when the temperature is reduced. Again the triplet state can be described in terms of an open shell arrangement for the two unpaired electrons. Typically, these excited states are labelled in terms of the orbital of origin of the excited electron. Thus, for example $n \rightarrow \pi^*$ represents the transition of a lone pair electron to an anti-bonding molecular orbital. These electronic transitions can be further described in terms of the molecular orbital of origin of the electron density and the destination molecular orbital for the electron density. Such transitions include ligand field (LF) d-d transitions, intra-ligand (IL) or ligand centred (LC) transitions,

and charge transfer transitions which can be further subdivided into metal-ligand charge transfer (MLCT), ligand-metal charge transfer (LMCT), and metal-solvent charge transfer (MSCT).

Ligand field or d-d transitions originate from electron transitions between metal d orbitals. This results in an angular rearrangement of electron density, which has no net effect on the charge distribution across the metal or ligand. Although this has little effect on internal redox processes in the molecule it can effect its reactivity towards other species[11]. This may happen as a result of redirection of a metal orbital away from or towards a ligand thus changing the probability of nucelophilic attack, inducing isomerisation or increasing the metal-ligand bond length to such an extent that ligand loss may occur.

Intraligand (IL) or ligand-centred transitions occur as a result of electron transfer between two molecular orbitals, which are localised on a ligand. Although, IL transitions have little effect on the charge distribution between the metal and ligand they can effect dramatic changes in the donor-acceptor properties, equilibrium geometry, and dipole moments of the excited state species[11].

A third and very important type of electron transitions are charge transfer transitions. This typically occurs between molecular orbitals localised on the metal and molecular orbitals localised on the ligand. As previously mentioned these can be subdivided into MLCT, LMCT and LSCT transitions. Such transitions cause a redistribution of electron charge between the transition metal and the ligand. Such transitions typically induce oxidation–reduction processes of the metal or ligand. These changes in the redox chemistry of the molecule can also change its reactivity (changing a previously inert metal centre to a labile one). Charge transfer transitions typically occur at lower energy than IL transitions and demonstrate a strong relationship with the redox properties of the complex. Thus a complex with a low energy MLCT transition will require very little energy to induce an oxidation-reduction reaction. In the case of MLCT transitions, oxidation of the metal increases the positive charge on the metal and with it the chance of nucelophilic attack. Conversely, LMCT results in oxidation of the ligand and transfer of the electron to a metal d orbital.

In addition, charge transfer to the solvent medium can also occur. Metal-solvent charge transfer (MSCT) or charge transfer to solvent (CTTS) transitions result in oxidation of the complexed species and a solvated electron.[11]

1.4. The technique of matrix isolation

Matrix isolation involves the trapping of guest molecules or atoms in a host matrix and first employed by George Pimentel and co-workers.[12] Matrix isolation is achieved by co-condensing a mixture of the evaporating sample complex and matrix gas at freezing temperatures onto a solid support. The host material (matrix) is often a crystalline polymer, or a glass formed by freezing a liquid or solidifying a gas. The advantage of matrix solution is that the trapped species in the rigid host matrix is prevented from diffusing at such low temperatures and thus cannot undergo bimolecular reactions, except with the host matrix itself. This technique allows the *in situ* irradiation of the sample material on the inert matrix and observation of the intermediate species formed, which in fluid media might only be observed with great difficulty. A range of spectroscopic techniques such as UV-vis, Raman, Mössbauer, ESR, emission and IR spectroscopy are used in conjunction with matrix isolation. Matrix isolation may also be used for characterising reaction intermediates, generating and studying novel reactive species, which might otherwise be too short-lived or unstable to study and freezing out and study of species in particular molecular conformations. Although much of the initial study in matrix isolation took place in organic glasses using the methods applied by Lewis[13], solidified noble gases, N_2 and CH_4 have a number of distinct advantages over the former choice of matrix host. They are chemically inert and transparent over the various regions of the spectrum. However, these inert gas matrices also commonly form complexed species with photo-fragments of the parent complex. To form such rigid matrices low temperatures are required (12-20 K). This is achieved by the use of liquid helium (and in the past liquid hydrogen). However due to this restrictive temperature range and the limited sample diffusion kinetic information cannot be obtained using these techniques. The "cage" formed by the solidified matrix gas around the reactant species can block certain possible photochemical pathways by preventing escape of the reactant species or intermediate species, thus promoting regeneration of the parent species. However, the situation is slightly more complicated for metal carbonyls. On photolysis of a metal carbonyl species in a "cage" a fragment is formed with ejection of CO. Although the fragment and CO molecule inhabit the same cage they might not recombine if the vacant site on the metal centre rotates away from the CO molecule.

1.5. The technique of Time resolved infra red (TRIR) spectroscopy

Time resolved infrared (TRIR) spectroscopy applies to the observation of a transient species or system via infrared spectroscopy vs. time. Specifically, it applies to the investigation and monitoring of transient excited state species generated photochemically in liquid solution. TRIR has proven to be particularly useful in the study of C-H bond activation, ligand substitution reactions, migratory insertion reactions and other photocatalysed reactions[14]. Although the similar technique of Time resolved optical (TRO) spectroscopy which utilises UV-vis detection is of great use, the broad and often featureless absorption bands observed following excitation cannot provide any structural information. IR bands allow for the observation of distinct species and functional groups with distinct absorption frequencies, such as the C≡O stretching vibration observed in metal carbonyl systems.

Thus, infrared spectroscopy is particularly useful for the study of decay and kinetic data as well as the elucidation of possible excited state structures. Time resolved infrared (TRIR) spectroscopy involves the generation of excited state transient species by a laser pulse. The solution is then monitored and transient species detected by IR spectroscopy operating in a very fast time-range. Typically a ns optical pumping source such as a XeCl excimer laser using the 308 nm output or a Nd:YAG laser operating at the third harmonic of 355 nm is used for organometallic systems. Due to the need for signal averaging and the eventuality of sample decomposition on repetitive excitation a flow-cell set-up through the sample cell and IR is also required. The IR source is typically a continuous source such as a globar (black body source) but CO lasers and semiconductor diode lasers may also be used. The latter two are particularly useful in the investigation of metal carbonyl systems due to the higher level of monochromatic photon flux. Signals are then detected by HgCdTe or InSb diode IR detectors although photovoltaic detectors may also be used[14].

The time resolved infrared (TRIR) spectroscopic studies on *cis*- and trans- (η^6-1,2-diphenylethene)$Cr(CO)_3$ discussed in chapter 4 were carried out at the Rutherford Appleton laboratories in Didcot, Oxfordshire in the United Kingdom using the Picosecond infrared absorption and transient excitation (PIRATE) facility. The TRIR spectroscopy instrumentation in use at the Rutherford Appleton Laboratory (RAL) is

described in a number of annual reports published by the Central Laser Facility at the Rutherford Appleton Laboratory.[15]

1.6. Computational Chemistry

Computational chemistry as the name suggests is a computer based area of theoretical chemistry with the basic purpose of solving chemistry related problems and calculations. In this sense, theoretical chemistry relies on mathematical methods and equations and the laws of physics to study and often predict, as far as is possible, the behaviour of molecules and other species in a particular environment. These include the structure, energy, charge, dipoles, vibrational frequencies, and electronic configurations of a molecular species.

Over the last few decades with the advent of faster, cheaper and ultimately more powerful computers, computational chemistry has itself become an important area of chemistry. This is partially due to the ever-increasing power and capabilities of today's computers but also due to cost effectiveness. However, it is also important not to replace practical "wet" chemistry with theoretical chemistry. Instead it is better to combine these two complementary areas of study. In recent times, as the use of high-speed computers in computational chemistry has increased so too has the power and sophistication of the software used. High specification computational chemistry programmes such as GAMESS(UK)[16], Gaussian[17] and Jaguar[18] are now available for solving a number of computational chemistry problems at varying degrees of accuracy and complexity from *ab-initio* Hartree-Fock to Density Functional Theory (DFT).

1.7. Ab-initio Calculations

Quantum chemical calculations are based calculations that attempt to solve the Schrödinger equation using the molecular Hamiltonian operator, which is a mathematical function describing the motion of electrons and nuclei in a polyatomic species. Solving Schrödinger's equation using the Hamiltonian operator gives equation 1, where Ψ is an eigenfunction and E is an eigenvalue describing a particular value or values of the system.

$$\mathrm{H}\Psi = E\Psi \qquad \text{(eqn. 1)}$$

However, the form of the molecular Hamiltonian used in quantum chemistry takes into account 2 contributions related to the kinetic and potential energies of the electrons and nuclei in the system[19]. Mathematically, this is written as

$$\mathrm{H} = -\sum_i \frac{\eta^2}{2m_e}\nabla_i^2 - \sum_k \frac{\eta^2}{2m_k}\nabla_k^2 - \sum_i \sum_k \frac{e^2 Z_k}{r_{ik}} + \sum_{i<j} \frac{e^2}{r_{ij}} + \sum_{k<l} \frac{e^2 Z_k Z_l}{r_{kl}} \qquad \text{(eqn. 2)}$$

where i and j describe electrons, k and l describe nuclei, $\hbar$ is the reduced Planck's constant ($h/2\pi$), m_e is the electron mass, m_k is the nucleus mass, ∇^2 is the Laplacian operator, e is the charge on the electron, Z is the atomic number, r_{ik}, r_{ij}, and r_{kl} the distance between particles i & k, i & j, and k & l respectively. If the Schrödinger equation is solved for a one-electron Hamiltonian, only the one-electron kinetic energy and nuclear attractions terms come into play. Thus the Hamiltonian operator can be expressed as

$$\mathrm{H} = \sum_{i=l}^{N} h_i \qquad \text{(eqn. 3)}$$

where N is the total number of electrons and h_i is the one-electron Hamiltonian (eqn. 4). M is defined as the total number of nuclei, and the term $V_i\{j\}$ represents the interaction potential with all other electrons occupying orbitals.

$$h_i = -\frac{1}{2}\nabla_i^2 - \sum_{k=1}^{M} \frac{Z_k}{r_{ik}} + \mathrm{V}_i\{j\} \qquad \text{(eqn. 4)}$$

However, eigenfunctions produced by the one-electron Hamiltonian must satisfy the one-electron Schrödinger equation (eqn. 5), where h_i is the one electron Hamiltonian operator, ψ_i is the one-electron eigenfunction and ε_i is the eigenvalue.

$$h_i\psi_i = \varepsilon_i\psi_i \qquad \text{(eqn. 5)}$$

However, a problem arises in that the original purpose of conducting quantum chemical calculations is to obtain values for ψ, although ψ is required in one-electron Hamiltonians. To overcome this, Hartree proposed the iterative "Self-consistent Field" (SCF) method. During the initial step of the SCF process the wavefunctions, ψ, for all occupied molecular orbitals are guessed. By solving equation 4 for each differential a new value for ψ may be obtained. This results in the formation of new one-electron Hamiltonians with this new ψ value, which in turn lead to the generation of a newer more accurate ψ values. This process continues until convergence is achieved, at which point successive values of ψ are within an accepted tolerance

Hartree's SCF method was then further extended by Fock to include Slater determinants (Φ_{SD}) (eqn. 6). In a Slater determinant N represents the number of electrons, $\{\chi_i(x_i)\}$ are spin orbitals composed of a spatial orbital and a spin function[20]. This not only allows for the determination of molecular orbitals as eigenfunctions of a one-electron system but also takes into account exchange effects from coulombic electron-electron repulsions. Typically, Hartree-Fock (HF) equations present the wavefunctions of closed-shell (spin-paired, doubly occupied) systems as a single Slater determinant, which is known as Restricted Hartree-Fock (RHF).

$$\Phi_{SD} = \frac{1}{\sqrt{N!}}\det\{\chi_1(\vec{x}_1)\chi_2(\vec{x}_2)\Lambda\ \chi_N(\vec{x}_N)\} \qquad \text{(eqn. 6)}$$

Ab-initio quantum chemical calculations are those based purely on theoretical values without the presence of any empirical or experimental values. The simplest form of ab-initio calculation is the Hartree-Fock (HF). In this scheme only an average value for coulombic electron-electron interactions is considered. The HF scheme allows for

the determination of the ground state wavefunction and ground state energy of polyatomic species. In the Hartree-Fock scheme the Schrödinger equation is treated as a simplified eigenvalue equation of the Hamiltonian operator with a finite and definite set of solutions. Using this HF approach, electrons are assigned to certain closed-shell orbitals and the energy of each individual electron calculated by assuming an average distribution of the other electrons present in the system.

Many quantum chemical calculations begin with the Hartree-Fock level of theory with subsequent corrections for coulombic electron-electron repulsions[21]. Further approximations are usually added leading to further calculations using semi-empirical or empirical methods such as the Hückel method or Density Functional Theory (DFT) (Figure 4).

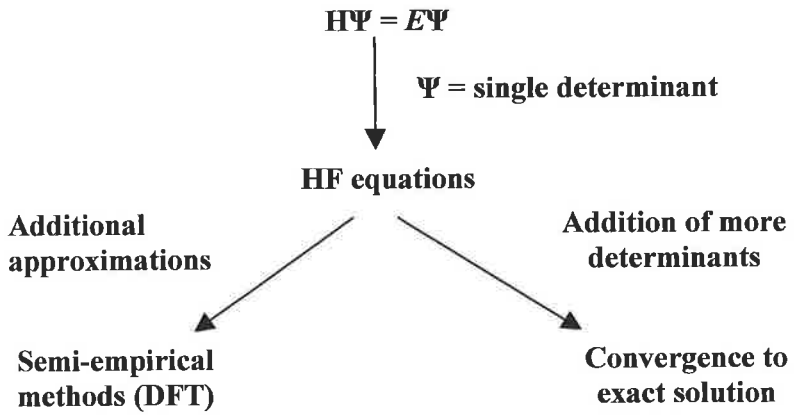

Figure 4 The use of the Hartree-Fock (HF) method as a starting point in quantum chemical calculations[21]

1.8. Density Functional Theory (DFT)

Hartree-Fock (HF) and other ab initio model chemistries, which are based on a multi-body wavefunction and a single Slater determinant, which serves as a model wavefunction. In contrast, Density Functional Theory (DFT) replaces this wavefunction with a mathematical function known as the Density Functional. This function is an expression of the electron density of the electronic ground state of a molecule. In Density Functional Theory, the electron density is a function of just three variables - the kinetic energy, the coulombic energy due to electrostatic interactions between the charged particles and the exchange correlation function, which arises from electron-electron repulsions. Nuclear–nuclear repulsions are taken as constant according to the Born-Oppenheimer approximation as they occur on a much slower timescale.

The first attempts to use electron density instead of wavefunctions as the basic quantity in quantum chemical calculations of atomic and molecular species were carried out by Thomas and Fermi in 1927. However, the Thomas-Fermi model is simplistic in that it only takes into account kinetic energy of nuclear-electron and electron-electron interactions based on a non-interacting uniform electron gas[20]. Only in 1964 with the publication of a set of two theorems by Hohenberg and Kohn did Density Functional Theory gain popular support among the chemistry community.
The first of these theorems states that two N-electron systems with different external potentials cannot have the same (degenerate) ground-state electron density. Thus, two N-electron systems having two different external potentials will give rise to two different Hamiltonians. Each Hamiltonian belonging to two different ground state wavefunctions and having corresponding non-degenerate ground state eigenvalues[22]. This means that in a molecule free of external molecular potentials the only potential acting upon in is the nuclear electrostatic potential. If the nuclear positions and the number of electrons are known then the Hamiltonian can be determined, this then allows for determination of the ground-state wavefunction, which in turn allows for the determination of the ground-state molecular electronic structure. This in turn yields the electron number and the external potential. Thus the ground-state molecular electronic structure is a functional of the ground-state electron density (eqn. 7) where $\rho(r)$ is the electron density.

$$E = E[\rho(r)] \qquad \text{(eqn. 7)}$$

The second Hohenberg-Hohn theorem, which is a variation of the variational principle (eqn. 8), states that the functional that delivers the ground state energy of the system only does so if the input electron density is the true ground state density.

$$E_0 \leq E[\tilde{\rho}] = T[\tilde{\rho}] + E_{Ne}[\tilde{\rho}] + E_{ee}[\tilde{\rho}] \qquad \text{(eqn.8)}$$

These expressions can be divided into system (electron density) dependent expression E_{Ne}, due to nuclei –electron interactions, and system independent expressions. The system independent expressions can be united to give a new expression called the Hohenberg-Kohn functional $F_{HK}[\rho_0]$. Substitution into equation 8. then gives us equation 9.

$$E_0[\rho_0] = \int \rho_0(\vec{r}) V_{Ne} d\vec{r} + F_{HK}[\rho_0] \qquad \text{(eqn. 9)}$$

This means that for any electron density greater than a constant and where the integration of the density results in the correct number of electrons, which also has an associated external potential the resulting total energy functional from equation 8 represents the ground state energy E_0.

Thus overall the electron density of the system determines the external potential, which in turn determines the Hamiltonian, which in turn determines the wavefunction. However, this still leaves the problem of having to solve the Schrödinger equation. This difficulty was overcome in 1965 by the introduction of the new Kohn-Sham Self consistent field methodology. In this Kohn and Sham proposed that the computation of the kinetic energy of a non-interacting reference electrons system built from a set of orbitals which has the same overall ground state electron density as the real interacting system. This set of non-interacting electrons are moving in an effective potential which is inclusive of external potentials and coulombic electron-electron interactions, which are the exchange and correlation energies. Thus using the Kohn-Sham methodology electron densities are defined by a set of energies and the ground

state electronic energy (eqn. 10) determined from the non-interacting kinetic energy ($T_s[\rho]$), the coulombic electron-electron repulsion ($U[\rho]$), the exchange functional ($E_x[\rho]$), the correlation functional ($E_c[\rho]$) and the interaction energy with the external potential. The final integral in the equation defines the interaction with the external potential.

$$E[\rho] = T_S[\rho] + U[\rho] + E_X[\rho] + E_C[\rho] + \int d\vec{r} v_{ext}(\vec{r})\rho(\vec{r}) \qquad \text{(eqn. 10)}$$

The non-interacting kinetic energy should be similar to a portion of the true value provided it has the same electron density as the real interacting system being studied. The exchange and correlation functionals contain the non-classical electrostatic contributions of self-interaction, exchange and correlation but also some of the kinetic energy. The latter contribution accounting for the difference between the calculated non-interacting system kinetic energy and that obtained from the real interacting system.

Density functional Theory using the Kohn-Sham methodology can be applied in various ways depending on the application. In recent much more complex functionals have been developed, many of which are inconsistent with the HF uniform electron gas model. In the area of physics, for example, the Perdew-Burke-Enzerhof (PBE) exchange model is popular. However, more importantly and in the case of this study, in the case of chemistry the B3LYP hybrid functional has become popular. This functional, which is a hybrid based on the DFT exchange functional BLYP (Becke, Lee, Yang, Paar) is coupled with an exact exchange functional from HF model chemistry.

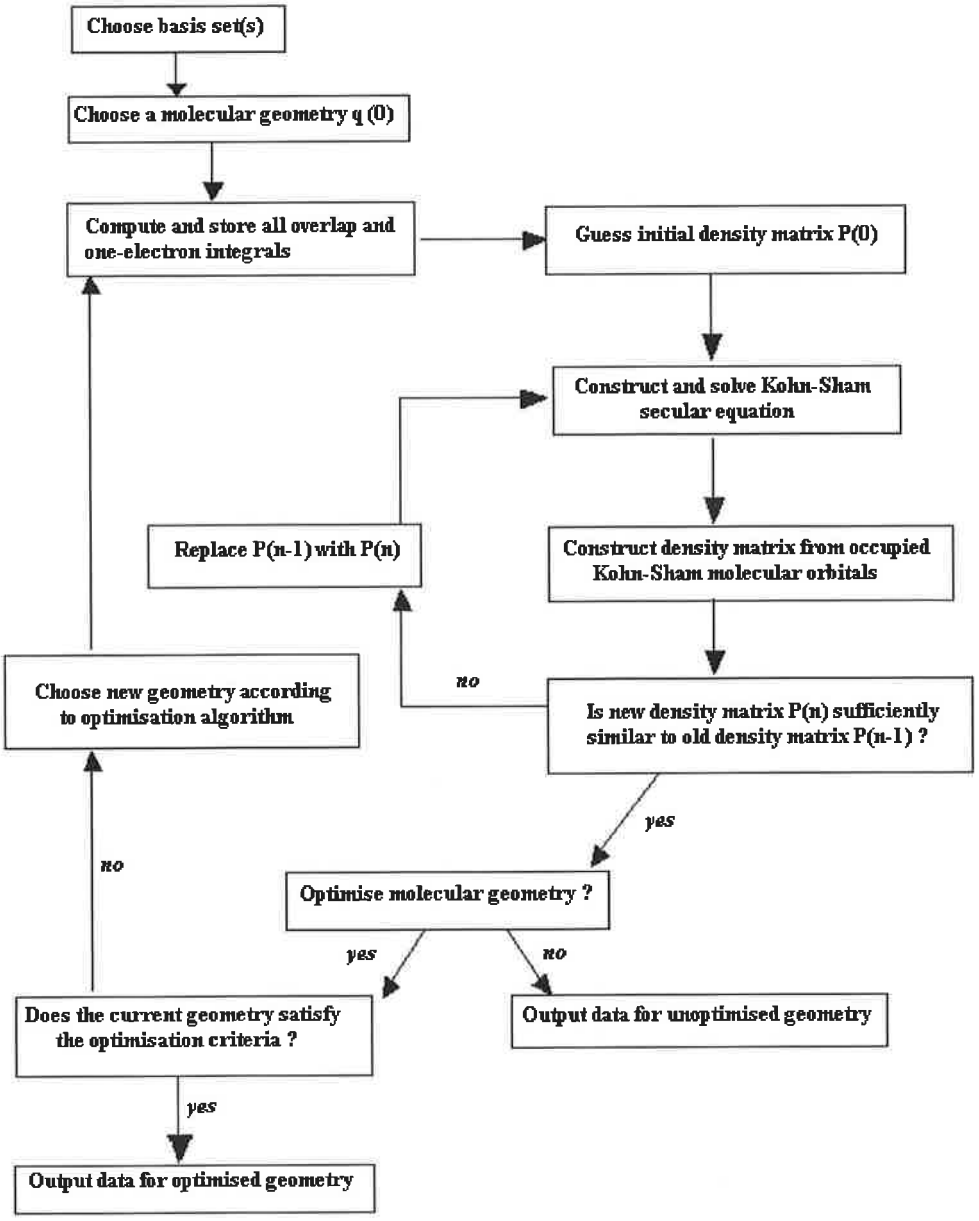

Figure 5 Flow chart of the Kohn-Sham Self Consistent Field (KS SCF)[19]

Figure 5 outlines the Kohn-Sham SCF procedure. The first step is to choose a basis set from the many basis sets used in DFT calculations. However, the initial basis set used is the one from which the Kohn-Sham orbitals for the non-interacting model system are formed. The molecular geometry must then be chosen. The overlap integrals, kinetic energy and nuclear-attraction integrals are then computed.

In HF SCF theory the kinetic energy and nuclear-attraction integrals are essentially one-electron integrals while in KS SCF theory all integrals are essentially regarded as one-electron integrals. Following this new orbitals are determined from the solution of the secular equation and the electron density determined from these orbitals. These values are compared to the previous iteration. Convergence is achieved when successive iterations result in similar values. Once the SCF is converged, the ground-state electronic energy is calculated. The geometry-optimised structure corresponding to this ground state electronic energy is then compared to a stationary point.

1.9. Time-Dependent Density Functional Theory (TD-DFT)

Density Functional Theory is termed a ground state theory although the ground state electron density contains information on the excited states. The reason for this is that it is not yet known how to extract this information from the ground state density. Over the last decade or so one of the methods developed to calculate excitation energies has been Time Dependent Density functional Theory (TD-DFT). TDDFT utilises the fact that in an interacting quantum many-particle finite system subjected to a time dependent potential all physical properties are determined by the time dependent density and the state of the system in that arbitrary moment in time. In TD-DFT the matrix elements of the Hamiltonian are replaced with the Kohn-Sham orbital energies and a number of exchange energies. Generally speaking TDDFT is more successful for predicting low energy excitations as the Kohn-Sham orbital energies decrease in accuracy the higher up the virtual manifold one goes. For optimum results using the TDDFT method it has been suggested that the excitation energy should be smaller than the molecular ionisation potential and that electron promotion should not take place into molecular orbitals possessing positive Kohn-Sham eigenvlaues. Although efforts are underway to improve and increase the extent to which higher energy excitations higher up the virtual manifold can be accurately predicted. i.e to extend the possibility of using TDDFT to predict higher energy excited states than is currently possible, TDDFT is currently the best method for calculating low energy excited states.

1.10. Alternative model chemistries

In many other cases modelling of molecular systems can be achieved without the need for quantum mechanical calculations thereby avoiding the need to solve the Schrödinger equation. Apart than Hartree-Fock and Density Functional Theory, other model chemistries exist which are based on the Force Field (FF) method. These Force Field methods do not need to calculate the electronic energy and instead write it as a function of the nuclear coordinates. Such methods are referred to as Molecular Mechanics (MM) due to their treatment of a molecule as a ball and stick, ie as atoms held together by bonds. Molecular mechanics methods also take into account the fact that most molecules consist of various similar sub-units such as C-H bonds, C-C bonds, C=O bonds etc. Thus it can be assumed that in most molecules C-H bond lengths will be relatively similar and thus their vibrational frequencies will be comparable. Another similar method is molecular dynamics (MD) in which atoms and molecules in a simulation are allowed interact for a defined period of time under the laws of physics.

1.11. Quantum Chemical Calculations

1.11.1. Computer Hardware & Software used

Quantum chemical calculations comprising of geometry optimisations and Time-dependent Density Functional Theory (TDDFT) studies were carried out on a HP workstation xw8200 containing an Intel Xeon processor. The programmes used were Gaussian 03[23], Gaussview 3.09[24], GaussSum 2.0.[25]

1.11.2. Model Chemistries and Basis Sets used

The ground state electronic structures of the compounds in this study were calculated using the Gaussian 03[23] programme. Initial geometry optimisations were carried out at the Hartree-Fock (HF) level of theory and subsequently with Becke's three parameter hybrid functional[26] (B3) with the Lee-Yang-Paar (LYP) correctional functional[27] (B3LYP). The size of the basis set was increased incrementally from STO-3G to LanL2DZ. The final geometry optimisation was carried out using the LanL2DZ basis set, which incorporates the Los Alamos core potential and the Dunning-Huzinaga double-ζ basis functions (DZ) for carbon, nitrogen, and hydrogen atoms[28]. The energies of the 20 lowest lying singlet-singlet energy transitions were then calculated at the optimised geometry using time dependent density functional theory (TDDFT). For calculations of complexes containing heavy metal atoms such as tungsten geometry optimisation was initiated at the RHF/LanL2DZ level of theory. For each basis set a fine integration grid was used. The orbital population of the 20 lowest lying excited states was visualised using Gaussview[24] and extraction of the percentage contributions of the metal orbitals, CO and the ligands in the excited state structures was performed by locally created GaussSum software[25]. Partial density of states (PDOS) and spectra were generated using the GaussSum software[25] by convoluting the molecular orbital information with Gaussian curves of unit height and FWHM of 0.4 eV. The contribution of a group to a molecular orbital was calculated using Mulliken population analysis. UV-Vis absorption spectra were also simulated using the GaussSum programme[25].These simulated spectra were compared to the measured UV-Vis absorption spectra using the Microcal Origin 6.0 spreadsheet programme[29]. All transitions calculated for the energy range being studied were included and the band areas are proportional to the oscillator strengths of the individual transitions.

Although not strictly correct, the calculated Kohn-Sham energy surfaces are referred herein as molecular orbitals. Although this is not strictly the correct description for the Kohn-Sham density functions it is a commonly more understandable way of describing these energy surfaces.

1.12. Bibliography

1 Ch. Elschenbroich, A. Salzer, *Organometallics – A concise Introduction*, VCH Verlagsgesellschaft mbH, Weinheim, **1992**

2 L. Mond, C. Langer and F. Quincke, *J. Am. Chem. Soc.*, **1890**, 749

3 L. Mond and C. Langer, *J. Am. Chem. Soc*, **1891**, 1090

4 T.E Bitterwolf, *J. Organomet. Chem.*, **2004**, 689, 3939-3952 and references contained therein

5 M.L.H Green, A.N. Stear, *J. Organomet. Chem.*, **1964**, 1, 230-234

6 M. Gerloch, E.C. Constable , *Transition Metal chemistry*, VCH Verlaggesellschaft mbH, Weinheim, **1994**

7 R. Janes and E. Moore, *Metal-ligand bonding*, , Royal Society of Chemistry Cambridge, **2004**

8 M. Wrighton, *Chem. Rev.*, **1974**, 74, 401-429

9 N. Sutin, C. Creutz, *J. Chem. Educ.*, **1983**, 60, 10, 809-813

10 P. Suppan, *Chemistry and Light*, The Royal Society of Chemistry, Cambridge, **1994**

11 M. Montalti, A. Credi, L. Prodi, M. T. Gandolfi, *Handbook of Photochemistry*, CRC Taylor & Francis, 3rd Edn., Boca Raton **2006**

12 E. Whittle, D.A Dows, G.C.Pimentel, *J. Chem. Phys.*, **1954**, *22*, 1943

13 G.N. Lewis, D. Lipkin, *J. Am. Chem. Soc.*, **1942**, *64*, 2801

14 K. McFarlane, B. Le, J. Bridgewater, P.C. Ford, *J. Organomet. Chem.* **1998**, 554, 49-61

15 M. Towrie, P.D. Bailey, R. Barton, P. Matousek, A.W. Parker, M.W. George, D.C. Grills, *Laser Science and Development – Lasers for Science Facility, The PIRATE Development*, Central Laser Facility Annual Report **2000/2001**, 165-167, http://www.clf.rl.ac.uk/reports/2000-2001/pdf/75.pdf

16 GAMESS (UK) is available online from Computing for Science at http://www.cfs.dl.ac.uk/

17 For information on Guassian 03 and Gaussview 3.09 see www.Gaussian.com

18 Jaguar is available from Schrödinger Inc. at www.schrodinger.com

19 C.J. Cramer, *Essentials of Computational Chemistry - Theories and Models*, John Wiley & Sons Ltd., Chicester, **2002**

20 W. Koch, M.C. Holthausen, *A Chemist's Guide to Density Functional Theory*, Wiley-VCH Verlag GmbH, Weinheim, **2000**

21 F. Jensen, *Introduction to Computational Chemistry*, John Wiley & Sons Ltd., Chicester, **1999**

22 J.M. Brown, P. Hofmann, *Organometallic Bonding and Reactivity – Fundamental Studies*, Springer Verlag Berlin, **1999**

23 Gaussian 03, Revision C.02, Frisch, M. J.; Trucks, G. W.; Schlegel, H. B.; Scuseria, G. E.; Robb, M. A.; Cheeseman, J. R.; Montgomery, Jr., J. A.; Vreven, T.; Kudin, K. N.; Burant, J. C.; Millam, J. M.; Iyengar, S. S.; Tomasi, J.; Barone, V.; Mennucci, B.; Cossi, M.; Scalmani, G.; Rega, N.; Petersson, G. A.; Nakatsuji, H.; Hada, M.; Ehara, M.; Toyota, K.; Fukuda, R.; Hasegawa, J.; Ishida, M.; Nakajima, T.; Honda, Y.; Kitao, O.; Nakai, H.; Klene, M.; Li, X.; Knox, J. E.; Hratchian, H. P.; Cross, J. B.; Bakken, V.; Adamo, C.; Jaramillo, J.; Gomperts, R.; Stratmann, R. E.; Yazyev, O.; Austin, A. J.; Cammi, R.; Pomelli, C.; Ochterski, J. W.; Ayala, P. Y.; Morokuma, K.; Voth, G. A.; Salvador, P.; Dannenberg, J. J.; Zakrzewski, V. G.; Dapprich, S.; Daniels, A. D.; Strain, M. C.; Farkas, O.; Malick, D. K.; Rabuck, A. D.; Raghavachari, K.; Foresman, J. B.; Ortiz, J. V.; Cui, Q.; Baboul, A. G.; Clifford, S.; Cioslowski, J.; Stefanov, B. B.; Liu, G.; Liashenko, A.; Piskorz, P.; Komaromi, I.; Martin, R. L.; Fox, D. J.; Keith, T.; Al-Laham, M. A.; Peng, C. Y.; Nanayakkara, A.; Challacombe, M.; Gill, P. M. W.; Johnson, B.; Chen, W.; Wong, M. W.; Gonzalez, C.; and Pople, J. A.; Gaussian, Inc., Wallingford CT, **2004**.

24 GaussView, Version 3.09, Roy Dennington II, Todd Keith, John Millam, Ken Eppinnett, W. Lee Hovell, and Ray Gilliland, Semichem, Inc., Shawnee Mission, KS, **2003**

25 Noel M. O'Boyle, Johannes G. Vos, GaussSum 0.9, Dublin City University, **2005**. Available at http://gausssum.sourceforge.net.

26 A.D. Becke, *J. Chem. Phys.*, **1993**, 98, 5648

27 Lee, C.; Yang, W.; Parr, R. G. *Phys. Rev. B* **1988**, *37*, 785

28 Dunning, T. H., Jr.; Hay, P. A. In *Modern Theoretical Chemistry*; Schaefer, H. F., III, Ed.; Plenum: New York, **1977**; Vol. 3, p 1.

29 Origin 6.0, Microcal Software Inc. www.microcal.com

Chapter 2

C-F bond activation, the photochemistry and DFT studies of fluorinated manganese pentacarbonyl systems

Chapter two begins with an introduction to the properties of the carbon-fluorine bond and a short review of recent reports of C-F bond activation in the literature. This is followed by a literature survey, which focuses on the photochemistry and computational studies of a number of metal carbonyl compounds. The photochemistry of a series of fluorinated metal carbonyls of the type $XMn(CO)_5$ (X = fluorinated substitutent), was probed via matrix isolation studies at 20 K, using both IR and UV-vis as detection methods. Theoretical studies were performed, and compared to the experimental data.

2.1 Literature Survey

2.1.1. C-F activation

The C-F bond is the strongest known carbon-halogen bond. As such the cleavage or activation of this bond is of great industrial interest. A notable characteristic of fluorocarbon complexes is their general inertness under most conditions, a characteristic arising from the unusually high strength of the C-F bond. This property of fluorocarbon complexes arises from the small size and high electronegativity of the fluorine atom.[1] Because of a damaging build up of chlorofluorocarbons (CFC's) or freons in the ozone layer and also the potency of perfluoroalkanes as greenhouse gases[2] there is a need to develop methods of activating the C-F bond to form more readily removed compounds. This would not only aid in reducing the amount of these harmful substances in the environment but also may help in the design of new catalysts for preparing chlorofluorocarbon replacements. In a number of organic molecules, replacement of hydrogen with fluorine has resulted in the generation of a large number of pharmaceutical, bioorganic and agricultural chemicals.[1, 3] Many industrial and pharmaceutical applications of such chemicals rely on the unusual thermal and chemical stability imparted on the complex as a result of the C-F bond. It has been demonstrated that organometallic systems can be used to activate C-H bonds and also provide a greater understanding of the activation. Most existing C-F activation mechanisms involve transition metals and oxidative addition reactions. It has been observed that fluoroarene or perfluoroarene ligands react with transition metals by way of a migratory insertion of the metal into the C-F bond. The first demonstration of room temperature C-F bond activation using an organometallic compound, carried out by Richmond et al.[4], (Scheme 1) used $W(CO)_3(PrCN)_3$ and a 1,2-pentafluorophenylimino-aminobenzene system. Interestingly C-F activation was observed only on the tethered perfluorophenyl ring while in perfluorobenzene in the solution was unaffected.

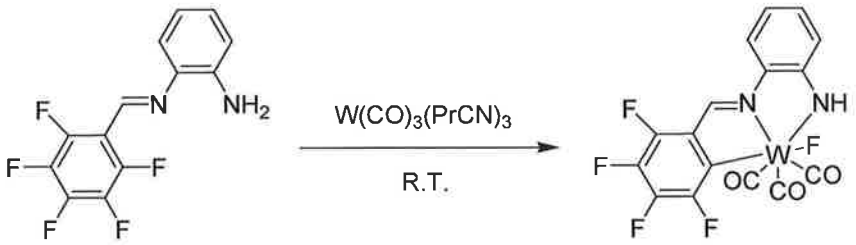

Scheme 1 Oxidative addition reaction of $W(CO)_3(PrCN)_3$ with pentafluorphenyl ligand[4]

Kiplinger et al.[5] have shown that further treatment of these tungsten metallacycles with alkynes can yield η^2-vinyl or metallacyclopropenes. A number of groups have also reported the activation of C-F bonds using complexes of low-valent transition metals such as iron, cobalt or zinc. C-F activation by intermolecular oxidative addition of C_6F_6 to $[Ni(PEt_3)_2(COD)]$ has been reported by Fahey and co-workers.[6] More recently, Richmond et al[7]. have described C-F activation of the ligand 2-$NMe_2C_6H_4N{=}CHC_6F_5$ on treatment with $Ni(COD)_2$. Muller et al[8]. expanded on this reaction by use of aromatic amines such as picoline, lutidine and collidone to activate carbon-halogen bonds generating five-membered Ni metallcycles under mild conditions. This occurs via insertion of Ni into the *ortho* C-F bond on the phenyl ring of the imine ligands (Scheme 2).

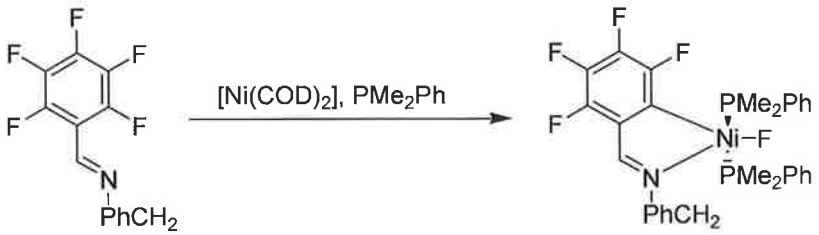

Scheme 2 C-F activation of a fluorinated amine using Nickel[8]

Until recently the only cobalt initiated C-F activation reaction had been observed by Richmond and co-workers[9] in a study involving the synthesis of ionic cobaltocenium fluoride $[(C_6H_5)_2Co]F$ following the treatment of perfluorodecalin with $(C_6H_5)_2Co$ in toluene. However, new studies by Li and co-workers[10] have shown that C-F activation may also occur via a cyclometallation reaction, using cobalt(0), resulting in the formation of an *ortho*-chelated cobalt (III) complex containing a C-Co-F moiety (Scheme 3) .

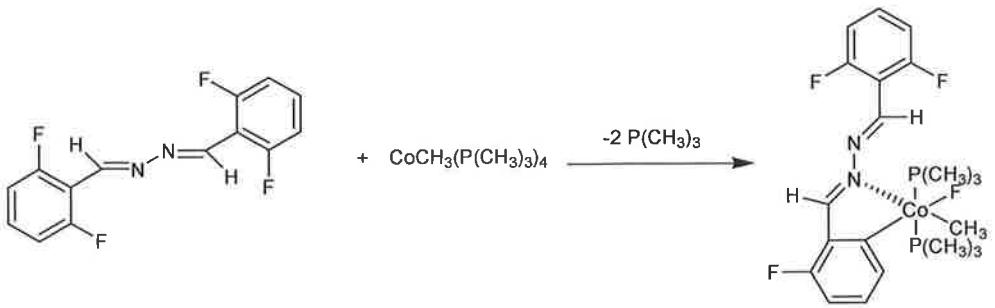

Scheme 3 Formation of *ortho* chelated Co(III) complex by C-F activation

It has also been shown by Akiyama et al.[11] that group 5 transition metal complexes that the product energy is sufficiently lower than the starting material to allow for C-H and C-F bond cleavage. Treatment of o-phenyl-α,α,α-trifluorotoluene in dimethoxyethane (DME) with $NbCl_5$ and $LiAlH_4$ resulted, via C-F activation of the trifluoromethyl group, in the generation of fluorene as the predominant product (61%) with other expected reduction products accounting for the remaining percentage (Scheme 4). Using other group 5 metal salts such as VCl_5 and $TaCl_5$ resulted in reduced fluorene yields.

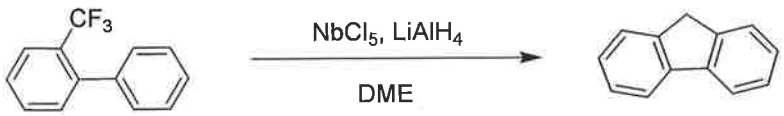

Scheme 4 C-F bond activation by group V metal salts yielding fluorene

Although a number of processes such as oxidative addition and electron transfer shown in the above examples may result in activation of the C-F bond, photons may also provide the necessary energy to activate the C-F bond.[1] It has been shown by Pola et al.[12] that 193 nm irradiation of liquid hexafluorobenzene resulted in C-F bond activation leading to the generation of a number of fluorinated organic products. More recently, Asplund and co-workers[13] have studied the photochemical formation of a tungsten tricarbonyl species from a tetracarbonyl species as a model intermediate for this kind of oxidative addition reaction. Irradiation of the tetracarbonyl parent species with 355 nm resulted in C-F bond activation leading to the generation of the tricarbonyl species shown in Scheme 5.

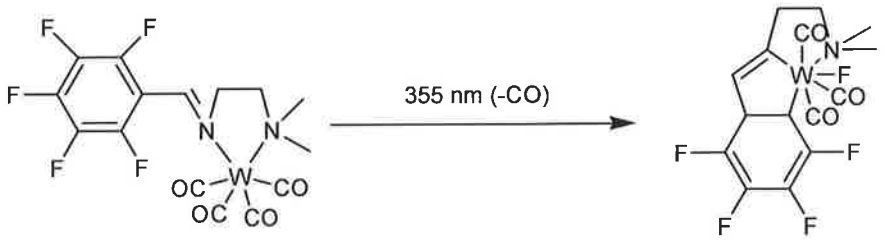

Scheme 5 Photochemically induced C-F activation with tungsten tetracarbonyl[13]

It has also been observed by Jones and Perutz[14] that >285 nm UV irradiation of $(C_5Me_5)Rh(PMe_3)(\eta^2\text{-}C_6F_6)$ underwent oxidative addition to yield $CpRh(PMe_3)(C_6F_5)F$.

As mentioned previously the exchange of hydrogen for a fluorine atom in many organic systems can affect the solubility, hydrophobicity and bulk properties of these materials.[15] These allow for the development of a wide range of pharmaceuticals, fine chemicals, and imaging agents such as ^{18}F-deoxyfluoroglucose. Much of the impetus behind the study of the organometallic chemistry of these fluorinated organic materials lies in their potential use in the catalysis of C-F bond activation and the development of new synthetic methods for C-F bond construction.[16] To this end, previous efforts have concentrated on the development of Pd(0)/(II) based catalysts for C-F bond formation[17] in a manner similar to those observed in Sonogashira[18] or Negishi[19] type cross-coupling reactions. These early efforts proved unsuccessful. However, an alternative approach has been proposed by Sanford et al[16]. This involves the reaction of Pd^{II} aryl/alkyl intermediate with a fluorinating reagent to allow oxidative transformation of the Pd-C bond to a C-F bond. In this study, which results in Pd^{II} catalysed C-H bond activation and subsequent C-F bond formation 8-methylquinoline in benzene is treated with palladium acetate ($Pd(OAc)_2$) and a suitable F^+ reagent. This resulted in the generation of 8-fluoromethylquinoline in good yields (Scheme 6).

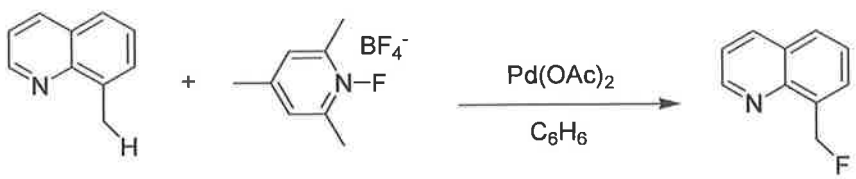

Scheme 6 Pd^{II} catalysed C-F bond formation in 8-methylquinoline

2.1.2. The photochemistry of dinuclear group 7 metal carbonyl complexes

The commonly available carbonyl compounds of manganese and rhenium are $M_2(CO)_{10}$, M = Mn or Re. These metal carbonyl compounds contain a M-M bond between two zerovalent transition metals. The photochemistry of symmetric metal-metal bonded compounds such as $Re_2(CO)_{10}$ and $Mn_2(CO)_{10}$ has been the subject of vigorous investigation and early studies often resulted in the production of asymmetric photogenerated species, consequently leading to the belief that a radical species might be involved. Subsequent investigations of $Re_2(CO)_{10}$ in CCl_4 by Wrighton[20] et al. resulting in formation of $ClRe(CO)_5$ showed that homolytic cleavage of the M-M bond resulting in $^{\bullet}Re(CO)_5$ radical formation was the precursor for the rearrangement observed. It was soon realised that such M-M bond homolysis was also relevant to other bimetallic compounds such as $Mn_2(CO)_{10}$ and $Cp_2Fe_2(CO)_4$.[21] Irradiation of dimanganese decacarbonyl in particular, produces the substituted pentacarbonyl species $Mn(CO)_5L$ (Scheme 7). Six-coordinate compounds such as $M(CO)_6^+$ and $RM(CO)_5$, (M = Re or Mn) with the metal in the +1 oxidation state as well as products resulting from CO loss have been generated photochemically.

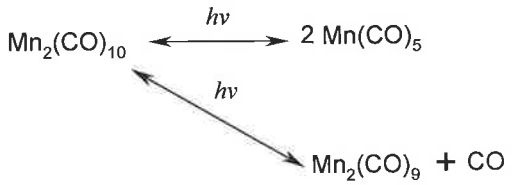

Scheme 7 Schematic diagram indicating generation of pentacarbonyl and nonacarbonyl species following photolysis of $Mn_2(CO)_{10}$

In photochemical studies carried out by Hepp et al.[22] excitation of $Mn_2(CO)_{10}$ in a rigid alkane (methylcyclohexane or 3-methylpentane) matrix at 77 K resulted in growth of a band at 2132 cm^{-1} (free CO) and a strong absorption at 1760 cm^{-1}. Following further investigation of $Mn_2(CO)_{10}$ containing 30% ^{13}CO, this band at 1760 cm^{-1} was attributed to the bridging CO moiety of the CO loss product $Mn_2(CO)_9$ (Scheme 7). Heating of an alkane matrix containing $Mn_2(CO)_9$ and CO to room temperature resulted in regeneration of the parent species. Heating of an alkane matrix containing both $Mn_2(CO)_9$ and PPh_3, CCl_4 or 2-MeTHF resulted in coordination of the donor ligand onto the vacant site. However, the 2-MeTHF substituted derivative

proved to be thermally labile on addition of PPh_3 to the solution, resulting in loss of the loosely bound 2-MeTHF ligand and formation of $Mn_2(CO)_9(PPh_3)$. Thus the primary process following irradiation of $Mn_2(CO)_{10}$ in a glassy alkane matrix at 77 K is dissociative CO loss compared to excitation in solution at 298 K in which case the primary product is $Mn(CO)_5$ resulting from homolysis of the Mn-Mn bond. This may be because the efficiency of geminal recombination in a fluid medium at 298 K is greater than that in a rigid matrix at 77 K. Further studies by Hepp et al.[22] investigated the relative efficiency of Mn-Mn bond homolysis compared to Mn–C scission in fluid solution at 298 K. Irradiation was carried out in solution containing $Mn_2(CO)_{10}$, a trapping ligand (PPh_3 or CH_3CN) and the radical scavenger CCl_4 in order to investigate whether CCl_4 suppressed formation of $Mn_2(CO)_8L_2$ thus indicating whether $Mn_2(CO)_8L_2$ is formed directly following formation of $Mn_2(CO)_9$ or via substitution of $Mn(CO)_5$ to form $Mn(CO)_4L$ followed by coupling to another $Mn(CO)_5$ radical. Where CCl_4 was absent both $Mn_2(CO)_9L$ and $Mn_2(CO)_8L_2$ are the major products, however the presence of CCl_4 precludes the formation of the latter product with $Mn_2(CO)_9L$ as the only product. However, in any case in 298 K solution the presence of CCl_4 only approx. 30% of irradiated $Mn_2(CO)_{10}$ is converted to $Mn_2(CO)_9L$ indicating the main product (~70%) to be the radical species $^{\bullet}Mn(CO)_5$.

Further studies were carried out by Church et al.[23] to determine the nature of the photogenerated products $Mn_2(CO)_9$ and $Mn(CO)_5$ and the reaction pathways leading to regeneration of the parent species. Flash photolysis studies of $Mn_2(CO)_{10}$ in argon-saturated cyclohexane or n-heptane resulted in the generation of two transient signals, which can be assigned to generation of the $^{\bullet}Mn(CO)_5$ and $Mn_2(CO)_9$ species respectively. Using infra-red monitoring a single IR band was observed for the $^{\bullet}Mn(CO)_5$ radical species at 1988 cm^{-1}. Matrix isolation studies[24] confirmed that the $^{\bullet}Mn(CO)_5$ radical exhibited two ν_{co} bands at 1988 and 1978 cm^{-1} The absence of the band at 1978 cm^{-1} is due to these unresolved E and A_1 bands in the C_{4v} pentacarbonyl species in hydrocarbon solution. This is similar to what has been observed in gas-phase photodissocation studies of $Mn_2(CO)_{10}$ by Seder et al.[25] in which a band at 1993 cm^{-1} due to $Mn_2(CO)_{10}$ is not observed as a result of overlap with the E and A_1 vibrations of $Mn(CO)_5$. Kinetic analysis of the pentacarbonyl species clearly showed that the process occurred near the near diffusion-controlled limit and resulted from

radical reformation recombination to form $Mn_2(CO)_{10}$. Dissociative loss of CO played no part in the decay. For the CO loss species, $Mn_2(CO)_9$, five terminal ν_{co} bands were observed as well as a bridging CO band at 1760 cm^{-1} previously described, which Church and co-workers[23] propose is unsymmetrical in nature. Flash photolysis was carried out with UV-Vis detection to link the previously observed IR bands of the transient species to their electronic absorption counterparts. Two transient bands were observed at 820 nm and 480 nm, which are attributed to $Mn(CO)_5$ and $Mn_2(CO)_9$ respectively. Absorption and decay kinetics indicate that on initial photolysis of $Mn_2(CO)_{10}$ the concentrations of both $Mn(CO)_5$ and $Mn_2(CO)_9$ formed are approximately the same.

These results are further substantiated by a similar study by Yesaka and co-workers[26] in which $Mn_2(CO)_{10}$ was photolysed in cyclohexane and monitored by UV-Vis spectroscopy. Following photolysis in cyclohexane two transient bands were observed at 827 nm and 500 nm, which following examination of their decay kinetics were assigned to $Mn(CO)_5$ and $Mn_2(CO)_9$. The decay of the 827 nm signal due to $Mn(CO)_5$ followed second-order kinetics and can be viewed in terms of recombination of the $Mn(CO)_5$ radicals (Reaction 1).

$$^{\bullet}Mn(CO)_5 + {}^{\bullet}Mn(CO)_5 \rightarrow Mn_2(CO)_{10}$$

Reaction 1 Recombination reaction of $Mn(CO)_5$ radicals

The absorption band at 500 nm attributed to the dissociative CO loss species $Mn_2(CO)_9$, which was observed at 480 nm by Church and co-workers[23] also decays according to second-order kinetics to form $Mn_2(CO)_{10}$. Confirmation of the assignment of the latter absorption band at 500 nm to $Mn_2(CO)_9$ was carried out by observing the time-dependent change in intensity of this band in the presence of EtCN. It was observed that the EtCN ligand reacts with the $Mn_2(CO)_9$ photoproduct to yield the stable species $Mn_2(CO)_9$(EtCN). A study by Vaida and co-workers[27] has also shown that both dissociative CO loss and M-M bond homolysis resulted from UV photolysis at 355 nm of $Mn_2(CO)_{10}$ in ethanol generating two transient absorption bands at 780 nm and 480 nm, thus indicating a shift of approximately 20 nm of the two transient bands at 827 nm and 500 nm in cyclohexane. In the presence of CCl_4 it

was observed that following photolysis the transient band at 827 nm decayed following first-order kinetics and that the reaction of the radical species with CCl_4 was much faster than the recombination reaction yielding $Mn_2(CO)_{10}$. Under the same conditions decay of the $Mn_2(CO)_9$ species also followed first–order kinetics, with a $k_{obs} = 2.1 \times 10^2\ s^{-1}$, believed to arise from reaction of the photogenerated $Mn_2(CO)_9$ with CCl_4 or the CCl_3 radical present from an earlier reaction with $^{\bullet}Mn(CO)_5$. According to studies by Sarakha and Ferraudi[28] investigations of the quantum yields of both the pentacarbonyl and nonacarbonyl following flash photolysis of $Mn_2(CO)_{10}$ in cyclohexane showed that the CO loss product is favoured with decreasing wavelength, $\Phi = 0.64$ at 266 nm compared to 0.12 at 355 nm. Conversely as the photolysis wavelength is increased to the ~340 nm region the quantum yield (Φ_p) of the pentacarbonyl product reaches a maximum with $\Phi_p = 0.33$ at 337 nm compared to 0.12 at 308 nm. These results agree with those obtained by Kobayashi and co-workers[29]. Sarakha and Ferraudi[28] suggest that the irradiation wavelength dependence of the ratio between the quantum yields ($\Phi_N/2\Phi_p$) of the pentacarbonyl(Φ_p) and nonacarbonyl(Φ_N) that the processes leading to the photoproducts may both begin in the low-lying excited states but that upper states predominantly form $Mn_2(CO)_9$.

2.1.3. The photochemistry of $RMn(CO)_5$ type complexes, where R = H, CH_3, CH_3CO, CF_3 or CF_3CO.

As previously described, UV irradiation of $Mn_2(CO)_{10}$ can result in the formation of the C_{4v} radical species, $^{\bullet}Mn(CO)_5$. Six-coordinate metal-carbonyl-alkyl compounds $RMn(CO)_5$, where R = H, CH_3, CH_3CO, CF_3 or CF_3CO also yield this radical species on irradiation at certain wavelengths, with the predominant photoproducts being tetracarbonyl species arising from loss of the carbon monoxide ligand. Photolysis of $HMn(CO)_5$ in an argon matrix by Rest et al.[30] yielded CO and $HMn(CO)_4$ resulting from dissociative CO loss. This suggested that $HMn(CO)_5$ has a high quantum yield for CO loss and a much lower quantum yield for H ejection. Although the tetracarbonyl $HMn(CO)_4$ with IR absorption bands at 1970, 2001 and 2094 cm^{-1} is the primary product another set of bands observed can be attributed to a 2nd photoproduct which may be due to the product $HMn(CO)_3$. ESR experiments[30] also suggest that $^{\bullet}Mn(CO)_5$ may have also be formed as a minor product. Similar studies of $Mn(CO)_4NO$ in a CO matrix[31] have also resulted in the formation of this C_{4v} carbonyl species indicating that H ejection is involved in its formation from $HMn(CO)_5$.

Subsequent matrix isolation studies on $HMn(CO)_5$ in a CO matrix were carried by Church and co-workers[24] to investigate whether promotion of the recombination reaction of $HMn(CO)_4$ with CO to regenerate $HMn(CO)_5$ would result in the H ejection reaction leading to preferential $^{\bullet}Mn(CO)_5$ radical formation. After 80 minutes UV photolysis of $HMn(CO)_5$ in a CO matrix the radical species $^{\bullet}HCO$, with a vibrational stretching band at 1860 cm^{-1} and a new carbonyl species were observed. The new carbonyl species has three IR bands 1987, 1978 and 1992 cm^{-1}, similar to $HMn(CO)_5$ but are shifted to lower energy compared to the parent species. The band at 1992 cm^{-1} was due to matrix splitting effects following irradiation ($\lambda > 375$ nm) and annealing (20 K to 33 K) of the matrix. Another band (A_1 vibrational mode) should be present for the $^{\bullet}Mn(CO)_5$ radical species but may have been masked by the strong absorptions of the CO matrix. According to calculations using energy-factored force fields and comparisons with spectra of partially ^{13}CO enriched carbonyl the $^{\bullet}Mn(CO)_5$ species is predicted to be C_{4v} with bands at 2105, 1978 and 1987 cm^{-1} ($2a_1$ and e modes respectively). It is also suggested that irradiation in a CO matrix increases the

rate at which $HMn(CO)_4$ recombines with CO to form the pentacarbonyl hydride as opposed to increasing the rate at which H is lost to form the radical. Thus, in an argon matrix dissociative CO loss resulting in tetracarbonyl formation, Fig.5 (1), is the major photochemical process and radical formation, Fig.5 (2), is of minor importance. However, in a CO matrix the CO loss process is effectively quenched and the quantum yield for homolysis increases with increasing availability of free CO in the matrix, resulting in predominant formation of the HCO and $Mn(CO)_5$ radicals respectively (Scheme 8).

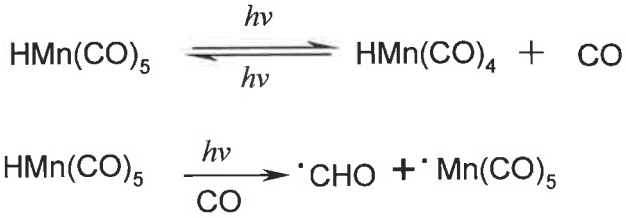

Scheme 8 Photochemical processes following irradiation of $HMn(CO)_5$

Further to this work, Electron Spin Resonance (ESR) spectroscopy studies of matrix isolated $HMn(CO)_5$ in both argon and CO matrices were carried out by Symons et al.[32] to confirm the assignment by Church and co-workers[24] of the C_{4v} carbonyl species to the elusive $^{\cdot}Mn(CO)_5$ radical. Results show that in an argon matrix the main photochemical process is tetracarbonyl formation although $^{\cdot}Mn(CO)_5$ formation does still occur as a minor reaction. $H^{\cdot}$ loss initially appears to occur near sites of free CO, presumably resulting from CO loss, which consequently trap the hydrogen atom as $^{\cdot}HCO$. During photolysis $^{\cdot}HCO$ is observed growing in prior to $H^{\cdot}$, which only appears on extended irradiation. However, in a CO matrix, due to suppression of the CO loss mechanism and cage recombination effects of the hydrogen atom loss process, only $^{\cdot}HCO$ and the pentacarbonyl radical are observed, with no H atom detected.

The formation of C-C bonds as a result of methyl migration reactions in compounds of the type $Mn(CO)_5R$, especially where $R = CH_3$, has been the subject of particularly extensive study due to its role as a catalyst.[33] A classic model of this migratory insertion reaction is observed following irradiation of $CH_3Mn(CO)_5$ in the presence of

a ligand such as CO, generating the acyl derivative $CH_3COMn(CO)_5$. Although it is clear that the reaction proceeds via migration of a methyl group to a neighbouring carbonyl, rather than CO insertion onto a vacant site on the Mn metal centre, the intermediate species involved in forming the acyl product have proved difficult to characterise and as a result has been the subject of much study.

Early matrix isolation studies by Rest[34] involved photolysis of both $CH_3Mn(CO)_5$ and its acyl derivative $CH_3COMn(CO)_5$. Photolysis ($230 < \lambda < 280$ nm) of $CH_3Mn(CO)_5$ in an argon matrix at 15 K produced new IR absorption bands at 1956, 2002, 2092 cm^{-1} due to the formation of the tetracarbonyl species, $CH_3Mn(CO)_4$ with free CO also observed at 2138 cm^{-1}. Irradiation at $\lambda > 280$ nm and annealing the matrix to 30 K resulted in quantitative reversal of the tetracarbonyl species and CO to $CH_3Mn(CO)_5$. Irradiation in a CO matrix demonstrated that the generation of $CH_3Mn(CO)_4$ from $CH_3Mn(CO)_5$ is partially inhibited compared to the reaction in an argon matrix. This may be due to matrix cage effects in which an intermediate is surrounded by CO molecules. This intermediate has however sufficient activation energy to regenerate the parent species $CH_3Mn(CO)_5$. Photolysis ($300 < \lambda < 360$ nm) of $CH_3COMn(CO)_5$ in an argon matrix at 15 K produced new IR bands at 1613, 1957, 1993, 2006, 2014, 2087 cm^{-1} associated with formation of both $CH_3COMn(CO)_4$ and $CH_3Mn(CO)_5$ and a band at 2138 cm^{-1} due to free CO. Those at 1993, 2014 and 2113 cm^{-1} can be assigned to species $CH_3Mn(CO)_5$ while the other bands are due to formation of the acyl tetracarbonyl photoproduct $CH_3COMn(CO)_4$. Extended photolysis at $\lambda > 320$ nm resulted in loss of bands due to species $CH_3COMn(CO)_5$ and the tetracarbonyl species and continued growth of the bands due to species $CH_3Mn(CO)_5$. The band at 1613 cm^{-1} may be assigned as a ketonic stretching band of the acyl tetracarbonyl derivative, which was thought to have trigonal bipyramidal (C_{3v}) structure as its terminal CO stretching bands are similar to those observed for the tetracarbonyl derivative, $CH_3Mn(CO)_4$. However, subsequent matrix isolation studies by McHugh et al.[35] of $CH_3Mn(CO)_5$ and $CH_3COMn(CO)_5$ in a variety of matrices aided by ^{13}CO labelling studies have shown that this assignment of $CH_3Mn(CO)_4$ having C_{3v} structure with CH_3 in the axial position is incorrect due to accidental superposition of the terminal CO stretching bands, and may in fact have C_{2v} geometry[35]. Electron diffraction studies have shown that $CH_3Mn(CO)_5$ should adopt C_{4v} geometry and energy-factored force field calculations predict that this

species should have 3 IR active bands at 2106 cm^{-1}(A_1), 2012 cm^{-1}(E) and 1948 cm^{-1} (A_1), which are in good agreement with the bands observed experimentally in previous matrix isolation studies of $CH_3Mn(CO)_5$ by Rest.[34] UV irradiation ($280 < \lambda > 380$ nm) of $CH_3Mn(CO)_5$ in a CH_4 matrix corresponding to the electronic absorption bands (222s, 274w nm) produced new bands at 2136 cm^{-1} due to free CO and 2086, 1997 and 1952 cm^{-1} and a decrease in intensity of the parent bands. Monochromatic photolysis of $CH_3Mn(CO)_5$ also produces these bands although the efficiency was reduced due to the lower extinction coefficient of the 274 nm absorption. Photolysis with monochromatic light (254 nm) produced more efficient photolysis but also lead to secondary photolysis products resulting from irradiation of the primary photoproduct $CH_3Mn(CO)_4$. Photolysis at $\lambda > 320$ nm and annealing the matrix to ambient temperatures also caused reversal of the primary photoreaction to yield species $CH_3Mn(CO)_5$. Results in an argon matrix were similar although further matrix splitting effects were observed and band positions were slightly shifted. In order to determine the geometry of $CH_3Mn(CO)_4$ photolysis of the ^{13}CO enriched species *cis*-[$Mn(^{12}CO)_4(^{13}CO)(CH_3)$] was carried out in a methane matrix. This yielded new absorption bands at 2086, 2082, 2075, 1997, 1989, 1964, 1951 and 1922 cm^{-1} as well as an increase in the free CO band at 2136 cm^{-1}. Long-wavelength irradiation resulted in the reversal of this reaction and the appearance of a new band at 1947 cm^{-1}, assigned as the A_1 mode of *trans*-[$Mn(^{12}CO)_4(CH_3)$]. From these studies it was predicted that $CH_3Mn(CO)_4$ adopts the C_{2v} structure. However, later studies[36] have proven that two isomers of $CH_3Mn(CO)_4$ are formed and have the geometries C_{4v} and C_s, the latter being previously mistaken for C_{2v} in the ^{13}CO enrichment studies.[35] In CO matrices following irradiation of $CH_3Mn(CO)_5$ formation of the tetracarbonyl $CH_3Mn(CO)_4$ was also observed. This is in accordance with the formation of $Cr(CO)_5$ from $Cr(CO)_6$ in CO matrix isolation studies.[35] No conversion however was observed of $CH_3Mn(CO)_5$ to its acyl derivative $CH_3COMn(CO)_5$ following photolysis in a CO matrix. Later work by Horton-Mastin et al.[36] described that irradiation of $CH_3Mn(CO)_5$ in both Ar and CH_4 matrices resulted in two isomers of the expected $CH_3Mn(CO)_4$ species. The photochemistry of the acyl derivative $CH_3COMn(CO)_5$ will be discussed later.

Previous workers[35] assigned a C_{2v} symmetry to $CH_3Mn(CO)_4$. However, Horton-Mastin and coworkers[36] describe that the ^{13}CO enrichment studies, originally used in assigning this geometry cannot always distinguish between a square–pyramidal structure C_s and a trigonal-bipyramidal structure C_{2v}. Although, it has been shown that the structural data originally obtained[35] are consistent with both structures, the two structures are distinguishable by their UV-vis spectra. Photolysis of the C_{4v} species, $CH_3Mn(CO)_5$ resulted in five new IR bands and a band at 2138 cm^{-1} due to free CO. Following further irradiation four of the bands remain with constant relative intensities, this indicating they belong to the same photogenerated species, while the other band changes in intensity indicating it is due to a second species. The former four bands correspond to the bands previously[35] assigned to $CH_3Mn(CO)_4$, while the second species may be assigned as a 2nd isomer of $CH_3Mn(CO)_4$ as its absorption band is not due to $^{\bullet}Mn(CO)_5$ and it can be formed by irradiating the known C_s isomer with visible light (Scheme 9). This second C_{4v} species should only have two absorption bands, the stronger E band observed while the a_1 believed to be weak might not be observed in the spectrum.

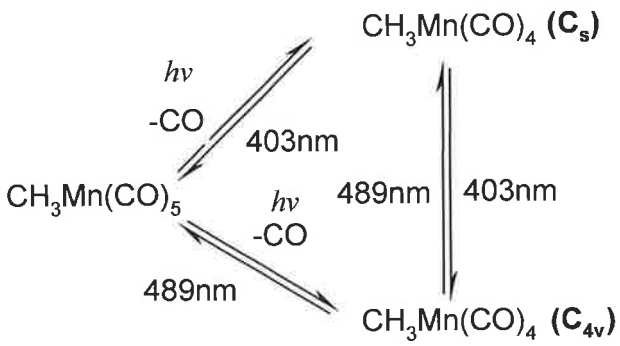

Scheme 9 Illustration showing generation of both isomers of $CH_3Mn(CO)_4$ from $CH_3Mn(CO)_5$ and their inter-conversion on irradiation with visible UV light[36].

It was observed that in the UV-visible spectrum of the photoproducts of $CH_3Mn(CO)_5$ two absorption maxima are observed. This indicates the formation of two species. On switching from an Ar to a CH_4 matrix, a blue shift of the absorption maxima of both species, is observed. One of the bands is already assigned as the C_s isomer of $CH_3Mn(CO)_4$, while the other must be due to another isomer of $CH_3Mn(CO)_4$. This second isomer may be assigned as having C_{4v} geometry as such blue shifts observed

of the absorption maxima are often associated with 16-electron, five coordinate square-pyramidal or pseudo-square-pyramidal structures (Scheme 10).

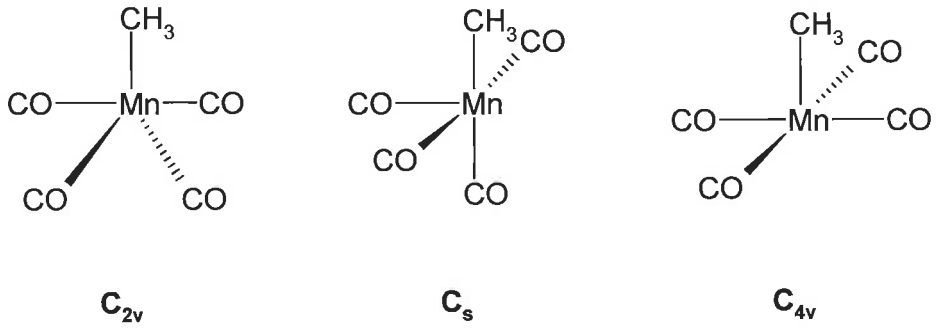

C_{2v} C_s C_{4v}

Scheme 10 Isomers of $CH_3Mn(CO)_4$. C_{2v} geometry was proven to be incorrect and in fact two isomers of $CH_3Mn(CO)_4$ exist and are assigned as C_s (major) and C_{4v} (minor).

The structural isomerisation observed for $CH_3Mn(CO)_4$ is very similar to that observed for $HMn(CO)_4$ in Density Functional Theory (DFT) calculations and vibrational spectra studies by Frigyes et al.[37] Here it was found that two isomers of $HMn(CO)_4$ exhibit energy minima. The lower energy isomer having C_s geometry as in its methyl analogue and a second isomer having C_{4v} geometry, lying approx. 12.5 kJ/mol higher in energy. A third structure was found to be more a quasi-stable intermediate than a true structural isomer.

Although it is clear from the above studies that irradiation of $CH_3Mn(CO)_5$ in a variety of matrices predominantly produces $CH_3Mn(CO)_4$ and to a lesser extent $^{\bullet}Mn(CO)_5$, the transient species involved in formation of the tetracarbonyl photoproduct is unclear and as a result this species has been the subject of much study, particularly in the area of time resolved Infra-red (TRIR) spectroscopy. TRIR studies by Boese et al.[38] have shown that on laser flash photolysis (308 nm) of $CH_3Mn(CO)_5$ in cyclohexane at room temperatures, bleaching of the parent species is observed as well as formation of a transient species with ν_{co} bands at 1992, 1986 and 1952 cm^{-1}. These bands are consistent with the *cis*-substituted tetracarbonyl *cis*-$Mn(CO)_4(L)CH_3$. Flash photolysis (337 nm) resulted in the observation of a single absorption band at λ_{max} = 383 nm, attributed to the formation of the species *cis*-$Mn(CO)_4(C_6H_{12})CH_3$. Irradiation of $CH_3Mn(CO)_5$ in a frozen methane glass[36] also yielded a similar spectrum due to this *cis*-labilised species, although the λ_{max}

absorption band occurred at a slightly lower energy. Photolysis of a $CH_3Mn(CO)_5$ in a 77 K methylcyclohexane glass produced a spectrum similar to that of the intermediate *cis*-$Mn(CO)_4(C_6H_{12})CH_3$ indicating the MCH solvento-species to be *cis*-$Mn(CO)_4(MCH)CH_3$. (Scheme 11). Flash photolysis in the presence of CO resulted in near-quantitative regeneration of $CH_3Mn(CO)_5$ although the rate of regeneration does appear to be solvent-dependent. In the case of cyclohexane, regeneration of $CH_3Mn(CO)_5$ following photolysis of the transient species *cis*-$Mn(CO)_4(solv)CH_3$ follows second-order kinetics. Photolysis of the deuterated analogue of $CH_3Mn(CO)_5$, $CD_3Mn(CO)_5$, in cyclohexane in the presence of CO resulted in the same spectrum and same second-order rate constant (5.0×10^8 M^{-1} s^{-1} at 298 K) as observed for $CH_3Mn(CO)_5$. Flash photolysis of $CH_3Mn(CO)_5$ in cyclohexane in the presence of 1 Atm N_2 again lead to the formation of the solvent substituted transient intermediate *cis*-$Mn(CO)_4(C_6H_{12})CH_3$, which subsequently decayed exponentially to give the N_2 substituted species $Mn(CO)_4(N_2)CH_3$ with IR bands at 2004 and 1975 cm^{-1}, with the ν_{NN} stretch out of the range of the TRIR instrumentation.

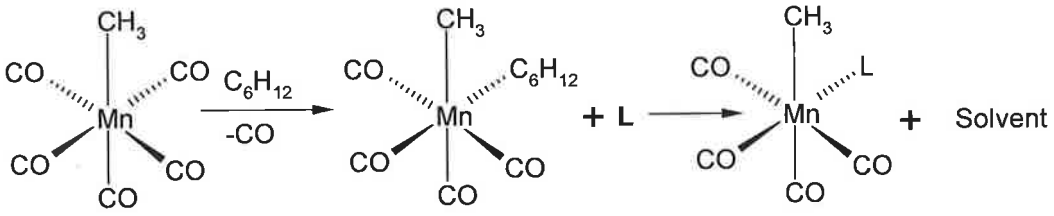

Scheme 11 Photolysis of $CH_3Mn(CO)_5$ resulting in formation of solvento-transient intermediate and subsequently the *cis*-ligand substituted tetracarbonyl product.

Similarly, photolysis in cyclohexane in the presence of PPh_3 initially results in the solvento-tetracarbonyl species, which then reacts with the ligand to product an a *cis*-substituted tetracarbonyl species with bands similar to those of the known *cis*-$Mn(CO)_4(PPh_3)CH_3$ species.[39] Analogous studies of $CH_3Mn(CO)_5$ in 295 K perfluoromethylcyclohexane (PMFC) under argon indicate loss of $CH_3Mn(CO)_5$ and formation of a new intermediate species $CH_3(PFMC)Mn(CO)_4$ with terminal CO stretches at 2008 and 1964 cm^{-1}, which are somewhat shifted to higher energy compared to those observed in cyclohexane. On extended photolysis this intermediate in the presence of photoliberated CO decays to regenerate species $CH_3Mn(CO)_5$. Flash photolysis of $CH_3Mn(CO)_5$ in the stronger donor solvent THF resulted in

formation of the transient species $CH_3(THF)Mn(CO)_4$, with bands at 1974, 1964 and 1921 cm^{-1}. Although this intermediate does react with dissociated CO to regenerate species $CH_3Mn(CO)_5$, it does so at a rate too slow (1.4×10^2 M^{-1} s^{-1}) to be monitored using TRIR, necessitating the use of Time-Resolved Optical (TRO) spectroscopy. These results indicated that 308 nm photolysis at ambient temperatures in the absence of added ligands produced an absorption spectrum with λ_{max} = 370 nm and 430 nm (sh.) in the visible region of the spectrum. Although these two electronic absorption bands due to the transient species $Mn(CO)_4(THF)CH_3$ are somewhat blue-shifted (~70 nm higher in energy) compared to the *cis-* and *trans-* isomers of $CH_3Mn(CO)_4$ observed following photolysis of $CH_3Mn(CO)_5$ in inert gas matrices[36], these bands are assigned as *cis-* and *trans*-$Mn(CO)_4(THF)CH_3$ respectively, with the former species being the major product. Following photolysis of $CH_3Mn(CO)_5$ in 77 K methyltetrahydrofuran (MTHF) glass a spectrum very similar to that observed in flash photolysis experiments in ambient temperature THF is observed using Time-Resolved Infrared (TRIR) monitoring.

Migratory insertion of CO into a metal-alkyl bond to form metal-acyl complexes is a fundamental reaction in organometallic chemistry and one of great importance in the carbon-carbon bond formation step in numerous industrially relevant catalytic carbonylation reactions such as alkene hydroformylation. Early matrix isolation work on the acyl derivative $CH_3COMn(CO)_5$ in argon and CO matrices by Rest et al.[34] was described earlier. Subsequent matrix isolation studies of this acyl species have been performed by McHugh and co-workers.[35] Here it is suggested that carbonylation can occur via three different mechanisms: **a)** alkyl migration, **b)** CO insertion and **C)** co-operative movement of co-ordinated methyl and CO groups although it has been shown that mechanism **b)** is the common mechanism of carbonylation. Photolysis ($280 < \lambda < 370$ nm) of matrix isolated $CH_3COMn(CO)_5$ in a methane matrix resulted in formation of species $CH_3Mn(CO)_5$ and free CO as well as bands due to another transient species with bands at 2084, 1992, 1948 cm^{-1} and a ketonic stretching band at 1610 cm^{-1}. The generation of 3 new carbonyl bands that cannot be assigned as either the radical $^{\bullet}Mn(CO)_5$ or the tetracarbonyl $CH_3Mn(CO)_4$ and the generation of a new ketonic CO band indicates the formation of the intermediate transient species $CH_3COMn(CO)_4$. Further investigation involving photolysis in a methane matrix of

the ^{13}CO-enriched $CH_3{}^{13}COMn(CO)_5$ analogue also produced three ν_{CO} bands identical to those for the aforementioned species, confirming the assignment as $CH_3COMn(CO)_4$. Efforts to eliminate formation of $CH_3Mn(CO)_5$ by selective photolysis with monochromatic light proved unsuccessful and indicated that even in a CO matrix decarbonylation of $CH_3COMn(CO)_5$ to regenerate $CH_3Mn(CO)_5$ occurs via the intermediate $CH_3COMn(CO)_4$. No evidence was found for formation of this species on photolysis of $CH_3Mn(CO)_5$, which may be because $CH_3Mn(CO)_5$ is thermodynamically more stable than $CH_3COMn(CO)_4$ or that this species requires a higher activation energy than $CH_3Mn(CO)_5$. As with species $CH_3Mn(CO)_5$, its acyl derivative $CH_3COMn(CO)_5$ has also been the subject of much TRIR investigation. In studies by Boese et al.[40] pulse laser excitation (λ_{exc}=308 nm) of $CH_3COMn(CO)_5$ in ambient temperature cyclohexane or methylcyclohexane resulted in disappearance of the parent bands due to $CH_3COMn(CO)_5$ and formation of new bands at 1990, 1952 and 1607 cm^{-1} due to a long-lived transient species $CH_3COMn(CO)_4$ which subsequently reacted via methyl migration to generate $CH_3Mn(CO)_5$ in competition with regeneration of $CH_3COMn(CO)_5$ in the presence of CO or underwent trapping by another ligand such as 4-phenylpyridine to yield the species *cis*-$Mn(CO)_4(L)(CH_3CO)$ (Scheme 12).

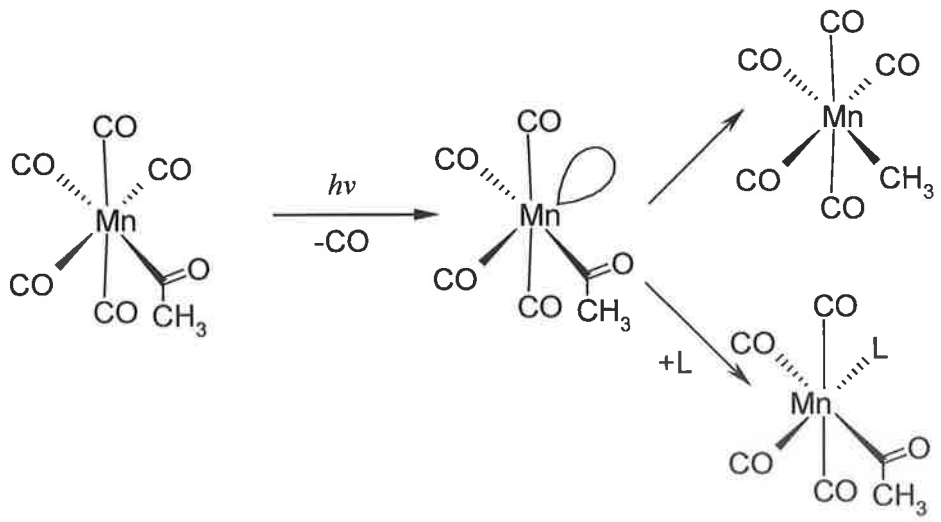

Scheme 12 Formation of intermediate species $CH_3COMn(CO)_4$ following photolysis of $CH_3COMn(CO)_5$

In a later experiment by Boese and Ford,[41] ambient temperature photolysis of the ^{13}CO labelled analogue $CH_3{}^{13}COMn(CO)_5$ in cyclohexane resulted in the generation of *cis*-$CH_3Mn(CO)_4(^{13}CO)$ with bands at 2102, 2033, 2011. 1992 and 1975 cm^{-1}, which can be assigned as photolabilisation of the *cis*-CO ligand and methyl migration to the vacant site on the metal centre.

Continuous photolysis (313 nm) of $CH_3COMn(CO)_5$ at room temperature in a range of hydrocarbon, halocarbon and other organic solvents resulted in CO loss and generation of $CH_3Mn(CO)_5$, with good efficiency under argon (Φ = 0.63 in cyclohexane).[40] The reaction was however strongly inhibited under 1 atm. CO (Φ = 0.16 in cyclohexane).

Low temperature (20 K) photolysis with 308 nm laser irradiation resulted in the formation of a transient species $CH_3COMn(CO)_4$ observed by FTIR with a lifetime of hours in a range of solvents. In methylcyclohexane new ν_{co} bands were observed at 2080, 1988, 1941 and 1607 cm^{-1}, the latter three similar to those observed in the TRIR spectrum following photolysis in ambient temperature cyclohexane (1991, 1952 and 1607 cm^{-1})[41] and those observed by McHugh et al.[35] following photolysis of $CH_3COMn(CO)_5$ in methane matrices at 12 K. When the TRIR experiment[41] was repeated using the ^{13}CO labelled complex $CH_3{}^{13}COMn(CO)_5$ approximately 10% of $CH_3Mn(CO)_4(^{13}CO)$ was also observed. Similar spectra are also observed in perfluoromethylcyclohexane and a range of methylated THF, indicating labilisation of a CO ligand adjacent to the acyl ligand resulting in the generation of a tetracarbonyl species. On switching from the weakly coordinating solvent perfluoromethylcyclohexane, to the strong donor THF, a notable shift in the carbonyl bands to lower frequency is observed. However, the THF and MeTHF spectra are somewhat more complicated than the cyclohexane spectra. Three terminal ν_{co} bands are observed in THF (1981, 1931 cm^{-1} and a shoulder at 1965 cm^{-1}). The former two are due to the predominant intermediate species formed also observed in cyclohexane, while the latter shoulder is consistent with formation of *cis*-trans-isomers. This is analogous to formation of *cis/trans*-$CH_3Mn(CO)_4THF$ following 308 nm irradiation of $CH_3Mn(CO)_5$ as observed by Boese et al[38] Similarly in 2-MeTHF and 2,5-Me_2THF solutions, a band at 1965 cm^{-1} (shifted to 1962 cm^{-1} in Me_4THF) attributed to the trans isomer is observed. In Me_4THF solutions the band at 1965 cm^{-1}

due to the *trans*-isomer displays 1st order decay kinetics 3.3 (± 0.6) × 10^4 s^{-1} at 298 K. Further evidence of formation of *cis/trans*-$CH_3COMn(CO)_4(THF)$ and *trans-cis* isomerisation was observed by Boese[41] in TRO experiments in 2-MeTHF. Flash photolysis of $CH_3COMn(CO)_5$ in 2-MeTHF under 0.1 Atm. CO resulted in transient absorbance over the range 380-450 nm. On monitoring at 430 nm a 1st order decay of the absorbance 3.5 (± 0.7) × 10^4 s^{-1} at 298 K was observed, while there was little change observed at 390 nm. This is in good agreement with the decay rate observed for the 1965 cm^{-1} band of the trans-isomer and confirms assignment of the 430 nm absorbance as that of *trans*-$CH_3COMn(CO)_4(THF)$.

It has been demonstrated that the intermediate species $CH_3COMn(CO)_4$ is much less reactive than other "unsaturated" metal carbonyl intermediates such as $Cr(CO)_5$, which exists as a solvento species even in weakly coordinating solvents. The intermediate transient species $CH_3COMn(CO)_4$ might be assigned as a solvento species resulting from coordination of a solvent molecule onto the vacant site on the metal centre. One would expect that going from THF to 2,5-Me_2-THF the ν_{co} bands of a solvento species $CH_3COMn(CO)_4(S)$ would shift to a higher energy. However, as shown above transient species recorded in THF, 2-MeTHF and Me_2THF gave identical ν_{co} stretching bands. More recently however, it has been demonstrated by Boese et al.[41] via kinetic data and MM2 calculations that the solvento species (Figure 1-A) may prevail in both THF and 2,5-Me_2THF, with a mixture of both the *cis*- and *trans*-isomer occurring in THF, 2,5-Me_2THF and 2-MeTHF possible formed by trapping of the unsaturated species generated by labilisation of the *cis*- and *trans*-CO. In the much more sterically crowded solvent Me_4THF the bands observed occur at higher frequencies and are more similar to those observed in cyclohexane. The reaction of *cis*-$CH_3COMn(CO)_4(S)$ with 4-phenylpyridine in Me_4THF is 2-3 order of magnitude faster than in THF and is more similar to the analogous intermediate observed in hydrocarbon solution in which an η^2-acyl structure (Figure 1-B) is suggested.

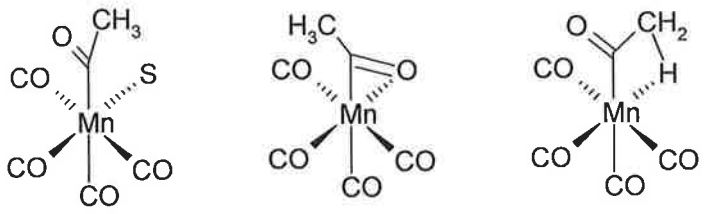

(A) (B) (C)

Figure 1 Prospective structures for intermediate species – (A) Solvento structure, (B) η^2-acyl structure and (C) agostic structure

The low-reactivity of the intermediate species $CH_3COMn(CO)_4$ in alkane and perfluoroalkane solutions is unusual when compared to the reactivity of similar previously mentioned intermediates such as *cis*-$Mn(CO)_4(CH_3)S$. This low-reactivity of $CH_3COMn(CO)_4$ in weak hydrocarbon solvents, must arise as a result of some unique stability arising via an agostic interaction with the methyl group (Figure 1-C) or chelation of the metal with an η^2-bound carbonyl group (Figure 1-B).[40, 41, 42] Such chelation would be more important in weakly coordinating solvents such as cyclohexane or perfluorocyclohexane than in the strongly donating THF, in which the solvento species dominates. However, according to *ab initio* calculations on $CH_3COMn(CO)_4$ carried out by Axe et al.[40, 43] and later Density Functional Theory (DFT) calculations by Derecskei-Kovacs et al.[44] the η^2-acyl structure should be more stable than the agostic structure. This assignment of the η^2-acyl structure as the stable structure in alkane and perfluoroalkane is further supported by a shift in the frequency of the acyl band at 1607 cm^{-1} to lower frequencies in going from species $CH_3COMn(CO)_5$ to the intermediate $CH_3COMn(CO)_4$ and by comparison of this frequency shift to those commonly observed for other stable mono- and dihapto coordinating acyl complexes.[45] Early studies by Boese et al.[41] showed that the kinetic behaviour and TRIR spectra of the transient species $CH_3COMn(CO)_4$ resulting from photodissociation of CO from $CH_3COMn(CO)_5$ are solvent dependent. In weakly coordinating solvents such as cyclohexane and the sterically crowded Me_4-THF the previously described η^2-acyl structure was the dominant product. The kinetics observed were very slow in comparison to those expected for a solvento species in cyclohexane. This is best seen by comparison with the solvento species *cis*-$CH_3Mn(CO)_4(S)$[41] resulting from flash-photolysis of $CH_3Mn(CO)_5$. More recent work by Masick et al.[46] has shown that this species is 5 orders of magnitude more reactive

towards CO (k_{co} = 4.5 × 10^8 M^{-1} s^{-1}) at 298 K compared to $CH_3COMn(CO)_4$, which has a rate constant of 1.07 × 10^4 M^{-1} s^{-1} in 298 K alkane solution,[46] and is even smaller in THF solution. While k_{co} values for $CH_3Mn(CO)_4(S)$ are solvent dependent, those for $CH_3COMn(CO)_4$ appear to be independent of solvent in weak donor solvents such a cyclohexane. When $P(OMe)_3$ is the incoming ligand there is a difference in reactivity of 3 orders of magnitude between the cyclohexane and THF solutions[42](Table 1). The fact that $CH_3COMn(CO)_4$ is much less reactive toward ligand substitution than $CH_3Mn(CO)_4(S)$ in cyclohexane, but still shows substantial decreases in reactivity in THF further supports the assignment of $CH_3COMn(CO)_4$ as the chelate complex (Figure 1-B) in the former solvent and other weakly coordinating solvents and the solvento species (Figure 10-A) in the latter solvent. The similar reactivities of $CH_3COMn(CO)_5$ to $P(OMe)_3$ and CO in THF, 2-MeTHF and 2,5-Me_2THF also indicate intermediate species with similar coordination modes, ie a solvento structure.

Table 1 Comparison of k_L values for reaction of $CH_3COMn(CO)_4$ and $CH_3Mn(CO)_4(S)$ with various ligands in a range of solvents. [42]

Solvent	Ligand	k_L for $CH_3COMn(CO)_4$ ($M^{-1}s^{-1}$) (295 K)	k_L for $CH_3Mn(CO)_4(S)$ ($M^{-1}s^{-1}$) (295 K)
Cyclohexane	PhPy	7.5 (± 1.5) × 10^6	2.5 (± 0.3) × 10^9
Cyclohexane	PPh_3	2.3 (± 0.5) × 10^6	1.0 (± 0.2) × 10^9
Cyclohexane	$P(OMe)_3$	1.4 (± 0.3) × 10^6	1.1 (± 0.2) × 10^9
THF	$P(OMe)_3$	1.7 (± 0.3) × 10^3	–
Me_4-THF	$P(OMe)_3$	6 × 10^5	–
Cyclohexane	CO	6.5 (± 1.3) × 10^3	4.5 (± 0.5) × 10^8
PFMC	CO	1.5 (± 0.3) × 10^4	1.0 (± 0.5) × 10^{10}
THF	CO	< 5 × 10^2	1.4 (± 0.3) × 10^2

Apart from $CH_3Mn(CO)_5$ and its acetyl analogue $CH_3COMn(CO)_5$, species $CH_3Mn(CO)_5$ and $CH_3COMn(CO)_5$ respectively, their fluorinated analogues $CF_3Mn(CO)_5$ and $CF_3COMn(CO)_5$ have also been synthesised and investigated using photochemical techniques. In experiments carried out by Boese et al.[41] continuous wave photolysis (313 nm) of $CF_3COMn(CO)_5$ in 296 K cyclohexane resulted in

bleaching of the bands due to the parent species (2118, 2038, 2017 and 1956 cm^{-1}) and formation of the methyl analogue $CF_3Mn(CO)_5$ with carbonyl bands at 2119, 2047, 2022 cm^{-1}. Irradiation at 308 nm of $CF_3COMn(CO)_5$ in cyclohexane resulted in the generation of a transient species $CF_3COMn(CO)_4$ with TRIR bands at 2054, 2013, 2007, 1976 and 1617 cm^{-1}, which was observed to be much more reactive than the intermediate $CH_3COMn(CO)_4$ resulting from photolysis of the acetyl analogue $CH_3COMn(CO)_5$. These bands are similar to those observed by Boese et al.[38] in the TRIR spectrum following laser flash photolysis of $CF_3Mn(CO)_5$ in cyclohexane. The transient species formed displays four bands in the CO stretching region at ν_{co} 2063, 2028, 1995 and 1985 cm^{-1}. As was the case with species $CH_3Mn(CO)_5$ these results suggest that labilisation of *cis*-CO is the predominant photoreaction. The back – reaction in the presence of CO resulting in regeneration of the parent complex displayed second-order decay kinetics with k_{obs} = 1.6 (± 0.3) × 10^7 M^{-1} s^{-1} (298 K) compared to 4.5 (± 0.5) × 10^8 M^{-1} s^{-1} (298 K)for the analogous decay in the presence of CO of the intermediate species resulting from photolysis of $CH_3Mn(CO)_5$.

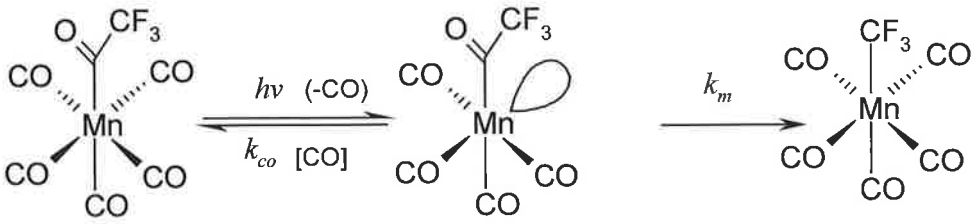

Figure 2 Formation of $CF_3Mn(CO)_4$ on photolysis of $CF_3COMn(CO)_5$ and subsequent CO dependent formation of $CF_3Mn(CO)_5$ or $CF_3COMn(CO)_5$.[41]

Under argon, the intermediate $CF_3COMn(CO)_4$ decays exponentially to give $CF_3Mn(CO)_5$ (Figure 2) with an observed rate constant k_{obs} = 2.5 × 10^4 s^{-1}, while under a CO atmosphere it disappeared following first order kinetics, dependent on the pressure of CO present to generate $CF_3Mn(CO)_5$ and regenerate $CF_3COMn(CO)_5$. However in THF and Me_2THF, $CF_3COMn(CO)_4$ does not demonstrate any appreciable decay on the TRIR timescale even under 1 atm. CO. The TRIR bands are also shifted to lower frequencies (2005 cm^{-1} and 1965 cm^{-1}) in THF and (2004 cm^{-1} and 1968 cm^{-1}) in Me_2-THF respectively.

Flash photolysis (308 nm) of the analogous monofluoroacetyl complex $CH_2FMn(CO)_5$ in cyclohexane solution also led to the formation of an intermediate transient species, which reacted quickly in the presence of CO to regenerate the parent species. The bands for this transient species in cyclohexane occur at 2052, 2002, 1987 and 1966 cm^{-1}, somewhat red shifted to lower frequency compared to those of the intermediate $CF_3COMn(CO)_4$ resulting from flash photolysis of $CF_3COMn(CO)_5$ in cyclohexane, this difference perhaps occurring as result of an increased donor ability in going from CF_3 to CH_2F.

2.2. Aims and Objectives

The following section involves the syntheses of a number of novel fluorinated manganese pentacarbonyl systems. The photochemical properties of these systems are investigated using matrix isolation in a variety of matrix gases. The aim of these photochemical studies is investigate whether irradiation results in photoinduced C-F bond activation. The photochemistry of these systems is then compared to the theoretical data observed in Density Functional Theory calculations

2.3. Experimental

2.3.1. Materials

All reactions were carried out under an inert atmosphere of argon or nitrogen. All solvents were supplied by the Aldrich Chemicals Company. Dichloromethane, chloroform, diethyl ether, pentane, cyclohexane and ethanol were dried over $MgSO_4$ prior to use. All solvents used in laser flash photolysis experiments were of spectroscopic grade and were used without further purification. Tetrahydrofuran (THF) was distilled from sodium/benzophenone ketyl solution and used immediately. Methane, dinitrogen and carbon monoxide gases were supplied by Air Products Ltd. Dimanganese decacarbonyl was supplied by Aldrich Chemical Company and was used without further purification. Silica Gel (Merck) was used as received. All mobile phases for column chromatography were dried over $MgSO_4$ before use. Acetophenone, octane, iodomethane, sodium metal, mercury, trifluoroacetic anhydride, iodopentafluorobenzene, (Aldrich. Chemical Co.), 2,2,2-trifluoroacetophenone, (Fluorochem. Ltd.) were all used without further purification.

2.3.2. Equipment

All synthesis were performed using conventional laboratory glassware under an inert argon atmosphere. All solutions were deoxygenated by purging with pure argon or nitrogen for ~10 mins. Column chromatography was carried out using neutral silica gel pH 6.5 – 7.5 or neutral aluminium oxide. All infrared spectra were obtained on a Perkin-Elmer 200 FT-IR spectrometer in a 0.1mm sodium chloride liquid solution cell using spectroscopic grade pentane, cyclohexane and THF. ^{1}H, ^{13}C and COSY spectra were recorded on a Bruker model AC 400 MHz spectrometer in $CDCl_3$ or d_6-acetone and were calibrated according to the deuterated solvent peak. ^{19}F NMR spectra were also recorded on a Bruker model AC 400 MHz spectrometer in $CDCl_3$ with trifluoroacetic acid as the standard. All UV spectra were measured in spectroscopic grade solvents on a Hewlett-Packard 8452A-photodiode-array spectrometer using a 1cm quartz cell. Elemental analysis of C, H, & N were carried out by the Chemical services Unit, University College Dublin using an Exeter Analytical CE-440 elemental analyser.

2.3.3. Synthesis

2.3.3.1. $CF_3COMn(CO)_5$

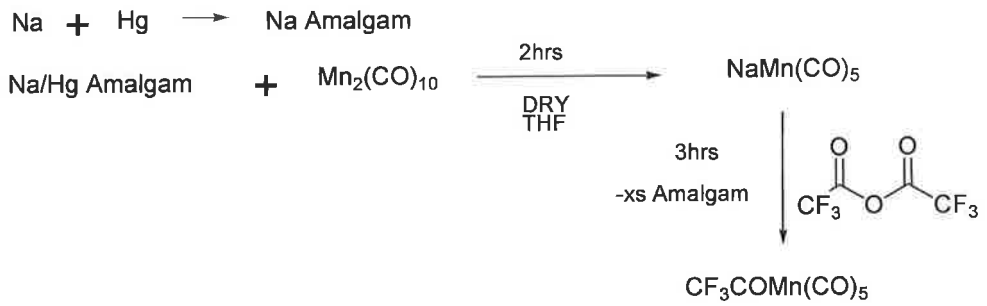

Scheme 13 Synthesis of $CF_3COMn(CO)_5$

This compound was synthesised according to the method outlined by Beck et al.[47] with minor alterations.

Trifluoroacetylpentacarbonylmanganese $CF_3COMn(CO)_5$ was prepared by adding a solution of $Mn_2(CO)_{10}$ (0.3 g, 0.75 mMol) in ~10 ml to a sodium amalgam (0.11 g Na in 0.68 ml Hg). This was stirred vigorously under an inert atmosphere for 1hr and allowed to cool to ambient temperatures. This resulted in the formation of the sodium salt $[Mn(CO)_5]^-Na^+$. Any excess amalgam was then removed. The sodium salt was then treated under inert conditions with trifluoroacetic anhydride (0.217 ml, 1.5 mMol). This was added to the reaction solution at -10 °C and left stirring vigorously under inert conditions for 3 hours to yield a light green coloured liquid, which turned light yellow-white in colour following solvent removal under reduced pressure. This yielded the product $CF_3COMn(CO)_5$, which is used directly in the preparation of the non-acetylated analogue $CF_3Mn(CO)_5$.

IR ν_{co} : ($CHCl_3$) 2133 (w), 2073 (w) and 2040 cm^{-1} (s) 1652 cm^{-1}; UV-Vis (Pentane) : 250 nm

2.3.3.2. $CF_3Mn(CO)_5$

The synthesis for the non-acetylated analogue is also outlined in the references.[47(a,b,c)] The method used for isolation of this compound is that suggested by Boese and Ford[48].

The non-acetylated analogue $CF_3Mn(CO)_5$ was prepared by heating the previously described $CF_3COMn(CO)_5$. The pure acetylated product $CF_3COMn(CO)_5$ was transferred to a schlenk tube and evacuated. The sealed evacuated Schlenk tube containing the acetyl product was then placed in an oven at 110 °C for approx. 2 hours and then cooled to room temperature. This resulted in the deposition of pure $CF_3Mn(CO)_5$ onto the inner walls of the schlenk tube.

Yield: IR ν_{co} : 2070 (w), 2042 (s) and 2021 cm^{-1} (m)

UV-Vis (Pentane) : 250 (s) and 360 (sh.) nm

2.3.3.3. (2-acetylphenyl-C,O)Mn(CO)$_4$

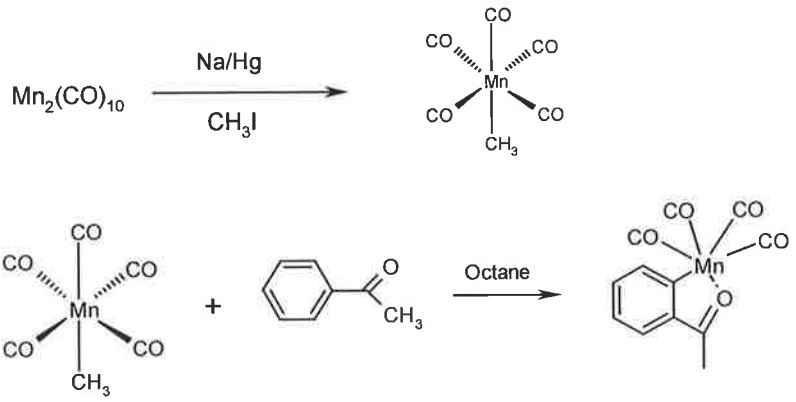

Scheme 14 Synthesis of (2-acetylphenyl-C,O)tetracarbonyl manganese

This compound was synthesized and isolated according to the method outlined by Mckinney et al.[49]

A sodium amalgam was prepared by adding small pieces of sodium (0.22 g, 9.56 mMol) to mercury (22.50 g, 112 mMol) under an inert argon atmosphere. This was then left to cool following formation of the amalgam. To the Na/Hg amalgam was then added dimanganese decacarbonyl $Mn_2(CO)_{10}$ (0.66 g, 1.69 mMol) in dry THF. This formed $NaMn(CO)_5$. The excess and unreacted amalgam was removed by transferring the $NaMn(CO)_5$ solution to a new round bottomed flask via a double ended needle. This solution was placed in an ice-bath and to it was added drop-wise via a syringe under inert conditions a solution of iodomethane, CH_3I (0.32 ml, 5.04 mMol) in dry THF. Following vigorous stirring for approx. 1 hr. under inert conditions a solution of $CH_3Mn(CO)_5$ was formed. This was purified by sublimation at 40 °C into a liquid N_2/acetone slush cooled sublimer. The pure product was collected as white crystals.

To a argon purged solution consisting of 16.5 ml octane and 0.65 ml acetophenone. was added $CH_3Mn(CO)_5$ (0.15 g, 0.714 mMol). This solution was then heated to reflux temperature for 30 mins changing from colourless to yellow, indicating the formation of the yellow coloured (2-acetylphenyl-C,O)tetracarbonylmanganese product. Following cooling, the crude product was purified by column chromatography on silica gel with a 50:50 hexane – chloroform mobile phase.

Solvents were removed under reduced pressure, to yield a bright yellow crystalline product. This was then recrystallised from a hexane/CH_2Cl_2 mixture.

Yield : 0.135 g, 66%; IR (pentane) : 2085 cm^{-1}, 1994 cm^{-1} & 1944 cm^{-1}; UV-Vis (pentane) : 250 and 470 nm; ^{1}H-NMR (400 MHz, $CDCl_3$): δ 2.6(s, CH_3), 7.17(td), 7.41(td), 7.83(dd), 8.09 (dd),

2.4. Results

2.4.1. Photochemistry of $CF_3Mn(CO)_5$

2.4.1.1. Photolysis of $CF_3Mn(CO)_5$ in a CH_4 matrix

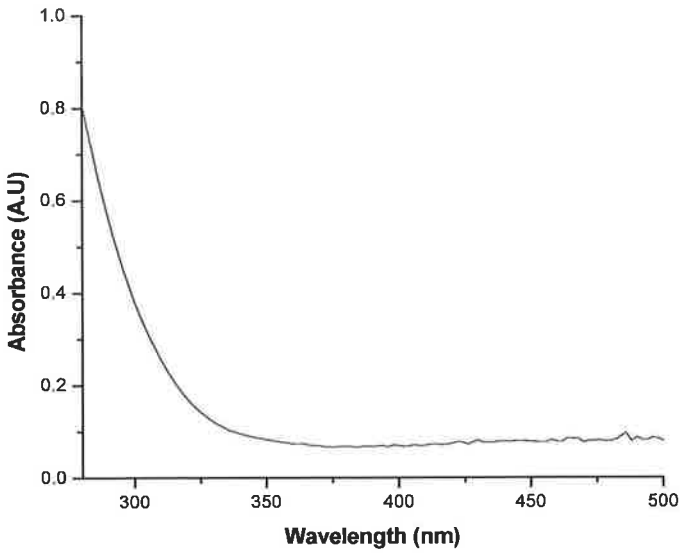

Figure 3 UV-Vis spectrum of $CF_3Mn(CO)_5$ in pentane

$CF_3Mn(CO)_5$ is a white-cream coloured crystalline solid with a UV-Vis spectrum exhibiting a single high energy band at approximately 280 nm in pentane solution.

On deposition of $CF_3Mn(CO)_5$ in a methane matrix three carbonyl bands were observed at 2141, 2045 and 2019 cm^{-1} (Figure 4). Weak bands also observed at deposition at 2070 and 1975 cm^{-1} are assigned to the weak B_1 vibrational mode of $CF_3Mn(CO)_5$ and naturally present ^{13}CO respectively.[50] Monochromatic photolysis (λ_{exc} = 313 nm, 90 min) of $CF_3Mn(CO)_5$ in a methane matrix at 12 K produced new carbonyl absorption bands at 2166, 2115, 2099, 2137, 2033, 2006, 1988, 1971 cm^{-1} and an increase in intensity of the free CO band at 2137 cm^{-1} with concomitant bleaching of the parent bands. The bands at 2033, 2006 and 1971 cm^{-1} can be assigned to the tetracarbonyl species $CF_3Mn(CO)_4$ arising from dissociative CO loss while that at 1988 cm^{-1} is due to homolytic cleavage of the C-Mn bond leading to formation of the C_{4v} $^{\bullet}Mn(CO)_5$ radical species (Figure 4). Photolysis in the visible

region (λ_{exc} = 405 nm, >410 nm) resulted in regeneration of the parent bands and depletion of the tetracarbonyl and $^{\bullet}Mn(CO)_5$ radical product bands indicating regeneration of the 18-e$^-$ pentacarbonyl parent species $CF_3Mn(CO)_5$.

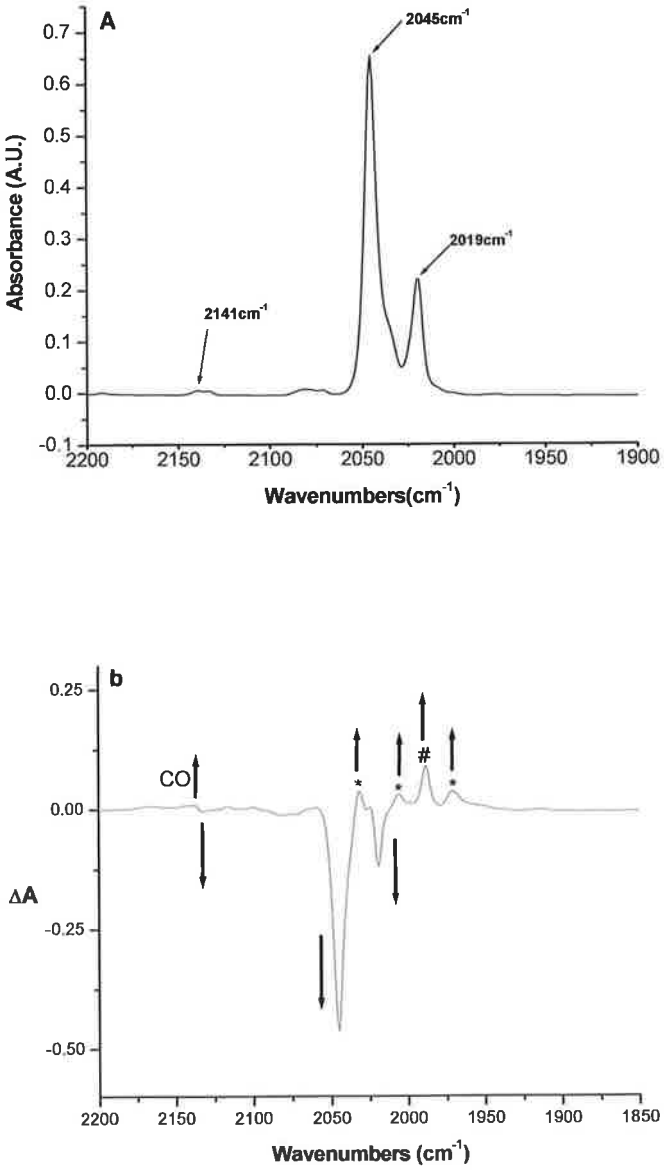

Figure 4 (A) IR Spectrum following deposition of $CF_3Mn(CO)_5$ in CH_4 matrix at 20 K, (B) Difference spectrum following irradiation (λ_{exc} = 313 nm) indicating formation of tetracarbonyl bands (*) and the $^{\bullet}Mn(CO)_5$ radical (#).

2.4.1.2. Photolysis of $CF_3Mn(CO)_5$ in a N_2 matrix

Following deposition of $CF_3Mn(CO)_5$ in a N_2 matrix three carbonyl bands were observed at 2140, 2048 and 2022 cm^{-1}. Photolysis (λ_{exc} = 313 nm, 100 mins) in a pure dinitrogen matrix produced a decrease in intensity of the parent bands at 2048 and 2022 cm^{-1} and generation of two species (Figure 5). A tetracarbonyl species, $CF_3Mn(CO)_4N_2$ with ν_{co} stretching bands at 2036, 2009 & 1992 cm^{-1} and a ν_{NN} band at 2171 cm^{-1} and a tricarbonyl $CF_3Mn(CO)_3(N_2)_2$ with a ν_{co} band at 2119 and 1918 cm^{-1} and two weak ν_{NN} bands at 2282 and 2236 cm^{-1}. The product bands also observed at 2104 and 1978 cm^{-1} indicate formation of the $^{\bullet}Mn(CO)_5$ radical species, the expected band at ~ 1988 cm^{-1} masked by the absorption band at 1992 cm^{-1}.

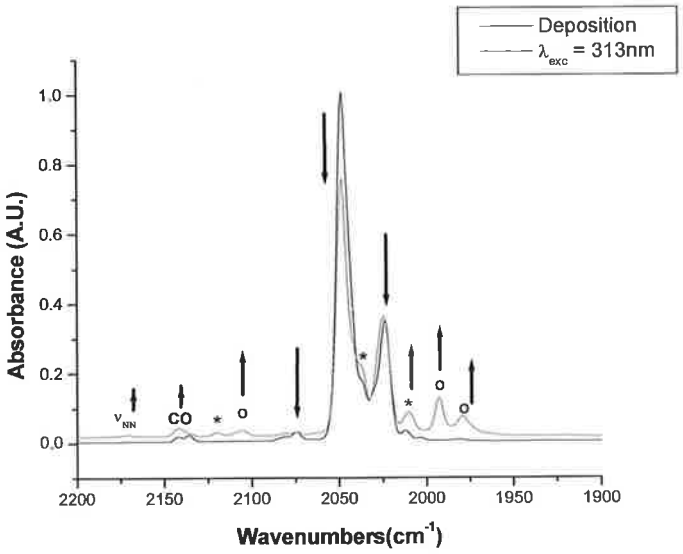

Figure 5 Overlay of vibrational spectra of $CF_3Mn(CO)_5$ in N_2 matrix. Following initial deposition (black) and following photolysis at λ_{exc} = 313 nm (red). Bands due to the $^{\bullet}Mn(CO)_5$ radical species (o) and the tetracarbonyl $CF_3Mn(CO)_4N_2$ (*) are indicated

Photolysis at 405 nm resulted in a decrease in intensity of the parent bands and the product bands at 1978, 1992, 2104 cm^{-1} and 2171 cm^{-1} with concomitant generation of product bands at 2090, 2064 and 1980 cm^{-1}, and an increase in intensity of the two N_2 vibrational bands at 2236 and 2282 cm^{-1} due to the N_2 disubstituted species, $CF_3Mn(CO)_3(N_2)_2$.

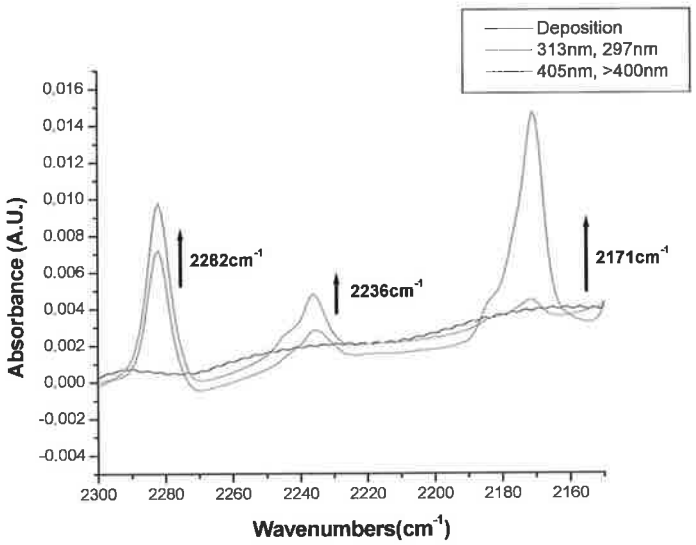

Figure 6 Overlay of vibrational spectra of $CF_3Mn(CO)_5$ in N_2 matrix. In black is the vibrational spectrum following deposition. Following photolysis at λ_{exc} = 313 nm (Red), and following photolysis at $\lambda > 400$ nm.(Green)

Subsequent broadband irradiation ($\lambda_{exc} > 400$ nm) resulted in regeneration of the parent bands as well as loss of the bands due to the $^{\bullet}Mn(CO)_5$ radical species and the tetracarbonyl species $CF_3Mn(CO)_4N_2$. The product bands at 2090, 2064, 1980, 2282 and 2236 cm^{-1}, initially observed on 405 nm irradiation increased in intensity (Figure 6) suggesting the formation of a second isomer of the tricarbonyl species - *fac*-$CF_3Mn(CO)_3(N_2)_2$ via secondary photolysis of the previously formed tetracarbonyl species, $CF_3Mn(CO)_4N_2$

2.4.1.3. Photolysis of $CF_3Mn(CO)_5$ in a 2% or 20% CO-doped CH_4 matrix

Deposition of $CF_3Mn(CO)_5$ in both a 2% or 20% CO doped methane matrix resulted in the generation of three carbonyl bands at 2140, 2044 and 2020 cm^{-1}. Irradiation in 2% or 20% CO-doped methane matrices yielded similar results and consequently only those observed for the 20% CO-doped methane matrix will be discussed.

Figure 7 shows the IR spectral changes following UV irradiation at $\lambda_{exc} = 313$ nm for 110 mins which showed bleaching of the parent carbonyl bands and the formation of product bands at 2033, 2004 and 1973 cm^{-1} assigned to $CF_3Mn(CO)_4$ and 1988 cm^{-1} to the 17-e^- $^{\bullet}Mn(CO)_5$ radical species. The band at 2137 cm^{-1} can be assigned to free CO in the CO - doped methane matrix.

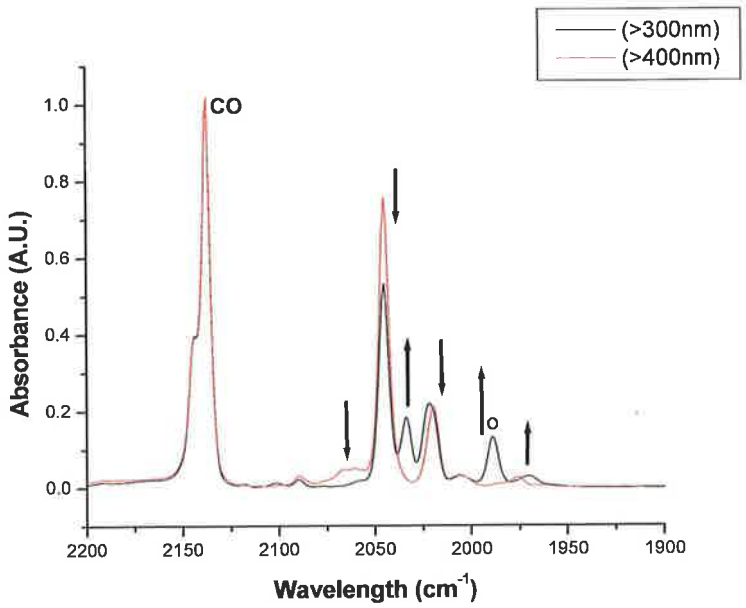

Figure 7 FTIR spectra, following photolysis at λ >300 nm (in black) illustrating formation of the $^{\bullet}Mn(CO)_5$ radical (°) and tetracarbonyl photoproducts and following λ > 400 nm (in red) illustrating regeneration of the parent bands on irradiation at higher wavelengths.

When the excitation wavelength was changed to 297 nm further depletion of both the parent bands and the product bands at 2033, 1988 and 1973 cm^{-1} was observed, with continued growth of the product band at 2004 cm^{-1}. Subsequent irradiation at > 400 nm, for 90 mins resulted in the depletion of the product bands and regeneration of the parent bands at 2044, 2020 cm^{-1} (Figure 8).

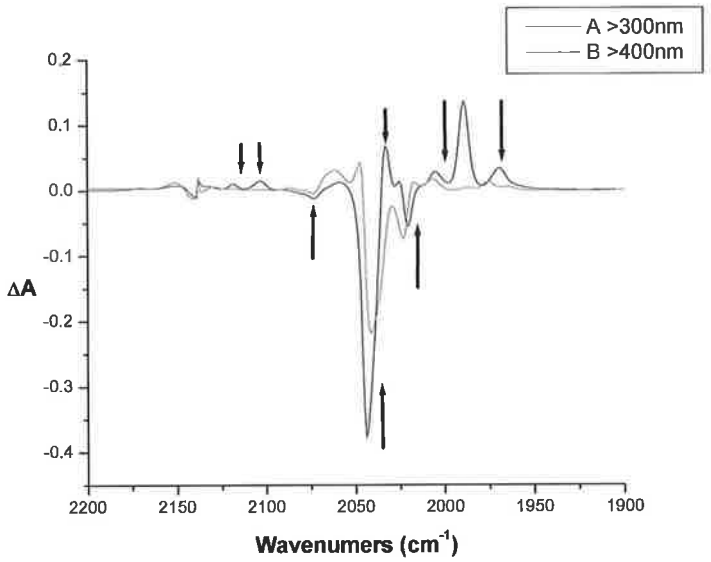

Figure 8 Difference Spectrum of $CF_3Mn(CO)_5$ in 20% CO-CH_4 matrix following (A) deposition and photolysis λ > 300 nm, (B) following photolysis at λ > 400 nm, indicating regeneration of parent species

2.4.2. Photochemistry of $CF_3COMn(CO)_5$

2.4.2.1. Photolysis of $CF_3COMn(CO)_5$ in a methane matrix

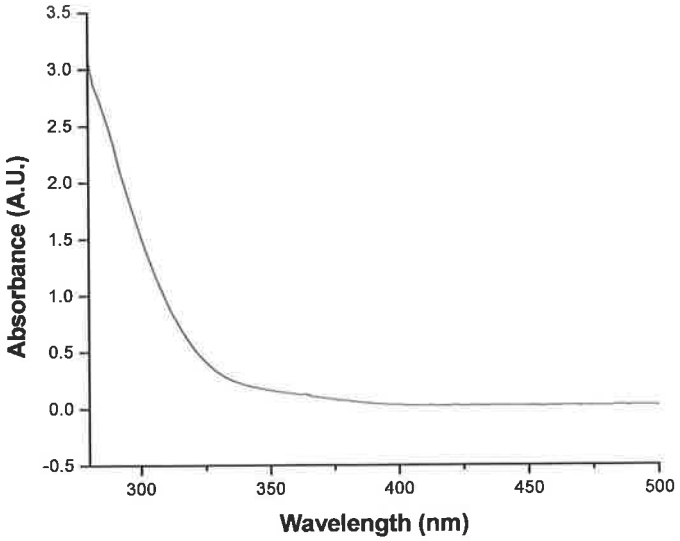

Figure 9 UV-Vis absorption spectrum of $CF_3COMn(CO)_5$ in pentane

$CF_3COMn(CO)_5$ is a white-cream coloured crystalline solid with a UV-Vis spectrum exhibiting a single broad high energy absorption at 280 nm in pentane solution

On deposition of $CF_3COMn(CO)_5$ in a methane matrix ν_{co} bands were observed at 2133, 2071, 2042, 2035 (sh.), 2020 & 1670 cm^{-1}. Monochromatic irradiation at λ_{exc} = 313 nm for 45 mins resulted in depletion of the parent bands and loss of the band at 2133 cm^{-1} (CO A_1 symmetric stretch)[51] with generation of product bands at 1134 (w), 1596 cm^{-1} and 2104, 1985, and 1974 cm^{-1} which are assigned to the $^{\bullet}CF_3CO$ and $^{\bullet}Mn(CO)_5$ radicals respectively.

The product bands generated at 2138, 2020 and 2005 cm^{-1} may be assigned to free CO and the coordinatively unsaturated $CF_3Mn(CO)_4$ as they are in good agreement with those previously observed for this species. This is further suggested by the observed decrease in the intensity of the ketonic CO band at 1670 cm^{-1} indicating acyl CO loss. As can be seen in Figure 10 subsequent high energy irradiation at 297 and 289 nm produced very little change in the intensity of the parent or product carbonyl bands.

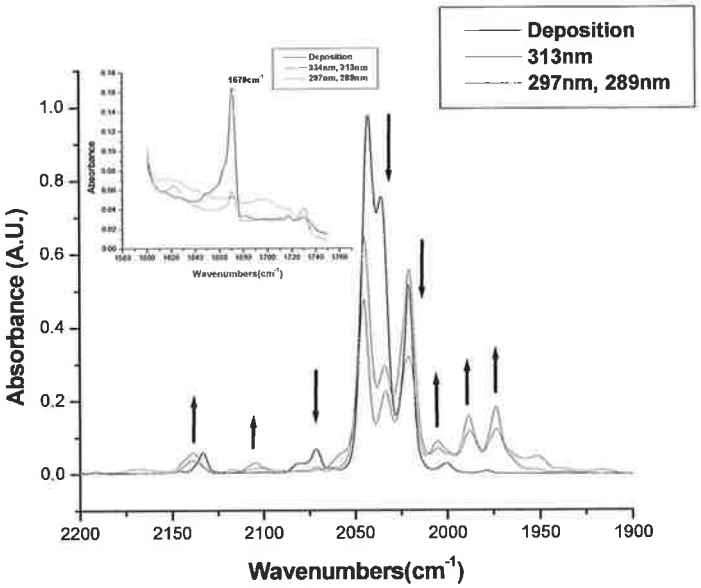

Figure 10 Overlay of IR spectra of $CF_3COMn(CO)_5$ on photolysis in a methane matrix at 12 K. Deposition spectrum (black) shows parent bands before irradiation. Spectrum following extended photolysis at 313 nm is shown in red. Spectrum following photolysis at 297 nm and subsequently 289 nm is shown in green. Inset shows depletion of ketonic stretching vibration on photolysis at 313 nm.

Photolysis at λ_{exc} = 405 nm for 60 mins resulted in an increase in intensity of the parent bands as well as a substantial decrease in the intensity of the product bands at, 2005, 1988, 1973 cm^{-1} thus indicating loss of the radical species, the coordinatively unsaturated tetracarbonyl and concomitant regeneration of the parent species on high energy irradiation. No change was observed in the weak bands at 1596, 1543 and 1525 cm^{-1}. Subsequent broadband photolysis (λ_{exc} > 400 nm) resulted in further regeneration of the parent species and further loss of the bands due to both the radical species and the coordinatively unsaturated tetracarbonyl species $CF_3Mn(CO)_4$.

2.4.2.2. Photolysis of $CF_3COMn(CO)_5$ in a N_2 matrix

Deposition of $CF_3COMn(CO)_5$ in a N_2 matrix resulted in the generation of ν_{co} bands at 2025, 2074, 2082 (sh.), 2043 and acyl CO bands at 1670 & 1660 cm^{-1}. As shown in Figure 11 and Figure 12 high energy irradiation (λ_{exc} = 313 nm, 110 mins) produced a decrease in intensity of the parent bands at 2025, 2043, 2074 and 1670 cm^{-1} with loss of the bands at 2037 (sh.), 1660 and 1670 cm^{-1} on extended photolysis and concomitant generation of product bands at 1597, 1978, 1992 2109, 2009, 2046, 2140 and 2170cm^{-1} which are assigned to the generation of three species – the $^{\bullet}CF_3CO$ and $^{\bullet}Mn(CO)_5$ radicals and a tetracarbonyl species $CF_3COMn(CO)_4N_2$. The presence of another weak N_2 band at 2282 cm^{-1} and a carbonyl band at 2120 cm^{-1} are tentatively assigned to generation of another N_2 substituted species, $CF_3COMn(CO)_3(N_2)_2$ (Figure 13).

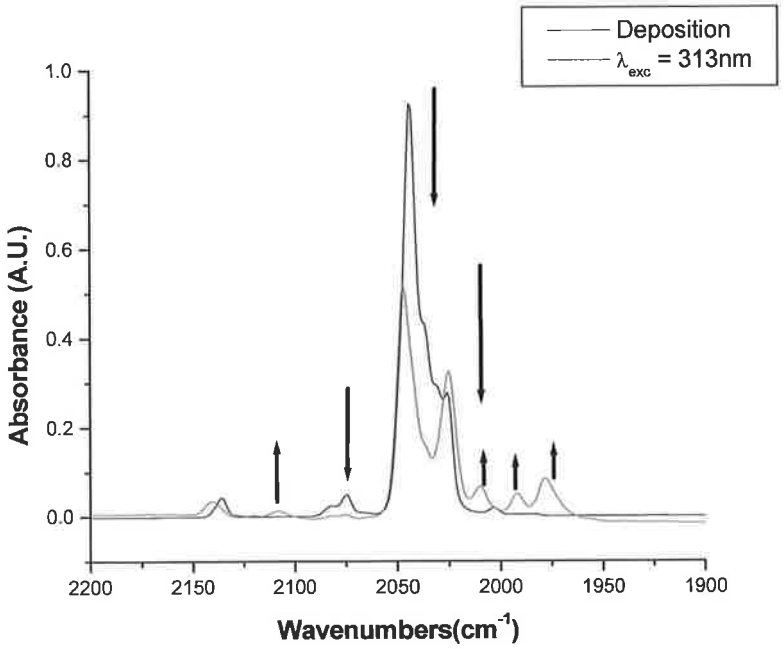

Figure 11 IR spectra of $CF_3COMn(CO)_5$ in a N_2 matrix. Following deposition (black) and following photolysis at 313 nm (red).

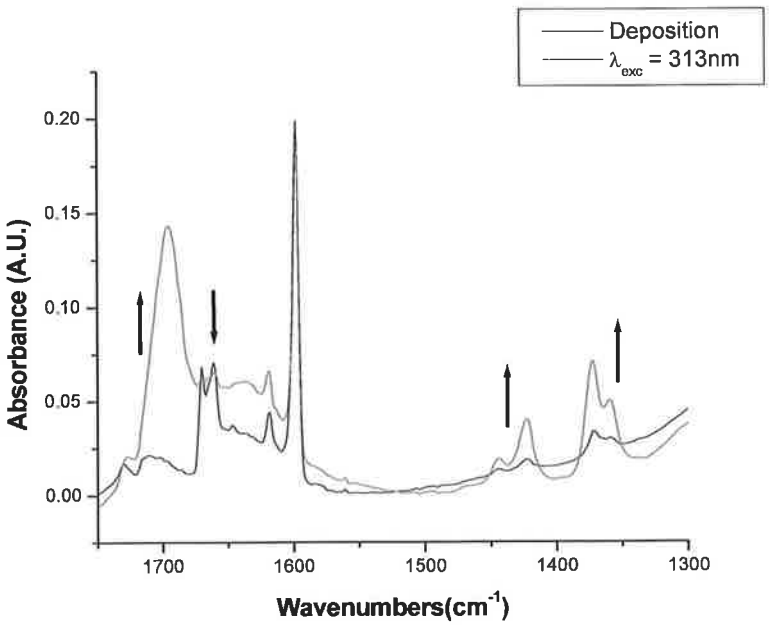

Figure 12 Overlay spectrum in ketone region prior to photolysis (black) and following photolysis at 313 nm (red).

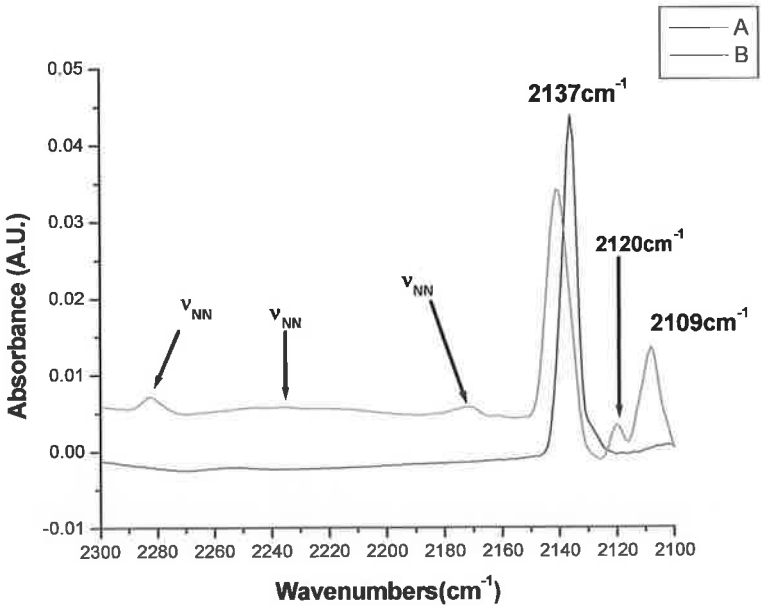

Figure 13 Overlay spectrum following deposition (black) and following photolysis at 313 nm (Red). On photolysis at 313 nm two product bands are generated at 2120 and 2109 cm^{-1}, while two ν_{NN} bands are generated at 2170 and 2283 cm^{-1}

UV Irradiation (λ_{exc} = 297 nm, 95 mins) produced an increase in intensity of the product bands and a weak product N_2 stretching vibration at 2236 cm^{-1} while the parent bands and the product bands at 1991 & 1978 cm^{-1} decreased in intensity. This indicates a further increase in intensity of both the $CF_3Mn(CO)_4N_2$ and $CF_3COMn(CO)_3(N_2)_2$ species respectively with concomitant loss of both the parent species and the radical species at this wavelength. Subsequent UV irradiation at λ_{exc} = 289 nm for 80 mins resulted in a further increase in intensity of the product bands due to both $CF_3COMn(CO)_4N_2$ and $CF_3COMn(CO)_3(N_2)_2$ with an associated decrease in intensity of the parent and radical bands.

Visible irradiation at 405 nm of the acetylated $CF_3COMn(CO)_5$ in an N_2 matrix resulted in a further increase in intensity of the bands due to the N_2 disubstituted species $CF_3COMn(CO)_3(N_2)_2$ while those due to the parent species and $CF_3COMn(CO)_4N_2$ continued to decrease in intensity. Broadband irradiation at >400 nm produced a further increase in intensity of the bands due to $CF_3COMn(CO)_3(N_2)_2$ with complete loss of those due to $CF_3COMn(CO)_4N_2$. Regeneration of the parent bands was also observed indicating that reversal of the phortoreaction must take place on irradiation at a wavelength higher than 405 nm.

2.4.2.3. Photolysis of $CF_3COMn(CO)_5$ in a 2% CO-doped CH_4 matrix

On deposition of $CF_3COMn(CO)_5$ in a 2% CO-doped methane matrix at 20 K carbonyl bands were observed at 2071, 2042, 2037, 2022 and 1670 cm^{-1}. Photolysis at 334 nm for 30 mins resulted in an increase in intensity of the parent band at 2072 cm^{-1} and a decrease in intensity of those at 2037 and 2020 cm^{-1} with concomitant production of 2055, 2017, 2003, and 2138 cm^{-1} due to generation of a tetracarbonyl species *cis*-$CF_3COMn(CO)_4$[52] and free CO respectively. A product band generated at 1984 cm^{-1} is tentatively assigned to generation of the *trans*-isomer of the coordinatively unsaturated tetracarbonyl species $CF_3COMn(CO)_4$ resulting in labilisation of the CO *trans* to the CF_3CO moiety.

On changing the excitation wavelength to 313 nm and 297 nm irradiation produced two new photoproducts - the $^{\bullet}Mn(CO)_5$ radical with bands at 1972, 1988 and 2101 cm^{-1} and the coordinatively unsaturated tetracarbonyl $CF_3Mn(CO)_4$ with bands at 2006 and 2045 cm^{-1}, formation of the latter species further suggested by an increase in intensity of the free CO band at 2138 cm^{-1}. Concomitantly a further increase in intensity is observed for *cis*-$CF_3COMn(CO)_4$ while the ketonic vibrational band at 1670 cm^{-1} disappeared indicating complete loss of the parent acetylated species $CF_3COMn(CO)_5$.

Irradiation in the visible region at 405 nm resulted in loss of the bands attributed to the $^{\bullet}Mn(CO)_5$ radical with a concomitant generation of bands at 2117, 2060 and 1984 cm^{-1} which are tentatively assigned to generation of $CF_3Mn(CO)_5$. Broadband irradiation ($\lambda > 400$ nm, 60 mins) resulted in the further increase in intensity of the bands at, 2064, 2006, 2137 cm^{-1} and of the parent bands at 2045 and 2020 cm^{-1}. On prolonged irradiation at $\lambda > 400$ nm product bands were produced at 1991, 1976 cm^{-1}.

2.4.2.4. Photolysis of $CF_3COMn(CO)_5$ in a 10% CO-doped CH_4 matrix

Following photolysis in a 2% CO-doped methane matrix the percentage of carbon monoxide present in the methane matrix was increased in order to increase the probability of methyl migration (CO insertion) taking place. The IR spectrum of $CF_3COMn(CO)_5$ in a 10% CO-doped methane matrix is shown in Figure 14.

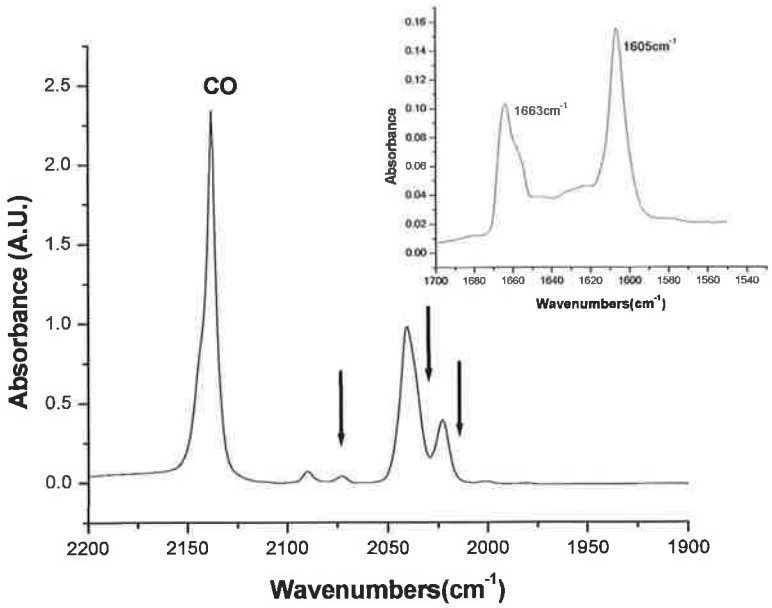

Figure 14 IR spectrum (carbonyl region) of $CF_3COMn(CO)_5$ in a 10% CO-doped CH_4 matrix following deposition. Inset shows two ketonic stretching vibrations at 1605 cm^{-1} and 1663 cm^{-1} due to the acyl moiety of the parent species.

On deposition of $CF_3COMn(CO)_5$ in a 10% CO-CH_4 matrix ν_{CO} bands were observed at 2073, 2040 and 2022 cm^{-1} as well as an acyl CO band at 1664 cm^{-1}. Photolysis (λ_{exc} = 313 nm, 140 mins) resulted in a decrease in the intensity of the parent bands with simultaneous generation of the $^{\bullet}Mn(CO)_5$ radical species and the coordinatively unsaturated product $CF_3Mn(CO)_4$ (Figure 15) and loss of the ketonic CO stretching band at 1664 cm^{-1} on extended irradiation (Figure 16).

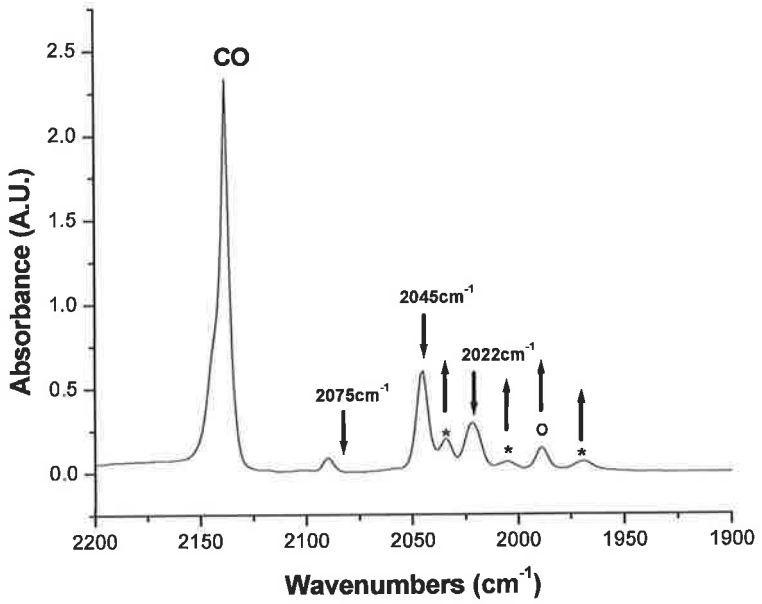

Figure 15 IR spectrum in 10% CO-doped CH_4 matrix following extended photolysis at 313 nm. The parent band at 2075 cm^{-1} has disappeared on extended photolysis. Product bands due to $CF_3COMn(CO)_4$ (*) and the radical $^{\bullet}Mn(CO)_5$ (o) are observed increasing in intensity.

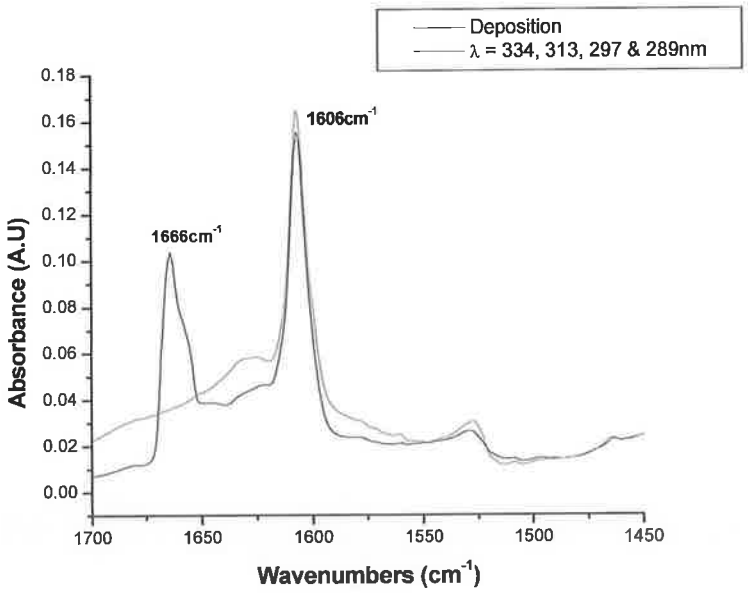

Figure 16 Overlay of ketone region of the IR vibrational spectrum of $CF_3COMn(CO)_5$ in a 10% CO-doped CH_4 matrix on initial deposition (black) and following monochromatic photolysis at λ = 334 nm, 313 nm, 297 nm and 289 nm (red). Acyl band at 1666 cm^{-1} disappeared on extended irradiation indicating loss of the $CF_3COMn(CO)_5$ parent species.

Photolysis at both 289 nm and 297 nm resulted in further depletion of the parent bands as well as a decrease in intensity of the product bands due to both the radical and tetracarbonyl species. UV photolysis (λ_{exc} = 405 nm, 30 mins) resulted in regeneration of parent bands at 2045 and 2021 cm^{-1} with a parallel decrease in intensity of the product band at 2033 cm^{-1}.

2.4.3. Photochemistry of (2-acetylphenyl-C,O)Mn(CO)$_4$

2.4.3.1. Photolysis of (2-acetylphenyl-C,O)Mn(CO)$_4$ in a methane matrix

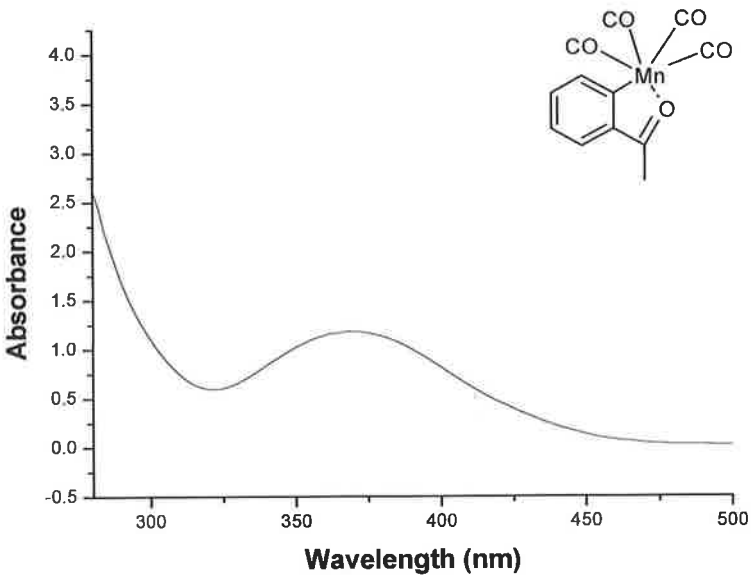

Figure 17 UV-Vis absorption spectrum of (2-acetylphenyl-C,O)Mn(CO)$_4$ in pantane

(2-acetylphenyl-C,O)Mn(CO)$_4$ is a bright yellow coloured crystalline solid with a UV-Vis spectrum exhibiting a high energy band at approximately 280 nm and a broad low energy band at 370 nm in pentane solution

On deposition of (2-acetylphenyl-C,O)Mn(CO)$_4$ in a methane matrix three ν_{co} bands were observed at 2085, 1995 and 1944 cm^{-1} and a ketonic CO band at 1590 cm^{-1}.
UV irradiation at 405nm for 60 mins resulted in a decrease in intensity of the parent bands at 2085, 1995 and 1944 cm^{-1} with associated generation of product bands at 2030 and 1922 cm^{-1}, which grew in at the same rate. A third weak band generated at 1903 cm^{-1} may also be due to (2-acetylphenyl-C,O)Mn(CO)$_3$. No change is observed in the ketone CO band at 1590 cm^{-1}. As illustrated in Figure 18 photolysis at 365nm for 90 mins resulted in a further decrease in intensity of the parent bands and a continued increase in the intensity of the product bands at 2030, 1923 and 1903 cm^{-1}.

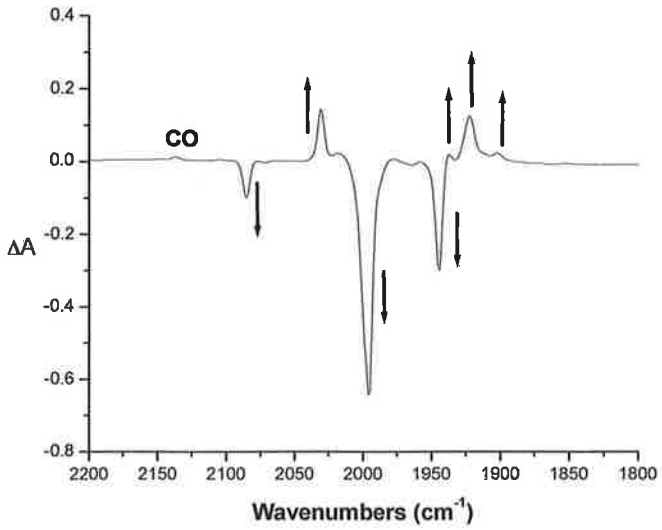

Figure 18 Difference spectrum of (2-acetylphenyl)$Mn(CO)_4$ following deposition and following monochromatic photolysis at 405 nm and 365 nm.

Subsequent broadband photolysis ($\lambda > 550$ nm, 20 mins) resulted in regeneration of the parent bands and a decrease in intensity of the product bands at 2030 and 1923 cm^{-1} indicating loss of the (2-acetylphenyl-C,O)$Mn(CO)_3$ photoproduct. As expected regeneration of the parent bands is coupled with a decrease in intensity of the free CO band at 2138cm^{-1}, indicating re-coordination of the CO ligand.

2.4.3.2. Photolysis of (2-acetylphenyl-C,O)Mn(CO)$_4$ in a N_2 matrix

On deposition of (2-acetylphenyl-C,O)Mn(CO)$_4$ in a N_2 matrix three carbonyl bands were observed at 2087, 1999 and 1948 cm^{-1} and a ketonic CO band at 1590 cm^{-1}. Monochromatic irradiation at 405 nm for 80 mins and 365 nm for 60 mins resulted in bleaching of the parent bands, CO loss as indicated by generation of a band a 2138 cm^{-1} and associated generation of the N_2 substituted tricarbonyl (2-acetylphenyl-C,O)Mn(CO)$_3$N$_2$ with a ν_{NN} band at 2261 cm^{-1} and ν_{co} bands at 2036, 1929 and 1907 cm^{-1}.

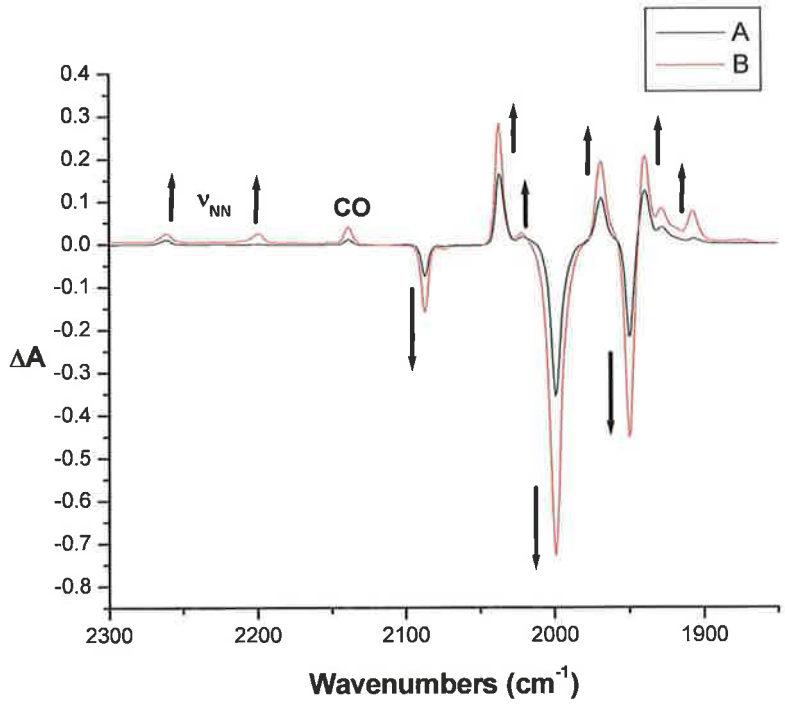

Figure 19 Overlay of two difference spectra, (A) initial photolysis at 405 nmdeposition spectrum and (B) following photolysis at 405 nm and 365 nm.

On extended photolysis at 405 nm weak bands were also observed at 2199 (ν_{NN}), 2021, 1968 & 1938 cm^{-1} suggesting generation of the bis N_2 species. (2-acetylphenyl-C,O)Mn(CO)$_2$(N$_2$)$_2$. This is outlined below in Scheme 15.

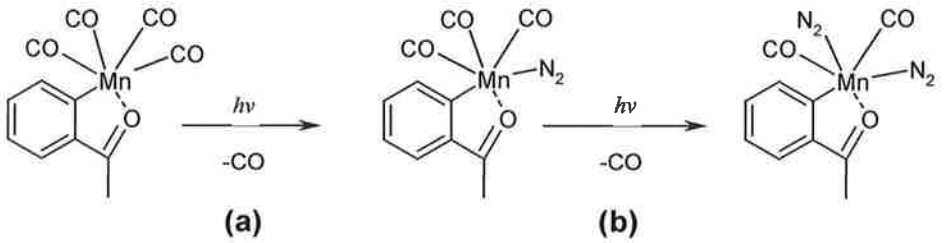

Scheme 15 Coordination of dinitrogen onto two vacant sites following CO loss on photolysis after 405 nm irradiation for (a) 30 mins and (b) 80mins

Subsequent photolysis at 313 nm for 60 mins produced a decrease in intensity for all bands except the product bands at 1929 and 1907 cm^{-1} and parent band at 2087 cm^{-1} which continued to increase in intensity.

2.4.3.3. Photolysis of (2-acetylphenyl-C,O)$Mn(CO)_4$ in a 2% CO-doped CH_4 matrix

On deposition of (2-acetylphenyl-C,O)$Mn(CO)_4$ in a 2% CO-CH_4 matrix resulted in generation of three carbonyl bands at 2085, 1995 & 1944 cm^{-1} as well as a ketonic CO band at 1590 cm^{-1}.

As shown in Figure 20 monochromatic UV irradiation of (2-acetylphenyl-C,O)$Mn(CO)_4$ at 405 nm or 365 nm in a 2% CO-doped methane matrix resulted in bleaching of the parent bands with parallel generation of the tricarbonyl product (2-acetylphenyl-C,O)$Mn(CO)_3$ as suggested by an increase in intensity of the free CO band at 2138 cm^{-1} and generation of product bands at 2031, 1923 and 1901 cm^{-1}. The generation of weak bands at 1940 and 1967 cm^{-1} suggest formation of the dicarbonyl (2-acetylphenyl-C,O)$Mn(CO)_2$ as a minor product (Figure 21).

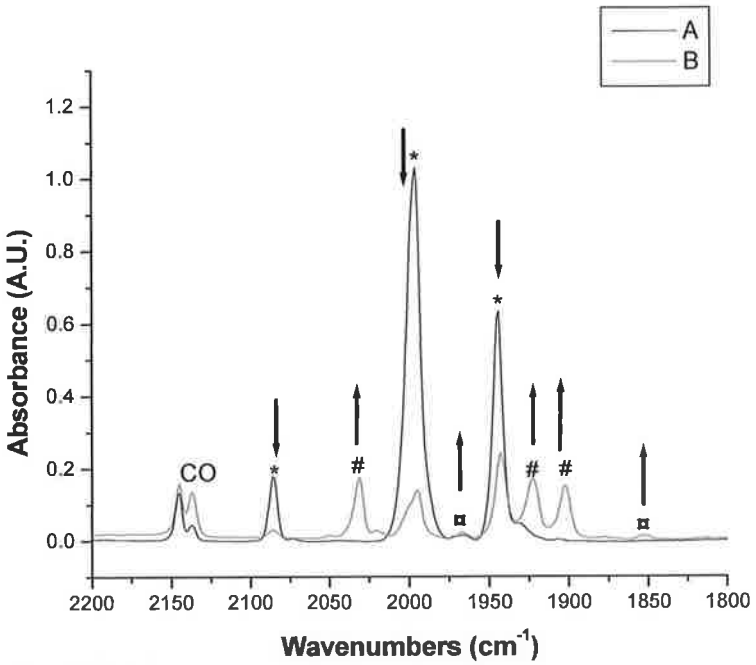

Figure 20 Overlay of IR vibrational spectra of (2-acetylphenyl-C,O)$Mn(CO)_4$ in a 2% CO-CH_4 matrix following Deposition (A, Black) and following photolysis at 405 nm, 365 nm and 313 nm (B, Red). Depleting parent bands are indicated by *, while bands due to the tricarbonyl (2-acetylphenyl-C,O)$Mn(CO)_3$ are indicated by #. Other carbonyl bands indicated by ¤ may be due to the generation of a dicarbonyl species.

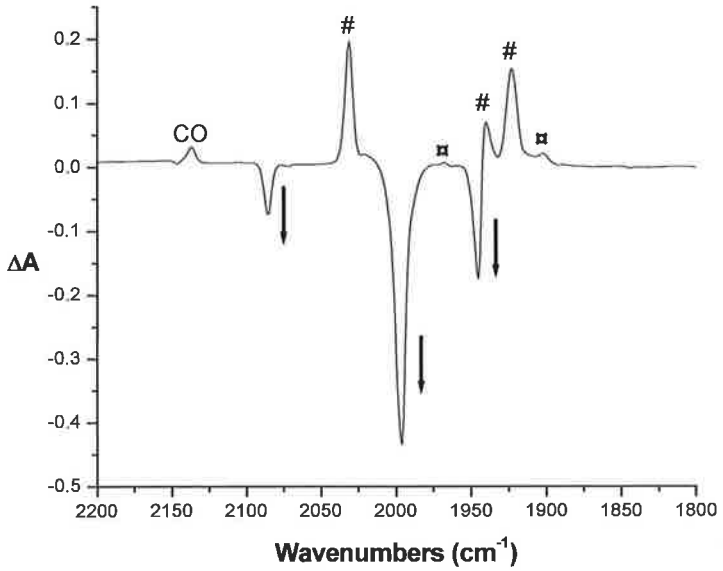

Figure 21 IR Difference spectrum of (2-acetylphenyl-C,O)Mn(CO)$_4$ in a 2% CO-CH$_4$ matrix following irradiation at 450 nm and subsequently 365 nm. Those bands indicated by # are due to generation of a tricarbonyl species while those indicated by ¤ may be due to a dicarbonyl species

Broadband photolysis (λ > 520 nm, 60 mins) resulted in regeneration of the parent bands and depletion of the product bands at 2137, 2031, 1922 and 1901 cm^{-1} indicating loss of free CO and (2-acetylphenyl-C,O)Mn(CO)$_3$ respectively. The product bands at 1940 and 1967 cm^{-1} due to (2-acetylphenyl-C,O)Mn(CO)$_2$ produced on 405 nm photolysis continued to increase in intensity. Subsequent photolysis at λ > 410 nm for 90 mins resulted in regeneration of the parent bands and a decrease in intensity depletion of free CO and the bands of both the tricarbonyl and dicarbonyl compounds.

2.4.3.4. Photolysis of (2-acetylphenyl-C,O)Mn(CO)$_4$ in a 10% CO-doped CH_4 matrix

Following photolysis of (2-acetylphenyl-C,O)Mn(CO)$_4$ in a 2% CO doped methane matrix the experiment was repeated using a 10% CO doped methane matrix. As observed in the previous experiments deposition gave rise to 4 IR active bands at 2085, 1995, 1944 and 1590 cm^{-1}. Irradiation at 405 nm produced three product bands at 2030, 1923 and 1902 cm^{-1} as well as an increase in intensity of the free CO band at 2138 cm^{-1} indicating formation of the tricarbonyl (2-acetylphenyl-C,O)Mn(CO)$_3$ as observed in both the methane and N_2 matrices. 365 nm irradiation resulted in further loss of the parent species and further generation of the previously mentioned tricarbonyl (2-acetylphenyl-C,O)Mn(CO)$_3$. Prolonged irradiation at this wavelength produced two very weak bands at 1938 and 1966 cm^{-1} assigned to the dicarbonyl (2-acetylphenyl-C,O)Mn(CO)$_2$ (Figure 22).

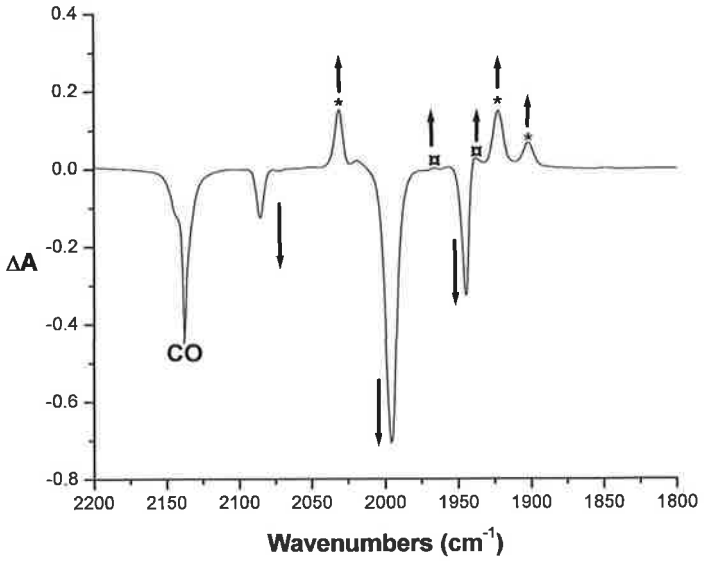

Figure 22 Difference spectrum between initial deposition and following photolysis at 405 nm, 365 nm and 313 nm. Bands due to the tricarbonyl (2-acetylphenyl-C,O)Mn(CO)$_3$ are indicated by * , while those due to the minor product (2-acetylphenyl-C,O)Mn(CO)$_2$ are indicated by ¤.

As observed in the 2% CO doped methane matrix >520 nm irradiation resulted in regeneration of the parent species, continued generation of (2-acetylphenyl-C,O)Mn(CO)$_2$ and depletion of the bands of (2-acetylphenyl-C,O)Mn(CO)$_3$.

Subsequent broadband photolysis at $\lambda_{exc} > 410$ nm for 90 mins resulted in an increase in intensity of both the parent bands the bands due to the tricarbonyl product.

2.5. Quantum chemical calculations

2.5.1. Calculations on compounds of the type $Mn(CO)_5L$

2.5.1.1. Geometry Optimisation

The structures of compounds of the type $Mn(CO)_5L$, where L = CF_3CO, CF_3 and CHF_2 were optimised using the B3LYP/LANL2DZ level of theory. Geometry optimisation was initiated at the RHF/STO-3G theory level with the size of the basis set increased incrementally to LANL2DZ followed by further optimisation with this basis set and the B3LYP method. As is evident from Figure 23 in each case the $Mn(CO)_5$ moiety was found to adopt a C_{4V} geometry as proposed in the literature.[24,53]

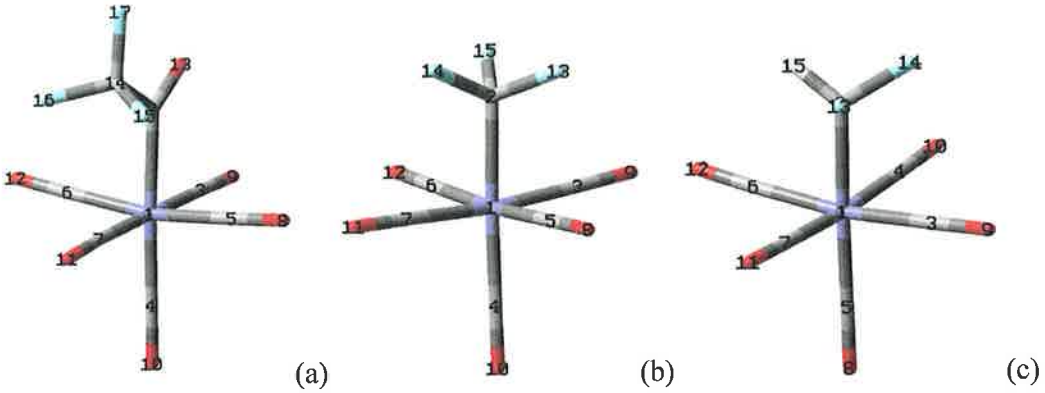

Figure 23 Geometry optimised structures of (a) $CF_3COMn(CO)_5$, (b) $CF_3Mn(CO)_5$ and (c) $CHF_2Mn(CO)_5$ attained using the B3LYP/LANL2DZ level of theory

The calculated bond lengths (Å) and bond angles (°) for the optimised structures of $CF_3COMn(CO)_5$, $CF_3Mn(CO)_5$ and $CHF_2Mn(CO)_5$ shown in Figure 23 are outlined in Table 2, Table 3, Table 4 respectively. For each compound the data is compared for the different basis sets and model chemistries used and against data from the literature containing both theoretical[37,43] and experimental values[54] for similar compounds of the type $Mn(CO)_5L$. All three compounds share the same geometry and point group (see above) and have similar values for bond lengths and bond angles. This may be partially attributed to the fact that the optimised structures were generated with the same theoretical approach and the same model chemistries and basis sets were used. The majority of the bond length and bond angle differences present are due to the varying substituent ligands L, where L = CF_3CO, CF_3 and CHF_2.

	RHF/ 3-21G	RHF/ LANL2DZ	B3LYP/ LANL2DZ	Literature[37, 43, 54]	Deviation % B3LYP - Literature
Bond lengths					
Mn1-C2	2.076	2.211	2.078	2.056	1.07
Mn1-C5	1.957	2.028	1.853	1.874, 1.864	1.12, 0.59
Mn1-C6	1.957	2.028	1.853	1.874, 1.864	1.12, 0.59
Mn1-C3	2.068	2.180	1.869	1.874, 1.864	0.26, 0.26
Mn1-C7	2.007	2.159	1.864	1.874, 1.864	0.53, 0
Mn1-C4	1.967	2.104	1.841	1.874, 1.864	1.76, 1.23
All equatorial C≡O	1.124	1.131	1.166	1.143, 1.157	2.01, 0.77
C4-O10	1.129	1.130	1.171	1.143, 1.160	2.44, 0.94
C2-O13	1.225	1.234	1.239		
C2-C14	1.522	1.559	1.571		
C14-F15/16	1.364	1.386	1.408	1.370	2.77
C14-F17	1.337	1.358	1.382	1.370	0.87
Bond angles					
C4-Mn1-C3	89.8	90.3	90.2	92.1, 97.1	2.06, 7.10
C4-Mn1-C5	99.4	93.7	95.2	92.1, 97.1	3.36, 1.95
C4-Mn1-C6	99.4	93.7	95.2	92.1, 97.1	3.36, 1.95
C4-Mn1-C7	96.5	90.3	89.1	92.1, 97.1	3.25, 8.23
C3-Mn1-C6	89.7	89.8	90.1	89.1	1.12
C6-Mn1-C7	89.2	90.2	89.9	89.1	0.89
C7-Mn1-C5	89.2	90.2	89.9	89.1	0.89
C5-Mn1-C3	89.7	89.8	90.1	89.1	1.12
Mn1-C3-O9	178.5	179.2	178.6	177.3	0.73
Mn1-C5-O8	171.3	175.9	178.9	177.3	0.90
Mn1-C6-O12	171.3	175.8	178.9	177.3	0.90
Mn1-C7-O11	179.9	178.9	175.7	177.3	0.90
Mn1-C4-O10	176.5	179.5	179.6	177.3	1.29
Mn1-C2-O13	121.7	122.5	124.9		
O13-C2-C14	116.1	114.1	115.9		
C2-C14-F15	108.5	109.1	110.2		
C2-C14-F16	108.5	109.1	110.2		
C2-C14-F17	117.4	118.5	115.0		
F16-C14-F17	108.3	106.9	107.3		
F15-C14-F16	105.2	105.4	106.5		
F15-C14-F17	108.3	106.9	107.3		

Table 2 Comparison of selected bond lengths (Å) and bond angles (°) for $CF_3COMn(CO)_5$ on increasing the size of the basis set with literature values[37, 43, 54]

	RHF/ 3-21G	RHF/ LANL2DZ	B3LYP/ LANL2DZ	Literature[37, 43, 54]	Deviation % B3LYP - Literature
Bond lengths					
Mn1-C2	2.023	2.136	2.075	2.012, 2.056	3.13, 0.92
Mn1-C5	1.942	2.050	1.863	1.864	0.05
Mn1-C6	4.170	2.050	1.863	1.864	0.05
Mn1-C3	2.015	2.047	1.862	1.864	0.10
Mn1-C7	2.014	2.050	1.862	1.864	0.10
Mn1-C4	1.954	2.005	1.843	1.865, 1.874	1.17, 1.65
C3-O9	1.123	1.130	1.165	1.157, 1.143	0.69, 1.92
C4-O10	1.128	1.133	1.171	1.160, 1.143	0.94, 2.44
C5-O8	1.130	1.130	1.165	1.157, 1.143	0.69, 1.92
C6-O12	1.126	1.130	1.165	1.157, 1.143	0.69, 1.92
C7-O11	1.123	1.130	1.165	1.157, 1.143	0.69, 1.92
C2-F13	1.355	1.415	1.428	1.370	4.23
C2-F14	1.355	1.409	1.422	1.370	3.79
C2-F15	1.517	1.405	1.428	1.370	4.23
Bond angles					
C4-Mn1-C3	96.09	93.30	92.77	97.10, 92.10	4.45. 0.72
C4-Mn1-C5	105.97	93.00	92.54	97.10, 92.10	4.69, 0.47
C4-Mn1-C6	63.18	93.00	92.54	97.10, 92.10	4.69, 0.47
C4-Mn1-C7	95.3	93.08	92.67	97.10, 92.10	4.56, 0.61
C3-Mn1-C6	134.39	89.95	90.37	89.10	1.42
C6-Mn1-C7	57.27	89.70	89.48	89.10	0.42
C7-Mn1-C5	91.37	89.70	89.38	89.10	0.31
C5-Mn1-C3	91.53	89.95	90.28	89.10	1.32
Mn1-C3-O9	175.51	177.43	179.80	177.30	1.41
Mn1-C5-O8	175.30	178.01	179.41	177.30	1.19
Mn1-C6-O12	173.31	178.01	179.47	177.30	1.22
Mn1-C7-O11	175.75	178.27	179.55	177.30	1.26
Mn1-C4-O10	171.31	179.78	179.67	177.30	1.33
Mn1-C2-F13	127.02	114.71	114.09	114.00	0.07
Mn1-C2-F14	126.79	117.58	116.24	114.00	1.96
Mn1-C2-F15	71.15	114.71	114.00	114.00	0
F13-C2-F14	106.17	102.72	103.78		
F13-C2-F15	101.72	102.36	103.42		
F14-C2-F15	101.72	102.72	103.78		

Table 3 Comparison of selected bond lengths (Å) and bond angles (°) for $CF_3COMn(CO)_5$ on increasing the size of the basis set with literature values[37, 43, 54]

	RHF/ 3-21G	RHF/ LANL2DZ	B3LYP/ LANL2DZ	Literature[37,43,54]	Deviation % B3LYP-Literature
Bond lengths					
Mn1-C2	2.122	2.148	2.096	2.023, 2.056	3.60, 1.94
Mn1-C5	1.959	1.993	1.840	1.864	1.28
Mn1-C6	1.935	2.009	1.843	1.865, 1.874	1.18, 1.65
Mn1-C3	2.036	2.050	1.860	1.865, 1.874	0.27, 0.74
Mn1-C7	1.996	2.040	1.857	1.865, 1.874	0.42, 0.90
Mn1-C4	1.996	2.040	1.857	1.865, 1.874	0.42, 0.90
C3-O9	1.123	1.130	1.166	1.143, 1.157	2.01, 0.77
C4-O10	1.124	1.131	1.167	1.143, 1.157	2.09, 0.86
C5-O8	1.130	1.134	1.172	1.160, 1.143	1.03, 2.53
C6-O12	1.129	1.134	1.170	1.143, 1.157	2.36, 1.12
C7-O11	1.124	1.131	1.167	1.143, 1.157	2.09, 0.86
C2-F13	1.431	1.454	1.447	1.370	5.62
C2-F14	1.431	1.454	1.447	1.370	5.62
C2-H15	1.080	1.082	1.096		
Bond angles					
C5-Mn1-C3	95.32	93.66	94.13	97.10, 92.10	3.05, 2.20
C5-Mn1-C4	96.99	93.29	92.75	97.10, 92.10	4.47, 0.70
C5-Mn1-C6	96.99	94.75	94.16	97.10, 92.10	3.02, 2.23
C5-Mn1-C7	96.99	93.29	92.75	97.10, 92.10	4.47, 0.70
C3-Mn1-C4	87.89	89.40	89.87	89.10	0.86
C3-Mn1-C7	87.88	89.40	89.87	89.10	0.86
C7-Mn1-C6	89.90	90.11	89.73	89.10	0.70
C6-Mn1-C4	89.90	90.11	89.72	89.10	0.69
Mn1-C3-O9	177.22	177.62	179.40	177.30	1.18
Mn1-C4-O10	175.46	177.38	179.51	177.30	1.24
Mn1-C5-O8	178.44	179.86	179.89	177.30	1.46
Mn1-C6-O12	167.82	174.05	177.89	177.30	0.33
Mn1-C7-O11	175.46	177.38	179.51	177.30	1.24
Mn1-C2-F13	105.67	109.07	111.50	114.00	2.19
Mn1-C2-F14	105.67	109.07	111.50	114.00	2.19
Mn1-C2-H15	129.77	127.73	118.54		
F13-C2-F14	103.09	102.42	104.07		
F13-C2-H15	104.92	102.85	104.99		
F14-C2-H15	104.92	102.85	105.00		

Table 4 Comparison of selected bond lengths (Å) and bond angles (°) for $CHF_2Mn(CO)_5$ on increasing the size of the basis set with literature values[37, 43, 54]

Following geometry optimisation of the above structures a vibrational analysis of the ground state electronic structure was undertaken. The frequency calculation was carried out on the B3LYP/LANL2DZ optimised structures to investigate whether any negative frequencies were present, which would indicate that the geometry optimised structure was not at a minimum on the potential energy surface.

For each complex $CF_3COMn(CO)_5$, $CF_3Mn(CO)_5$ and $CHF_2Mn(CO)_5$ no negative frequencies were found indicating that the geometry optimised structures obtained were at the energy minimum. Each complex which is of the type $Mn(CO)_5L$, has C_{4v} symmetry and as such is predicted to have 3 IR active carbonyl bands – $2A_1$ and E. The E mode is expected to be very strong while both A_1^1 and A_1^2 are expected to be weak bands. The IR spectrum of $CF_3COMn(CO)_5$ is also predicted to have an acyl CO stretch in the region 1600-1700 cm^{-1}. In

Table 5, Table 6, and Table 7 the predicted IR active bands of the three complexes optimised at the B3LYP/LANL2DZ level of theory are compared to the experimental values obtained in this study. For both $CF_3COMn(CO)_5$ and $CF_3Mn(CO)_5$ the calculated IR stretching frequencies are scaled with respect to the experimental values obtained. In the case of $CHF_2Mn(CO)_5$, as no experimental data is available the calculated IR stretching frequencies are scaled with respect to literature values[47(b)].

IR active bands (Calculated)	IR active bands (experimental) [$CHCl_3$]	IR active bands (Literature) [CCl_4][a]	Assignment
1901	1652	1669	symmetric C=O stretch
2150	2040	2047	asymmetric C≡O stretch (E mode)
2156	2073	2076	asymmetric C≡O stretch (A_1 mode)
2202	2133	2138	asymmetric C≡O stretch (A1 mode)

Table 5 Comparison of IR active frequencies of $CF_3COMn(CO)_5$ calculated at the B3LYP/LANL2DZ theory level with those observed experimentally in chloroform. Calculated values have been corrected by an empirical factor of 1.021. [a] See reference 47(a)

IR active bands (Calculated)	IR active bands (experimental) [Pentane]	IR active bands (Literature) [C_6H_{12}][a]	Assignment
2040	2021	2025	asymmetric C≡O stretch (axial C≡O)
2059[b]	2042	2050	asymmetric C≡O stretch (E mode)
2061			asymmetric C≡O stretch (E mode)
2076	2070	2144	asymmetric C≡O stretch (eq. C≡O's)

Table 6 Comparison of IR active frequencies of $CF_3Mn(CO)_5$ calculated at the B3LYP/LANL2DZ theory level with those observed experimentally in pentane. Calculated values have been corrected by an empirical factor of 1.021.[a] See reference 47(a). [b]Splitting of the E vibrational mode is observed in the theoretical geometry optimised model

IR active bands (Calculated)	IR active bands (Literature) [Heptane][c]	Assignment
2028	2010	asymmetric C≡O stretch (axial C≡O)
2039	2029	asymmetric C≡O stretch (E mode)
2067	2062	asymmetric C≡O stretch (B_1 mode)
2132	2127	asymmetric C≡O stretch (A_1 mode)

Table 7 Comparison of IR active frequencies of $CHF_2Mn(CO)_5$ calculated at the B3LYP/LANL2DZ theory level with literature values in heptane. Literature values have been corrected by an empirical factor of 1.021.[c] See reference 47(b).

2.5.1.2. Calculation of the ground state electronic structure for $Mn(CO)_5L$

Following the prerequisite ground state geometry optimisations of $CF_3COMn(CO)_5$, $CF_3Mn(CO)_5$ and $CHF_2Mn(CO)_5$ at the B3LYP/LANL2DZ level of theory the ground state electronic structures for each of the complexes were calculated and the highest occupied (HOMO) and lowest virtual (LUMO) molecular orbitals were examined in order to provide a framework for the subsequent Time Dependent DFT (TDDFT) calculations. For each complex the valence orbitals are plotted according to their energies. Such valence orbitals are very important in that they play an active role in the determination of the electronic excitations and electronic character of the particular complex. The assignment of the type of molecular orbital was made on the basis of its relative composition and by inspection of the three dimensional representation. In each case the compositional assignment is relative in that the majority are of mixed character with a particular MO giving the major compositional contribution. Table 8 lists the most important molecular orbitals for each of the studies complexes. Five occupied MO's (HOMO to H-4) and nine unoccupied or virtual MO's (LUMO to L+8).

MO	$CF_3COMn(CO)_5$	$CF_3Mn(CO)_5$	$CHF_2Mn(CO)_5$
L+8	-1.33	-1.46	-1.22
L+7	-2.06	-1.51	-1.31
L+6	-2.17	-2.16	-1.85
L+5	-2.26	-2.18	-1.89
L+4	-2.28	-2.21	-1.96
L+3	-2.50	-2.34	-2.06
L+2	-2.55	-2.57	-2.31
L+1	-2.62	-2.59	-2.36
LUMO	-2.68	-2.75	-2.45
HOMO	-7.55	-8.69	-8.05
H-1	-8.63	-8.70	-8.39
H-2	-8.65	-8.94	-8.39
H-3	-8.93	-8.95	-8.70
H-4	-11.39	-10.83	-10.54

Table 8 The molecular orbitals of $CF_3COMn(CO)_5$, $CF_3Mn(CO)_5$ and $CHF_2Mn(CO)_5$ and their energies (eV). HOMO: Highest occupies molecular orbital. LUMO: Lowest unoccupied molecular orbital.H-1 is HOMO-1 and L+1 is LUMO+1

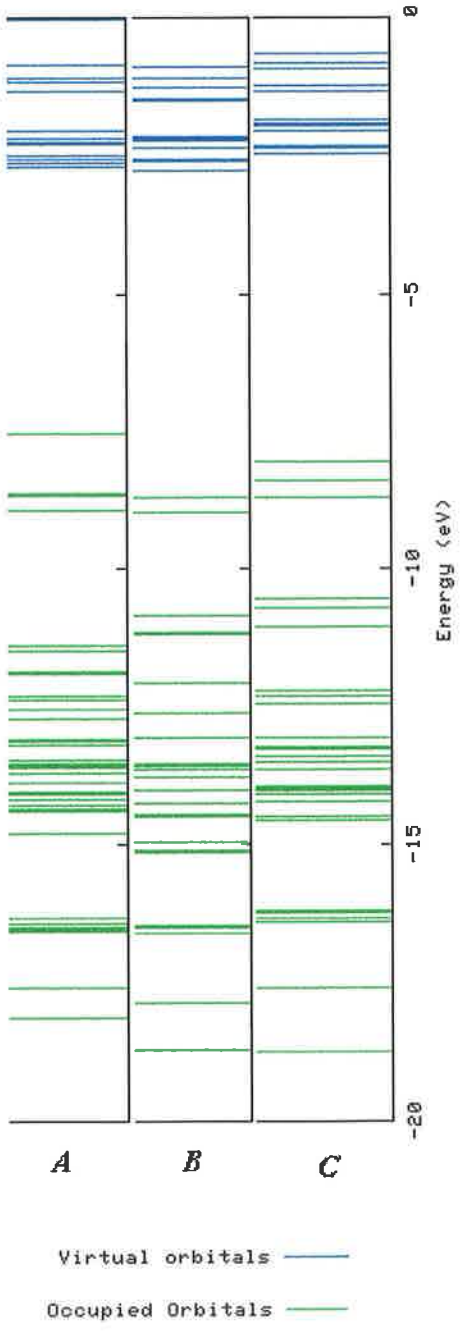

Figure 24 Energy level diagram of (A) $CF_3COMn(CO)_5$, (B) $CF_3Mn(CO)_5$ and (C) $CHF_2Mn(CO)_5$. Extracted from Density of states (DOS) diagram generated by the GaussSum 2.0 programme[55]

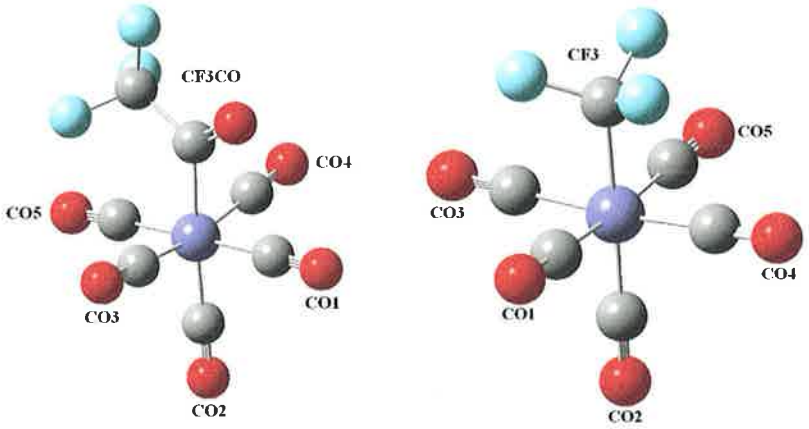

Figure 25 Geometry optimised structure of $CF_3COMn(CO)_5$ and $CF_3Mn(CO)_5$ indicating each of the groups contributing to the selected molecular orbitals

MO no.	Assignment	Energy (eV)	Mn %	CO1 %	CO2 %	CO3 %	CO4 %	CO5 %	CF_3CO %
71	L+4	-2.28	27	12	0	17	17	24	2
70	L+3	-2.50	9	46	2	3	3	27	11
69	L+2	-2.55	11	4	14	34	34	3	0
68	L+1	-2.62	7	29	1	13	13	26	10
67	LUMO	-2.68	6	3	9	7	7	7	61
66	HOMO	-7.55	19	1	2	2	2	0	74
65	H-1	-8.63	72	0	10	7	7	0	4
64	H-2	-8.65	75	6	9	0	0	8	2
63	H-3	-8.93	71	7	0	7	7	7	0
62	H-4	-11.39	1	0	0	5	5	0	88

Table 9 The contribution of manganese, each of the five CO orbitals and the CF_3CO orbitals in $CF_3COMn(CO)_5$ for each of the selected molecular orbitals

MO no.	Assignment	Energy (eV)	Mn %	CO1 %	CO2 %	CO3 %	CO4 %	CO5 %	CF_3 %
64	L+4	-2.21	11	35	23	19	11	1	0
63	L+3	-2.34	28	18	0	16	19	19	0
62	L+2	-2.57	8	7	8	38	34	5	0
61	L+1	-2.59	8	37	7	6	5	36	0
60	LUMO	-2.75	10	22	1	20	19	20	9
59	HOMO	-8.69	74	5	9	0	0	7	4
58	H-1	-8.70	75	0	9	7	7	0	2
57	H-2	-8.94	26	2	4	1	1	0	65
56	H-3	-8.95	70	7	0	7	7	7	2
55	H-4	-10.83	0	0	0	0	0	0	100

Table 10 The contribution of manganese, each of the five CO orbitals and the CF_3 orbitals in $CF_3Mn(CO)_5$ for each of the selected molecular orbitals

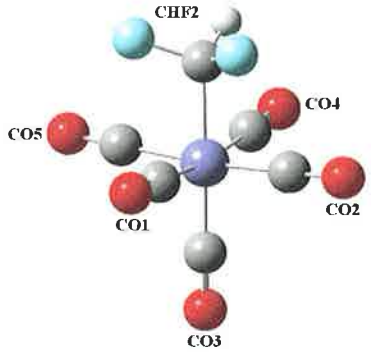

Figure 26 Geometry optimised structure of $CHF_2Mn(CO)_5$ indicating each of the groups contributing to the selected molecular orbitals

MO no.	Assignment	Energy (eV)	Mn %	CO1 %	CO2 %	CO3 %	CO4 %	CO5 %	CHF_2 %
60	L+4	-1.96	1	15	26	1	31	26	0
59	L+3	-2.06	28	27	17	2	9	17	0
58	L+2	-2.31	8	4	41	5	2	41	0
57	L+1	-2.36	8	29	2	5	53	2	0
56	LUMO	-2.45	8	16	20	2	25	20	10
55	HOMO	-8.05	22	1	1	4	2	1	69
54	H-1	-8.39	73	7	0	10	7	0	3
53	H-2	-8.39	74	0	7	9	0	7	3
52	H-3	-8.70	70	7	7	0	8	7	0
51	H-4	-10.54	0	0	2	0	0	2	96

Table 11 The contribution of manganese, each of the five CO orbitals and the CHF_2 orbitals in $CHF_2Mn(CO)_5$ for each of the selected molecular orbitals

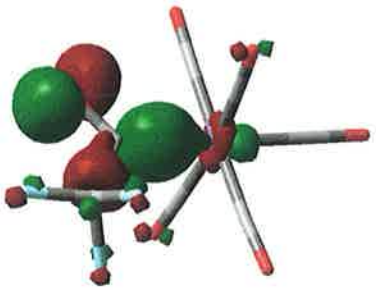

66 (O) – HOMO

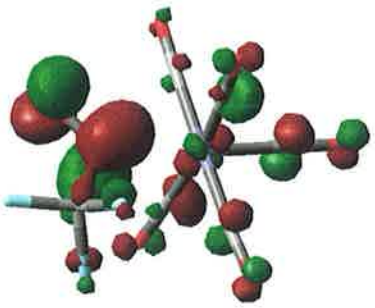

67(V) – LUMO

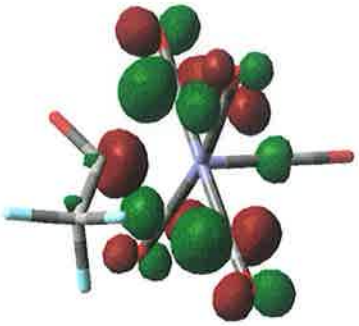

68 (V) – LUMO+1

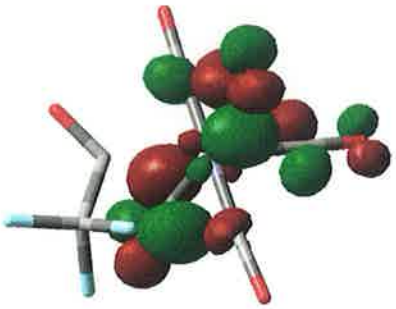

69 (V) – LUMO+2

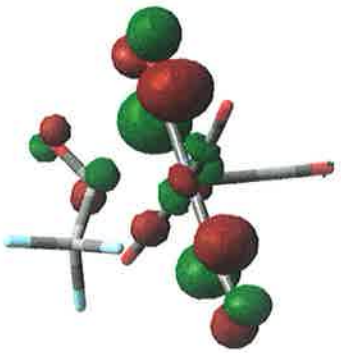

70 (V) – LUMO+3

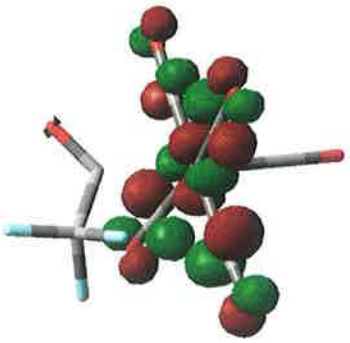

71 (V) – LUMO+4

Figure 27 Selected molecular orbitals of $CF_3COMn(CO)_5$

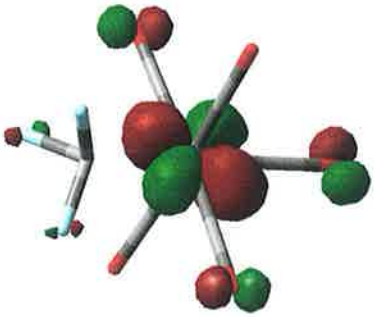

58 (O) – HOMO-1

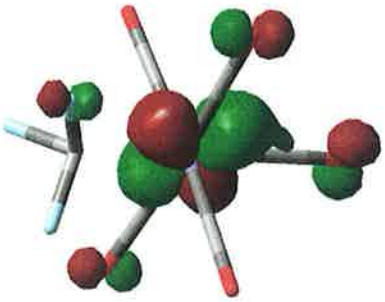

59(O) – HOMO

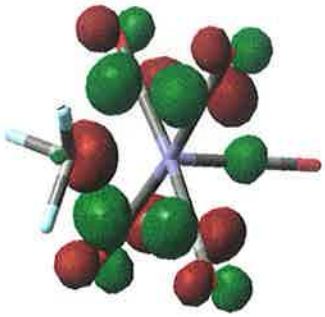

60 (V) – LUMO

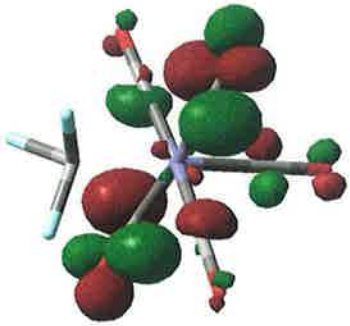

61 (V) – LUMO+1

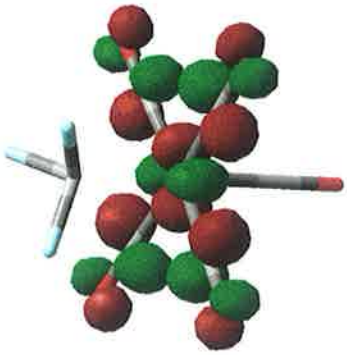

63 (V) – LUMO+3

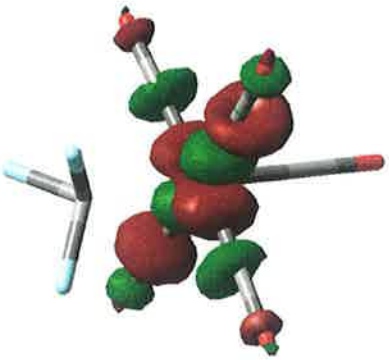

69 (V) – LUMO+9

Figure 28 Selected molecular orbitals for $CF_3Mn(CO)_5$

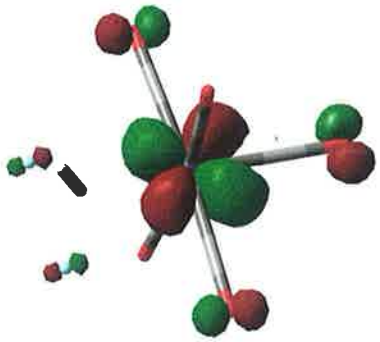

53 (O) – HOMO-2

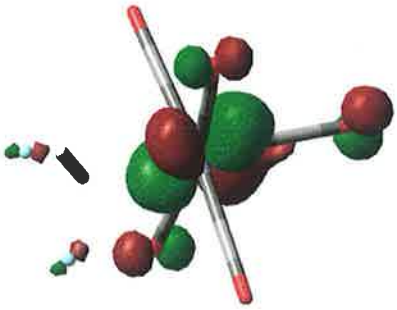

54 (O) – HOMO-1

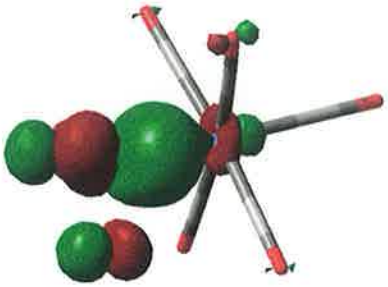

55 (O) – HOMO

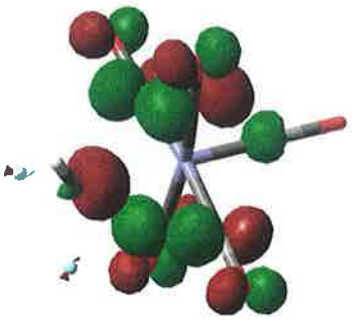

56 (V) – LUMO

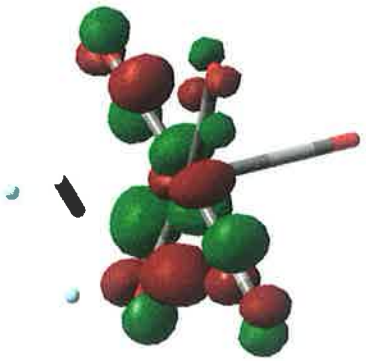

59 (V) – LUMO+3

65 (V) – LUMO+9

Figure 29 Selected molecular orbitals for $CHF_2Mn(CO)_5$

2.5.1.3. Time –dependent Density Functional Theory (TDDFT) calculations

State	E (eV) [λ (nm)[a]]	f [b]	$\psi_o \rightarrow \psi_v$ [c]	Predominant character [d]
1	3.2794 (378.07)	0.0006	HOMO->LUMO (77%), HOMO->L+3 (10%)	$\pi CO_{acyl} \rightarrow *\pi CO_{acyl}$ $\pi CO_{acyl} \rightarrow 2 \times *\pi CO_{cis}$
2	4.0525 (305.95)	0.0006	HOMO->L+2 (96%)	$\pi CO_{acyl} \rightarrow 2 \times *\pi CO_{cis}$, $*\pi CO_{trans}$
3	4.0577 (305.55)	0	HOMO->L+3 (75%), HOMO->L+4 (15%)	$\pi CO_{acyl} \rightarrow 2 \times *\pi CO_{cis}$ $\pi CO_{acyl} \rightarrow 4 \times *\pi CO_{cis}$, Mn-$d_{yz}$
4	4.1105 (301.63)	0.0186	HOMO->L+1 (82%) HOMO->L+6 (8%)	$\pi CO_{acyl} \rightarrow 4 \times *\pi CO_{cis}$ $\pi CO_{acyl} \rightarrow 4 \times *\pi CO_{cis}$
5	4.1822 (296.46)	0.0002	HOMO->L+3 (12%), HOMO->L+4 (78%)	$\pi CO_{acyl} \rightarrow 2 \times *\pi CO_{cis}$ $\pi CO_{acyl} \rightarrow 4 \times *\pi CO_{cis}$, Mn-$d_{yz}$
6	4.3302 (286.32)	0.0025	HOMO->L+5 (88%) HOMO->L+1 (3%)	$\pi CO_{acyl} \rightarrow 3 \times *\pi CO_{cis}$, $*\pi CO_{trans}$ $\pi CO_{acyl} \rightarrow 4 \times *\pi CO_{cis}$

Table 12 Selected calculated singlet excited states for $CF_3COMn(CO)_5$

State	E (eV) [λ (nm) [a]]	f [b]	$\psi_o \rightarrow \psi_v$ [c]	Predominant character [d]
1	4.4166 (280.73)	0	HOMO→L+3 (81%) H-1→L+9 (13%)	Mn-$d_{xy} \rightarrow *\pi CO_{cis}$, Mn-$d_{yz}$ Mn-$d_{xz} \rightarrow$ Mn-d_{yz}, p_y, p_z
2	4.4327 (279.70)	0	H-1→L+3 (83%) HOMO→L+9 (12%)	Mn-$d_{xz} \rightarrow *\pi CO_{cis}$, Mn-$d_{yz}$ Mn-$d_{xy} \rightarrow$ Mn-d_{yz}, p_y, p_z
3	4.581 (270.65)	0.0003	HOMO→L+1 (16%) HOMO→L+5 (16%) H-1→L+2 (11%)	Mn-$d_{xy} \rightarrow 2 \times *\pi CO_{cis}$, $*\pi CO_{trans}$ Mn-$d_{xy} \rightarrow *\pi CO_{trans}$, Mn-$d_{xz}$ Mn-$d_{xz} \rightarrow 2 \times *\pi CO_{cis}$, $*\pi CO_{trans}$
4	4.5953 (269.80)	0.0011	HOMO→L+9 (27%) HOMO→LUMO (16%) HOMO→L+10 (23%)	Mn-$d_{xy} \rightarrow$ Mn-$d_{x^2-y^2}$, p_y, p_z Mn-$d_{xy} \rightarrow *\pi CO_{cis}$ Mn-$d_{xy} \rightarrow$ Mn-dz^2, $*\pi CO_{trans}$, $*\pi CF_3$
5	4.6428 (267.04)	0.0017	H-1→LUMO (20%) H-1→L+9 (18%) H-1→L+10 (39%)	Mn-$d_{xz} \rightarrow *\pi CO_{cis}$ Mn-$d_{xz} \rightarrow$ Mn-d_{yz}, p_y, p_z Mn-$d_{xz} \rightarrow$ Mn-dz^2, $*\pi CO_{trans}$, $*\pi CF_3$
6	4.6715 (265.41)	0.0004	HOMO→L+5 (19%) H-1→L+2 (15%) H-1→L+4 (15%)	Mn-$d_{xy} \rightarrow *\pi CO_{trans}$, Mn-$d_{xz}$ Mn-$d_{xz} \rightarrow 2 \times *\pi CO_{cis}$, $*\pi CO_{trans}$ Mn-$d_{xz} \rightarrow$ Mn-d_{xy}, $*\pi CO_{cis}$, $*\pi CO_{trans}$

Table 13 Selected calculated singlet excited states for $CF_3Mn(CO)_5$

[a] Energy of vertical excitation from ground state, [b] Oscillator strength, [c] Occupied to unoccupied (virtual) orbital excitation, [d] Character of excited state

State	E (eV) [λ (nm)[a]]	f [b]	$\psi_o \rightarrow \psi_v$ [c]	Predominant character [d]
1	4.3558 (284.64)	0	H-1->L+3 (66%) H-1->L+1 (12%) H-2->L+9 (10%)	$Mn\text{-}d_{xz} \rightarrow Mn\text{-}d_{xz}, *\pi CO_{cis}$ $Mn\text{-}d_{xz} \rightarrow 2 \times *\pi CO_{cis}$ $Mn\text{-}d_{xy} \rightarrow Mn\text{-}d_{x^2-y^2}$
2	4.373 (283.52)	0	H-2->L+3 (74%) H-1->L+9 (10%) H-2->L+1 (10%)	$Mn\text{-}d_{xy} \rightarrow Mn\text{-}d_{xz}, *\pi CO_{cis}$ $Mn\text{-}d_{xz} \rightarrow Mn\text{-}d_{x^2-y^2}$ $Mn\text{-}d_{xy} \rightarrow 2 \times *\pi CO_{cis}$
3	4.5771 (270.88)	0	H-1->L+5 (28%) H-2->L+6 (18%) H-1->L+1 (18%)	$Mn\text{-}d_{xz} \rightarrow Mn\text{-}d_{xy}, *\pi CO_{trans}$ $Mn\text{-}d_{xy} \rightarrow Mn\text{-}d_{xz}, *\pi CO_{trans}$ $Mn\text{-}d_{xz} \rightarrow 2 \times *\pi CO_{cis}$
4	4.6403 (267.19)	0.0003	H-1->L+5 (26%), HOMO->L+3 (26%) H-2->L+6 (21%)	$Mn\text{-}d_{xz} \rightarrow Mn\text{-}d_{xy}, *\pi CO_{trans}$ $Mn\text{-}d_{z^2}, CHF_2 \rightarrow Mn\text{-}d_{xz}, *\pi CO_{cis}$ $Mn\text{-}d_{xy} \rightarrow Mn\text{-}d_{xz}, *\pi CO_{trans}$
5	4.6891 (264.41)	0.0001	HOMO->L+1 (43%) H-2->L+2 (18%) H-2->L+10 (13%)	$Mn\text{-}d_{z^2}, CHF_2 \rightarrow 2 \times *\pi CO_{cis}$ $Mn\text{-}d_{xy} \rightarrow 2 \times *\pi CO_{cis}$ $Mn\text{-}d_{xy} \rightarrow Mn\text{-}d_{z^2}$
6	4.7047 (263.53)	0	H-2->L+9 (30%) H-2->L+10 (30%) H-2->L+6 (-13%)	$Mn\text{-}d_{xy} \rightarrow Mn\text{-}d_{x^2-y^2}$ $Mn\text{-}d_{xy} \rightarrow Mn\text{-}d_{z^2}$ $Mn\text{-}d_{xy} \rightarrow Mn\text{-}d_{xz}, *\pi CO_{trans}$

Table 14 Selected calculated singlet excited states for $CHF_2Mn(CO)_5$

[a] Energy of vertical excitation from ground state, [b] Oscillator strength, [c] Occupied to unoccupied (virtual) orbital excitation, [d] Character of excited state

2.5.2. Calculations on (2-acetylphenyl-C,O)Mn(CO)$_4$

2.5.2.1. Geometry Optimisation

The structure of (2-acetylphenyl-C,O)Mn(CO)$_4$ was optimised using the B3LYP/LANL2DZ level of theory. Geometry optimisation was initiated at the RHF/STO-3G theory level with the size of the basis set increased incrementally to LANL2DZ followed by further optimisation with this basis set and B3LYP model chemistry.

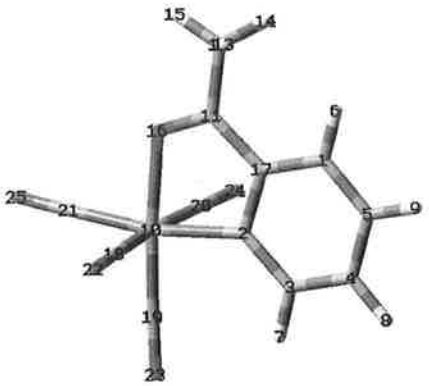

Figure 30 Geometry optimised structures of (2-acetylphenyl-C,O)Mn(CO)$_4$ using the B3LYP/LANL2DZ level of theory

The calculated bond lengths (Å) and bond angles (°) for the geometry optimised structures of (2-acetylphenyl-C,O)Mn(CO)$_4$ shown in Figure 30 are outlined in Table 10. The data obtained is compared between the different basis sets and model chemistries used and against data from the literature[49(b)] containing experimental values.

	RHF/ 3-21G	RHF/ LANL2DZ	B3LYP/ LANL2DZ	Literature[49 (b)]	Deviation % B3LYP - Literature
Bond lengths					
Mn10-C2	2.109	2.160	2.053	2.042	0.54
Mn10-O16	2.116	2.132	2.072	2.055	0.83
C11-O16	1.247	1.253	1.284	1.244	3.21
Mn10-C18	1.947	2.009	1.844	1.857	0.70
C18-O22	1.129	1.136	1.173	1.132	3.62
Mn10-C19	1.926	1.978	1.800	1.786	0.78
C19-O23	1.133	1.137	1.179	1.150	2.52
Mn10-C21	1.951	1.977	1.835	1.849	0.76
C21-O25	1.131	1.137	1.175	1.130	3.98
Mn10-C20	1.947	2.009	1.844	1.856	0.65
C20-O24	1.129	1.136	1.173	1.126	4.17
Bond angles					
C5-C1-C17	119.52	119.85	119.48	119.68	0.17
C1-C5-C4	119.09	118.94	119.28	119.43	0.12
C5-C4-C3	120.97	120.094	121.12	121.63	0.42
C4-C3-C2	121.95	122.29	121.17	120.73	0.36
C3-C2-C17	115.57	115.05	116.70	116.82	0.10
C3-C2-Mn10	131.28	133.73	130.85	130.92	0.05
C17-C2-Mn10	113.13	111.20	112.43	112.22	0.19
C17-C11-O16	118.82	118.79	117.31	117.52	0.18
C2-C17-C11	114.21	115.54	114.45	114.42	0.03
C1-C17-C11	122.90	121.55	123.32	123.72	0.32
C11-O16-Mn10	116.58	116.80	116.01	116.50	0.42
C2-Mn10-O16	77.24	77.64	79.79	79.40	0.49
C17-C11-C12	121.66	122.81	124.08	123.82	0.21
C2-Mn10-C18	80.28	85.39	85.30	87.81	2.85
C2-Mn10-C19	92.14	94.76	95.05	96.81	1.82
C2-Mn10-C20	80.28	85.38	85.30	83.30	2.40
C2-Mn10-C21	163.26	167.15	169.63	169.10	0.31
Mn10-C18-O22	168.42	173.81	177.58	176.72	0.48
Mn10-C19-O23	170.55	174.68	177.84	179.02	0.66
Mn10-C20-O24	168.42	173.81	177.58	175.23	1.34
Mn10-C21-O25	173.63	177.35	178.96	179.53	0.32

Table 15 Comparison of selected bond lengths (Å) and bond angles (°) for (2-acetylphenyl-C,O)Mn(CO)$_4$ on increasing the size of the basis set with literature values[49 (b)]

Following geometry optimisation of the above structures a vibrational analysis of the ground state electronic structure was undertaken. The frequency calculation was carried out on the B3LYP/LANL2DZ optimised structures to investigate whether any negative frequencies were present, which would indicate that the geometry optimised structure was not the minimum on the potential energy surface.

The Hessian matrix was examined and no negative elements were found indicating that the geometry optimised structure obtained was at the energy minimum on the

potential energy surface. In Table 16 the predicted IR active bands of the three complexes optimised at the B3LYP/LANL2DZ level of theory are compared to the experimental values obtained in this study. The calculated IR stretching frequencies are scaled with respect to the experimental values obtained.

IR active bands (Calculated)	IR active bands (experimental) (Pentane)	IR active bands (Literature) (cyclohexane)	Assignment
1979	1948	1947	asymmetric C=O stretch
2002[a]	1998	1997	asymmetric C≡O stretch
2008	-	-	asymmetric C≡O stretch
2080	2085	2082	symmetric C≡O stretch
1579	1588	1530	acyl CO stretch

Table 16 Comparison of IR active frequencies of (2-acetylphenyl-C,O)Mn(CO)$_4$ calculated at the B3LYP/LANL2DZ theory level with experimental values in pentane and literature values in cyclohexane[49(a)]. Literature values have been corrected by an empirical factor of 1.021. [a]Splitting of this vibrational mode is observed in the theoretical geometry optimised model.

2.5.2.2. Calculation of the ground state electronic structure for (2-acetylphenyl-C,O)Mn(CO)$_4$

Following the ground state geometry optimisations of (2-acetylphenyl-C,O)Mn(CO)$_4$ at the B3LYP/LANL2DZ level of theory the ground state electronic structures for each of the complexes were calculated and the highest occupied (HOMO) and lowest virtual (LUMO) molecular orbitals were examined in order to provide a framework for the subsequent Time Dependent DFT (TDDFT) excited state calculations. For each complex the frontier orbitals are plotted according to their energies. Such frontier orbitals are very important in that they play an active role in the determination of the electronic excitations and electronic character of the particular complex. The assignment of the type of molecular orbital was made on the basis of its relative composition and by inspection of the three dimensional representation. In each case the compositional assignment is relative in that the majority are of mixed character with a particular MO giving the major compositional contribution. Table 17 lists the most important molecular orbitals for (2-acetylphenyl-C,O)Mn(CO)$_4$. Six occupied MO's and seven unoccupied or virtual MO's.

MO	(2-acetylphenyl-C,O) $Mn(CO)_4$
L+9	-0.02
L+6	-0.76
L+5	-0.77
L+3	-0.97
L+2	-1.25
L+1	-2.0
LUMO	-2.63
HOMO	-6.75
H-1	-6.98
H-2	-7.25
H-3	-7.65
H-4	-7.78
H-5	-7.81

Table 17 The molecular orbitals of (2-acetylphenyl-C,O)$Mn(CO)_4$ and its energies (eV). HOMO: Highest occupied molecular orbital. LUMO: Lowest unoccupied molecular orbital.H-1 is HOMO-1 and L+1 is LUMO+1

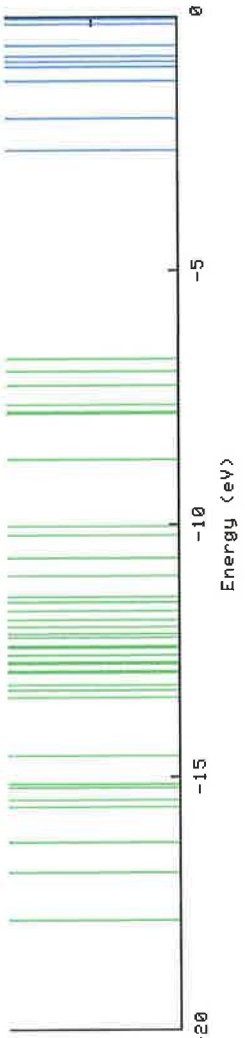

Figure 31 Energy level diagram of (2-acetylphenyl-C,O)$Mn(CO)_4$. Extracted from Density of States (DOS) diagram generated by the GaussSum 2.0 programme[55]

MO no.	Assignment	Energy (eV)	Mn	CO	CO	CO	CO	acyl CO	CH_3	Phenyl
77	L+9	-0.02	57	8	15	8	11	2	0	0
74	L+6	-0.76	26	11	1	11	49	0	0	1
73	L+5	-0.77	21	6	25	6	41	0	0	0
71	L+3	-0.97	26	14	41	14	1	1	0	3
70	L+2	-1.25	5	43	1	43	2	0	0	5
69	L+1	-2	23	32	1	32	9	2	0	1
68	LUMO	-2.63	2	0	1	0	1	52	3	41
67	HOMO	-6.75	38	3	0	3	6	3	0	47
66	H-1	-6.98	74	0	12	0	9	3	0	2
65	H-2	-7.25	58	6	8	6	0	5	0	17
64	H-3	-7.65	15	2	2	2	0	6	1	73
63	H-4	-7.78	19	2	1	2	5	1	0	69
62	H-5	-7.81	31	6	0	6	4	3	0	50

Table 18 The contribution of manganese, each of the four CO orbitals, the acyl group, the methyl group and the phenyl for each of the selected molecular orbital

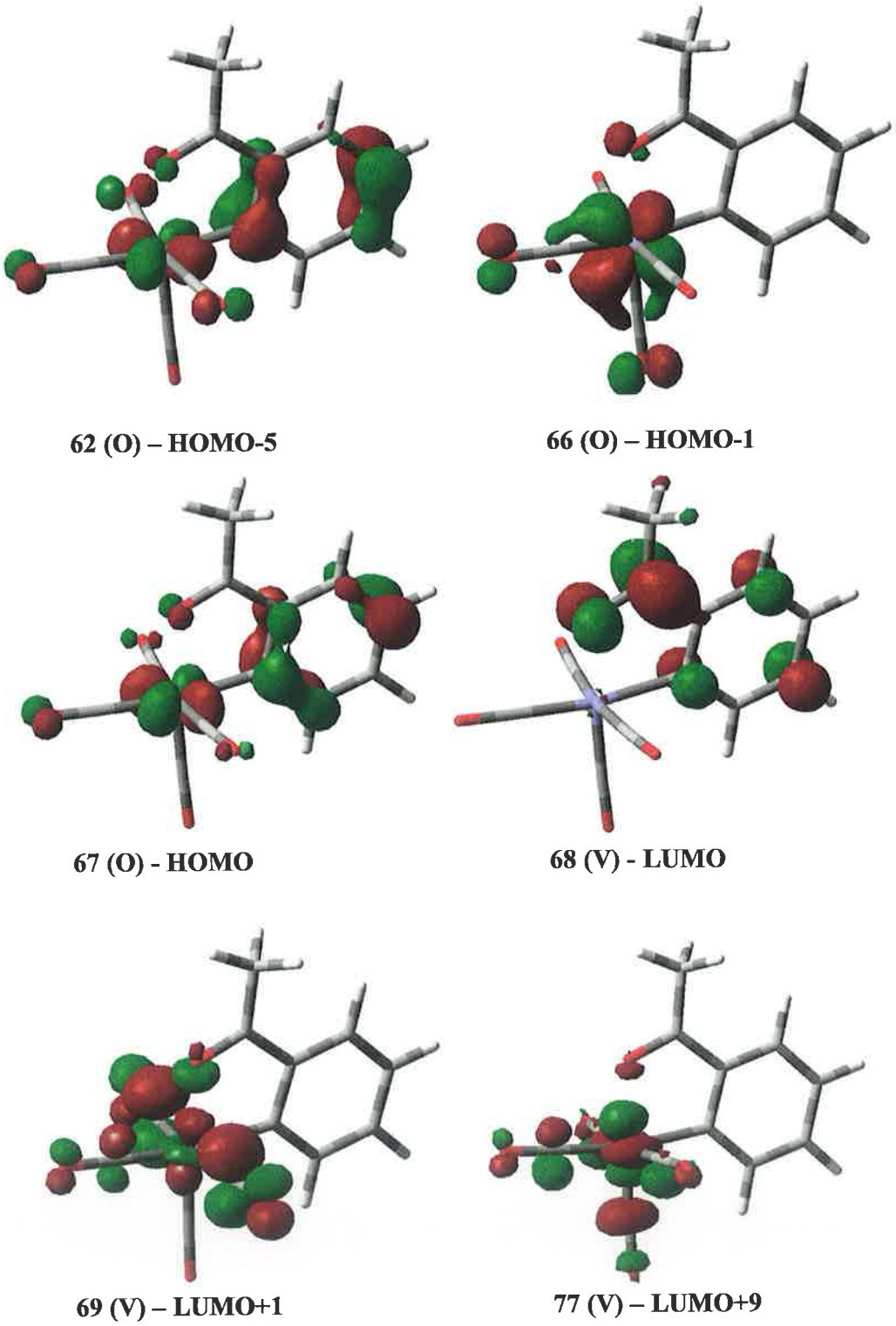

Figure 32 Selected molecular orbitals for (2-acetylphenyl-C,O)Mn(CO)$_4$

2.5.2.3. Time – Dependent Density Functional Theory (TDDFT) calculations

State	E (eV) λ (nm)[a]	f [b]	$\psi_o \rightarrow \psi_v$ [c]	Predominant character [d]
1	3.2879 (377.1)	0.0069	H-1->L+1 (73%) H-1->L+9 (13%)	Mn-$d_{xz} \rightarrow$ *πCO_{ax}, Mn-d_z^2 Mn-$d_{xz} \rightarrow$ *πCO, Mn-d_z^2
2	3.325 (372.88)	0.0201	HOMO->LUMO (88%) H-5->LUMO (2%)	Mn-d_{xy}, L $\rightarrow$ L, *πCO_{acyl} Mn-d_{xz}, *$\pi CO \rightarrow$ L, *πCO_{acyl}
3	3.3661 (368.33)	0.0005	H-1->LUMO (79%) HOMO->L+1 (14%)	Mn-$d_{xz} \rightarrow$ L, *πCO_{acyl} Mn-d_{xy}, L $\rightarrow$ *πCO_{ax}, Mn-d_z^2
4	3.4478 (359.6)	0.0004	H-1->LUMO (-17%), HOMO->L+1 (66%)	Mn-$d_{xz} \rightarrow$ L, *πCO_{acyl} Mn-d_{xy}, L $\rightarrow$ *πCO_{ax}, Mn-d_z^2
5	3.7038 (334.75)	0.0109	H-2->L+1 (58%), H-2->L+9 (-14%)	Mn-d_{yz},*$\pi CO_{ax} \rightarrow$*πCO_{ax}, Mn-d_z^2 Mn-d_{yz},*$\pi CO_{ax} \rightarrow$ *πCO, Mn-d_z^2
6	3.8093 (325.48)	0.0442	H-2->LUMO (88%) H-3->LUMO (4%)	Mn-d_{yz},*$\pi CO_{ax} \rightarrow$ L, *πCO_{acyl} Mn-d_{yz}, L $\rightarrow$ L, *πCO_{acyl}

[a]Energy of vertical excitation from ground state, [b] Oscillator strength, [c] Occupied to unoccupied (virtual) orbital excitation, [d] Character of excited state

Table 19 Selected calculated singlet excited states for (2-acetylphenyl-C,O)$Mn(CO)_4$

2.6. Discussion

2.6.1. Matrix Isolation

2.6.1.1. Matrix Isolation of compounds of the type $Mn(CO)_5L$

Monochromatic photolysis at 313 nm for 90 mins of matrix isolated $CF_3Mn(CO)_5$ in a methane matrix resulted in bleaching of the parent carbonyl bands and production of both the tetracarbonyl species $CF_3Mn(CO)_4$ and the radical species $^{\bullet}Mn(CO)_5$ (Figure 4(b)). The formation of the tetracarbonyl species is based on the generation of three carbonyl bands at 2033, 2006 and 1971 cm^{-1}. On comparison with the work by Church et al.[56] it can be concluded that the product band generated at 1988 cm^{-1} is due to the generation of the C_{4v} $^{\bullet}Mn(CO)_5$ radical species, occurring via homolytic cleavage of the C-Mn bond in the parent molecule. According to Church and co-workers[56] this radical species should have 3 IR active bands at 2105, 1988 and 1978 cm^{-1}. Product bands generated at 2166, 2115 and 2099 cm^{-1} are very weak and as such very difficult to unambiguously assign but may indicate minor formation of a dicarbonyl product species. Subsequent visible irradiation (405 nm or > 410 nm) resulted in regeneration of the parent species as indicated by regeneration of the parent bands and loss of product bands from both photoproducts.

Irradiation at 313 nm for 100 mins of $CF_3Mn(CO)_5$ in a N_2 matrix produced a decrease in intensity of the parent bands and concomitant generation of two N_2 substituted photoproducts and the $^{\bullet}Mn(CO)_5$ radical species. Generation of $CF_3Mn(CO)_4N_2$ is suggested by comparison of the bands generated at 2036, 2009,1992 and 2171 cm^{-1} with those observed by Boese and co-workers[57] for the coordinatively unsaturated $CF_3Mn(CO)_4$, although it should be noted the values in this study are on average 10 cm^{-1} higher. A tricarbonyl species, $CF_3Mn(CO)_3(N_2)_2$ with bands at 2119, 1918, 2282 and 2236 cm^{-1} was also generated. The N_2 stretching band of the tetracarbonyl species was significantly more intense than that of the tricarbonyl species indicating the former to be the predominant photoproduct at this wavelength. Subsequent irradiation at 405 nm resulted in further loss of the parent species, the tetracarbonyl photoproduct, a further increase intensity of the N_2 vibrational bands at 2236 and 2282 cm^{-1} and generation of product band at 2090, 2064 and 1980 cm^{-1}.

This suggests that on low energy irradiation the tricarbonyl species is the predominant photoproduct with loss of both $^{\bullet}Mn(CO)_5$ and $CF_3Mn(CO)_4N_2$. On broadband irradiation the parent compound was regenerated and a tricarbonyl species continued to be generated. This tricarbonyl was assigned as *fac*-$CF_3Mn(CO)_3(N_2)_2$ with two ν_{NN} stretches at 2282 and 2236 cm^{-1} and three νco stretching vibrations at 2090, 2064 and 1980 cm^{-1}. It is presumed that the tricarbonyl species observed on 313 nm irradiation was the *mer*-isomer – *mer*-$CF_3Mn(CO)_3(N_2)_2$. These species are outlined below in Figure 33. The assignment of this species as the *fac*-isomer is based on a detailed analysis of the results and comparison with those observed by Goff[58] for the species *fac*-$CH_3Mn(CO)_3(N_2)_2$ and the deuterated rhenium analogue *fac*-$CD_3Re(CO)_3(N_2)_2$ on respective irradiation of $CH_3Mn(CO)_5$ and $CD_3Re(CO)_5$ impregnated polymer disks in a N_2 matrix. There is deviation of 40 cm^{-1} in the band position of the species described by Goff[58] and those of the trifluoromethyl analogue described in this thesis.

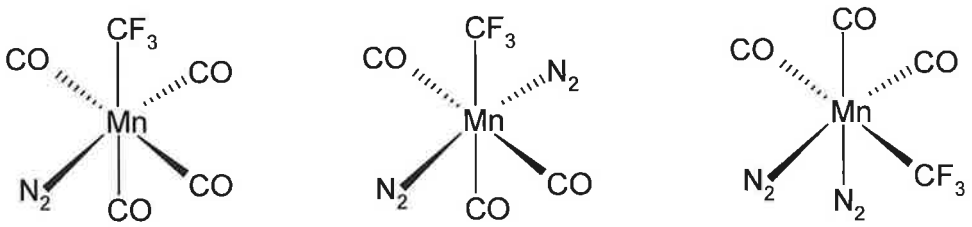

single N_2 substitution *mer*-isomer *fac*-isomer

Figure 33 Possible methods of coordination of dinitrogen onto the metal centre

As the parent species does not absorb in the region > 400 nm it may be concluded that irradiation at this wavelength aside from leading to regeneration of the parent species and loss of earlier photoproducts also resulted in the formation of another isomer of the tricarbonyl $CF_3Mn(CO)_3(N_2)_2$ via photolysis of the tetracarbonyl $CF_3Mn(CO)_4N_2$, which would be expected to absorb in this region.

Irradiation at 313 nm for 110 mins of $CF_3Mn(CO)_5$ in a 2% CO doped methane matrix resulted in depletion of the parent bands and generation of both the tetracarbonyl $CF_3Mn(CO)_4$ and the radical species $^{\bullet}Mn(CO)_5$. However, as observed by Rest and co-workers[59] on photolysis of $CH_3Mn(CO)_5$ in a CO matrix, formation of the tetracarbonyl species on irradiation of $CF_3Mn(CO)_5$ in a CO doped methane

matrix is partially inhibited compared to a pure methane matrix. This may arise from cage-effects within the matrix whereby CO molecules surround the intermediate tetracarbonyl species. On switching the photolysis wavelength to 297 nm or 289 nm little change was observed in the matrix, which suggests that a steady-state may have been reached on high energy irradiation. Subsequent irradiation at > 400 nm for 90 mins regenerated the parent species with concomitant loss of the product bands, which is consistent with a CO-loss species having been produced.

As observed for $CF_3Mn(CO)_5$, monochromatic irradiation at 313 nm for 45 mins of the trifluoroacetyl analogue $CF_3COMn(CO)_5$ in a methane matrix resulted in CO loss to yield the tetracarbonyl species $CF_3Mn(CO)_4$ and homolytic cleavage of the acyl C-Mn bond resulting in formation of the radical species $^{\bullet}Mn(CO)_5$ and the previously unseen fluorinated radical $CF_3{}^{\bullet}CO$. Formation of the pentacarbonyl species is again based on comparison of the IR bands of this photoproduct with those observed by Church et al.[56] in matrix isolation experiments on $CH_3Mn(CO)_5$ in a range of matrixes. Product bands observed at 1596 and 1134 cm^{-1}, were assigned to the CO stretching vibration and C-F stretching vibration of the CF_3 moiety, respectively. The band at 1596 cm^{-1} is in good agreement with that observed by Isobe et al.[60] at 1574 cm^{-1} for the CO stretching vibration of a $CF_3{}^{\bullet}CO$ radical. The CF_3 stretching vibration for this radical would be expected to occur in the region 1400-1100 cm^{-1} as suggested in the same study by Isobe and co-workers[60] where absorption bands observed at 1338 and 1115 cm^{-1} were assigned to the A_1 and E vibrational modes of the CF_3 moiety. These bands are however difficult to unambiguously assign as they are partially masked by the absorption bands of the CaF_2 plate. Subsequent visible irradiation (405 nm and > 400 nm) resulted in the expected regeneration of the parent absorption bands and loss of those of the previously generated photoproducts. Irradiation at 313 nm in a dinitrogen matrix as for the methane matrix resulted in bleaching of the parent bands with generation of the $^{\bullet}Mn(CO)_5$ and $^{\bullet}CF_3CO$ radical species. The generation of product bands at 2046, 2009, 2170 cm^{-1} and an increase in intensity of the free CO band is assigned to the formation of the N_2 substituted tetracarbonyl $CF_3COMn(CO)_4N_2$. A third product band expected in the region 1990 cm^{-1} may overlap with that of the radical species $^{\bullet}Mn(CO)_5$ in this region. Weak bands also generated at 2282 and 2120 cm^{-1} are tentatively assigned to the generation of the N_2 disubstituted species $CF_3COMn(CO)_3(N_2)_2$. Subsequent reduction of the irradiation

wavelength to 297 nm and 289 nm produced further bleaching of the parent bands as well as those from the two radical species. This occurred parallel to an increase in the relative intensities of both the N_2 substituted species $CF_3COMn(CO)_4N_2$ and $CF_3COMn(CO)_4(N_2)_2$. This suggests that on high energy irradiation dissociative CO loss and subsequent N_2 coordination appears to be the predominant photo reaction for this system.

Similarly irradiation of $CF_3COMn(CO)_5$ in a 2% or 10% CO-doped methane matrix produced *cis*-$CF_3COMn(CO)_4$, which was trapped by N_2 when carried out under an N_2 atmosphere. This assignment is based on the similarity of the product bands produced at 2055, 2017, 2003 and 1973 cm^{-1} with those observed by Boese et al.[61] at 2054, 2013, 2007, 1976 and 1617 cm^{-1} for $CF_3COMn(CO)_4$ following laser flash photolysis of $CF_3COMn(CO)_5$ in 296 K cyclohexane. Unusually no change is observed in the ketonic CO band at 1670 cm^{-1}, which shifts to 1695 cm^{-1} in both methane and dinitrogen matrices on CO loss. According to observations made by Boese et al.[61] the ketonic CO band of this tetracarbonyl species should be present at 1617 cm^{-1}. However, water in this region in the matrix at ~1600 cm^{-1} may be masking any signal. High energy irradiation at 313 nm and 297 nm produced both the $^{\bullet}Mn(CO)_5$ radical and the coordinatively unsaturated tetracarbonyl $CF_3Mn(CO)_4$. Formation of the latter species is suggested by generation of product bands at 2006 and 2045 cm^{-1} band an increase in intensity of the free CO band at 2138 cm^{-1}. On extended irradiation the bands due to *cis*-$CF_3COMn(CO)_4$ further increase in intensity with complete loss of the parent ketonic band at 1670 cm^{-1} suggesting complete loss of the parent species. Subsequent irradiation in the visible region at 405 nm and broadband irradiation at >400 nm resulted in loss of the radical species and regeneration of the parent bands. However, on extended broadband irradiation product bands were also generated at 1991 and 1976 cm^{-1}. This suggests that visible broadband irradiation not only results in regeneration of the parent species but also irradiation of previously formed photoproducts resulting in the formation of a number of ambiguous bands.

2.6.1.2. Matrix Isolation of (2-acetylphenyl-C,O)Mn(CO)$_4$

UV irradiation of 405 nm for 60 mins in a methane matrix at 12 K resulted in bleaching of the parent carbonyl bands and generation of three product bands at 2030, 1922 and 1903 cm^{-1} and a free CO band at 2138 cm^{-1}. These are assigned to generation of the CO loss species (2-acetylphenyl-C,O)Mn(CO)$_3$ based on comparison with bands observed by Stor et al.[62] for a range of manganese tricarbonyl systems of the type XMn(CO)$_3$(bpy), where X = Cl, Br or I. No observable change in the ketone band at 1690 cm^{-1} suggests that low energy photolysis results in CO loss and no cleavage of the Mn-O bond. On reducing the irradiation wavelength to 365 nm for 90 mins little further change in either the parent or product carbonyl bands was observed. Low energy broadband irradiation at > 550 nm for 20 mins resulted in regeneration of the parent bands, eventual loss of the tricarbonyl photoproduct and a decrease in intensity of the free CO band at 2138 cm^{-1}, indicating re-coordination of the CO ligand to the photoproduct to regenerate the parent species.

As observed in a methane matrix, monochromatic irradiation at 405 nm for 80 mins in a dinitrogen matrix resulted in bleaching of the parent band and generation of a tricarbonyl species which in a dinitrogen matrix is trapped by N_2 to yield (2-acetylphenyl-C,O)Mn(CO)$_3$N$_2$. Extended irradiation (80 mins) at this wavelength also produced a second set of weak bands at 2199(ν_{NN}), 2021, 1968and 1938 cm^{-1} which are tentatively assigned to generation of the disubstituted species (2-acetylphenyl-C,O)Mn(CO)$_2$(N$_2$)$_2$ (Scheme 16). The second expected ν_{NN} band for this species may overlap with that observed for the monosubstituted species at 2261 cm^{-1}. This is similar to observations made by Breheny et al.[63] on irradiation of (η^6-C$_5$H$_5$N)Cr(CO)$_3$ in a N_2 matrix, where the ν_{NN} band of the monosubstituted product (η^6-C$_5$H$_5$N)Cr(CO)$_2$(N$_2$) overlapped the low energy ν_{NN} band of the bis(dinitrogen) speies (η^6-C$_5$H$_5$N)Cr(CO)(N$_2$)$_2$.

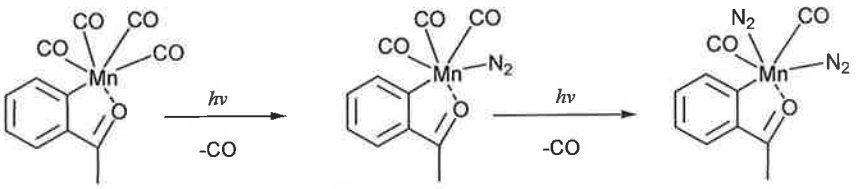

Scheme 16 Coordination of N_2 following CO on irradiation at 405 nm for (a) 30 and (b) 80 mins

Subsequent low energy irradiation at > 520 nm resulted in regeneration of the parent bands and a decrease in intensity of the product bands.

Irradiation at 405 nm for 60 mins in a 2% or 10% CO-doped methane matrix produced results comparable to those observed on irradiation in both a methane and dinitrogen matrix. In a CO doped methane matrix bleaching of the parent bands was observed with concomitant generation of product bands, previously assigned to the tricarbonyl product (2-acetylphenyl-C,O)$Mn(CO)_3$. This is further confirmed by an increase in intensity of the free CO band at 2138 cm^{-1}. The generation of two further weak bands suggests formation of a minor dicarbonyl photoproduct based on comparison with bands previously observed for the generation of (2-acetylphenyl-C,O)$Mn(CO)_2(N_2)_2$ in a dinitrogen matrix. As previously observed on irradiation in both methane and dinitrogen matrixes, broadband irradiation at > 520 nm for 60 mins resulted in regeneration of the parent bands and depletion of the product bands and a reduction in intensity of the free CO band. This suggests regeneration of the parent tetracarbonyl species.

2.6.2. Quantum Chemical Studies

2.6.2.1. DFT and TDDFT studies of compounds of the type $Mn(CO)_5L$

2.6.2.1.1. Geometry optimisation of compounds of the type $Mn(CO)_5L$

A comparison of the bond lengths for the three complexes (a) $CF_3COMn(CO)_5$, (b) $CF_3Mn(CO)_5$ and (c) $CHF_2Mn(CO)_5$, showed little difference in the Mn-C bond length between the CF_3CO (2.075 Å) and CF_3 (2.076 Å) complexes while unusually in the case of the CHF_2 analogue a Mn-C bond length of 2.096 Å was calculated. The presence of the carbonyl group in (a) appears to have no effect on the Mn-C bond length. However, the calculated Mn-C bond lengths for each of these systems are larger by 1-2 %, compared to measured values. DFT tends to slightly overestimate such bond lengths when using the LANL2DZ basis set.[37] Overall on varying the fluorinated substituents no significant difference in CO_{eq} or CO_{ax} bond length was observed between the three complexes, the average values for CO_{eq} and CO_{ax} being 1.16 Å and 1.17 Å, respectively. This is in contrast to observations of McQuillan et al.[64] and Pansak et al.[65] where theoretical (EHMO) calculations and vibrational studies of pentacarbonyl manganese and rhenium halides and $MeMn(CO)_5$ indicated that the axial bond lengths were consistently shorter than their equatorial counterparts by 0.03-0.04 Å. However, in these studies differences in bond length of this order are negligible as they lie within the range of experimental error for DFT calculations. For both $MeMn(CO)_5$ and $BrMn(CO)_5$ this effect has been attributed[64] to a π-effect which strengthens the Mn-CO bond. In the case of the acetylated analogue $CF_3COMn(CO)_5$ the presence of the acetyl CO does appear to affect the bond lengths and bond angles of the attached CF_3 moiety. The C-F bond length of the fluorine atom closest to the acetyl group is shorter at 1.382 Å compared to the other two C-F bonds which are both 1.408 Å in length. An increased bond angle of 115 ° between the acetyl group and the fluorine atom closest to it compared to 110 ° for the other two fluorine atoms further suggests repulsion between the acetyl group and the fluorine atom closest to it. The bond lengths and angles of $CF_3Mn(CO)_5$ suggest that the geometry of this compound may be distorted and may thus have C_{2v} geometry and not the expected C_{4v} geometry. This is suggested by a reduced bond length of 1.422 Å for one of the C-F bonds compared to the other two which are both 1.488 Å, while the Mn-C-F bond angle for this particular fluorine atom is 116 ° compared to 114 ° for the other two

fluorine atoms. This compares favourably with observations made by Goff et al.[58] for $CD_2HMn(CO)_5$.

2.6.2.1.2. The molecular orbitals of compounds of the type $Mn(CO)_5L$

As can be seen in Figure 27-Figure 29 the majority of the valence molecular orbitals for compounds (a) $CF_3COMn(CO)_5$, (b) $CF_3Mn(CO)_5$ and (c) $CHF_2Mn(CO)_5$ are concentrated on the metal carbonyl moiety of the complex and are as such almost independent of the fluorinated methyl substituent. However, in the trifluoroacetyl analogue, $CF_3COMn(CO)_5$, both the HOMO and LUMO are centred on the acetyl group, with 74 % and 61 % contributions from the acetyl group to the HOMO and LUMO, respectively. The LUMO also involves weak contributions from the five π^* CO orbitals and the Mn-d_{xy} orbital while the HOMO is solely dominated by the acetyl group. Weak contributions from the acetyl group are also observed for the L+1 and L+3 molecular orbitals. In the case of compound (c) $CHF_2Mn(CO)_5$ this is also the case with both the HOMO and LUMO centred on the CHF_2 moiety. However, for the LUMO significant contributions are also observed from the metal carbonyl system. Unusually, in the case of $CF_3Mn(CO)_5$ for all frontier molecular orbitals studied the trifluoromethyl moiety plays no significant part, with only very minor contributions observed for the HOMO and H-1 molecular orbitals. A comparison of the energies involved in the HOMO and LUMO for each complex shows the HOMO of $CF_3COMn(CO)_5$ to be lowest in energy at -7.55 eV compared to -8.05 eV for $CHF_2Mn(CO)_5$ and -8.69 eV for $CF_3Mn(CO)_5$. This suggests that the molecular orbitals centred on the acetyl group are more stable than those centred on either the metal carbonyl or the fluoromethyl group alone. However, conversely the LUMO of $CHF_2Mn(CO)_5$ is lowest in energy (-2.45 mV) and thus more stable. This orbital is centred predominantly on the π^* orbitials of the four *cis*-CO ligands with minor contributions from both the CHF_2 and *trans*-CO ligands (Figure 29). The metal centre appears to play no role in this molecular orbital. The situation is similar for $CF_3Mn(CO)_5$ where the LUMO is dominated by the four π^* *cis* CO orbitals at 81 % contribution, with little input from either the metal (10%), CF_3 (9%) or the *trans*-CO (1%) orbitals (Table 10). This is similar to observations made by Wilms et al.[66] in a DFT study on the primary photoprocesses of $MnCl(CO)_5$ where it was observed that the contributions for the LUMO based on Mulliken population analysis was centred

on the equatorial CO ligands (55 %) with smaller contributions from both Mn (20 %) and Cl (20 %). As observed in this study, no significant contributions from the *trans*-CO ligand was found.

In contrast, population analysis of $CF_3COMn(CO)_5$ shows the HOMO to be centred on the acetyl group (74 %) with small contributions from both the metal (19%) and the CO ligands (7 %). A similar trend is observed for the LUMO although the % contribution from the CO ligands does improve. The LUMO is again centred on the CF_3CO moiety (61 %) with contributions of 31 % from the *cis*-CO ligands, 9% from the *trans*-CO ligand and 6% from the Mn centre.

The energy gap between the HOMO and LUMO is smallest for $CF_3COMn(CO)_5$ at 4.87 mV while the energy gap is largest for $CF_3Mn(CO)_5$ at 5.94 mV. Overall the presence of the acetyl group in the trifluoroacetyl analogue appears to have a stabilising effect compared to the trifluoromethyl analogue, which possesses both a higher energy HOMO and LUMO. This effect is easily visualised in the energy level diagram for all three complexes in Figure 24. As can be seen in Table 12 the ground state molecular orbitals of $CF_3COMn(CO)_5$ are dominated by the CF_3CO moiety.

Overall, it can be seen from Table 13 and Table 14 that the photochemistry of both $CF_3Mn(CO)_5$ and $CHF_2Mn(CO)_5$ is dominated by MLCT type transitions involving charge transfer from the d orbitals of the Mn centre to the four π^* CO_{cis} orbitals, although a small amount of d-d type transitions are also observed particularly in the L+3, L+5 and L+9 molecular orbitals of $CF_3Mn(CO)_5$ and in the L+3, L+5, L+6 and L+9 molecular orbitals of $CHF_2Mn(CO)_5$. This is in good agreement with observations made by Wilms et al.[66] in DFT studies on $ClMn(CO)_5$. However, in contrast the accessible transitions of $CF_3COMn(CO)_5$ appears to be dominated by LMCT and ILCT type transitions involving charge transfer from the CF_3CO moiety (exclusively from the HOMO) to either the Mn metal centre or the four π^* CO_{cis} orbitals.

2.6.2.1.3.Correlation of TDDFT results with observed photochemistry

As previously suggested the lowest lying excited states for both compound (b) $CF_3Mn(CO)_5$ and (c) $CHF_2Mn(CO)_5$ are mainly MLCT in character. As previously suggested the lowest lying excited states for both compound (b) $CF_3Mn(CO)_5$ and (c) $CHF_2Mn(CO)_5$ are mainly MLCT in character, that is, involving charge transfer from the Mn-d orbitals to either the *cis*-CO ligands, the *trans*-CO ligands or both. Furthermore, significant d-d transitions are also observed where charge is transferred from one Mn-d orbital to another higher energy d orbital. However, as $CHF_2Mn(CO)_5$ could not be synthesised and the photochemistry thus not investigated experimentally only $CF_3Mn(CO)_5$ will be discussed when correlating experimental results with those predicted by Density Functional Theory. The observed photochemistry for $CF_3Mn(CO)_5$ displays both unique ligand loss via C-Mn bond cleavage but also dissociative CO loss or both. Thus the photochemistry and thus the transitions involved can be divided into two groups – those leading to radical formation and those leading to CO loss.

Time Dependent Density Functional Theory (TDDFT) studies were carried out to determine the 20 lowest lying singlet excited states for $CF_3Mn(CO)_5$. These calculations predict nine singlet excited states with relatively low or zero oscillator strengths occurring between 260 and 280 nm.

Calculated bands (nm)	Oscillator Strength (*f*)	Excited State Properties	Photoproduct produced
280.73	0	Mn → CO CT, LF	CF_3 loss, CO_{trans} loss
279.70	0	Mn → CO CT, LF	CF_3 loss
270.65	0.0003	Mn → CO CT	CF_3 loss
269.80	0.0011	Mn → Mn-d, CO-$p_{y,z}$ Mn → CO CT Mn → CO CT, LBCT	CF_3, CO_{trans} loss CF_3 loss CO_{cis} loss
267.04	0.0017	Mn → CO CT Mn →CO CT, LBCT Mn→CO CT, LBCT	CF_3 loss CF_3, CO_{trans} loss CO_{cis} loss
265.41	0.0004	Mn → CO CT, LF Mn→ CO CT, LF Mn→ CO CT, LF , LBCT	CF_3 loss CF_3, CO_{cis} loss CF_3, CO_{cis} loss

Table 20 The calculated low energy UV absorption bands for $CF_3Mn(CO)_5$, their excited state properties and the predicted photoproducts produced on irradiation into these bands.

This is in agreement with the measured electronic absorption spectrum of $CF_3Mn(CO)_5$ in pentane shown in Figure 3. In Figure 34 the six lowest energy excited state transitions are shown relative to the actual UV-Vis spectrum. However, the scale of the excited state transitions shown is arbitrary and does not reflect the oscillator strengths of the individual transitions.

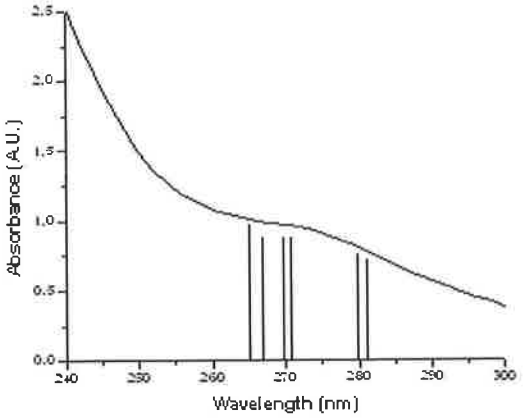

Figure 34 The position of the six lowest lying excited state (vertical lines) relative to the experimental UV-Vis absorption spectrum of $CF_3Mn(CO)_5$ in pentane.

The first and second lowest lying singlet excited states in $CF_3Mn(CO)_5$ predominantly involve charge transfer (MLCT and LF) from the HOMO and H-1 molecular orbitals respectively to the L+3 virtual molecular orbital. In both cases this involves LF transitions from a Mn-d orbital to another Mn-d orbital and MLCT transitions to the four *cis*-CO ligands, which are antibonding with respect to the ligand-metal bonding interaction. In both cases, in the L+3, the MO receiving electron density, the CF_3 and CO_{trans} are non-bonding with respect to the ligand-metal bonding interaction, resulting in labilsation of either group to yield either $^{\bullet}Mn(CO)_5$ or $CF_3Mn(CO)_4$. However, both transitions have a zero oscillator strength and thus may poorly contribute to the transitions responsible for the electronic absorption spectrum. The next two lowest lying excited states, occurring at 270 and 269 nm, both involve substantial mixing of transitions but are both predominantly MLCT in nature. That occurring at 270 nm involves charge transfer from the HOMO, which is predominantly metal centred to π^* orbitals centred on either two CO_{cis} ligands or the CO_{trans} ligand. In both cases the metal is again non-bonding with respect to the metal-CF_3 bonding interaction, resulting in the labilisation of the CF_3 moiety to give the $Mn(CO)_5$ radical species. The next transition occurring at 269 nm is again dominated by MLCT from the

HOMO to L+9 and L+10 virtual molecular orbitals. This involves CT from a metal centred MO to MO's which have contributions from both the metal centre and the four π* CO_{cis} ligands. Again both the CF_3 ligand and CO_{trans} are non-bonding with respect to the metal and are expected to be lost. The final two low lying excited states predominantly involve CT from the H-1 orbital, which is predominantly metal centred (although it does possess contributions from two CO_{cis} and the CO_{trans} ligands) to L+2, L+4, L+9, L+10 and LUMO. Overall, this results in labilisation of the CF_3 group as well as a CO_{cis} or CO_{trans} ligand.

Thus it would be expected that excitation with 313 nm light should populate the lowest energy excited states, which in the case of $CF_3Mn(CO)_5$, are dominated by Metal-To-Ligand Charge Transfer states. As a result, this leads to the predominant loss of the CF_3 moiety via C-Mn bond cleavage to yield the $Mn(CO)_5$ radical species. A number of transitions also involve the loss of either a CO_{cis} or CO_{trans} ligand. This affinity for CF_3 loss may be explained in terms of oxidation of the central Mn atom in the excited state, which results in decreased back donation to either the CF_3 or CO_{trans} group. Experimentally, lower energy irradiation at 405 nm resulted in regeneration of the parent species and generation of a CO loss species *fac*-$CF_3Mn(CO)_3(N_2)_2$, presumably via photolysis of the previously photogenerated tetracarbonyl species. TDDFT calculations were also carried out on $CF_3COMn(CO)_5$ to determine its 20 lowest lying singlet excited states.

Calculated Bands (nm)	Oscillator Strength (f)	Excited State Properties	Photoproduct Produced
378.07	0.0006	MLCT, LBCT, L-CO CT L-CO CT, MLCT, LBCT	CF_3CO loss, CO_{cis} loss CF_3CO loss, CO_{trans} loss
305.95	0.0006	L-CO CT, MLCT	CF_3CO loss
305.55	0.0000	L-CO CT, MLCT, LBCT L-CO CT, MLCT	CF_3CO loss, CO_{trans} loss CF_3CO loss, CO_{trans} loss
301.63	0.0186	L-CO CT, LBCT L-CO CT, MLCT	CF_3CO loss, CO_{trans} loss CF_3CO loss
296.46	0.0002	L-CO CT, MLCT, LBCT L-CO CT, MLCT	CF_3CO loss, CO_{trans} loss CF_3CO loss, CO_{trans} loss
286.32	0.0025	L-CO CT, MLCT L-CO CT, LBCT	CF_3CO loss, CO_{cis} loss CF_3CO loss, CO_{trans} loss

Table 21 The calculated low energy UV absorption bands for $CF_3COMn(CO)_5$, their excited state properties and the predicted photoproducts produced on irradiation into these bands.

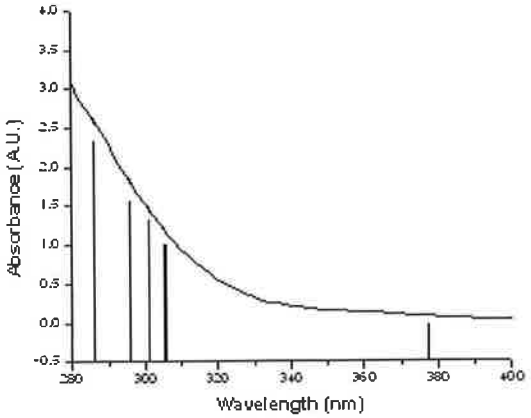

Figure 35 The position of the six lowest lying excited state (vertical lines) relative to the experimental UV-Vis absorption spectrum of $CF_3Mn(CO)_5$ in pentane.

The photochemistry of $CF_3COMn(CO)_5$, unlike $CF_3Mn(CO)_5$, is completely LMCT and LBCT in character involving charge transfer in each case from the HOMO, which is centred on the acyl group, with minor Mn-d character. This charge transfer takes place into both the metal centre but also the acyl and CO ligands resulting in both CF_3CO and CO loss. The six predicted lowest lying singlet excited states responsible for the electronic absorption spectrum of $CF_3COMn(CO)_5$ are shown relative to the actual UV-Vis spectrum of $CF_3COMn(CO)_5$ in pentane (Figure 35).

The lowest lying singlet excited state for $CF_3COMn(CO)_5$ occurs at 378 nm and is dominated (77 %) by a HOMO to LUMO charge transfer transition. This transition involves transfer of electron density from a molecular orbital centred on the acyl group (74 %), which is bonding with respect to the metal centre and predominantly non-bonding with respect to the metal carbonyl ligand to a virtual molecular orbital also centred on the acyl group, which is however anti-bonding with respect to the metal centre. A second weaker transition (HOMO $\rightarrow$ L+3) also contributes to this excited state. Again this involves transfer from a molecular centred on the acyl group to one which is anti-bonding for the acyl group with respect to the metal centre and anti-bonding for two of the CO_{cis} ligands. The CO_{trans} is non-bonding in this molecular orbital. Overall, this suggests that this transition will weakly result in both CF_3CO and CO_{trans} loss as the oscillator strength for this transition is quite low.

The second lowest excited state involves charge transfer from the HOMO to L+2, a molecular orbital which is predominantly CO in character, with the electron density centred on two of the CO_{cis} ligands and the CO_{trans} ligand. Almost no charge transfer takes place to the remaining two CO_{cis} ligands, while the acyl moiety is completely non-bonding with respect to the metal. Overall, this suggests that the predominant result of this transition will be loss of CF_3CO, although some minor CO_{cis} loss may also occur. The third lowest excited state is dominated by a HOMO → L+3 transition as discussed above. The involves charge transfer to a MO centred on two CO_{cis} ligands with minor Mn-d contributions. Overall, this is expected to result in labilisation of both the acyl and CO_{trans} moieties. However, this particular transition has an oscillator strength of zero and thus may not actually impact on the electronic absorption spectrum of this complex. Both the fourth and fifth lowest lying singlet excited states may be described as being L-CO CT in nature. The fourth and fifth excited states are largely HOMO→ L+1 (82 %) and HOMO → L+4 (78 %) in nature, respectively. In both cases, these transitions involves charge transfer from a molecular orbital centred on the acyl group with minor Mn-d character to a molecular orbital centred predominantly on the four π* CO_{cis} ligands, with little, and in the case of the fifth excited state, no, significant contributions from other groups in the complex. This suggests that in both cases the result of these transitions should be labilisation of both CF_3CO and CO_{trans}.

The sixth low lying excited state in somewhat different from those previously discussed for this complex. This excited state is largely HOMO → L+5 in nature. As before, this involves charge transfer from the largely acyl based HOMO to a molecular orbital centred on three of the π*-CO_{cis} ligands, the π*-CO_{trans} ligand and to a lesser extent the d_{xy} orbital of the metal centre. As before the CF_3CO moiety is non-bonding with respect to the metal centre and is thus expected to be easily labilised. However, unusually the CO_{cis} ligand, which is itself *trans* to the C=O group of the CF_3CO moiety is also non-bonding and as such may also be expected to be labilised. This molecular orbital is shown below in Figure 36.

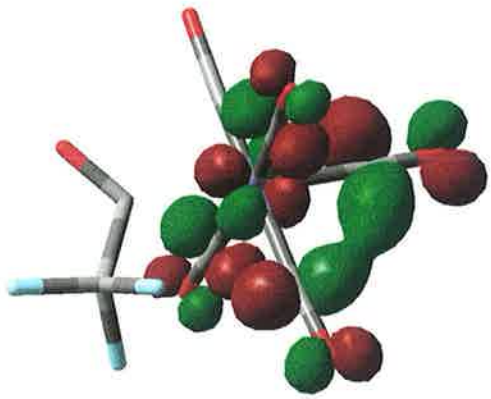

Figure 36 LUMO + 5 virtual molecular orbital (72) of $CF_3COMn(CO)_5$ involved in the 6th lowest lying singlet excited state

Based on the six lowest lying singlet excited states discussed above it would be expected that irradiation at 313 nm would involve direct excitation into a number of excited states, presumably those occurring between 300 and 310 nm (excited states 2-4). TDDFT predicts, as is evident above, that direct excitation of these charge transfer bands should result in labilisation of both the CF_3CO moiety and a CO ligand, resulting in effective C-Mn bond cleavage or CO loss. This is in agreement with matrix isolation studies of $CF_3COMn(CO)_5$ in a variety of matrix gases, where it was observed that direct 313 nm irradiation resulted in both effective C-Mn bond cleavage yielding the $Mn(CO)_5$ radical species but also the tetracarbonyl species and in the case of the N_2 matrix tricarbonyl formation via CO loss. Experimentally it has been observed that visible irradiation at 405 nm resulted in regeneration of the parent species, loss of the $Mn(CO)_5$ radical species and continued generation of the coordinatively unsaturated tetracarbonyl $CF_3COMn(CO)_4$. The theory predicts that excitation of the CT band of the parent complex in this region at 378 nm should result predominantly in loss of a CO_{cis} ligand, which is in agreement with experimental observations. However, irradiation at this wavelength was carried out after 313 nm irradiation and thus may also result in irradiation of previous photoproducts, resulting in regeneration of the parent species.

2.6.2.2. DFT and TDDFT studies of (2-acetylphenyl-C,O)$Mn(CO)_4$

2.6.2.2.1. Geometry optimisation of (2-acetylphenyl-C,O)$Mn(CO)_4$

The ground state geometry of (2-acetylphenyl-C,O)$Mn(CO)_4$ was optimised at the B3LYP/LANL2DZ level of theory. This showed a near planar structure of the ortho-metallated acetophenone type molecule containing a fused phenyl and Mn-contaning five-membered ring. This is in agreement with the crystal structure of (2-acetylphenyl-C,O)$Mn(CO)_4$ obtained by Kaesz and co-workers[49(b)]. As shown in Table 15 the geometry optimised bond lengths compare favourably with those obtained by Kaesz et al.[49(b)], although the M-CO bond lengths are generally overestimated in the theoretical model by approximately 0.046 Å, having a % deviation from the literature values of between 3.21 and 4.17 %. It has, however, been observed in the literature, that Density Functional Theory often overestimates C≡O bond lengths. The calculated bond lengths for the geometry optimised model also fit favourably with those for a number of other heterocyclic ring systems[49]. In contrast, the predicted metal carbonyl bond angles for match favourably with those observed experimentally.[49] The ketone CO bond length is also slightly overestimated in the theoretical model. The experimentally observed bond length is expected to be longer than for the free acetophenone ligand, in which the C=O bond length is 1.216 Å compared to that of 1.244 Å observed for (2-acetylphenyl-C,O)$Mn(CO)_4$. This increase in bond length is attributed to an increase in π delocalisation, with a concomitant decrease in both Mn-O and Mn-C bond lengths.

2.6.2.2.2. The molecular orbitals of (2-acetylphenyl-C,O)Mn(CO)$_4$

As is evident from Figure 32 and Table 19 the majority of the frontier molecular orbitals for (2-acetylphenyl-C,O)Mn(CO)$_4$ are composed of a mixture of metal centred, CO centred and ligand centred molecular orbitals. The exceptions to this are H-1, L+1 and L+9, both of which have their electron density centred on the metal carbonyl moiety with no contribution from the phenyl or five-membered ring systems. The H-1 molecular orbital is centred on the Mn-d_{xz} orbital (74 %) with minor contributions from the CO_{trans} ligand (9 %) and the CO_{cis} ligand in the plane of the ring system (12 %). In the L+1 molecular orbital electron density is concentrated on the Mn-d_z^2 orbital and two of the π^* CO ligands situated *cis* to the ring system but out of the plane of the ring system. In this MO the remaining CO_{cis} ligand and acetylphenyl ring system are non-bonding in nature with respect to the metal centre. Similarly, in the L+9 molecular orbital electron density is centred on the Mn-$d_{x^2-y^2}$ molecular orbital and the four CO ligands which are anti-bonding with respect to the metal centre. The HOMO possesses contributions from both the metal (38 %) and the phenyl ligand (47 %), being centred on the Mn-d_{xy} orbital and π orbital of the phenyl ring with little significant contribution from the CO ligands (12 %) or the acetyl group (3 %). However, the situation is different for the LUMO, which is dominated by electron density centred on the C=O of the acetyl group (52 %) and the π orbital of the phenyl ring (41 %), with no significant contribution from either the metal centre (2%) or the carbonyl ligands (2%). HOMO-5, like the HOMO, although predominantly centred on the phenyl ring (50 %) also contains a very significant contribution from the Mn-dyz orbital (31 %).The CO ligands only account for a combined total of 16 % contribution towards this molecular orbital.

2.6.2.2.3.The correlation of TDDFT results with observed photochemistry

Time Dependent Density Functional Theory (TDDFT) studies were carried out to determine the 20 lowest lying singlet excited states of (2-acetylphenyl-C,O)$Mn(CO)_4$. The lowest eight singlet excited states occur in the region 300-380 nm and thus it is transitions into these excited states that lead to the UV-Vis spectrum of (2-acetylphenyl-C,O)$Mn(CO)_4$ as shown in Figure 17. The lowest lying singlet excited states of (2-acetylphenyl-C,O)$Mn(CO)_4$ involve electronic transitions which are primarily MLCT in character involving charge transfer from a molecular orbital centred on the metal centre, and to a lesser extent the CO and phenyl ligands to molecular orbitals centred on the CO or phenyl ligands as well as the Mn-d orbital. However, as a result of mixing of MO character a certain amount of LFCT, LBCT and LMCT is also observed. However, both the 7^{th} and 8^{th} lowest lying excited states have very low oscillator strengths and may not contribute significantly to the observed UV-Vis spectrum.

Calculated Bands (nm)	Oscillator Strengths (*f*)	Excited State Properties	Photoproduct Produced
377.10	0.0069	MLCT, LBCT, LF	CO_{cis} loss
372.88	0.0201	MLCT, LBCT	Mn-C bond cleavage
368.33	0.0005	MLCT, LBCT	Mn-C bond cleavage, CO loss
359.60	0.0004	MLCT, LBCT, LF	CO_{cis} loss
334.75	0.0109	MLCT, LF	CO_{cis} loss
325.48	0.0442	LF, MLCT	Mn-C bond cleavage, CO loss
307.11	0.0001	LBCT, MLCT	Mn-C bond cleavage, CO loss
297.32	0.0003	MLCT, LBCT	CO_{trans} loss

Table 22 The calculated low energy UV absorption bands, their excited state properties and the predicted photoproducts produced on irradiation into these bands

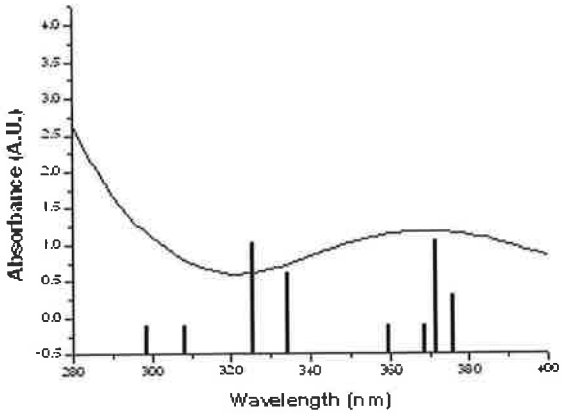

Figure 37 The position of the eight lowest lying excited state (vertical lines) relative to the experimental UV-Vis absorption spectrum of (2-acetylphenyl-C,O)Mn(CO)$_4$ in pentane.

The lowest lying excited state is predominantly metal-to-ligand charge transfer in character involving charge transfer from the H-1 molecular orbital, which is centred on the d_{xz} orbital of the metal centre (74 %) and two of the π*-CO ligands (21 %) to L+1, a molecular orbital centred on the Mn-d_z^2 orbital (23%) and two of the π*-CO_{cis} ligands (64 %) and the CO_{trans} ligand (9 %), all of which are anti-bonding in character with respect M-CO bonding interaction. Both the ring system and the CO_{cis} ligand, which is in the plane of the ring system are non-bonding in this molecular orbital. Thus this transition would be expected to result in labilisation of the CO_{trans} ligand. The second lowest singlet excited state is predominantly HOMO → LUMO in character, involving transfer of electron density from a molecular orbital with both Mn-d_{xy} (38 %) and phenyl ligand (47 %) character to a molecular orbital centred on the acyl group (52 %) and the π orbital (41 %) of the acetylphenyl ring system. The $Mn(CO)_4$ moiety in this MO is near non-bonding in nature and would thus be expected to labilise. However, the small amount of electron density (2%) centred on the metal may prevent labilisation of this group on irradiation.

The third excited state involves a HOMO-1 → LUMO and is for the most part MLCT in character. This involves transfer of electron density from a molecular orbital centred on the Mn-d_{xz} orbital (74 %), with minor contributions from a CO_{cis} and CO $_{trans}$ ligand (12 % and 9 % respectively) to a virtual molecular orbital which is almost entirely acetylphenyl ligand based. The acyl group accounts for 52 % composition

and the phenyl ring for 41 %, while the metal and the CO ligands have a negligible contribution to this molecular orbital. The four CO ligand orbitals are completely non-bonding and thus the CO ligands may be labilised by excitation into this MLCT band. However, as was observed for the 2nd excited state the 2% Mn-d orbital may prevent this from occurring. The fourth excited state is HOMO → L+1 in nature. This involves transfer of electron density from a molecular orbital with mixed character (Mn-d_{xy} (38 %) and phenyl ligand (47 %)) to a molecular orbital centred on the Mn-d_z^2 orbital (23%) and which is antibonding for two of the π*-CO_{cis} ligands (64 %) and the CO_{trans} ligand (9 %), with respect to the metal centre.

The fifth lowest lying singlet excited involves a H-2→ L+1 electronic transition. This transition contains MLCT (metal to CO), LF (d-d transitions) and LBCT (CO to CO CT) character. This excited state is characterised by transfer of electron density from an orbital centred on the Mn-d_{zy} orbital (58 %) with minor contributions from both the CO (20 %) and phenyl (17 %) ligands to a virtual orbital centred on centred on the 2 of the π* CO_{cis} ligands (64 %) and the Mn-d_z^2 orbital (23%), with the CO_{trans} ligand also making a minor contribution (9 %). The CO_{cis} ligand in the plane of the ring is completely non-bonding in nature with respect to the CO_{cis} ligand-metal interaction and would thus be expected to be labilised on irradiation into this MLCT band. The 6th lowest lying excited state is HOMO-2 → LUMO in nature and is characterised by transfer of electron density from an orbital which is mainly Mn-d_{zy} in character to a molecular orbital which is centred both on the acyl (52 %) and phenyl (41 %) moieties of the ligand. The $Mn(CO)_4$ is almost non-bonding (with the exception of 2% on the Mn-d orbital) and thus would not be expected to labilise. This may however, result in labilisation of any of the CO groups which are completely non-bonding with respect to the metal centre.

Experimentally, irradiation at 405 nm or 365 nm should result in direct excitation into the two lowest lying excited states which are responsible for the observed electronic absorption band at 370 nm in the UV-Vis spectrum of (2-acetylphenyl-C,O)$Mn(CO)_4$ in pentane (Figure 17). Direct excitation of these charge transfer states is expected to result in CO loss, especially that *trans* to the phenyl ligand. In both cases, the predicted CO loss is observed experimentally and in the case of the N_2 matrix the N_2 trapped species is observed. Formation of a dicarbonyl species may arise from

irradiation into the second lowest lying excited state, which is the principle transition responsible for the 370 nm band in the UV-Vis spectrum. This transition is expected to result in the CO loss from either the *cis* or *trans* position or both. Irradiation at >520 nm is beyond the absorption limit of the ground state parent species. Thus irradiating at this wavelength may irradiate the previously produced photoproducts, thereby resulting in loss of product band and regeneration of the parent species.

2.7. Conclusion

An investigation of the photochemistry of two fluorinated manganese pentacarbonyl complexes was undertaken using matrix isolation in a range of matrix gases. For both complexes the predominant photoproduct formed on high energy excitation (313 nm) in a methane matrix and CO-doped methane matrix was the $Mn(CO)_5$ radical as a result of heterolysis of the Mn-C bond. In a dinitrogen matrix, irradiation resulted in the formation of a number of CO loss species. Visible irradiation (405 nm) of both complexes, resulted in loss of product bands and regeneration of the parent absorption bands. These results are in good agreement with predictions made by Density Functional Theory, which suggests that the unoccupied molecular orbitals for both $CF_3COMn(CO)_5$ and $CF_3Mn(CO)_5$ are strongly centred on the *cis*-CO ligands, with very little bonding interaction with the fluorinated moiety. These studies have also shown that the fluorinated moiety has very little involvement in the excited state chemistry of these complexes.

2.8. Bibliography

1 T.G. Richmond, *Activation of unreactive Bonds & Organic Synthesis*, S. Murai(ed.), Springer-Verlag, NewYork, **1999**, 3, 243-269

2 J.T. Lyon, L. Andrews, *Organometallics*, **2006**, 25, 1341-1343 and references terein

3 K.L. Hull, W.Q. Anani, M.S. Sanford, *J. Am. Chem. Soc.* **2006**, 128, 7134-7135

4 T.G. Richmond, C.E. Osterberg, A. M. Arif, *J. Am. Chem. Soc.* **1987**,109, 26, 8091-8092

5 (a) J.L. Kiplinger, M.A. King, A. Fectenkötter, A. M. Arif, T.G. Richmond, *Organometallics*, **1996**, 15, 5292-5301, (b) J. L. Kiplinger, A.M. Arif, T. G. Richmond, *Organometallics*, **1997**, 16, 2, 246- 254, (c) M.H.A. Benvenutti, P.B. Hitchcock, J.L. Kiplinger, J.F. Nixon, T.G. Richmond, *J. Chem. Soc., Chem. Commun.* **1997**, 1539

6 D.R. Fahey, J.E. Mahan, *J. Am. Chem. Soc.* **1977**, 99, 2501

7 J.L. Kiplinger, T.G. Richmond, C.E. Osterberg, *Chem. Rev.* **1994**, 94, 373

8 R.M. Ceder, J. Granell, G. Muller, M. Font-Bardía, X. Solans, *Organometallics*, **1995**, 14, 5544-5551

9 B.K. Bennett, R.G. Harrison, T.G. Richmond, *J. Am. Chem. Soc.* **1994**, 116, 11165-11166

10 X. Li, H. Sun, F. Yu, U. Flörke, H-F. Klein, *Organometallics*, **2006**, 25, 4695-4697

11 T. Akiyama, K. Fuchibe, J. *Am. Chem. Soc.* **2006**, 128, 1434-1435

12 J. Pola, M. Urbanová, Z. Bastl, Z. Plzák, J. Subrt, I. Gregora and V. Vorlícek, *J. Mater. Chem.*, **1988**, 8, 187

13 M.C. Asplund, A.M. Johnson, J.A. Jakeman, *J. Phys. Chem. B*, **2006**, 110, 1, 20-24

14 R. M. Chin, L. Dong, S. B. Duckett, M. G. Partridge, W. D. Jones and R. N. Perutz, *J. Am. Chem. Soc.*, **1993**, 115, 7685

15 M. Shimuzu, T. Hiyama, *Angew. Chem. Int. Ed.* **2005**, 44, 214-231

16 K. L. Hull, W.Q. Anani, M.S. Sanford, *J. Am. Chem. Soc.*, **2006**, 128, 7134-7135

17 V.V. Grushin, *Chem. Eur. J.* **2002**, 8, 1006-1014 and references therein

18 K. Sonogashira, Y. Tohda, N. Hagihara *Tetrahedron Lett., 1975*, 4467

19 *Handbook of Organopalladium Chemistry for Organic Synthesis*; Negishi, E.I., Ed.; Wiley-Interscience, New York, **2002**

20 M.S. Wrighton and D. Bredesen, *J. Organomet. Chem.*, **1973**, 50, C35-C38

21 T.E Bitterwolf, *J. Organomet. Chem.*, **2004**, 689, 3939-3952 and references contained therein

22 A.F. Hepp and M.S. Wrighton, *J. Am. Chem. Soc.*, **1983**, 105, 5934-5935

23 S.P. Church, H. Hermann, F.-W Grevels, K. Schaffner, *J. Chem. Soc., Chem. Commun.*, **1984**

24 S.P. Church, M. Poliakoff, J.A. Timney and J. J. Turner, *J. Am .Chem. Soc.*, **1981**, 103, 7515

25 T.A. Seder, S.P. Church and E. Weitz, *J. Am. Chem. Soc.*, **1986**, 108, 7518-7524

26 H. Yesaka, T. Kobayashi, K. Yasufuku and S. Nagakura, *J. Am. Chem. Soc.*, **1983**, 105, 6249-6252

27 L.J. Rothberg, N.J. Cooper, K.S. Peters and V.J. Vaida, *J. Am. Chem. Soc.*, **1982**, 104, 3536

28 M. Sarakha and G. Ferraudi, *Inorg. Chem.*, **1999**, 38, 4605-4607

29 T. Kobayashi, H. Ohntani, H. Noda, S. Teratani, J. Yamazaki and K. Yasufuku, *Organometallics*, **1986**, 5, 110

30 A.J. Rest and J.J. Turner , *J. Chem. Soc., Chem. Commun.* **1969**, 375-377 and references cited therein

31 O. Crichton, M. Poliakoff, A.J. Rest, J.J. Turner, *J. Chem. Soc., Dalton Trans.* **1973**, 1321-1324

32 M.C.R. Symons and R.L. Sweany, *Organometallics*, **1982**, 1, 834-836

33 L.S. Reich and A. Schneider, *Polymerisation by Organometallic compounds*, Wiley-Interscience, New York, **1966**

34 A.J. Rest, J. *Organomet. Chem.*, **1970**, 25, C30-C32 (Preliminary communication)

35 T.M. McHugh and A.J. Rest, *J.Chem. Soc., Dalton Trans.*, **1980**, 12, 2323-2332 and references therein

36 A.Horton-Mastin, M. Poliakoff, J.J. Turner, *Organometallics*, **1986**, 5, 405-408

37 D. Frigyes and G. Fogarasi, *Organometallics*, **1999**, 18, 5245-5251

38 W.T. Boese and P.C. Ford, *Organometallics*, **1994**, 13, 3525-3531

39 C.S. Kraihanzel and P.K. Maples, *Inorg. Chem.*, **1968**, 9, 1806-1815

40 W.T. Boese, B. Lee, D.W. Ryba, S.T. Belt, P.C. Ford, *Organometallics*, **1993**, 12, 4739-4741 and references therein

41 W. T. Boese and P.C. Ford, *J. Am. Chem. Soc.*, **1995**, 117, 8381-8391

42 K. McFarlane, B. Lee, J. Bridgewater, P.C. Ford, *J. Organomet. Chem.*, **1998**, 554, 49-61

43 F. U. Axe and D.S. Marynick, *J. Am. Chem. Soc.*, **1988**, 110, 3728-3734

44 A. Derecskei-Kovacs and D.S. Marynick, *J. Am. Chem. Soc.*, **2000**, 122, 2078-2086

45 L.D. Durfee and I.P. Rothwell, *Chem. Rev.*, **1988**, 88, 1059-1079

46 S.M. Massick, V. Mertens, J. Marhenke, P.C. Ford, *Inorg. Chem.*, **2002**, 13, 41, 3553-3559

47 (a) W. Beck, W. Hieber and H. Tengler, *Chem. Ber.*, **1961**, 94, 862-872, (b) K. Noack, U. Schaerer and F. Calderazzo, *J. Organomet. Chem.*, **1967**, 8, 517-526, (c) R.B. King, *Organometallic Synthesis – Volume 1 (Transition metal compounds)*, Academic Press, **1965**, 148

48 W.T. Boese and P.C. Ford, *Organometallics*, **1994**,13, 3525-3531

49 (a) R. J. McKinney, G. Firestein, H.D. Kaesz, *Inorg. Chem.*, **1975**, 14, 9, 2057-2061, (b) C.B. Knobler, S. S. Crawford, H.D. Kaesz, *Inorg. Chem.*, **1975**, 14, 9, 2062-2066, (C) H.D. Kaesz, *Inorganic Syntheses*, 26, 156, Wiley publications, **1989**

50 K. Noack, U. Schaerer and F. Calderazzo, *J. Organomet. Chem.*, **1967**, 8, 517-526

51 S.K. Shin, J.L. Beauchamp, *J. Am. Chem. Soc.*, **1990**, 112, 2057-2066

52 W. T. Boese and P. C. Ford, *J. Am. Chem .Soc.*, **1995**, 117, 8381-8391

53 É.Bencze, J. Mink, I. Pápai, I.S. Butler, D. Lafleur, D.F.R. Gibson, *J. Organomet. Chem.*, **2000**, 616, 1-9

54 B. Beagley, G.G. Young, *J. Mol. Struct.*, **1977**, 40, 295-297

55 Noel M. O'Boyle, Johannes G. Vos, GaussSum 0.9, Dublin City University, 2005. Available at http://gausssum.sourceforge.net

56 S. P. Church, M. Poliakoff, J.A. Timney, J.J. Turner, *J. Am. Chem. Soc.;* **1981**, 103, 7515-7520

57 W.T. Boese, P.C. Ford, *Organometallics*, **1994**, 13, 3525-3531

58 Simon E. J. Goff, Ph.D Thesis, University of Nottingham, **1997**

59 A.J. Rest, *J. Organomet. Chem.*, **1970**, 25, C30-C32 (preliminary communication)

60 M. Kozuka, T. Isobe, *Bull. Chem. Soc. Japan*, **1976**, 49, 7, 1766-1771

61 W.T. Boese, P.C. Ford, *J. Am. Chem. Soc.*, **1995**, 117, 8381-8391

62 G. J. Stor, D.J. Stufkens, P. Vernooijs, E.J. Baerends, J. Fraanje, K. Goubitz, *Inorg. Chem.*, **1995**, 34, 1588-1594

63 C.J. Breheny, S.M. Draper, F.-W. Grevels, W.E. Klotzbücher, , C. Long, M.T. Pryce, G. Russell, *Organometallics*, **1996**, 15, 3679-3687

64 G.P. McQuillan, D.C. McKean, C. Long, A.R. Morrisson, I. Torto, *J. Am. Chem. Soc.*, **1986**, 108, 863-871 and references cited therein

65 D.A. Pansak, R.J. McKinney, *Inorg. Chem.*, **1979**, 18, 3407

66 M.P. Wilms, E.J. Baerends, A. Rosa, D.J. Stufkens, *Inorg. Chem.*, **1997**, 36, 1541-1551

Chapter 3

Photochemistry and DFT studies of fluorinated pyridine pentacarbonyl tungsten systems

Chapter three involves a review of the photochemistry of $M(CO)_5$ systems, where M = W or Cr, bound to pyridine or substituted pyridines. The photochemistry of systems of the type $FpyW(CO)_5$, was then investigated using matrix isolation at 20 K in a number of matrix gases. Spectroscopic changes were monitored via UV-Vis and IR spectroscopy. Theoretical studies using TDDFT were also preformed. These are compared to the experimental data observed in matrix isolation studies.

3.1. Literature Survey

3.1.1. The photochemical substitution reactions of pyridine and substituted pyridine derivatives of Cr, Mo and W carbonyl complexes

Carbonyl complexes of the Group 6 metals (Cr, Mo, or W) have an extensive photochemistry. Although substitution is the major reaction, reactions resulting in isomerisation are also known. It has been previously described [1] that photolysis of compounds of the type $M(CO)_6$, (M = Cr, Mo, or W), results in the generation of $M(CO)_5$ as well as tetracarbonyl and tricarbonyl species.

$$M(CO)_6 \xrightarrow[-CO]{h\nu} M(CO)_5 + CO$$

(Reaction 1. 1)

This is not surprising as reactions involving ligand exchange and substitution dominate the excited–state chemistry of $M(CO)_6$ type complexes. The photogenerated species $M(CO)_5$, which is itself highly photoactive can then regenerate $M(CO)_6$ via coordination of CO onto the vacant site on the metal or can generate $M(CO)_5L$, via coordination with another ligand L. This is outlined below in Reaction 1.2 and 1.3.

$$M(CO)_5 + CO \longrightarrow M(CO)_6$$

(Reaction 1. 2)

$$M(CO)_5 + L \longrightarrow M(CO)_5L$$

(Reaction 1. 3)

In early work Graham et al.[2] described the generation of $Cr(CO)_5$ from $Cr(CO)_6$ following photolysis in an argon matrix at 20 K. Later work by Graham et al.[1(b)] describes the observation of similar results corresponding to generation of $Cr(CO)_5$ following photolysis of $Cr(CO)_6$ in a solid methane matrix at 20K. Similarly studies by Perutz et al.[1(e)] involving UV photolysis of $Mo(CO)_6$ in a methane matrix produced $Mo(CO)_5$ as the main product with the two secondary photolysis products $Mo(CO)_4$ and $Mo(CO)_3$ also produced in small concentrations.

Although it is clear that photolysis of $M(CO)_6$ (M = Cr, Mo, or W) in Ar or CH_4 matrixes leads to the formation of $M(CO)_5$ among other minor photoproducts, the position of the visible absorption band due to this pentacarbonyl fragment is strongly dependent on the matrix material. This blue shift in the absorption in different matrices, especially in the case of $Cr(CO)_5$ in CO doped Ar matrices and CH_4 matrices, has been assigned by Turner et al.[1(c)] to $M(CO)_5$---matrix interactions, resulting in the formation of weakly interacting $Cr(CO)_5$---Ar and $Cr(CO)_5$---CO complexes. This assignment by Turner at al.[1(c)] is in agreement with observations by Kelly et al.[1(d)] following laser flash photolysis of $Cr(CO)_6$ in room temperature argon-flushed perfluoromethylcyclohexane where it is observed that $Cr(CO)_5$ in solution might be more weakly bonded and therefore more reactive in perfluorocarbon solvents compared to hydrocarbon solvents.

Pulsed laser flash photolysis studies by Dobson et al.[3] of $W(CO)_6$ in methylcyclohexane (MCH) in the presence of the trapping ligand 4-acetylpyridine, although resulting in the formation of $W(CO)_5$(4-acpy) also revealed the presence of the reactive solvento-intermediate $W(CO)_5$(MCH). Spectra immediately after the flash are attributed to the solvento-intermediate $W(CO)_5$(MCH), however a few μs later the spectrum reveals the presence of O-bound $W(CO)_5$(4-acpy), which then subsequently converts to the expected N-bound isomer of $W(CO)_5$(4-acpy) with two visible region absorptions (λ_{max} = 404, 440 nm). The initial O-bound isomer is produced as a result of displacement of MCH for the stronger donor ligand 4-acetylpyridine. This O-bound $W(CO)_5$(4-acpy) isomer then interconverts to its N-bound isomer. This is similar to the observations made by Wang and co-workers[3] on photolysis of $W(CO)_6$ in THF solution in the presence of 4-cyanopyridine resulting in the preferential formation of the CN bound isomer of $W(CO)_5$(4-CNpy).

The photosubstitution chemistry of $W(CO)_5L$, L = pyridine, piperidine, PPh_3, PBr_3 or other donor ligands has been examined in depth in studies by Dahlgren and Zink[4] Photolysis of the nitrogen-donor complexes $W(CO)_5L$, where L = acetonitrile, cyclohexylamine, pyridine or piperidine in cyclohexane in the presence of the 1M entering ligand L′, where L′= another amine or CO, resulted in all cases in the monosubstituted photoproduct $W(CO)_5L'$. This arises from dissociative loss of the N

donor ligand. To obtain quantum yields for CO loss from $W(CO)_5L$, where L = acetonitrile, cyclohexylamine, pyridine or piperidine, L was used as the entering ligand. Photolysis of $W(CO)_5(CH_3CN)$ in cyclohexane in the presence of the entering ligand CH_3CN showed low quantum yields (Φ) of <0.01 for the disubstituted product *cis*-$W(CO)_4(CH_3CN)_2$. This indicates that the quantum yields for CO dissociation from the N-donor complexes are very low. It was found that for the N-donor complexes the quantum efficiency for ligand (Φ_1) and CO (Φ_2) substitution are 0.5 and $<10^{-2}$ respectively.

However conversely, irradiation of the phosphorus donor complexes, $W(CO)_5L$, where L = PPh_3, PBr_3, PCl_3, PH_3, or P(*n*-Bu)$_3$, with the entering ligand L′ = PPh_3, failed to produce clean reactions as indicated by the lack of clear isosbestic points. This indicated that the photochemical reaction pathway of the phosphorus donor complexes must be different to that observed for the N-donor complexes. When the entering ligand (L′) and the donor ligand(L) are not identical (L′ ≠ L or CO) the photogenerated product will be $W(CO)_4LL'$, i.e. a tetracarbonyl species containing both the P-donor ligand L and the entering ligand L′. These products are themselves very photoactive and readily undergo secondary photolysis. In contrast to the quantum efficiencies observed above for ligand and CO substitution in the N-donor complexes substitution for the P-donor ligand complexes displays quantum efficiencies of $\Phi_1 \cong \Phi_2 \cong 0.3$ for substitution of L and CO respectively.

In early work by Wrighton and co-workers[5] the photoprocesses in substituted tungsten carbonyl complexes, specifically complexes of the type $W(CO)_5X$, where X = pyridine, *trans*-2-strylpyridine or *trans*-4-styrlpyridine. The photochemistry of these tungsten carbonyl complexes is dominated by ligand dissociation leading to photosubstitution in solution. IR spectra of these complexes in solution show that the band maxima of the CO stretching frequencies are similar in position indicating a similar degree of π-back bonding to the CO ligands in pyridine and styrlpyridine. Generally, $W(CO)_5X$ type complexes on photolysis undergo dissociative decay via three pathways shown below in Figure 1.

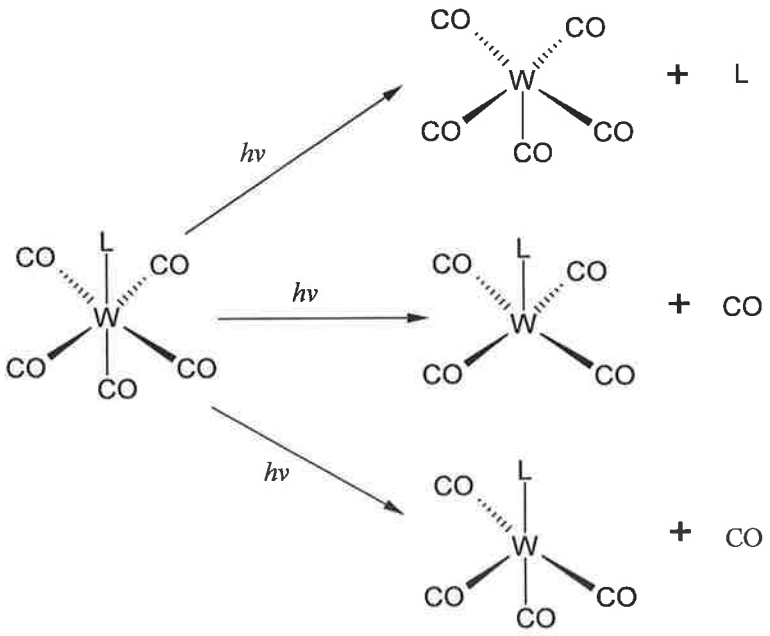

Figure 1 Decay pathway for complexes of the type $W(CO)_5L$, L=ligand

Photolysis of $W(CO)_5$ (pyridine) at 436 nm in ambient temperature isooctane solution in the presence of 3.66 M 1-pentane resulted in dissociative loss of the pyridine ligand (Φ = 0.63 for λ_{exc} 436 nm) and subsequent coordination of 1-pentene to generate $W(CO)_5$(1-pentene). On irradiation at shorter wavelengths the quantum efficiencies (Φ) for the dissociative loss of the pyridine ligand and formation of $W(CO)_5$(1-pentene) showed a notable decrease. Similarly, irradiation of $W(CO)_5$ (*trans*-4-styrlpyridine) at 436 nm in isooctane solution in the presence of 1-pentene results in the generation of $W(CO)_5$ (1-pentene), the quantum efficiency of which also reduces on going from an excitation wavelength of 436 nm to 254 nm. This is outlined below in Table 1.

Table 1 Quantum efficiencies for photoreactions of $W(CO)_5$(py) and $W(CO)_5$(*trans*-4-styrlpyridine)[5]

Reaction	$^{\Phi}$436 nm	$^{\Phi}$366 nm	$^{\Phi}$313 nm	$^{\Phi}$254 nm
$W(CO)_5$(Pyridine)	0.63	0.50	0.38	0.30
$W(CO)_5$ (*trans*-4-styrlpyridine)	0.16	0.08	0.05	0.0

The photosubstitution of CO was also determined by irradiating $W(CO)_5$(pyridine) in ambient-temperature isooctane in the presence of 0.25 M pyridine, which resulted in formation of only the *cis*-photoproduct *cis*-$W(CO)_4(pyridine)_2$. It was observed that

the quantum efficiencies (Φ) for the formation of *cis*-$W(CO)_4$(pyridine)$_2$ increased in going from λ_{exc} = 436 nm (Φ = 0.0) to 254 nm (Φ = 0.04). This observed decrease in pyridine substitution and increase in dissociative CO loss on decreasing wavelength indicates that two reactive excited states may be involved on irradiation in room temperature solution. The observation of only the *cis*-isomer may be due to the entering ligand coordinating to the coordinatively unsaturated species $W(CO)_4$(pyridine) before rearrangement. This reactivity of $W(CO)_5$(pyridine) is supported by photolysis studies of $W(CO)_5$(piperidine) in a ^{13}CO – enriched atmosphere where following photolysis ^{13}CO is selectively incorporated into equatorial positions in intermediate species.

Subsequent photolysis studies by Darensbourg and Murphy[6] of $M(CO)_5$ (amine), M = Cr, Mo, W ; amine = pyridine, piperidine, in the presence of ^{13}CO showed the occurrence of both CO and amine loss. Irradiation at 313 and 366 nm of $M(CO)_5$(amine), M = Cr, Mo or W ; amine = pyridine or piperidine, in hexane in the presence of ^{13}C-labelled CO resulted in both amine and CO dissociation, the latter resulting in formation of the ^{13}C-labelled *cis*-$M(CO)_4(^{13}CO)$(amine). It was observed that for both amine complexes for all three metals the quantum yields generally decrease in going down the triad, from Cr $\rightarrow$ W. For the W and Mo compounds of both amines there is a greater quantum efficiency for M-amine bond dissociation compared to M-CO bond cleavage at both 313 and 366 nm. In the case of chromium however, for both amine derivatives the quantum yields for both M-amine and M-CO cleavage are generally similar at 366 nm compared to 313 nm irradiation. This is outlined below (Table 2)[6] in which the quantum yield for both M-amine and M-CO bond cleavage for the amine derivatives of all 3 three metal carbonyls at both 313 nm and 366 nm are compared.

Table 2 Quantum yields for photodissociation of $M(CO)_5$(amine), M = Cr, Mo, W; amine = pip, py in hexane with 1.5atm ^{13}CO entering ligand.[6]

Complex	Product(s)	Φ366 nm	Φ313 nm
$Cr(CO)_5$(piperidine)	$Cr(CO)_5(^{13}CO)$	0.23	0.14
	cis-$Cr(CO)_4(^{13}CO)$(piperidine)	0.23	0.30
$Mo(CO)_5$(piperidine)	$Mo(CO)_5(^{13}CO)$	0.42	0.18
	cis-$Mo(CO)_4(^{13}CO)$(piperidine)	0.12	0.15
$W(CO)_5$(piperidine)	$W(CO)_5(^{13}CO)$	0.35	0.20
	cis-$W(CO)_4(^{13}CO)$(piperidine)	0.04	0.09
$Cr(CO)_5$(pyridine)	$Cr(CO)_5(^{13}CO)$	0.19	0.17
	cis-$Cr(CO)_4(^{13}CO)$(pyridine)	0.20	0.24
$Mo(CO)_5$(pyridine)	$Mo(CO)_5(^{13}CO)$	0.25	-
	cis-$Mo(CO)_4(^{13}CO)$(pyridine)	0.11	0.10
$W(CO)_5$(pyridine)	$W(CO)_5(^{13}CO)$	0.28	0.32
	cis-$W(CO)_4(^{13}CO)$(pyridine)	0.01	0.04

As previously mentioned irradiation of $M(CO)_5L$ can result in photosubstitution of either L (L = Ligand) or CO in solution at room temperature, with efficient loss of L, where L = pyridine or substituted pyridine, as the dominant reaction. Where L = pyridine a low lying MLCT absorption would be expected as the complex is low valent and there are available π^* pyridine levels. With variation of the substituents on the pyridine ligand a change in the MLCT band position should be observed. To this end, Wrighton et al.[7] carried out photochemical studies on $W(CO)_5$ (pyridine) and a number of substituted pyridine analogues. Following 436 nm irradiation at 298 K in isooctane the presence of 1-pentene resulted in the substitution of the pyridine or substituted pyridine ligand (L) and formation of $W(CO)_5$(1-pentene). This occurs with almost quantitative yield and very little formation of the tetracarbonyl substitution product $W(CO)_4$(L)(1-pentene) resulting from loss of the CO ligand. Irradiation at 514 nm shows very low quantum yields for the photosubstitution reaction of the pyridine ligand. The quantum yields for pyridine and a number of pyridine complexes on irradiation at 436 nm is shown below in Table 3.

Table 3 Quantum yields for photosubstitution of L in $W(CO)_5L$[7]

Ligand (L)	$^{\Phi}$436 nm	Lowest excited state
3,4-Dimethylpyridine	0.53	LF
4-Methylpyridine	0.55	LF
Pyridine	0.62	LF
3-Bromopyridine	0.66	LF
3-Acetylpyridine	0.75	LF
3-Benzoylpyridine	0.73	LF
3,5-Dibromopyridine	0.82	LF
4-Benzoylpyridine	0.12	MLCT
4-cyanopyridine	0.12	MLCT
4-Acetylpyridine	0.15	MLCT
4-Formylpyridine	0.05	MLCT
Piperidine	0.58	LF

It can be seen from Table 3 that those complexes, where the an MLCT absorption is the lowest excited state also have a very low quantum yield for photosubstitution of L (pyridine or substituted pyridine) on irradiation at 436 nm. It can be therefore concluded that with respect to photosubstitution of L, the W→ L CT state is much less reactive than the lowest energy Ligand field (LF) states.

Subsequent flash photolysis studies have been employed by Lees and co-workers[8] to investigate the intermediated produced on photolysis of $W(CO)_5L$, where L = 4-acetylpyridine, 4-benzoylpyridine, 4-cyanopyridine and 4-formylpyridine. It has been shown that complexes of these type in 77 K glasses show luminescence and that the position of the energy maxima changes depending on the electron-withdrawing effect of the coordinated ligand L. 465 nm irradiation of $W(CO)_5$(4-AcPy) and W(CO)5)4-BNPy) respectively in 298 K methylcyclohexane in the presence of 0.05 M ethanol resulted in the almost quantitative production of $W(CO)_5$(EtOH), uncomplicated by side reactions or subsequent photoproducts. The quantum yields for these photosubstitution reactions are Φ = 0.040 ($W(CO)_5$(4-AcPy)) and Φ = 0.035 ($W(CO)_5$(4-BNPy)) respectively. It was observed that in solutions not containing at least 0.025 M entering ligand (ethanol) that the isosbestic points rapidly disappeared However, no dependence of the quantum yield of the photosubstitution product on the

concentration of ethanol was observed, indicating that the ethanol quickly coordinates on to the $W(CO)_5$ intermediate produced on photolysis. The difference in the quantum yields for $W(CO)_5$(4-AcPy) and $W(CO)_5$(4-BNPy) in methylcyclohexane compared to those observed by Wrighton et al.[7] in isooctane can be accounted for by solvent effects.

However, in the case of $W(CO)_5$(4-cyanopyridine) the quantum yield (Φ) does not appear to be solvent dependent. Again, 465 nm photolysis of $W(CO)_5$(4-CNPy) at 298 K methylcyclohexane in the presence of 0.05M ethanol resulted in the formation of the photosubstitution product $W(CO)_5$(EtOH) with a quantum yield (Φ) of 0.062. The quantum yields of this photosubstitution reaction in isooctane (Φ=0.030), THF (Φ=0.030) and ethanol (Φ=0.029) which were carried out at 283 K as thermal substitution occurred at higher temperatures, indicates once again that the concentration of ethanol (0.05 M) does not influence the quantum yield of the photosubstitution product and acts as a good scavenger in trapping the $W(CO)_5$ intermediate species. The formation of this intermediate species, occurring from a low-lying MLCT state, is believed to result via distortion of the W-L bond forming either $W(CO)_5$ or the solvento-species $W(CO)_5S$, which is then scavenged by the entering ligand. The formation of such solvento-species $W(CO)_5S$ following irradiation of $W(CO)_5$Py has been shown to be dependent on both on the solvent used and the irradiation wavelength.

In studies by Langford et al.[9] this dependence is investigated in depth by monitoring these photoprocesses in the femtosecond to picosecond time domain. Femtosecond results have shown that for $W(CO)_5$(Pyridine) quantum yields are severely wavelength and medium dependent. The vibrationally relaxed species $W(CO)_5S$ is formed in less than 10 ps on irradiation of $W(CO)_5$py compared to 17ps for $W(CO)_6$. The reason for this faster relaxation time may be due to the ability of the dissociated py ligand to bear a greater share of the excess vibrational energy compared to the rigid diatomic CO ligand. Moreover various solvent parameters such as bulk solvent viscosity (η), acidity, bulk thermal conductivity (θ) and solvent reorientation all play a part in the ability of the solvento-species to initially form and the lifetime of that solvento-species. The generation of a solvent "cage effect", due to the presence of solvent molecules around the intermediate species, can make escape of geminate

partners more difficult, thus making recombination of the intermediate species more favourable. However, as solvent fluidity increases the cage effect decreases and with it the lifetimes of the transient species formed.

In later studies by Lees and co-workers[10] the photochemistry of the molybdenum analogues were investigated. Two $Mo(CO)_5L$ type complexes were studied, $Mo(CO)_5$(4-CNPy) with a lowest lying MLCT state and $Mo(CO)_5$(3-CNPy) with a lowest lying LF state. Irradiation was carried out at 283 K to reduce thermal substitution effects. Irradiation at 405, 436 or 458 nm in benzene solution in the presence of 0.1 M PPh_3 resulted in both cases in the generation of $Mo(CO)_5(PPh_3)$ resulting from photosubstitution of the ligand L, as shown in Figure 2.

$$Mo(CO)_5L \xrightarrow[0.1\ M\ PPh3]{h\nu} Mo(CO)_5(PPh_3) + L$$

L = 3-CNPy, 4-CNPy

Figure 2 Photosubstitution of $Mo(CO)_5L$ (L = 3-CNPy, 4-CNPy) at λ = 405, 436, 458nm[10]

In each case irrelevant of the irradiation wavelength, photolysis resulted in loss of the substituted pyridine ligand and generation of the species $Mo(CO)_5(PPh_3)$, while no evidence was observed for dissociative loss of CO. It was however, observed that the quantum efficiency (Φ) was highly dependent on the irradiation wavelength and also whether the lowest lying transition state of the complex was an MLCT or LF state. The quantum yields for both $Mo(CO)_5$(4-CNPy) and $Mo(CO)_5$(3-CNPy) following irradiation at 405, 436 or 458 nm, shown below in Table 4, indicate that although the excitation energy does play a part in the quantum yield it is the greater photoactivity of the complex with a lowest lying LF state ($W(CO)_5$(3-CNPy)) compared to that with a lowest lying MLCT state ($W(CO)_5$(4-CNPy)), which is the main determining factor.

Table 4 Quantum yields for photosubstitution of $Mo(CO)_5L$, L = 3-CNPy or 4-CNPy[7]

Complex	$^{\Phi}$405 nm	$^{\Phi}$436 nm	$^{\Phi}$458 nm
3-cyanopyridine	0.67	0.61	0.40
4-cyanopyridine	0.24	0.12	0.04

This is in agreement with the observations by Wrighton et al.[7] on irradiation of $W(CO)_5$(4-CNPy) and other substituted pyridine complexes in isooctane in the presence of 1-pentene, where those complexes with a lowest lying MLCT state produced much lower quantum yields than those with lowest lying LF states. The complex $W(CO)_5$(4-CNPy) also displays a quantum yield, which is more dependent on the excitation wavelength than its 3-CNPy analogue as it decreases from $\Phi = 0.24$ at $\lambda_{exc} = 405$ to $\Phi = 0.04$ at $\lambda_{exc} = 458$ nm. This may be due to increased population of the MLCT band resulting from long wavelength irradiation of the $W(CO)_5$(4-CNPy) complex. 458 nm photolysis of the 4-CNPy complex at varying temperatures showed little change in the quantum yield of ~0.05, indicating thermal activation effects play little part in population of the high energy states.

The photochemistry of the $Mo(CO)_5(PPh_3)$ is itself studied in great detail by Darensbourg and Murphy,[11] where photolysis in the presence of either PPh_3 or ^{13}CO results in the formation of *cis*- and *trans*- photoproducts. Irradiation at 366 and 313 nm of $Mo(CO)_5PPh_3$ in THF in the presence of PPh_3 resulted in photodissociation of CO with generation of both *cis*- and *trans*-isomers of $Mo(CO)_4(PPh_3)_2$, with the *cis*-isomer being the dominant photoproduct. The quantum yields for *cis*-$Mo(CO)_4(PPh_3)_2$ and *trans*-$Mo(CO)_4(PPh_3)_2$ at 366 nm ($\Phi_{366\ nm}$) are 0.50 and 0.08 respectively and for 313 nm photolysis $\Phi_{313\ nm} = 0.43$ and 0.07 respectively. Photolysis at these wavelengths of $Mo(CO)_5PPh_3$ in the presence of ^{13}CO generated *cis*- and *trans*-$Mo(CO)_4(^{13}CO)(PPh_3)$ in quantum yields similar to those observed for the $Mo(CO)_4(PPh_3)_2$ product. A small yield of ^{13}CO-enriched $Mo(CO)_6$ was also observed with quantum yields $\Phi_{366\ nm} = 0.11$ and $\Phi_{313\ nm} = 0.07$.

In studies by Glyn et al.[12] using pulsed laser photolysis (510 nm, 10 ns) of $W(CO)_5$(4-CNpy) in methylcyclohexane, it was observed that immediately after the flash, bleaching of the parent bands (~80%) and growth of two new bands at 1966 and 2000 cm^{-1} occurred. However, 5 μs after the flash these bands disappeared giving way to a

new band at 1954 cm^{-1}, assigned to the solvento species $W(CO)_5(MCH)$ with concomitant regeneration of the parent bands to 50% of the original intensity. After a subsequent 500 μs the band at 1954 cm^{-1} disappeared yielding near complete regeneration of the parent bands.The rate of decay of the bands at 1966 and 2000 cm^{-1} is equal to the rates of generation of the band at 1954 cm^{-1} and regeneration of the parent species. Incomplete recovery of the parent bands 500 μs after the laser pulse may be due to the formation of the dimer product $(CO)_5W(NC_5H_4CN)W(CO)_5$ as suggested by Lees and Adamson[13]. This would involve coordination of one W atom to the N atom of the pyridine ring while the other W is coordinated to the N atom of the CN group. The initial bands at 1966 and 2000 cm^{-1} may be respectively assigned as the a_1 and e modes of the square pyramidal (C_{4v}) $W(CO)_5$ group.

The shift of the ν_{co} bands to higher frequency compared to the ground state indicates that the TRIR spectrum following irradiation is that of an MLCT excited state. During the 10ns laser pulse most of the ground state $W(CO)_5$(4-CNpy) is converted via intersystem crossing to the ^{3}MLCT state. However, following this half the molecules of this excited state species decay back to the ground state species, while the other half form $W(CO)_5L$, where L is the entering ligand, via photoejection of the 4-cyanopyridine moiety (Figure 3).

$$W(CO)_5(CNpy) + L \longrightarrow W(CO)_5 + CNpy$$

Figure 3 Photoejection of 4-CNpy following irradiation of $W(CO)_5$(4-CNpy)

Under continuous photolysis the probability of return of the ^{3}MLCT state to the ground state via internal conversion from the ^{1}MLCT state is high. This can be seen in the quantum yields observed in photolysis experiments by Lees et al.[8] on $W(CO)_5$(4-CNpy) in a range of solvents.

Picosecond time-resolved absorption spectra of both $W(CO)_5$(4-cyanopyridine) and $W(CO)_5$(4-formylpyridine) following LF (355 nm) or MLCT (532 nm) excitations were observed by Lindsay et al.[14] Irradiation into the LF (355 nm) or MLCT (532 nm) absorption bands of $W(CO)_5$(4-formylpyridine) resulted in bleaching of the ground state absorption and generation of a long-lived excited state absorption in the visible

region. Following LF excitation this excited state absorption grows within 0-20 ps and remains unchanged after 20 ps. Another weak absorbance was observed after MLCT excitation (532 nm). This picosecond transient spectrum is assigned to the lowest MLCT excited state. LF excitation (355 nm) in toluene of $W(CO)_5$(4-cyanopyridine) generated an intense broad transient absorption (λ_{max} = 575 nm) with a lifetime of 45 ps. The transient absorption band observed on irradiation of $W(CO)_5$(4-CNpy) may be assigned as arising from a ^{3}MLCT excited state. With a lifetime of 292 ns it is far too long-lived to be due to either an LF or ^{1}MLCT state. The temporal changes observed in the picosecond absorption spectra of both complexes, are due to formation of the vibrationally cold ^{3}MLCT state via ^{1}MLCT $\rightarrow$ ^{3}MLCT (in the case of MLCT excitation at 532 nm) or ^{1}LF$\rightarrow$ ^{3}MLCT (LF excitation at 355 nm) intersystem crossing (ISC).

Záliš et al.[15] measured the TRIR spectra of $W(CO)_5$(4-CNpy), in methylcyclohexane. Following 500 nm excitation of the MLCT (CNpy) absorption band, population of the ^{3}MLCT excited state occurs via intersystem-crossing from the ^{1}MLCT (CNpy) state. Alternatively, 400 nm excitation of the MLCT (CO) absorption band populates the ^{3}MLCT excites state via both ^{1}MLCT (CNpy) intersystem crossing (ISC) and via an ultra fast internal conversion from ^{1}MLCT (CO) states as well as low-yield W-N bond. TRIR spectra show that on MLCT (CO) excitation at 400 nm only bands due to ^{3}MLCT (CNpy) and a weak transient absorption band at 1953 cm^{-1} due to low yield formation of $W(CO)_5$(methylcyclohexane) are observed. This 1953 cm^{-1} transient feature is not observed on 500 nm excitation as only the MLCT (CNpy) state is populated resulting in negligible quantum yields for the solvento-product. The excited state behaviour of W(CO)5(4-CNpy) in methylcyclohexane is very similar to that observed in acetonitrile.

As previously mentioned photolysis of $M(CO)_5X$, where M = Cr or Mo, W; X = pyridine or substituted pyridine, while often resulting in dissociative loss of X, can also, on photolysis, result in generation of the disubstituted isomer *cis*-$M(CO)_4X_2$, in the presence of an excess of X . The photochemistry of complexes of this type has been examined by Abrahamson et al.[16] 436 nm irradiation of *cis*-$W(CO)_4X_2$, where X = 3,4-dimethylpyridine, 4-ethylpyridine, pyridine, 3-benzotlpyridine, 4-

phenylpyridine, 3,5-dichloropyridine, 3,5-dichloropyridine, 3,5-dibromopyridine, 4-benzoylpyridine, 4-cyanopyridine or 4-formylpyridine in benzene in the presence of the trapping ligand L = *cis*-$Ph_2PCH{=}CHPPh_2$ resulted in all cases in the almost quantitative photoconversion to $W(CO)_4L$.

$$cis\text{-}\ W(CO)_4X_2 \xrightarrow[L,\ C_6H_6]{h\nu} W(CO)_4L + 2X$$

Figure 4 436nm irradiation of *cis*-$W(CO)_4X_2$ in benzene in the presence of the ligand L

This takes place via initial dissociative loss of X leading to the formation of the coordinatively unsaturated species $W(CO)_4X$, which then thermally reacts with the trapping ligand L to generate $W(CO)_4L$. Photolysis at 436 nm of *cis*-$W(CO)_4(py)_2$ and *cis*-$W(CO)_4$(3-Bz-py)$_2$ in the presence of the entering ligand PPh_3 resulted in the formation of *cis*-$W(CO)_4(PPh_3)$(py) and *cis*-$W(CO)_4(PPh_3)$(3-Bz-py) respectively. No evidence was observed for the generation of $W(CO)_3XL$ on photolysis (λ = 436 nm) of $W(CO)_4X_2$. This indicates that on photolysis the entering ligand L always displaces the ligand X from $W(CO)_4X$ and not CO. The quantum yields observed for formation of $W(CO)_4L$ varied between pyridine and substituted pyridines and in cases where MLCT is the lowest excited state neither the dissociative loss reactions of CO or X are very reactive.

Similarly, in later work by Chun et al.[17] 465 nm irradiation of *cis*-$W(CO)_4$(4-Me-py)$_2$ in 298 K benzene in the presence of 0.01 M 1, 10-phenanthroline resulted in the generation of $W(CO)_4$phen (Φ = 0.13) with no evidence for the dissociative loss of CO. It was observed that on long wavelength photolysis (465 nm & 514 nm) the photoreactivity of these complexes is dramatically reduced resulting in low quantum yields. This is attributed by Chun and co-workers[17] as being due to exclusive and direct population of the low-reactivity MLCT state. In contrast to this, irradiation at 360, 395 and 430 nm (LF excitation) results in higher quantum yields 0.32, 0.38 & 0.35 in the case of *cis*-$W(CO)_4$(4-Me-py)$_2$, indicating the higher energy LF states are considerably more photoreactive than the MLCT states. As observed by Abrahamson and Wrighton[16] the quantum yield (Φ) is highly dependent on the ligand L. Where L = 4-Ph-py, 3,5-Cl_2-py, 4-Bz-py, 4-CN-py extremely low quantum yields are observed as

the MLCT state is the lowest lying excited state compared to complexes where L = 4-Et-py, pyridine in which high quantum yields are observed indicating significant population of the lowest lying excited LF state.

In a recent review by Vlček[18] the unique spectroscopic and photochemical properties of a number of tetracarbonyl diimine complexes of the type $M(CO)_4$(α-diimine), where M = Cr, Mo or W and diimine = bpy , phenanthroline, pyridine-2-carbaldehyde, or 1,4-diazabutadiene were discussed. These systems can be viewed as consisting of two halves – a $M(CO)_4$ unit and a α-diimine unit. These systems all posses an intense band in the visible region, which is attributed to a M → diimine MLCT transition. These systems also exhibit a noticeable solvatochromic shift of this MLCT band to the blue on increasing solvent polarity. This blue shift of the MLCT band is also observed following pressure or temperature changes. The solvatochromism of the MLCT band is attributed to stabilisation of the ground and excited state by dipole interactions. These systems are generally more polar in the ground state due to charge distribution between the metal and the diimine unit as a result of σ-donation between the diimine unit and the metal centre. Conversely, the M→ diimine MLCT excited state reduced the dipole moment of the system. Overall, the observed solvatochromism is explained by the MLCT excited state transition and is determined by the extent of M → diimine backbonding and delocalisation of electron density in the diimine system.

As these systems are pseudo-octahedral , having C_{2v} geometry the equatorial and axial CO ligands have noticeably different reactivity and lability. The axial CO ligand of these systems is significantly substitution labile following irradiation in the presence of a coordinating solvent or trapping ligand. This results in the generation of the CO loss product *fac*-[$M(CO)_3$(L)(α-diimine). This photochemical substitution involves two or more excited state processes, which are populated by near-UV and visible photons. This is especially apparent when decreasing the irradiation wavelength (from near-UV to visible irradiation), whereby a notable decrease in the quantum yield is observed. Furthermore, the quantum yield is also strongly affected by the metal and diimine unit present. For photochemical substitution of these $M(CO)_4$(α-diimine) systems a dissociative and an associative pathway is available. The dissociative

pathway involves formation of a solvated tricarbonyl intermediate leading to formation of the ligand trapped tricarbonyl species *fac*-[M(CO)$_3$(L)(α-diimine). Traditionally, this process was attributed to a LF state however recently it has been suggested that dissociative CO loss occurs following population of a M → CO MLCT excited state. This is further suggested by theoretical calculations and ps-TRIR studies on systems such as Cr(CO)$_4$(bpy)[19,20] and W(CO)$_4$(phen)[21], which suggest that both the ^{1}LF and ^{3}LF states lie too high in terms of energy to be populated by low-energy near-UV or visible photons. Theoretical calculations suggest that a number of M → CO MLCT transitions lie above the lowest M → diimine transition. Furthermore, these calculations suggest that thermally induced back-population of the M → diimine MLCT state is energetically unfavourable and that near-UV irradiation of these systems populates a low lying M → CO MLCT excited state resulting in dissociative CO loss. In contrast visible irradiation results in population of the lower energy M → diimine MLCT state, with competing CO dissociation and rapid population via ISC of the non-radiative ^{3}MLCT state. Furthermore, in these systems the efficacy for population of this ^{3}MLCT state increases in the order Cr >> Mo > W due to increased spin-orbit coupling. This partially accounts for the decreasing quantum yield for dissociative CO loss observed for these systems on going down the group 6 triad.

This is in contrast to the associative CO loss process, whereby an excited state such as *[M(...L)(CO)$_4$(α-diimine)] is formed. The associative CO loss process involves an interaction between this *[M(...L)(CO)$_4$(α-diimine)] excited state and a nucleophile such as a phosphine trapping ligand. This occurs via population of the lowest lying M → diimine MLCT band by visible irradiation. This may then undergo ISC to the ^{3}MLCT state, although the efficiency for population of this triplet state does appear to be dependent not only on both the nature of the metal and diimine ligands present but also the excitation wavelength used. However, this is expected as higher energy irradiation would be expected to populate the higher energy M → CO MLCT band resulting in dissociative CO loss. Following population of this triplet state oxidation of the metal centre occurs resulting in formation of the excited state complex *[M+(CO)4(α-diimine-). If this excited state is sufficiently long lived as in the case of M(CO)$_4$(Phen), where M = Mo or W, it may undergo bimolecular interactions with an incoming nucleophile to form the ligand substituted tricarbonyl

complex. However, this associative pathway for CO loss is not observed for chromium systems such as $Cr(CO)_4(bpy)$[20] due to the smaller size of the Cr atom and the shorter excited state lifetimes. TRIR studies on $Cr(CO)_4(bpy)$[20] indicated that excitation at 400 or 500 nm resulted in population of a M $\rightarrow$ CO ^{1}MLCT state resulting in dissociative axial CO loss as well as relaxation via ISC to two non-radiative Cr $\rightarrow$ bpy ^{3}MLCT states, which then decay to the ground state over 8 and 87 ps. Due to the relatively short lifetimes no bimolecular interactions leading to associative CO loss are observed.

More recently, Vlček and co-workers[22] have also examined the ultrafast excited state dynamics observed in the $Re(CO)_3$ systems, *fac*-[Re(Cl)$(CO)_3$(*trans*-4-styrylpyrdine)$_2$] and *fac*-[Re(*trans*-4-styrylpyridine)$(CO)_3$(2,2′-bipyridine)]$^+$ prior to *trans-cis* isomerisation about the vinylic bond. Following 400 nm excitation of *fac*-[Re(Cl)$(CO)_3$(*trans*-4-styrylpyrdine)$_2$] bleaching of the parent bands was observed with concomitant generation of transient signals at 2012 and 1864 cm^{-1}. This is attributed to a ^1IL_t state based on comparison with [Re(4-Etpy)$(CO)_3$-(dppz)]$^+$ and other similar systems. This rapidly relaxes to the ^{3}IL state. Over 40 ps the 2012 cm^{-1} band narrows and that at 1864 cm^{-1} shifts to higher wavenumbers at 1926 and 1894 cm^{-1}. Concomitantly a band is generated at 2019 cm^{-1}, with a clear isosbestic point evident at 2017 cm^{-1}. These changes are attributed to a ^3IL_p transition state with the phenyl and pyridine rings in a perpendicular orientation. This excited transition state may then relax to the ground state to regenerate *fac*-[Re(Cl)$(CO)_3$(*trans*-4-styrylpyrdine)$_2$] or may form *fac*-[Re(Cl)$(CO)_3$(*trans*-4-styrylpyrdine)(*cis*-4-styrylpyrdine)] via a 90° rotation about the vinylic bond over the first 11-12 ps. Busby and co-workers[23] have also studied the ultrafast excited state dynamics of the comparable system *fac*-[Re(Cl)$(CO)_3$(*trans*-4-phenylazopyridine)$_2$] using ps-TRIR, TR-Vis and TR^3 spectroscopies. Initial excitation at 400 nm populates the ^{1}IL and ^{1}MLCT states localised on the *trans*-4-phenylazopyridine ligand, which then undergo ISC on a sub-picosecond time scale (< 1.4 ps) to populate the low energy ^{3}MLCT state also localised on the *trans*-4-phenylazopyridine ligand. Excitation leads to bleaching of the parent ground state bands with concomitant generation of bands at 2011, 1910 and 1872 cm^{-1} attributed to a transient species. This small shift to lower energy following transient formation is indicative of population of a ^{3}IL state

localised on the *trans*-4-phenylazopyridine ligand, although depopulation of the metal-based orbitals is not observed.

Vlček and co-workers have[22] also examined the excited state photochemistry of *fac*-[Re(*trans*-4-styrylpyrdine)$(CO)_3$(2,2`-bipyridine)]$^+$. Irradiation at 400 nm in CH_2Cl_2 solution resulted of the ground state bands and generation of higher energy bands at 1963, 1995 and 2061 cm^{-1}. This shift of the generated transient to higher wavenumbers is indicative of population of a Re → bpy ^{3}MLCT excited state via an optically excited ^{1}MLCT state. Following 10 ps the vibrationally hot band at 2061 cm^1 cools resulting a shift to 2074 cm^{-1}. A similar shift is observed in CH_3CN solution. The ^{3}MLCT state then rapidly decayed over 3.5 ps to populate a ^{3}IL state characterised by loss of the previously observed ^{3}MLCT bands and generation of a transient band at 2027 cm^{-1} and a broad absorption between 1910-1960 cm^{-1}. As observed in the IR spectrum of Re$(CO)_3$(*trans*-4-styrylpyrdine)$_2$ under similar conditions this excited state is assigned to a styrylpyrdine localised ^3IL_t state. This ^{3}IL state then decays to a ^{3}IL state with perpendicular geometry common to both the *trans*- and *cis*- isomers, *fac*-[Re(*trans*-4-styrylpyrdine)$(CO)_3$(2,2`-bipyridine)] and *fac*-[Re(*cis*-4-styrylpyridine) $(CO)_3$(2,2`-bipyridine)]. This common state then decays to the ground state, while retaining it perpendicular geometry, with a positive or negative 90° rotation about the C=C bond to form the *cis*- and *trans*-isomers respectively.

3.2. Aims and Objectives

The following section involves the syntheses of a number of novel fluorinated pyridine tungsten pentacarbonyl systems. The photochemical properties of these systems are investigated using matrix isolation in a variety of matrix gases. The aim of these photochemical studies is investigate whether irradiation results in photoinduced C-F bond activation. The photochemistry of these systems is then compared to the theoretical data observed in Density Functional Theory calculations

3.3. Experimental

3.3.1. Materials

All reactions were carried out under an inert atmosphere of Argon or nitrogen. All solvents were supplied by the Aldrich Chemicals Company. Dichloromethane, chloroform, diethyl ether, pentane, cyclohexane and ethanol were dried over $MgSO_4$ prior to use. All solvents used in laser flash photolysis experiments were of spectroscopic grade and were used without further purification. Tetrahydrofuran (THF) was distilled from sodium/benzophenone ketyl solution and used immediately. Methane, dinitrogen and carbon monoxide gases were supplied by Air products Ltd. Chromium and tungsten hexacarbonyl were supplied by Aldrich chemical company and were used without further purification. Silica Gel (Merck) was used as received. All mobile phases for column chromatography were dried over $MgSO_4$ before use. Pentafluoropyridine, 2,3,5,6-tetrafluoropyridine and pyridine (Aldrich. Chemical Co.), 3-fluoropyridine, 2-fluoropyridine, 2,6-difluoropyridine (Fluorochem. Ltd) were all used without further purification

3.3.2. Equipment

All syntheses were performed using conventional laboratory glassware under an inert argon atmosphere. All solutions were deoxygenated by purging with pure argon or nitrogen for ~10 mins. Column chromatography was carried out using neutral silica gel pH 6.5 – 7.5 or neutral Aluminium oxide. All infrared spectra were obtained on a perkin-Elmer 200 FT-IR spectrometer in a 0.1mm sodium chloride liquid solution cell using spectroscopic grade pentane, cyclohexane and THF. ^{1}H and ^{13}C spectra were recorded on a Bruker model AC 400 MHz spectrometer in $CDCl_3$ or Acetone-d_6 and were calibrated according to the deuterated solvent peak. ^{19}F NMR spectra were also recorded on a Bruker model AC 400 MHz spectrometer in $CDCl_3$ with trifluoroacetic acid as the standard. All UV spectra were measured in spectroscopic grade solvents on a Hewlett-Packard 8452A-photodiode-array spectrometer using a 1cm quartz cell. Elemental analysis of C, H, & N were carried out by the Chemical Services Unit, University College Dublin using an Exeter Analytical CE-440 elemental analyser

3.3.3. Synthesis

3.3.3.1. $W(CO)_5Py$

This was synthesised according to the general photochemical method outlined by Strohmeier[24] and described by Hermann and Salzer[25].

200 mls dry THF was added to a photolysis immersion well and purged for approx. 10 mins with argon. To the THF was then added $W(CO)_6$ (0.1 g, 0.284 mMol). The immersion well was equipped with an oil bubbler and a constant flow of nitrogen through the reaction mixture. A flow of cold water was set through the outer section of the well to keep the flask cool. A UV-light source was then placed in the centre of the lamp and the lamp is covered in order to keep it in complete darkness and prevent any possible secondary photolysis or destruction of photo-generated species. This colourless solution was then stirred vigorously under photolysis conditions for approximately 3 hrs. Following this the reaction solution had turned yellow in colour indicating formation of the THF adduct, $W(CO)_5THF$. This solution was then carefully transferred to a clean round bottom flask under a steady argon flow. To this yellow solution was added pyridine (0.03 mL, 0.36 mmol). This was then covered with aluminium foil and stirred vigorously overnight under inert conditions to yield a bright yellow solution. The solvent was removed under reduced pressure to yield a bright yellow solid. This crude solid was purified by dissolving in cold n-pentane. The insoluble tetracarbonyl side-product was removed by filtration. The desired pentacarbonyl product was then precipitated from solution by cooling with liquid nitrogen and then filtered.

Yield: 0.038g, 38%, IR ν_{co} : (pentane) 2073 (w), 1934 (s) and 1922 cm^{-1} (sh.) UV-Vis (pentane) : 382 nm; ^{1}H-NMR (400MHz, $CDCl_3$) : δ 8.73 (1 H), 7.73 (1 H), 7.22 (2 H)

3.3.3.2. 2-FPyW(CO)$_5$

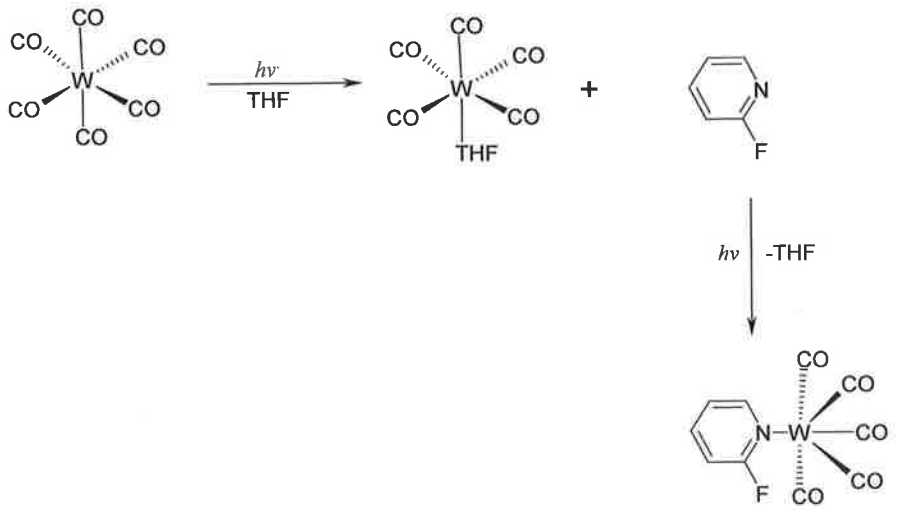

Scheme 1 Synthesis of 2-Fluoropyridinepentacarbonyltungsten

This compound was synthesised according to the method used for W(CO)$_5$Py.[24,25]

200 mls dry THF was added to a photolysis immersion well and purged for approx. 10 mins with argon. To the THF was then added W(CO)$_6$ (0.3 g, 0.852 mmol). This colourless solution was then stirred vigorously under photolysis conditions for approximately 3 hrs. Following this the reaction solution had turned yellow in colour indicating formation of the THF adduct, W(CO)$_5$THF. This solution was then carefully transferred to a clean round bottom flask under a steady argon flow. To this yellow solution was added 3-fluoropyridine (0.12 mL, 0.85 mmol). This was then covered with aluminium foil and stirred vigorously overnight under inert conditions to yield a bright yellow solution. Solvent removal resulted in the formation of bright yellow crystals. To remove any oxide which may have formed this solid was dissolved in pentane and filtered through celite. The solvent was then removed from the filtrate under reduced pressure to yield a bright yellow solid.

Yield: 0.105 g, 29%, M.p 55-60 °C. ^{1}H NMR (400 MHz, $CDCl_3$) : 8.70 ppm (d), 8.10 ppm(d), 7.95 ppm(m), 7.16 ppm(m), ^{13}C-NMR (100 MHz, $CDCl_3$) :201.4, 197.4, 186.8, 153.6, 150.9, 146.9, 93.9, 47.2, 26.0; ^{19}F-NMR (376 MHz, $CDCl_3$) : - 48.1 ppm; IR ν_{co} (pentane) : 2075 cm^{-1}, 1932 cm^{-1} and 1925 cm^{-1}, UV-Vis (pentane) : 285 nm and 387 nm

3.3.3.3. $W(CO)_5$-3FPy

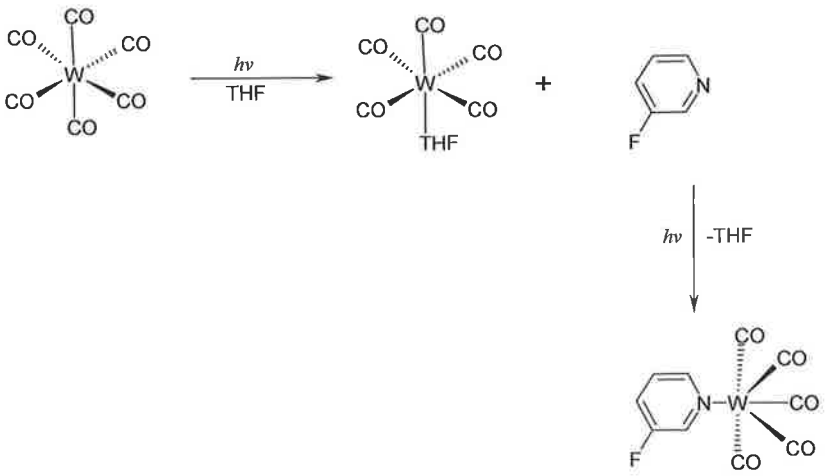

Scheme 2 Synthesis of 3-Fluoropyridine pentacarbonyltungsten

This compound was synthesised according to the method used for $W(CO)_5Py$.[24,25]

200 mls dry THF was added to a photolysis immersion well and purged for approx. 10 mins with argon. To the THF was then added $W(CO)_6$ (0.3 g, 0.852 mmol). This colourless solution was then stirred vigorously under photolysis conditions for approximately 3 hrs. Following this the reaction solution had turned yellow in colour indicating formation of the THF adduct, $W(CO)_5THF$. This solution was then carefully transferred to a clean round bottom flask under a steady argon flow. To this yellow solution was added 3-fluoropyridine (0.12 mL, 0.85 mmol). This was then stirred vigorously overnight under inert conditions to yield a bright yellow solution. Solvent removal resulted in the formation of bright yellow crystals. To remove any oxide which may have formed this solid was dissolved in pentane and filtered through celite. The solvent was then removed from the filtrate under reduced pressure to yield a bright yellow solid.

Yield:0.130g, 36% M.P 55-60 °C. ^{1}H NMR: (400 MHz, $CDCl_3$) : 8.66 ppm (dd), 8.60 ppm(d), 7.50 ppm(m), 7.24 ppm(m), UV-Vis (pentane) : 205 nm, 242 nm (sh.) and 395 nm (w, br.);^{13}C (100 MHz, $CDCl_3$) : δ 197.6, 165.0, 151.3, 151.2, 147.1, 126.9, 123.7, 33.3, 22.1, ^{19}F-NMR (376 MHz, $CDCl_3$) :-114 ppm (s, 1F), IR ν_{co} (pentane) : 2074 cm^{-1}, 1937 cm^{-1} and 1925cm^{-1}

3.4. Results

3.4.1. Photochemistry of 2-FPyW(CO)$_5$

3.4.1.1. Photolysis of 2-FPyW(CO)$_5$ in a methane matrix

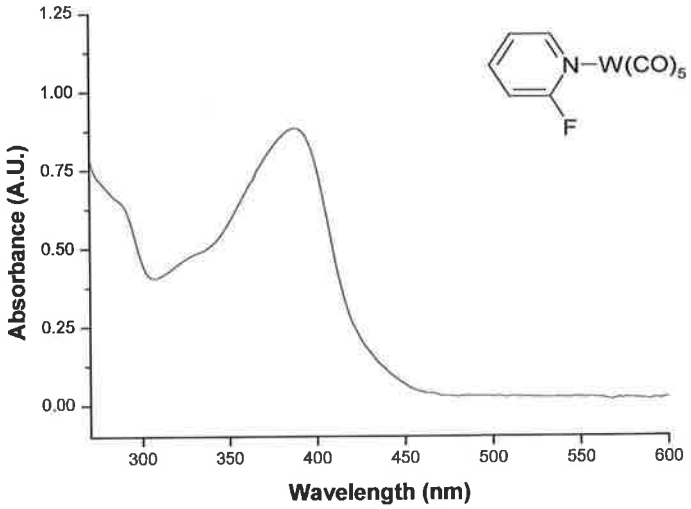

Figure 5 UV-Vis absorption spectrum of 2-FPyW(CO)$_5$ in pentane

2-Fluoropyridine pentacarbonyl tungsten is a bright yellow solid with a UV-Vis spectrum exhibiting three intense absorption bands – two high energy bands at approximately 238 nm (2.09 x 10^8 M^{-1} cm^{-1}) and 284 nm (2.03 x 10^7 M^{-1} cm^{-1}) and a low energy band at 390 nm (1.95 x 10^7 M^{-1} cm^{-1}) in pentane solution.

Monochromatic visible irradiation at 436 nm of 2-fluoropyridinepentacarbonyl tungsten in a methane matrix at 12 K resulted in bleaching of the parent bands at 1914, 1935 and 2077 cm^{-1} with concomitant production of two photoproducts. The predominant photoproduct was W(CO)$_5$ with IR active bands at 2087 and 1957 cm^{-1} with a third expected band in the region 1930-1935 cm^{-1}, which is masked by parent absorptions. This assignment is in agreement with that suggested by McHugh et al.[26] on formation of W(CO)$_5$ following irradiation of W(CO)$_5$(3-Brpy) based on generation of bands at 2097, 1963 and 1932 cm^{-1}. The weak product bands generated at 1997, 1900 and 1874 cm^{-1} are tentatively assigned to generation of *cis*-(2-

Fpy)(CH_4)W(CO)$_4$ based on comparison with the bands as observed by Dobson et al.[27] for a number of complexes of the type *cis*-W(CO)$_4$L(solvent), where L = PPh_3, P(O-*i*-Pr)$_3$ or P(OEt)$_3$. Irradiation also resulted in the generation of an ambiguous band at 1925 cm^{-1}. The product band at 2138 cm^{-1} due to free CO shows little change in intensity on irradiation at this wavelength thus confirming loss of the 2-Fpy ligand to be the predominant photoreaction.

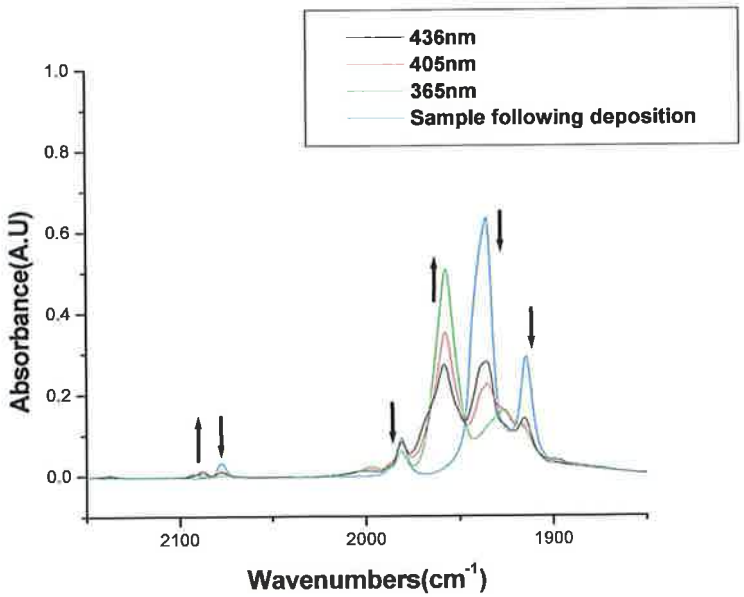

Figure 6 IR spectra of 2-FPyW(CO)$_5$ following monochromatic photolysis in a CH_4 matrix.

Broadband photolysis (λ_{exc}>520 nm) resulted in the regeneration of the parent bands and an increase in intensity of the product bands of both *cis*-W(CO)$_4$(2-Fpy)(CH_4) and W(CO)$_6$. This indicates that on low energy broadband photolysis regeneration of the parent species and generation of the product species occurs competitively, which may occur as a result of photolysis of the photoproducts as well as the parent compound.

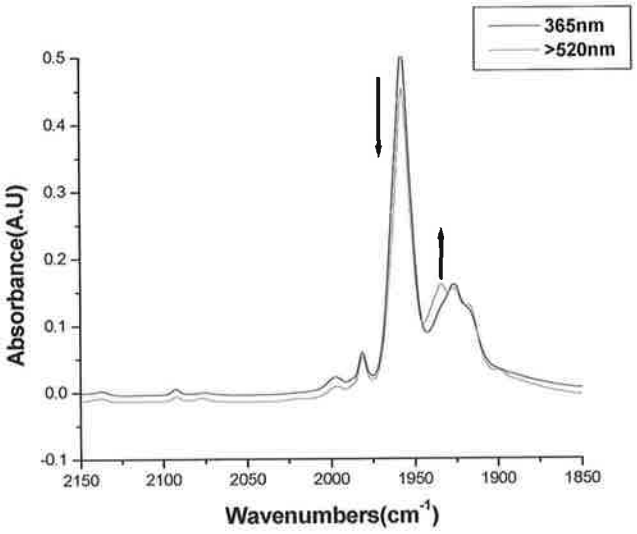

Figure 7 IR-Spectrum following photolysis at 365 nm (black) and following broadband photolysis at >520 nm (red). Reversal of reaction is observed with regeneration of the parent bands and depletion of the product bands.

3.4.1.2. Photolysis of 2-FPyW(CO)$_5$ in dinitrogen matrix

Deposition of 2-FPyW(CO)$_5$ in a N_2 matrix resulted in the generation of carbonyl bands at 1921, 1941 and 2077 cm^{-1}. A band was also observed at 1984 cm^{-1} indicating that some decomposition of the parent compound may have occurred on deposition.

Monochromatic irradiation at 436 nm of 2-FPyW(CO)$_5$ in a N_2 matrix at 12 K resulted in strong bleaching of the parent bands at 1921, 1941 and 2077 cm^{-1} and a decrease in intensity of the hexacarbonyl band at 1984 cm^{-1} with concomitant generation of a strong carbonyl bands at 1971, 1968, 2089, 2229 cm^{-1} which are assigned to generation of W(CO)$_5$ via cleavage of the W-N bond and subsequent coordination of N_2 onto the free coordination site on the metal centre to yield W(CO)$_5$N$_2$ as the major product. These bands are in agreement with those observed by McHugh et al.[26] for this species following photolysis of 3-BrPyW(CO)$_5$ in a N_2 matrix. The product band generated at 2008 cm^{-1} is tentatively assigned to the CO loss species W(CO)$_4$(2-FPy)N$_2$, while the N_2 stretch for this species may overlap with that occurring at 2229 cm^{-1} for W(CO)$_5$N$_2$. Irradiation at 405 nm resulted in further bleaching of the parent bands and an increase in intensity of the bands due to both W(CO)$_5$N$_2$ and the tetracarbonyl W(CO)$_4$(2-FPy)N$_2$, while no change was observed in the intensity of the hexacarbonyl band at 1984 cm^{-1}.

Photolysis at 365 nm for 40 mins resulted in regeneration of the parent species, with little depletion observed for either the pentacarbonyl or tetracarbonyl photoproducts, indicating the photoreaction may have reached a steady state. Broadband irradiation at $\lambda > 520$ nm resulted in growth of both the parent bands and the product bands indicating a competitive reaction between regeneration of the parent complex and a forward reaction involving loss of either the pyridine or CO ligand.

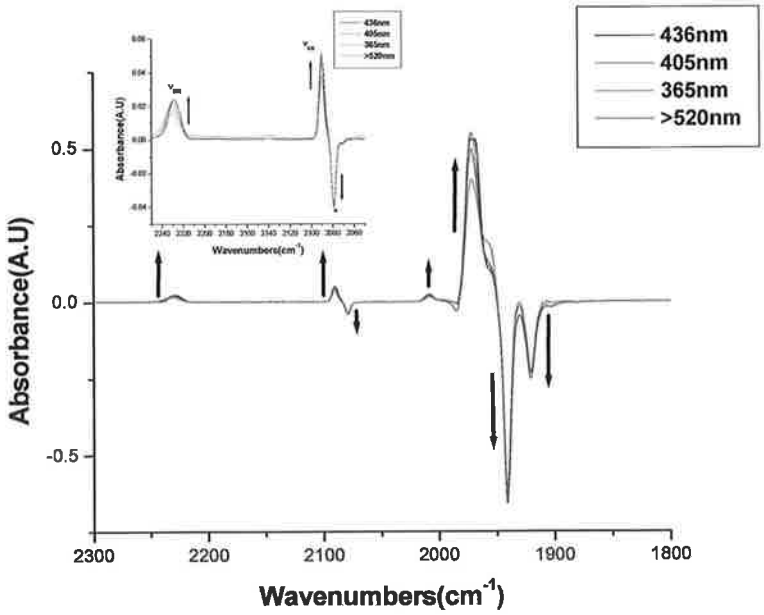

Figure 8 Overlay of IR difference spectra of $(C_5H_3FN)W(CO)_5$ in a N_2 matrix following photolysis at 436 nm (black), 405 nm (red), 365 nm (green) and >520 nm (blue). The inset spectrum shows the growth of the ν_{NN} band, the growth of a product band at 2089 cm^{-1} and the depletion of the parent band at 2077 cm^{-1}.

3.4.1.3. Photolysis of 2-FPyW(CO)$_5$ in 2% CO-CH$_4$ Matrix

On deposition of 2-FPyW(CO)$_5$ in a 2% CO doped methane matrix three carbonyl bands were observed at 1914, 1937 and 2077 cm^{-1}. Studies were carried out in 2% and 5% CO doped methane matrices respectively to investigate whether hexacarbonyl formation occurred and whether the concentration of the CO present affected the formation of the 2-FPy ligand loss and tetracarbonyl formation. The results observed for both 2% and 5% CO doped matrices were similar and thus only those relating to the 2% CO doped methane matrix will be outlined and discussed.

Monochromatic irradiation of 2-FPyW(CO)$_5$ at 436 nm in a 2% CO doped methane matrix resulted in generation of product bands at 2088, 2046, 2006, 1981, 1968, 1885, 1868 and 1842 cm^{-1} with concomitant bleaching of the parent bands at 1914, 1937 and 2077 cm^{-1}. The growth of the band at 1981 cm^{-1} indicates formation of the hexacarbonyl W(CO)$_6$, while the product bands 2046, 2006 and 1885 cm^{-1} are tentatively assigned to formation of the photoproduct *cis*-W(CO)$_4$(2-Fpy) and that at 2137 cm^{-1} to free CO present in the matrix. The product bands at 2088 and 1968 cm^{-1} are at a lower wavelength than those expected for W(CO)$_5$ (2097, 1962, 1930 cm^{-1}) and thus may be due to formation of a photoproduct resulting from coordination of W(CO)$_5$ to the pyridine ring through an η^2-π interaction as observed by Alamiry[28] on photolysis of Cr(CO)$_5$(acetylpyridine) in an Ar matrix and by Dobson et al.[29] in laser flash photolysis experiments of Cr(CO)$_6$ in arene solution.

The bands observed at 1842 and 1868 cm^{-1}, which are similar to those observed by Boxhoorn et al.[30] for Cr(CO)$_3$pyrazine, may be due to generation of the 14 electron species W(CO)$_3$(2-FPy).

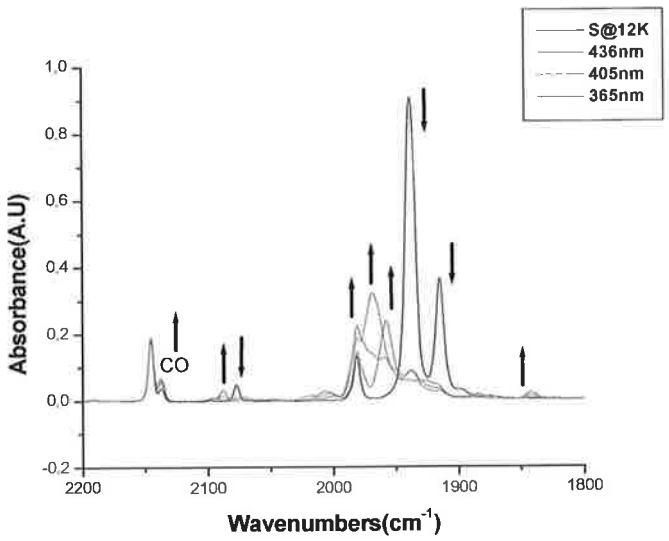

Figure 9 Overlay of IR spectra of 2-FPyW(CO)$_5$ in a 2%CO-CH$_4$ matrix following monochromatic photolysis at 436 nm (red), 405 nm (green) & 365 nm (blue). The spectrum in black is 2-FPyW(CO)$_5$ following deposition in 2% CO-CH$_4$ at 12 K.

On 405nm irradiation the parent bands, the product bands due to the hexacarbonyl W(CO)$_6$ and the CO loss products *cis*-W(CO)$_4$(2-FPy) and W(CO)$_3$(2-FPy) increased in intensity while the bands due to η^2-π bound W(CO)$_5$(2-FPy) depleted indicating that at 405 nm CO loss is more energetically favourable than the thermodynamically unstable coordination of pyridine to W(CO)$_5$ via the π-electrons of the pyridine ring. The generation of new product bands at 2092 and 1926 cm^{-1} and growth of those at 1841 and 1957 cm^{-1} on irradiation at 365 nm indicates generation of the species W(CO)$_5$ via W-N bond cleavage. The bands at 2092, 1957 and 1926 cm^{-1} are comparable to those observed by McHugh et al.[26] at 2092, 1962 and 1930 cm^{-1} for W(CO)$_5$ formation. This is further substantiated by generation of a band, although partially masked by the matrix absorptions, at 1000 cm^{-1}, due to the dissociated 2-fluoropyridine ligand. The product bands from the η^2-π bound W(CO)$_5$(2-Fpy) and 1980 cm^{-1} due to W(CO)$_6$ disappear on extended irradiation indicating at low wavelengths, loss of the pyridine ligand is the dominant reaction. Broadband irradiation (>520 nm) demonstrates the photochromic nature of pyridine coordinated pentacarbonyls as regeneration of the parent species is observed along with some further W(CO)$_5$ formation while the CO loss products decreased in intensity.

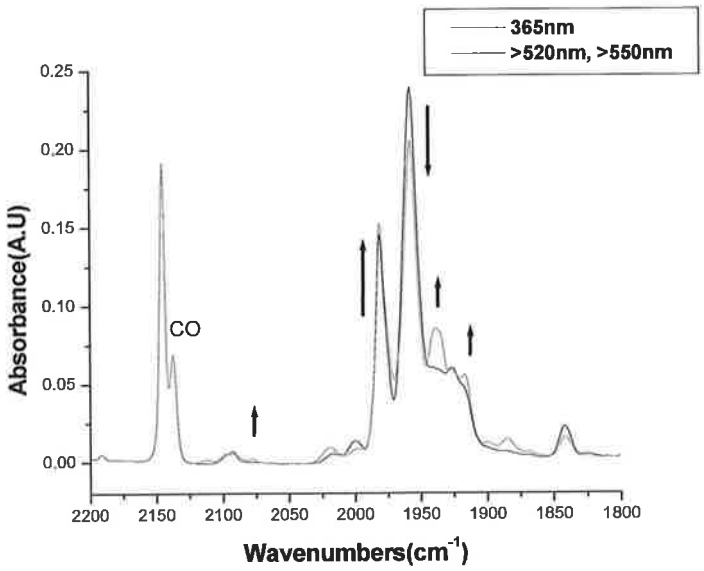

Figure 10 Overlay of IR spectra of 2-FPyW(CO)$_5$ in a 2% CO-CH$_4$ matrix following broadband photolysis at >520 nm and >550 nm. Regeneration of the parent and an increase in intensity of the W(CO)$_6$ band is observed.

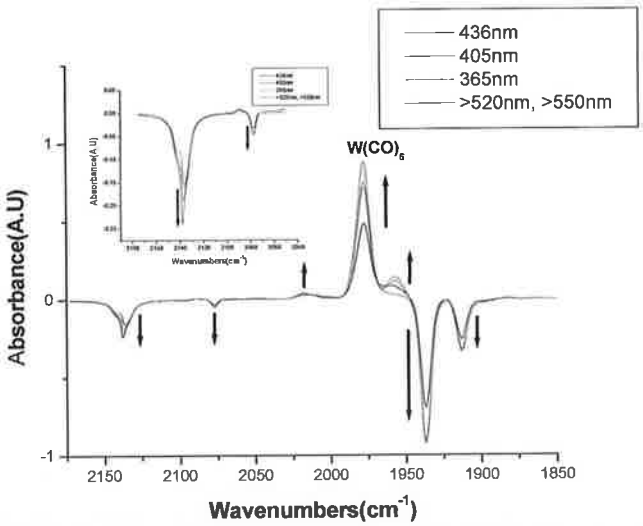

Figure 11 Overlay of IR difference spectra of 2-FPyW(CO)$_5$ in a 5%CO-CH$_4$ matrix following photolysis at 436 nm (Black), 405 mn (Red), 365 nm(Green) and >520 nm,>550 nm(Blue). Depletion of 3 parent bands and free CO band is observed with formation of 2 photoproducts – a tetra- and a hexacarbonyl species at 365 nm and 405 nm respectively.

3.4.2. Photochemistry of 3-FPyW(CO)$_5$

3.4.2.1. Photolysis of 3-FPyW(CO)$_5$ in a methane matrix

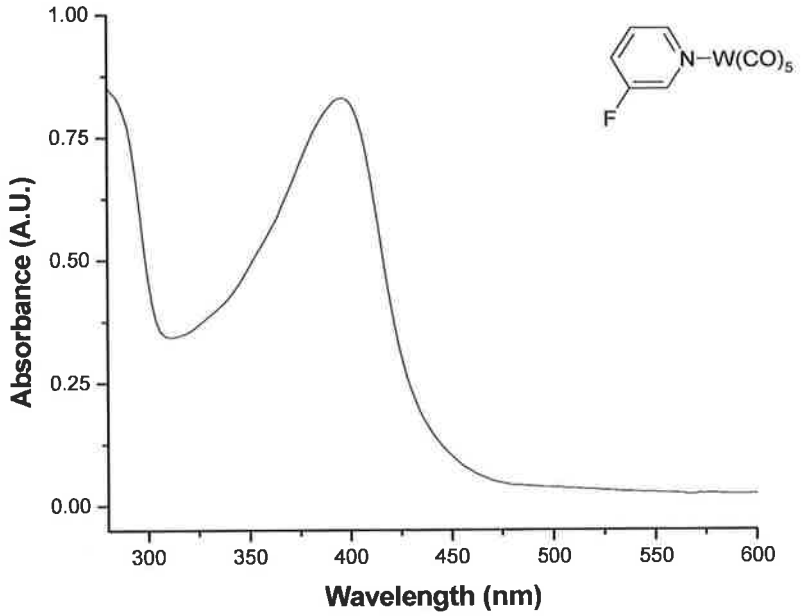

Figure 12 Electronic absorption spectrum of 3-FpyW(CO)$_5$ in Pentane

3-Fluoropyridine pentacarbonyl tungsten is a bright yellow coloured solid with a UV-Vis spectrum exhibiting three intense absorption bands – two high energy bands at approximately 232 nm (1.07 x 10^8 M^{-1} cm^{-1}) and 288 nm (9.59 x 10^6 M^{-1} cm^{-1}) and a low energy band at 388 nm (6.57 x 10^6 M^{-1} cm^{-1}) in pentane solution.

On deposition of 3-fluoropyridinepentacarbonyltungsten in a methane matrix four carbonyl bands were observed at 1941, 1933, 1919 and 2075 cm^{-1}. Initial photolysis at 436 nm for 30 mins resulted in depletion of the parent bands and concomitant generation of product bands at 1956 and 2086 cm^{-1} (Figure 13). These bands are tentatively assigned to generation of the W-N bond cleavage product W(CO)$_5$ which may be interacting with the 2-fluoropyridine moiety either via an agostic interaction through a C-H bond or via the π-electrons of the pyridine ring.

Subsequent irradiation at 405 nm for 60 mins resulted in a further decrease in intensity of the parent bands with an associated increase in intensity of the product bands at 1956, 2086 cm^{-1}, assigned to formation of an η^2-π or agostic C-H bound $(C_5H_3FN)W(CO)_5$.[27,28] On extended irradiation at this wavelength further product bands were generated at 1001 and 2091 cm^{-1} (Figure 14).

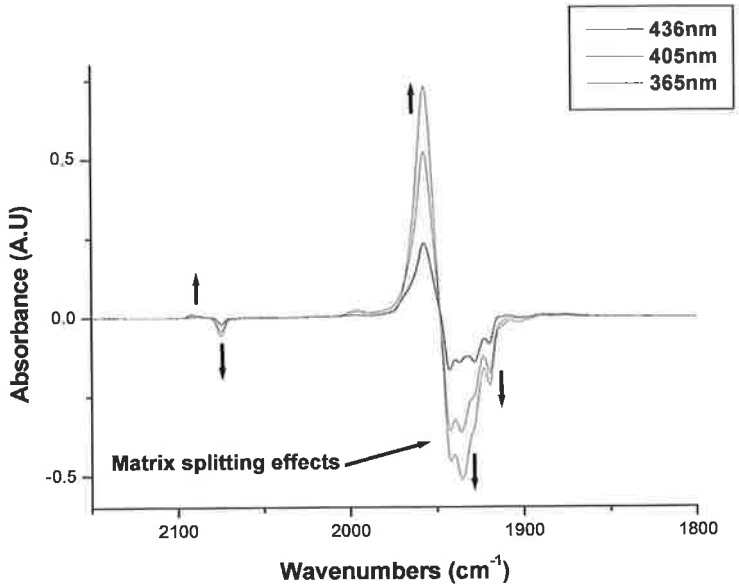

Figure 13 IR difference spectra of $(C_5H_3FN)W(CO)_5$ in a CH_4 matrix indicating bleaching of the parent bands and generation of a photoproduct.

Following photolysis at 365 nm for 30 mins a further bleaching of the parent bands at 2075 cm^{-1}, 1932 cm^{-1} was observed. Concomitantly an increase in intensity of the product bands at 1956 cm^{-1} and 2091 cm^{-1} was observed. This indicates that high energy photolysis resulted in the preferential formation of $W(CO)_5$ via W-N bond cleavage. On further monochromatic irradiation at 334 nm & 313 nm further bleaching of the parent bands was observed with further generation of the ligand loss product $W(CO)_5$.

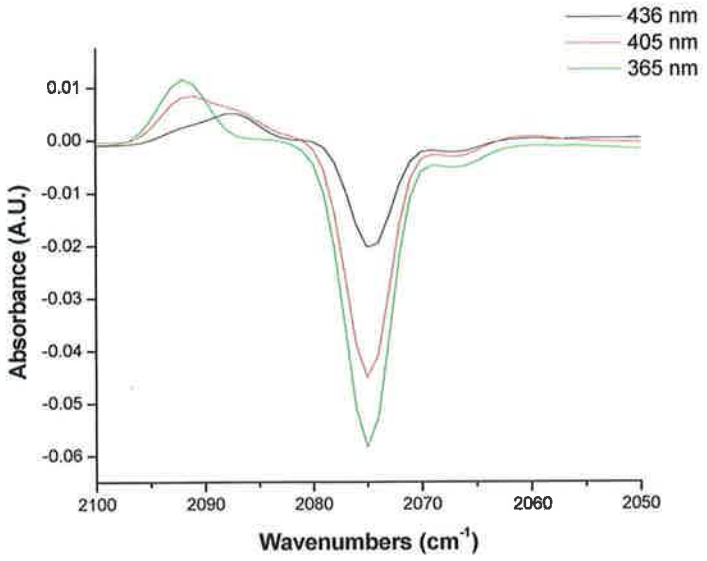

Figure 14 IR difference spectra of $(C_5H_3FN)W(CO)_5$ in a CH_4 matrix, Detail from Fig. 22 in the region 2100 cm^{-1} – 2050 cm^{-1} indicating band depletion at 2075 cm^{-1} band growth at 2090 cm^{-1}.

3.4.2.2. Photolysis of 3-FPyW(CO)$_5$ in a N_2 matrix

Following deposition of 3-FPyW(CO)$_5$ in a N_2 matrix three ν_{co} stretching bands were observed at 1930, 1949 and 2075 cm^{-1}. Two weak bands were also observed at 1926 and 1940 cm^{-1}, which may be due to matrix splitting.

As is evident in Figure 16 irradiation at 436 nm for 60 mins resulted in bleaching of the parent carbonyl bands at 1930, 1949 and 2075 cm^{-1} with concomitant generation of product bands at 1891, 1926, 1940, 1971, 2004, 2089 and 2228 cm^{-1}. Little generation of free CO indicates cleavage of the W-N bond and formation of the N_2 substituted species W(CO)$_5$N$_2$ to be the predominant reaction (Figure 16). The other weaker bands generated at 1891, 2004, 2137 and 2195 cm^{-1} are tentatively assigned to generation of a 3-PyW(CO)$_4$N$_2$. Irradiation at 405 nm for 40 mins results in bleaching of the parent bands and the bands at 1926 cm^{-1} and 1940 cm^{-1}. The strong band at 1971 cm^{-1} also decreased in intensity while that at 2089 cm^{-1} increased in intensity.

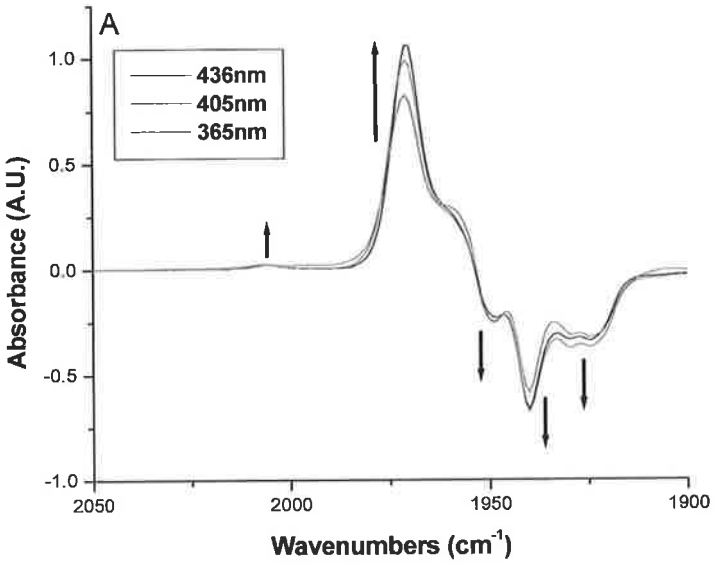

Figure 15 The area of the spectrum 2275 cm^{-1} to 2050 cm^{-1} indicating bleaching of parent bands and generation of product bands

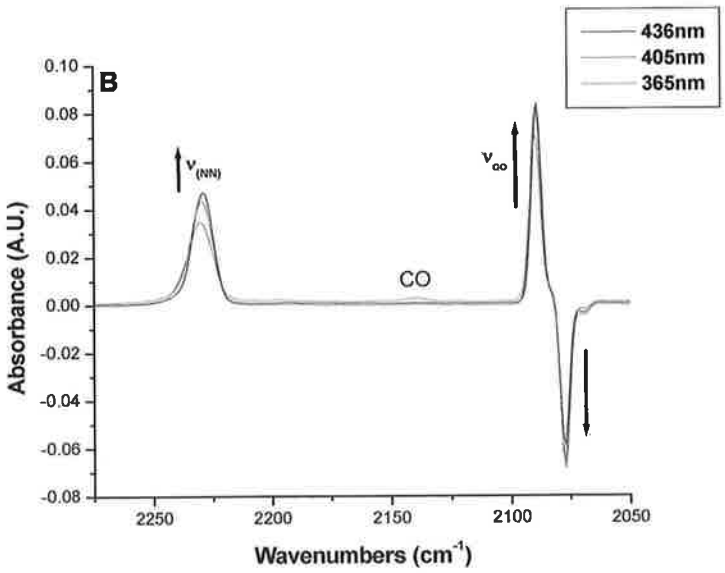

Figure 16 Dinitrogen stretch at 2228 cm^{-1} is indicated by ν_{NN}. A very weak free CO band is observed at 2137 cm^{-1} on photolysis at 365 nm.

Photolysis at 365 nm (Figure 17) resulted in further bleaching of the parent bands and product bands with concomitant generation of new product bands at 1938 and 1958 cm^{-1}. Broadband photolysis (λ_{exc} >520 nm, 30 mins) resulted in an increase in intensity of the product bands at 1939 cm^{-1} and 2228 cm^{-1} while little change is observed for the parent band at 2077 cm^{-1} or product band at 2089 cm^{-1}.

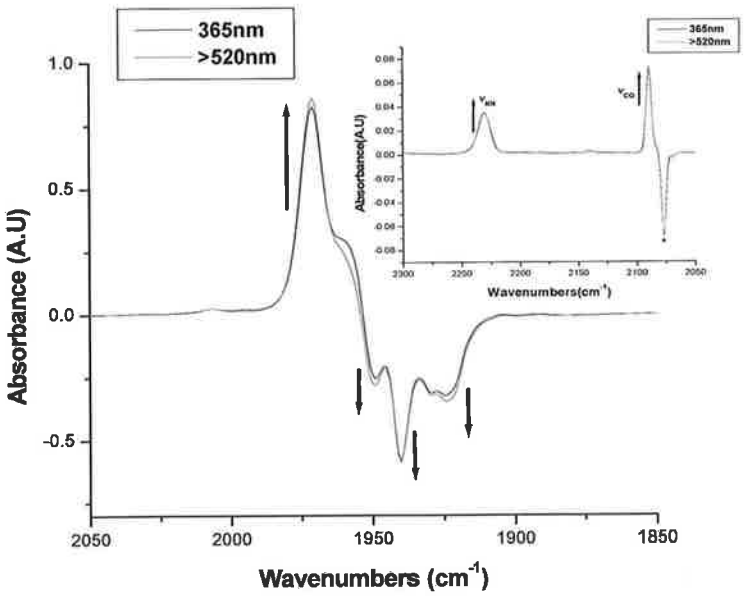

Figure 17 Broadband Photolysis of 3-FPyW(CO)$_5$ in a N_2 matrix

Main spectrum shows 2050 cm^{-1}-1850 cm^{-1} region of the spectrum on photolysis at 365 nm (black) and subsequently following photolysis at >520 nm (red). The inset spectrum shows the region 2300-2050 cm^{-1}.

3.4.2.3. Photolysis of 3-FPyW(CO)$_5$ in a 5% CO-doped CH_4 matrix

On deposition of 3-FPyW(CO)$_5$ in a 5% CO doped methane matrix three carbonyl bands were observed at 2075, 1935 and 1918 cm^{-1}.

Initial irradiation at 436 nm for 60 mins resulted in a decrease in intensity of the parent bands with simultaneous generation of product bands at 2089, 1968 due to formation of a pentacarbonyl species. Subsequent irradiation at 405 nm for 60 mins resulted in a further bleaching of the parent bands with a continued increase in intensity of the band at 1979 cm^{-1} indicating further formation of W(CO)$_6$.

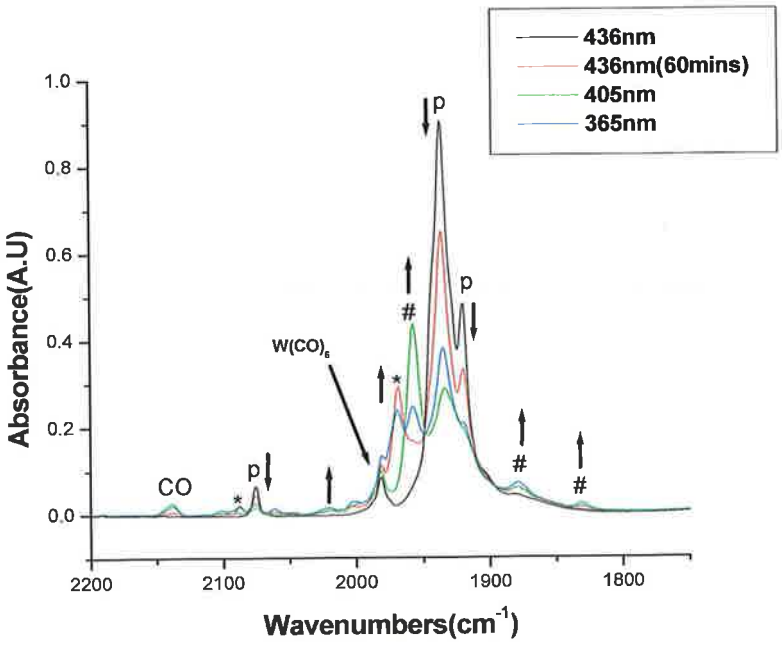

Figure 18 IR spectra of 3-FPyW(CO)$_5$ in a 5% CO doped CH_4 matrix. 20 mins photolysis at 436 nm (black), extended photolysis for 60 mins at 436 nm (red). Irradiation at 405 nm (green) and after irradiation at 365 nm(blue). Parent carbonyl bands are indicated with P, while those due to generation of the pentacarbonyl species W(CO)$_5$ are indicated by *. The bands indicated by # are due to another CO loss species observed on 405nm irradiation.

Following this the sample was irradiated at 365 nm for 40 mins. This resulted in a decrease in intensity of the parent bands and the product bands due to both W(CO)$_5$ and W(CO)$_6$. On irradiation at > 520 nm regeneration of the parent bands is observed with concomitant loss of the product bands due to both the W(CO)$_5$ and W(CO)$_6$ product species.

3.5. Quantum Chemical Calculations

3.5.1. Calculations on compounds of the type $W(CO)_5L$

3.5.1.1. Geometry Optimisation

The structures of compounds of the type $W(CO)_5L$, where L = 2-fluoropyridine, 3-fluoropyridine or 4-fluoropyridine, were optimised using the B3LYP/LANL2DZ level of theory. Due to the size of the tungsten atom geometry optimisation was initiated at the RHF/ LANL2DZ theory level followed by further optimisation with this basis set and B3LYP model chemistry. As is evident in Figure 19 the theory predicts that in each case the complex will adopt the C_{4v} local symmetry of the $W(CO)_5$ moiety although the literature[31] does suggest that compounds of the type $W(CO)_5$pyridine may adopt C_{2v} local symmetry.

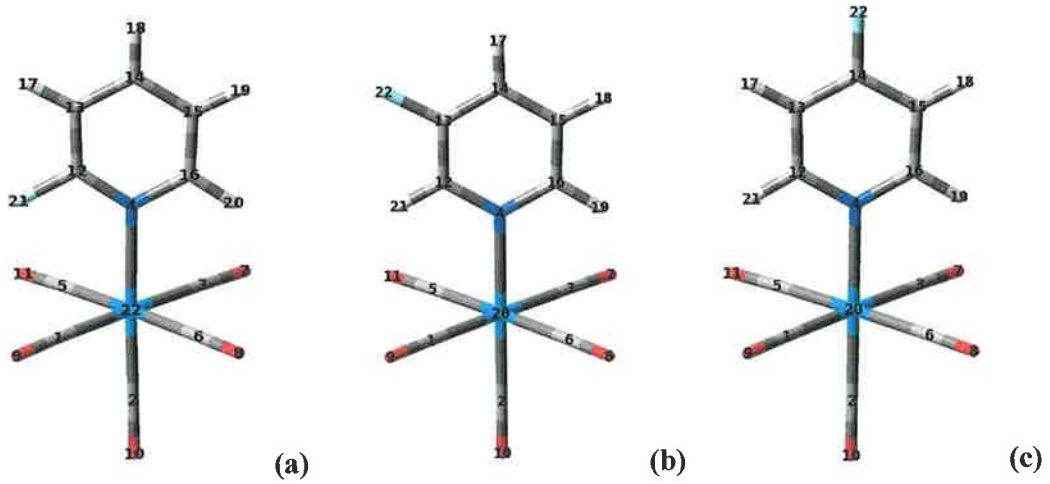

Figure 19 Geometry optimised structures of (a) 2-FpyW(CO)$_5$, (b) 3-FPyW(CO)$_5$ and (c) 4-FPy W(CO)$_5$ attained using the B3LYP/LANL2DZ level of theory

The calculated bond lengths (Å) and bond angles (°) for the geometry optimised structures of (a) 2-FPyW(CO)$_5$, (b) 3-FPyW(CO)$_5$ and (c) 4-FPyW(CO)$_5$ shown in Figure 19 are outlined in Table 5-Table 7. For each compound the data is compared between the different basis sets and model chemistries used and against data experimental[31,32,33] values from the literature for similar compounds of the type $W(CO)_5L$, where L = pyridine, substituted pyridine or piperidine. In the case of 4-FPyW(CO)$_5$ the theoretical data is compared to theoretical data obtained for (4-CN)PyW(CO)$_5$[31]. All three compounds share the same geometry and point group and have similar values for bond lengths and bond angles.

	RHF/ LANL2DZ	B3LYP/ LANL2DZ	Literature[31,32,33]	Deviation % B3LYP-Literature
Bond lengths				
N4-W22	2.367	2.305	2.26, 2.33	1.99, 1.07
W22-C1	2.078	2.044	2.07, 2.04	1.25, 0.19
C1-O9	1.146	1.180	1.12	5.35
W22-C5	2.078	2.044	2.07, 2.04	1.25, 0.19
C5-11O	1.146	1.180	1.12	5.35
W22-C3	2.054	2.032	2.026, 2.04	0.29, 0.39
C3-7O	1.151	1.184	1.12	5.71
W22-C6	2.054	2.032	2.026, 2.04	0.29, 0.39
C6-8O	1.151	1.184	1.12	5.71
W22-C2	1.996	1.986	1.982, 2.00	0.20, 0.70
C2-O10	1.159	1.187	1.13	5.04
N4-C16	1.356	1.375	-	-
C15-C16	1.382	1.396	-	-
C15-C14	1.400	1.411	-	-
C14-C13	1.386	1.402	-	-
C13-C12	1.386	1.397	-	-
C12-N4	1.318	1.345	-	-
C12-F21	1.356	1.382	-	-
Bond angles				
C2-W22-C1	89.90	89.23	89.4, 87.8	0.19, 1.62
C2-W22-C5	89.88	89.23	89.4, 87.8	0.19, 1.62
C2-W22-C3	89.74	89.21	89.4, 87.8	0.21, 1.60
C2-W22-C6	89.72	89.21	89.4, 87.8	0.21, 1.60
W22-C1-O9	177.96	177.73	176.7, 178.3	0.58, 0.32
W22-C5-O11	177.94	177.73	176.7, 178.3	0.58, 0.32
W22-C3-O7	178.93	178.58	176.7, 178.3	1.06, 0.15
W22-C6-O8	178.90	178.58	176.7, 178.3	1.06, 0.15
W22-C2-O10	179.90	179.91	-	-
W22-N4-C16	119.56	120.20	-	-
W22-N4-C12	123.58	123.72	121.4, 120.8	1.91, 2.41
N4-C16-H20	116.46	115.95	-	-
N4-C12-F21	116.61	116.45	-	-
N4-C16-C15	122.56	122.76	122.3, 123.4	0.38, 0.52
C16-C15-C14	118.91	119.33	118.8, 119.1	0.45, 0.19
C15-C14-C13	118.97	118.69	118.8, 119.1	0.09, 0.34
C14-C13-C12	117.06	117.40	118.8, 119.1	1.17, 1.18
C13-C12-N4	125.63	125.72	122.3, 123.4	2.79, 1.88

Table 5 Comparison of selected bond lengths (Å) and bond angles (°) for 2-FPyW(CO)$_5$ on increasing the size of the basis set with literature values[31,32,33]

	RHF/ LANL2DZ	B3LYP/ LANL2DZ	Literature[31,32,33]	Deviation % B3LYP-Literature
Bond lengths				
N4-W20	2.345	2.288	2.26, 2.33	1.23, 1.80
W20-C1	2.066	2.038	2.07, 2.04	1.54, 0.09
C1-O9	1.148	1.182	1.12	5.53
W20-C5	2.066	2.038	2.07, 2.04	1.54, 0.09
C5-11O	1.148	1.182	1.12	5.53
W20-C3	2.063	2.037	2.026, 2.04	0.54, 0.15
C3-7O	1.149	1.183	1.12	5.62
W20-C6	2.063	2.037	2.026, 2.04	0.54, 0.15
C6-8O	1.149	1.183	1.12	5.62
W20-C2	2.001	1.991	1.982, 2.00	0.45, 0.45
C2-O10	1.158	1.186	1.13	4.95
N4-C16	1.345	1.367	-	-
C15-C16	1.390	1.401	-	-
C15-C14	1.392	1.406	-	-
C14-C13	1.381	1.397	-	-
C13-C12	1.380	1.396	-	-
C12-N4	1.343	1.364	-	-
C13-F22	1.368	1.389	-	-
Bond angles				
C2-W20-C1	89.82	89.47	89.4, 87.8	0.07, 1.90
C2-W20-C5	89.82	89.41	89.4, 87.8	0.01, 1.83
C2-W20-C3	89.88	89.47	89.4, 87.8	0.07, 1.90
C2-W20-C6	89.88	89.41	89.4, 87.8	0.01, 1.83
W20-C1-O9	178.74	178.67	176.7, 178.3	1.11, 0.20
W20-C5-O11	178.74	178.61	176.7, 178.3	1.08, 0.17
W20-C3-O7	178.92	178.81	176.7, 178.3	1.19, 0.28
W20-C6-O8	178.92	178.75	176.7, 178.3	1.16, 0.25
W20-C2-O10	179.96	179.94	-	-
W20-N4-C16	120.82	121.06	121.4, 120.8	0.28, 0.21
W20-N4-C12	120.65	121.00	121.4, 120.8	0.33, 0.16
N4-C16-C15	122.64	122.75	122.3, 123.4	0.37, 0.52
C16-C15-C14	119.31	119.75	118.8, 119.1	0.79, 0.54
C15-C14-C13	116.81	116.50	118.8, 119.1	1.93, 2.18
C14-C13-C12	121.74	121.99	118.8, 119.1	2.68, 2.42
C13-C12-N4	120.96	121.05	122.3, 123.4	1.02, 1.90

Table 6 Comparison of selected bond lengths (Å) and bond angles (°) for 3-FPyW(CO)$_5$ on increasing the size of the basis set with literature values[31,32,33]

	RHF/ LANL2DZ	B3LYP/ LANL2DZ	Literature[31]	Deviation % B3LYP-Literature
Bond lengths				
N4-W20	2.346	2.292	2.330	1.63
W20-C1	2.064	2.037	2.069	1.54
C1-O9	1.149	1.183	1.156	2.33
W20-C5	2.064	2.037	2.069	1.54
C5-11O	1.149	1.183	1.156	2.33
W20-C3	2.064	2.037	2.069	1.54
C3-7O	1.159	1.183	1.156	2.33
W20-C6	2.064	2.037	2.069	1.54
C6-8O	1.149	1.183	1.156	2.33
W20-C2	2.002	1.991	2.015	1.19
C2-O10	1.158	1.187	1.161	2.23
N4-C16	1.346	1.367	1.352	1.10
C15-C16	1.387	1.400	1.388	0.86
C15-C14	1.383	1.397	1.402	0.35
C14-C13	1.383	1.397	1.402	0.35
C13-C12	1.387	1.400	1.388	0.86
C12-N4	1.346	1.367	1.352	1.10
C14-F22	1.362	1.386	1.433	3.27
Bond angles				
C2-W20-C1	89.88	89.39	89.6	0.23
C2-W20-C5	89.88	89.39	89.6	0.23
C2-W20-C3	89.88	89.39	89.6	0.23
C2-W20-C6	89.88	89.39	89.6	0.23
W20-C1-O9	178.91	178.66	178.8	0.08
W20-C5-O11	178.91	178.66	178.8	0.08
W20-C3-O7	178.91	178.66	178.8	0.08
W20-C6-O8	178.91	178.66	178.8	0.08
W20-C2-O10	180.00	180.00	-	-
W20-N4-C16	120.91	121.17	121.4	0.19
W20-N4-C12	120.91	121.17	121.4	0.19
N4-C16-C15	123.03	123.12	123.5	0.30
C16-C15-C14	117.17	117.43	118.9	1.23
C15-C14-C13	121.41	121.22	-	-
C14-C13-C12	117.17	117.43	118.9	1.23
C13-C12-N4	123.03	123.12	123.5	0.30

Table 7 Comparison of selected bond lengths (Å) and bond angles (°) for 4-FPyW(CO)$_5$ on increasing the size of the basis set with literature values[31]

Following geometry optimisation of the above structures a vibrational analysis of the ground state electronic structure was undertaken. The frequency calculation was carried out on the B3LYP/LANL2DZ optimised structures to investigate whether any negative frequencies were present, which would indicate that the geometry-optimised structure was not a minimum on the potential energy surface.

For each complex (a) 2-FPyW(CO)$_5$, (b) 3-FPyW(CO)$_5$ and (c) 4-FPyW(CO)$_5$ no negative frequencies were found indicating that the geometry optimised structures obtained were at an energy minimum.. Each complex which is of the type W(CO)$_5$L, has C_{4v} symmetry and as such is predicted to have 3 IR active carbonyl bands – $2A_1$ and E. The E mode is expected to be very strong while both A_1^1 and A_1^2 are expected to be weak bands. In Table 8-Table 10 the predicted IR active bands of the three complexes optimised at the B3LYP/LANL2DZ level of theory are compared to the experimental values obtained in this study. For both 2-FPyW(CO)$_5$ and 3-FPyW(CO)$_5$ the calculated IR stretching frequencies are scaled with respect to the experimental values obtained. In the case of 4-FPyW(CO)$_5$, as no experimental data is available the calculated IR stretching frequencies are scaled with respect to literature values.

IR active bands (Calculated)	IR active bands (experimental) [Pentane]	IR active bands (Literature) [Methyl Cyclohexane]	Assignment
2064	2073	2075	asymmetric C≡O stretch (A_1 mode)
1971a	-	-	asymmetric C≡O stretch (B mode)
1938[b]	1934	1936	asymmetric C≡O stretch (E mode)
1931	-	-	
1929	1922	1928	asymmetric C≡O stretch (A_1 mode)

Table 8 Comparison of IR active frequencies of 2-FPyW(CO)$_5$ calculated at the B3LYP/LANL2DZ theory level with experimental values in pentane and literature values in methylcyclohexane. Calculated values have been corrected by an empirical factor of 1.021. [a]The predicted B vibrational mode is not observed experimentally. [b]Splitting of the E vibrational mode is observed in the theoretical geometry optimised model.

IR active bands (Calculated)	IR active bands (experimental) [Pentane]	IR active bands (Literature) [Methyl Cyclohexane]	Assignment
2062	2074	2075	asymmetric C≡O stretch (A_1 mode)
1967[a]	-	-	asymmetric C≡O stretch (B mode)
1937[b]	1937	1936	asymmetric C≡O stretch (E mode)
1932	-	-	
1930	1925	1928	asymmetric C≡O stretch (A_1 mode)

Table 9 Comparison of IR active frequencies of 3-FPyW(CO)$_5$ calculated at the B3LYP/LANL2DZ theory level with experimental values in pentane and literature values in cyclohexane Calculated values have been corrected by an empirical factor of 1.021. [a]The predicted B vibrational mode is not observed experimentally [b]Splitting of the E vibrational mode is observed in the theoretical geometry optimised model.

IR active bands (Calculated)	IR active bands (Literature) [Methyl Cyclohexane]	Assignment
2062	2075	asymmetric C≡O stretch (A_1 mode)
1936[a]	1936	asymmetric C≡O stretch (E mode)
1930	-	
1929	1928	asymmetric C≡O stretch (A_1 mode)

Table 10 Comparison of IR active frequencies of 4-FPyW(CO)$_5$ calculated at the B3LYP/LANL2DZ theory level with literature values for 4-CNPyW(CO)$_5$ in methylcyclohexane. Literature values have been corrected by an empirical factor of 1.021. [a]Splitting of the E vibrational mode is observed in the theoretical geometry optimised model.

3.5.1.2. Calculation of the ground state electronic structure for $W(CO)_5L$

Following optimisations of the ground state geometries of (a) 2-FPyW$(CO)_5$, (b) 3-FPyW$(CO)_5$ and (c) 4-FPyW$(CO)_5$ at the B3LYP/LANL2DZ level of theory the ground state electronic structures for each of the complexes were calculated and the highest occupied (HOMO) and lowest virtual (LUMO) molecular orbitals were examined in order to provide a framework for the subsequent Time-Dependent DFT (TD-DFT) calculations. For each complex the valence orbitals are plotted according to their energies. Such orbitals are very important in that they play an active role in the determination of the electronic excitations and electronic character of the particular complex. The assignment of the type of molecular orbital was made on the basis of its relative composition and by inspection of the three dimensional representation. In each case the compositional assignment is relative, in that the majority are of mixed character with a particular MO giving the major compositional contribution. Table 11 lists the most important molecular orbitals for each of the studies complexes. Five occupied MO's (HOMO to H-4) and six unoccupied or virtual MO's (LUMO to L+5).

MO	2-FPyW$(CO)_5$	3-FPyW$(CO)_5$	4-FPyW$(CO)_5$
L+5	-1.32	-1.41	-1.45
L+4	-1.74	-1.92	-1.92
L+3	-1.75	-1.96	-1.96
L+2	-2.08	-2.18	-2.37
L+1	-2.34	-2.56	-2.55
LUMO	-2.81	-2.88	-2.68
HOMO	-6.26	-6.38	-6.36
H-1	-6.29	-6.45	-6.45
H-2	-6.67	-6.85	-6.85
H-3	-8.78	-8.76	-9.12
H-4	-9.81	-9.72	-9.44

Table 11 The molecular orbitals of (a) 2-FPyW$(CO)_5$, (b) 3-FPyW$(CO)_5$ and (c) 4-FPy W$(CO)_5$ and their energies (eV). HOMO: Highest occupies molecular orbital. LUMO: Lowest unoccupied molecular orbital.H-1 is HOMO-1 and L+1 is LUMO+1

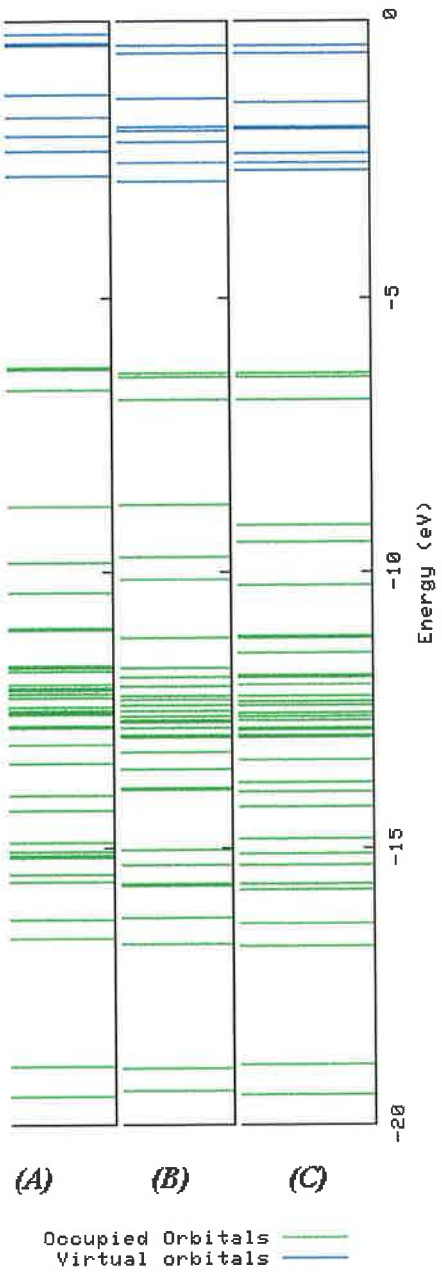

Figure 20 Energy level diagram of (a) 2-FpyW(CO)$_5$, (b) 3-FpyW(CO)$_5$ and (c) 4-FpyW(CO)$_5$. Extracted from Density of states (DOS) diagram generated by the GaussSum 2.0 programme[34]

MO no.	Assignment	Energy (eV)	W %	CO_{cis} %	CO_{trans} %	2-FPy %
73	L+5	-1.32	0	92	0	8
72	L+4	-1.74	11	88	1	0
71	L+3	-1.75	9	88	1	1
70	L+2	-2.08	1	8	0	91
69	L+1	-2.34	22	78	0	0
68	LUMO	-2.81	1	2	2	94
67	HOMO	-6.26	60	22	13	5
66	H-1	-6.29	63	22	13	0
65	H-2	-6.67	61	38	0	0
64	H-3	-8.78	0	0	0	100

Table 12 The contribution of tungsten, each of the five CO orbitals and the 2-fluoropyridine orbitals in 2-FPyW(CO)$_5$ for each of the selected molecular orbitals

MO no.	Assignment	Energy (eV)	W %	CO_{cis} %	CO_{trans} %	3-FPy %
73	L+5	-1.41	0	80	0	20
72	L+4	-1.92	9	88	0	3
71	L+3	-1.96	11	88	1	0
70	L+2	-2.18	1	20	0	79
69	L+1	-2.56	22	80	0	1
68	LUMO	-2.88	1	4	2	93
67	HOMO	-6.38	60	24	12	5
66	H-1	-6.45	64	24	13	0
65	H-2	-6.85	61	40	0	0
64	H-3	-8.76	0	0	0	100

Table 13 The contribution of tungsten, each of the five CO orbitals and the 3-fluoropyridine orbitals in 3-FPyW(CO)$_5$ for each of the selected molecular orbitals

MO no.	Assignment	Energy (eV)	W %	CO_{cis} %	CO_{trans} %	4-FPy %
73	L+5	-1.45	0	88	0	13
72	L+4	-1.92	9	88	0	4
71	L+3	-1.96	11	88	1	0
70	L+2	-2.37	1	12	0	87
69	L+1	-2.55	22	80	0	1
68	LUMO	-2.68	1	4	2	92
67	HOMO	-6.36	60	24	13	5
66	H-1	-6.45	64	24	13	0
65	H-2	-6.85	61	40	0	0
64	H-3	-9.12	0	0	0	100

Table 14 The contribution of tungsten, each of the five CO orbitals and the 4-fluoropyridine orbitals in 4-FPyW(CO)$_5$ for each of the selected molecular orbitals

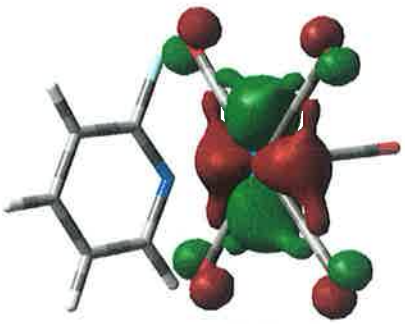

65 (O) – HOMO-2

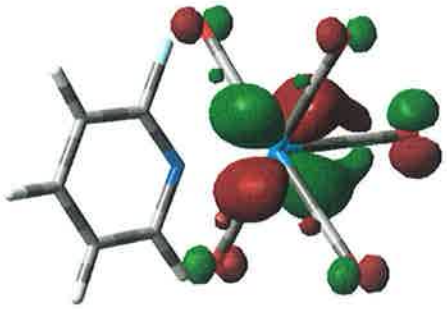

66 (O) – HOMO-1

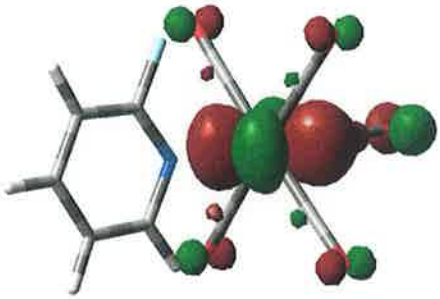

67 (O) - HOMO

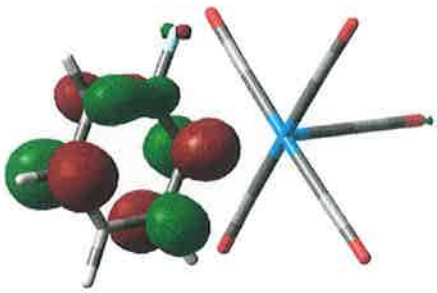

68 (V) – LUMO

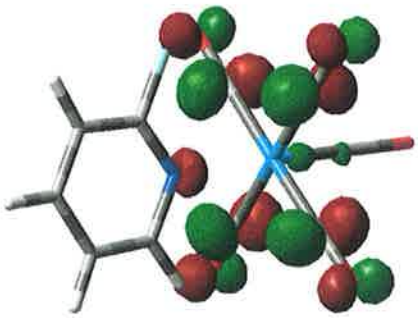

69 (V) – LUMO+1

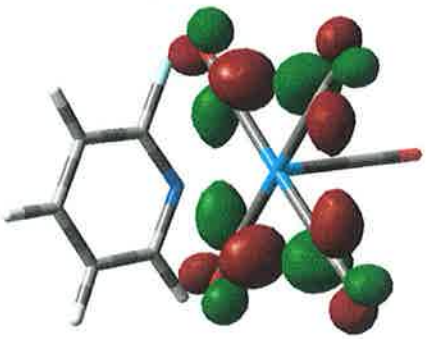

71 (V) – LUMO+3

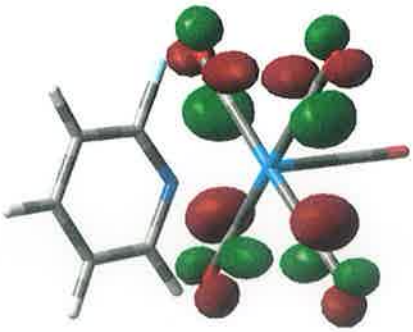

72 (V) – LUMO+4

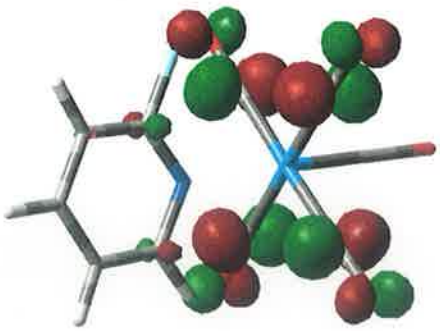

73 (V) – LUMO+5

Figure 21 Selected molecular orbitals for 2-FPyW(CO)$_5$

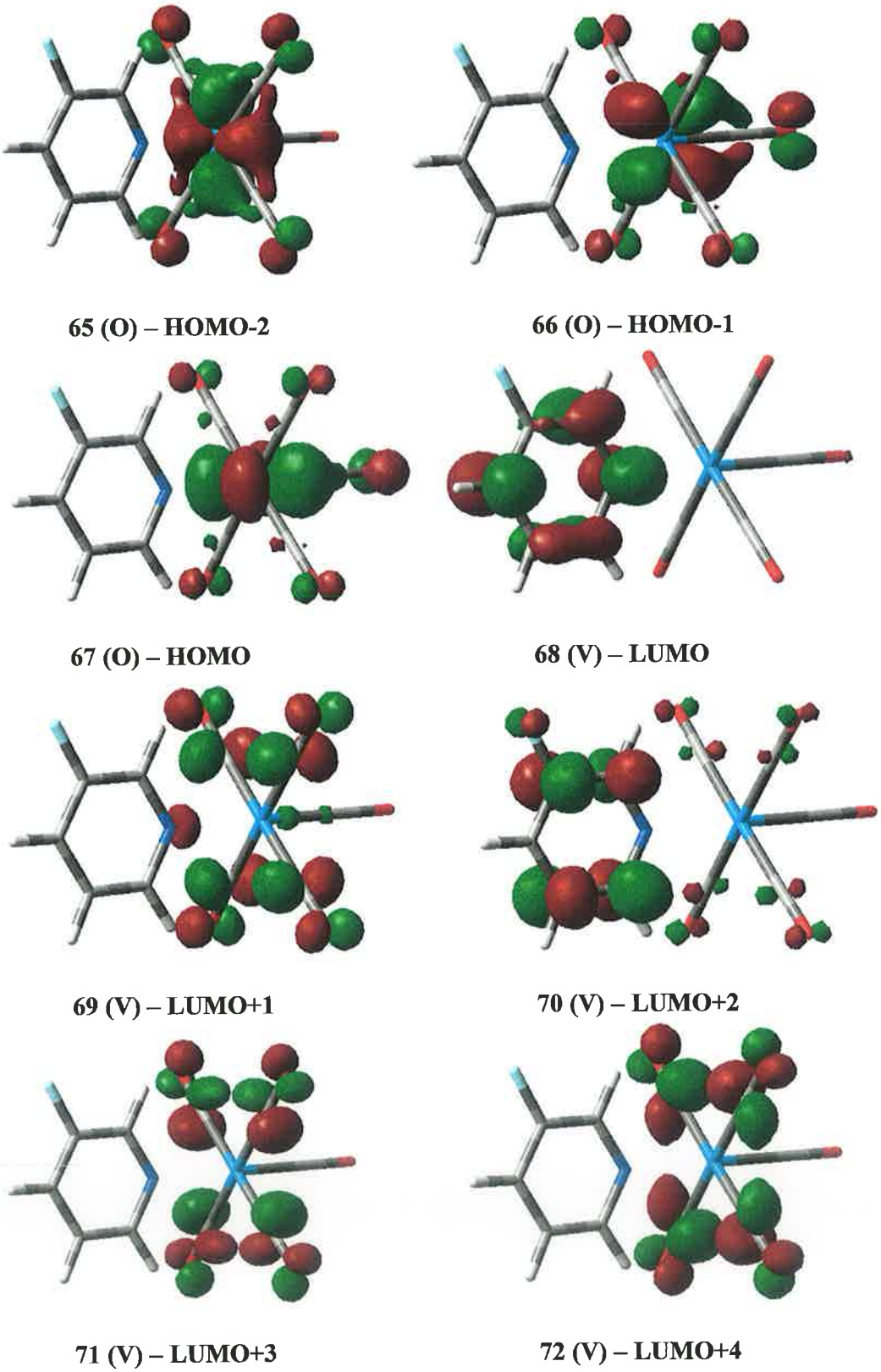

Figure 22 Selected molecular orbitals for 3-FPyW(CO)$_5$

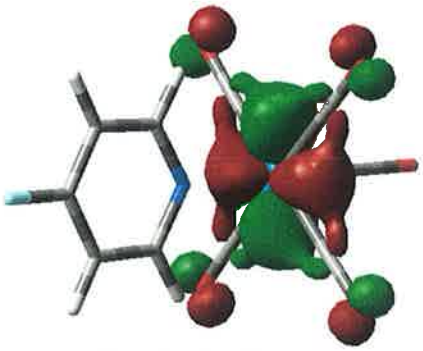

65 (O) – HOMO-2

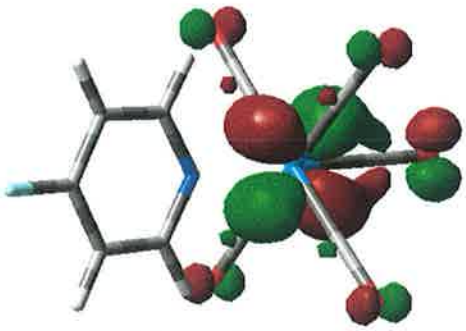

66 (O) – HOMO-1

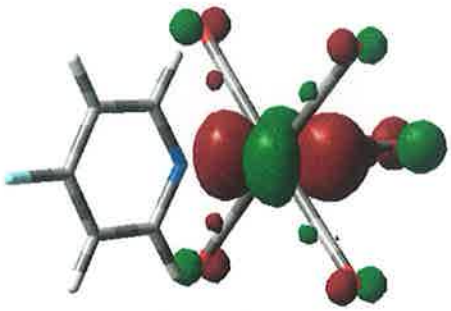

67 (O) – HOMO

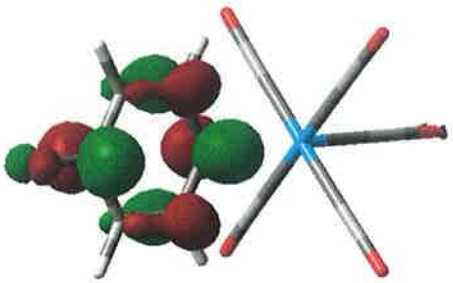

68 (V) – LUMO

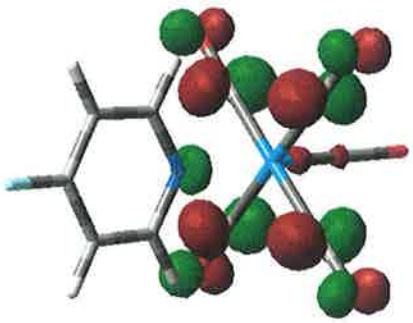

69 (V) – LUMO+1

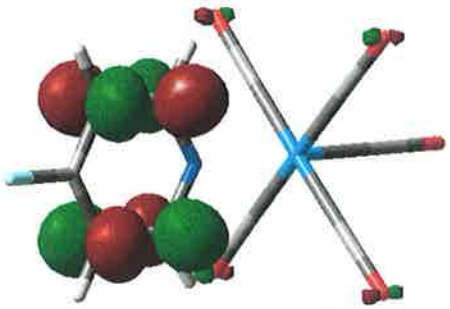

70 (V) – LUMO+2

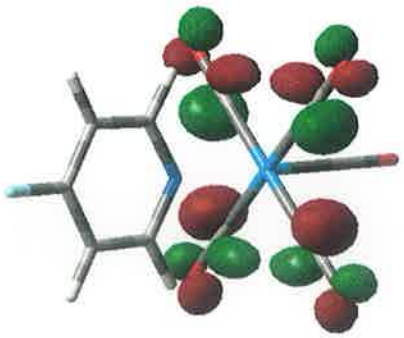

71 (V) – LUMO+3

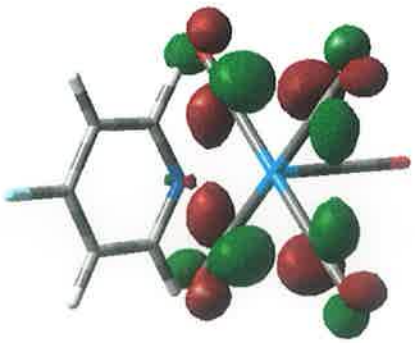

72 (V) – LUMO+4

Figure 23 Selected molecular orbitals for 4-FPyW(CO)

3.5.1.3. Time –dependent Density Functional Theory (TDDFT) calculations

State	E (eV) [λ (nm)[a]]	f [b]	$\psi_o \rightarrow \psi_v$ [c]	Predominant character [d]
2	2.9105 (425.99)	0.1213	HOMO→ LUMO (89%)	W-d_{xz}, *πCO → L
3	3.0260 (409.74)	0.0091	H-2→ LUMO (71%) HOMO → L+1 (15%) H-2 → L+3 (11%)	W-d_{yz} , *πCO_{cis} → L W-d_{xz}, *πCO → *πCO_{cis} W-d_{yz} , *πCO_{cis} → *πCO_{cis}
4	3.0496 (406.56)	0.0092	H-1 → L+1 (74%) H-2 → L+1 (10%) H-2 → L+4 (10%)	W-d_{xy}, *πCO → *πCO_{cis} W-d_{yz} , *πCO_{cis} → *πCO_{cis} W-d_{yz} , *πCO_{cis} → *πCO_{cis}
5	3.1462 (394.07)	0.0037	H-2 → LUMO (84%) HOMO → L+1 (11%)	W-d_{yz} , *πCO_{cis} → L W-d_{xz}, *πCO → *πCO_{cis}
6	3.1878 (388.94)	0.0043	H-2 → L+1 (78%) H-1 → L+1 (8%)	W-d_{yz} , *πCO_{cis} → *πCO_{cis} W-d_{xy}, *πCO → *πCO_{cis}
9	3.4941 (354.84)	0.0219	HOMO → L+2 (89%) H-2 → L+4 (6%)	W-d_{xz}, *πCO → L W-d_{yz} , *πCO_{cis} → *πCO_{cis}

Table 15 Selected calculated singlet excited states for 2-FPyW(CO)$_5$

State	E (eV) [λ (nm)[a]]	f [b]	$\psi_o \rightarrow \psi_v$ [c]	Predominant character [d]
2	2.9468 (420.75)	0.1298	HOMO → LUMO (87%)	W-d_{xy}, *πCO → L
3	2.9615 (418.65)	0.0118	HOMO → L+1 (80%) H-2 → L+4 (11%)	W-d_{xy}, *πCO → *πCO_{cis} W-d_{yz} , *πCO_{cis} → *πCO_{cis}
4	3.0204 (410.49)	0.0120	H-1 → L+1 (81%) H-2 → L+3 (13%)	W-d_{xy}, *πCO → *πCO_{cis} W-d_{yz} , *πCO_{cis} → *πCO_{cis}
8	3.3658 (368.36)	0.0082	HOMO → L+4 (46%) H-1 → L+3 (36%) H-2 → L+1 (11%)	W-d_{xy}, *πCO → *πCO_{cis} W-d_{xy}, *πCO → *πCO_{cis} W-d_{yz} , *πCO_{cis} → *πCO_{cis}
9	3.4619 (358.14)	0.0058	HOMO → L+2 (74%) H-1 → L+3 (13%) H-2 → L+3 (11%)	W-d_{xy}, *πCO → L W-d_{xy}, *πCO → *πCO_{cis} W-d_{yz} , *πCO_{cis} → *πCO_{cis}
15	4.0230 (308.19)	0.0035	H-1 → L+5 (67%) H-2 → L+4 (24%)	W-d_{xy}, *πCO → *πCO_{cis}, L W-d_{yz} , *πCO_{cis} → *πCO_{cis}

Table 16 Selected calculated singlet excited states for 3-FPyW(CO)$_5$

[a]Energy of vertical excitation from ground state, [b] Oscillator strength, [c] Occupied to unoccupied (virtual) orbital excitation, [d] Character of excited state

State	E (eV) [λ (nm)[a]]	f[b]	$\psi_o \rightarrow \psi_v$[c]	Predominant character[d]
1	2.9515 (420.07)	0.0122	HOMO → L+1 (81%) H-2 → L+4 (11%)	W-d_{xz}, *πCO → *πCO_{cis} W-d_{yz}, *πCO_{cis} → *πCO_{cis}
3	3.0143 (411.32)	0.0112	H-1 → L+1 (80%) H-2 → L+3 (13%)	W-d_{xy}, *πCO → *πCO_{cis} W-d_{yz}, *πCO_{cis} → *πCO_{cis}
4	3.0768 (402.96)	0.0805	HOMO → LUMO (63%) H-2 → L+1 (16%)	W-d_{xz}, *πCO → L W-d_{yz}, *πCO_{cis} → *πCO_{cis}
5	3.1599 (392.36)	0.0341	H-2 → L+1 (72%) HOMO → LUMO (22%)	W-d_{yz}, *πCO_{cis} → *πCO_{cis} W-d_{xz}, *πCO → L
9	3.3759 (367.26)	0.0234	HOMO → L+4 (47%) H-1 → L+3 (36%) H-2 → L+1 (10%)	W-d_{xz}, *πCO → *πCO_{cis} W-d_{xy}, *πCO → *πCO_{cis} W-d_{yz}, *πCO_{cis} → *πCO_{cis}
15	3.9528 (313.66)	0.0018	H-1 → L+5 (66%) H-2 → L+4 (31%)	W-d_{xy}, *πCO → *πCO_{cis}, L W-d_{yz}, *πCO_{cis} → *πCO_{cis}

Table 17 Selected calculated singlet excited states for 4-FPyW(CO)$_5$

[a]Energy of vertical excitation from ground state, [b] Oscillator strength, [c] Occupied to unoccupied (virtual) orbital excitation, [d] Character of excited state

3.6. Discussion

3.6.1. Matrix Isolation

3.6.1.1. Matrix Isolation of compounds of the type $W(CO)_5L$

Monochromatic irradiation at 436 nm for 30 mins of 3-fluoropyridine$W(CO)_5$ in a methane matrix resulted in bleaching of the parent carbonyl bands with concomitant generation of product bands at 1956 and 2086 cm^{-1}. These bands are at higher energies to those observed by McHugh et al.[26] for $W(CO)_5$ following irradiation of the analogous compound $(C_5H_3BrN)W(CO)_5$ under similar conditions. This difference in band position may be explained in terms of re-coordination of the dissociated $W(CO)_5$ group to the 2-FPy moiety via an agostic interaction through a C-H bond or via the π-electrons of the pyridine ring, as shown in Figure 24. Coordination through an agostic C-H interaction or π-interaction of the pyridine ring is thermodynamically more unstable but kinetically more stable than coordination through the nitrogen atom of the pyridine ring. In similar studies by Alamiry,[28] broadband irradiation at > 400 nm of $Cr(CO)_5Py$ and $Cr(CO)_5(acpy)$ in a 12 K argon matrix resulted in the generation of product bands, which were at higher energies compared to those of the known $Cr(CO)_5Ar$.

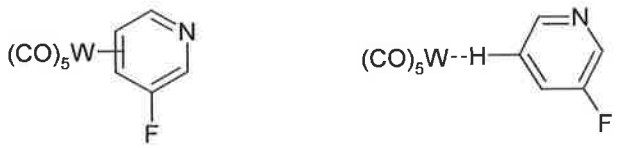

η^2–π Interaction Agostic C-H Interaction

Figure 24 Suggested coordination of $W(CO)_5$ through either the π electron of the pyridine ring or through an agostic interaction through a C-H bond of the pyridine ring. [28,29]

Similarly this type of π-coordination to the pyridine ring was also observed by Dobson et al.[27] on photolysis of $Cr(CO)_6$ in a variety of arene solutions. The absence of photogenerated CO also further suggests that this process occurring does not involve dissociative CO loss. Further irradiation at 405 nm for 60 mins resulted in

further bleaching of the parent bands and further generation of the η^2-π or agostic bound $(C_5H_3FN)W(CO)_5$. Subsequent higher energy irradiation at 365 nm for 30 mins resulted in the generation of two product bands at 1956 and 2091 cm^{-1}. These are in good agreement with those observed by McHugh et al.[26] for $W(CO)_5$ and are thus assigned to the generation of $W(CO)_5$ following W-N bond cleavage. A third band observed by McHugh et al.[26] for this species at 1930 cm^{-1} may be masked by the parent absorption band at 1933 cm^{-1}. Additionally, the case for generation of $W(CO)_5$ via W-N cleavage is further substantiated by the presence of a band at 1001 cm^{-1}, which may be assigned to an IR active band of the dissociated 3-FPy ligand[26].

In contrast to irradiation in a methane matrix, irradiation 3-FPyW(CO)_5 at 436 nm for 60 mins in a dintrogen matrix resulted in cleavage of the W-N bond leading to the predominant N_2 substituted photoproduct $W(CO)_5N_2$. These bands are in excellent agreement with those observed by McHugh et al.[26] for this photoproduct following irradiation of $(3\text{-BrPy})W(CO)_5$ in an N_2 matrix. Weaker product bands generated at 1891, 2004, and 2195 cm^{-1} are tentatively assigned to generation of a small quantity of the N_2 substituted tetracarbonyl 3-FPyW(CO)_4N_2. This assignment is based on comparison with the product bands observed by Dobson et al.[27] for the generation of *cis*-$Cr(CO)_4Py$. This is further suggested by generation of a free CO at 2137 cm^{-1}. Subsequent irradiation at 405nm produced further bleaching of the parent bands and further generation of the product bands. On changing the irradiation wavelength to 365 nm further bleaching of the parent bands was observed. The product bands assigned to $W(CO)_5N_2$ also decreased in intensity with concomitant generation of ambiguous product bands at 1938 and 1958 cm^{-1}. Following low energy broadband irradiation at >520 nm for 30 mins little change in the parent band intensity was observed. However, an increase in intensity of the $W(CO)_5N_2$ bands was observed.

As observed for irradiation in a dinitrogen matrix, irradiation of 3-FPyW(CO)_5 at 436 nm for 60 mins in a 5 % CO-doped methane matrix resulted in bleaching of the parent carbonyl bands and cleavage of the W-N bond resulting in $W(CO)_5$ generation, some of which coordinates with the free CO present in the matrix to generate the hexacarbonyl $W(CO)_6$ as indicated by generation of a band at 1979 cm^{-1}. Irradiation at 405 nm for 60 mins resulted in further bleaching of the parent bands with concomitant growth in the hexacarbonyl band. Complete loss of the bands previously assigned to

$W(CO)_5$ is observed. This suggests that at 405 nm irradiation there is a greater efficiency for cleavage and coordination to yield $W(CO)_6$. On reducing the irradiation wavelength to 365 nm for 40 mins both parent bands and product bands decreased in intensity. This suggests that irradiation at this wavelength also results in absorption of a second photon leading to secondary photolysis. Broadband irradiation at >520 nm resulted in regeneration of the parent species with concomitant loss of the product bands due to both $W(CO)_5$ and $W(CO)_6$.

Irradiation of 2-Fluoropyridine$W(CO)_5$ in a methane matrix resulted in bleaching of the parent absorption bands with concomitant generation of two photoproducts. In contrast, to irradiation of 3-Fluoropyridine$W(CO)_5$ where formation of an η^2-π or agostically bound 3-FPy$W(CO)_5$, irradiation in this case resulted in direct generation of $W(CO)_5$ via W-N bond cleavage. The bands assigned to this species are in excellent agreement with those observed by McHugh et al.[26] for the same species. Weak product bands also generated at 1997, 1900, and 1874 cm^{-1} are tentatively assigned to generation of *cis*-(2-FPy)$(CH_4)W(CO)_4$ based on comparison with bands observed by Dobson et al.[27] for a number of complexes of the type *cis*-$W(CO)_4L$(Solvent). However, very little CO loss is observed indicating W-N bond cleavage to be the predominant reaction on irradiation at this wavelength. Low energy broadband irradiation at > 520 nm resulted in regeneration of the parent species but also an increase in intensity of both sets of photoproduct bands. As observed for the 2-fluoropyrdine analogue, irradiation at 436 nm of 3-fluoropyridine$W(CO)_5$ resulted in strong bleaching of the parent absorption bands with concomitant generation of $W(CO)_5N_2$, via W-N bond cleavage and N_2 coordination onto the vacant site. A product band also generated at 2008 cm^{-1} is tentatively assigned to generation of the tetracarbonyl 2-FPy$W(CO)_4N_2$. This minor photoproduct was also observed for the 3-fluoropyrdine analogue under similar irradiation conditions. Subsequent irradiation at 405 nm produced further bleaching of the parent absorption bands and further generation of both the pentacarbonyl and tetracarbonyl photoproducts. On moving the irradiation wavelength to 365 nm for 40 mins regeneration of the parent absorption bands was observed with little difference in either the pentacarbonyl or tetracarbonyl photoproduct bands observed, thereby suggesting a steady state may have been reached. Subsequent low energy broadband irradiation at > 520 nm resulted in further

growth of both parent band and product bands indicating a competitive reaction between regeneration of the parent complex and a forward reaction involving loss of either the pyridine or CO ligand.

3.6.2. Quantum Chemical Studies

3.6.2.1. DFT and TDDFT Studies of compounds of the type $W(CO)_5L$

3.6.2.1.1. Geometry optimisation of compounds of the type $W(CO)_5L$

A comparison of the W-N bond lengths for the three mono-fluorinated pyridine complexes (a) 2-fluoropyridine, (b) 3-fluoropyridine and (c) 4-fluoropyridine showed that the position on the pyridine ring of the fluorine atom had very little effect on the W-N bond lengths, which were calculated to be 2.305 Å for 2-FPyW$(CO)_5$, 2.288 Å for 3-FPyW$(CO)_5$ and 2.292 Å for 4-FPyW$(CO)_5$. These values were also in good agreement with literature values[31,32,33] for similar compounds and had a % deviation from the literature values of between 1.07 and 1.99 %. However, as can be seen the W-N bond lengths for the 2- and 4-substituted analogues are longer than of the 3-fluorine derivative. This trend is also observed for the CO_{trans} bond length where again 2-FPy > 4-FPy > 3-Fpy. This indicates that the position of the fluorine atom on the pyridine ring does affect the W-N bond lengths. However, the effect of the position of substitution is even more evident when we examine the four CO_{cis} ligands. In 2-FPyW$(CO)_5$, where the F atom is closest to the metal carbonyl moiety a notable bond shortening effect is observed for the two CO_{cis} ligands closest to the F atom. The CO bond length for these two CO ligands is 1.180 Å, while those on the opposite side of the pyridine ring, away from the fluorine atom have a CO bond length of 1.184 Å. This marked difference may be explained in terms of the larger atomic radius of the fluorine atom, exerting a repulsive force on the W-CO groups below. This is further suggested by the decreased dihedral bond angle, from 180 °, of these two carbonyl groups, which are 177.73 ° compared to the remaining two CO_{cis} ligands not affected by the F atom, which possess a bond angle of 178.58 °. Overall, this may be viewed as a reduction in the bond order and a bending out of the plane and away from the F atom of the two carbonyl groups involved. A small difference of 0.18 ° in the bond angle of the CO_{cis} ligands *cis* to the F atom and *trans* to the F atom is also observed As would be expected this effect is lost on substitution of the F atom into the 4-position of the pyridine ring. In this case, the carbonyl bond length is predicted to be 1.183 Å for all four CO_{cis} ligands and 1.187 Å for the CO_{trans} ligand. Similarly, the presence of the F atom in the 4 position has the effect of repelling all four CO_{cis}

ligands equally away from the pyridine ring, such that they all have a bond angle of 178.66 °.

This suggests that although 2-FPyW(CO)$_5$ and 3-FPyW(CO)$_5$ might be expected to have C_{4v} geometry, the presence of the F atom in either the 2- or 3- position distorts this geometry, specifically the metal carbonyl moiety, such that the four CO_{cis} ligands may actually have C_{2v} geometry.

3.6.2.1.2. The molecular orbitals of compounds of the type $W(CO)_5L$

As is evident from Figure 21-Figure 23, the position of the fluorinated substituent on the pyridine ring in each of the $W(CO)_5L$ complexes appears to have very little impact on the molecular orbitals of the three complexes. For each complex, the Kohn-Sham molecular orbitals are predominantly centred on the metal pentacarbonyl moiety with some also being centred on the π orbitals of the pyridine ring. In a number of molecular orbitals a small amount of electron density is also localised on the F atom. In the case of 2-$FPyW(CO)_5$, only the LUMO is centred on the π orbitals of the pyridine ring (94 %) with no significant contribution from the $W(CO)_5$ moiety. For 3-$FPyW(CO)_5$, only the LUMO and L+2 molecular orbitals are centred on the pyridine ring, having contributions from the pyridine ring of 93% and 79%, respectively. No significant contribution from the $W(CO)_5$ is observed in the case of the LUMO and a relatively low contribution (21%) in the case of the L+2 molecular orbital. Similarly, the molecular orbitals of 4-$FPyW(CO)_5$ are predominantly centred on the metal carbonyl, with the exception of the LUMO and L+2, with pyridine π orbital contributions of 92 and 87 %, respectively. As observed for 3-$FPyW(CO)_5$, the L+2 molecular orbital also possesses a small contribution from the $W(CO)_5$ moiety (13%). Overall, as the position of the F-substituent moves from 2-4, the % contribution of the pyridine ring to the LUMO decreases and the overall energy of the MO increases, with the exception of 4-fluropyridine which has a LUMO energy of -2.68 eV compared to -2.88 eV for 3-$FPyW(CO)_5$ and -2.81 eV for the 4-$FPyW(CO)_5$ analogues. These observations are in agreement with studies TDDFT studies by Záliš et al.[31], where it was observed that the LUMO of both $W(CO)_5Py$ and $W(CO)_5$(4-CNPy) are dominated (96%) by π*-py character. As the position of substitution of the F atom on the pyridine ring moves further away from the metal carbonyl system the HOMO-LUMO energy band gap increases from -3.45 eV to -3.68 eV, giving an energy difference of -0.23 eV. This change in LUMO energy may be due to the F substituent becoming a better acceptor on changing position and also on the strong effect on the LUMO, that derivitisation in the 4-position of the pyridine ring is expected to apply. According to a study by Kanis et al.[35] involving the acceptor properties of various pyridine or substituted Cr(CO)Py complexes, as the pyridine substituent becomes a better acceptor the energy of the π* orbital of the pyridine is reduced. The HOMO-LUMO energy gap observed compares well to previously

observed 4-position derivitsation sensitivity[28,35,36] and is in agreement with observed trends in wavelength excitation of the charge transfer band (λ_{CT}). This thus suggests that the fluorine substituent is a better acceptor in the 3-position than the other two positions. Furthermore, as the LUMO and to a lesser extent the L+2 molecular orbitals, are pyridine π^* centred for each complex the energy of the LUMO is very sensitive to the position of the fluorine substituent, especially with respect to substitution in the 4-position. Kanis[35] found that on moving from NH_2 to H and subsequently to CHO as the 4-position substituent on the pyridine ring, that the energy of the LUMO decreased from -1.07 eV for NH_2, -1.39 eV for H and -2.15 eV for CHO. In each of the fluorinated pyridine complexes the higher energy virtual orbitals, after the LUMO, are largely low-lying π^* CO_{cis} orbitals.

It was also observed that the nature of the 4-position substituent had very little effect on the metal centred HOMO, which showed energies of -7.91 eV for NH_2, -8.07 eV for H and -8.22 eV for CHO. Similarly, little change is observed in the H-2 molecular orbital. For both 3-FPyW$(CO)_5$ and 4-FPyW$(CO)_5$ the energies of the HOMO are very similar, at -6.38 eV and -6.36 eV respectively, while the energy of the H-2 MO is -6.85 eV for both. In both cases the H-2 molecular orbital is entirely based on the pentacarbonyl system, specifically the W-d_{xy} orbital and the four π^* CO_{cis} ligands. However, in contrast compound (a) 2-FPyW$(CO)_5$ possesses a HOMO which is substantially lower at -6.26 eV compared to either the 3- or 4-FPy derivatives. The H-2 molecular orbital is also notably lower in energy at -6.67 eV. For all three compounds the HOMO is centred on the metal centre, with the tungsten d orbital contributing to 60-64 % of this molecular orbital. The remainder of the HOMO in each case consists of CO_{cis} contributions (22 % for 2-FPyW$(CO)_5$ and 24 % for both the 3- and 4- analogues.), 13 % CO_{trans} and 5% on the π orbitals of the substituted pyridine ring. This considerable π^* CO contribution arises as a result of W $\rightarrow$ CO π^* back bonding effects. For all three compounds the H-2 molecular orbital is again centred on the metal centre (61%) with the remainder solely located on the four π^* CO_{cis} ligands (38-40 %). As can be seen a transition involving these orbitals would be strongly MLCT in nature involving charge transfer from an orbital almost wholly metal based to an orbital almost wholly ligand based.

It has been shown that in the photochemistry of complexes of the type $W(CO)_5L$, where L = pyridine or substituted pyridine, is inconsistent with the genral observations suggesting that the photochemistry and photophysics of such compounds should be LF based, possessing transitions dominated by metal centred molecular orbitals. The molecular orbitals of the three fluorinated pyridine pentacarbonyl complexes presented are in agreement with observations by Záliš et al.[31] and Zakrzewski et al.[32,36], where it has been observed that, to a large extent the molecular orbitals are delocalised and a greater number possess W-d character than predicted by LF theory. In contrast the photochemistry of compounds of the type $W(CO)_5L$, where L = pyridine or substituted pyridine, is largely directed by MLCT type transitions. However, it should also be noted that when undertaking Density Functional Theory studies in systems containing tungsten, smaller basis sets such as 3-21g and 6-311g cannot be used due to the larger atomic radius and weight of the tungsten atom. Thus optimisation of such system must begin at the LANL2DZ level. This makes the results obtained for tungsten systems inherently more unreliable than those obtained for analogous Cr systems.

3.6.2.1.3. The correlation of TDDFT results with the observed photochemistry

Time Dependent Density Functional Theory (TDDFT) studies were carried out to determine the 20 lowest lying singlet excited states of (a) 2-FPyW(CO)$_5$, (b) 3-FPyW(CO)$_5$ and (c) 4-FPyW(CO)$_5$. However, as 4-FPyW(CO)$_5$ was not synthesised and the photochemistry could this not be examined it has only been included for comparative purposes and will not be discussed in this section.

The lowest nine singlet excited states occur in the region 350-460 nm and thus it is transitions into these excited states that lead to the UV-Vis spectrum of 2-FPyW(CO)$_5$ as shown in Figure 12. The lowest lying singlet excited states of 2-FPyW(CO)$_5$ involve electronic transitions which are primarily MLCT in character involving charge transfer from a molecular orbital centred on the metal centre, and to a lesser extent the CO and pyridine ligands to molecular orbitals centred on either the pyridine ring (LUMO) or the CO ligands (higher energy virtual MO's). Although the first nine lowest lying singlet excited states contribute to the electronic absorption spectrum (Table 18), only the six most intense, in terms of their oscillator strengths, will be discussed.

Calculated Bands (nm)	Oscillator Strength (*f*)	Excited State Properties	Photoproduct Produced
454.04	0	W-d → py CT	W-N bond cleavage
425.99	0.1213	W-d → py CT	W-N bond cleavage
409.74	0.0091	W-d, CO → CO_{cis}	W-N bond cleavage, CO_{trans} loss
406.56	0.0092	W-d, CO → CO_{cis}	W-N bond cleavage, CO_{trans} loss
394.07	0.0037	W-d → py CT	W-N bond cleavage
388.94	0.0043	W-d, CO → CO_{cis}	W-N bond cleavage, CO_{trans} loss
370.97	0.0002	W-d, CO → CO_{cis}	W-N bond cleavage, CO_{trans} loss
363.56	0.0025	W-d, CO → CO_{cis}	W-N bond cleavage, CO_{trans} loss
354.84	0.0219	W-d → py CT	W-N bond cleavage

Table 18 The calculated low energy UV absorption bands for 2-FPyW(CO)$_5$, their excited state properties and the predicted photoproducts produced on irradiation into these bands

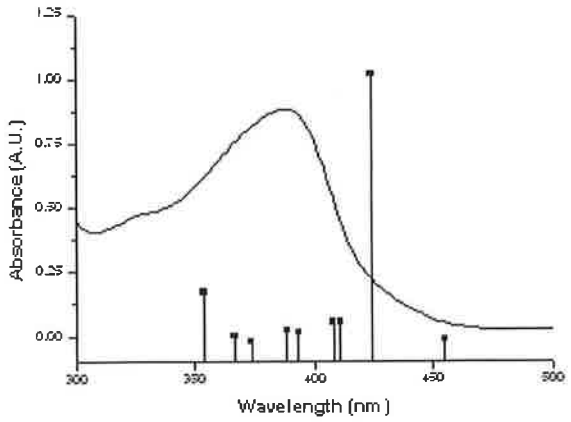

Figure 25 The position of the nine lowest lying excited state (vertical lines) relative to the experimental UV-Vis absorption spectrum of 2-FPyW(CO)$_5$ in pentane

The lowest lying singlet excited state of 2-FPyW(CO)$_5$ is characterised by a H-1 to LUMO transition. This transition is purely MLCT in nature and involves transfer of electron density from a molecular orbital centred on the W-d_{xy} orbital (63 %), CO_{cis} (22 %) and CO_{trans} (13 %) ligands to an unoccupied molecular orbital centred on the π orbital of the 2-fluoropyrdine moiety (94 %), which is non-bonding with respect to the W(CO)$_5$ moiety. This suggests that labilisation of this moiety should occur on irradiation into the charge transfer band. However, this band has a zero oscillator strength and thus may not significantly contribute to the electronic absorption spectrum. The second lowest lying excited state has the greatest oscillator strength of the transitions responsible for the electronic absorption spectrum. This state is HOMO → LUMO in nature and as such predominantly involves MLCT type transition from the d_{xz} orbital (60 %) to the π orbital of the pyridine ligand (94 %). However, LBCT is also present. This involves charge transfer from the CO_{cis} (22 %) and CO_{trans} (13 %) of the HOMO to the π orbital of the pyridine ligand. As this transition also involves transfer of charge into the largely π based LUMO, the metal carbonyl moiety will be non-bonding in nature, thus resulting in labilisation of the carbonyl moiety.

The third lowest excited state, occurring at 409.74 nm, is characterised by a HOMO → L+1 transition. This involves transfer of electron density from a molecular orbital centred on the W-d_{xz} orbital (60 %) with minor contributions from the CO_{cis} (22 %) and CO_{trans} (13 %) ligands. This electron density is transferred into the L+1 MO,

which is dominated by four π* CO_{cis} ligands (78 %) with a minor contribution from the d orbital (22 %). This receiving MO is almost non-bonding with respect to both the 2-fluorpyrdine ligand and the CO_{trans} ligand is thus expected to result in labilisation of either ligand. The fourth lowest lying excited state, located at 406.56 nm, is dominated by the H-1 to L+1 transition. This involves transfer of electron density from a molecular orbital centred on the W-d_{xy} orbital (63 %), CO_{cis} (22 %) and CO_{trans} (13 %) ligands to a virtual molecular orbital centred on the four π* CO_{cis} ligands (78 %). Excitation is expected to result in labilisation of either the 2-fluoropyrdine ligand or the CO_{trans} ligand.

The fifth lowest lying excited state is H-2 to LUMO in nature and thus involves charge transfer from a MO centred on the W-d_{zy} orbital (61 %) and the 4 π* CO_{cis} ligands (38 %) to a molecular orbital centred on the π orbital of the pyridine ligand (94 %). Similarly, the sixth excited state involves charge transfer from a metal based orbital (H-2) to a MO centred on the four 4 π* CO_{cis} ligands (78 %). Excitation is expected to result in labilisation of either the 2-fluoropyrdine ligand or the CO_{trans} ligand. The ninth excited state also contributes to the electronic absorption spectrum in the region 355 nm. The transition responsible for this absorption band is HOMO → L+2 in nature involving CT from a largely based MO to a largely pyridine ligand (91 %) based MO.

The molecular orbital and transitions responsible for the electronic absorption spectrum of 3-FPyW$(CO)_5$ are very similar to those observed for 2-FPyW$(CO)_5$. However, only the second, third, fourth, eighth, ninth, and fifteenth lowest lying excited states will be discussed as they have the highest oscillator strengths and thus are the transitions mainly responsible for the electronic absorption spectrum. The 2nd lowest lying excited state involves a HOMO → LUMO transition, whereby electron density is transferred from a molecular orbital centred on the d_{xy} orbital (60 %) and the 4 π* CO_{cis} orbitals (24 %) to a molecular orbital centred on the π orbital of the pyridine ring (93 %). This has the effect of labilising the pentacarbonyl moiety resulting in W-N bond cleavage.

Calculated Bands (nm)	Oscillator Strength (*f*)	Excited State Properties	Photoproduct Produced
443.73	0	W-d, CO → py CT	W-N bond cleavage
420.75	0.1298	W-d → py CT	W-N bond cleavage
418.65	0.0118	W-d, CO → CO CT	W-N bond cleavage, CO loss
410.49	0.0120	W-d, CO → CO CT	W-N bond cleavage, CO loss
368.36	0.0082	W-d, CO → CO CT	W-N bond cleavage, CO loss
358.14	0.0058	W-d, CO → py, CO CT	W-N bond cleavage, CO loss
308.19	0.0035	W-d, CO → py, CO CT	W-N bond cleavage, CO loss

Table 19 The calculated low energy UV absorption bands, their excited state properties and the predicted photoproducts produced on irradiation into these bands

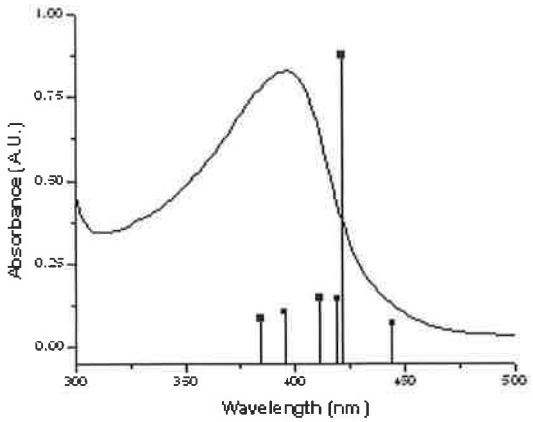

Figure 26 The position of the six lowest lying excited state (vertical lines) relative to the experimental UV-Vis absorption spectrum of 3-FPyW(CO)$_5$ in pentane

The third lowest lying excited state is similar in nature in that it too is MLCT in character involving charge transfer from the HOMO to L+1, a ligand based molecular orbital centred on the 4 π* CO_{cis} orbitals (80 %) with a minor contribution of 22 % coming from the metal d orbital. This has the result of increasing the CO_{cis} bond length, which are now anti-bonding in nature and labilising the CO_{trans} and pyridine ring which are now non-bonding in nature.

The fourth lowest lying excited state is H-1 → L+1 in nature. This transition involves charge transfer from a molecular orbital composed of metal d_{xy} orbital (64 %) and CO_{cis} (24 %) and CO_{trans} (13 %) contributions to an unoccupied molecular orbital localised on the 4 π* CO_{cis} orbitals (80 %) and the metal d orbital (22 %). Both the pyridine ring and CO_{trans} ligand are expected to be labilised as they are non-bonding

with respect to the metal centre in this molecular orbital. The eighth lowest lying excited state is dominated by a HOMO to L+4 transition state. This state involves transfer of electron density from the metal based HOMO to the 4 π^* CO_{cis} based (88 %) L+4 MO, which is entirely non-bonding for both the pyridine and CO_{trans} ligands. This is expected to result in labilisation of these ligands on excitation at the appropriate wavelength.

The ninth lowest lying excited state is similar to the second lowest lying state in that in involves charge transfer from the HOMO to a molecular orbital (L+2) almost entirely centred on the pyridine ring (79 %) and as such can be described as being a wholly MLCT based transition. However, the remaining 20 % of the electron density is transferred to the 4 π antibonding CO_{cis} ligands and thus a small contribution from M $\rightarrow$ CO CT and LBCT is also observed. Overall, this has the effect of labilising the CO_{trans} ligand. The highest energy transition involved in the electronic absorption spectrum occurs at 308 nm and is centred on the metal centre (64 %) and CO ligands (37 %), which in turn transfer electron density to the L+5 MO centred on the four CO_{cis} antibonding molecular orbitals (80 %) and to a lesser extent the π orbital of the pyridine ring (20 %). The CO_{trans} ligand is non-bonding with respect to the metal centre and is therefore labilised, resulting in CO loss from the *trans* position on UV-excitation in this area.

3.7. Conclusion

The photochemistry of two monofluorinated pyridine tungsten pentacarbonyl systems was investigated using matrix isolation in methane, dinitrogen and CO-doped methane matrixes. The photoproducts observed appear to be dependent on both the irradiation wavelength and the matrix gas. Visible irradiation (436 nm/405 nm) in a methane matrix resulted in W-N bond cleavage and re-coordination of the dissociated $W(CO)_5$ moiety to the pyridine ligand via either a C-H agostic interaction or via a π interaction on the pyridine ring. In both a CO doped methane matrix and a dinitrogen matrix the $W(CO)_5$ radical species was trapped forming $W(CO)_6$ and $W(CO)_5N_2$ respectively. In both cases tetracarbonyl formation was only observed as a minor photoproduct. Low energy broadband irradiation led to the regeneration of the parent species. This photochemistry is predicted in TD-DFT calculations, which show that in almost every case the excited state transitions involve promotion of electron density into a MO, which is non-bonding with respect to the pentacarbonyl moiety. The presence and position of the fluorine substituent on the pyridine ring does not appear to have any effect on the excited state chemistry compared to known unfluorinated examples and as such no indications of C-F bond activation are observed.

3.8. Bibliography

1 a) G.L. Geoffrey and M.S. Wrighton, *Organometallic Photochemistry*, Academic Press, New York, **1979,** b) M.A. Graham, R.N. Perutz, M. Poliakoff and J.J. Turner, *J. Organomet. Chem.*, **1972**, 34, C34-C35, c) J.K. Burdett, M.A. Graham, R.N. Perutz, M. Poliakoff, A. J. Rest, J.J. Turner, R.F. Turner, *J. Am. Chem. Soc.*, **1975**, 97, 17, 4805-4807, d) R. Bonneau and J.M .Kelly, *J. Am. Chem. Soc.*, **1980**, 102, 3, 1220-1221, e) R.N. Perutz and J. J. Turner, *J. Am. Chem. Soc.*, **1975**, 97, 17, 4800-4804

2 a) M.A. Graham, A.J. Rest and J.J. Turner, *J. Organomet. Chem.*, **1970**, 24, C54
b) M.A. Graham, M. Polikaoff and J.J. Turner, *J. Chem. Soc A*, **1971**, 2939

3 Z. Wang and A.J. Lees, *J. Organomet. Chem.*, **1989**, 363, 335

4 R. M. Dahlgren and J.I. Zink, *Inorg. Chem.*, **1977**, 16, 12, 3154 - 3160

5 M. Wrighton, G.S. Hammond, H.B. Gray, *Mol. Photochem.*, **1973**, 5, 2, 179-193

6 D. J. Darensbourg and M. A. Murphy, *Inorg. Chem.*, **1978**, 17, 4, 884

7 M.S. Wrighton, H. B. Abrahamson, D.L. Morse, *J. Am. Chem. Soc.*, **1976**, 98, 14, 4105-4109

8 A.J. Lees and A.W. Adamson, *J. Am. Chem. Soc.*, **1982**, 104, 3804-3812

9 C.H. Langford and L.E. Shaw, *Coord. Chem. Rev.*, **1997**, 159, 221-233

10 R.M. Kolodziej and A.J. Lees, *Organometallics*, **1986**, 5, 450-455

11 D.J. Darensbourg and M.A. Murphy, *J. Am. Chem. Soc.*, **1978**, 100, 2, 463-468

12 P. Glyn, F.P.A. Johnson, M.W. George, A.J. Lees and J.J. Turner, *Inorg. Chem.*, **1991**, 30, 3543-3546 and references therein

13 A.J. Lees and A.W. Adamson, *J. Am. Chem. Soc.*, **1980**, 102, 6874

14 E. Lindsay, A. Vlček and C.H. Langford, *Inorg. Chem.*, **1993**, 32, 3822-3825

15 S. Záliš, M. Busby, T. Kotrba, P. Matousek, M. Towrie and A. Vlček, *Inorg. Chem.*, **2004**, 43, 1723-1734

16 H. B. Abrahamson and M. S. Wrighton, *Inorg. Chem.*, **1978**, 17, 12, 3385-3388

17 S. Chun, E.E. Getty and A.J. Lees, *Inorg. Chem.*, **1984**, 23, 2155-2160

18 A. Vlček, *Coord. Chem. Rev.*, **2002**, 230, 225-242 and references cited therein

19 D. Guillaumont, C. Daniel, A. Vlček, *J. Phys. Chem. A*, **2001**, 105, 1107-1114

20 I.R. Farrell, P. Matousek, M. Towrie, A.W. Parker, D.C. Grills, M.W. George, A. Vlček, *Inorg. Chem.*, **2002**, 41, 4318-4323

21 I.R. Farrell, J. Van Slageren, S. Záliš, A. Vlček, *Inorg. Chim. Acta*, **2001**, 315, 44

22 M. Busby, P. Matousek, M. Towrie, A. Vlček, *J. Phys. Chem. A*, **2005**, 109, 3000-3008

23 M. Busby, P. Matousek, M. Towrie, A. Vlček, *Inorg. Chim. Acta*, **2006**, 360, 885-896

24 W. Strohmeier, *Angew. Chem. Int. Ed. Engl.*, 1**964**, 3, 11, 730-737

25 W.A. Hermann and A. Salzer, *Synthetic methods of organometallic and inorganic chemistry – Vol 1,* Georg Thieme Verlag, Stuttgart **1996**

26 T.M. McHugh, A.J. Rest, J.R. Sodeau, *J. Chem. Soc. Dalton Trans.,* **1979**, 1, 184-189

27 G. R. Dobson, P. M. Hodges, M. A. Healy, M. Poliakoff, J. J. Turner, S. Firth and K. J. Asali, *J. Am, Chem. Soc.,* **1987**, 109, 4218-4224

28 Mohammed Abid Hassan Alamiry, Ph.D Thesis, Dublin City University, **2005**

29 S. Ladogana, G.R. Dobson and J.P. Smit, *Inorg. Chim. Acta*, **1998**, 278, 202, S. Ladogana, G.R. Dobson and J.P. Smit, *Inorg. Chim. Acta*, **1998**, 271, 105

30 G. Boxhoorn, J. Stufkens and A. Oskam, *Inorg. Chim. Acta*, **1979**,33, 215

31 S. Záliš, M. Busby, T. Kotrba, P. Matousek, M. Towrie, A. Vlček Jr., *Inorg. Chem.*, **2004**, 43, 1723-1734

32 A. Hameed, A. Rybarczyk-Pirek, J. Zakrzewski, *J. Organomet. Chem.*, **2002**, 656, 102-107

33 L. Tutt, J. I. Zink, *J. Am. Chem. Soc.*, **1986**, 108, 5830-5836

34 Noel M. O'Boyle, Johannes G. Vos, GaussSum 0.9, Dublin City University, 2005. Available at http://gausssum.sourceforge.net

35 D.R. Kanis, P.G. Lacroix, M.A. Ratner, T.J. Marks, *J. Am. Chem. Soc.*, **1994**, 116, 10089-10102

36 J. Zakrzewski, J.A. Delaire, C. Daniel, I. Cote-Bruand, *New J. Chem.,* **2004**, 28, 1514-1519

Chapter 4

A photochemical and computational study of *cis-trans* isomerisation in (η^6-1,2-diphenylethene)$Cr(CO)_3$

Chapter four begins with a review of the literature of cis-trans/trans-cis isomerisation, particularly in stilbene and butadiene type compounds. This is then followed by a literature review of the photochemistry of (arene)$M(CO)_3$ type compounds. For comparison a review of the photochemistry of a number of photoisomerisable $Re(CO)_3L$ complexes is also included, as these systems contain both isomerisable stilbene-like units and carbonyl units. Predominantly the chapter centres on the photoinduced cis-trans isomerisation of cis-(η^6-1,2-diphenylethene)$Cr(CO)_3$. The photochemistry of these compounds is then examined using techniques such as, matrix isolation, time resolved infra red (TRIR) spectroscopy and steady-state photolysis. These results are then compared to theoretical results achieved using quantum chemical calculations. The electrochemistry of these metal carbonyl systems is then briefly examined.

4.1 Literature Survey

4.1.1 Isomerisation Reactions

The primary step in visual perception involves the *cis* → *trans* photoisomerisation of unsaturated centres in the retinal chromophore[1]. Consequently, photoisomerisation of alkenes has been extensively studied as model compounds in such systems, the *cis* → *trans* isomerisation reaction of stilbene being one of the most heavily studied photosensitised reactions known. Wavelength dependent photochemistry has been observed in the photoisomerisation reaction of *cis*- and *trans*-stilbene.[2] Irradiation of the *trans*-isomer at 313 nm results in the generation of a photostationary state dominated (90%) by the *cis*-isomer. This occurs via a non-planar intermediate. The predominant formation of the *cis*-isomer is explained in terms of distortion from planarity due to non-bonding interactions between the two phenyl rings. This inhibits resonance in the *cis*-isomer and thus increases both the ground state and excited state energy of the system ensuring the energy difference between these is much larger than that in the *trans*-isomer. It is suggested that this non-planar intermediate is twisted about the double bond and is a triplet state common to both isomers.[2,3] This twisted triplet state is achieved when the ground state reaches its maximum energy following a 90 ° twist. This twisted triplet state is also energetically similar to the *trans* triplet state, as confirmed by the similarities of their observed rate constants for sensitisation of the *trans*-isomer. This twisted triplet state has as yet to be detected as the energy difference between it and the *trans* triplet state is very small at 2.1 kcal/mol (8.7 kJ/mol), leading to rapid intersystem crossing. Photoinduced *cis-trans* isomerisation has also been studied on the ps timescale by Miyazawa et al[4]. Ultrafast excitation of *cis*-stilbene at 532 nm in room temperature hexane solution resulted in isomerisation to the *trans*-stilbene isomer with no cyclisation to form dihydrophenanthrene observed.

It has also been observed that irradiation of *cis*-stilbene may lead to cyclisation and generation of phenanthrene via a dihydrophenathrene intermediate[5]. Irradiation of a number of aminostilbenes in the absence of oxygen generates a reactive dihydrophenanthrene intermediate. In the continued absence of oxygen this then

regenerates the parent species but in the presence of oxygen it is oxidised to form the substituted phenanthrene species (
Scheme 1).

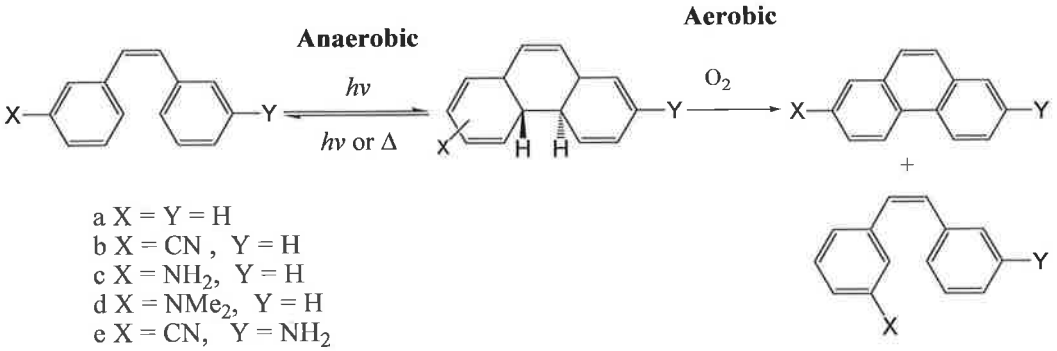

Scheme 1 Reaction pathway on irradiation of *cis*-amino-stilbenes[5]

This photoinduced isomerisation reaction, involving conrotary opening and closing of the central bond is of industrial interest as it has potential in applications such as optical data storage. Other similar system such as metacyclopheanadiene and diarylethenes are also of great interest in the area of three dimensional optical data storage as irradiation of these materials also greatly changes their π-conjugation and their optical properties[6].

Further to this gas phase studies on bistilbene have recently been performed on a conductive Ag/Ge (111)-(√3-√3)*R*30° surface.[7] *cis*-Stilbene molecules absorbed on a Ag/Ge (111)-(√3-√3)*R*30° surface at 100 K were irradiated with 248 nm UV irradiation. Scanning Tunnelling Microscopy (STM) imaging showed that *cis-trans* isomerisation took place pairwise with two *cis*-stilbene molecules transformed into two *trans*-stilbene molecules. This isomerisation took place mainly at *cis-trans* domain boundaries on the Ag/Ge surface. Similarly *trans*-stilbene absorbed on a Ag/Ge (111)-√3 surface at 100 K was irradiated with 308 nm UV irradiation. This resulted in the pairwise generation of two molecules of *cis*-stilbene, while on extended irradiation the reaction almost reached 100 % yields. Overall STM suggests that *cis-trans* isomerisation in the solid phase occurs via a one bond flip (OBF) mechanism where the tilted phenyl groups of the *cis*-stilbene molecule flip flat onto

the surface while moving laterally along the surface to fill the available adsorption site.

In contrast, recent solid and liquid phase studies of the photoisomerisation reactions of 2,2′-dimethylstilbene,[8] stilbene and the ring fused analogue *trans*-1,1′-bis(indanylidene)[9] suggest that this one bond flip mechanism may not apply to solid state isomerisation. Instead it is proposed that the Hula Twist mechanism, originally introduced to account for the *cis-trans* isomerisation of the confined visual chromophore in rhodopsin[10], is involved in solid state isomerisation. This process is outlined below in Scheme 3.

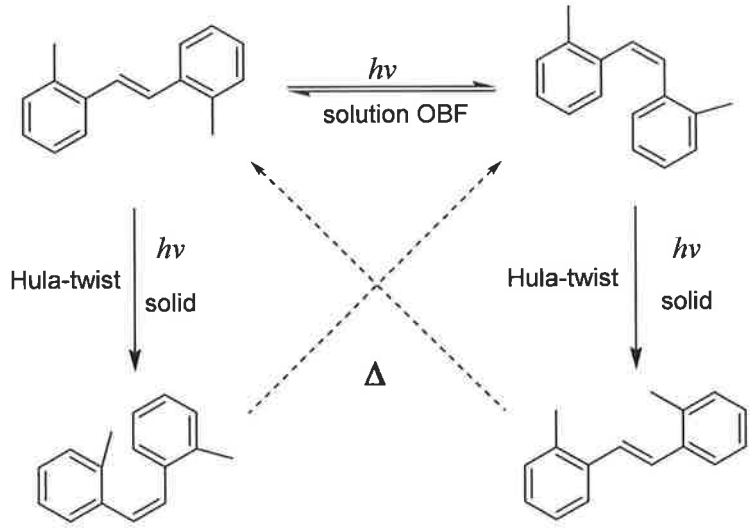

Scheme 3 Predicted photoisomerisation pathways for 2,2′-dimethylstilbene. Solution phase one-bond flip (OBF) isomerisation is shown horizontally. Isomerisation in a frozen glass by Hula-twist (HT) is shown vertically[8].

This is further suggested by the observation of the Hula Twist mechanism in a recent study on pre-vitamin D in an organic glass.[11] Irradiation at $\lambda > 280$ nm of *trans*-2,2′-dimethylstilbene and *cis*-2,2′-dimethylstilbene in a 273 K 2-methylpentane fluid solution[8] resulted in absorption difference spectra which were essentially mirror images indicating that in both cases the same equilibrium mixture is reached via torsional relaxation (one bond flip) of the double bond. However, this process is volume demanding and is not expected to occur in confined media where the less volume demanding Hula Twist mechanism would be more efficient. On irradiation of both isomers under similar conditions at 80 K in a 2-methylpentane glass

isomerisation via the Hula Twist (HT) mechanism was observed, the *cis*-isomer being an estimated 100 times more reactive than the *trans*-isomer. It was observed that subsequent warming of this low temperature HT product to 273 K resulted in the facile conversion to the more stable OBF product (Scheme 3).

Similar work has recently been carried out on the involvement of this Hula Twist mechanism in the *cis-trans* photoisomerisation of stilbene and the ring fused analogue *trans*-1,1′-bis(indanylidene)[9]. Irradiation at 270 nm of free *cis*-stilbene and *trans*-stilbene in the gas phase results in rotation of the ethylenic double bond by 90° to form an excited state singlet energy minimum common to both isomers. The lifetime for reaching this "common" minimum on the potential energy surface is much lower for the *cis*-isomer (300 fs)[9] compared to that of the *trans*-isomer 10 to > 100 ps depending on the excess energy. Following this 90° C=C twist the process proceeds by a rotation of a neighbouring single bond, i.e by a Hula Twist mechanism or in the case of the fused ring analogue via pyramidalization of the ethylenic C atoms. Study of the ultrafast dynamics of these species has shown that for both isomers of free stilbene the lower energy path is via the Hula Twist mechanism while in the fused ring analogue departure from the singlet energy minimum via a one – bond flip is the lower energy path.

Recent studies have also shown that the Hula-Twist mechanism also applies to the isomerisation reactions of styrenes[12] and dienes.[13,14] In a recent study by Yang and co-workers,[14] irradiation of the *Z,E* and *Z,Z* isomers (Figure 1) of 1,4-diphenyl-1,3-butadiene (DPB) in an ether/isopentane/ethanol glass at 77 K resulted in the formation of a number of new isomers. Typically, irradiation of the *Z,Z* isomer of DPB in liquid solution results in the formation of the *Z,E* isomer via a one-bond flip mechanism. However, irradiation of the *Z,Z* isomer in the sterically confined conditions of a 77 K glass also results in the formation of a new *Z,E′* isomer via a Hula-Twist mechanism. This then reacts further via another Hula-Twist mechanism to give the isomer *Z,E"*. Irradiation of the *Z,E* isomer under similar conditions was found to yield only a single *E,E* isomer of DPB via a Hula-Twist mechanism. Further investigation with *o,o'*-dimethyl DPB under similar irradiation conditions showed this isomer to be the unstable *E,E"* conformer.

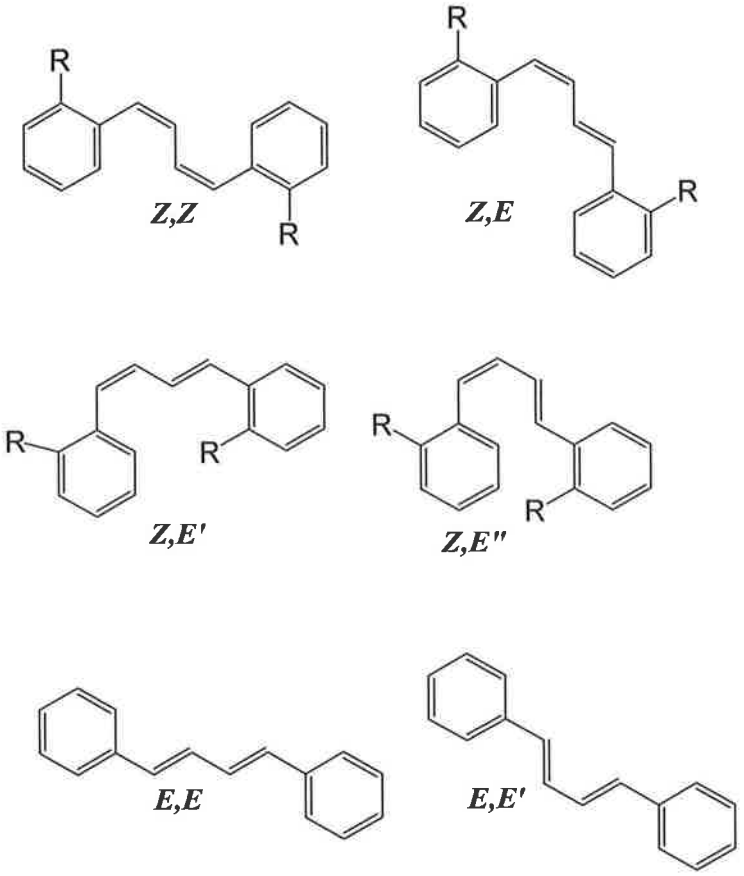

Figure 1 Conformational Isomers observed on irradiation of 1,4-diphenyl-1,3-butadiene[14]

Isomerisation of stilbene and stilbene like systems has also been investigated in constrained environments such as zeolites. In studies by Kuriyama and co-workers[15], irradiation at 254 nm of stilbene in room temperature cyclohexane produced a *cis:trans* ratio of 76:24. Conversely in both NaY zeolite and KY zeolite the predominant product was the *trans*-isomer, at 95 % and 76 % , respectively. Lower energy irradiation in cyclohexane solution again predominantly produced the *cis*-isomer (96 %), while in the zeolites the *trans*-isomer again dominated at 45:55 and 25:75 for the NaY and KY zeolites respectively. This provides further evidence that that isomerisation in stilbene is strongly effected by the surrounding environment.[16,17]

Previously Cohen et al.[18] coined the idea of a reaction cavity in order to explain and rationalise the photodimerisation reactions they observed in crystals. This process has since been observed by a number of groups for stilbene and azobenzene systems[19]. More recently, Natarajan and co-workers.[20] have investigated the *cis* → *trans*

isomerisation of *cis*-1-styrlpyrene and other 1,2-diaryl oelefins in the solid state (Scheme 4). Irradiation of solid *cis*-1-styrylfluoranthene at room temperature for 18 hrs lead to 25 % conversion to *trans*-1-styrylfluoranthene compared to 85 % in room temperature benzene solution. Increasing the temperature of the solid to 50 ° C increased the yield to 60 %. Similarly, it was observed that > 350 nm irradiation of solid *cis*-1-styrlpyrene resulted in isomerisation, yielding 55 % trans-1-strylpyrene. On increasing the temperature to 50 ° C a quantitative yield of 100 % isomerisation to *trans*-1-styrlpyrene was observed. In both cases *trans* → *cis* isomerisation was not observed. However, in contrast to both *cis*-1-styrylfluoranthene and *cis*-1-styrlpyrene on irradiation of *cis*-1,2-diazulene-ethene at $\lambda > 425$ nm as a solid at both room temperature and 50 ° C no isomerisation was observed. This is unusual as irradiation of a benzene solution of *cis*-1,2-diazulene-ethene under similar conditions resulted in a 0:100 *cis:trans* photostationary state. An analysis of the X-ray crystal structure of *cis*-1-styrylfluoranthene suggests that irradiation in the solid state will result in rotation of the side of the alkene attached to the phenyl group. In the case of cis-1-styrlpyrene the x-ray crystal structure reveals the presence of a void near the phenyl moiety, with the alkene molecules aligned in a criss-cross arrangement. This allows for rotation of the alkene and phenyl moiety. In solution this isomerisation process takes place via a conventional one-bond flip or torsional relaxation process. However, in the constrained environments of a crystal, where a large free volume or reaction cavity is absent, this isomerisation must take place via a Hula-Twist process. This involves simultaneous rotation of two adjacent bonds. The authors[20] do however note that this process may also occur via a conventional one-bond flip mechanism if the phenyl ring side of the molecule flips, although isomerisation by the Hula-Twist process is more probable in a constrained environment.

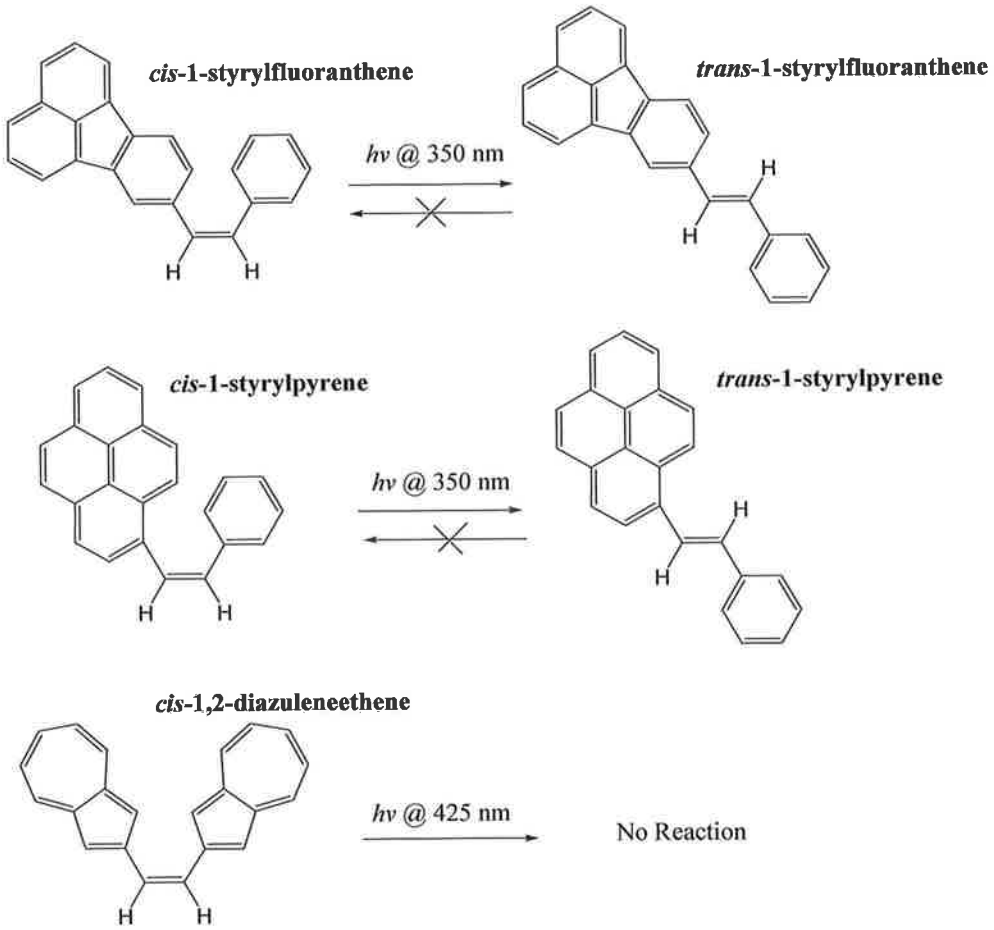

Scheme 4 Isomerisation of a number of 1,2-diaryl olefins in the solid state[20]

Recently the structural factors influencing *cis-trans* isomerisation have also been the subject of investigation. Photochemical studies on a number of methoxy and cyano substituted stilbenes have been performed to investigate the structural effects these substituents have on the *cis-trans* or *E-Z* isomerisation reactions[21].

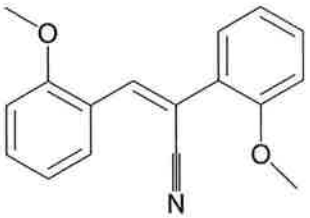

(*Z*)-1-cyano-1,2-bis-(2-methoxyphenyl)ethane

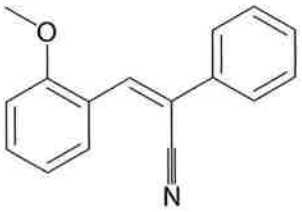

(*Z*)-1-cyano-2-(2-methoxyphenyl)-1-phenylethene

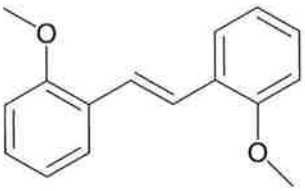

(*E*)-1,2-bis(2-methoxyphenyl)ethene

Figure 2 Structures of of (Z)-1-cyano-1,2-bis-(2-methoxyphenyl)ethane, (Z)-1-cyano-2-(2-methoxyphenyl)-1-phenylethene and (E)-1,2-bis(2-methoxyphenyl)ethane[21]

Photochemical studies of (Z)-1-cyano-1,2-bis-(2-methoxyphenyl)ethane, (Z)-1-cyano-2-(2-methoxyphenyl)-1-phenylethene and (E)-1,2-bis(2-methoxyphenyl)ethene (shown in Figure 2) were carried out in dry ethanol with a non-monochromatic source (max. λ = 365 nm). Following 1000 mins irradiation of the above three complexes it was observed in each case that the predominant isomer formed was the *cis*-isomer, with a final percentage contribution of above 80% in each case. This is in striking contrast to the ground state theoretical and the experimental fractions of the *cis*-isomers observed on thermal isomerisation in the presence of I_2, where a maximum experimental % *cis* value of 11.2 % was observed for (Z)-1-cyano-1,2-bis-(2-methoxyphenyl)ethane.

However, *trans-cis* isomerisation of stilbene type compounds has also been observed. Irradiation of a series of heavily substituted *trans*-stilbene dendrimers at 330 mn resulted in efficient *trans-cis* isomerisation in the excited state with a lifetime of approximately 10ns[22]. Recent work by Ozawa et al.[23] has shown that *trans-cis*

isomerisation of *trans*-stilbene may also be induced photochemically in the presence of the ionic liquid 1-butyl-3-methylimidazolium hexafluorophosphate ([bmim]PF_6). Görner[24] has also recently investigated the photoinduced reactions of *trans* isomers of a number of nitrostilbenes and substituted nitrostilbenes in the presence of amine solutions of diethylamine or triethylamine using both steady state (366 nm) and pulse (354 nm) photolysis. The photochemistry of these nitrostilbenes involves triplet states, which are significantly reduced in the amine solutions having rate constants for quenching in the order $k = 1 \times 10^8$ M^{-1} s^{-1}. In each case irradiation of the *trans*-nitrostilbene results in generation of a radical anion.

More heavily substituted ethenes have also been studied in terms of photochemical *trans-cis* isomerisation. Complexes of the type 1,2-diethynylethene (DEEs) and tetraethynylethene (TEEs) with electron donating (*p*-dialkylaminophenyl) or electron-accepting (*p*-nitrophenyl) groups were used as there wavelength dependence and *trans-cis* isomerisation differs greatly from the previously reported basic stilbenes.[25] However, as previously observed generation of the *cis*-isomer appears to be the predominant photoproduct in all cases. Monochromatic irradiation of a range of donor/acceptor substituted (E)-DEEs and (E)-TEEs in dilute *n*-hexane at 27 °C into the lowest energy absorption maximum of each complex resulted in all cases in *trans-cis* isomerisation. In all cases well-defined isosbestic points were observed with no detectable decomposition products. It was observed that the donor-acceptor nature of the substituents had a large impact on the ratio of each isomer formed at the photostationary state and on the partial quantum yields for *trans-cis* ($\Phi_{t\rightarrow c}$) and *cis-trans* ($\Phi_{c\rightarrow t}$) isomerisation. For the acceptor-acceptor substituted DEE's and TEE's the total quantum yields were the highest with 0.41 and 0.72 respectively, while in both cases little preference was observed for formation of either the *cis*-or *trans*-isomer. The donor-donor substituted DEEs and TEEs showed similar results with little preference in the equilibrium product distribution for formation of either isomer. In both A-A and D-D substituted cases the partial quantum yield $\Phi_{c\rightarrow t}$ was 2-5 times larger than $\Phi_{t\rightarrow c}$. However, in contrast the total quantum yields for the donor-acceptor substituted DEEs and TEEs were much lower, Φ_{total} = 0.088, 0.030 and 0.015 respectively while the partial quantum yield for *trans-cis* isomerisation ($\Phi_{t\rightarrow c}$) were 10-15 times higher than that for *cis-trans* isomerisation. This suggests almost quantitative conversion of these D-A functionalised molecules to the *cis*-isomers.

The relative "photostability" of the isomerisation reaction can also be examined in terms of the rate of isomerisation or more specifically the half-life ($t_{½}$) of the irradiated species. The A-A functionalised complexes rapidly undergo isomerisation, having $t_{½}$ = 9 and 6 mins respectively, whereas the D-D and D-A functionalized complexes are more resistant to isomerisation in *n*-hexane. Overall, the highly functionalised DEEs and TEE show photochemical behaviour that is in stark contrast to that of corresponding stilbene molecules. Although the partial quantum yields $\Phi_{c\rightarrow t}$ and $\Phi_{t\rightarrow c}$, show a large dependence on the nature of the functionality, by and large $\Phi_{c\rightarrow t}$ appears to be independent of substitution about the central stilbene frame, while conversely $\Phi_{t\rightarrow c}$ appears to be highly dependent on the nature of the substituted functionality. Solvent effects are also involved as it was observed that on increasing the polarity of the solvent used from n-hexane to CH_3CN to DMF irradiation of a (E)-D-A substituted TEE the photoequilibrium constant decreased, the partial and total quantum yields also decreased quite dramatically while the photostationary state shifted towards the *trans*-isomer, the latter especially evident in CH_3CN.

Crim and co-workers[26] have also recently examined the vibrational energy flow rates for both *cis*-and *trans*-stilbene in both deuterated chloroform and deuterated acetone. This was achieved through excitation of selected C-H vibrational bands with the subsequent energy flow monitored for both isomers by transient electronic spectroscopy. In both cases, following a rapid rise time, the transient species showed two different decay lifetimes. For the *cis*-isomer $\tau_1 = 2.6 \pm 1.5$ ps and $\tau_2 = 24.1 \pm 2.1$ ps and for the *trans*-isomer $\tau_1 = 1.4 \pm 0.6$ ps and $\tau_2 = 10.2 \pm 1.1$ ps. The decay times of the *cis*-isomer are on average longer than those of the *trans*-isomer by a factor of 2. However, no change in decay times was observed on changing either the solvent or excitation wavelength, thus suggesting that the process occurring is predominantly intramolecular in character.

The excited state dynamics and isomerisation of stilbene[27,28] and azobenzene[29] systems have been studied using ultrafast spectroscopic techniques – namely Time Resolved UV-Vis (TRVIS) and Time Resolved InfraRed (TRIR) and Time –Resolved Resonance Raman (TR^3) spectroscopies. *cis*-Stilbene in *n*-hexane was excited at 267 nm with probing in the range 630 nm near the singlet transient absorption band. The spectrum observed has been attributed to the S_1 *cis*-stilbene state with a lifetime of ~ 1

ps. This is also similar to other S_1-*cis*-stilbene lifetimes of 0.38 ps observed in acetonitrile and 1.8 ps observed in cyclohexane. This contrasts strongly with the observed S_1 *trans*-stilbene state, which has a decay lifetime on the ~ 100 ps timescale. Isomerisation from *cis*-stilbene is near barrierless and thus occurs rapidly (1 ps). Excitation at 260 nm into the S_2 ($\pi \rightarrow \pi^*$) of azobenzene produced a band which decayed after approximately 900 fs. A longer lived component with a lifetime (τ) of 10 ps was also observed and assigned to recovery of the bleach of the ground state absorption bands. The photochemistry of azobenzene was also investigated following excitation of the $S_1(n \rightarrow \pi^*)$ band. Excitation of this state at 503 nm resulted in the generation of excited state transient absorption bands between 390-420nm with an excited state lifetime of 2.5 ps.

4.1.2 Photoisomerised $Re(CO)_3L$ complexes

Both the chromophore $(bpy)Re(CO)_3$ and more notably stilbene are of particular interest in the design of photoswitchable molecular devices. This is because the luminescence of $(bpy)Re(CO)_3$ can be initiated by electron or energy transfer while the *trans-cis* photoisomerisation reaction of stilbene can be initiated by either direct excitation of the singlet excited state or energy transfer to a triplet excited state.[30]

Recently it was observed that irradiation of complexes of the type $(bpy)Re(CO)_3(L)$, where L = 4-(4-diethylaminostyryl)pyridine) [py-DEAS] or 4-(4-aza-15-crown-5-styryl)pyridine) [py-AZAS][31] in the range 350-450 nm resulted in population of either an ILCT or MLCT excited state.

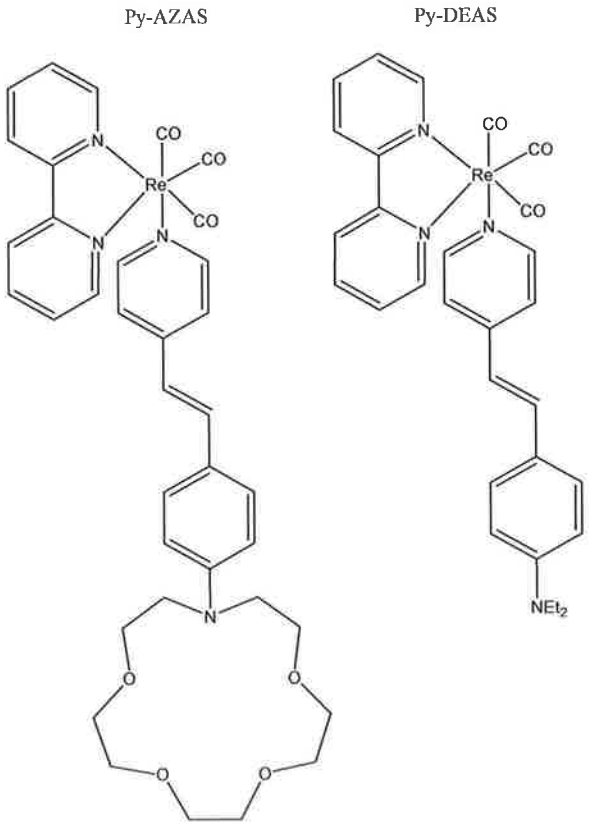

Figure 3 Structures of *fac*-(bpy)Re(CO)$_3$(*trans*-Py-AZAS) and *fac*-(bpy)Re(CO)$_3$(*trans*-Py-DEAS)

The products had a similar UV-Vis absorption spectrum, suggesting that no significant photoreaction occurred at this wavelength. Typically excitation into the MLCT band of (bpy)Re(CO)$_3$ at 380 nm results in a moderate emission with a quantum yield, $\Phi_{em} = 10^{-2}$. However, subsequent excitation of this band and between 300-500 nm of the py-DEAS derivative resulted in very low intensity emission with a quantum yield, $\Phi_{em} < 6 \times 10^{-4}$. In contrast, on protonation of the amine N-atom and the azacrown, following addition of HCl to *fac*-(bpy)Re(CO)$_3$(*trans*-py-DEAS) or *fac*-(bpy)Re(CO)$_3$(*trans*-py-AZAS) respectively, significant photochemistry was observed. Irradiation of *fac*-(bpy)Re(CO)$_3$(*trans*-py-DEAS-H$^+$) with λ_{exc} = 400-450 nm, populates the MLCT state, which results in changes to the UV-Vis absorption spectrum consistent with *cis* → *trans* isomerisation and an increase in emission intensity. However, for both *fac*-(bpy)Re(CO)$_3$(*trans*-Py-DEAS) and its protonated analogue *fac*-(bpy)Re(CO)$_3$(*trans*-PY-DEAS-H$^+$), the emission intensity and lifetime is much lower than that observed for typical (bpy)Re(CO)$_3$ complexes. This suggests that the MLCT excited state decays to the ground state via a non-radiative pathway in both cases. Similar results were observed for *fac*-(bpy)Re(CO)$_3$(*trans*-Py-AZAS), with *cis* → *trans* isomerisation only observed on protonation to yield *fac*-(bpy)Re(CO)$_3$ (*trans*-Py-AZAS-H$^+$).

A recent review by Murakami-Iha and co-workers[32] has shown a number of further examples of photo-induced *trans* → *cis* isomerisation reactions of similar rhenium complexes of the type *fac*-[Re(CO)$_3$(NN)(*trans*-L)]$^+$. Irradiation of a number of complexes of the type *fac*-[Re(CO)$_3$(NN)(*trans*-L)]$^+$, where NN = 1,10-phenanthroline (phen), 5-chloro-1,10-phenanthroline (Cl-Phen), 4,7-diphenyl-1,10-phenanthroline (ph$_2$phen) or dipyrido[3,2-a:2′,3′-c]phenazine (dppz) and L = ,2-bis(4-pyridyl)ethylene (bpe) or 4-styrylpyrdine (stpy), in acetonitrile solution resulted in spectral changes in the UV-Vis spectrum, which are assigned to photoinduced *trans* → *cis* isomerisation. The nature of either the bidentate or L ligand used has a profound effect on the quantum yield for isomerisation. Following irradiation at 313 nm of a *trans*-bpe complex where NN = phen, the quantum yield, $\Phi_{313\ nm} = 0.41$ while it is reduced to 0.19 where NN = dppz. This shows a less efficient sensitisation of the *trans*-bpe triplet IL excited state in the dppz complex compared to the phen complex. This fact has been used to modulate the energy of either the MLCT or ILCT excited states. Further monitoring of the photoinduced isomerisation of *fac*-

$[Re(CO)_3(phen)(trans\text{-}bpe)]^+$ has been carried out by Dattelbaum et al[33]. using time-resolved infrared (TRIR) spectroscopy. This study shows that in *fac*-$[Re(CO)_3(phen)(trans\text{-}bpe)]^+$ the lowest lying excited state is characterised by a ^3IL ($^3\pi\rightarrow\pi^*$) transition, with electron density localised on the *trans*-bpe ligand. It is this excited state which is responsible for *trans-cis* isomerisation. This ^3IL state decays to the parallel triplet excited state (3p*) of the *trans*-bpe ligand with a lifetime (τ) of 28 $\pm$ 1 ns, at a rate (k) of 3.6×10^7 s^{-1}. This suggests that the $^3p^*$ excited state is formed by intramolecular sensitisation ^1MLCT, $^1IL \rightarrow {}^3MLCT \rightarrow {}^3IL \rightarrow {}^3p^*$ and that it is the ^3IL state which is the immediate precursor leading to *trans-cis* isomerisation[32,33].

Similar observations have been made by Busby et al[34]. in ultrafast TRIR and Time resolved visible spectroscopic studies on *fac*-$[(Re(Cl)(CO)_3(papy)_2)]$ and *fac*-$[Re(papy)(CO)_3(bpy)]^+$, where papy = *trans*-4-phenylazopyridine and bpy = 2,2′-bipyrdine. Irradiation of *fac*-$[(Re(Cl)(CO)_3(papy)_2)]$ at 405 nm in CH_2Cl_2 solution, showed spectral changes assigned to isomerisation to form *fac*-[(Re(Cl)(CO)$_3$(t-papy)(c-papy)]. However, unusually, this appears to be fully thermally reversible following 15 mins in the dark. Likewise, irradiation of *fac*-$[Re(papy)(CO)_3(bpy)]^+$ at 350 nm results in *trans* $\rightarrow$ *cis* isomerisation of the papy ligand[34,35]. As is observed in many stilbene systems, isomerisation to form the *cis*-isomer also switches on the emission, presumably via a ^3MLCT state. TRIR spectroscopic studies of *fac*-$[(Re(Cl)(CO)_3(papy)_2)]$ and *fac*-$[Re(papy)(CO)_3(bpy)]^+$ indicate that both complexes share a common lowest lying excited state, which are however populated by two very different mechanisms. Excitation of *fac*-$[(Re(Cl)(CO)_3(papy)_2)]$ at 400 nm populates both the $^1\pi\pi^*$ (papy) and ^1MLCT (papy) states, which rapidly undergo ISC to the $^3n\pi^*$ state. This is in contrast to previous studies[32,33,37] on similar complexes where the ^3MLCT state was populated following ISC from the $^1\pi\pi^*$ and ^1MLCT states. It may be the case that, either the ^1MLCT (papy) state is in fact populated but decays too quickly to be measured or that population of this state is circumvented by faster ISC to populate the $^3n\pi^*$ state via the $^1\pi\pi^*$ and ^1MLCT states. In the case of, *fac*-$[Re(papy)(CO)_3(bpy)]^+$, irradiation results in population of the $^1\pi\pi^*$ (papy), ^1MLCT (papy) and, ^1MLCT (bpy) states, which then undergo ISC to populate both the $^3n\pi^*$ and ^3MLCT state. This is similar to the mechanism observed for *fac*-$[(Re(Cl)(CO)_3(papy)_2)]$. However, the ^3MLCT state, also populated by ISC, is formed

vibrationally "hot". This state cools and undergoes solvent relaxation between 1.5 – 6 ps, which is manifested in the IR spectrum by a shift in the A^1 band from 2055 cm^{-1} to 2063 cm^{-1}. This ^{3}MLCT (bpy) state then undergoes interconversion (IC) to populate the $^3n\pi^*$ state. Overall, this may be viewed as charge transfer from the $^*Re(CO)_3(bpy)$ moiety to the papy ligand. For both complexes, the populated $^3n\pi^*$ state results in narrowing and red-shifting of the higher energy CO band over time. The authors[34] rationalise this change in CO band positions in terms of rotation about the central N=N bond. This rotation removes the planarity of the complex and decouples the excited N=N-Ph unit. This is then expected to lead to a twisted ground state geometry, which will then return to either the *trans* and or the *cis* isomer. The process occurs in 120 ps for *fac*-[(Re(Cl)$(CO)_3(papy)_2$)] and 100 ps for *fac*-[Re(papy)$(CO)_3(bpy)]^+$.This process is similar to that observed by Vlček et al[36]. for similar styrylpyrdine systems. Here it was observed the sub-ps ISC from the singlet excited state to the triplet state occurs. This is followed by formation of an intermediate via partial rotation about the N=N bond and then slower ISC to either the *cis*- or *trans*- ground state geometry. However, in the case of the papy systems[34] this process occurs approximately 200 times faster.

Excitation of a series of *trans*-trinuclear diimine rhenium(I) tricarbonyl complexes with a 1,3,5-tris-(4-ethenylpyridyl)benzene bridging ligand in room temperature CH_3CN solution showed very weak luminescence, while in those where NN = 4,4′-Me_2bpy; 5-NO_2phen none was observed[37]. Emission quantum yields (Φ_{em}) are very low ($\Phi_{em} \sim 10^{-3}$) and lifetimes are short, being in the range 4.9 - 20.5 ns. This is ascribed to intermolecular sensitization of the triplet π-π^* (^{3}IL) excited state localized on the ethylenic C=C bond of the bridging ligand. Irradiation at 366 nm of the above complexes in CH_3CN increases the intensity of the band due to the ligand localized $^3\pi$-π^* excited state and decreases the MLCT band. This increases the intensity of the previously, albeit weakly, observed ^{3}MLCT excited state emission. Extended irradiation under these conditions increases the lifetimes to hundreds of seconds. Monitoring this photoinduced isomerisation showed that the *cis,cis,cis*-1,3,5-tris-(4-ethenylpyridyl)benzene-bridged complex was the predominant product with yields between 75-95%. Interestingly it was observed that these spectral changes were reversible on heating this solution to 60 °C for 5 h with no degradation of the complex

observed. On reversal of this photoinduced *trans-cis* isomerisation the quantum yields and lifetimes returned to pre-irradiation levels

The sensitisation of the ^{3}IL state by the ^{1}MLCT state, observed in the examples above, is in agreement with a recent computational study employing TD-DFT to study the geometry and excited states of $[Re(CO)_3(2,2'\text{-bpy})(\text{trans-4-strylpyrdine})]^+$.[38] This study showed that the lowest lying excited states are dominated by MLCT and ^{1}ILCT transitions. The photoisomerisation dynamics are governed by ISC from these singlet states to the low-lying Franck-condon ^{3}MLCT state. This is followed by conversion to a ^{3}IL state, which involves rotation of the C=C bond of about 90 °. When this perpendicular conformation (^{3}p*) of the ^{3}IL is reached, ISC to the ground state is observed, which results in *trans* → *cis* isomerisation of the styrylpyrdine ligand.

4.1.3 Photochemistry of (η^6-arene)$Cr(CO)_3$ systems

Although several transition metals readily complex with arene ligands, those of chromium are perhaps the most intensely studied and cited of these types of complexes. Analogous systems containing the remaining two group 6 transitions metals, molybdenum and tungsten, are somewhat less common due to the lesser stability of the complexes of the latter two transition metals. Over the last number of years the photochemistry of (η^6-arene)$Cr(CO)_3$ type systems[39] has been heavily investigated. Up until recently,[1b] it has been assumed that CO loss was the only photochemical pathway available to these systems. Wrighton et al[40]. have observed that direct excitation of complexes of the type (benzene)$Cr(CO)_3$ or (mesitylene)$Cr(CO)_3$ resulted in efficient CO substitution in the presence of pyridine with little evidence found for loss of the arene group. However, it has been shown that in the case of (η^6-pyridine)$Cr(CO)_3$, wavelength dependent photochemistry exists[39]. Depending on the wavelength of photolysis either CO loss or a photoinduced hapticity change may proceed. A combination of matrix isolation and ^1H NMR identified photoproducts confirming a hapticity change and giving evidence for the formation of (η^1-pyridine)$Cr(CO)_5$.[1(b)]

Photoinduced hapticity changes have been previously observed for a number of (arene)$Cr(CO)_3$ type complexes. In studies in the 1960's using ^{14}C-labelled arene systems, Strohmeier et al,[41,42] investigated the photochemical induced arene exchange. Irradiation of a number of (arene)$M(CO)_3$ complexes, where arene = benzene, chlorobenzene, toluene, heptatriene, M = Cr, Mo or W, in ^{14}C- labelled benzene, chlorobenzene, toluene, or heptatriene resulted in each case in exchange or the arene system for the labelled system to varying degrees. However, in each case the predominant reaction was dissociative CO loss resulting in formation of the dicarbonyl species. Overall, the % conversion for the chromium complexes was highest, especially for (benzene)$Cr(CO)_3$ and (heptatriene)$Cr(CO)_3$, which were 56.6 % and 87.5 %, respectively.

More recently, Howell et al.[43] have investigated the uncatalysed arene-exchange reaction observed following irradiation of a number of labile (arene)$Cr(CO)_3$ compounds in hydrocarbon solvents such as decalin or cyclooctane. Irradiation of $Cr(CO)_3$ complexes of pyrene and naphthalene and the "external" arene ligand toluene in decalin resulted in exchange of the polycyclic ligand for toluene. An analysis of the kinetic data suggested that the toluene independent mechanistic path follows a ring-slip or haptotropic shift intermediate, (η^n-arene)$Cr(CO)_3$ with another path through an (η^n-arene)$Cr(CO)_3$(η^{6-n}-toluene) intermediate, where n = 6-1. Extended Hückel level MO calculations indicated the $\eta^6 \rightarrow \eta^2$ path to be energetically most favourable for the naphthalene system while for the pyrene system the $\eta^6 \rightarrow \eta^1$ system is more favourable. This deduction is also suggested by, and is in agreement with, an earlier theoretical study by Albright et al[44]. on haptotropic processes in (naphthalene)$Cr(CO)_3$, (phenalene)$Cr(CO)_3$ and a number of other anionic and cationic species. Similarly, in a study by Treichel et al.,[45] it was observed that dissolution of a mono-deuterated dimethoxynapthalene $Cr(CO)_3$ complex in C_6D_6 the $Cr(CO)_3$ moiety underwent haptotropic migration to the undeuterated ring of the naphthalene system with equilibrium mixtures of the two eventually observed. Notably, very little arene exchange with the solvent or decomposition of the $Cr(CO)_3$ moiety was observed.

Bamford et al[46]. found that irradiation of (benzene)$Cr(CO)_3$ and (toluene)$Cr(CO)_3$ in hydrocarbon solution, predominantly resulted in CO loss, producing the dicarbonyl species, which subsequently decomposed to yield the free arene. In the presence of CO, the parent (arene)$Cr(CO)_3$ species was regenerated, while the presence of CCl_4, appeared to enhance arene-Cr bond scission by reaction with the dicarbonyl species and the excited state (arene)$Cr(CO)_3$ species. The rate of arene loss was observed to be even higher in methyl methacrylate solution. The authors[46] assigned this improved generation of arene to formation of a solvated (arene)$Cr(CO)_3$ excited state species, which then relaxes to generate either the arene and the solvated methylmethacrylate complex, (methylmethacrylate)$Cr(CO)_3$ or the solvated dicarbonyl species (arene)$Cr(CO)_2$(methylmethacrylate) and CO.

Similarly, it has been observed by Kreiter et al[47]. that UV irradiation of (η^6-1,3,5-cyclohepatriene)$Cr(CO)_3$ at 203 K in THF resulted in CO loss and generation of the 16-electron coordinatively unsaturated dicarbonyl species (η^6-1,3,5-cyclohepatriene)$Cr(CO)_2$(THF). This thermally sensitive dicarbonyl was then reacted with 2,3-dimethylbutadiene to yield the 1:1 adduct [{$\eta^{5:3}$-6-(2′,3′-dimethyl-3′-butene-1′,2′-diyl)-cyclohepta-2,4-dien-1-yl}$Cr(CO)_3$]. This was then reacted with CO to generated a stable $Cr(CO)_3$ cycloadduct complex.

Matrix isolation studies have been under taken by George et al[48]. on [(η^6-$C_6H_5C_2H_5$)$Cr(CO)_3$] and [$(CO)_4Mn(\mu$-η^3:η^6-$C_3H_4C_6H_5$)$Cr(CO)_3$] in a number of matrix gases. Photolysis of [(η^6-$C_6H_5C_2H_5$)$Cr(CO)_3$] in an argon matrix at > 300 nm resulted in formation of the dicarbonyl species [(η^6-$C_6H_5C_2H_5$)$Cr(CO)_2$] via CO loss. Photolysis of [$(CO)_4Mn(\mu$-η^3:η^6-$C_3H_4C_6H_5$)$Cr(CO)_3$] in an argon matrix at > 254 nm, resulted in CO loss from the Mn centre leading to [$(CO)_3Mn(\mu$-η^3:η^6-$C_3H_4C_6H_5$)$Cr(CO)_3$] formation with the $Cr(CO)_3$ moiety remaining intact. This may be due to the population of an excited state, which was not labile with respect to the $Cr(CO)_3$ moiety or to readily reversible CO loss from the $Cr(CO)_3$ moiety. In contrast, irradiation of [$(CO)_4Mn(\mu$-η^3:η^6-$C_3H_4C_6H_5$)$Cr(CO)_3$] in a N_2 matrix at > 400 nm, resulted in CO loss from the chromium metal centre to yield the N_2 trapped species [$(CO)_4Mn(\mu$-η^3:η^6-$C_3H_4C_6H_5$)$Cr(CO)_2N_2$], based on comparison of a similar N_2 trapped species observed by Rest et al[49]. on irradiation of [(η^6-C_6H_6)$Cr(CO)_3$] in a N_2 matrix, where the dicarbonyl [(η^6-C_6H_6)$Cr(CO)_2N_2$] was observed. Higher energy irradiation at > 300 nm resulted in continued generation of [$(CO)_4Mn(\mu$-η^3:η^6-$C_3H_4C_6H_5$)$Cr(CO)_2N_2$], but also generation of a second dicarbonyl species, involving loss from the Mn metal centre, [$N_2(CO)_3Mn(\mu$-η^3:η^6-$C_3H_4C_6H_5$)$Cr(CO)_2N_2$].

In a similar matrix isolation study by Rest and co-workers[50] a series of dinuclear manganese and chromium metal carbonyls were irradiated in a range of matrix gases. Irradiation of [$Cr_2(\mu$-η^6:η^6-$C_{12}H_{10}$)$(CO)_6$] at > 550 nm ,with a $290 < \lambda < 370$ nm filter, in a methane matrix generated the CO loss species [$Cr_2(\mu$-η^6:η^6-$C_{12}H_{10}$)$(CO)_5$] with concomitant bleaching of the parent absorption. Subsequent lower energy (> 415 nm) irradiation immediately resulted in photochemical reversion leading to regeneration of

the parent species, while higher energy (λ < 280, > 550 nm) irradiation resulted in further generation of the dicarbonyl product and eventual decomposition. Irradiation in argon and dinitrogen matrixes under similar conditions gave similar results. However, in a N_2 matrix, the N_2 substituted species was generated on coordination of N_2 onto the vacant site following CO ejection (Scheme 5). Unusually, photochemically induced CO loss was only observed from a single $Cr(CO)_3$ moiety in the dinuclear species, with no tetracarbonyl formation observed.

Similarly, irradiation of $[Cr(\eta^6\text{-}C_7H_8)(CO)_3]$ with λ_{exc} > 300 nm in a 12 K methane matrix resulted in formation of product bands at 1944 and 1864 cm^{-1} assigned to the dicarbonyl species $[Cr(\eta^6\text{-}C_7H_8)(CO)_2]$. In the presence of N_2, the dicarbonyl $[Cr(\eta^6\text{-}C_7H_8)(CO)_2(N_2)]$ was observed (Scheme 5) while irradiation in a CO matrix at > 300 nm produced both $Cr(CO)_6$ and a tetracarbonyl species $[Cr(\eta^6\text{-}C_7H_8)(CO)_4]$. Assignment of this latter species is based on comparison with the spectra of $[Mo(\eta^6\text{-}C_7H_8)(CO)_3]$ in a CO matrix[51].

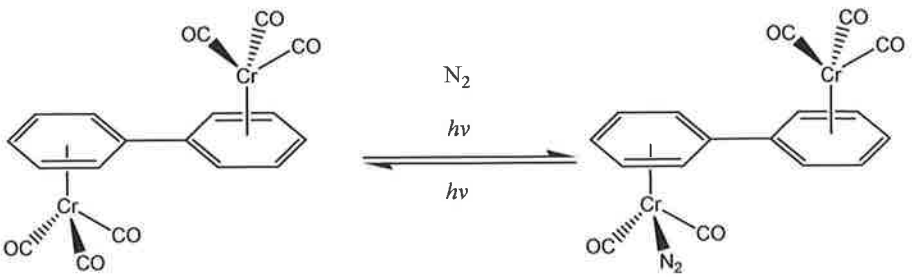

$[Cr_2(\mu\text{- eta}^6\text{: eta}^6\text{-}C_{12}H_{10})(CO)_6]$

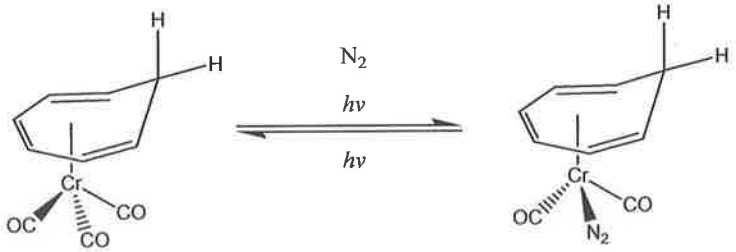

$[Cr(\text{ eta}^6\text{-}C_7H_8)(CO)_3]$

Scheme 5 Irradiation of $[Cr_2(\mu\text{-}\eta^6\text{:}\eta^6\text{-}C_{12}H_{10})(CO)_6]$ and $[Cr(\eta^6\text{-}C_7H_8)(CO)_3]$ in a N_2 matrix

As observed for the dinuclear species low energy irradiation (> 475 nm) and to a lesser extent, annealing, resulted in regeneration of the parent species and loss of the product bands. Higher energy irradiation, as previously observed, ($\lambda < 280 > 550$ nm) in an N_2 matrix resulted in further dinitrogen substituted dicarbonyl formation

In recently published work by Mischenko et al[52]., the photodecomposition products of compounds of the type [(arene)$Cr(CO)_3$], where arene = styrene, stilbene, 1-4-diphenyl-1,3-butadiene, have been discussed. Irradiation of [(styrene)$Cr(CO)_3$] at 313 and 336 nm, [(stilbene)$Cr(CO)_3$] at 366 and 405 nm, and [(1-4-diphenyl-1,3-butadiene)$Cr(CO)_3$] at 313 and 436 nm, resulted in each case, in CO loss and formation of the relevant dicarbonyl species. The authors[52] propose the subsequent formation of a binuclear complex in which the chromium atom from one dicarbonyl species is coordinated to the vinylic double bond of a neighbouring molecule as well as the phenyl ring. This then decomposes resulting in further CO loss, with a quantum yield for decomposition in the styrene complex of 0.68. This is further suggested by analysis of IR spectra following irradiation. Overall, the authors propose a reaction scheme whereby on irradiation an excited state molecule is formed, which then relaxes to reform the parent tricarbonyl and emits a photon of light or relaxes resulting in CO loss and dicarbonyl formation. This dicarbonyl then interacts with another intact tricarbonyl molecule via interaction with the vinylic bond. Further irradiation results in further CO loss leading to complete dicarbonyl formation and thus formation of a binuclear arene chromium complex.

McCabe et al[53]. have also recently reported the synthesis and photochemistry of an unusual [(η^6-fulgide)$Cr(CO)_3$] system, where fulgide = [1-(3′, 4′, 5′-trimethoxyphenyl) ethylidene(isopropylidene)succinic anhydride. Irradiation at 254 nm of the *Z*-isomer of [(η^6-fulgide)$Cr(CO)_3$] in dioxane-d^8, resulted in isomerisation to the E isomer.

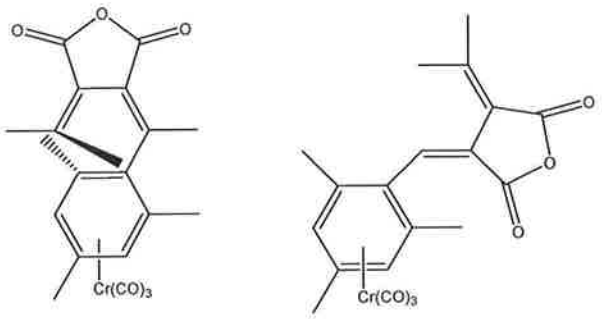

Z-isomer *E*-isomer

Figure 4 The structures of Z- and E- [η^6 – (1-(2′, 4′, 6′-trimethylphenyl)-methylidene (isoprpylidene) succinic anhydride)$Cr(CO)_3$]

Similarly, irradiation at 350 nm of the *Z*-isomer in C_6D_6 resulted in isomerisation but also loss of the $Cr(CO)_3$ moiety, resulting in both the free *Z*- and *E*-fulgide ligand. Interestingly, an *E*-fulgide ring closure product was also observed. Similar results were observed on irradiation of the *E*-isomer. In the same way, irradiation of the *Z*-isomer of the trimethylphenyl fulgide $Cr(CO)_3$ analogue complex, in C_6D_6 resulted in isomerisation and subsequent unique ligand loss.

A number of arene-$Cr(CO)_3$ type complexes have also been synthesised in the areas of drug design and as organometallic synthetic precursors. Gervasio et al[54]. have successfully synthesised a number of complexes of polycyclic aromatic hydrocarbon (PAH) ligands of the type [(η^6-PAH)$Cr(CO)_3$], where PAH = pyrene, perylene, chrysene and 1,2-benzanthacene. A further example of this type of $Cr(CO)_3$ complex is [(η^6-phenanthrene)$Cr(CO)_3$], the synthesis and characterisation of which is described in the appendix. Vasil'kov[55] has also recently investigated the electrochemical properties of a series of fluoranthene chromium tricarbonyl complexes. Recently, Ashe et al[56]. have synthesised and characterised an unusual $Cr(CO)_3$ complex of 1,2-dihydro-1,2-oxaborine via a tris-acetonitrile $Cr(CO)_3$ ($Cr(CO)_3(MeCN)_3$) adduct. Motterlini et al[57]. have also recently investigated the use of $Fe(CO)_3$ complexes of substituted pyrones as CO releasing molecules in inducing apoptosis in cancerous cells.

4.2 Aims and Objectives

This work in this chapter involves study of the photochemistry of both *cis*-(η^6-1,2-diphenylethene)$Cr(CO)_3$ and *trans*-(η^6-1,2-diphenylethene)$Cr(CO)_3$, in particular the photoinduced isomerisation of the *cis*-isomer to yield the *trans* isomer. These systems were also further characterised using cyclic voltammetry. Density Functional Theory calculations were also undertaken to further investigate the excited state properties resulting in the observed photochemistry.

4.3 Experimental

4.3.1 Materials

All operations were performed under inert gas atmospheres, and the purity of all isolated products was verified by microanalysis. Spectroscopic grade cyclohexane was used as obtained (Aldrich spectroscopic grade). Both *cis*- and *trans*-stilbene were obtained from the Sigma Aldrich chemical Co. and used without further purification. Gases used for the matrix experiments and for the flash photolysis experiments (Ar, N_2, and CO) were BOC research grade (99.999% purity).

4.3.2 Equipment

Spectra were recorded on the following instruments: IR, Perkin-Elmer 2000 FT-IR (2 cm^{-1} resolution), UV/vis Hewlett-Packard 8452A; NMR, Bruker AC 400. Emission spectra (accuracy±5 nm) were recorded at 298 K using a LS50B luminescence spectrophotometer, equipped with a red sensitive Hamamatsu R928 PMT detector, interfaced with an Elonex PC466 employing Perkin–Elmer FL WinLab custom built software.

The matrix isolation apparatus used is described in detail in Chapter 1. *cis*-(η^6-1,2-diphenylethene)$Cr(CO)_3$ was sublimed from a right angled tube at 338 K as the gas stream entered the vacuum shroud. Deposition of *trans*-(η^6-1,2-diphenylethene)$Cr(CO)_3$ using a variety of techniques proved unsuccessful. The *cis*-isomer was deposited onto the windows at 20 K, and monitored in the infrared until the absorbance of (the most intense) one of the metal carbonyl bands was approximately 1 A.U. When the required absorbance was achieved the sample was photolysed and monitored on a Spectrum One FTIR spectrophotometer fitted with a CsI beam splitter. Spectra were recorded at 1 cm^{-1} resolution with 16 scans. UV/vis spectra were recorded on a Perkin-Elmer Lambda EZ201 spectrophotometer. Matrices were photolysed through a quartz window with a 300 W Xe arc or 200 W Hg lamp in combination with a water filter. Photolysis wavelengths were selected with cut-off or interference filters: $\lambda_{exc.}$ = 405, 365, or > 410 or 500 nm.

Density Functional calculations were carried out with the Gaussian 03 programme[58] on geometry optimized structures, initially using the restricted Hartree-Fock (RHF) functional and subsequently Becke's[59] three-parameter hybrid functional with the

LYP[60] correctional functional (B3LYP). The size of the basis set used was increased incrementally from STO-3G to LanL2DZ. The final geometry optimisation was carried out using the LanL2DZ basis set, which uses the Dunning-Huzinaga double-ζ basis functions (DZ) for carbon, nitrogen, and hydrogen atoms.[61] The energies of the 20 lowest lying singlet-singlet energy transitions were then calculated at the optimised geometry using time dependent density functional theory (TDDFT). The orbital population of the 20 lowest lying excited states was visualised using Gaussview[62] and extraction of the percentage contributions of the metal orbitals, CO and the ligands in the excited state structures was performed by locally created GaussSum software. [63]

4.3.3 Synthesis

Both *cis*- and *trans*-(η^6-1,2-diphenylethene)$Cr(CO)_3$ were synthesised according to the method outlined by Hrnviar et al.[64] and Pryce[65] with minor alterations.

4.3.3.1 *cis*-(η^6-1,2-diphenylethene)$Cr(CO)_3$

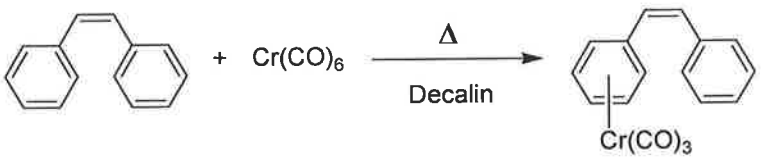

Scheme 6 Synthesis of *cis*-(η^6-1,2-diphenylethene)$Cr(CO)_3$

To 20 mL argon purged decahydronapthalene (Decalin) was added $Cr(CO)_6$ (0.300 g, 0.136 mmol) and *cis*-stilbene (0.242 mL, 0.136 mmol). This solution was then refluxed under inert conditions for 4 hours to yield a bright yellow coloured solution. The resulting solution was allowed cool to room temperature and the reaction flask immersed in liquid nitrogen to promote precipitation of the desired product. The resulting yellow crystalline solid was filtered and any remaining solvent and excess $Cr(CO)_6$ removed under reduced pressure. This yellow solid was then recrystallised from benzene/pentane.

Yield: 0.150 g, 35.3 %

IR (cyclohexane) : 1981 and 1916 cm^{-1}; UV-Vis (cyclohexane) : 220, 263, 328 & 422 nm ; ^{1}H-NMR (400 MHz, d_3-acetonitrile) : 7.31 ppm (s, 5H), 6.76 ppm (d, 1H), 6.23 ppm (d, 1H), 5.48 ppm (m, 5H)

4.3.3.2 *trans*-(η^6-1,2-diphenylethene)$Cr(CO)_3$

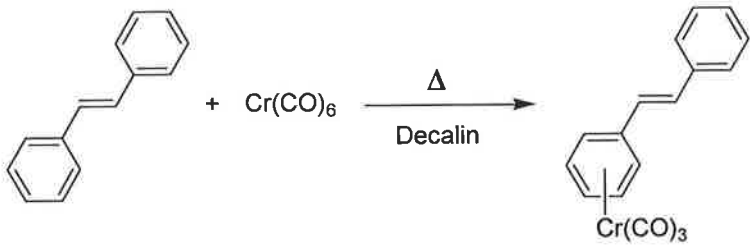

Scheme 7 Synthesis of *trans*-(η^6-1,2-diphenylethene)$Cr(CO)_3$

To 20 mL argon purged decahydronapthalene (Decalin) was added $Cr(CO)_6$ (0.300 g, 1.362 mmol) and *trans*-stilbene (245.5 g, 1.362 mmol). This solution was then refluxed under inert conditions for 4 hours to yield a bright yellow coloured solution. The resulting solution was allowed cool to room temperature and the reaction flask placed in a freezer at -20 °C overnight to promote precipitation of the desired product. The resulting orange-red crystalline solid was filtered and any remaining solvent and excess $Cr(CO)_6$ removed under reduced pressure. This orange-red solid was then recrystallised from benzene/pentane.

Yield: 210 g, 49.5 %

IR (cyclohexane): 1981 and 1916 cm^{-1}; UV-Vis (cyclohexane) : 218, 285 & 420 nm; ^{1}H-NMR (400 MHz, d_3-acetonitrile): 7.54 ppm (d, 2H), 7.39 ppm (m, 3H), 7.16 ppm (d, 1H), 6.82 ppm (d, 1H), 5.83 ppm (d, 2H), 5.66 ppm (t, 2H), 5.50 ppm (t, 1H)

Anal. Calcd. for $C_{17}H_7CrO_3$, C 65.60 %, H 2.27, Found C 64.10 %, H 3.78 %

4.4 Results

4.4.1 Matrix Isolation of *cis*-(η^6-1,2-diphenylethene)Cr(CO)$_3$

4.4.1.1 Photolysis of *cis*-(η^6-1,2-diphenylethene)Cr(CO)$_3$ in a methane matrix

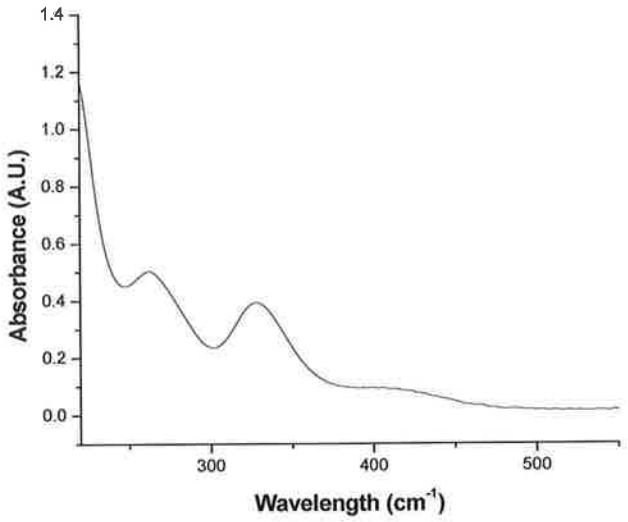

Figure 5 UV-Vis spectrum of *cis*-(η^6-1,2-diphenylethene)Cr(CO)$_3$ in cyclohexane

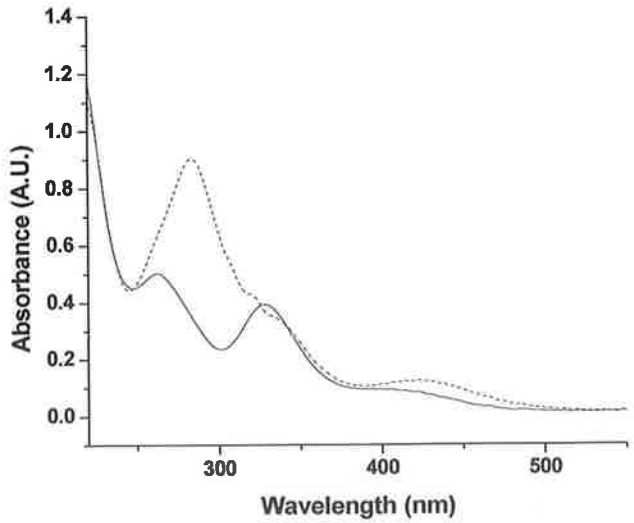

Figure 6 UV-Vis spectra of *cis*-(η^6-1,2-diphenylethene)Cr(CO)$_3$ (2.99 x 10^{-5} M) (—) and *trans*-(η^6-1,2-diphenylethene)Cr(CO)$_3$ (----) (3.55 x 10^{-5} M) in cyclohexane solution

cis-(η^6-1,2-diphenylethene)$Cr(CO)_3$ is a bright yellow coloured crystalline solid with a UV-Vis spectrum exhibiting two high energy bands centred at 263 nm (ε = 1.6 x 10^4 M^{-1} cm^{-1}) and 328 nm (ε = 1.3 x 10^4 M^{-1} cm^{-1}) in a cyclohexane solution. A weaker feature is also observed in the visible region at approximately 420 nm. For comparison and identification of the *cis* → *trans* isomerisation process the UV-Vis spectrum of *trans*-(η^6-1,2-diphenylethene)$Cr(CO)_3$ is also shown. The spectrum of the *trans* isomer contains a feature centered at 285 (ε = 2.5 x 10^4 M^{-1} cm^{-1}), as well as a weaker MLCT band at 420 nm also observed for the *cis*-isomer.

Following deposition of *cis*-(η^6-1,2-diphenylethene)$Cr(CO)_3$ in a methane matrix two carbonyl bands were observed at 1978 and 1911 cm^{-1}. Because the ν_{CO} vibrations for both the *cis* and the *trans*-complexes occur at the same wavenumbers, *cis* → *trans* isomerisation is best monitored by UV-Vis spectroscopy. Following irradiation of *cis*-(η^6-1,2-diphenylethene)$Cr(CO)_3$ in a methane matrix for 80 mins at 20 K ($\lambda_{exc.}$ = 405 nm), strong absorption bands were generated at 295 and 445 nm suggesting formation of *trans*-(η^6-1,2-diphenylethene)$Cr(CO)_3$ (Figure 7).

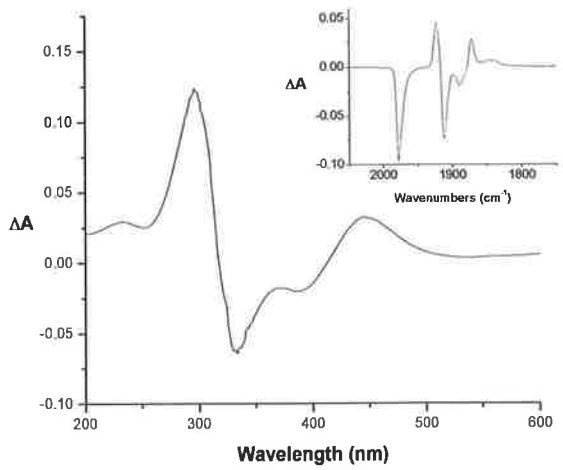

Figure 7 The UV-vis difference spectrum of *cis*-(η^6-1,2-diphenylethene)$Cr(CO)_3$ in a methane matrix following irradiation at 405 nm for 80 mins. The inset shows the IR difference spectrum of the same matrix following irradiation with λ_{exc} = 313 nm for 60 mins.

Following irradiation of the methane matrix for 60 mins with $\lambda_{exc.}$ = 313 nm, bleaching of the parent bands was observed with concomitant formation of ν_{CO} bands at 2139, 1924 and 1873 cm^{-1} *trans*-(η^6-1,2-diphenylethene)$Cr(CO)_2$.

4.4.1.2 Photolysis of *cis*-(η^6-1,2-diphenylethene)$Cr(CO)_3$ in a N_2 matrix

Following deposition of *cis*-(η^6-1,2-diphenylethene)$Cr(CO)_3$ in a methane matrix two carbonyl bands were observed at 1980 and 1915 cm^{-1}. Photolysis of *cis*-(η^6-1,2-diphenylethene)$Cr(CO)_3$ in a dinitrogen matrix at 20 K with λ_{exc} = 313 nm for 110 mins resulted in the depletion of the parent bands with concomitant generation of three product bands at 2151, 1940 and 1899 cm^{-1} assigned to *cis*-(η^6-1,2-diphenylethene) $Cr(CO)_2N_2$ as shown in Figure 8.

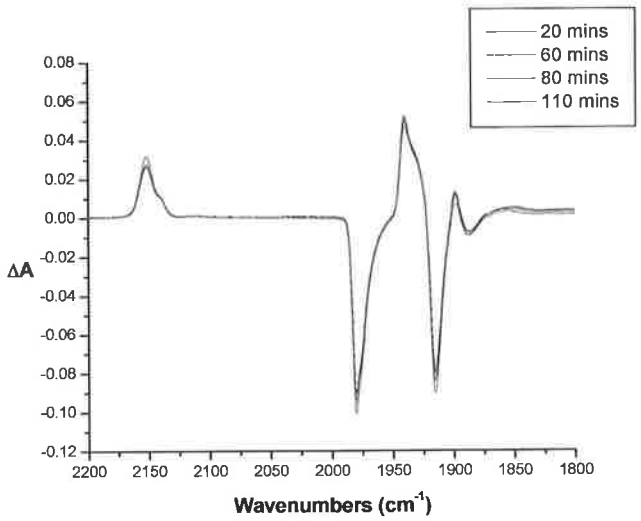

Figure 8 Difference spectrum obtained following irradiation (λ_{exc} = 313 nm) of *cis*-(η^6-1,2-diphenylethene)$Cr(CO)_3$ in a N_2 matrix.

Following 300 mins irradiation at 405 nm weak spectral changes were evident in the IR spectrum (Figure 9). This showed the depletion of the parent carbonyl bands at 1980 and 1915 cm^{-1} with concomitant generation of two carbonyl bands of equal intensity at very similar wavenumbers – 1975 and 1910 cm^{-1} thus suggesting formation of another isomeric form of the tricarbonyl species.

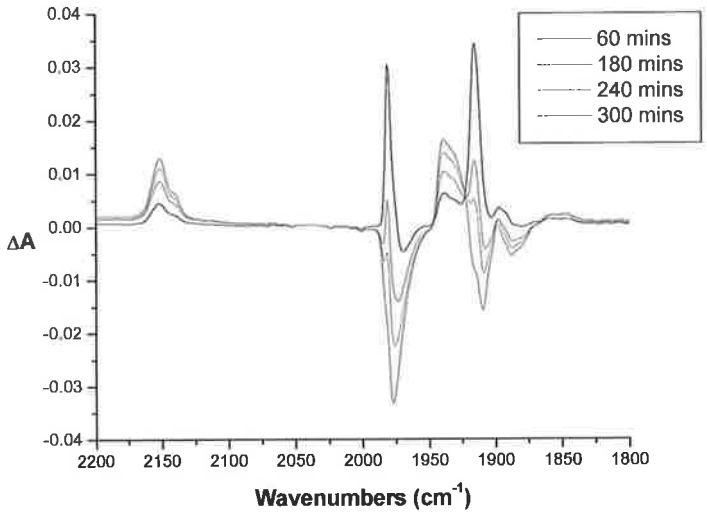

Figure 9 Difference spectrum obtained following irradiation (λ_{exc} = 405 nm, 300 mins) of *cis*-(η^6-1,2-diphenylethene)$Cr(CO)_3$ in a N_2 matrix.

However, as the IR stretching vibrations for both the *cis* and the *trans*-isomer occur in almost the same position in the IR spectrum any *cis*→*trans* isomerisation is best observed by monitoring in the UV-Vis region of the spectrum. Following 300 mins irradiation at 405 nm the electronic absorption difference spectrum (pre- and post-irradiation) indicated the generation of an absorption band at 285 nm. This band is not present in the electronic absorption spectrum of *cis*-(η^6-1,2-diphenylethene)$Cr(CO)_3$ but is, in that of *trans*-(η^6-1,2-diphenylethene)$Cr(CO)_3$. Shown in is the UV-vis spectrum following deposition, and after irradiation at 405 nm. These spectra are compared to the known UV-vis spectrum of *trans*-(η^6-1,2-diphenylethene)$Cr(CO)_3$. The subtraction spectrum obtained (Figure 10) highlights the absorption feature observed at ~285 nm.

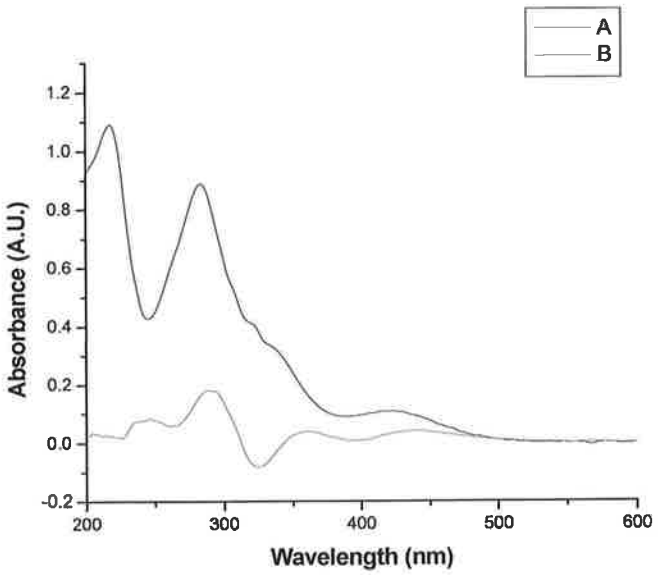

Figure 10 Electronic difference spectrum following 405 nm irradiation for 300 mins of *cis*-(η^6-1,2-diphenylethene)$Cr(CO)_3$ in a N_2 matrix (B, shown in red) compared to the known electronic absorption spectrum of *trans*-(η^6-1,2-diphenylethene)$Cr(CO)_3$ (A, shown in black).

4.4.1.3 Photolysis of *cis*-(η^6-1,2-diphenylethene)$Cr(CO)_3$ in a 10% CO-doped CH_4 matrix

On deposition of *cis*-(η^6-1,2-diphenylethene)$Cr(CO)_3$ in a 10% CO-doped methane matrix carbonyl bands were observed at 1976 and 1909 cm^{-1} due to the parent complex and at 2137 cm^{-1} due to free CO present in the matrix. Following visible irradiation (λ_{exc} = 405 nm, 60 mins) the parent bands decreased in intensity while very weak product bands were generated concomitantly at 2066, 2036, 2013 and 1920 cm^{-1}. As shown in Figure 11 on subsequently changing the photolysis wavelength to 313 nm for 80 mins the product band at 2066, 2036, and 2013 cm^{-1} decreased in intensity while the product band at 1920 cm^{-1} increased in intensity. A further product band was also generated at 2137 cm^{-1}. The free CO band at 2137 cm^{-1} also increased in intensity further suggesting the occurrence of a CO loss process.

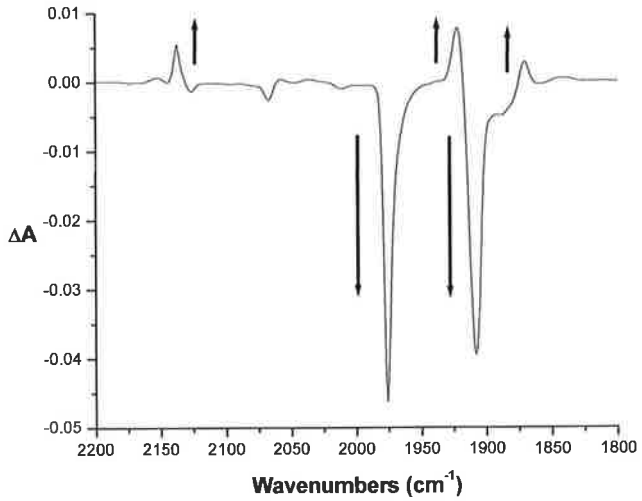

Figure 11 IR difference spectrum following irradiation at 313 nm for 80 mins of *cis*-(η^6-1,2-diphenylethene)$Cr(CO)_3$ in a 10% CO-doped methane matrix. Depletion of the parent bands and an increase in intensity of product bands and free CO are indicated.

4.4.2 Photochemistry of *cis*-(η^6-1,2-diphenylethene)$Cr(CO)_3$

4.4.2.1 Steady-state photolysis of *cis*-(η^6-1,2-diphenylethene)$Cr(CO)_3$ in argon purged cyclohexane

Steady-state photolysis of *cis*-(η^6-1,2-diphenylethene)$Cr(CO)_3$ in argon purged cyclohexane was carried out to investigate whether *cis* → *trans* isomerisation occurs under non-inert conditions. An argon purged solution of *cis*-(η^6-1,2-diphenylethene)$Cr(CO)_3$ in cyclohexane was placed in a quartz cuvette. The concentration of the solution was made such that the optical density (O.D) of the 263 nm absorption band was approximately 1 A.U. This sample was then irradiated at $\lambda >$ 400 nm at 60s intervals for a total of 360s (6 mins). The UV-Vis absorption spectrum was monitored between each interval to investigate any spectral changes taking place.

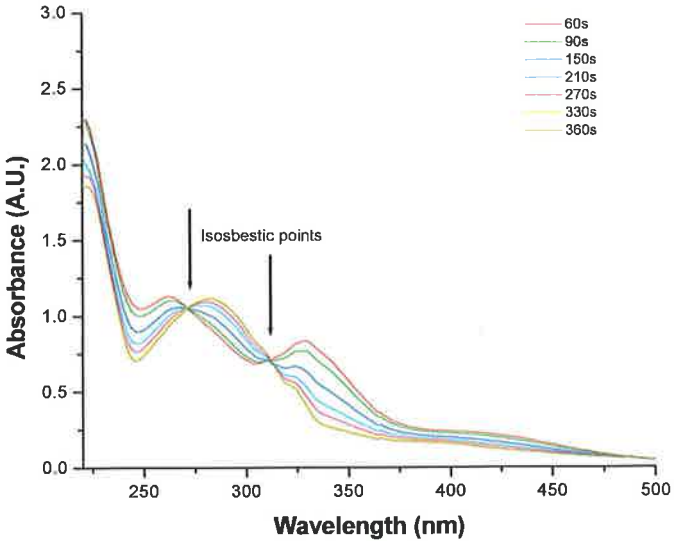

Figure 12 Spectral changes in UV-Vis spectrum of *cis*-(η^6-1,2-diphenylethene)$Cr(CO)_3$ following irradiation at > 400 nm in argon purged cyclohexane.

As is evident in Figure 12 on increasing the irradiation time from 60s to 360s at > 400 nm the parent bands due to *cis*-(η^6-1,2-diphenylethene)$Cr(CO)_3$ gradually decreased in intensity while a new absorption band was generated at 283 nm. This absorption band is not observed in the UV-Vis absorption spectrum of *cis*-(η^6-1,2-diphenylethene)$Cr(CO)_3$ but is indicative of *trans*-(η^6-1,2-diphenylethene)$Cr(CO)_3$. *Cis* → *trans* isomerisation is further suggested by the generation following irradiation

of two isosbestic points at 270 and 311 nm respectively. The band at 420 nm in *cis*-(η^6-1,2-diphenylethene)$Cr(CO)_3$ assigned to an MLCT based transition does however decrease in intensity during photolysis suggesting that some loss of the metal carbonyl may occur.

4.4.2.2 Steady-state photolysis of *cis*-(η^6-1,2-diphenylethene)$Cr(CO)_3$ in CO saturated cyclohexane

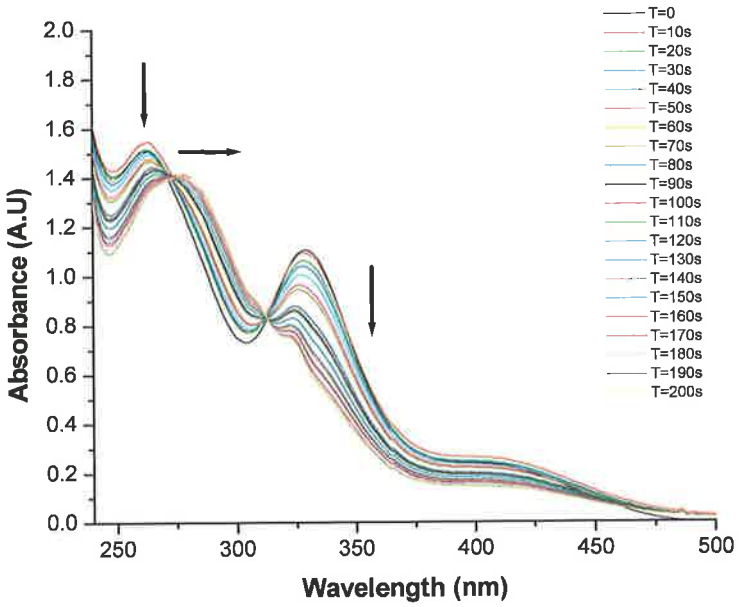

Figure 13 Spectral changes over time (200s) on irradiation of *cis*-(η^6-1,2-diphenylethene)$Cr(CO)_3$ in CO saturated cyclohexane at 10s intervals with $\lambda_{exc} > 400$ nm

A solution of *cis*-(η^6-1,2-diphenylethene)$Cr(CO)_3$ in spectrophotometric grade cyclohexane was made such that the O.D of the absorption band at 330 nm would be approximately 1.0 A.U. This solution was then saturated by bubbling through with pure CO gas for 10 mins. The initial UV-Vis absorption spectrum of *cis*-(η^6-1,2-diphenylethene)$Cr(CO)_3$ in a CO saturated cyclohexane solution indicates the typically observed absorption bands at 263, 330 and 422 nm. Irradiation of this solution at $\lambda_{exc} > 400$ nm results in loss of the 330 nm band an a red shift of that at 263 nm to 278 nm. This depletion and shift of the absorption bands in the presence of CO suggests isomerisation to form *trans*-(η^6-1,2-diphenylethene)$Cr(CO)_3$

4.4.2.3 Solid state photolysis

Solid state photolysis of *cis*-(η^6-1,2-diphenylethene)$Cr(CO)_3$ was carried out according to a method described by Natarajan et al.[20] with minor alterations. In a minimum volume of spectroscopic grade cyclohexane was dissolved a small amount of *cis*-(η^6-1,2-diphenylethene)$Cr(CO)_3$. This solution was then placed dropwise on a clean glass slide. Each successive drop was allowed dry before reapplication. This resulted in a thin film of the compound on the glass slide. This glass slide was then covered with another glass slide. The edges were then sealed with parafilm. This sample was then irradiated at 405 nm for 150 mins (2.5 hrs). Following irradiation the sample had become much paler in colour. The resulting pale yellow residue was then dissolved in cyclohexane and a UV-Vis absorption spectrum obtained. In Figure 14 the UV-Vis absorption spectrum of *cis*-(η^6-1,2-diphenylethene) $Cr(CO)_3$ in cyclohexane is compared with that of the pale yellow residue obtained following irradiation at 405 nm for 150 mins.

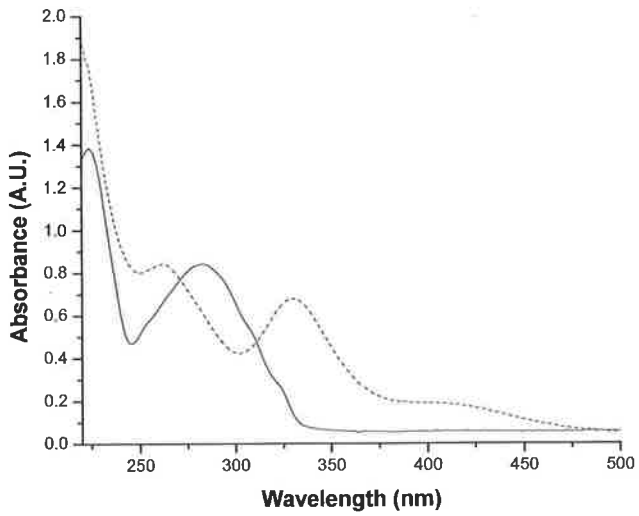

Figure 14 UV-Vis absorption spectrum of *cis*-(η^6-1,2-diphenylethene)$Cr(CO)_3$ in cyclohexane (----) and of residue following 405 nm irradiation for 150 mins (——)

This showed the generation of two absorption bands at 224 and 282 nm with loss of that at 420 nm. This suggests that although *cis* → *trans* isomerisation does occur forming *trans*-stilbene loss of the $Cr(CO)_3$ also occurs. This was further confirmed by comparison of the UV-Vis absorption spectrum of the residue following photolysis at

405 nm with that of the *trans*-stilbene ligand. Although this process appears to be predominantly photochemically driven, thermal effects may also be involved in loss of the $Cr(CO)_3$ moiety.

4.4.2.4 Time-Resolved Infrared Spectroscopy (TRIR)

Photolysis ($\lambda_{exc.}$ = 400 nm) of *cis*-(η^6-1,2-diphenylethene)Cr(CO)$_3$ in pentane solution at room temperature resulted in bleaching of the ground-state ν_{CO} bands at 1915 and 1980 cm^{-1} within the 2 ps rise time of the instrument (Figure 15). Three new bands were generated at 1891, 1961 and 1998 cm^{-1}. A fourth band was also evident at 1947 cm^{-1} but is partially masked by that at 1961 cm^{-1}. As is evident in Figure 15 the 1998 cm^{-1} band undergoes vibrational cooling between 7 and 10 ps, resulting in a shift to higher energy (2008 cm^{-1}).

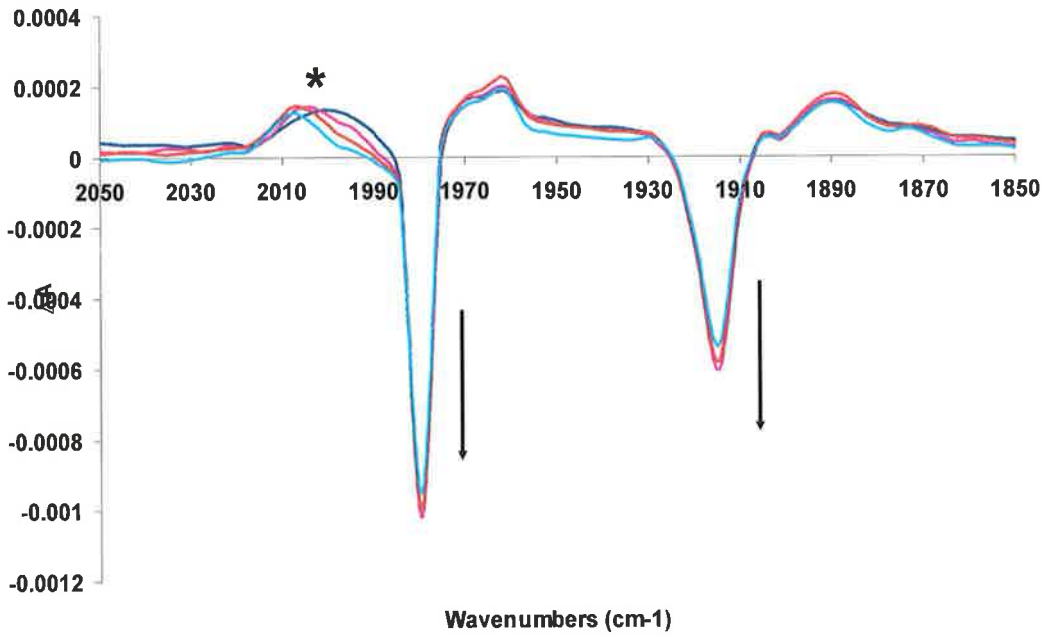

Figure 15 Difference time resolved infrared spectrum in pentane solution, following 3 ps (—), 5 ps (—), 7 ps (—) and 10 ps (—) indicating vibrational cooling of 1998 cm^{-1} band to 2008 cm^{-1}, indicated by *.

Subsequent to this the lower energy bands at 1891 and 1961 cm^{-1} decay over 100 ps with concomitant recovery of the parent bands and the production of two further ν_{co} bands at 1873 and 1924 cm^{-1}, corresponding to the CO-loss species *trans*-(η^6-1,2-diphenylethene)Cr(CO)$_2$ (Figure 16). This assignment is based on comparison with the bands observed at 1924 and 1873 cm^{-1} for the formation of this species in a 20 K methane matrix and with those previously observed by Creaven and co-workers[66] at

1927 and 1877 cm^{-1} for the formation of (η^6-benzene)$Cr(CO)_2$(solvent) in *n*-heptane solution at room temperature

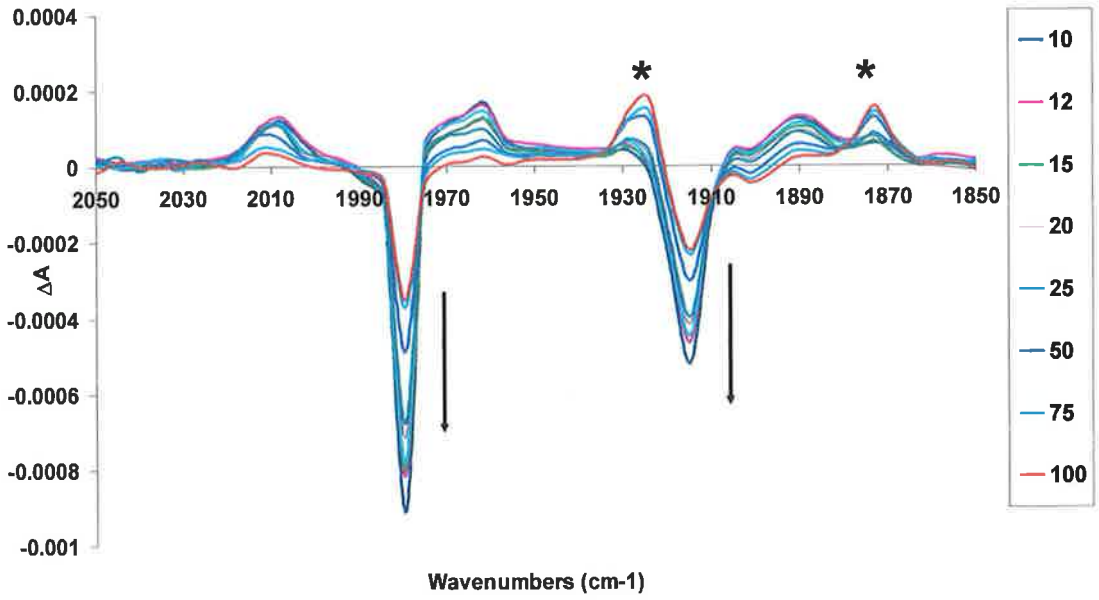

Figure 16 Difference time resolved infrared spectrum in pentane solution, following 10 ps (—), 12 ps (—), 15 ps, (—), 20 ps (—), 25 ps (—), 50 ps (—), 75 ps (—) and 100 ps (—) indicating decay of the excited state bands and recovery of the parent absorptions. Generation of the dicarbonyl species *cis*-(η^6-1,2-diphenylethene)$Cr(CO)_2$ with bands at 1873 and 1929 cm^{-1} is indicated by *.

The remaining excited state bands at 1947 and 2007 cm^{-1} begin to decay 50 ps after the initial pulse and have completely decayed to the ground state by 250 ps. Furthermore the parent bands recover approximately 60% of their initial depletion during formation of the dicarbonyl species, *cis*-(η^6-1,2-diphenylethene)$Cr(CO)_2$ over 100 ps.

4.4.2.5 Luminescence studies

Emission spectra were recorded in cyclohexane at room temperature. The emissive characteristics of *cis*- and *trans*-(η^6-1,2-diphenylethene)$Cr(CO)_3$ were compared to those of the free ligand using $\lambda_{exc.}$ = 332 nm. The general shape of the luminescence spectrum (Figure 17) is unaffected by complexation to the $Cr(CO)_3$ unit suggesting that the nature of the emissive state is similar for both free and complexed stilbenes. The luminescence intensity however, is significantly reduced upon complexation.

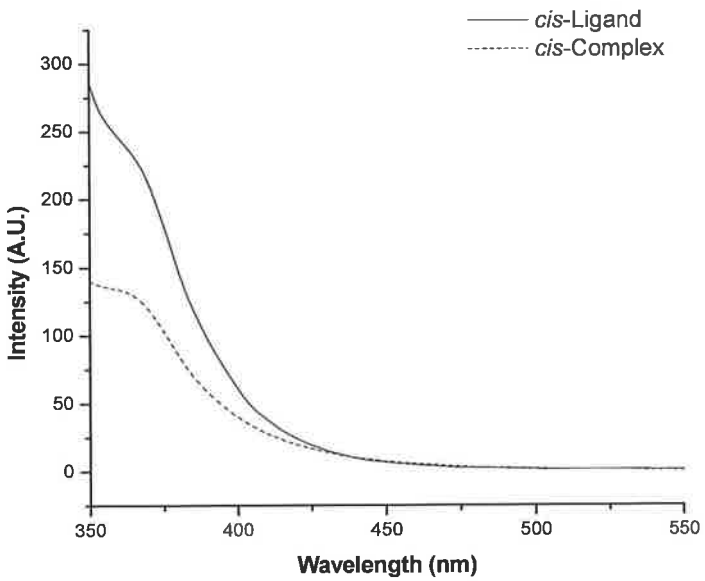

Figure 17 Emission spectra of *cis*-stilbene (——) and *cis*-(η^6-1,2-diphenylethene)$Cr(CO)_3$ (-----) in cyclohexane, following excitation at 332 nm (O.D = 0.2 A.U. at 332 nm)

Room temperature excited state lifetimes of either *cis*-(η^6-1,2-diphenylethene)$Cr(CO)_3$ or *trans*-(η^6-1,2-diphenylethene)$Cr(CO)_3$ could not be determined as they were too short lived using the available instrumentation.

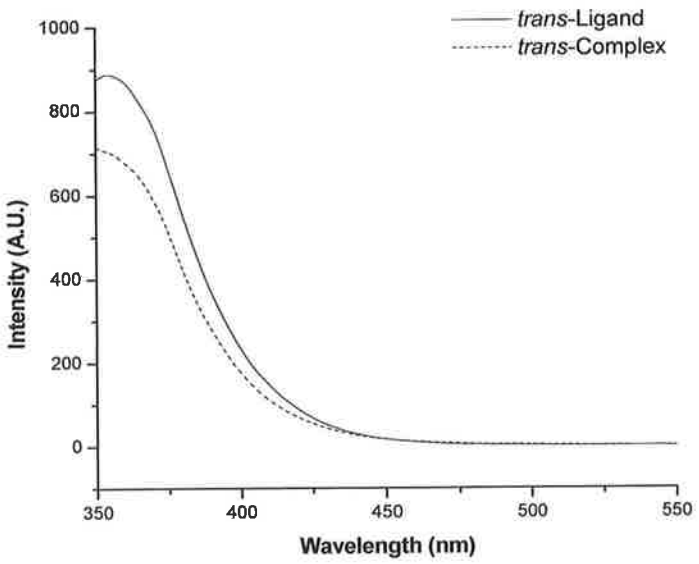

Figure 18 Emission spectra of *trans*-stilbene (——) and *trans*-(η^6-1,2-diphenylethene)$Cr(CO)_3$ (-----) in cyclohexane, following excitation at 332 nm (O.D = 0.2 A.U. at 332 nm)

Low temperature emission spectra of both *cis*-(η^6-1,2-diphenylethene)$Cr(CO)_3$ and *trans*-(η^6-1,2-diphenylethene)$Cr(CO)_3$ were recorded at 77 K in a 4:1 EtOH:MeOH glass. The overall profile and position of the emission spectra is the same, as observed at 298 K in cyclohexane solution.

4.4.3 Photochemistry of *trans*-(η^6-1,2-diphenylethene)Cr(CO)$_3$

4.4.3.1 Time Resolved Infrared (TRIR) spectroscopy

Photolysis ($\lambda_{exc.}$ = 400 nm) of *trans*-(η^6-1,2-diphenylethene)Cr(CO)$_3$ in pentane solution at room temperature resulted in bleaching of the ground-state ν_{CO} bands of (η^6-1,2-diphenylethene)Cr(CO)$_3$ at 1915 and 1980 cm^{-1} within the 2 ps rise time of the instrument. Three new bands were generated at 1891, 1961 and 2003 cm^{-1}. A fourth band was also evident at 1947 cm^{-1} but is partially masked by that at 1961 cm^{-1}. As is evident in Figure 19 the 2003 cm^{-1} band undergoes vibrational cooling between 7 and 10 ps, resulting a shift to higher energy (2012 cm^{-1}).

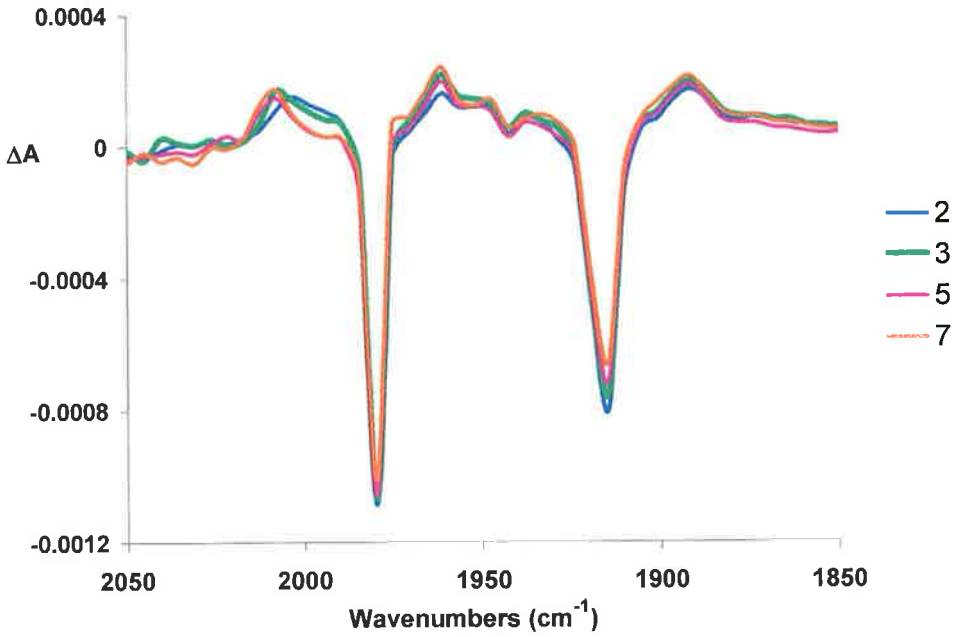

Figure 19 Difference time resolved infrared spectrum in pentane solution, following 3 ps (—), 5 ps (—), 7 ps (—) and 10 ps (—) indicating vibrational cooling of 2003 cm^{-1} band to 2012 cm^{-1}, indicated by *.

Subsequent to this the lower energy bands at 1891 and 1961 cm^{-1} decay over 100 ps with concomitant recovery of the parent bands and the production of two further ν_{co} bands at 1873 and 1929 cm^{-1}, corresponding to the CO-loss species *trans*-(η^6-1,2-diphenylethene)Cr(CO)$_2$ (Figure 20). This assignment is based on comparison with the bands observed at 1924 and 1873 cm^{-1} for the formation of this species in a 20 K methane matrix and with those previously observed by Creaven and co-workers[66] at

1927 and 1877 cm^{-1} for the formation of (η^6-benzene)$Cr(CO)_2$(solvent) in *n*-heptane solution at room temperature.

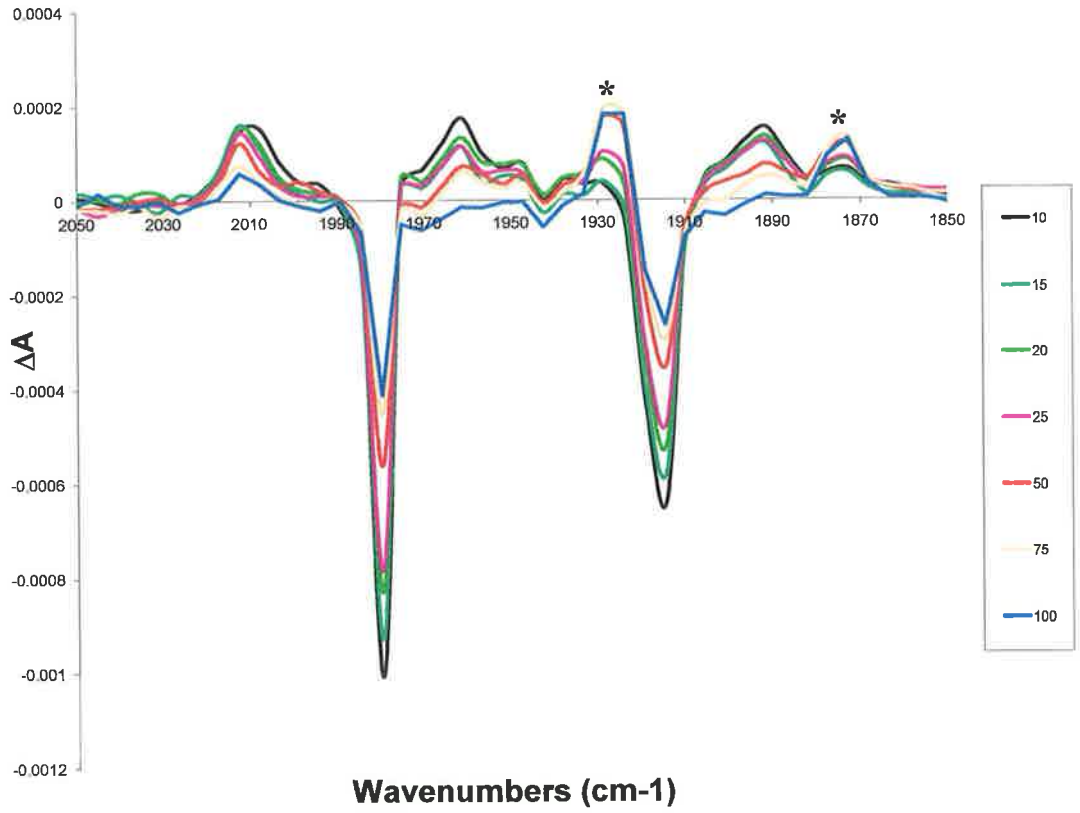

Figure 20 Difference time resolved infrared spectrum in pentane solution, following 10 ps (—), 15 ps (—), 20 ps (—), 25 ps (—), 50 ps (—), 75 ps ( ) and 100 ps (—) indicating decay of the excited state bands and recovery of the parent absorptions. Generation of the dicarbonyl species *trans*-(η^6-1,2-diphenylethene)$Cr(CO)_2$ with bands at 1873 and 1929 cm^{-1} is indicated by *.

The remaining excited state bands at 1947 and 2012 cm^{-1} begin to decay 50 ps after the initial pulse and have completely decayed to the ground state by 250 ps. Furthermore the parent bands recover approximately 60% of their initial depletion during formation of the dicarbonyl species, *trans*-(η^6-1,2-diphenylethene)$Cr(CO)_2$ over 100 ps.

4.4.4 Density Functional Theory (DFT) and Time-dependent DFT calculations

4.4.4.1 Geometry Optimisation

The structures of both *cis*- and *trans*-(η^6-1,2-diphenylethene)$Cr(CO)_3$ were optimised using the B3LYP/LANL2DZ level of theory. Geometry optimisation was initiated at the RHF/STO-3G theory level with the size of the basis set increased incrementally to LANL2DZ followed by further optimisation with this basis set and B3LYP model chemistry.

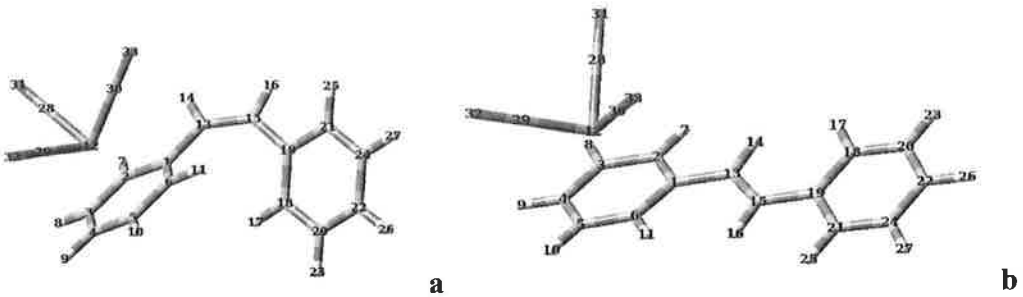

a b

Figure 21 Geometry optimised structures of (a) *cis*-(η^6-1,2-diphenylethene)$Cr(CO)_3$ and (b) *trans*-(η^6-1,2-diphenylethene)$Cr(CO)_3$ attained using the B3LYP/LANL2DZ level of theory

The calculated bond lengths (Å) and bond angles (°) for the geometry optimised structures of **(a)** *cis*-(η^6-1,2-diphenylethene)$Cr(CO)_3$ and **(b)** *trans*-(η^6-1,2-diphenylethene) $Cr(CO)_3$ shown in Figure 21 are outlined in Table 1. For each compound the geometrical parameters following geometry optimisation at the B3LYP/LANL2DZ level of theory is compared with X-ray crystallography results[65,67] of *trans*-(η^6-1,2-diphenylethene)$Cr(CO)_3$ and theoretical[68,69] values for the uncoordinated *cis*-stilbene ligand.

	cis-(η^6-1,2-diphenylethene) $Cr(CO)_3$	*trans*-(η^6-1,2-diphenylethene) $Cr(CO)_3$	X-ray[a] (e.s.d's)	Literature [68,69,43]	[b]Deviation %
Bond lengths					
C1-C13	1.477	1.467	1.479 (4)	1.467	0.68, 0.81
C13-C15	1.360	1.359	1.299 (4)	1.351	0.66, 4.61
C15-C19	1.481	1.471	1.481 (4)	1.467	0.95, 0.67
C1-Cr12	2.358	2.367	2.243 (2)	-	-
C2-Cr12	2.307	2.320	2.219 (3)	-	-
C3-Cr12	2.313	2.316	2.201 (3)	-	-
C4-Cr12	2.314	2.313	2.206 (19)	-	-
C5-Cr12	2.308	2.310	2.196 (3)	-	-
C6-Cr12	2.301	2.306	2.216 (19)	-	-
Cr12-C28	1.832	1.832	1.838 (3)	1.84	0.43, 0.32
Cr12-C29	1.830	1.829	1.843 (3)	1.84	0.54, 0.76
Cr12-C30	1.832	1.832	1.852 (3)	1.84	0.43, 1.07
C28-O31	1.188	1.188	1.151 (3)	1.14	4.21, 3.21
C29-O31	1.188	1.188	1.153 (3)	1.14	4.21, 3.03
C30-O33	1.187	1.187	1.145 (3)	1.14	4.1, 3.66
Bond angles					
C2-C1-C6	117.69	117.38	118.6 (2)	118.0	0.28 ,1.03
C1-C6-C5	121.08	121.24	119.8 (2)	120.8	0.23, 1.20
C4-C5-C6	120.10	120.21	120.5 (2)	120.5	0.33, 0.24
C3-C4-C5	119.69	119.48	119.2 (2)	119.4	0.24, 0.23
C2-C3-C4	119.87	119.99	121.0 (3)	120.1	0.19, 0.83
C1-C2-C3	121.41	121.59	120.8 (3)	121.2	0.17, 0.65
C1-Cr12-	93.57	92.99	88.60 (10)	-	4.95
C1-Cr12-	156.92	156.35	146.95 (11)	-	6.39
C1-Cr12-	113.07	113.74	110.57 (11)	-	2.86
C2-Cr12-	121.43	120.56	123.61(11)	-	2.46
C2-Cr12-	148.77	149.60	159.68 (11)	-	6.31
C2-Cr12-	89.85	90.27	94.17 (11)	-	4.14
C3-Cr12-	157.17	156.23	146.72 (11)	-	6.48
C3-Cr12-	112.81	113.74	123.49 (12)	-	7.89
C3-Cr12-	93.42	92.97	87.91 (11)	-	5.75
C4-Cr12-	149.08	149.76	161.67 (9)	-	7.36
C4-Cr12-	89.43	89.82	93.74 (10)	-	4.18
C4-Cr12-	121.21	120.30	124.91 (11)	-	3.69
C5-Cr12-	113.11	113.74	109.62 (10)	-	3.75
C5-Cr12-	93.26	93.08	87.71 (11)	-	6.12
C5-Cr12-	156.97	156.14	146.47 (11)	-	6.60
C6-Cr12-	89.72	89.91	94.87 (9)	-	5.22
C6-Cr12-	121.24	120.62	110.24 (10)	-	9.41
C6-Cr12-	148.99	149.65	160.17 (10)	-	6.56

Table 1 Comparison of selected bond lengths (Å) and bond angles (°) for *cis*-(η^6-1,2-diphenylethene)$Cr(CO)_3$ and *trans*-(η^6-1,2-diphenylethene)$Cr(CO)_3$ with X-ray crystallography results and literature values for the *cis*- and *trans*-stilbene ligands.[a] Crystallography results are for *trans*-(η^6-1,2-diphenylethene)$Cr(CO)_3$ only.[b]For *cis*-isomer % deviation is deviation from *cis*-stilbene ligand[68,69].For *trans*-isomer % deviation is from x-ray data[67].

Following geometry optimisation of the above structures a vibrational analysis of the ground state electronic structure was undertaken. The frequency calculation was carried out on the B3LYP/LANL2DZ optimised structures to investigate whether any negative frequencies were present, which would indicate that the geometry optimised structure was not a minimum on the potential energy surface. Both *cis*-(η^6-1,2-diphenylethene)$Cr(CO)_3$ and *trans*-(η^6-1,2-diphenylethene)$Cr(CO)_3$ are of the type $LM(CO)_3$, where L = 1,2-diphenylethene, and are predicted to have C_{3v} local geometry. C_{3v} complexes of this type are predicted to have 2 IR active carbonyl bands – A_1 and E. In Table 2 the predicted IR active bands of both complexes optimised at the B3LYP/LANL2DZ level of theory are compared to the experimental values obtained in this study. The calculated IR stretching frequencies are scaled with respect to the experimental values obtained.

IR active bands (Calculated)		**IR active bands (Experimental) (Cyclohexane)**		**Assignment**
cis	*trans*	*cis*	*trans*	
1976	1974	1981	1981	C≡O symmetric stretch (A_1 mode)
1917	1916[a]	1916	1916	C≡O asymmetric stretch (E mode)
1915	1914			

Table 2 The experimental and calculated ν_{CO} values for *cis*-(η^6-1,2-diphenylethene)$Cr(CO)_3$ and *trans*-(η^6-1,2-diphenylethene)$Cr(CO)_3$ based on an optimized geometry at B3LYP/LANL2DZ Model Chemistry. The calculated values have been corrected by an empirical factor of 1.021. [a]Splitting of the E vibrational mode is observed in the theoretical model for both the *cis*- and *trans*-isomer.

4.4.4.2 Calculation of the ground state electronic structure for *cis*-(η^6-1,2-diphenylethene)$Cr(CO)_3$ and *trans*-(η^6-1,2-diphenylethene)$Cr(CO)_3$

Following the ground state geometry optimisations of both *cis*-(η^6-1,2-diphenylethene)$Cr(CO)_3$ and *trans*-(η^6-1,2-diphenylethene)$Cr(CO)_3$ at the B3LYP/LANL2DZ level of theory the ground state electronic structures for each complex was calculated and the highest occupied (HOMO) and lowest virtual (LUMO) molecular orbitals were examined in order to provide a framework for the subsequent Time dependent DFT (TDDFT) excited state calculations. For each complex the frontier orbitals are plotted according to their energies. Such frontier orbitals are very important in that they play an active role in the determination of the electronic excitations and electronic character of the particular complex. The assignment of the type of molecular orbital was made on the basis of its relative composition and by inspection of the three dimensional representation. In each case the compositional assignment is relative in that the majority are of mixed character with a particular MO giving the major compositional contribution. Table 3 lists the most important molecular orbitals for both *cis*-(η^6-1,2-diphenylethene)$Cr(CO)_3$ and *trans*-(η^6-1,2-diphenylethene)$Cr(CO)_3$. Six occupied MO's and seven unoccupied or virtual MO's.

MO	*cis*-(η^6-1,2-diphenylethene)$Cr(CO)_3$	*trans*-(η^6-1,2-diphenylethene)$Cr(CO)_3$
L+8	0.25	0.27
L+7	0.22	0.22
L+6	-0.36	-0.35
L+5	-0.61	-0.57
L+4	-0.75	-0.72
L+3	-0.77	-0.75
L+2	-0.85	-0.79
L+1	-1.45	-1.45
LUMO	-2.17	-2.30
HOMO	-5.83	-5.78
H-1	-5.94	-5.93
H-2	-6.21	-6.21
H-3	-6.76	-6.65
H-4	-7.37	-7.32

Table 3 The molecular orbitals of *cis*-(η^6-1,2-diphenylethene)$Cr(CO)_3$ and *trans*-(η^6-1,2-diphenylethene)$Cr(CO)_3$ and their energies (eV). HOMO: Highest occupies molecular orbital. LUMO: Lowest unoccupied molecular orbital.H-1 is HOMO-1 and L+1 is LUMO+1

MO no.	Assignment	Energy (eV)	Cr %	CO %	CO %	CO %	*cis*-(1,2-diphenylethene %
85	L+8	0.25	30	27	36	3	4
84	L+7	0.22	22	27	3	33	15
83	L+6	-0.36	42	16	16	22	3
82	L+5	-0.61	17	6	2	5	70
81	L+4	-0.75	42	15	13	8	22
80	L+3	-0.77	43	9	15	13	19
79	L+2	-0.85	3	1	1	4	92
78	L+1	-1.45	4	4	6	0	86
77	LUMO	-2.17	5	1	1	3	90
76	HOMO	-5.83	56	6	5	14	20
75	H-1	-5.94	61	11	12	3	12
74	H-2	-6.21	72	9	8	9	2
73	H-3	-6.76	7	0	1	1	91
72	H-4	-7.37	0	0	0	0	100

Table 4 The contribution of chromium, each of the three CO orbitals and the *cis*-(η^6-1,2-diphenylethene orbitals in *cis*-(η^6-1,2-diphenylethene)$Cr(CO)_3$ for each of the selected molecular orbitals

MO no.	Assignment	Energy (eV)	Cr %	CO %	CO %	CO %	*trans*-(1,2-diphenylethene %
85	L+8	0.27	28	20	32	18	2
84	L+7	0.22	44	28	9	14	4
83	L+6	-0.35	42	18	16	21	3
82	L+5	-0.57	3	0	2	3	93
81	L+4	-0.72	32	9	7	12	41
80	L+3	-0.75	45	16	14	12	14
79	L+2	-0.79	24	5	10	6	56
78	L+1	-1.45	4	6	3	1	86
77	LUMO	-2.30	5	1	1	3	90
76	HOMO	-5.78	52	5	5	13	25
75	H-1	-5.93	61	11	12	13	12
74	H-2	-6.21	72	9	8	9	2
73	H-3	-6.65	11	1	1	2	85
72	H-4	-7.32	0	0	0	0	100

Table 5 The contribution of chromium, each of the three CO orbitals and the *trans*-(η^6-1,2-diphenylethene orbitals in *trans*-(η^6-1,2-diphenylethene)$Cr(CO)_3$ for each of the selected molecular orbitals

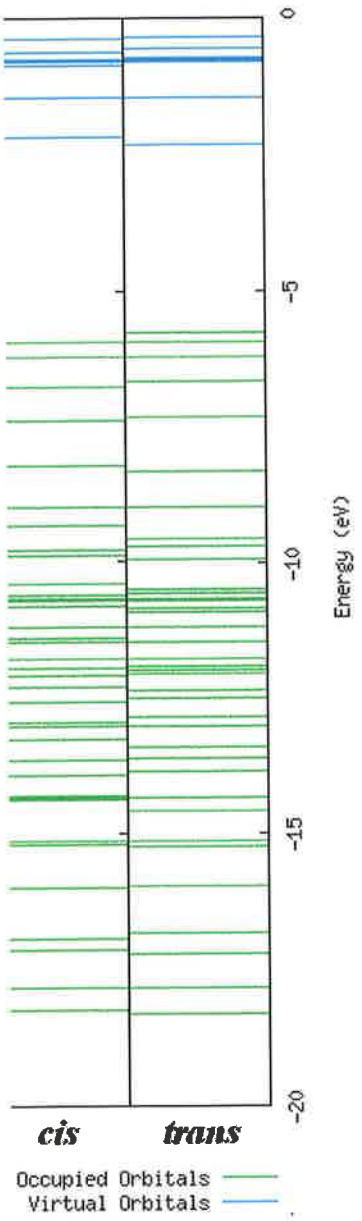

Figure 22 Energy level diagram of *cis*-(η^6-1,2-diphenylethene)$Cr(CO)_3$ and *trans*-(η^6-1,2-diphenylethene)$Cr(CO)_3$. Extracted from Density of States (DOS) diagram generated by the GaussSum 2.0 programme[63].

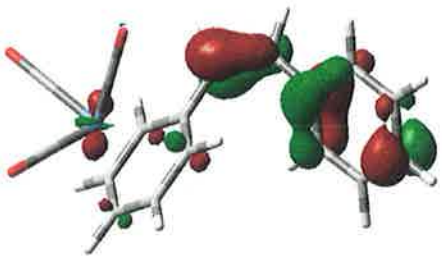

73 (O) – HOMO-3

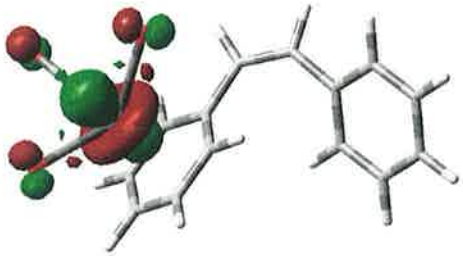

74 (O) – HOMO-2

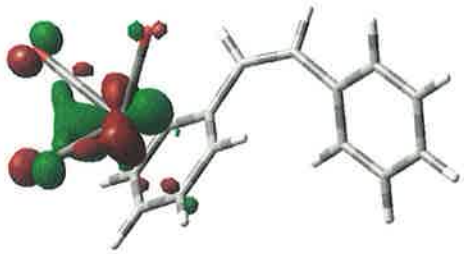

75 (O) – HOMO-1

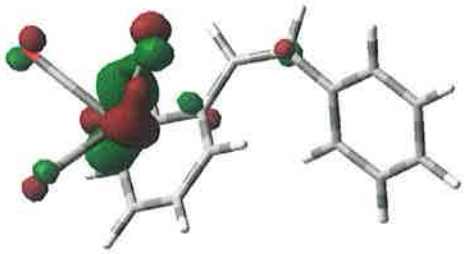

76 (O) – HOMO

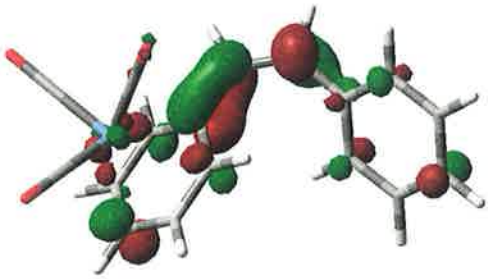

77 (V) – LUMO

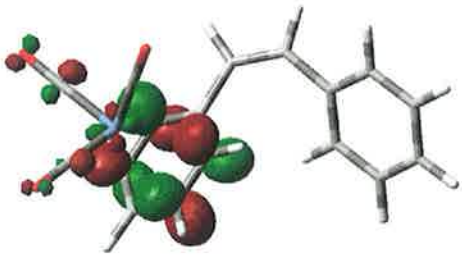

78 (V) – LUMO+1

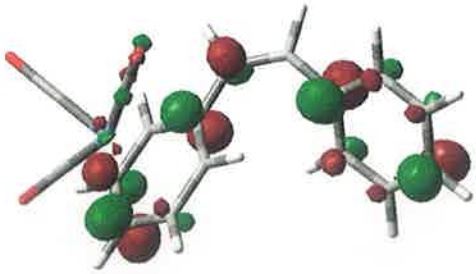

79 (V) – LUMO+2

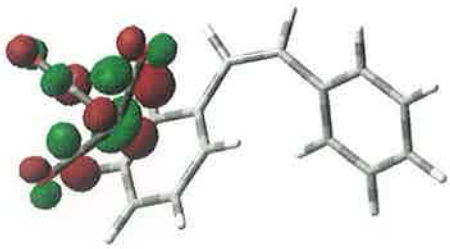

83 (V) – LUMO+6

Figure 23 Selected molecular orbitals of *cis*-(η^6-1,2-diphenylethene)$Cr(CO)_3$

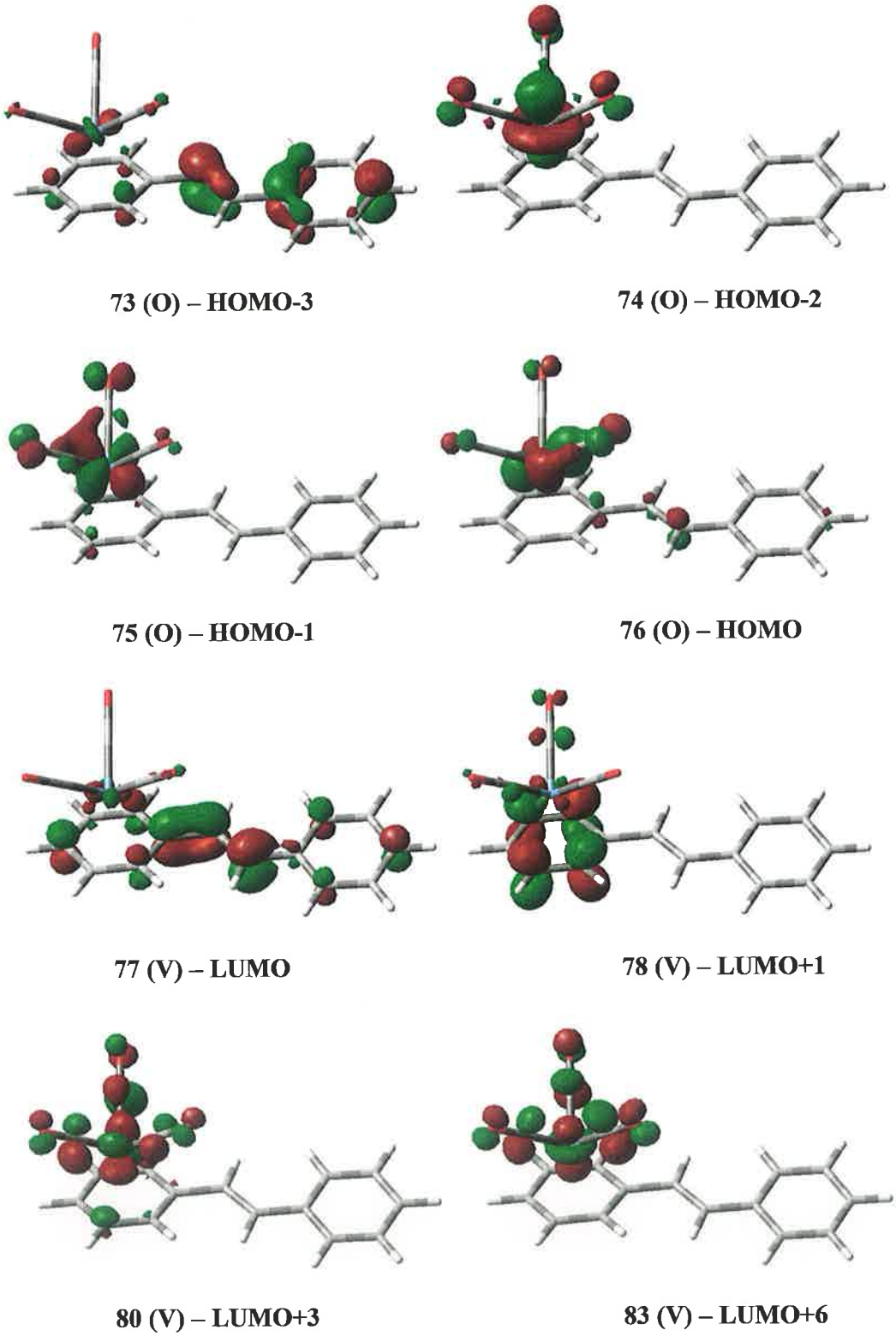

Figure 24 Selected molecular orbitals of *trans*-(η^6-1,2-diphenylethene)$Cr(CO)_3$

4.4.4.3 Time –dependent Density Functional Theory (TDDFT) calculations

State	E (eV) [λ (nm)[a]]	f [b]	$\psi_o \rightarrow \psi_v$ [c]	Character [d]
1	2.8431 (436.09)	0.0045	H-1 → LUMO (89%)	d_{xy}, CO → L, C=C bond
2	2.9641 (418.29)	0.0802	H-1 → L+1 (11%) HOMO → LUMO (68%)	d_{xy}, CO → L d_{xy} → L, C=C bond
3	3.0732 (403.44)	0.0032	H-2 → LUMO (84%)	d_z^2, CO → L, C=C bond
12	3.8748 (319.98)	0.2846	H-1 → L+1 (52%)	d_{xy}, CO → L
13	3.9802 (311.51)	0.0271	HOMO → L+6 (75%)	d_{xy} → d_z^2, 3 x π* CO
14	4.0398 (306.91)	0.0233	H-1 → L+6 (71%)	d_{xy}, CO → d_z^2, 3 x π* CO
15	4.0833 (303.64)	0.0882	H-3 → LUMO (63%) HOMO → L+2 (13%)	L, d_z^2 → L, C=C bond d_{xy} → L

Table 6 Selected calculated singlet excited states for *cis*-(η^6-1,2-diphenylethene)Cr(CO)$_3$

State	E (eV) [λ (nm)[a]]	f [b]	$\psi_o \rightarrow \psi_v$ [c]	Character [d]
2	2.85 (435.03)	0.1304	HOMO → LUMO (70%)	d_{xy}, CO → L, C=C bond
8	3.4304 (361.43)	0.0124	H-2 → L+3 (32%) H-2 → L+4 (12%)	d_z^2, CO → d_{xz}, 3 x π* CO d_z^2, CO → d_{yz}, 3 x π* CO, L
12	3.8192 (324.63)	0.4422	H-3 → LUMO (19%) H-1 → L+1 (46%)	L, d_z^2 → L, C=C bond d_{xy}, CO → L
13	3.9597 (313.11)	0.042	HOMO → L+6 (66%)	d_{xy}, CO → d_z^2, 3 x π* CO
14	4.0283 (307.78)	0.0916	H-3 → LUMO (19%) H-1 → L+6 (44%) HOMO → L+6 (14%)	L, d_z^2 → L, C=C bond d_{xy}, CO → d_z^2, 3 x π* CO d_{xy}, CO → d_z^2, 3 x π* CO
15	4.0531 (305.90)	0.1254	H-3 → LUMO (32%) H-1 → L+1 (10%) H-1 → L+6 (31%)	L, d_z^2 → L, C=C bond d_{xy}, CO → L d_{xy}, CO → d_z^2, 3 x π* CO

Table 7 Selected calculated singlet excited states for *trans*-(η^6-1,2-diphenylethene)Cr(CO)$_3$

[a]Energy of vertical excitation from ground state, [b] Oscillator strength, [c] Occupied to unoccupied (virtual) orbital excitation, [d] Character of excited state

4.4.5 Electrochemistry of *cis*- and *trans*- (η^6-1,2-diphenylethene)$Cr(CO)_3$

Electrochemical studies were carried out on *cis*- and *trans*-(η^6-1,2-diphenylethene)$Cr(CO)_3$ in a 0.1 M $TBAPF_6$/acetonitrile electrolyte solution with a Teflon shrouded platinum working electrode, a platinum wire counter electrode and a non-aqueous Ag/Ag^+ reference electrode. The filling solution for the non-aqueous Ag/Ag^+ reference electrode was 0.1 M $TBAPF_6$ and 0.1 mM $AgNO_3$ in anhydrous acetonitrile. All potentials are quoted in volts vs. Ag/Ag^+ reference electrode with respect to the Fc^+/Fc redox pair. Scan rate was 100 mV S^{-1} unless otherwise stated. E_{ap} corresponds to an irreversible anodic process. [c] E_{cp} corresponds to an reversible cathodic process.[d] $E_{½}$ corresponds to a reversible electrode process, it is assumed that $E_{½} \approx E^{o'}$. The half-wave potential $E_{½} = (E_{ap} + E_{cp})/2$ and $\Delta E_p = E_{ap} - E_{cp}$. . Table 8 indicates the electrochemical data obtained for the complexes in this study

Table 8 Electrochemical properties at room temperature

Complex	E_{ap} or $E_{½}$ (V) [ΔE_p (mV)]	E_{cp} or $E_{½}$ (V) [ΔE_p (mV)]
cis- (η^6-1,2-diphenylethene)$Cr(CO)_3$	0.331, 0.498, 1.387	-0.022, -0.361
trans- (η^6-1,2-diphenylethene)$Cr(CO)_3$	0.395, 0.604 , 1.466	-0.300 (86), -0.353

Electrochemical monitoring of the solution of either *cis*- (η^6-1,2-diphenylethene) $Cr(CO)_3$ or *trans*- (η^6-1,2-diphenylethene)$Cr(CO)_3$ in pentane following successive oxidation and reduction cycles did not suggest any electrochemically induced isomerisation process. However, some deposition of both isomers, most likely due to decomposition, onto the platinum electrode surface was observed

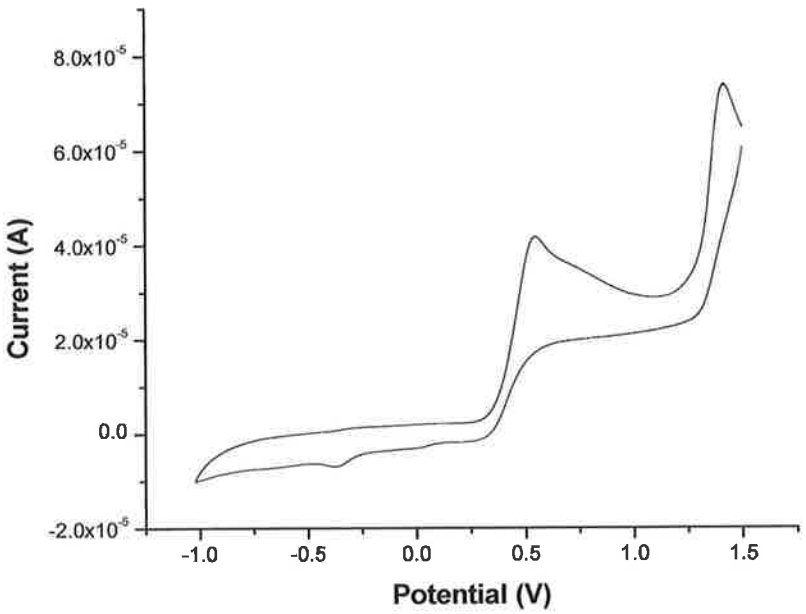

Figure 25 Cyclic voltamagramm of *cis*-(η^6-1,2-diphenylethene)$Cr(CO)_3$ dissolved in dry Acetonitrile containing 0.1 M TBAPF6. The working electrode was a 1 mm diameter platinum electrode and the scan rate was 0.1 Vs^{-1}.

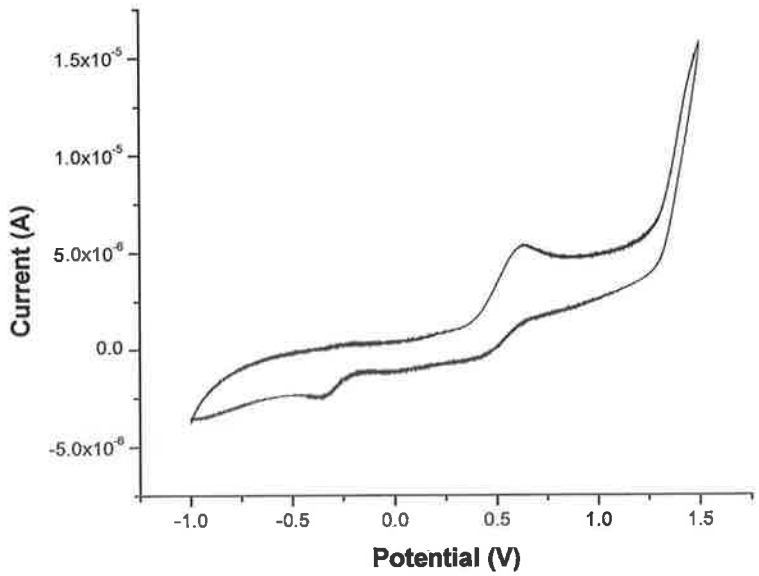

Figure 26 Cyclic voltamagramm of *trans*-(η^6-1,2-diphenylethene)$Cr(CO)_3$ dissolved in dry Acetonitrile containing 0.1 M TBAPF6. The working electrode was a 1 mm diameter platinum electrode and the scan rate was 0.1 Vs^{-1}.

4.5 Discussion

4.5.1 Photochemistry

Irradiation of *cis*-(η^6-1,2-diphenylethene)$Cr(CO)_3$ in a methane matrix for 80 mins at 405 mn resulted in the generation of two strong absorption bands at 295 and 445 nm.

These spectroscopic changes in the UV-vis spectrum, presented in Figure 7 suggest formation of the *trans* isomer, *trans*-(η^6-1,2-diphenylethene)$Cr(CO)_3$. Under these conditions the only changes observed in the IR spectrum were a slight reduction in intensity of the ν_{CO} vibrations, with no evidence for the formation of product bands.

Following irradiation of the methane matrix for 60 mins with $\lambda_{exc.}$ = 313 nm, the parent bands at 1978 and 1911 cm^{-1} decreased in intensity, with the formation of ν_{CO} bands at 2139, 1924 and 1873 cm^{-1}. The weak feature at 2139 cm^{-1} is assigned to free CO in the matrix, and the remaining bands at 1924 and 1873 cm^{-1} are assigned to (η^6-1,2-diphenylethene)$Cr(CO)_2$. These results suggest that, irradiation with $\lambda_{exc.}$ = 405 nm results in isomerisation, yielding *trans*-(η^6-1,2-diphenylethene)$Cr(CO)_3$. This photoproduct then undergoes CO loss on higher energy irradiation to yield *trans*-(η^6-1,2-diphenylethene)$Cr(CO)_2$.

Similarly, irradiation of *cis*-(η^6-1,2-diphenylethene)$Cr(CO)_3$ at 313 nm for 110 mins in a N_2 matrix resulted in bleaching of the parent absorption bands and generation of the N_2 coordinated dicarbonyl species *cis*-(η^6-1,2-diphenylethene)$Cr(CO)_2N_2$. Subsequent lower energy irradiation at 405 nm for 300 mins resulted in minor changes in the IR spectrum. However, as both isomeric forms of the stilbene system have identical carbonyl bands the changes observed in photoinduced isomerisation are based on differences in the UV-Vis spectra. The electronic difference spectrum (Figure 10) indicates generation of a new absorption band at 285 nm, which is indicative of formation of *trans*-(η^6-1,2-diphenylethene)$Cr(CO)_3$.

Similarly, in steady state-photolysis studies of *cis*-(η^6-1,2-diphenylethene)$Cr(CO)_3$ in either argon or CO purged cyclohexane, irradiation with $\lambda_{exc} > 400$ nm resulted in bleaching and eventual loss of the electronic absorption band at 330 nm with concomitant generation of a band at approximately 280 nm, indicative of the

formation of *trans*-(η^6-1,2-diphenylethene)$Cr(CO)_3$. However, extended irradiation at > 400 nm was observed to also result in a decrease in intensity of the low energy MLCT band at 420 nm, suggesting that prolonged irradiation may result in thermally induced labilisation of the $Cr(CO)_3$ moiety resulting in formation of the *trans*-stilbene ligand. Initial irradiation of *cis*-(η^6-1,2-diphenylethene)$Cr(CO)_3$ in argon or CO purged cyclohexane solution at λ_{exc} > 400 nm in 30-60s cycles, was however observed to result in the rapid loss of the $Cr(CO)_3$ moiety and formation of the *cis*-stilbene ligand, based on comparison with an authentic UV-Vis absorption spectrum of the *cis*-stilbene ligand in cyclohexane solution. *cis*-(η^6-1,2-diphenylethene)$Cr(CO)_3$ was also irradiated in the solid state at 405 nm using a method similar to that described by Natarajan et al[20]. However, although *cis-trans* isomerisation did occur loss of the $Cr(CO)_3$ moiety was also observed. This is similar to observations made by Natarajan et al.[20], who observed photoinduced *cis-trans* isomerisation of both *cis*-1-styrylfluoranthene and *cis*-1-styrylpyrene in the solid state.

4.5.2 Time-resolved infrared (TRIR) studies

It is clear from the difference TRIR spectra shown in Figure 19 and Figure 20 that following 400 nm laser pulse excitation two excited states are formed with concomitant bleaching of the ground state absorptions. One of the excited states is higher in energy than the ground state, with bands at 1947 and 2003 cm^{-1}. The other set of bands is lower in energy with bands at 1891 and 1961 cm^{-1}. Within 7 ps after the laser pulse narrowing of the 2003 cm^{-1} band and a shift to higher energy, 2012 cm^{-1}, occurs. This is indicative of vibrational cooling and compares favourably with observations made by Vlček and co-workers[34,36] in a number of metal carbonyl systems. This is followed by gradual decay of the two bands at 1891 and 1961 cm^{-1} at a rate of 2×10^6 s^{-1} with concomitant growth of bands at 1873 and 1929 cm^{-1} ascribed to the CO loss product *trans*-(η^6-1,2-diphenylethene)$Cr(CO)_2$ and recovery of the parent absorptions. This suggests that dicarbonyl formation is preceded by decay of the lower energy excited state. Following 50 ps the higher energy excited state with bands at 1947 and 2012 cm^{-1} also begins to decay to the ground state, with complete loss evident by 250 ps. Decay of this excited state does not appear to result in CO labilisation and may decay non-radiatively or may be involved in the isomerisation process. Similarly, irradiation of the *cis*-isomer produced new bands at 1891, 1961 and 1998 cm^{-1} A fourth very weak band is also evident at ~ 1950 cm^{-1}, which is significantly overlapped by the band at 1961 cm^{-1}. The band at 1998 cm^{-1} undergoes vibrational cooling within the initial 7-10 ps resulting in a shift to 2008 cm^{-1}. Again this appears to be followed by decay of the lower energy excited state bands and generation of product bands assigned to the dicarbonyl species, *cis*-(η^6-1,2-diphenylethene) $Cr(CO)_2$. Studies were also undertaken with monitoring in the vinylic region to investigate whether isomerisation was involved in these excited state processes and whether it preceded CO loss. However, due to the very weak intensity of the C=C bonds no spectral changes in this region could be observed.

4.5.3 DFT and TDDFT calculations

4.5.3.1 Geometry optimisation of *cis*- and *trans*-(η^6-1,2-diphenylethene)$Cr(CO)_3$

A comparison of the bond lengths of both *cis*- and *trans*-(η^6-1,2-diphenylethene)$Cr(CO)_3$ and the uncomplexed ligands shows that complexation has little effect on bond length. In both cases the C=C olefinic bond length, calculated from the B3LYP/LANL2DZ geometry optimised models is in good agreement with those observed for both *cis* or *trans*-stilbene by Chen et al[69]. and Kertesz[68]. *cis*-(η^6-1,2-diphenylethene)$Cr(CO)_3$ is predicted to have a C=C bond length of 1.360 Å, compared to 1.351 Å for the uncomplexed ligand, giving a % deviation of 0.66. Similarly, the *trans*-isomer of the complex is predicted to have a C=C bond length of 1.359 Å which is similar to the value of 1.350 Å, also having a % deviation of 0.66. However, when the predicted value for *trans*-(η^6-1,2-diphenylethene)$Cr(CO)_3$ (1.359 Å) is compared to that obtained experimentally in X-ray crystallographic studies[65,67] (1.299 Å) a difference of 0.06 Å corresponding to a 1.41 % deviation is observed. This difference between experimentally observed C=C bond length and predicted bond length has been previously observed by both Kertesz[68] and Chen[69] in styrene and stilbene systems and may be due either a packing effect on the solid crystal or dynamic disorder in the crystal at room temperature. The remaining predicted ligand bond lengths are very similar to those previously predicted and experimentally observed for the *cis*-and *trans*-stilbene ligands. However, analysis in both isomers of the $Cr(CO)_3$ moiety shows a marked disparity between the C-Cr and C≡O bond lengths predicted in this study and those observed experimentally for *trans*-(η^6-1,2-diphenylethene)$Cr(CO)_3$, and the values in the literature for the uncomplexed ligands. The C-Cr bonds between the coordinated phenyl ring and the central chromium atom are predicted to be in the range 2.30-2.31 Å, compared to experimentally observed values of 2.19-2.20 Å. Similarly, the predicted C≡O bond length for *trans*-(η^6-1,2-diphenylethene)$Cr(CO)_3$ is 1.18 Å, while the value observed experimentally in X-ray crystallographic studies for that isomer is 1.15 Å. Again a marked difference of 0.03 Å is observed. However, overestimation of predicted metal carbonyl bond lengths in DFT studies using LANL2DZ model chemistry has been previously observed[70]. In general the predicted ground state geometries are consistent with those derived from the single crystal X-ray diffraction studies.[65]

Examination of the geometry optimised model of *cis*-(η^6-1,2-diphenylethene)$Cr(CO)_3$ shows distortion from planarity to avoid steric hindrance from the phenyl rings. Analysis of the B3LYP/LANL2DZ geometry optimised model indicates a dihedral angle of the coordinated phenyl ring from the plane of about 34 °. This is somewhat less than the value of 50.5 ° observed by Chen et al[69]. for the *cis*-stilbene ligand but very similar to the value of 33.8 ° for this angle observed with B3LYP/6-31++G** theory by Kertesz et al[68]. However, literature values of τ for *cis*-stilbene generally in the range 42-45 ° in both theoretical and experimental studies[69,70,71]. Nevertheless, as previously observed, this distortion from planarity does not appear to significantly alter the bond lengths of the *cis*-stilbene ligand. This is consistent with previous observations.

Conversely, in this study *trans*-(η^6-1,2-diphenylethene)$Cr(CO)_3$ was found to have a dihedral angle (τ) of 11.4 ° indicating the near-planar geometry of the *trans*-stilbene complex. However, many studies have shown near-planarity in the *trans*-stilbene ligand with experimental and theoretical values ranging from 3.6[72] and 5.2[73] to 27.2°[71]. In contrast, gas-phase electron diffraction studies have shown that the two phenyl rings are distorted from planarity by approximately 32 °. In general, there appears to be little agreement in the level of distortion from planarity in *trans*-stilbene. This inconsistency is probably as a result of the three possible symmetries this compound may possess – C_{2h}, C_2 and C_i. Various groups have assigned one of these particular geometries to their *trans*-stilbene model during geometry optimisation using varying theoretical techniques and have come up with a variety of results. In studies employing MM3, B3LYP/6-31G, B3LYP/6031G** methods *trans*-stilbene was found to be a planar molecule while in other studies employing HF/6-31G, HF/6-31G** and MP2/6-31G** the molecule is non-planar possessing a dihedral angle (τ) of up to 20°[69]. However, as observed in the *cis*-isomer loss of planarity does not seem to have any profound effect on bond lengths of the *trans*-stilbene ligand.

4.5.3.2 The molecular orbitals of *cis*- and *trans*-(η^6-1,2-diphenylethene)$Cr(CO)_3$

As is evident from Table 4 and Table 5 and Figure 23 and Figure 24 the valence orbitals of both *cis*- and *trans*-(η^6-1,2-diphenylethene)$Cr(CO)_3$ are composed of a mixture of metal centred, CO centred and ligand centred molecular orbitals, with the majority centred on the d orbitals of the chromium metal centre and the π CO ligand orbitals. In the case of *cis*-(η^6-1,2-diphenylethene)$Cr(CO)_3$, the exceptions to this general observation are the HOMO-3, LUMO, LUMO+1 and LUMO+2 molecular orbitals, while similarly for the *trans*-isomer the same molecular orbitals are the exceptions, with the exclusion of the LUMO+2 orbital, which does not appear to be heavily involved in the excited state photochemistry of the *trans*-isomer. In the case of these molecular orbitals the electron density is centred on either the Cr coordinated phenyl ring or the olefinic C=C bond. The H-3 molecular orbital is, in both isomers, centred on the vinylic double bond and the uncoordinated phenyl ring of the stilbene system (91 % and 85 % for *cis* and *trans*, respectively), with minor contributions from the chromium d_z^2 orbital (7 % and 11 % for *cis* and *trans*, respectively). Energetically the H-3 MO of the *cis*-isomer is lower at -6.65 eV compared to -6.76 eV for the *trans*-isomer. In both isomers the LUMO's are identical in their percentage composition , both being centred (90 %) on the π orbitals of the phenyl rings and the C-C bonds of the central bridge between the two phenyl rings, which are π-antibonding with respect to one another. There are also minor contributions in the MO from the Cr-d_{xz} orbital (5 %). Similarly, in both isomers the L+1 molecular orbitals is centred on the $Cr(CO)_3$ coordinated phenyl ring (86 %) with the remaining 14 % centred on two of the π* orbitals of the CO ligands (12 %) and the Cr-d_{xz} orbital (4 %). The remaining CO ligand is entirely non-bonding in this molecular orbital and would thus be expected to be labilised on irradiation. In both isomers the L+1 MO is energetically identical at -1.45 eV. The L+2 molecular orbital, which also contains significant ligand contributions to its composition is also involved in the excited state of the *cis*-isomer but not in that of the *trans*-isomer. In L+2 the electron density is spread across the length of the stilbene ligand (92 %) with minor contributions from the metal d orbitals (3 %) and the CO ligands (6 %). In both isomers, the HOMO is centred on the metal centre, at 56 % for the *cis*-isomer and 52 % for the *trans*-isomer. However, large contributions from the 3 π* CO ligands are also present, at 25 % and 23 % for the *cis*- and *trans*-isomer, respectively.

4.5.3.3 The correlation of TDDFT results with the photochemistry of *cis*- and *trans*-(η^6-1,2-diphenylethene)$Cr(CO)_3$

Time dependent Density Functional Theory (TDDFT) studies were carried out to determine the 20 lowest lying singlet excited states of *cis*- and *trans*-(η^6-1,2-diphenylethene)$Cr(CO)_3$. The lowest eight singlet excited states occur in the region 300-380 nm and thus it is transitions into these excited states that lead to the UV-Vis spectra of *cis*- and *trans*-(η^6-1,2-diphenylethene)$Cr(CO)_3$ as shown in Figure 6, Figure 27, and Figure 28. Although the 20 lowest lying singlet excited states have been determined for both isomers, only those excited states which are responsible for the observed electronic absorption spectrum, due to their high oscillator strengths will be discussed. For *cis*-(η^6-1,2-diphenylethene)$Cr(CO)_3$ these excited states are 1, 2, 3, 12, 13, 14, 15 and for *trans*-(η^6-1,2-diphenylethene)$Cr(CO)_3$ these excited states are 1, 2, 8, 12, 13, 14, 15. As shown in Table 9 and Table 10 each of these excited states involves a transition which is predominantly metal-to-ligand charge transfer in character, involving charge transfer from the chromium metal centre to either the CO or stilbene ligand. However, as a result of mixing of MO character a certain amount of LFCT, LBCT and LMCT is also observed.

Excited State	Calculated Bands (nm)	Excited State Properties	Photoproduct Produced
1	436.09	MLCT, LBCT, LFCT	CO loss, rotation about C=C bond
2	418.29	MLCT, LBCT, LFCT	CO loss, rotation about C=C bond
3	403.44	MLCT, LBCT, LFCT	CO loss, rotation about C=C bond
12	319.98	MLCT, LBCT	CO loss
13	311.51	MLCT, LBCT, LFCT	$Cr(CO)_3$ dissociation
14	306.91	LFCT, MLCT	$Cr(CO)_3$ dissociation
15	303.64	LBCT, MLCT	CO loss, rotation about C=C bond

Table 9 The calculated low energy UV absorption bands of *cis*-(η^6-1,2-diphenylethene)$Cr(CO)_3$, their excited state properties and the predicted photoproducts produced on irradiation into these bands

The lowest lying excited state of *cis*-(η^6-1,2-diphenylethene)$Cr(CO)_3$ is located at 436.09 nm and is predominantly metal-to-ligand charge transfer in nature involving transfer of electron density from the H-1 molecular orbital, centred on the Cr-d_{xy} (61 %) and the two of the π^* CO ligands (25 %) and the coordinated phenyl ring (12 %) to the LUMO, a molecular orbital centred on the stilbene ligand, most notably on the π^* orbitals of the vinylic C=C bond. Similarly, both the 2nd and 3rd lowest lying

excited states of the *cis*-isomer involve transfer of electron density from molecular orbitals which are centred on the Cr metal centre and the π-Cr orbitals to the LUMO, which is centred on the olefinic C=C bond of the stilbene ligand (90 %) and to a much lesser extent the Cr metal centre (5 %) and the carbonyl ligands (5 %). The transition occurring at 418.29 nm, which is predominantly HOMO → LUMO in character, is the main transition responsible for the absorption band at approximately 420 nm in the observed electronic absorption spectrum. Overall, irradiation into these MLCT bands would have the result of populating the LUMO, which in turn would result in transfer of electron density to the π*C=C bond and the metal centre. To combat this anti-bonding π orbital a near 180 ° rotation about the vinylic C=C bond is observed resulting in formation of *trans*-(η^6-1,2-diphenylethene)$Cr(CO)_3$.

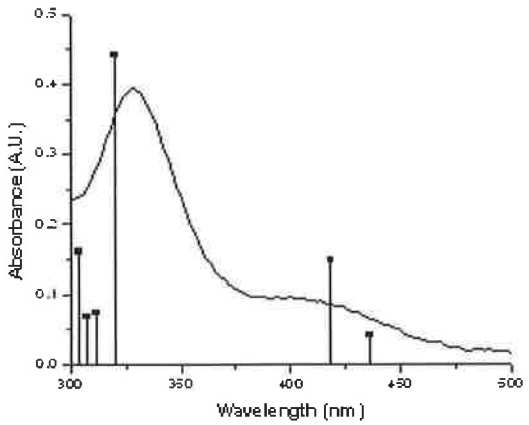

Figure 27 The position of the selected lowest lying excited state (vertical lines) relative to the experimental UV-Vis absorption spectrum of *cis*-(η^6-1,2-diphenylethene)$Cr(CO)_3$.

The higher energy band, with a λ_{max} of 330 nm, observed for *cis*-(η^6-1,2-diphenylethene) $Cr(CO)_3$ in cyclohexane is due to a number of transitions between 285 and 320 nm, although that occurring at 320 nm appears to be the excited state predominantly responsible for this electronic transition. This excited state occurring at 320 nm is MLCT in nature and involves transfer of electron density from the H-1 orbital, which is centred on the Cr-d_{xy} (61 %) and three CO ligands (26 %) to the L+1 molecular orbital, which is strongly bonding with respect to the Cr-CO interaction to the phenyl ring bearing the $Cr(CO)_3$ unit (86 %), the Cr-d_{xy} orbital (4 %) and two of the π* CO ligand orbitals (10 %). The remaining CO ligand is non-bonding with respect to the metal centre in this molecular orbital. Irradiation would thus be

expected to labilize the Cr to CO interaction. The excited states occurring at 311.51 and 306.91 nm involve charge transfer from the HOMO and H-1 molecular orbitals respectively, both of which are strongly metal centred, to the L+6 virtual orbital. This transition involves transfer of electron density from a MO centred on the metal (56 % for HOMO and 61 % for H-1), with minor contributions in both cases from the CO ligands, to L+6, a molecular orbital centred on the Cr-d_z^2 orbital (42 %) and the three π^* CO ligand orbitals (54 %). In the L+6 molecular orbital, the stilbene ligand is almost non- bonding (only 3 %) with respect to the metal centre and may thus be expected to be labilised on extended irradiation.

Excited State	Calculated Bands (nm)	Excited State Properties	Photoproduct Produced
1	455.04	MLCT, LBCT, LFCT	CO loss, rotation about C=C bond
2	435.03	MLCT, LBCT	CO loss, rotation about C=C bond
8	361.43	MLCT, LBCT	CO loss
12	324.63	MLCT, LBCT, LFCT	CO loss
13	313.11	MLCT, LFCT	$Cr(CO)_3$ dissociation
14	307.78	LFCT, MLCT	$Cr(CO)_3$ dissociation
15	305.90	LBCT, MLCT	CO loss, rotation about C=C bond

Table 10 The calculated low energy UV absorption bands of *trans*-(η^6-1,2-diphenylethene)$Cr(CO)_3$, their excited state properties and the predicted photoproducts produced on irradiation into these bands

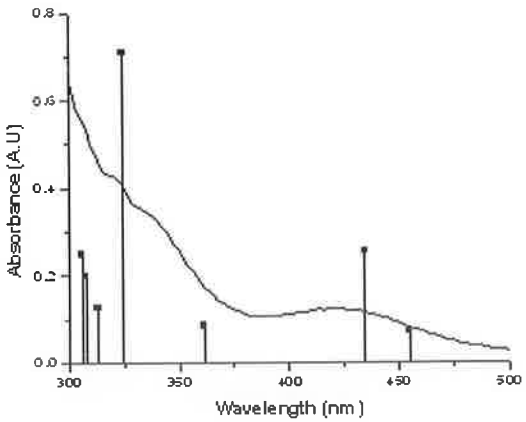

Figure 28 The position of the selected lowest lying excited state (vertical lines) relative to the experimental UV-Vis absorption spectrum of *trans*-(η^6-1,2-diphenylethene)$Cr(CO)_3$.

Similarly, the photochemistry of the *trans*-isomer, *trans*-(η^6-1,2-diphenylethene) $Cr(CO)_3$, is dominated by the same transitions involving population of the same molecular orbitals. The lowest lying singlet excited state occurs at 455.04 nm and involves a H-1 → LUMO charge transfer transition. This transition entails transfer of electron density from a molecular orbital (H-1), which is strongly Cr-d_{xy} (61 %) and CO ligand (35 %) in character to a virtual molecular orbital (LUMO) which is strongly ligand based (90 %), especially in the area of the C=C olefinic bond, which is anti-bonding in nature. To overcome this, a rotation about the C=C bond must occur, which should theoretically result in *trans* → *cis* isomerisation. Similarly, the 2nd lowest lying excited state, which is principally responsible for the electronic transition at 425 nm involves population of the LUMO via the HOMO, which like the H-1 orbital previously mentioned is also Cr metal and CO ligand based. Again population of the LUMO would be expected to result in rotation about the C=C bond to give the *cis*-isomer of the complex. Although isomerisation following population of the LUMO is observed on irradiation of the *cis*-isomer, this may be hindered in the *trans*-isomer by an energy barrier as suggested in ps-TR[3] studies of *cis*-stilbene by Matousek et al.[27] Another singlet excited state occurring at 361.43 nm involves a H-2 → L+3 charge transfer transition. This transition entails charge transfer from the Cr-d_z^2 orbital (72 %) and the CO ligand orbitals (26 %) to the L+3 orbital, which is centred on the Cr-d_{xz} orbital (45 %) and the three π^* CO ligand orbitals (42 %) as well as minor contributions from the coordinated phenyl ring of the stilbene ligand (14 %). This transition involves charge transfer from a metal centred and CO based molecular orbital to another Cr and CO based molecular orbital. As a result no labilisation would be expected to occur on irradiation.

As observed for *cis*-(η^6-1,2-diphenylethene)$Cr(CO)_3$, the high energy band observed at approximately 300 nm in the electronic absorption spectrum is a result of a number of excited states, although the excited state at 324 nm is the principal contributor to this transition band. This excited state is H-1 → L+1 in character and thus involves transfer of electron density from a molecular orbital centred on the Cr-d_{xy} (61 %) and CO ligands (35 %) to L+1, an unoccupied molecular orbital, which is strongly bonding with respect to the Cr-CO interaction to the phenyl ring bearing the $Cr(CO)_3$ unit (86 %) and also possesses strong contributions from the metal centre (4 %) and

two of the π* CO ligand orbitals (10 %), while in the remaining CO ligands is non-bonding with respect to the Cr centre. Such a transition would be expected to labilize the Cr to CO interaction, resulting in dissociative loss of CO. The next two higher energy singlet excited states, at 3.9597 eV and 4.0283 eV, both involve population of the L+6 virtual orbital from a metal centred occupied orbital (HOMO or H-1). This involves charge transfer to an orbital centred on the Cr-d_z^2 orbital (42 %) and π* CO ligand orbitals (54 %) with no apparent bonding interactions with the stilbene ligand. Thus irradiation of these MLCT, LFCT bands would be expected to result in Cr-C bond cleavage and subsequent loss of the stilbene ligand. The final highest energy transition, which will be discussed involves population of the LUMO from the H-3 molecular orbital. This transition requires transfer of electron density from a molecular orbital centred on the stilbene ligand (85 %), especially on the olefinic C=C bond which is bonding in nature and to a lesser extent the Cr-d_z^2 orbital (11 %) to an another ligand based molecular orbital (90 %), which is anti-bonding with respect to the C=C bond. As a result irradiation of this ligand based charge transfer transition should result in rotation about the C=C bond to yield the *cis*-isomer.

Experimentally, irradiation of *cis*-(η^6-1,2-diphenylethene)$Cr(CO)_3$ at 405 nm or greater should result in direct excitation of the 418 nm MLCT band resulting in population of the LUMO. Direct excitation of the MLCT bands in this region are expected to result in isomerisation about the olefinic C=C bond resulting in formation of *trans*-(η^6-1,2-diphenylethene)$Cr(CO)_3$. Furthermore, an analysis of the excited state MO structures suggests that CO loss may also occur as a minor photoproduct on irradiation at this wavelength. Irradiation at 313 nm results in excitation of the H-1 → L+1 transition, which will result in CO labilisation following charge transfer (MLCT) from the metal centre to a carbonyl group.

4.5.4 Electrochemistry

An analysis of the electrochemistry of both *cis*- and *trans*-(η^6-1,2-diphenylethene) $Cr(CO)_3$ indicates the presence of a number of apparently irreversible oxidation and reduction steps. For *cis*-(η^6-1,2-diphenylethene)$Cr(CO)_3$ a strong irreversible oxidation potential is observed at 1.38 V vs. Ag/Ag^+, while in the case of *cis*-(η^6-1,2-diphenylethene) $Cr(CO)_3$ this is present at 1.46 V vs. Ag/Ag^+. However, this may, in both cases, be due to oxidation of the surface of the Pt electrode on oxidation at high potentials. A second strong irreversible oxidation is observed at 0.49 V vs. Ag/Ag^+ in the case of *cis*-(η^6-1,2-diphenylethene)$Cr(CO)_3$, while in *trans*-(η^6-1,2-1,2-diphenylethene) $Cr(CO)_3$ this is observed at the more positive potential of 0.60 V vs. Ag/Ag^+. In both cases, this irreversible one-electron oxidation is assigned to oxidation of the Cr(0) metal centre to yield a highly reactive $17e^-$ radical species, with subsequent decomposition. This irreversible oxidation of (arene)$M(CO)_3$ systems has been previously been observed by a number of authors[55,74,75]. The values obtained in this study are similar to those obtained by Vasil'kov[55] for fluoranthene$Cr(CO)_3$ systems, where irreversible oxidations were observed at 0.82 and 0.85 V vs. SCE. Similarly, Antonini et al.[74] observed a one electron irreversible molybdenum centred oxidation from +0.91 to +0.9 6 V vs. SCE for a number of (arene)$Mo(CO)_3$ systems. However, in contrast Yeung et al[75]. have observed a 1 electron reversible oxidation process for $(C_6H_6)Cr(CO)_3$ in a Bu_4NPF_6/CH_2Cl_2 solution 0.98 V vs. Ag/AgCl. In this study a quasi-reversible reduction process was observed for *trans*-(η^6-1,2-diphenylethene) $Cr(CO)_3$ at 0.30 V vs. Ag/Ag^+ (ΔE_p = 86 mV). This may also be present in the the *cis*-isomer as a reductive potential was observed at -0.36 V vs. Ag/Ag^+, with the corresponding positive potential too weak to be observed. For both tricarbonyl complexs, cyclic voltammetry studies suggest the occurrence of a poorly reversible process involving formation of an unstable radical or cationic species, possibly $[(\eta^6$- 1,2-diphenylethene)$Cr(CO)_3]^+$, which is subsequently reduced to regenerate the starting material or decomposes. However, Dessy et al.[76] have suggested that bi-electronic reduction may induce formation of the highly reactive dianion species, which will result in decomposition and loss of the product.

4.6 Conclusion

Both matrix isolation studies in a number of frozen matrixes and steady-state photolysis studies under both CO and argon atmospheres indicate that *cis*-(η^6-1,2-diphenylethene)$Cr(CO)_3$ undergoes photoisomerisation to the *trans* isomer following the absorption of low energy photons (λ_{exc} > 400 nm). Theoretical calculations using TDDFT indicate this occurs as a result of population of the antibonding C=C centred LUMO. UV-Vis data obtained during matrix isolation studies suggests that CO-occurs only from the *trans* complex, *trans*-(η^6-1,2-diphenylethene)$Cr(CO)_3$. The CO-loss photoproduct was observed following high-energy photolysis at λ_{exc} = 313 nm of *cis*-(η^6-1,2-diphenylethene) $Cr(CO)_3$. TDDFT studies indicate that higher energy irradiation leads to population of an MLCT state localised on the coordinated phenyl ring, which results in labilisation of CO. ps-TRIR studies indicate that this dicarbonyl species, *trans*-(η^6-1,2-diphenylethene)$Cr(CO)_2$ is formed following decay of an excited state species with bands at 1891 and 1961 cm^{-1}. Similarly, irradiation of the *cis*-complex at 400 nm produces four bands attributed to two excited state processes. Depletion of the lower energy excited state bands at 1891 and 1961 cm^{-1} results in CO loss yielding the dicarbonyl *cis*-(η^6-1,2-diphenylethene)$Cr(CO)_2$ with bands at 1873 and 1923 cm^{-1}. Overall TRIR studies suggests that irradiation of either the *cis*- or *trans*-complex produces two excited state species. One of these undergoes vibrational cooling within the first 7-10 ps and another set decays over 100 ps with concomitant growth of the dicarbonyl bands. Electrochemical analysis of both the *cis*- and *trans*-isomer indicates a number of apparently irreversible processes taking place. In both cases the irreversible reduction of the Cr metal centre is observed, subsequently leading to decomposition. Furthermore, there is evidence to suggest that in solution a bi-anionic species may also be formed, which also results in the decomposition of the complex.

4.7 Bibliography

1 W. Gartner, *Angew. Chem. Int. Ed.* **2001**, 40, 2977.

2 G. Pattenden, In *Light, chemical change and life: A source book in Photochemistry*, J.D. Coyle, R.R. Hill, D.R. Roberts, 1st Ed.; The Open University Press, **1982**, 5.1, 167

3 F.D. Lewis, In *Advances in Photochemistry*, D.H. Volman, K. Gollnick, G.S. Hammond, John Wiley and Sons Inc., New York, **1986**, 13, 165-235

4 T. Miyazawa, S.Y. Koshihara, Y. Segawa, M. Kira, *Chem. Lett.*, **1995**, 24, 3, 217

5 F.D. Lewis, T.L. Kurth, R.S. Kalgutkar, *J. Chem. Soc. Chem. Commun.*,**2001**, 1372-1373

6 A.E. Clark, *J. Phys. Chem. A*, **2006**, 110, 3790-3796

7 C.-S. Tsai, J.-K. Wang, R.T. Skodje, J.-C. Lin, *J. Am. Chem. Soc.*; **2005**, 127, 10788-10789

8 Y. Imamoto, T. Kuroda, M. Kataoka, S. Shevyakov, G. Krishnamoorthy, R.S.H. Liu, *Angew. Chem. Int. Ed.***2003**, 42, 3630-3633

9 W. Fuß, C. Kosmidis, W.E. Schmid, S.A. Trushin, *Angew. Chem. Int. Ed.* **2004**, 43, 4178-4182

10 (a) R.S.H. Liu, A.E. Asato, *Proc. Natl. Acad. Sci. USA* **1985**, 82, 259-263 (b) R.S.H. Liu, D.T. Browne, *Acc. Chem. Res.* **1986**, 19, 42-48

11 A.M. Müller, S. Lochbrunner, W.E. Schmid, W. Fuß, *Angew. Chem. Int. Ed.* **1998**, 37, 505-507

12 G. Krishnamoorthy, A.E. Asato, R.S.H. Liu, *Chem. Commun.*, **2003**, 2170-2171

13 G. Krishnamoorthy, S. Schieffer, S. Shevyakov, A.E. Asato, K. Wong, J. Head, R.S.H. Liu, *Res. Chem. Interm.*, **2004**, 30, 397-405

14 L.-Y. Yang, R.S.H. Liu, K.J. Boarman, N.L. Wendt, J. Liu, *J. Am. Chem. Soc.*, **2005**, 127, 2404-2405

15 Y. Kuriyama, H. Takeya, S. Oishi, M. Kojima, *Chem. Lett.*, **1998**, 843

16 N. Strashnikova, V. Papper, P. Parkhomyuk, G. I. Likhtenshtein, V. Ratner, R. Marks, *J. Photochem. Photobil. A.*, **1999**, 122, 133

17 W.M. Horspool, In *Photochemistry*, A. Gilbert, N.S. Allen, A. Cox, I. Dunkin, A. Harriman, A.C. Pratt, The Royal Society of Chemistry, Cambridge, **2000**, 31, 112-140

18 M.D. Cohen, *Angew. Chem., Int. Ed. Engl.*, **1795**, 14, 386

19 J. Harada, K. Ogawa, *J. Am. Chem. Soc.*, **2001**, 123, 10884-10888

20 A. Natarajan, J.T. Mague, K. Venkatesan, T. Arai, V. Ramamurthy, *J. Org. Chem.*, **2006**, 71, 1055-1059

21 C.M.L. Vande Velde, F. Blockhuys, C. Van Alsenoy, A.T.H. Lenstra, H.J. Geise, *J. Chem. Soc., Perkin Trans. 2*, **2002**, 1345-1351

22 W.M. Horspool, In *Photochemistry*, I. Dunkin, N.S. Allen, A. Gilbert, The Royal Society of Chemistry, Cambridge, **2003**, 34, 69-110

23 R. Ozawa, H. Hamaguchi, *Chem. Lett.*, **2001**, 736

24 H. Görner, *Phys. Chem. Chem. Phys.*, **2002**, 4, 482

25 R.E. Martin, J. Bartek, F. Diederich, R.R Tykwinski, E.C. Mesiter, A. Hilger, H.P. Lüthi, *J. Chem. Soc., Perkin Trans. 2*, **1998**, 233-241

26 M. J. Cox, F.F. Crim, *J. Phys. Chem. A*, **2005**, 109, 11673-11678

27 P. Matousek, G. Gaborel, A.W. Parker, D. Phillips, G.D. Scholes, W.T. Toner, M. Towrie, Rutherford Appleton Laboratory, *CLF Annual Report* **1996/1997**, 126-127

28 P. Matousek, A.W. Parker, D. Phillips, G.D. Scholes, W.T. Toner, M. Towrie, *Chem. Phys. Lett.*, **1997**, 278, 56-62

29 I.K. Lednev, T.-Q. Ye, P. Matousek, M. Towrie, S. Umpathy, R.E. Hester, J.N. Moore, Rutherford Appleton Laboratory, *CLF Annual Report* **1996/1997**, 124-125

30 H. Görner, H.J. Kuhn, in *Advances in Photochemistry*, ed D.C. Neckers, D.H. Volman, G. von Bünau, John Wiley & Sons, New York, **1995**, Vol 19, P1

31 J.D. Lewis, R.N. Perutz, J.N. Moore, *Chem. Commun.*, **2000**, 1865-1866

32 A.S. Polo, M. K. Itokazu, K.M. Frin, A.O. de Toledo Patrocínio, N.Y. Murakami-Iha, *Coord. Chem. Rev.*, **2006**, 250, 1669-1680

33 D.M. Dattelbaum, M.K. Itokazu, N.Y. Murakami Iha, T.J. Meyer, J. Phys. Chem. A, 2003, 107, 4092-4095

34 M. Busby, P. Matousek, M. Towrie, A. Vlček Jr., *Inorg. Chim. Acta*, **2007**, 360, 885-896

35 V.W.-W. Yam, V.C.-Y. Lau, L.-X. Wu, *J. Chem. Soc. Dalton Trans.*, **1998**, 1461

36 M. Busby, P. Matousek, M.Towrie, A. Vlček Jr., *J. Phys. Chem. A*, **2005**, 1009, 3000-3008

37 S.-S. Sun, A.J. Lees, *Organometallics*, **2002**, 21, 39-49

38 J. Bossert, C. Daniel., *Chem. Eur. J.*, **2006**, 12, 4835-4843

39 (a) C.J. Breheny, J.M. Kelly, C.Long, S.O'Keeffe, M.T. Pryce, G.Russell, M. M. Walsh; *Organometallics*, **1998**, 17, 3690-3695 (b) C.J Breheny, S.M Draper, F.-W. Grevels, W.E Klotzbücher, C. Long, M.T Pryce, G Russell, *Organometallics*, **1996**, 15, 3679-3687, (c) B.S Creaven, M.W George, A.G Ginsburg, C Hughes, J.M. Kelly, C. Long, I.M. McGrath, M.T. Pryce,. *Organometallics*, **1993**, 12, 3127.

40 M.S. Wrighton, J.L. Haverty, *Z. Naturforsch.* B, **1975**, B30, 254-258

41 W. Strohmeier, D. von Hobe, *Z. Naturforsch.* B, **1963**, 18, 11, 981-982

42 W. Strohmeier, H. Hellmann, *Chem. Ber.*, **1963**, 96, 2859-2866

43 J.A.S. Howell, N.F. Ashford, D.T. Dixon, J.C. Kola, T.A. Albright, S.K. Kang, *Organometallics*, **1991**, 10, 1852-1864

44 T.A. Albright, P. Hofmann, R. Hoffmann, C.P. Lillya, P.A. Dobosh, *J. Am. Chem. Soc.*, **1983**, 105, 3396-3411

45 R.U. Kirss, P.M. Treichel, Jr., *J. Am. Chem. Soc.*, **1986**, 108, 853-855

46 C.H. Bamford, K. G. Al-Lamee, C.J. Konstantinov, *J. Chem. Soc. Faraday Trans I*, **1977**, 73, 1406-1419

47 C.G. Kreiter, R. Eckert, W. Frank, G.J. Reiß, *Inorg. Chim. Acta*, **1996**, 251, 95-100

48 P.A. Hamley, M.K. Kuimova, A.J. Blake, C. Highes, S.B.L. Lyons, M. Poliakoff, A.H. Wright, M.W. George, *J. Chem. Soc. Dalton Trans.*, **2003**, 1545-1550

49 A.J. Rest, J.R. Sodeau, D.J. Taylor, *J. Chem. Soc. Dalton Trans.*, **1978**, 651

50 P.E. Bloyce, R.H. Hooker, A.J. Rest, T.E. Bitterwolf, N.J. Fitzpatrick, J.E. Shade, *J. Chem. Soc., Dalton Trans.*, **1990**, 833-841

51 R.H. Hooker, A.J. Rest, J. Chem. Soc., Dalton Trans., 1982, 2029

52 O.G. Mischenko, S.V. Klement'eva, S.V. Maslennikov, A.N. Artemov, I.V. Spirinia, *Zh. Obshch. Khim.*, **2006**, 76, 12, 1996-1999

53 R.W. McCabe, S.P. Saberi, *Inorg. Chim. Acta*, **1995**, 228, 215-218

54 A. Arrais, E. Diana, G. Gervasio, R. Gobetto, D. Marabello, P.L. Stanghellini, *Eur. J. Inorg. Chem.*, **2004**, 1505-1513

55 A. Y. Vasil'kov, *Elektrokhimiya.*, **2003**, 39, 12, 1499-1503

56 J. Chen, Z. Bajko, J.W. Kampf, A.J. Ashe, III, *Organometallics*, **2007**, 26, 1563-1564

57 P. Sawle, J. Hammad, I.J.S. Fairlamb, B. Moulton, C.T. O'Brien, J.M. Lynam, A.K. Duhme-Klair, R. Foresti, R. Motterlini, *J. Pharmacol. Exp. Ther.*, **2006**, 318, 1, 403-410

58 Gaussian 03, Revision C.02, M. J. Frisch, G. W. Trucks, H. B. Schlegel, G. E. Scuseria, M. A. Robb, J. R. Cheeseman, J. A. Montgomery, Jr., T. Vreven, K. N. Kudin, J. C. Burant, J. M. Millam, S. S. Iyengar, J. Tomasi, V. Barone, B. Mennucci, M. Cossi, G. Scalmani, N. Rega, G. A. Petersson, H. Nakatsuji, M. Hada, M. Ehara, K. Toyota, R. Fukuda, J. Hasegawa, M. Ishida, T. Nakajima, Y. Honda, O. Kitao, H. Nakai, M. Klene, X. Li, J. E. Knox, H. P. Hratchian, J. B. Cross, V. Bakken, C. Adamo, J. Jaramillo, R. Gomperts, R. E. Stratmann, O. Yazyev, A. J. Austin, R. Cammi, C. Pomelli, J. W. Ochterski, P. Y. Ayala, K. Morokuma, G. A. Voth, P. Salvador, J. J. Dannenberg, V. G. Zakrzewski, S. Dapprich, A. D. Daniels, M. C. Strain, O. Farkas, D. K. Malick, A. D. Rabuck, K. Raghavachari, J. B. Foresman, J. V. Ortiz, Q. Cui, A. G. Baboul, S. Clifford, J. Cioslowski, B. B. Stefanov, G. Liu, A. Liashenko, P. Piskorz, I. Komaromi, R. L. Martin, D. J. Fox, T. Keith, M. A. Al-Laham, C. Y. Peng, A. Nanayakkara, M. Challacombe, P. M. W. Gill, B. Johnson, W. Chen, M. W. Wong, C. Gonzalez, and J. A. Pople, Gaussian, Inc., Wallingford CT, 2004.

59 A.D. Becke, *J. Chem. Phys.*, **1993**, 98, 5648.

60 C. Lee, W. Yang, R.G. Parr, *Phys. Rev. B* **1988**, *37*, 785.

61 T. H., Jr Dunning, P.E. Hay, In *Modern Theoretical Chemistry*; Schaefer, H. F., III, Ed.; Plenum: New York, **1977**; Vol. 3, p 1.

62 GaussView, Version 3.09, Roy Dennington II, Todd Keith, John Millam, Ken Eppinnett, W. Lee Hovell, and Ray Gilliland, Semichem, Inc., Shawnee Mission, KS, **2003**

63 Noel M. O'Boyle, Johannes G. Vos, GaussSum 0.9, Dublin City University, **2005**. Available at http://gausssum.sourceforge.net.

64 P. Hrnviar, M. Hudeck, G.K.I Magomedov, S. Toma, *Collect. Czech. Comm.*;**1991**, 56, 1477

65 Mary T. Pryce, Ph.D Thesis, Dublin City University, **1994**

66 B.S. Creaven, M.W. George, A.G. Ginzburg, C. Hughes, J.M. Kelly, C. Long, I.M. McGrath, M.T. Pryce, *Organometallics,* **1993**, *12*, 3127-3131

67 A. Coleman, S.M. Draper, C. Long, M.T. Pryce, *Organometallics*, **2007**, 26, 17, 4128-4134

68 C.H. Choi, M. Kertesz, *J. Phys. Chem. A*, **1997**, 101, 3823-3831

69 P.C. Chen, Y.C. Chieh, *J. Mol. Struct(Theochem)*. **2003**, 624, 191-200

70 D. Frigyes and G. Fogarasi, *Organometallics*, **1999**, 18, 5245-5251

71 (a) J.F. Arenas, I.J. Tocón, J.C. Otero, J.I. Marcos, *J. Phys. Chem.*, **1995**, 99, 11392-11398; (b) M. Traeteberg, E.B. Frantsen, *J. Mol. Struct.*, **1975**, 26, 69

72 J.A. Bouwstra, A. Shouten, J. Kroon, *Acta Crystallogr.*, **1984**, C40, 428

73 A. Hoekstra, P. Meertens, A. Vos., *Acta Crystallogr.,* **1975**, B31, 2813

74 A. Antonini, F. Calderazzo, U. Englert, E. Grigiotti, G. Pampaloni, P. Zanello, *J. Organomet. Chem.*, **2004**, 589, 2158-2168

75 L.K. Yeung, J.E. Kim, Y.K. Chung, P.H. Rieger, D.A. Sweigart, *Organometallics*, **1996**, 15, 3891-3897

76 (a) R.E. Dessy, R.B. King, M. Waldrop, *J. Am. Chem. Soc.*, **1966**, 88, 5112-5117

(b) R.E. Dessy, F.E. Stary, R.B. King, M. Waldrop, *J. Am. Chem. Soc.*, **1966**, 88, 3, 471-476

Chapter 5

The synthesis, photochemistry, photophysical and electro chemical properties of a series of Pyrene-Thiophene dyads and the corresponding metal carbonyl complexes

Chapter five begins with a general introduction to Sonogashira-Hagihara type cross coupling reactions. This is then followed by a literature survey on the synthesis and photochemistry of luminescent organometallic dyad systems. The synthesis of these novel systems using the Sonogashira-Hagihara method is described. The photophysical properties are then examined using room and low temperature fluorescence and life-time studies. The photochemistry of the $Co_2(CO)_6$ complexes are examined by steady-state photolysis studies in the presence of a trapping ligand. Electrochemical data is also included.

5.1 Literature Survey

5.1.1 Pyrenylacetylene systems

In recent years the construction of organometallic structures containing a transition metal and a π-conjugated system have attracted much interest. By carefully incorporating a luminescent organic chromophore the excited state lifetimes of such species can be greatly lengthened. Luminescent probes that absorb in the visible region of the spectrum and that possess long lived excited states are of great industrial interest for use in both industrial and clinical sensor devices. Potential applications include luminescent probes[1], labels for biomaterials[2, 3], DNA probes[4], devices for artificial photo-synthesis[5,6], molecular switches and logic gates[7] and optoelectronic devices[8] such as organic field-effect transistors (OFETS) and light-emitting diodes[9]. Incorporation of these opto-electronic materials into a polymeric film or substrate allows for the development of smart materials such as intelligent or smart polymers.[9]

Materials containing a conjugated chromophore such as pyrene or phananthrene, and transition metals such as Ru or Pt are highly luminescent[1]. In most cases the excited state behaviour of these compounds is predominantly dictated by ^{3}MLCT decay as the $^3\pi$-π^* charge transfer contributions are much higher in energy. This results, in the frequently observed charge transfer based luminescence. It has, however, been observed that by strategically placing the acetylide unit the energy of the ^{3}IL state can be altered.[1,10] Castellano and co-workers have reported that the ^{3}MLCT excited state can be used as an internal sensitizer for the formation of a ^{3}IL excited state on an adjacent pyrenylacetylide ligand resulting in the observation of extremely long lived phosphorescence. [11,12] In many cases, where both the ^{3}MLCT and ^{3}IL states were energetically similar, the photophysical properties were mixed with varying degrees of ^{3}MLCT or $^3\pi$-π^* character.

In recent years, such π-conjugated oligimers have gained much interest and as a result many reviews and articles have been published regarding the synthesis, characterisation, photochemistry and photophysics of such materials. A recent review by Fages et al. [13] gave an overview of polypyridine ligands with extended π-conjugation. These systems are of great interest due to their interesting electronic and optical properties. Of particular interest are light emitting systems, in which the

optical and electronic properties can be easily manipulated and tuned by changes in the length and/or degree of conjugation in the system. Especially, when such systems incorporate a binding unit, a unit sensitive to a specific ion or type of metal ion for example, are the uses of such systems apparent. Thus the transformation of the emissive properties of such systems in the presence of metal ions or protons means that these systems may be used in chemosensing or optical switching devices[14, 15]. In most cases a polypyridyl unit, such as 2,2′-bipyridine, 1,10-phenantroline or terpyridine acts as the chelating ligand for "capture" of metal ions. The polypyridyl ligands are themselves non-fluorescent, except in their monoprotonated state, where they weakly emit. The addition of acetylenic bridging ligands greatly improves the emissive qualities of these ligands by increasing the π-conjugation and thus stabilising the $\pi \rightarrow \pi^*$ excited state. Further addition of a highly conjugated luminescent chromophore such as pyrene, anthracene or phenanthrene greatly enhances the emissive properties of the system (Figure 1). The addition of the pyrene moiety allows such systems the ability to easily form extremely sensitive intramolecular charge transfer states. A number of such systems have been synthesised by Ziessel and co-workers[2,8,16] with a number of ruthenium complexes also synthesised from these ligands (Figure 1).

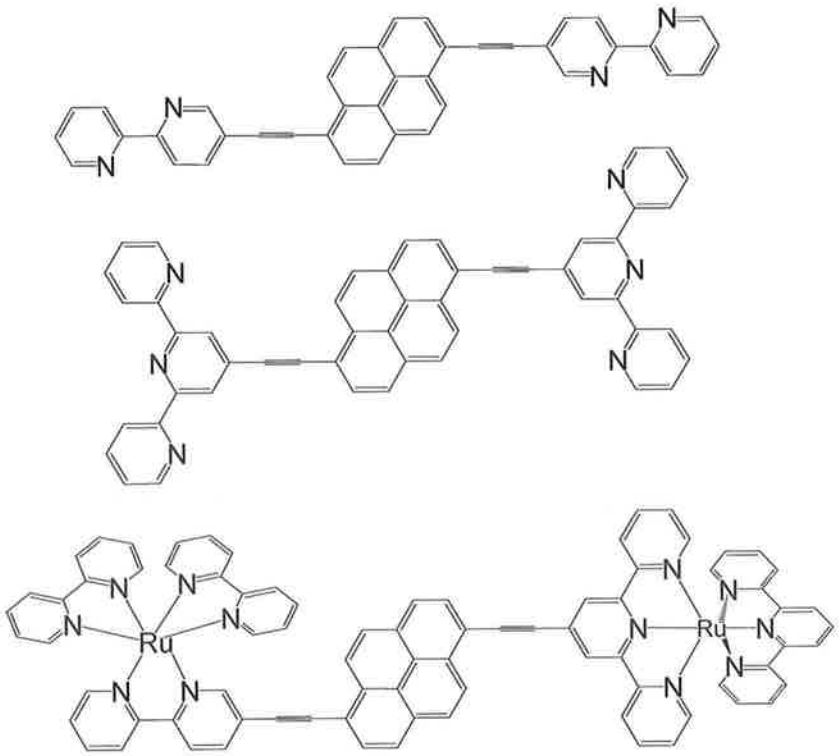

Figure 1 A number of polypyridyl-pyrenlacetylide ligands and their ruthenium complexes

Constable and co-workers[17] have also synthesised a number of similar polypyridyl based components of large metallomacrocyclic and dedritic systems. Such systems react with metal ions to give metallopolymers or metallocycles[17].

More recently, Schmittel and co-workers[18] have developed rigid bisphenanthroline based polypyridyl systems containing an acetylenic bridging ligand (Figure 2). The ability of these phenanthroline systems to form self assembled monolayers at a solid-liquid interface was then examined using scanning tunnelling microscopy.

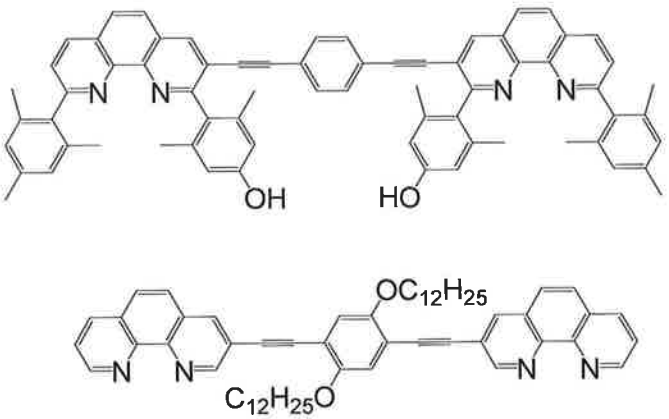

Figure 2 Rigid bisphenanthroline based polypyridyl systems used for self-assembled monolayers[18]

A number of bioactive polypyridyl and pyrenylacetylene based compounds have also been synthesised by Ziessel et al[2]. These contain chiral L-tyrosine fragments grafted to a polypyridine ligand via an acetylenic bridge (Figure 3). These chiral bioactive systems were synthesised in order to construct artificial systems, which mimic the photosystem II pathway observed in natural photosynthesis.

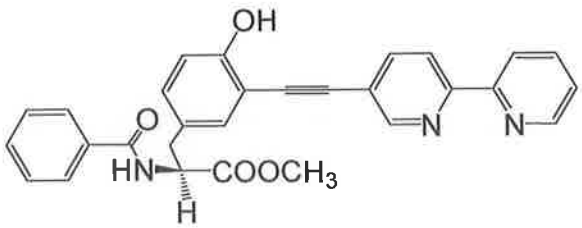

Figure 3 Chiral bioactive L-tyrosine fragment[2]

Similarly, Okamoto and co-workers[4] have also synthesised a pyrenylacetylene based nucleobase for use in the fluorimetric sensing of salt-induced B-Z DNA conformational transition. In these nucleobases a guanine (^{Pet}G) or cyctosine (^{Py}C) derivative is tethered to a pyrene system at the C8 or C5 position, respectively, via an acetylenic bridge (Figure 4).

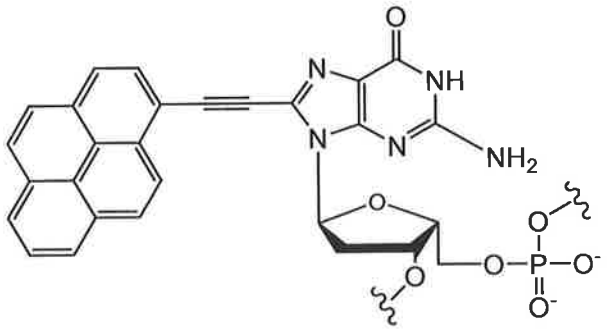

Figure 4 Pyrenylacetylene labelled ^{PET}G guanine derivative[4]

Recently, Hummelen and co-workers[7] have shown the use and application of anthraquinone based redox switches in molecular electronic devices. These anthraquinone based systems contain thioacetyl terminal groups for binding to a gold electrode surface (Figure 5). UV-Vis spectroelectrochemical experiments have shown that this system can be reversibly switched on (linear conjugation) and switched off (cross-conjugation) via a two-electron redox reaction.

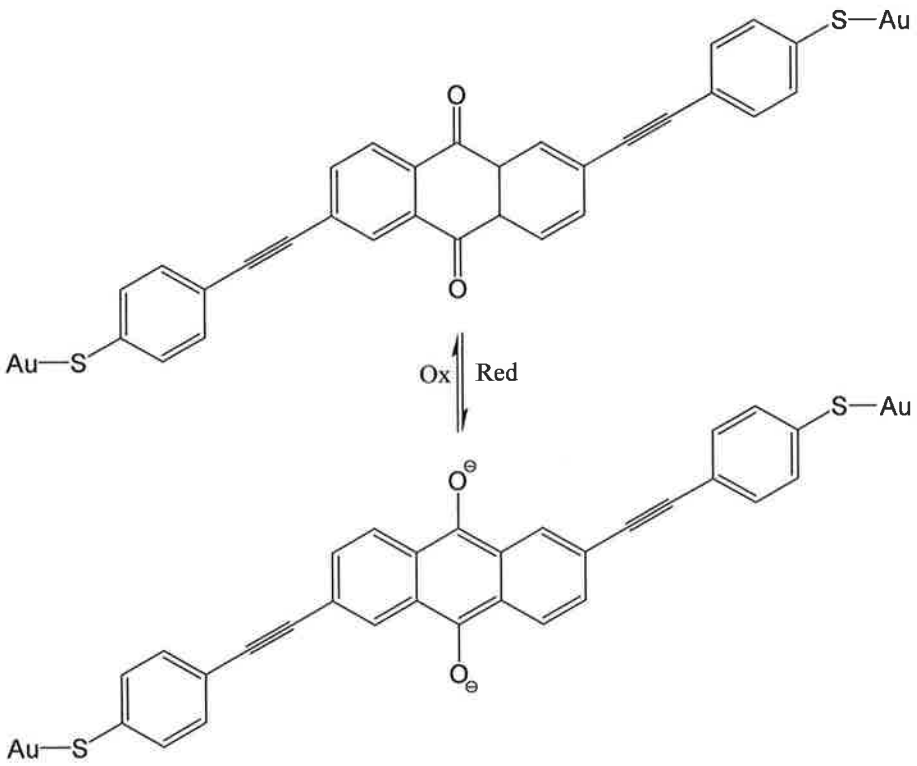

Figure 5 2-electron redox switching of anthraquinone based molecular switch[7]

The recent review by Fages et al.[13] and an earlier review by Lees et al.[19] serve to show the enormous interest in the area of polypyridyl, other heterocyclic systems and highly conjugated supramolecular systems and their abundant applications in the area of chemosensing, bio-labels, and molecular switches among others.

However, ethynylene systems containing other heteroaromatic rings have also attracted much interest, specially in the case of thiophene. The thiophene unit is known to enhance π conjugations along the ligand structure. An early study of the preparation of polyacetylene and polymetallaacetylene oligimers and polymers was undertaken by Lo Sterzo and co-workers[20]. In this study the authors describe the one-pot synthesis of aromatic acetylides via a Stille type cross-coupling reaction between aromatic iodides and tributyl(ethynyl)tin. This method resulted in high yields of polyacetylene or in the case of a metal carbonyl bound arene, the polymetallaacetylene. The $M(CO)_3$ labelled steroidal systems can be used in immunoassay FTIR studies. Furthermore, this method avoids the use of hazardous free alkynes and trimethyltinchloride.

Overall, this method was found to yield highly conjugated systems possessing a high degree of stereo-regularity and processability, making applications such as optoelectronic devices more feasible.

Recently, Otera et al.[21] have synthesised a large number of arylene ethynylene systems containing thiophene, pyridine and ferrocene subunits using a double elimination reaction of β-substituted sulfones. A typical example of the systems synthesised is shown in Figure 6. This method avoided the possibility of contamination by Pd or Cu catalysts typically observed during Sonogashira or Negishi cross coupling reactions.

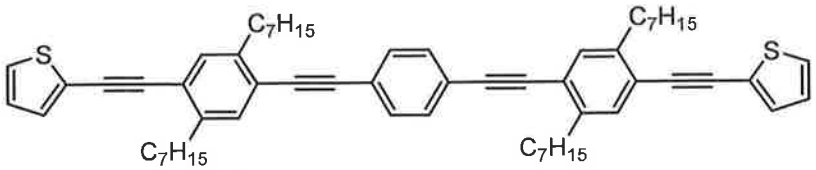

Figure 6 An example of the heteroaromatic ring systems synthesised

A number of Ru and Os metallo-supramolecular thiophene oligomers and polymers have also been synthesised by Barigelletti and co-workers[22]. These systems contain alternating thiophene and bipyridine subunits bridged by ethynyl linkers. A number of $Ru(bpy)_2$, $Os(bpy)_2$ or $Re(CO)_3Cl$ units are coordinated to the bpy subunit of the oligomeric chain. Room temperature luminescence studies have shown that emission from these complxes is largely ^{3}MLCT based and that these excited states are delocalised over the ligand. In the case of the Ru/Os dinuclear species efficient transfer from the Ru centre to the Os unit is observed following excitation, which results in purely Os based emission. Similar observations involving double electron transfer were made for the Re/Os dinuclear species.

Due to their potential applications in opto-electronic devices donor-acceptor conjugated complexes are of considerable interest. Recently, Raposo et al.[23] have synthesised a number of dicyanovinyl-substituted thienylpyrroles. Both absorption spectroscopy and electrochemical studies suggested that these compounds are promising candidates for non-linear optical chromophores.

Similarly, Roncali et al.[24] have incorporated these dicyanovinyl-thiophene units into rigid thiophene based π-conjugated systems. These systems are of interest as they act as push-pull non-linear optical chromophores. Furthermore, Roncali et al.[9,25] have incorporated these into a star-shaped molecule with a triphenylamine core (Figure 7).

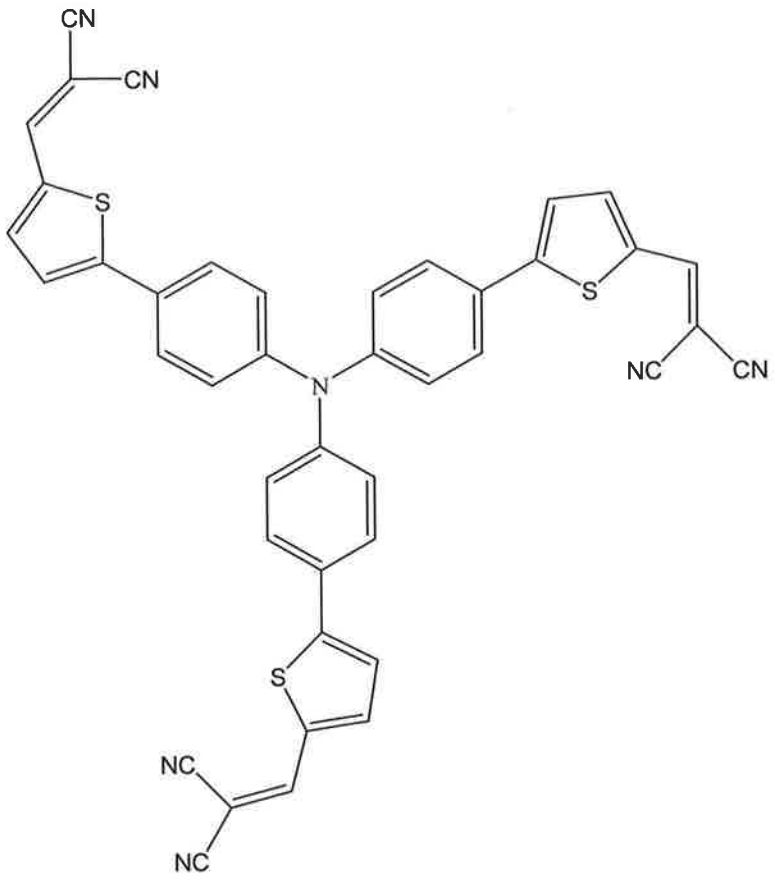

Figure 7 Star shaped Triphenylamine-Thienylenevinylene compound[9]

Fluorescence studies on these systems have shown that the addition of the electron-withdrawing dicyanovinyl group brings about an intramolecular charge transfer (ICT) process that results in a red-shift of the absorption bands to approximately 500 nm and a red-shift of approximately 100 nm of the room temperature luminescence is observed in addition to a significant reduction in emission intensity.

Pappenfus and Mann[26] have further developed this idea of a large oligothiophene structure to include an aromatic benzene core surrounded by a number of terthiophene arms, linked to the arene core by ethynlyne linkages (Figure 8).

The presence of the ethynyl bridges allows for greater conjugation between the oligothiophene arms and the benzene core, which allows improved coplanarity of the system.

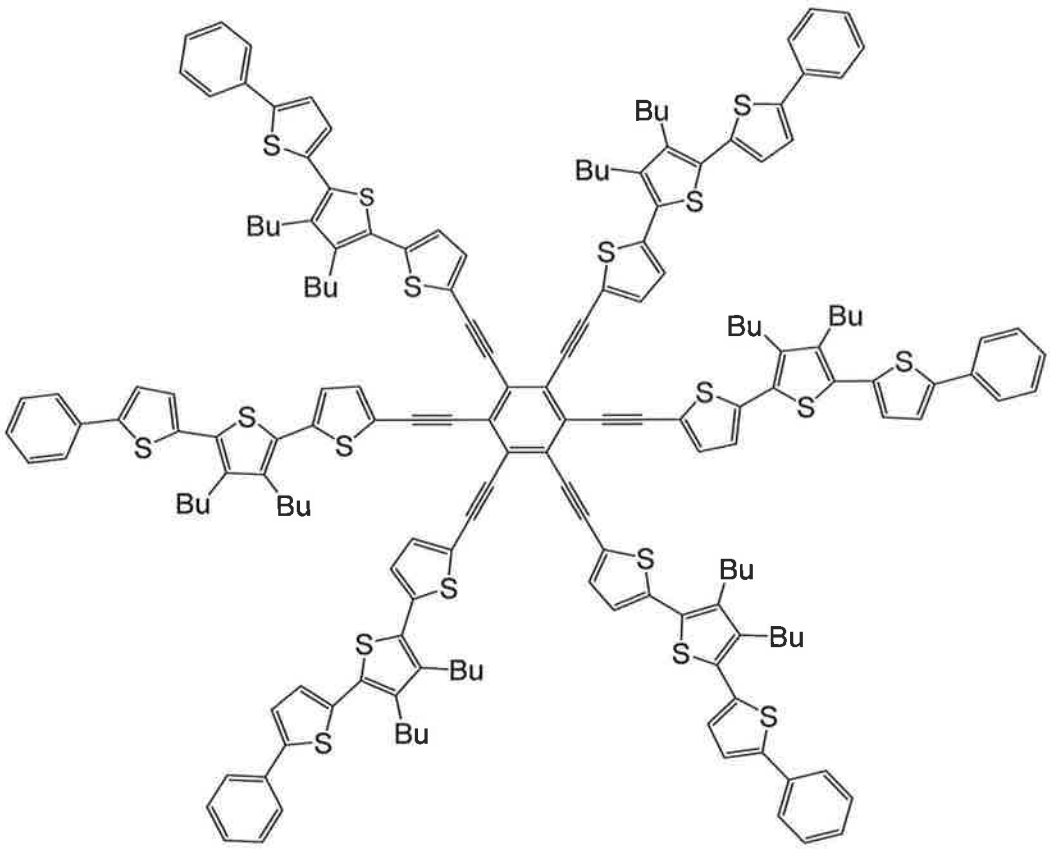

Figure 8 Radial Oligothiophene system with an arene core[26]

Examination of the absorption spectra of these systems indicated that the λ_{max} for the lowest energy $\pi \rightarrow \pi^*$ transition shifts to the red on increasing the number of oligothiophene arms on the arene (benzene or thiophene) core. Comparatively, the absorption spectrum of the oligothiophene arm itself only absorbs weakly in the visible region. This suggests that overall coordination of the oligothiophene arms to the arene core induces delocalisation of the π-system. Furthermore, solid state studies show an increased red-shift of the absorption bands compared to chloroform solution. This is attributed to increased planarity of the solid state molecule. As observed for the absorption spectra of these radial systems, the fluorescence maxima in

dichloromethane solution are substantially red-shifted as the number of oligothiophene arms increases and further red-shifted in the solid state.

Many of the previous examples of supermolecular structures have incorporated an ethynyl, pyridyl or phenyl based bridging ligand between terminal ends of the ligand. However, in recent years incorporation of a thiophene based linkage has attracted much interest. There are many reasons for this. Firstly a thiophene subunit is a good electronic conductor, meaning it enhances π-conjugation and thus π-delocalisation along the length of the molecule. This promotes electronic coupling between terminal ends of the molecule and improves excited state charge transfer processes. Moreover, the thiophene subunit may be readily functionalised to allow for solubility in water, tethering to a surface, electropolymerisation and for the creation of self-assembled monolayers.

In recent work by Benniston et al.[27] a pyrene subunit was tethered to a [2,2′:6′,2″]-terpyridine unit via a diethynyl thiophene ligand. The absorption spectrum in CH_3CN solution showns the presence of a low energy band at 426 nm, which is attributed to an intramolecular charge transfer (ICT) transition. Addition of $Zn(ClO_4)_2$ in CH_3CN solution results in Zn^{2+} cation binding to the terpyridine receptor (Scheme 1). This has the overall effect of red-shifting the absorption maximum into the visible region of the spectrum. Room temperature emission studies of this ligand in CH_3CN show it to be highly fluorescent, with an emission maximum centred at 488 nm, a fluorescence quantum yield of 0.32 and a singlet lifetime of 1.2 ns. The observed emission is broad and almost structureless and is not a mirror image of the lowest energy absorption. In addition a notable Stoke's shift of approximately 62 nm observed in acetonitrile solution suggests that the room temperature emission results from population of a photoexcited pyr^{+}-$thio^{-}$ charge transfer state (Figure 9).

Coordination of the Zn^{2+} cation to the terpyridine terminal raises the reduction potential of the terpyridine unit thereby directing the electronic charge from the thiophene subunit to the terminal metal complex. This is further suggested by ^{1}H-NMR studies, which indicate an up-field shift of the thienyl protons following formation of the Zn complex.

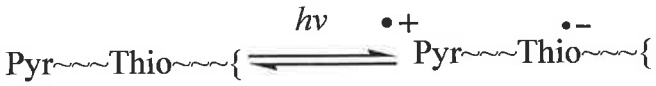

Figure 9 Pictorial representation of intramolecular charge transfer state[27]

This charge-shift results in a decrease in the fluorescence yield and significant quenching of the observed emission. However, cation coordination also produced a weak emission at 600 nm assigned to $[Zn(terpy)_2]^{2+}$, which is itself quenched at high Zn^{2+} concentrations.

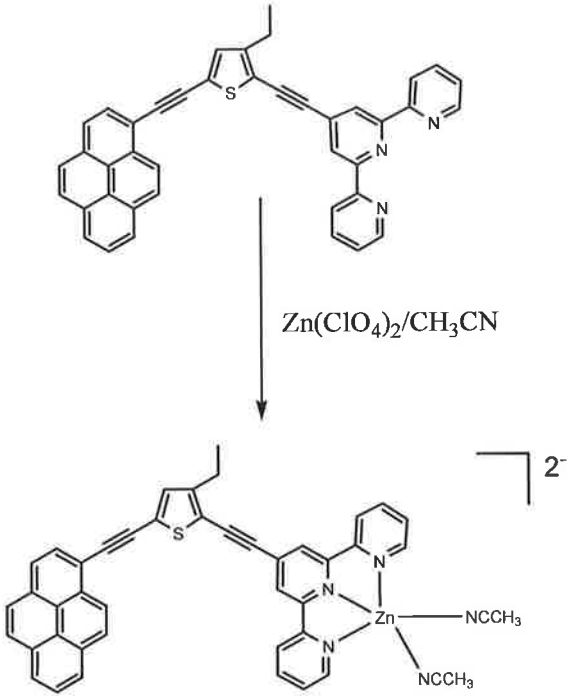

Scheme 1 Coordination of the Zn^{2+} cation to the pyrene-thiophene-terpy array[27]

This pyrene-thiophene-terpyridine array has been further evolved in later work by the same authors [28] by incorporation of a bisethynylanthracene bridge between the thiophene and terpyridine subunits in place of the previous ethynyl linkage (Figure 10). Replacing the ethynyl group with the bisethynylanthracene unit allows for greater tuning of the extent to which electron delocalisation occurs along the ligand.

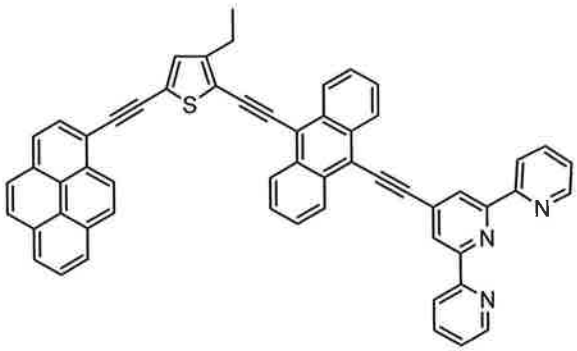

Figure 10 Incorporation of the bis(ethynyl)anthracene linkage into the Pyrene-thiophene-terpyridine array[28]

The absorption spectrum of this ligand displayed a broad low energy absorption at 490 nm, red-shifted by approximately 70 nm compared to the non-anthracene containing ligand. Fluorescent studies indicated that this ligand is also highly fluorescent in CH_3CN solution with an emission maximum centred at 540 m, a fluorescence quantum yield, of $\Phi_F = 0.35$ and a singlet lifetime of 1.9 ns. The emission band was observed to be broad and structureless suggesting population of an ICT state. The triplet state was detected by laser flash photolysis following excitation at 355 nm in deoxygenated DMSO. This state decays according to first order kinetics and has a $^3\tau$ of 18 μs. Following complexation with Zn^{2+} the absorption maximum was again red-shifted while the fluorescence lifetime in acetonitrile solution decreased to 0.16 ns with an associated decrease in intensity of the emission band. Laser flash photolysis in deoxygenated DMSO gave a triplet state lifetime of 95 μs for the Zn complex. Although similar effects are observed on cation binding, in contrast to the previous ligand, in which the anthracene unit is absent, binding of the cation to this ligand does not result in complete delocalisation or "off-loading " of electron density onto the terpyridine ligand. Instead the presence of the Zn(II) cation enhances triplet formation via perturbation of the anthracene ligand. It has also been observed that the pyrene-thiophene-anthracene-terpyridine ligand binds via the nitrogen donors of the terpy ligand to the Ru^{2+} cation. This system however does not emit at room temperature in acetonitrile solution, suggesting the ligand based triplet state is lower in energy than the MLCT triplet state.

Both the anthracene and non-anthracene containing ligands are very sensitive to cation binding which is clearly evident in reduced emission following metal binding.

Additionally, further studies suggests that these ligands respond in a similar way, following coordination of Na^{+}, H^{+}, Ca^{2+}, Li^{+}, Ba^{2+}, Al^{3+} and Fe^{2+} ions, suggesting further applications as metal ion or pH sensors.

Lately, the photochemical and photophysical properties of these pyrenylethynylene systems have received much attention due to their unique optical and electronic properties. Many of these systems involve the coordination of ruthenium to bipyridine and terpyridine type ligands[29,30]. Typically, these complexes contain a $Ru(bpy)_3^{2+}$ subunit coordinated to a pyrenylethynylene unit. The photochemistry of these complexes exhibits ^{3}IL and π–π^* ^{3}IL excited states respectively, resulting in the observance of room temperature phosphorescence. In the case of Br or ethynyltoluene bound substituents the excited states are MLCT in nature, involving charge transfer from Ru to the bpy ligands. However, where the substituents on the bpy ligand is a pyrene unit the excited state is ^{3}IL in nature.

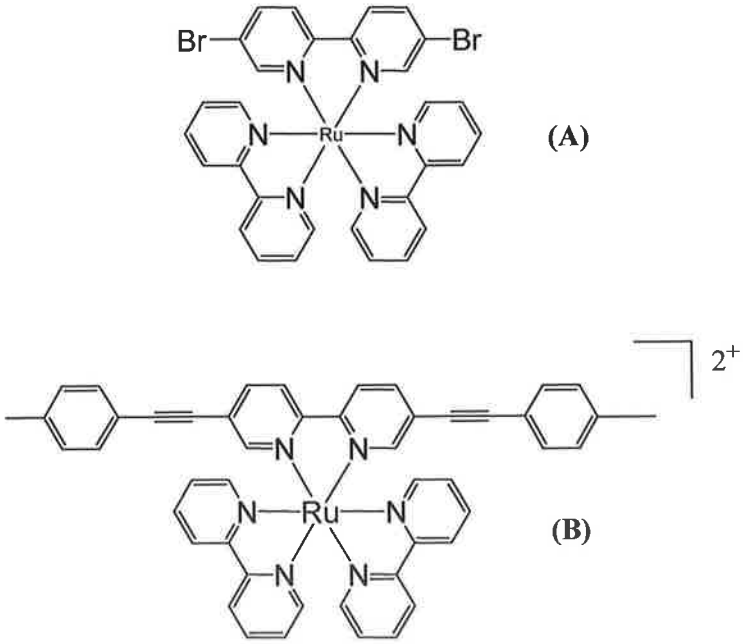

Figure 11 Structures of (A) [Ru(II)(2,2′-bipyridine)$_2$(5,5′-dibromo-2,2′-bipyridine)](PF$_6$)$_2$ and (B) [Ru(II)(2,2′-bipyridine)$_2$(5,5′-(*p*-ethynyltoluene))-2,2′-bipyridine]$^{2+}$

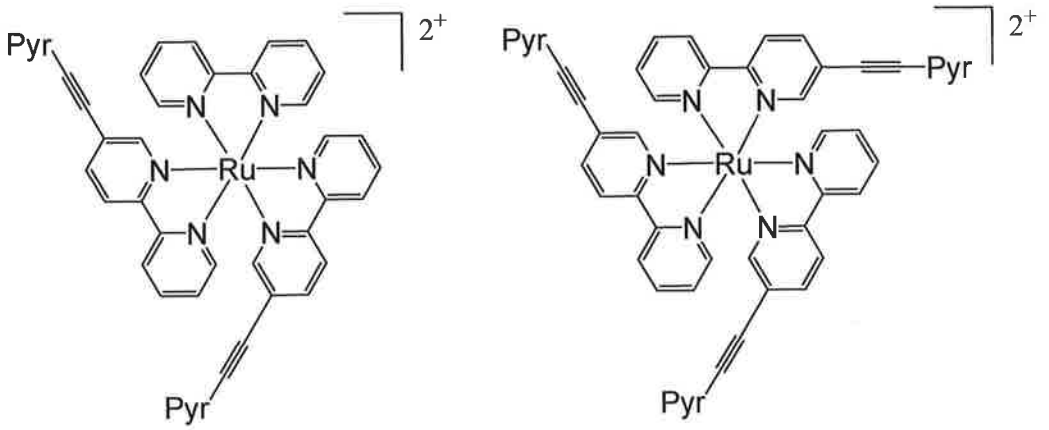

(1) (2)

Figure 12 Structures of (1) [Ru(II)(2,2′-bipyridine)$_2$(5-{1-ethynylpyrene})-2,2′-bipyridine]$_2^{2+}$ and (2) [Ru(II)(2,2′-bipyridine)$_2$(5-{1-ethynylpyrene})-2,2′-bipyridine]$_3^{2+}$ (pyr = pyrene)

Luminescence studies of these ethynylpyrene bound complexes (Figure 12 and Figure 13) in deoxygenated CH_3CN shows structured emission spectra and excitation spectra which are superimposable with the absorption spectra thereby suggesting the existence of a single excited state. Fluorescence quantum yields of Φ_F = 0.011, 0.009 and 0.013, and triplet lifetimes of 53.1, 54.3 and 4.86 μs were observed.

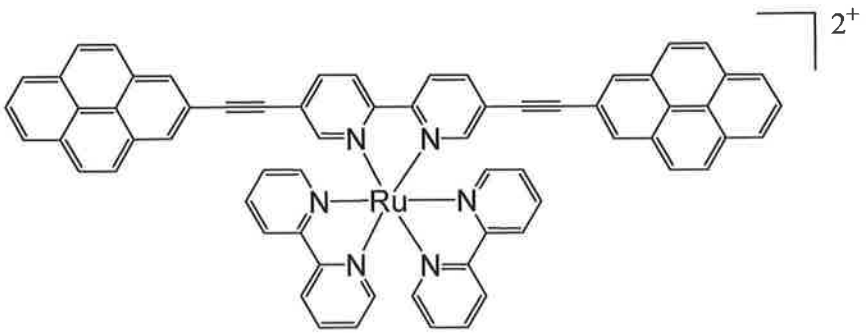

Figure 13 [Ru(II)(2,2′-bipyridine)$_2$(5,5′-{1-ethynylpyrene})-2,2′-bipyridine]$^{2+}$

The complex containing a linear diethynyl bpy unit (Figure 13) is approximately an order of magnitude lower than the other asymmetric pyrenyl systems (Figure 12). The authors attribute this 10-fold difference in lifetime to the energetic proximity of the ^{3}MLCT and ^{3}IL states, which results in mixed character excited state photophysics. In a 4:1 EtOH:MeOH glass at 77 K the lifetimes are similar to those observed in room temperature solution with negligible thermally induced Stoke's shifts observed.

These small thermally induced Stoke's shifts are indicative of ^{3}IL based excited state. A ^{3}IL excited state is further suggested by ns-laser flash photolysis studies in deoxygenated CH_3CN. Comparable studies of the free pyr-bpy ligand in the presence of the triplet sensitizer thioxanthone show similar results to that of its $Ru(bpy)_2$ complex further suggesting that the excited state photophysics of these compounds are ^{3}IL based and localised on the pyr-bpy ligand. Conversely, excitation of the bis(ethynyl)bpy complex shown in Figure 13 in acetonitrile solution at 532 nm results in a transient difference spectrum, which is somewhat red-shifted in comparison to the difference spectrum of a triplet-sensitized Me-THF solution of the Pyr-bpy-Pyr ligand following 355 nm excitation. This red-shift may be due to the increased planarity of the diimine structure by the Ru(II) centre (Figure 13).

Castellano et al.[31] have also synthesised an analogous complex $[Ru(py\text{-}phen)_3]^{2+}$ using the bidentate phenanthroline ligand in place of bpy. Excitation between 300-540 nm resulted in long lived (148 μs) MLCT based emission, which given the unusually long lifetime resulted in a dynamic self-quenching reaction at room temperature. Laser flash photolysis and ultrafast transient absorption spectroscopy measurements suggest formation of a pyrene triplet excited state, with the same room temperature decay kinetics as the room temperature MLCT based luminescence, thus suggesting formation of a thermal excited state equilibrium at room temperature.

The photochemical and photophysical properties of both the Pyr-bpy and Pyr-bpy-Pyr (Figure 14) ligand have also been separately studied[29,32,51]. The absorption spectrum of Pyr-bpy in acetonitrile is dominated by $\pi \rightarrow \pi^*$ based transitions and absorbs weakly in the visible region, to about 425 nm. Addition of Zn(II) to an acetonitrile solution of Pyr-bpy results in a noticeable red-shift of the $\pi \rightarrow \pi^*$ transitions further into the visible region. This shift is attributed to improved planarity of the bpy ligand on Zn^{2+} binding resulting in enhanced π-conjugation along the axis of the ligand.

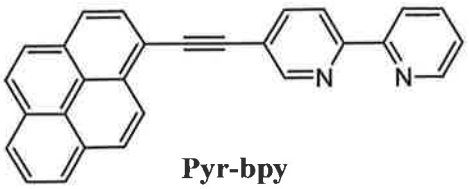

Pyr-bpy

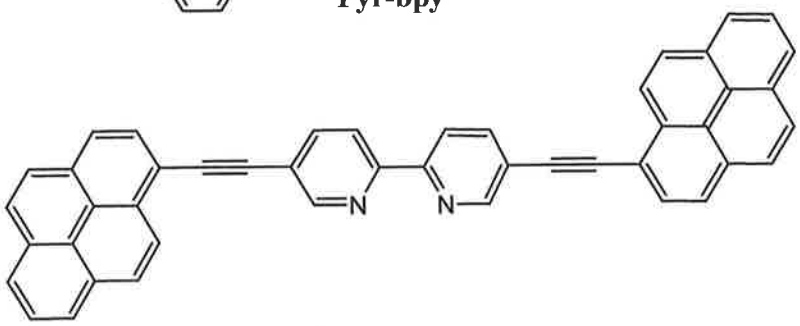

Pyr-bpy-Pyr

Figure 14 Structures of the fluorescent Pyr-bpy and Pyr-bpy-Pyr ligands[32]

Room temperature fluorescence in acetonitrile solution shows a broad, structureless emission band centred at 475 nm, indicating a Stoke's shift of approximately 50 nm. This broad unstructured emission band and Stoke's shift suggests that emission is observed from an intramolecular charge-transfer (ICT) excited state. Conversely, in non-polar solvents the emission maximum is blue-shifted to higher energies with the observance of a pyrene-like $\pi \rightarrow \pi^*$ emission. The ICT state was determined to decay according to first order kinetics with a lifetime of 3 ns, with no possible detection of the pyrene-like $\pi \rightarrow \pi^*$ emission in polar solvents indicating that it must have a lifetime of approximately 30 ps. However, in non-polar solvents the pyrene like $\pi \rightarrow \pi^*$ state is the energetic minimum and thus is observed. No room temperature phosphorescence was observed even in the presence of a ethyl iodide. In 77 K 4:1 EtOH:MeOH glass Pyr-bpy is highly fluorescent. Laser excitation at 355 nm in acetonitrile solution results in population of the lowest lying triplet (pyrene like $\pi \rightarrow \pi^*$) state, which decays according to first order kinetics and has a lifetime of 130 μs. Phosphorescence was also detected in micellar media and was observed to have a triplet lifetime of 45 ms. Excitation at 355 nm with a shorter-duration laser pulse populated the ICT, which decays by first order kinetics with a decay lifetime of 2.7 ns. The transient difference spectrum also indicates the presence of the pyrene like $\pi \rightarrow \pi^*$ state, which is formed via internal conversion from the initially formed ICT state. Excitation in acetonitrile solution with sub-ps transient absorption spectroscopy results in immediate formation

of the ICT state without detection of the pyrene-like $\pi \rightarrow \pi^*$ state, suggesting that interconversion from the ICT to this state occurs rapidly. Thus the initially formed singlet state is deactivated by both radiative and non-radiative means resulting in fluorescence and intersystem crossing to populate the pyrene-like $\pi \rightarrow \pi^*$ triplet excited state. However, conversely, irradiation in a non-polar solvent results in formation of the pyrene-like $\pi \rightarrow \pi^*$ singlet excited state, with a lifetime of 10 ps. The fact that the pyrene-like triplet state is lower in energy than pyrene and the unusually long phosphorescence lifetimes suggest that the pyrene like triplet state is delocalised over the length of the Pyr-bpy ligand.

Harriman et al.[33] have also recently developed a series of ethynylpyrene bound bora-3a, 4a-diaza-*s*-indacene (Bodipy) dyes. Such systems have many applications in the areas of biolabels, solar cells, laser dyes and fluorescent sensors. These systems consist of a Bodipy dye unit tethered to two pyrene or perylene units via the boron centre (Figure 15). These systems have strong absorptions far in the visible region, up to 525 nm, which are attributed to the Bodipy dye while at higher energy sets of sharp bands observed are due to either the pyrene or perylene subunits. Regardless of the aromatic polycycle present, (pyrene, perylene or both) a single sharp emission band is observed at 530 nm in room temperature deoxygenated MeTHF. This signal decays according to first-order kinetics with a lifetime of 6.5 ns and a fluorescence quantum yield of 0.90. The observed emission band is essentially a mirror image of the lowest energy absorption band and possesses a small Stoke's shift of 160 nm. This suggests that following population of the excited state little change in geometry is observed.

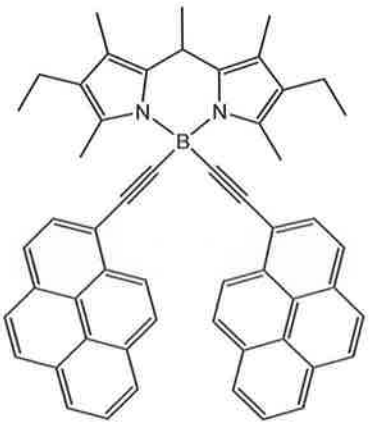

Figure 15 Structure of a bis ethynylpyrene Bodipy dye

Overall, this suggests that the emission observed results from the Bodipy subunit. Furthermore, neither the fluorescence quantum yield nor the singlet excited state lifetime of the Bodipy system in MeTHF solution changed in the temperature range 300 to 80 K. ns. Laser flash photolysis studies suggest that the triplet lifetime may be approximately 0.01 ns. However, these are largely speculative as triplet state formation is largely inefficient as it cannot compete with singlet state radiative decay in the absence of a triplet sensitizer. No fluorescence from either the pyrene or perylene units was observed in these systems and time resolved fluorescence studies indicated that pyrene or perylene associated emission would have a lifetime of < 50 ps. Thus it appears the Bodipy subunit acts as a photon "sink" with near quantitative transport of the photons collected by the polycyclic units to the Bodipy unit.

A number of bpy bound platinum diimine type complexes containing trimethylsilylacetylene [34], phenylacetylene, [35,36,37] napthylacetylene [36] or pyrenyl acetylene[36,37] terminal units have been synthesised.

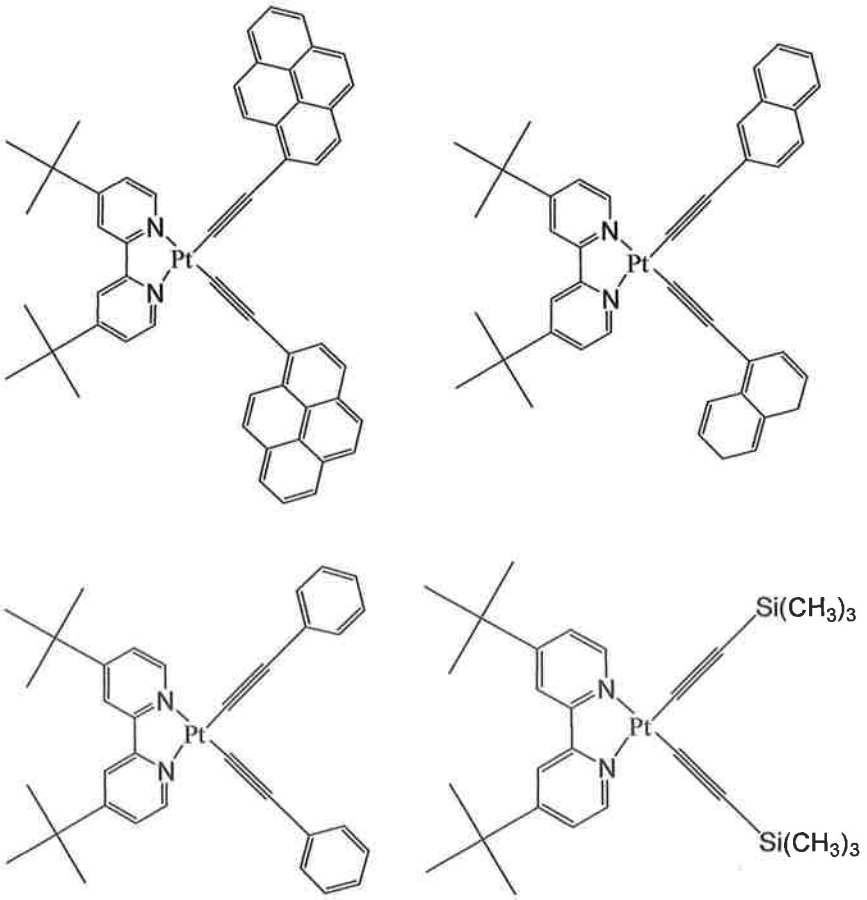

Figure 16 A range of pyrene, naphthalene, phenyl and TMS tethered Pt (II) diimine complexes

The photophysical properties of the bis-trimethylsilylacetylene complex have been investigated by Hua et al.[34] The absorbance spectrum of this complex has been shown to feature a dominant low energy Pt-ligand based MLCT transition. Both electrochemical studies and Density Functional Theory calculations have shown this transition to be predominantly HOMO-LUMO in nature, involving substantial charge transfer from the metal centre and acetylenic linkages to the substituted bpy ligand. This bis-trimethylsilylacetylene complex is a high quantum yield green emitter with a broad fluorescence spectrum centred at 526 nm observed on excitation in CH_2Cl_2 solution. The fluorescence quantum yield measured in degassed CH_2Cl_2 solution was 0.13 while the excited state lifetime was measured at 236 ns. The low energy and high quantum yield emission of this complex means that it may provide a possible alternative for green colour-matched triplet-state emitters for optoelectronic devices such as light-emitting electrochemical cells. Interestingly, the emission profile of this complex is almost super-imposable with that of $Ir(ppy)_3$. Similarly, a phenyl bound analogue (Figure 16) also containing the σ-donor acetylene units has also been studied by Castellano et al.[35,36,37] Excitation of this species at 480 nm in CH_2Cl_2 solution was found to result in a broad MLCT based emission band centred at approximately 560 nm with a lifetime of 1.25 μs. This is further suggested by low temperature studies in a 4:1 EtOH: MeOH glass.

However, of greater interest and relevance to this study are those systems containing one or more pyrenylacetylene units. A number of pyrenylacetylene species, such as that shown in Figure 16 have been synthesised by Castellano et al.[35,37] These compounds contain low energy pyrene based $\pi \rightarrow \pi^*$ transitions between 350-400 nm and a lower energy Pt→bpy MLCT band at 450 nm as previously observed in the TMS and phenyl derivatives. Similar, $\pi \rightarrow \pi^*$ transitions are observed for the *trans*-$Pt(PBu_3)_2(C{\equiv}Cpyrene)_2$ complex shown in Figure 17 suggesting that this transition is entirely localised on the pyrenylacetylene units. Unlike, the TMS and phenyl derivatives, the room temperature luminescence spectra of the pyrenylacetylene compounds were measured in deoxygenated Me-THF as they were O_2 sensitive. Following 400 nm excitation in deoxygenated Me-THF solution a very structured and sharp emission spectrum was observed at 658 nm for the $Pt(dbbpy)(C{\equiv}C\text{-}pyrene)_2$ (Figure 16) system. This emission was red-shifted by approximately 100 nm,

compared to the phenyl derivative and was observed to be quantitatively similar to the room temperature phosphorescence spectrum of *trans*-$Pt(PBu_3)_2(C{\equiv}Cpyrene)_2$ (Figure 17). In both systems, the observed emission is assigned to ^{3}IL phosphorescence from the pyrenylacetylene subunit. Similarly it has been observed that excitation in CH_2Cl_2 solution at 480 nm results in triplet sensitisation of the pyreneylacetylene ^{3}IL phosphorescence[35]. This suggests that solvatochromic effects play little part in room temperature emission.

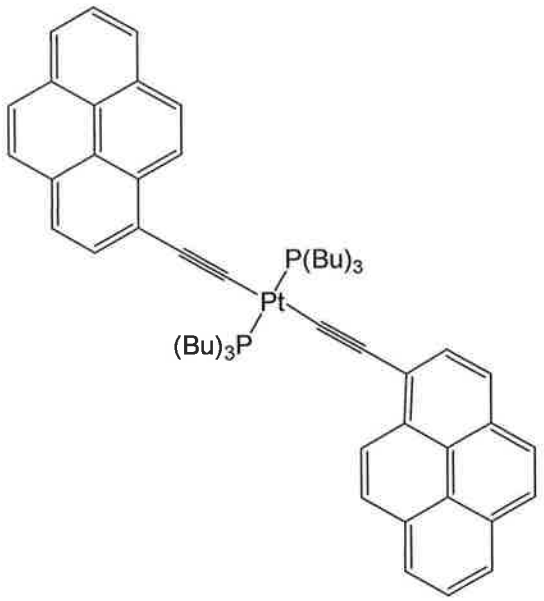

Figure 17 Structure of *trans*-$Pt(PBu_3)_2(C{\equiv}C$-pyrene$)_2$[37]

The nanosecond transient absorption difference spectrum of the phenyl derivative in Me-THF showed the presence of a "relaxed" ^{3}MLCT excited state. In contrast, excitation of the pyrenylacetylene derivative ($Pt(dbbpy)(C{\equiv}C$-pyrene$)_2$) at 416 nm in both Me-THF[37] and CH_2Cl_2[35] results in a difference spectrum showing generation of two absorption bands at 450 and 540 nm as well as bleaching of the ground state parent species. This further indicates that solvent polarity does not effect that position of the excited state or its dynamics. This transient decays according to first-order kinetics and has a decay lifetime of 25 μs, similar to the value of 24 μs observed for this species in time resolved luminescence studies. Overall, this suggests that in both the transient and luminescence spectroscopy studies the same excited state is involved. This state is believed to result from triplet sensitisation of the ^{3}IL state, resulting in bleaching of the pyrene-based ground state.

Further to this femtosecond transient absorption spectroscopic measurements have also been undertaken on these species by the Castellano[37] group.

Excitation of *trans*-$Pt(PBu_3)_2(C{\equiv}Cpyrene)_2$ (Figure 17) at 400 nm populates the lowest lying singlet $\pi \rightarrow \pi^*$ excited state localised on the pyrenylacetylene subunit as indicated by generation of a transient signal at 630 nm. However, this transient then decays via intersystem crossing over 5.2-5.6 ps to populate the triplet manifold as indicated by generation of transients at 500 and 550 nm. However, in the case of ($Pt(dbbpy)(C{\equiv}C\text{-}pyrene)_2$) the excited state dynamics are not so straightforward. In ultrafast spectroscopic studies this complex was excited at 400 nm to optically pump both the ^{1}MLCT and ^{1}IL excited states. At all delay times a transient, assigned to the ^{3}IL state, is generated between 500-550 nm. This decays according to first order kinetics over 210 fs. At longer wavelengths tentative evidence was observed for the presence of both the ^{1}IL and ^{3}MLCT excited states. Similarly, excitation at 480 nm results in a transient feature at 540 nm, which decays over 240 fs to populate the ^{3}IL state. Overall, this suggests that excitation at 400 m, populates either the ^{1}IL and ^{1}MLCT states, which subsequently decay to populate the ^{3}IL state. In contrast, excitation at 480 nm results in direct population of the ^{1}MLCT state, which then undergoes intersystem crossing to populate the lower energy ^{3}IL state. In any case, the presence of the MLCT state allows for rapid sensitisation (210-240 fs) of the ^{3}IL excited state. Substantial electronic coupling between the Pt(II), dbbpy and pyrenylacetylene orbitals results in rapid migration of energy throughout the system. Interestingly, in *trans*-$Pt(PBu_3)_2(C{\equiv}Cpyrene)_2$, which does not involve significant population of the ^{3}IL state, direct intersystem crossing between the singlet and triplet MLCT states is slower by one order of magnitude.

5.1.2 Dicobalt hexacarbonyl complexes

Although the photochemical properties of complexes of the type (alkyne)$Co_2(CO)_6$ have received little interest, these type of complexes are an important precursor in the formation of derivatised cyclopentenones via the Pauson-Khand reacton (PKR). These cyclopentenones are invaluable synthetic intermediates in a number of natural product syntheses[38]. The Pauson-Khand reaction is a cobalt mediated cycloaddition reaction involving co-cyclisation of an alkyne, an alkene and carbon monoxide. Although it is generally accepted that the first step in cyclisation in the Pauson-Khand reaction involves loss of CO and subsequent alkene coordination to one of the two enantiotopic Co atoms, the exact mechanism and the succeeding mechanisms have yet to be elucidated. It has, however, been generally observed[39] that the coordinating alkene positions itself nearest the stearically less bulky acetylenic substituent and that C-C bond formation occurs between this acetylenic carbon and the alkene, resulting in the majority of cases with the bulky acetylinic substituent in the α-position of cyclopentenone, next to the C=O bond (Figure 18).

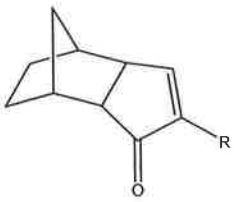

R = bulky substituent

Figure 18 Generalised cyclopentenone structure, indicating presence of the bulky substituent R in the α-position

Although the Pauson-Khand reaction is promoted by the presence of $Co_2(CO)_8$ much study has been undertaken to investigate what other factors may "speed-up" this sluggish reaction and improve the yields obtained. Many groups have used additives such as phosphine oxides, sulfoxides and amines to enhance the rate of reaction in PK reactions. It has also been observed that the pressure of the CO present in the reaction vessel may also have an effect on the rates and yields of the reaction[40]. Furthermore, modifications to the conditions of the reaction have also been shown to have an effect on the rate of reaction and yield with ultrasound[41], UV irradiation[42], natural light[43] and microwave radiation[44].

However, although the thermal substitution chemistry of (alkyne)$Co_2(CO)_6$ has been the subject of much interest[45], little attention has been given to the study of the (alkyne)$Co_2(CO)_6$, Pauson-Khand precursor. One of the earliest studies of these systems was undertaken by Gordon et al[46]. and involved a study of matrix isolated phenylacetylenedicobalthexacarbonyl, [$PhCCHCo_2(CO)_6$], in order to understand the mechanism and intermediate species behind the photo-induced Pauson-Khand reaction, in particular the photochemically-induced catalytic Pauson-Khand reaction. Irradiation of $PhCCHCo_2(CO)_6$ at 254 nm in an argon matrix resulted in the formation of the coordinatively unsaturated $PhCCHCo_2(CO)_5$ species in low yield as a steady-state was reached after conversion of approximately 25 % on the starting material. Broadband irradiation at > 400 nm resulted in a reversion of this process leading to regeneration of the hexacarbonyl parent species. However, no useful data regarding the acetylene group could be detected due to the common problem of water vapour present in the matrix. Irradiation under similar conditions at 254 nm with a 10 % N_2 doped argon matrix resulted in an increased percentage conversion to the pentacarbonyl species as well as sharper more defined bands. Apart from the N_2 coordinated pentacarbonyl species, $PhCCHCo_2(CO)_5N_2$, a number of other unknown species were formed. However, subsequent photolysis at 390 nm, while having little effect on the N_2 adduct, did result in the formation of the previously observed coordinatively unsaturated pentacarbonyl $PhCCHCo_2(CO)_5$. As observed in the argon matrix broadband irradiation at > 400 nm resulted in bleaching of the product bands with concomitant regeneration of the parent bands. Irradiation at 254 nm in a 100 % N_2 matrix again not only resulted in the rapid formation of the N_2 coordinated pentacarbonyl $PhCCHCo_2(CO)_5N_2$, but also another N_2 coordinated photoproduct , as indicated by the generation of a second ν_{NN} band. Overall, it was observed that the yield and rate of pentacarbonyl formation increased as the N_2 matrix gas concentration increased, suggesting that matrix cage-effects may be an important factor in the argon matrix resulting in rapid recombination of the photoejected CO with the pentacarbonyl, while irradiation at 250 nm had little effect, as $PhCCHCo_2(CO)_6$ appeared to be photochemically inert at this wavelength.

Long et al[47]. have taken this investigation a step further by examining the photochemistry of (alkyne)$Co_2(CO)_6$ complexes, and their role as intermediates in the photo-chemically induced Pauson-Khand reaction using steady-state and laser flash

photolysis techniques. Specifically, the photochemistry of $(\mu_2\text{-}RC_2H)Co_2(CO)_6$, where R = H or C_6H_5 (Figure 19), have been examined using laser flash photolysis and steady-state photolysis in the presence of a trapping ligand.

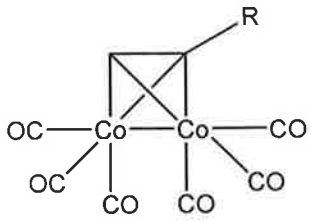

R = H or Ph

Figure 19 Basic structure of $(\mu_2\text{-}RC_2H)Co_2(CO)_6$ system

Broadband irradiation at > 340 nm in the presence of either PPh_3 or pyridine resulted in generation of the monosubstituted pentacarbonyl, $PhCCHCo_2(CO)_5L$, where L = PPh_3 or pyridine. Extended irradiation was also found to produce the secondary photoproduct $PhCCHCo_2(CO)_4(L)_2$. Broadband irradiation at > 400 nm produced similar results, although the yields obtained and rates of reaction observed were considerably slower due to lower absorbance in this area. Similarly, steady-state irradiation in cyclohexane solution in the presence of triphenylphosphine or pyridine exclusively produced the monosubstituted pentacarbonyl, $PhCCHCo_2(CO)_5(PPh_3)$ or $PhCCHCo_2(CO)_5$(pyridine). Increasing the irradiation energy to >340 nm was found to predominantly produce the disubstituted derivative, especially in the presence of PPh_3, most likely as a result of secondary photolysis.

Laser flash photolysis studies were also carried out in cyclohexane solution. Pulsed photolysis at 355 nm resulted in bleaching of the parent hexacarbonyl absorption within the 20ns rise time of the monitoring beam, while no absorptions were observed as far as 600 nm. The depletion was observed to rapidly recover to its pre-irradiation absorbance level according to first-order kinetics with a k_{obs} value of 4×10^7 s^{-1} (298 K). The addition of CO had no effect on the rate of recovery indicating that the depletion observed is not due to a CO loss product. Similar observations were made in the presence of a 20 fold excess of pyridine. This adds credence to the observations of Gordon and co-workers[46] suggesting that $PhCCHCo_2(CO)_6$ is not CO substitution labile at this wavelength and that irradiation at this wavelength results in rapid Co-Co

homolytic bond cleavage followed by rapid recombination resulting in no permanent or long lived bleaching (Scheme 2). In contrast, pulsed photolysis at 532 nm produced a transient absorption at 400 nm assigned to the pentacarbonyl $PhCCHCo_2(CO)_5$. In the presence of 1 atm. CO the decay lifetime was significantly reduced. The observed rate constant, k_{obs}, was observed to be linearly dependent on the CO concentration present, with a second order rate constant of 1.2 x 10^6 dm^3 mol^{-1} s^{-1} (298 K). Similarly, irradiation under these conditions in the presence of an excess of triphenylphosphine produced a transient absorption at 400 nm assigned to generation of the monosubstituted species $PhCCHCo_2(CO)_5(PPh_3)$ (Scheme 2). The lifetime and yields was, as in the case of CO, again dependent on the concentration of PPh_3 present. The second order rate constant was measured at 3.0 x 10^6 dm^3 mol^{-1} s^{-1} (298 K).

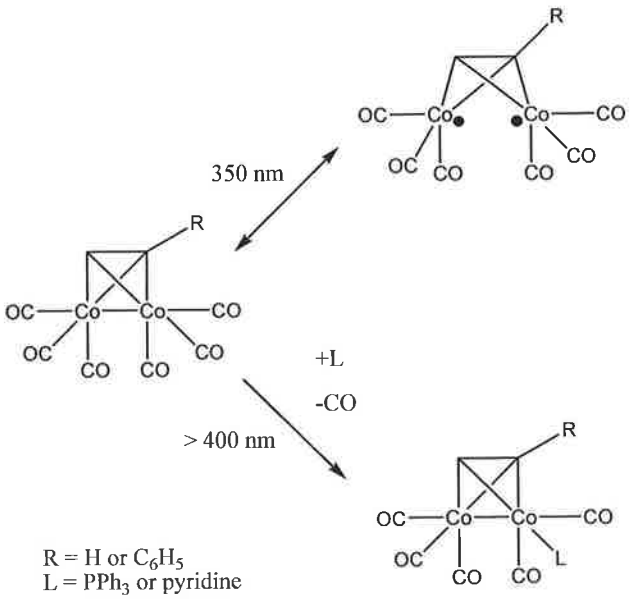

Scheme 2 Observed wavelength dependent photochemistry of (μ_2-RC_2H)$Co_2(CO)_6$ in cyclohexane solution, in the presence of either PPh_3 or pyridine[46]

In a more recent contribution, Ford and co-workers [48] have investigated the photoproducts formed on irradiation of the hydroformylation catalyst precursor $Co_2(CO)_6(PMePh_2)_2$ using time-resolved infrared (TRIR) spectroscopy. Irradiation at 365 nm of a solution of $Co_2(CO)_6(PMePh_2)_2$ in benzene under argon resulted in very weak spectral changes, which were tentatively assigned to formation of cobalt cluster complex of the type $Co_4(CO)_8(PMePh_2)_4$. This may occur via dissociative CO loss from a $[Co_2(CO)_6(PMePh_2)_2]$* excited state to yield $Co_2(CO)_5(PMePh_2)_2$. This

unsaturated species may then react with the photolytically released CO to regenerate $Co_2(CO)_6(PMePh_2)_2$ or with other molecules of $Co_2(CO)_6(PMePh_2)_2$ to form higher order Co clusters, albeit it with low quantum efficiency. Rapid bimolecular interactions between any radical species formed will result in regeneration of $Co_2(CO)_6(PMePh_2)_2$. Furthermore, as shown in Scheme 3 this $[Co_2(CO)_6(PMePh_2)_2]^*$ excited state may also dissociatively lose a $PMePh_2$ ligand to give the coordinatively unsaturated dimer $Co_2(CO)_6(PMePh_2)$, which could itself react with either CO or other dimers to generate cobalt clusters.

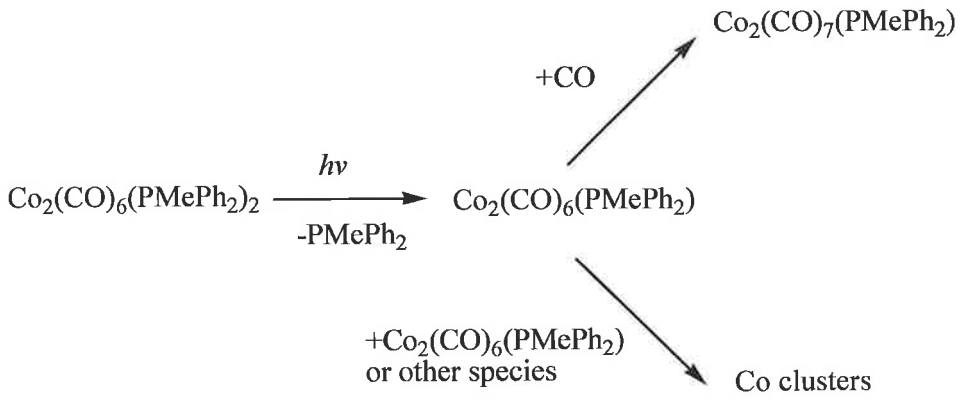

Scheme 3 Reaction of unsaturated dimer with CO or another Co_2 species[48]

However, in contrast irradiation at 365 nm of a benzene solution of $Co_2(CO)_6(PMePh_2)_2$ under 1 atm. CO resulted in bleaching of the absorption centred at 365 nm with concomitant generation of a band at 340 nm suggesting formation of $Co_2(CO)_7(PMePh_2)$. This spectral change occurred rapidly but ceased after 90 s irradiation suggesting a photostationary state, as shown in Scheme 4, had been reached. Formation of the $PMePh_2$ loss product was further suggested by IR spectroscopy, where product bands generated at 1987, 2022 and 2078 cm^{-1} compare favourably with those previously observed for the formation of $Co_2(CO)_7(PPh_3)$.

$$Co_2(CO)_6(PMePh_2)_2 + CO \underset{h\nu}{\overset{h\nu}{\rightleftharpoons}} Co_2(CO)_7(PMePh_2) + PMePh_2$$

Scheme 4 Photostationary state observed on irradiation at 365 nm under 1 atm CO

However, interestingly completely different photochemistry was observed on irradiation of $Co_2(CO)_6(PMePh_2)_2$ in the chlorinated solvent dichloroethane. Irradiation at 365 nm of a dichloroethane solution under argon resulted in rapid bleaching of the 386 nm parent absorption band, assigned as a Co-Co $\sigma \rightarrow \sigma^*$ transition, with no generation of new product bands in the UV-visible region. This depletion is due to photo-induced Co-Co band homolysis and formation of the 17-electron metal based radical $^{\bullet}Co(CO)_3(PMePh_2)$. In benzene recombination of two radical species to regenerate the Co-Co bond occurs rapidly, however in chlorinated solvents these 17-e^- radical species may also extract a chlorine from the dichloroethane to yield mononuclear chlorinated products. Formation of the monochlorinated photoproduct was further suggested by IR monitoring of the reaction solution, which indicated loss of the $Co_2(CO)_6L_2$ characteristic carbonyl bands and generation of bands at 1981 cm^{-1} and 1917 cm^{-1}, with the former band in good agreement with those observed for other similar species such as $Co(CO)_3(PEt_3)Cl$. Moreover, it has also been observed that the quantum yield for loss of $Co_2(CO)_6(PMePh_2)_2$ to form the chlorinated product, increased parallel to an increase in dichloroethane concentration from a 0.127 M solution to neat dichloroethane. This further supports the generation of the $^{\bullet}Co(CO)_3(PMePh_2)$ as increased Cl concentration results in less Co-Co bond regeneration following homolytic cleavage and increased trapping of the ligand by chlorine. However, radical formation also allows for the formation of a number of more complex photoproducts such as the coordination of the $^{\bullet}Co(CO)_3(PMePh_2)$ radical with photodissociated CO or $PMePh_2$ to yield $Co(CO)_4$ or $^{\bullet}Co(CO)_2(PMePh_2)_2$, respectively.

Further to this, time resolved infrared (TRIR) spectroscopic studies were carried out to further elucidate the photochemical pathways involved following irradiation and to gain information on the kinetics involved in these reaction pathways. Flash photolysis at either 308 nm or 355 nm in C_6D_6 solution under argon resulted in both cases in bleaching of the parent carbonyl bands with concomitant growth of a major product band at 1940 cm^{-1} which is shifted to lower energy by approximately 12 cm^{-1} compared to the parent absorption at 1952 cm^{-1}. Kinetic traces of the absorbance changes suggest the occurrence of two photo processes, although 355 nm irradiation results in a more intense 1940 cm^{-1} product band. The faster process has a 2nd order rate constant of 2 x 10^7 M^{-1} s^{-1} at 308 nm and 8 x 10^7 M^{-1} s^{-1} at 355 nm irradiation,

while the slower process has a higher rate constant of 9.6 x 10^5 M^{-1} s^{-1} following 308 nm irradiation compared to 2.4 x 10^5 M^{-1} s^{-1} following 355 nm photolysis. This suggests that the slower process is preferentially formed on 308 nm excitation. Previous studies of polynuclear metal carbonyls[48,49,50] suggests that CO dissociation is the preferential reaction observed following shorter wavelength irradiation. In contrast, pulsed laser photolysis of $Co_2(CO)_6(PMePh_2)_2$ in C_6D_6 solution under a CO atmosphere again results in bleaching of the parent absorption at 1952 cm^{-1} and growth of a product absorption at 1939 cm^{-1}. Analysis of the transient decay of the absorbance at 1939 cm^{-1} generated under CO following 308 nm irradiation, via a double exponential fit, suggests that two photoprocesses, which both absorb at 1940 cm^{-1} and both react with free CO. The faster component, with a second-order rate constant of 2.6 x 10^6 M^{-1} s^{-1} in C_6D_6, is attributed to $Co_2(CO)_5(PMePh_2)_2$ reacting with CO to regenerate the parent species, while the slower component, with a second order rate constant of 1.5 x 10^5 M^{-1} s^{-1} in C_6H_6, is attributed to reaction of photogenerated radical species $^{\bullet}Co(CO)_3(PMePh_2)$ with CO to form $Co(CO)_4$ via ligand dissociation.

5.2. Aims and Objectives

The aim of this study was to synthesise a number of novel pyrene-thiophene dyads linked by an ethynyl bridge and to investigate their photochemical, photophysical and electrochemical properties and what effect altering the thiophene terminal unit would have on these properties The associated dicobalt hexacarbonyl complexes of these dyads were also synthesised and their properties investigated in a similar manner to those of the dyads.

5.3. Experimental

5.3.1. Materials

All manipulations were carried out under an atmosphere of argon or nitrogen using standard schlenk techniques. All solvents were supplied by the Aldrich Chemicals Co. Dichloromethane, chloroform, diethyl ether, pentane and cyclohexane were dried over $MgSO_4$ prior to use. Ethanol and methanol were distilled over magnesium turnings and iodine before use. Tetrahydrofuran (THF) was distilled from sodium/ benzophenone ketyl solution and used immediately. Diisopropylamine was distilled over potassium hydroxide prior to use. All solvents used in emission and lifetime experiments were of spectroscopic grade and were used without further purification.. Silica Gel (Merck) was used as received. All mobile phases for column chromatography were dried over $MgSO_4$ before use. 5-bromo-2-thiophene carboxaldehyde was purified by distillation using a Büchi Kügelrohr apparatus. The starting materials 1-Trimethylsilyletynylpyrene and 1-ethynylpyrene were synthesised according to literature methods[51]. All other chemicals were obtained commercially and were used without further purification. All solutions were deoxygenated by purging with pure argon or nitrogen for ~10 mins. Column chromatography was carried out using neutral silica gel pH 6.5 – 7.5 or neutral Aluminium oxide.

5.3.2. Equipment

IR spectra were recorded on a Perkin-Elmer 2000 FT-IR spectrophotometer (2 cm^{-1} resolution) in a 0.1mm sodium chloride liquid solution cell using spectroscopic grade pentane, cyclohexane, dichloromethane. ^{1}H-NMR and ^{13}C-NMR were recorded on a Bruker AC 400 spectrophotometer in $CDCl_3$ or d_6-acetone and were calibrated according to the deuterated solvent peak. All UV-Vis spectra were measured in spectroscopic grade solvents on a Hewlett-Packard 8452A-photodiode-array spectrometer using a 1cm quartz cell. Elemental analysis of C, H, & N were carried out by the Chemical services Unit, University College Dublin using an Exeter Analytical CE-440 elemental analyser. All syntheses were performed using conventional laboratory glassware under an inert argon or nitrogen atmosphere. Melting points were measured on a Gallenkamp melting point apparatus. ESI mass spectra were obtained using a Bruker-Esquire LC_00050 electrospray ionization at positive polarity with cap-exit voltage of 77.2 V. Spectra were recorded in the scan range 100-1000 m/z with an acquisition time of 300-3000 μs and a potential of 30-70 V. Recorded spectra were the summation of 10 scans. Due to poor solubility and ionisation problems, mass spectrometry measurements could not be obtained for the dicobalt complexes using the available ESI instrumentation. Emission spectra (accuracy ± 5 nm) were recorded at 298 K using a LS50B luminescence spectrophotometer, equipped with a red sensitive Hamamatsu R928 PMT detector, interfaced with an Elonex PC466 employing Perkin–Elmer FL WinLab custom built software. Luminescence lifetime measurements were made using an Edinburgh Analytical Instruments (EAI) Time-Correlated Single-Photon Counting apparatus (TCSPC) as described by Browne et al.[52] Emission lifetimes were calculated using a single exponential fitting function, involving a Levenberg-Marquardt algorithm with iterative reconvolution (Edinburgh Instruments F900 software) and are ±10%. The χ^2 and residual plots were used to judge the quality of the fits. Cyclic voltammetry experiments were carried out using a CH instruments Model 600a electrochemical workstation at a scan rate of 0.1 VS^{-1}. Electrochemical studies were conducted using a three-electrode system with a 0.1 M solution of $TBAPF_6$ in anhydrous acetonitrile as the supporting electrolyte. The working electrode was either a 3 mm diameter Teflon shrouded glassy carbon or platinum electrode, which were polished before each use. The counter electrode was a platinum wire and the reference electrode was a non-

aqueous Ag/Ag^+ electrode. Deoxygenation of the solutions was achieved by bubbling through with argon for approximately 10 mins and a blanket of argon was maintained over the solution during all experiments. The filling solution for the non-aqueous Ag/Ag^+ reference electrode was 0.1 M $TBAPF_6$ and 0.1 mM $AgNO_3$ in anhydrous acetonitrile. All potentials are quoted with respect to the potentials of the ferrocene/ferrocenium couple ($E^{0'}$ = 0.31 V vs. Ag/Ag^+).

5.3.3. Synthesis

5.3.3.1. Introduction to Sonogashira-Hagihara cross coupling

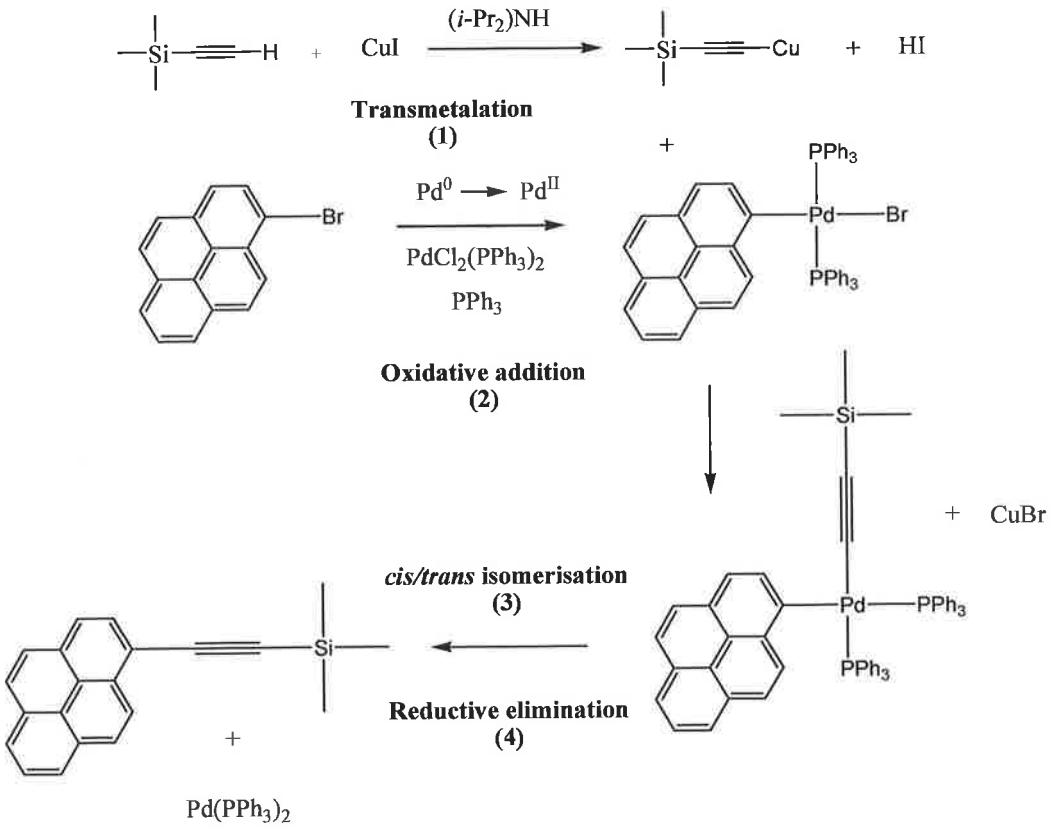

Scheme 5 Reaction mechanism for Sonogashira cross coupling reaction, using generation of trimethylsilylethynylpyrene as the sample compound.

The palladium catalysed Sonogashira cross coupling reaction[58] involves the coupling of terminal alkynes with aryl or vinyl halides in the presence of an amine base (Scheme 5). This procedure typically involves a Pd^0 catalyst such as $Pd(PPh_3)_4$ or $Pd(PPh_3)_2Cl_2$ and a copper (I) iodide co-catalyst in the absence of air or moisture, although less sensitive methods have been investigated[53]. In the case of $Pd(PPh_3)_2Cl_2$, two molar equivalents of PPh_3 must also be present in the reaction mixture. The Pd catalyst is oxidised to the Pd^{II} state and a cyclic reaction involving oxidative addition of the reactant to the palladium takes place. At the same time, transmetalation occurs, whereby, Cu(I) coordinates to the alkyne terminal end. This is followed by isomerisation of the Pd^{II} coordinated species and oxidative elimination to yield the final product.

The amine acts to neutralise any acidic species produced during the reaction. Apart from the original publication by Sonogashira and Hagihara[58] on this type of reaction a large number of other detailed publications exist. Suzuki and Miyaura[54] have compiled a very detailed review of Pd catalysed cross coupling reactions in organoboron compounds, while Negishi and Anastasia[55] have recently compiled a very detailed general overview of palladium-catalysed alkynlation reactions. Furthermore, Hanan et al[56]. have described the use of a Negishi cross-coupling reaction in the creation of a new binding site in a $Ru(bpy)_2$ complex. For a detailed review on the synthesis via Sonogashira and Negishi cross-coupling reactions of regioselective nitrogen-, oxygen, and sulphur containing heterocyclic systems, the reader is directed to a recent review by Bach et al.[57]

All ligands synthesised in this study were prepared using a Sonogashira cross-coupling reaction[58] with 1-ethynylpyrene in each case providing the pyrenyl group. 1-ethynylpyrene was initially prepared from 1-bromopyrene via a trimethylsilyl protected derivative.[51,59] The dicobalt hexacarbonyl ($Co_2(CO)_6$) substituted complexes were prepared by stirring the appropriate ligand and $Co_2(CO)_8$ in pentane at room temperature overnight under inert conditions. In the case of PyrCCThCHO and PyrCCThmal, dichloromethane was added to improve solubility of the ligand. The Sonogashira cross coupling reactions were catalysed by $PdCl_2(PPh_3)$(6 mol %), CuI (6 mol %) and PPh_3 (6 mol %) in the presence of *i*-Pr_2NH to remove the nascent acid formed.

5.3.3.2. TrimethylsilylpyrenylacetyleneCo$_2$(CO)$_6$

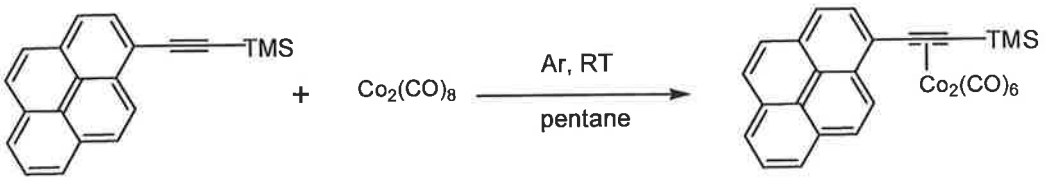

To a flame dried round bottom flask was added pentane (10 mL), which was purged with argon for 10 minutes. To this solution was then added 1-trimethylsilylethynylpyrene (0.150 g, 0.50 mmol) and $Co_2(CO)_8$ (0.170 g, 0.50 mmol). This solution was then stirred overnight at room temperature under inert conditions to yield a dark green solution. The crude product was then subsequently purified by column chromatography with silica gel and eluted with pentane to yield a dark green solution. Solvent was removed by rotary evaporation to yield a green residue, which was then recrystallised from hot hexane to yield the pure product.

Yield: 0.20 g, 0.34 mmol, 68% (based on PyrCCTMS)

IR (pentane) : 2086, 2051, 2024 cm^{-1}; UV-Vis (pentane) : 200, 238, 272, 284, 330, 344, 364, 384 nm; ^{1}H-NMR (400 MHz, $CDCl_3$) : 8.60ppm (d, 1H), 8.10ppm (m, 8H), 0.5ppm (s, 9H); ^{13}C–NMR (100 MHz, $CDCl_3$) : δ 134.42, 133.91, 131.26, 130.83, 130.54, 130.40, 130.18, 129.95, 129.39, 129.16, 129.10, 126.32, 126.10, 125.88, 125.71, 125.25, 124.18, 124.05, 123.88, 123.75, 123.30,

5.3.3.3. PyrenylacetyleneCo$_2$(CO)$_6$

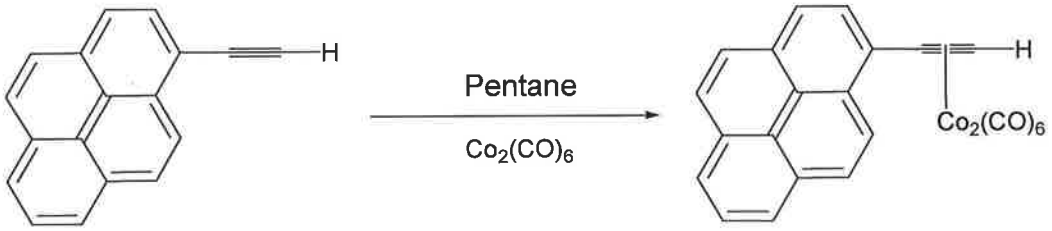

To a flame dried round bottom flask was added 1-ethynylpyrene (0.100 g, 0.44 mmol) and $Co_2(CO)_6$ (0.150 g, 0.44 mmol) and 15 mL n-pentane and 5 mL CH_2Cl_2 to improve the solubility of the ligand. This solution was then stirred overnight under inert conditions and under aluminium foil to exclude light. This resulted in the formation of a dark green-brown coloured solution. Solvent was removed by rotary evaporation .The dark brown residue was then purified by column chromatography on silica gel with a 20:80 CH_2Cl_2: petroleum ether mobile phase. The desired product eluted off the column as the first dark brown band. Solvent was removed by rotary evaporation to yield the desired product.

Yield: 0.160 g, 0.31 mmol, 70% (based on PyrCCH)

IR (pentane) : 2092, 2057, 2031 cm^{-1} ; UV-Vis (pentane) : 202, 234, 268, 386, 578 nm; ^{1}H-NMR (400 MHz, $CDCl_3$) : 8.6 ppm (s, 1H), 8.2 ppm (m, 8H), 7.0 ppm (s, 1H), 2.2 ppm (s, 1H); ^{13}C-NMR (100 MHz, $CDCl_3$) : 131.60, 131.37, 131.25, 131.12, 130.88, 128.05, 128.01, 127.50, 126.38, 125.79, 125.62, 124.83, 124.60, 124.18

5.3.3.4. 2-pyrenylacetylene-thiophene

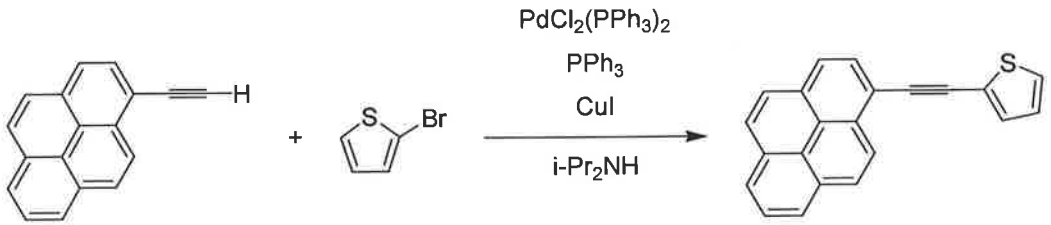

To freshly distilled and argon purged diisopropylamine (25 mL) was added 1-ethynylpyrene (0.200 g, 0.88 mmol), $PdCl_2(PPh_3)_2$ (0.037 g, 0.053 mmol, 6%), CuI (0.010 g, 0.053 mmol, 6%), PPh_3 (0.028 g, 0.106 mmol, 12 %). This solution was purged with argon for a further 5 mins. To this was then added 2-bromothiophene (0.085 mL, 0.88 mmol). This solution was then allowed to stir overnight under inert conditions and subsequently heated to reflux under inert conditions for 5 hours to yield a bright yellow solution. Solvent was removed under reduced pressure. The yellow residue was purified by column chromatography on silica gel with a 4:1 petroleum ether: CH_2Cl_2 mobile phase. The desired product eluted off the column as the first intense yellow band. Solvent was removed by rotary evaporation yielding a brightly coloured yellow solid.

Yield : 0.240g, 0.78 mmol, 88 %

IR (CH_2Cl_2) : ($\nu_{C\equiv C}$) 2199, ($\nu_{C=C}$) 1549 cm^{-1}; UV-Vis (CH_2Cl_2) : 236, 286, 304, 370, 396 nm; ^{1}H-NMR (400 MHz, $CDCl_3$) : 8.61 ppm (d, 1H), 8.15 ppm (m, 8H), 7.45 ppm (q, 1H, ^3J = 2.4 Hz, ^4J= 1.2 Hz), 7.37 ppm (q, 1H, ^3J = 4.0 Hz, ^4J= 1.2 Hz), 7.08 ppm (q, 1H, ^3J = 3.6 Hz ^4J= 1.6 Hz); ^{13}C-NMR (100 MHz, $CDCl_3$) : δ 131.0, 128.4, 127.4, 127.2, 126.4, 126.3, 126.2, 125.3, 124.7, 124.6, 124.4, 123.5, 116.4, 91.4, 87.2, 40.3, 28.7, 28.0, 21.6, 19.4, 13.3, 10.4; M.P. = 115-117 ° C; Mass Spec. ESI m/z 308.1; Anal. Calcd. for $C_{22}H_{12}S$, C 85.68 %, H 3.92 %, Found C 85.18 %, H 3.96 %

5.3.3.5. 2-pyrenylacetylene-thiophene$Co_2(CO)_6$

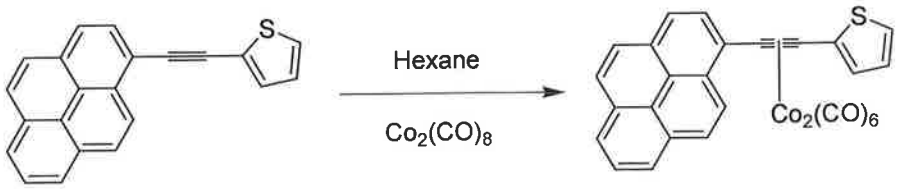

To argon purged hexane (20 mL) was added 2-pyrenylacetylene (0.104 g, 0.336 mmol) and $Co_2(CO)_8$ (0.116 g, 0.336 mmol) and a few drops of CH_2Cl_2 to improve solubility of the ligand. This solution was then stirred overnight under inert conditions and in darkness to exclude light. Overnight stirring resulted in the formation of a dark green-brown coloured solution . Solvent was removed by rotary evaporation to yield a dark green-brown residue. This was purified by column chromatography on silica gel with a hexane mobile phase. The desired product eluted off the column as an intense dark green-brown band. This fraction was collected and solvent removed by rotary evaporation to yield a dark green-brown coloured solid.

Yield : 0.070 g, 0.11 mmol, 33% (based on PyrCCTh)
IR (CH_2Cl_2) : 2089, 2056, 2028, 1602 cm^{-1}; UV-Vis (CH_2Cl_2) : 236, 286, 304, 352, 370, 396, 509 nm; ^{1}H-NMR (400 MHz, $CDCl_3$) : 8.61 ppm (d, 1 H) 8.13 ppm (m, 8H), 7.44 ppm (d, 1H, ^2J = 2.4 Hz), 7.37 ppm (d, 1H, ^2J = 4.8 Hz), 7.09 ppm (t, 1H, ^3J = 4.4 Hz, ^3J = 3.6); ^{13}C-NMR (100 MHz, $CDCl_3$) : δ 131.22, 129.39, 128.42, 128.38, 127.82, 127.40, 127.23, 127.00, 126.98, 126.64, 126.52, 126.44, 126.32, 126.26, 126.21, 124.67, 124.63, 124.67, 124.63, 124.60, 124.43, 123.43; Mass Spec. ESI m/z 308 [M^+-$Co_2(CO)_6$], 230.2 [$Co_2(CO)_4$], 202.2 [$Co_2(CO)_3$]

5.3.3.6. 2-bromo, 5-pyrcylacetylene-thiophene

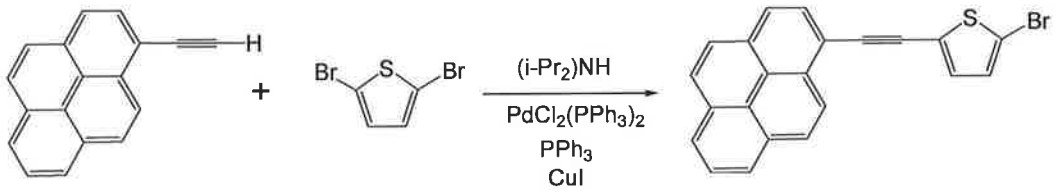

To 20 mL of freshly distilled diisopropylamine was added 1-ethynylpyrene (0.400 g, 1.77 mmol), 2,5-dibromothiophene (0.199 mL, 1.77 mmol), $PdCl_2(PPh_3)_2$ (0.0742 g, 0.106 mmol), CuI (0.0201 g, 0.106 mmol), and triphenylphosphine (0.055 g, 0.212 mmol). This dark brown coloured solution was then heated to reflux temperature overnight under inert conditions to yield an orange coloured solution. Solvent was removed under reduced pressure and the product was purified by column chromatography on silica gel with a 80:20 petroleum ether : dichloromethane mobile phase. The first bright yellow band to elute off the column was assigned to the desired product. Solvent was removed by rotary evaporation.

Yield: 0.210 g, 0.54 mmol, 30.6%

IR (CH_2Cl_2) : 2194 cm^{-1}; UV-Vis (CH_2Cl_2): 238, 286, 310, 378, 400, 436 nm; ^{1}H-NMR (400 MHz, $CDCl_3$) : 8.5 ppm (d,1H), 8.0 ppm (m,8H), 7.0 ppm (d, 1H, ^2J = 3.8 Hz), 7.2 ppm (d, 1H, ^2J = 3.8 Hz); ^{13}C-NMR (100 MHz, d^6-acetone) : 134.15, 132.74, 132.23, 132.05, 130.39, 130.06, 129.87, 129.59, 128.16, 127.63, 127.48, 127.34, 126.99, 125.76, 117.41, 101.01, 92.96, 87.50; M.P.: 133-135 ° C

5.3.3.7. 2-bromo, 5-pyrenylacetylene-thiophene$Co_2(CO)_6$

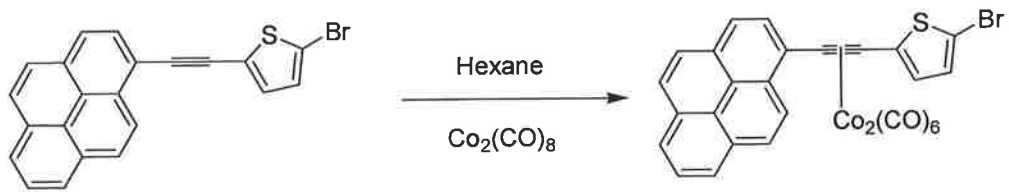

To argon purged hexane (20 mL) was added 2-bromo-5-ethynylpyrene-thiophene (0.100 g, 0.258 mmol) and $Co_2(CO)_8$ (0.088 g, 0.258 mmol). This solution was then stirred overnight under inert conditions to yield a dark green-brown coloured solution. Solvent was removed under reduced pressure to yield a dark green-brown residue which was purified by column chromatography on silica gel with petroleum ether (40:60°). The desired product eluted off the column as a dark green band. Solvent was removed by rotary evaporation to yield a dark green solid.

Yield : 0.098 g, 0.14 mmol, 54% (based on PyrCCThBr)
IR (CH_2Cl_2) : 2090, 2057, 2030 cm^{-1}; UV-Vis (Hexane) : 204, 236, 284, 308, 368, 396, 578 nm; ^{1}H-NMR (400 MHz, $CDCl_3$) : 8.43 ppm(d, 1H, J = 8 Hz), 8.24 ppm (m, 8H), 7.18 ppm (d, 1H, J = 4.0 Hz), 7.15 ppm (d, 1H, J = 4.0 Hz) ;

5.3.3.8. (5-(1-pyrenylacetylene)-2-thiophene)carboxaldehyde

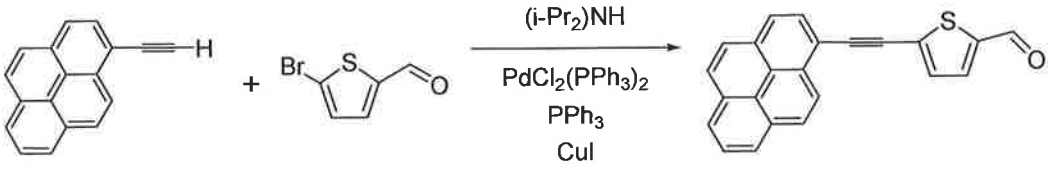

To 20 mL of freshly distilled, argon purged diisopropylamine was added 1-ethynylpyrene (0.226 g, 1.00 mmol), $PdCl_2(PPh_3)_2$ (0.0420 g, 0.06 mmol, 6%), CuI (0.0114 g, 0.06 mmol, 6%) and triphenylphosphine (0.0314 g, 0.12 mmol, 12%). To this was then added distilled 5-bromo-2-thiophenecarboxaldehyde (0.118 mL, 1.00 mmol). This solution was then stirred overnight under aluminium foil and under inert conditions to yield a bright yellow precipitate in solution. The solvent was removed under reduced pressure to yield a bright yellow solid, which was purified by column chromatography on silica gel and a 30:70 pentane/CH_2Cl_2 mobile phase. The desired product was isolated as a bright yellow-orange solid.

Yield: 0.230 g, 0.68 mmol, 68%

IR ($CHCl_3$) 1672, 2197 cm^{-1}; UV-Vis (CH_2Cl_2): 246, 286, 326, 352(sh.), 390(sh.), 404, 420, 372 nm; ^{1}H-NMR (400 MHz, $CDCl_3$): 9.86 ppm (s, 1H,), 8.50 ppm (d, 1H), 8.10 ppm (m, 8H), 7.69 ppm (d, 1H, J^2 = 3.9 Hz), 7.42 ppm (d, 1H, J^2 = 3.9 Hz); ^{13}C-NMR (100 MHz, $CDCl_3$) δ 133.13, 132.51, 132.10, 132.06, 131.18, 130.96, 129.67, 128.93, 128.85, 127.22, 126.48, 126.09, 126.04, 125.09, 124.61, 124.41, 124.17

M.P 120-122 °C; Mass Spec.: ESI m/z 336.1; Anal Calcd for $C_{23}H_{12}OS$: C 82.17 %; H 3.59 %; Found C 82.03 %, H 3.60%

5.3.3.9. (5-(1-pyrenylacetylene)-2-thiophene)carboxaldehyde$Co_2(CO)_6$

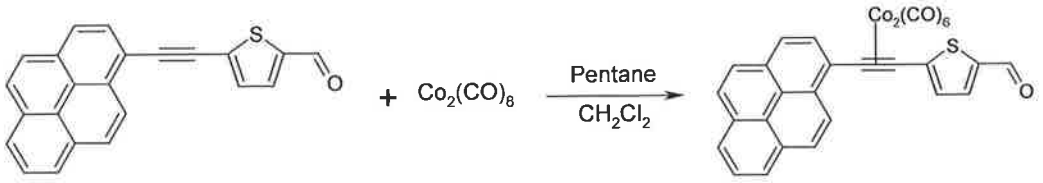

To a flame dried round bottom flask was added [5-(1-ethynylpyrene)-2-thienyl]carboxaldyde (0.100 g, 0.297 mmol) and dicobalt octacarbonyl (0.111 g, 0.326 mmol). To this was added pentane (20 mL) and 4-5 drops CH_2Cl_2 to improve the solubility of the aldehyde. This solution was then stirred overnight under inert conditions and under aluminium foil. This resulted in the formation of a dark green solution. Solvent was removed by rotary evaporation to yield a dark green solid. This was purified by column chromatography on silica gel with a 70:30 CH_2Cl_2: pentane mobile phase and the solvent removed by rotary evaporation to yield a dark green crystalline solid.

Yield: 0.152 g, 0.24 mmol, 83% (based on PyrCCThCHO)
IR (CH_2Cl_2) : 2093, 2060, 2033, 1664 cm^{-1}; UV-Vis (CH_2Cl_2) : 236, 282, 366, 390 and 602 nm; ^{1}H-NMR (400 MHz, $CDCl_3$) : 9.9 ppm (s, 1H), 8.3 ppm (d, 1H), 8.1 ppm (8H, m), 7.7 ppm (d, 1H, ^2J = 3.9 Hz), 7.2 ppm (s, 1H, ^2J = 3.9 Hz); ^{13}C-NMR (100 MHz, $CDCl_3$) : 182.80, 182.55, 182.49, 175.35, 143.49, 137.31, 133.46, 132.89, 131.69, 130.73, 128.30, 126.54, 125.99, 125.87, 125.62, 119.95, 118.94, 108.67; Anal Calcd for $C_{29}H_{12}O_7SCo_2$: C 55.97 %, H 1.94%, Found C 55.65 %, H 1.20 %

5.3.3.10. (5-(1-pyrenylacetylene)-2-thiophene)ethylene malonitrile

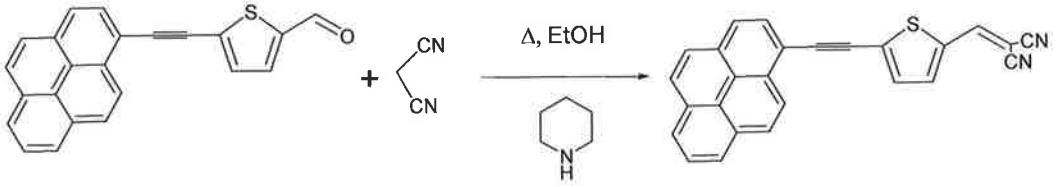

This dicyanovinyl derivative was synthesised via a Knoevenagel condensation reaction of the carboxaldehyde. To argon purged ethanol (40 mL), was added 5-(1-ethynylpyrene)-2-thiophene carboxaldehyde (0.230 g, 0.68 mmol), malonitrile (0.044 g, 0.042 mL, 0.68 mmol) and 3-4 drops piperidine. This yellow solution was then heated to reflux temperatures for 1 hr under inert conditions to yield a dark red solution. Solvent was removed under reduced pressure yielding a dark red-maroon coloured solid. This residue was purified by column chromatography on silica gel and eluted with CH_2Cl_2. The red-orange band was collected and the solvent removed by rotary evaporation to yield the desired red product.

Yield: 0.21 g, 0.55 mmol, 79%,

IR (CH_2Cl_2): ($\nu_{C=C}$) 1574, ($\nu_{C\equiv N}$) 2227, ($\nu_{C\equiv C}$) 2187 cm^{-1}; UV-Vis (CH_2Cl_2): 478 , 396, 356, 284, 274, 240 nm; ^{1}H-NMR (400 MHz, $CDCl_3$): 8.5 ppm (d, 1H), 8.2 ppm (m, 8H), 7.8 ppm (s, 1H), 7.7 ppm (d, 1H, J^2 = 4.0 Hz), 7.45 ppm (d, 1H, J^2 = 4.0 Hz); ^{13}C-NMR (100 MHz, $CDCl_3$) δ 148.7, 137.5, 134.6, 131.5, 131.2, 130.86, 130.13, 129.91, 128.78, 128.18, 126.18, 125.55, 125.28, 125.22, 123.96, 123.65, 112.88, 99.62; M.P.: 120-122 °C; Mass Spec.: ESI m/z 384.1; Anal Calcd for $C_{26}H_{12}N_2S$: C 81.22%; H 3.14%; N 7.28%; Found C 79.37 %, H 3.33 %, N 7.12 %.

5.3.3.11. (5-(1-pyrenylacetylene)-2-thiophene)ethylene malonitrile$Co_2(CO)_6$

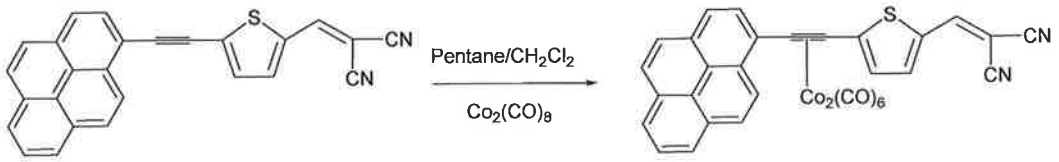

To 20 mL pentane was added 5-(1-ethynylpyrene)-2-thienyl]methylene malonitrile (0.100 g, 0.26 mmol), dicobalt octacarbonyl (0.097 g, 0.286 mmol, 10 % excess) and a few drops of CH_2Cl_2 to improve solubility This solution was then stirred overnight at room temperature under inert conditions to yield a dark green coloured solution. Solvent was removed by rotary evaporation and the resulting green-brown residue purified by column chromatography on silica gel with a 40:60 CH_2Cl_2:pentane mobile phase. The second dark green band due to the desired product was collected and the solvent removed by rotary evaporation to yield a dark green solid.

Yield: 0.107 g, 0.16 mmol, 62% (based on PyrCCThmal)

IR (CH_2Cl_2): (ν_{co}) 2093, 2062, 2035, (ν_{CN}) 2226, ($\nu_{C=C}$) 1569 cm^{-1}; UV-Vis (CH_2Cl_2) : 236, 276, 286, 350, 368, 386, 590 nm; ^{1}H-NMR (400 MHz, $CDCl_3$) : 8.30 ppm (d, 1H), 8.20 ppm (m, 8H), 7.75 ppm (s, 1H), 7.75 ppm (d, 1H, ^2J = 4.0 Hz), 7.30 ppm (d, 1H, ^2J = 4.0 Hz); ^{13}C-NMR (100 MHz, d^6-acetone) δ 172.3, 171.7, 166.6, 162.1, 158.4, 157.6, 157.1, 152.3, 151.6, 142.0, 140.8, 131.4, 130.8, 129.2, 128.4, 127.7, 127.0, 126.9, 126.7, 125.8, 119.9, 111.6, 109.6, 108.9, 104.6, 100.5, 100.0, 95.4, 55.1 ; Anal Calcd for $C_{32}H_{12}N_2O_6SCo_2$: C 57.33%; H1.80%; N 4.17%; Found C 57.03 %, H 1.85 %, N 4.18 %

5.3.3.12. [(5-bromo-2-thienyl)methylene]malonitrilebis$W(CO)_5$

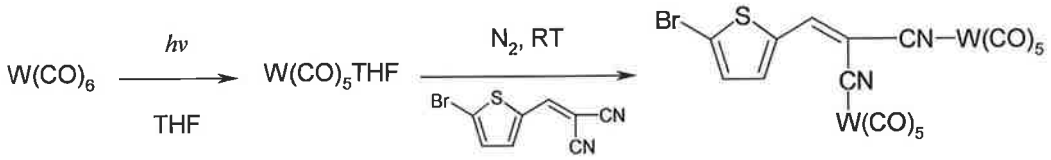

To a photolysis immersion well containing dry, argon purged tetrahydrofuran (THF) was added $W(CO)_6$ (1.055 g, 2.99 mmol). This was then photolysed under inert conditions for 4 hrs using a mercury lamp and formation of the desired $W(CO)_5THF$ adduct was confirmed by IR monitoring. This yellow solution was transferred under argon to a round bottom flask. To this was then added the gold coloured (5-bromo-2-thienyl)methylene malonitrile (0.300 g, 1.25 mmol). The solution, which quickly became red in colour was stirred overnight under inert conditions to yield a deep red coloured solution. The solvent and excess $W(CO)_6$ were removed under reduced pressure to give a red solid. This residue was purified by column chromatography on silica gel and eluted with CH_2Cl_2 to give a red solution yielding the desired red product on removal of the solvent by rotary evaporation. This complex demonstrated solvatochromism on dissolving in pentane or cyclohexane as it became strongly purple in colour, while in more polar solvents such as CH_2Cl_2, $CHCl_3$ or acetone it was red.

Yield: 0.86 g, 0.96 mmol, 77 % (based on BrThmal)

IR (CH_2Cl_2): ($\nu_{C=C}$) 1551 cm^{-1}; ($\nu_{C\equiv N}$) 2214 cm^{-1} (ν_{co}) 2075, 2070, 1948, 1918 cm^{-1}

(cyclohexane) : ($\nu_{C=C}$) 1551 cm^{-1}; ($\nu_{C\equiv N}$) 2214 cm^{-1} (ν_{co}) 2074, 1948, 1920 cm^{-1}

UV-Vis (CH_2Cl_2): 514, 374, 288, 248 nm

(cyclohexane): 574, 380, 284, 246 nm

^{1}H-NMR (400 MHz, $CDCl_3$) : 8.0 ppm (s, 1H), 7.6 ppm (d, 1H, ^2J = 4 Hz), 7.3 ppm (d,1H, ^2J = 4 Hz); ^{13}C-NMR (100 MHz, $CDCl_3$) : 194.66, 194.48, 190.12, 140.12, 136.14, 132.15

5.3.3.13. 2-pyrenylacetylene-5-trimethylsilylacetylene-thiophene

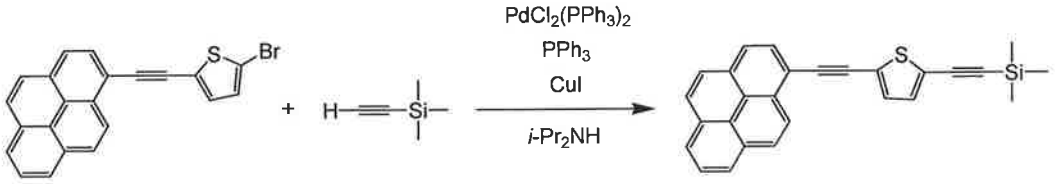

To freshly distilled and argon purged diisopropylamine (20 mL) was added 2-ethynylpyrene-5-bromo-thiophene (0.237 g, 0.612 mmol), $PdCl_2(PPh_3)_2$ (0.514 g, 0.073 g, 6%), CuI (0.0139 g, 0.073 g, 6%) and PPh_3 (0.0385 g, 0.147 mmol, 12%). This solution was purged for a further 5 mins with argon. To this solution was added trimethylsilylacetylene (0.259 mL, 0.612 mmol). This solution was then heated to reflux temperatures and stirred overnight under inert conditions yielding a luminescent green-purple solution. Solvent was removed under reduced pressure to yield a dark green-brown solid. The crude product was purified by column chromatography on silica gel with a 9:1 pentane:CH_2Cl_2 mobile phase. The desired product eluted off the column as the first green coloured luminescent band. Solvent was removed by rotary evaporation to yield a dark green-brown solid.

Yield : 0.102 g, 0.25 mmol, 42%

IR (CH_2Cl_2) : ($\nu_{c\equiv c}$) 2144, 2065 cm^{-1}, ($\nu_{c=c}$) 1644 cm^{-1}; UV-Vis (CH_2Cl_2) : 240, 274, 286, 310, 324, 388, 414 nm; ^{1}H-NMR (400 MHz, $CDCl_3$) : 8.55 ppm (d, 1H), 8.15 ppm (m, 8H), 7.27 ppm (d, 1H, ^2J =4 Hz), 7.16 ppm (d, 1H, ^2J = 4 Hz), 0.3 ppm (s, 9H).13C-NMR (100 MHz, $CDCl_3$) : δ 185.93, 185.60, 130.66, 130.27, 130.09, 129.74, 128.36, 127.12, 126.80, 126.28, 125.17, 124.61, 124.40, 124.38, 70.60, 69.14

5.3.3.14. 2-pyrenylacetylene-5-trimethylsilylacetylene-thiophene

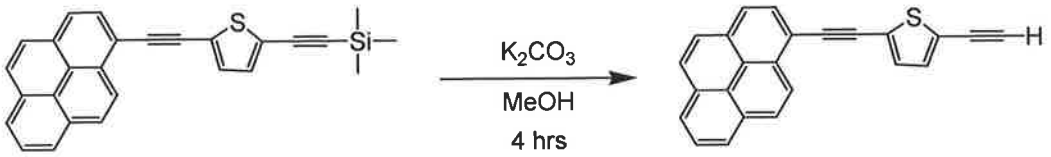

To freshly distilled and argon purged methanol (10 mL) was added 2-ethynylpyrene-5-trimethylsilylacetylene-thiophene (0.1022 g, 0.25 mmol).This was left to stir and once that latter had dissolved, K_2CO_3 (0.0052 g, 0.0375 mmol, 15%) was added. This solution was then allowed stir at room temperature for 4-5 hours. The solvent was then removed under reduced pressure and the resulting residue dissolved in 50 mL CH_2Cl_2. This solution was then washed with 4 x 25 mL aliquots of a 5% w/v aq. $NaHCO_3$ solution. The organic fractions were combined and dried over magnesium sulphate. The combined fractions were filtered and the solvent removed by rotary evaporation to yield a cream coloured solid with near quantitative yields.

Yield : 0.082 g, 0.25 mmol, 98%

IR (pentane): ($\nu_{c\equiv c}$) 2038, 2159 cm^{-1}; UV-Vis (pentane) : 284, 302, 316, 374, 382 and 404 nm; ^{1}H-NMR (400 MHz, $CDCl_3$) : 8.6 ppm (d, 1H), 8.2 ppm (m, 8H), 7.3 ppm (d, 1H, ^2J = 3.8 Hz), 7.2 ppm (d, 1H, ^2J = 3.8 Hz), 3.4 ppm (s, 1H); ^{13}C-NMR (100 MHz, d^6-acetone) : 141.87, 141.76, 136.83, 136.26, 134.43, 134.45, 133.39, 134.43, 13.20, 130.48, 129.92, 129.64, 129.11, 128.17, 127.65, 127.02, 125.78, 89.03, 84.96; M.P : 125-127 ° C

5.4. Results

5.4.1. UV-vis absorption spectra

Room temperature electronic and emission spectra in CH_2Cl_2 were obtained for all compounds in this study. Listed in Table 1 are the absorption maxima (λ_{max}) and extinction coefficient values (ε) for all compounds in this study. All compounds exhibit strong absorption bands in the UV-Vis region of the spectrum normally associated with ligand localised $\pi \rightarrow \pi^*$ transitions[28]. All UV-Vis spectra were recorded in spectrophotometric grade CH_2Cl_2, with the exception of PyrCCTMS and PyrCCThCCH, which were recorded in pentane. For all ligands and complexes in this study the electronic absorption spectra contain bands between 240 and 280 nm, which may be assigned to ligand based transitions on both the pyrene and thiophene groups. A typical UV-Vis spectrum for these type of systems and their Co2(CO)6 complexes in shown below in Figure 20. For the $Co_2(CO)_6$ complexes a weak low energy band is also observed between 580-600 nm. This may be assigned to a weak Co ($d\pi$) $\rightarrow$ ligand (π) charge-transfer (MLCT) transition. In the complex [BrThmal$(W(CO)_5)_2$] a broad low energy band is observed at 500 nm. This is similarly assigned as being MLCT in nature, involving charge transfer from tungsten to the thiophene-based ligand.

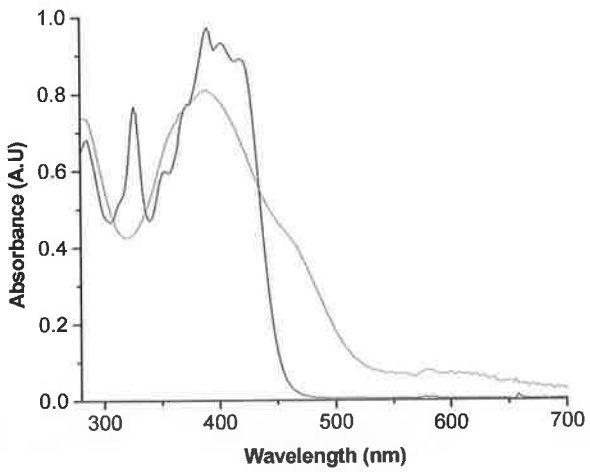

Figure 20 Representative UV-Vis spectra of the pyrene-thiophene dyads in CH_2Cl_2 solution. Shown are PyrCCThCHO (—) and the associated complex PyrCCThCHO$Co_2(CO)_6$ (—). The remaining UV-Vis spectra of the dyads in the study are shown in the appendix .

Table 1 Absorption properties and extinction coefficients (ε) for compounds in this study

	λ_{max} (nm), ε (x 10^7 $M^{-1}cm^{-1}$)
PyrCCTMS	238 (3.22), 248 (3.19), 272 (2.50), 284 (1.60), 330 (1.86), 344 (2.99), 364 (1.30), 384 (2.03)*
$PyrCCTMSCo_2(CO)_6$	236 (4.17)†,272 (2.94)† 284 (2.77)†, 330 (1.34)†, 344 (1.64)†, 364 (1.90)†, 388 (2.41)†, 580 (1.02)*
PyrCCH	272 (2.30), 284 (1.04), 314 (7.11)*, 328 (1.84), 342 (2.11), 360 (1.31), 384 (3.75)*
$PyrCCHCo_2(CO)_6$	236 (4.93), 268 (3.16), 386 (3.06), 580 (2.35)*
PyrCCTh	286 (3.13), 304 (2.70), 370 (3.24), 396 (2.15)
$PyrCCThCo_2(CO)_6$	236 (1.79)†, 286 (4.64)†, 304 (4.01)†, 352 (4.29)†, 370(3.92)†, 396 (2.60)†, 580
PyrCCThBr	286 (3.39), 310 (2.97), 378 (4.06), 400 (3.06)
$PyrCCThBrCo_2(CO)_6$	238 (4.93)†, 286 (3.44)†, 310 (2.42)†, 354 (2.49)†, 378 (3.33)†, 402 (3.31)†, 580 (7.33)*
PyrCCThCHO	286 (3.04), 326 (3.11), 352 (2.33), 372 (3.46), 390 (3.92), 402 (3.88), 420 (3.59)
$PyrCCThCHOCo_2(CO)_6$	238 (4.85), 280 (3.82), 360 (2.23), 388 (2.42), 580 (1.69)*
PyrCCThmal	274 (1.88), 284 (2.07), 294 (1.26), 356 (3.37), 396 (1.93), 478 (2.92)
$PyrCCThmalCo_2(CO)_6$	236 (6.07), 276 (4.95), 282 (5.04), 350 (3.33), 368 (3.81), 386 (4.35), 590 (3.06)*
$BrThmal(W(CO)_5)_2$	288 (2.11), 362 (2.28), 374 (2.70), 516 (1.05)
PyrCCThCCTMS	240, 274, 286, 310, 324, 388, 414
PyrCCThCCH	274 (8.07)*, 284 (1.13), 302 (8.07)*, 316 (1.20), 374 (2.03), 382 (1.56), 404 (1.54)

* ε = x 10^6 M^{-1} cm^{-1}; † ε = x 10^8 M^{-1} cm^{-1}

5.4.2. Fluorescence studies

Room temperature emission studies of the ligands and complexes in this study were carried out in CH_2Cl_2 as were lifetimes using the single photon counting (SPC) technique. For all organic ligands in this series, irradiation of each of the different absorption bands resulted in the same emission band. Solutions were prepared such that they were isoabsorptive at a selected wavelength, having an optical density in solution of approximately 0.3 A.U. Complexation with $Co_2(CO)_6$ however strongly quenched the strong emission observed for the uncomplexed ligands. No shift in the position of these bands were observed, which suggests that following complexation the origin of the emission band is ligand based. As is evident in Table 2 visible excitation led to structured luminescence in all pyrenyl-acetylide compounds in this study.

Table 2 Luminescence properties (298 K and 77 K) of the ligands and the complexes

	298 K[a]		77 K[b]	
	λ_{em} (nm)	τ (ns)	λ_{em} (nm)	τ (ns)
PyrCCTMS	387, 406	2.1, 2.1	384, 404, 420	2.7, 70.9
PyrCCTMS$Co_2(CO)_6$	391, 409	2.3, 2.4	384, 405	42.2, 1.01
PyrCCH	385, 405	17.0	382, 393, 403, 420	91.7, 27.6
PyrCCH$Co_2(CO)_6$	395, 425, 540	17.9	377, 420, 482, 530	3.35, 0.44
PyrCCTh	404, 425	0.16	404, 425	4.91, 1.77
PyrCCTh$Co_2(CO)_6$	400, 424	0.14	400, 424	0.87, 74.8
PyrCCThBr	410, 430	0.64	410, 430, 445	0.45, 30.9
PyrCCThBr$Co_2(CO)_6$	410, 430	0.63	360,404, 430, 443	0.75, 1.29
PyrCCThCHO	503	0.88	444, 468	55, 1.0
PyrCCThCHOCo_2CO_6	503	0.23	445	0.52, 70.9
PyrCCThmal	612	1.16	520	1.73
PyrCCThmal$Co_2(CO)_6$	612	0.99	516	0.96
BrThmal$(W(CO)_5)_2$	390[d]	-	385, 420, 435	-
PyrCCThCCH	420, 440	1.1, 0.2	415, 440, 455	3.72, 1.49

Room temperature (298 K) luminescence spectra and excited state lifetimes recorded in spectrophotometric grade dichloromethane [b]Spectrum recorded in hexane.[c] Low-temperature (77 K) luminescence spectra and excited state lifetimes recorded in 4:1 EtOH:MeOH. [d]Emission intensity too weak to be accurately measured using available instrumentation.

5.4.3. Cyclic voltammetry studies

Cyclic voltammetry studies were carried out on all ligands and complexes in a 0.1 M $TBAPF_6/CH_3CN$ electrolyte solution with a Teflon shrouded platinum working electrode (3 mm diameter), a platinum wire counter electrode and a non-aqueous Ag/Ag^+ reference electrode. The filling solution for the non-aqueous Ag/Ag^+ reference electrode was 0.1 M $TBAPF_6$ and 0.1 mM $AgNO_3$ in anhydrous acetonitrile. All potentials are quoted in volts vs. Ag/Ag^+ reference electrode with respect to the Fc^+/Fc redox pair. Scan rate is 100 mV S^{-1} unless otherwise stated. E_{ap} corresponds to an irreversible anodic process. E_{cp} corresponds to an reversible cathodic process. $E_{½}$ corresponds to a reversible electrode process, it is assumed that $E_{½} \approx E^{o\prime}$. The half-wave potential $E_{½} = (E_{ap}-E_{cp})/2$ and $\Delta E_p = E_{ap}-E_{cp}$. Table 3 indicates the electrochemical data obtained for all ligands and complexes in this study

Table 3 Electrochemical properties at room temperature

Complex	E_{ap} or $E_{½}$ (V) [ΔE_p (mV)]	E_{cp} or $E_{½}$ (V) [ΔE_p (mV)]
PyrCCTMS	0.41, 0.75, 0.97	-1.95, -1.75, -1.60
PyrCCTMS-$Co_2(CO)_6$	0.16, 0.39, 0.51, 0.64, 0.86, 0.97	-1.95, -1.76, -1.56, -1.28, -1.16
PyrCCH	0.649, 1.09	-0.39, -1.35
PyrCCH-$Co_2(CO)_6$	0.51, 0.64, 0.95, 1.07,	-1.27(71)
PyrCCTh	0.02, 0.90	-2.11, -1.56, -1.81, -1.21(81)
PyrCCTh-$Co_2(CO)_6$	0.56, 0.92	-1.91, -1.71, -1.20 (86)
PyrCCThBr	0.95, 1.07	-2.08(49), -1.84, -1.22,
PyrCCThBr-$Co_2(CO)_6$	0.67, 0.95, 1.02	-1.07, -1.19, -1.88
PyrCCThCHO	1.02	-1.88 (98), -1.67(56)
PyrCCThCHO-$Co_2(CO)_6$	0.56, 0.69, 0.99(45),	-1.86(44), -1.66(59), -1.48, -1.18, -1.09
PyrCCThmal	0.48, 1.03	-1.64, -1.36, -1.10(42)
PyrCCThmal-$Co_2(CO)_6$	0.92, 0.71, 0.56, 0.36,	-1.37, -1.14(74)
BrThmal$(W(CO)_5)_2$	0.77, 0.32	-1.26(81), -1.06, -0.90, -0.82, -0.62
PyrCCThCCH	1.00	-1.06, -1.26, -1.83

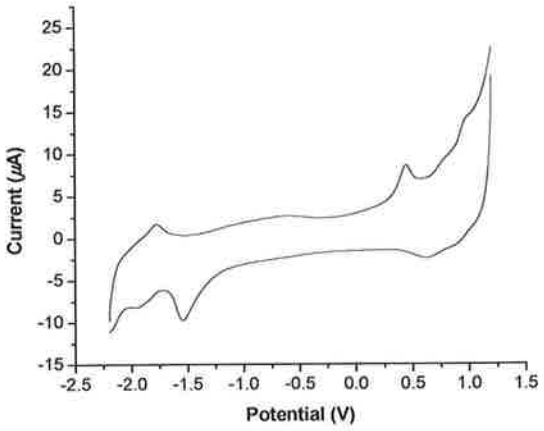

PyrCCTMS

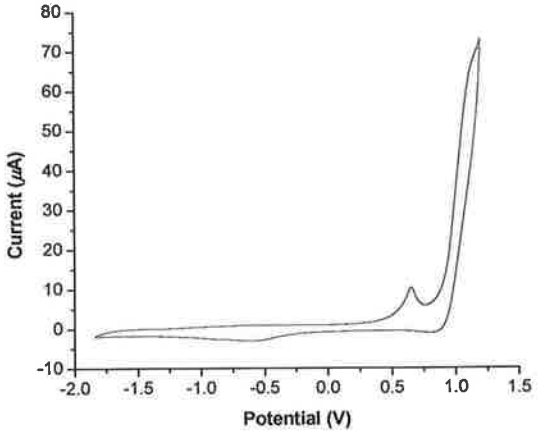

PyrCCH

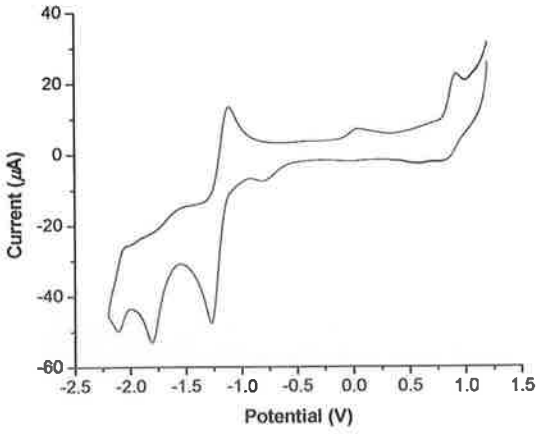

PyrCCTh

Figure 21 Cyclic Voltammogram of PyrCCTMS, PyrCCH and PyrCCTh showing oxidation and reduction waves

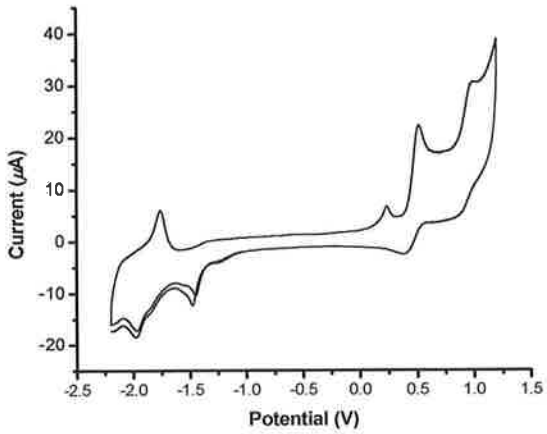

PyrCCTMS$Co_2(CO)_6$

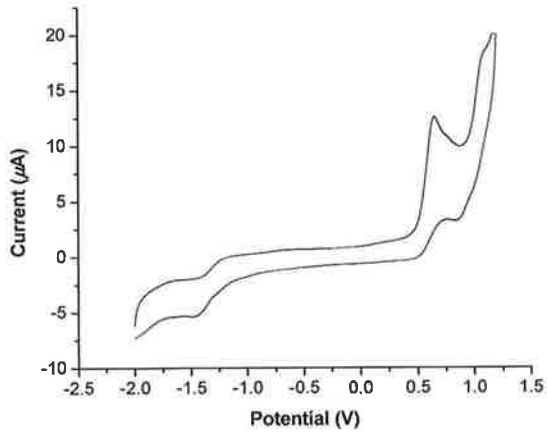

PyrCCH$Co_2(CO)_6$

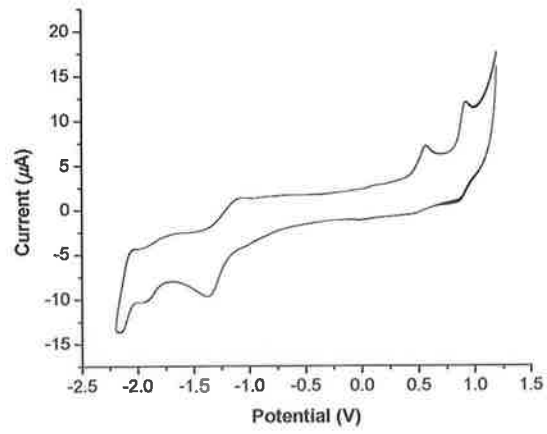

PyrCCTh$Co_2(CO)_6$

Figure 22 Cyclic Voltammogram of PyrCCTMS$Co_2(CO)_6$, PyrCCH$Co_2(CO)_6$ and PyrCCTh$Co_2(CO)_6$ showing oxidation and reduction.

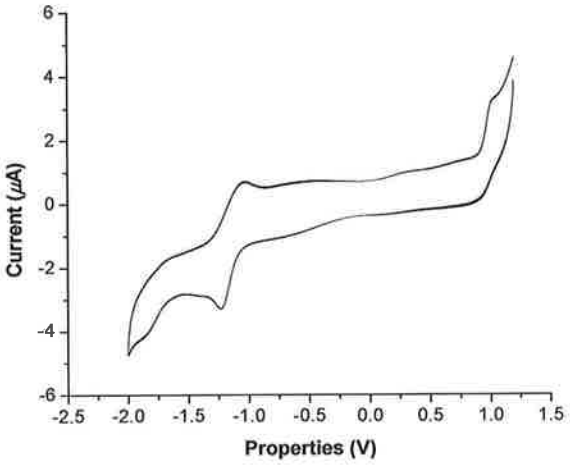

PyrCCThCCH

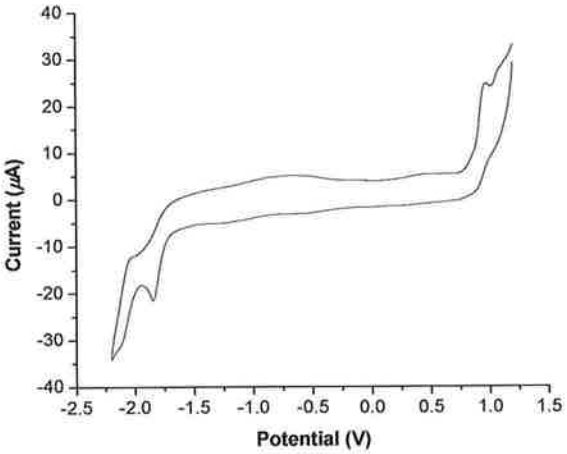

PyrCCThBr

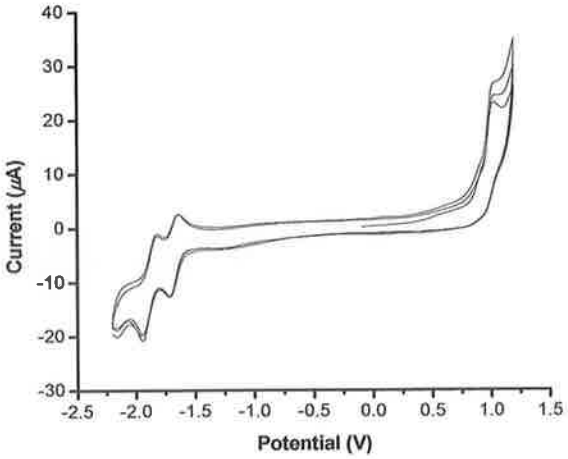

PyrCCThCHO

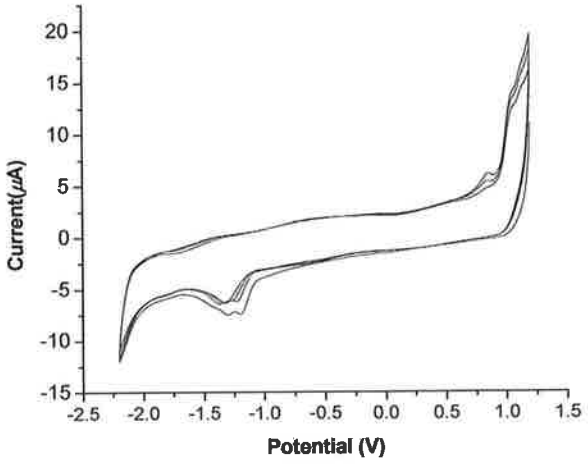

PyrCCThmal

Figure 23 Cyclic Voltammogram of PyrCCThCCH, PyrCCThBr, PyrCCThCHO and PyrCCThmal showing oxidation and reduction waves.

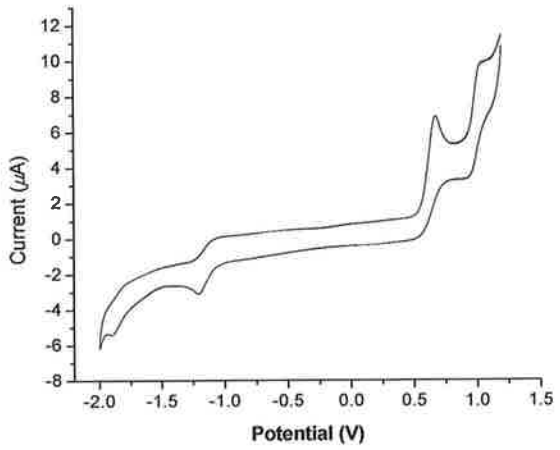

PyrCCThBrCo$_2$(CO)$_6$

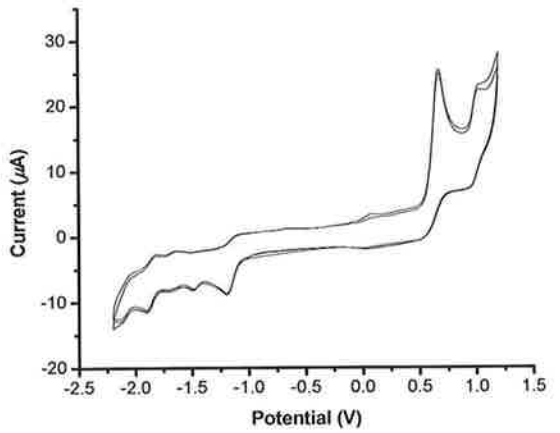

PyrCCThCHOCo$_2$(CO)$_6$

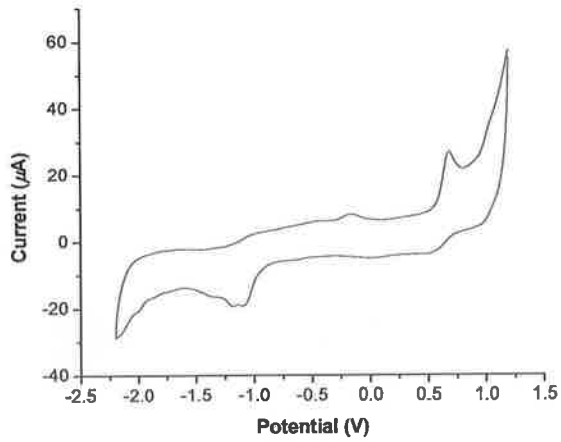

PyrCCThmalCo$_2$(CO)$_6$

Figure 24 Cyclic Voltammogram of PyrCCThBrCo$_2$(CO)$_6$, PyrCCThCHOCo$_2$(CO)$_6$ and PyrCCThmalCo$_2$(CO)$_6$ showing oxidation and reduction waves

5.4.4. Steady-State Photolysis

Broadband photolysis of the dicobalt hexacarbonyl complexes in this study with visible light (λ_{exc} > 520 nm and λ_{exc} > 400 nm) in the presence of the trapping ligand PPh_3 resulted in formation of a pentacarbonyl species. In each case, product bands were assigned by comparison with carbonyl bands of $Co_2(CO)_5$ type species in the literature. Overall, irradiation at > 520 nm appears to result in the weak production of the PPh_3 trapped pentacarbonyl species, although the efficiency for formation of this species does appear to be dependent on the terminal units in the complex. Following higher energy irradiation at > 400 nm an improved efficiency for pentacarbonyl formation is observed. Furthermore, for a number of systems formation of the tetracarbonyl as a minor photoproduct is also observed. The bands observed and assigned to formation of the pentacarbonyl and tetracarbonyl species respectively are in good agreement with those observed previously for similar $Co_2(CO)_5$ and $Co_2(CO)_4$ systems by Chia[45], Gordon[46], and Long[47].

Table 4 The M-CO band positions in pentane for the parent dicobalt hexacarbonyl complexes and the photoproducts observed in this study

Complex	ν_{co} ($cm^{-1} \pm 2\ cm^{-1}$)
PyrCCTMS$Co_2(CO)_6$ (*Parent*)	2086, 2051, 2024
PyrCCSiMe$_3$($Co_2(CO)_5$)(PPh_3)	2059, 2012. 2001, 1984
PyrCCSiMe$_3$($Co_2(CO)_4$)(PPh_3)$_2$	1968, 1941
PyrCCH$Co_2(CO)_6$ (*Parent*)	2092, 2057, 2030
PyrCCH($Co_2(CO)_5$(PPh_3)	2064, 2017, 2005,
PyrCCH($Co_2(CO)_4$(PPh_3)$_2$	1979, 1971, 1947
PyrCCTh$Co_2(CO)_6$ (*Parent*)	2090, 2057, 2031
PyrCCTh$Co_2(CO)_5$(PPh_3)	2064, 2021, 2007,
PyrCCTh$Co_2(CO)_4$(PPh_3)$_2$	1973, 1924
PyrCCThBr$Co_2(CO)_6$ (*Parent*)	2091, 2058, 2033
PyrCCThBr$Co_2(CO)_5$(PPh_3)	2064, 2022, 1974
PyrCCThCHO$Co_2(CO)_6$ (*Parent*)	2093, 2060, 2033
PyrCCThCHO($Co_2(CO)_5$)(PPh_3)	2067, 2022, 2013, 2001, 1975
PyrCCThmal$Co_2(CO)_6$ (*Parent*)	2093, 2062, 2035
PyrCCThmal($Co_2(CO)_5$)(PPh_3)	2067, 2025, 2014, 2001, 1977
PyrCCThmal($Co_2(CO)_4$)(PPh_3)$_2$	1964, 1948

5.5. Discussion

5.5.1. Room temperature emission studies and lifetimes measurements

As shown in Figure 25 both PyrCCTMS and PyrCCH exhibit sharp, strong room-temperature dual emission bands at 385 nm and 405 nm with a weak shoulder also exhibited in both at approximately 428 nm following excitation into all of the observed absorbance bands. A very small shift in band position of 2 cm^{-1} is observed between PyrCCTMS and PyrCCH, thereby suggesting that in both cases the same excited state is responsible for the observed emission.

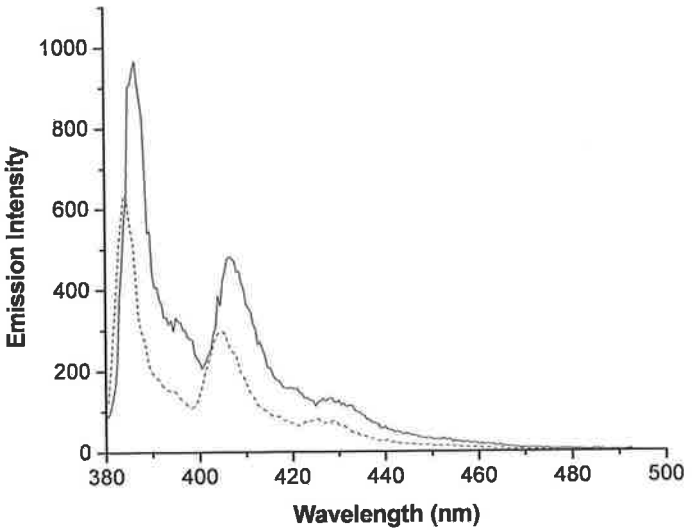

Figure 25 Emission spectra for PyrCCTMS (—) and PyrCCH (----) in CH_2Cl_2 solution at room temperature (298 K) following 345 nm excitation

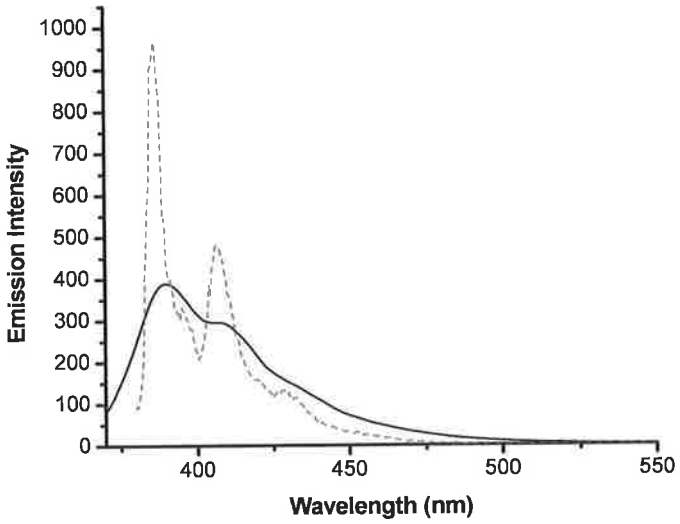

Figure 26 Room temperature (298 K) emission spectra of PyrCCTMS and the hexacarbonyl complex PyrCCTMS$Co_2(CO)_6$ in CH_2Cl_2. The emission spectra of the uncomplexed ligand is represented by (----) while that of the $Co_2(CO)_6$ complex is indicated by (—).

On complexation with $Co_2(CO)_6$ to give PyrCCTMS$Co_2(CO)_6$ and PyrCCH$Co_2(CO)_6$) the emission bands for the products are much broader and are significantly reduced in intensity (Figure 26). However, no shift in band position or generation of new emission bands were observed. This suggests that for both, PyrCCTMS and PyrCCH and the corresponding complexes, PyrCCTMS$Co_2(CO)_6$ and PyrCCH$Co_2(CO)_6$, the emission observed is solely ligand based, with no significant MLCT contribution. Furthermore, little change in the singlet excited state lifetime ($^1\tau$) is observed in going from PyrCCTMS ($^1\tau$ = 2.1 ns for both emission bands) to the $Co_2(CO)_6$ complex PyrCCTMS$Co_2(CO)_6$ ($^1\tau$ = 2.3 ns and 2.4 ns). However, interestingly the PyrCCH ligand possesses a much longer lived singlet excited state ($^1\tau$ = 17.0 ns). In contrast to the TMS precursor, coordination of the metal carbonyl system not only results in a decrease in intensity of the emission band but also in significant broadening and a red-shift of approximately 25 nm in the λ_{max} position to approximately 425 nm. However, little change is observed in the excited state lifetime of 17.9 ns observed for PyrCCH$Co_2(CO)_6$, compared to that of 17.0 ns observed for the uncomplexed ligand.

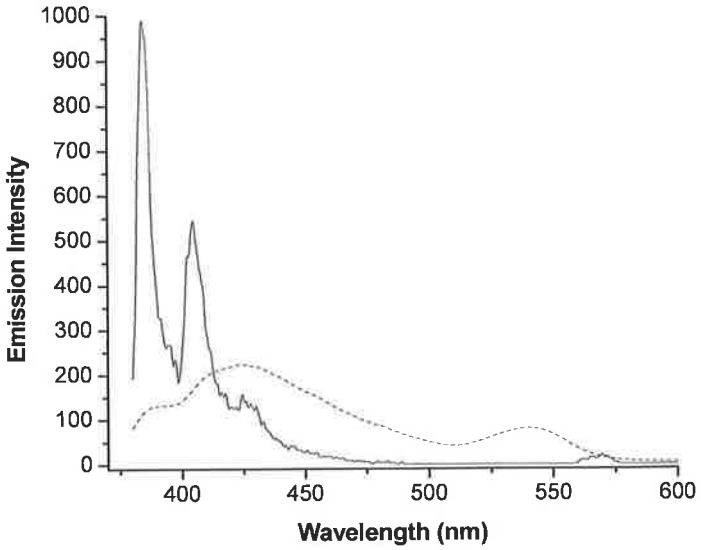

Figure 27 Overlay of emission spectra of PyrCCH (—) and its complex $PyrCCHCo_2(CO)_6$ (---) in room temperature CH_2Cl_2 following 280 nm excitation respectively.

This ligand based emission from compounds bearing a pyrenylacetylide unit has been previously observed and assigned by a number of authors, as arising from IL charge transfer excited states.[11,29,30] The excitation spectra of both ligands in CH_2Cl_2 are also superimposable with their absorption spectra above 280 nm further suggesting emission from a ligand based excited state.

PyrCCTh is the least electron withdrawing thiophene based analogue in this study. As shown in Figure 28, PyrCCTh exhibits two intense emission bands at 404 and 425 nm following excitation at 298 K in CH_2Cl_2 solution, although the most intense emission is observed following 370 nm excitation. These emission bands are similar to those observed for both PyrCCTMS and PyrCCH although they are shifted to higher energy by approximately 20 cm^{-1}. This shift to high energy of the emission bands may be explained in terms of increased electronegativety on coordination of the thiophene subunit. The emission bands are also significantly shorter lived with a singlet lifetime in the order of 0.2 ns, approximately an order of magnitude lower than the PyrCCTMS analogue.

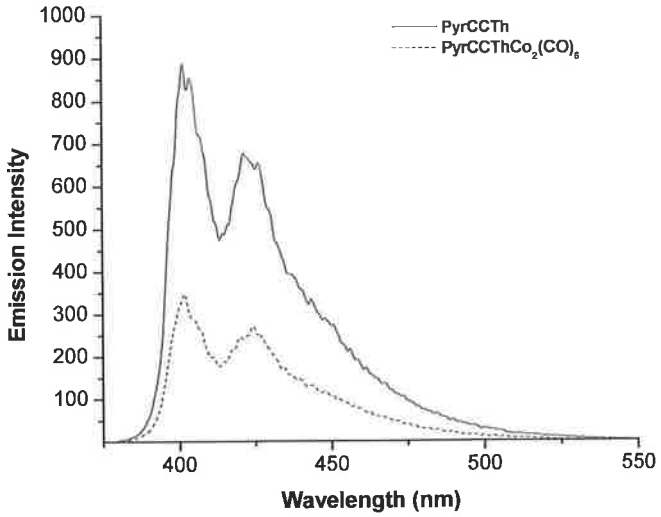

Figure 28 Room temperature emission spectra of PyrCCTh (—) and its $Co_2(CO)_6$ complex (---) following excitation at 305 nm in CH_2Cl_2 solution.

As previously observed for both PyrCCTMS and PyrCCH, complexation of PyrCCTh with $Co_2(CO)_6$ does not significantly shift the position of the emission bands although it does markedly reduce the emission intensity (Figure 28). Furthermore, the excited state lifetime of the dicobalt complex, $PyrCCThCo_2(CO)_6$, is 0.14 ns. This suggests that the room temperature emission is again ligand based with no significant contributions from the coordinated metal centres.

Extending the π-conjugation of this system by the addition of another ethynyl unit in the 5-position of the thiophene ring results in a broadening of the absorbances in the region 380-400 nm as well as an extension to the blue, by approximately 20 nm, of the absorbance maximum. Excitation of each of the absorbance bands of PyrCCThCCH, results in two partially overlapping emission bands at 420 nm and 440 nm respectively, as shown in Figure 29. However, the most intense emission spectrum is observed following excitation at 320 nm, with the observed emission bands becoming progressively weaker in intensity on excitation of the higher energy absorbance bands at 306 and 276 nm. As demonstrated in Figure 29 the emission profile of PyrCCThCCH is very similar to those observed for PyrCCTMS, PyrCCH and PyrCCTh although the emission maxima at 420 and 440 nm are red-shifted by 33 nm, 10 nm and 15 nm, respectively.

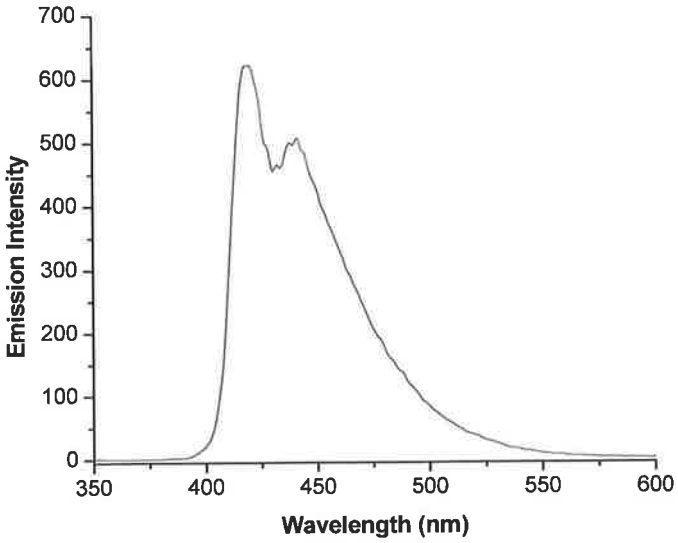

Figure 29 Room temperature emission band of PyrCCThCCH following 320 nm excitation in CH_2Cl_2 solution.

The lifetime decay of this dual emission was measured in CH_2Cl_2 and it was found that the best fit, was achieved using a bi-exponential function, where $\chi^2 = 1.093$, giving excited state lifetimes of 1.1 ns and 0.2 ns for the 420 nm and 440 nm emission bands respectively. The former excited state lifetime of 1.1 ns due to the 420 nm centred emission band is similar to that observed for PyrCCTMS, while the latter shorter lifetime of the 440 nm centred emission is similar to that observed for PyrCCTh. These lifetimes are however, noticeably shorter lived than that observed for PyrCCH.

PyrCCThBr similarly displays two sharp, intense partially overlapping emission bands at 410 nm and 430 nm. This dual emission is observed on excitation at all absorbance wavelengths, although the most intense as shown in Figure 30, are observed following 286 nm excitation in CH_2Cl_2 solution. The excited state singlet lifetime of this dual emission was measured as 0.64 ns in room temperature CH_2Cl_2 solution.

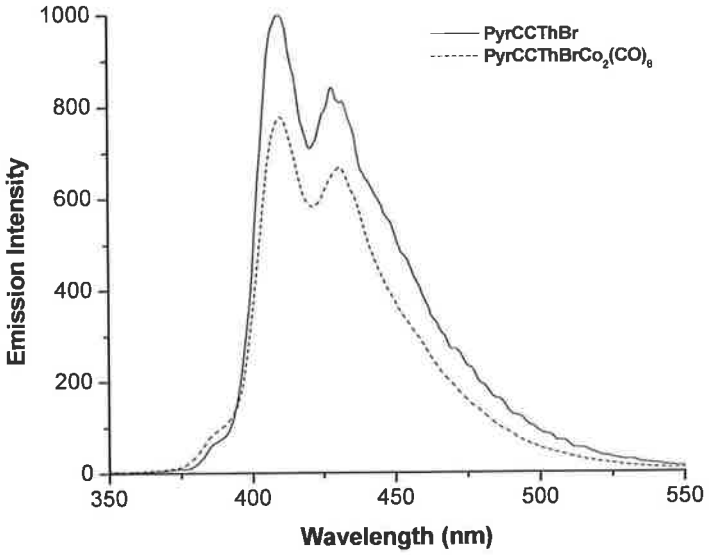

Figure 30 Room temperature emission bands of PyrCCThBr (—) and $PyrCCThBrCo_2(CO)_6$ (---) following 286 nm excitation in CH_2Cl_2 solution

Following complexation to yield the dicobalt hexacarbonyl complex, $PyrCCThBrCo_2(CO)_6$, room temperature emission was observed at 410 and 430 nm following excitation at 286 nm. As observed for the free ligand excitation at 286 nm results in the most intense emission spectrum. As is evident from Figure 30 complexation of the PyrCCThBr ligand with $Co_2(CO)_6$ does not appear to result in a change in the emission band position. Moreover, as previously observed, complexation results in a reduction in emission band intensity. This small reduction in intensity of approximately 20 % is striking, especially when compared to previous fluorescence quenching following complexation of PyrCCTMS, PyrCCH, and PyrCCTh, where a 50 -70 % reduction in band intensity was observed on complexation. The lifetime of the complex was measured at 0.63 ns, which is similar to that observed for the PyrCCThBr ligand, suggesting that overall that little change in either the emission band intensity of excited state lifetime is observed on complexation..

In contrast to the previously discussed systems, all of which display dual emission, both PyrCCThCHO and PyrCCThmal exhibit a single broad, intense room temperature emission band centred at 503 nm and 612 nm respectively. This red-shift

of approximately 100 nm (Figure 31) observed on changing from an aldehyde to a dicyanovinyl terminal end, may be assigned to intramolecular charge transfer (ICT), arising as a result of improved electron-accepting ability of the dicyanovinyl unit.

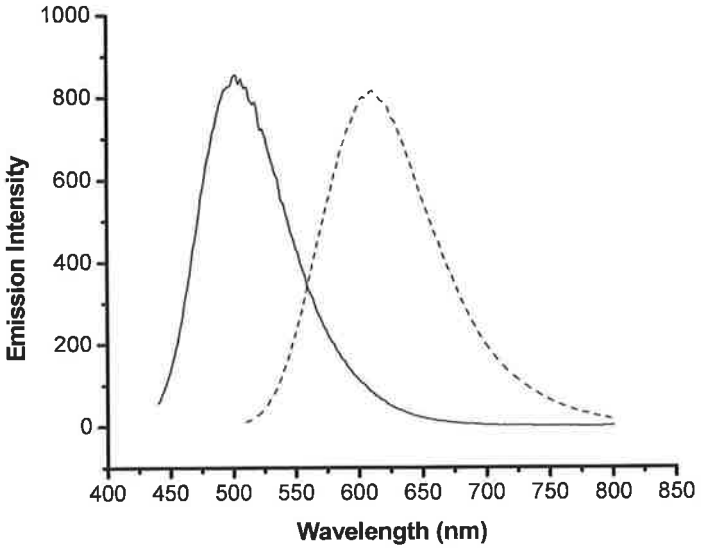

Figure 31 Room temperature emission spectra of PyrCCThCHO (—) and PyrCCThmal (----) in CH_2Cl_2, illustrating the red-shift of approximately 100 nm of the emission band of the dicyanovinyl derivative.

The singlet lifetimes ($^1\tau$) of the emissive excited states of species PyrCCThCHO and PyrCCThmal have been measured as 0.88 and 1.16 ns respectively. These lifetimes are similar to literature values for similar pyrene-thiophene compounds[27,28]. The fluorescence intensity does not appear to be reduced in the presence of oxygen, presumably as a result of the very short lifetimes observed. The emission observed may be assigned to ligand based intramolecular charge transfer involving a photo-excited pyrene$^+$-thiophene$^-$ state (Scheme 6) as proposed by Benniston and co-workers.[27]

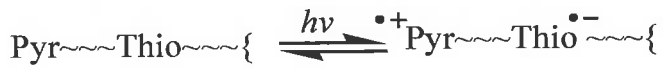

Scheme 6 Pictorial representation of the intramolecular charge transfer process observed on excitation of pyrene-thiophene dyad systems[27]

On coordination of $Co_2(CO)_6$ leading to formation of PyrCCThCHO$Co_2(CO)_6$ and PyrCCThmal$Co_2(CO)_6$, a significant reduction in intensity of the emission bands are

observed. However, as previously observed no shift in the emission band is observed. This suggests that the emission of the complexed species is, as before, entirely ligand based. The excited state singlet lifetimes of the complexes, $PyrCCThCHOCo_2(CO)_6$ having a lifetime of 0.23 ns and $PyrCCThmalCo_2(CO)_6$ a lifetime of 0.99 ns are also reduced compared to the free ligands. However, the reduction in the excited state lifetime is much more significant in the complexed aldehyde system, $PyrCCThCHOCo_2(CO)_6$ due to possible intermolecular interactions.

In the compound $[BrThmal(W(CO)_5)_2]$, in which the pyrenylacetylene chromophore is absent, a very weak broad ligand based emission bands is exhibited between 350 and 400 nm. Coordination of the metal carbonyl units does not appear to affect the emission properties of the ligand, which exhibits the same very weak bands. This further suggests that the emission observed is entirely ligand based.

5.5.2. Low temperature (77 K) and lifetime measurements

Low temperature (77 K) studies were also carried out on the compounds in this study in a 4:1 EtOH:MeOH glass. Comparison of the room temperature (298 K) and 77 K emission spectra and excited state singlet lifetimes of PyrCCTMS, PyrCCH, and their dicobalt complexes, indicate that at lower temperature the emission bands are red-shifted compared to those observed at room temperature.

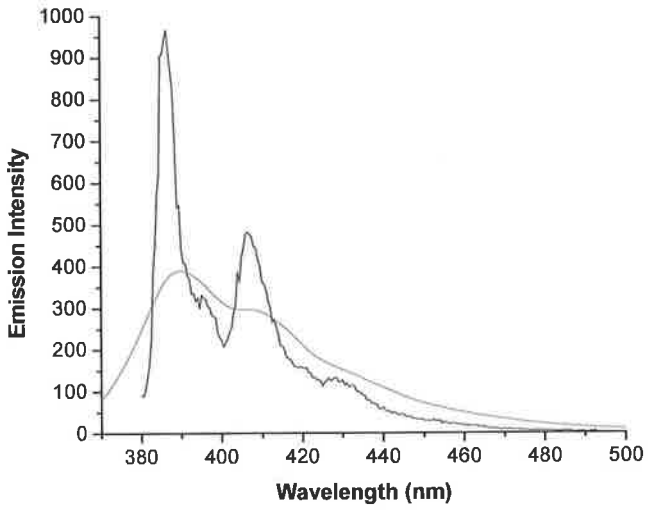

(A)

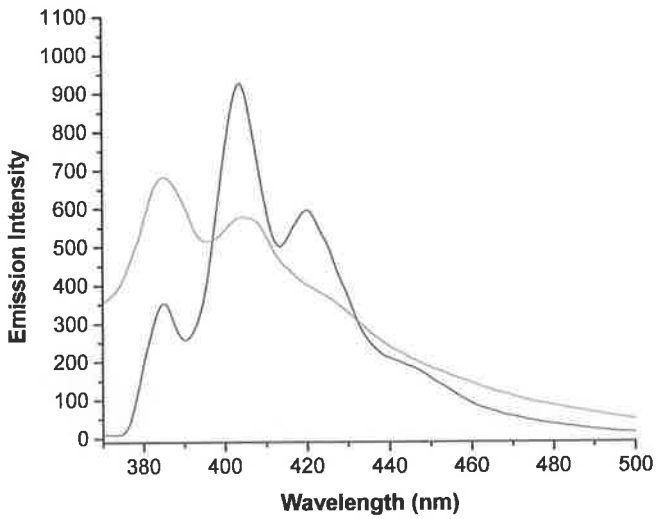

(B)

Figure 32 (A) Room temperature (298 K) emission spectra of PyrCCTMS (—) and PyrCCTMS$Co_2(CO)_6$ (—) in CH_2Cl_2 and (B) low temperature (77 K) emission spectra of PyrCCH (—) and PyrCCH$Co_2(CO)_6$ (—) following excitation at 340 nm

As is evident in Figure 32 the room temperature emission spectrum of PyrCCTMS in CH_2Cl_2 solution exhibits two sharp emission bands at 387 and 406 nm with an excited state lifetime of 2.1 ns for both emission bands following 345 nm excitation. However, excitation at this wavelength in a 77 K 4:1 EtOH:MeOH glass results in a red-shift by approximately 15 nm of the dual emission bands to lower energies. Fitting this dual emission spectrum with a bi-exponential function results in two lifetimes, τ_1 - a shorter lifetime of approximately 2.77 ns and τ_2 – a longer lifetime of approximately 70 ns. The latter lifetime of 70 ns is the major component for this excited state possessing a % relative contribution of 95 % to this excited state. As can be seen in Figure 26 and Figure 32 complexation of PyrCCTMS with $Co_2(CO)_6$ results in significant broadening and a reduction in intensity of the room temperature emission bands. Similarly, at low temperature the same broad, featureless emission band is observed for the complex PyrCCTMS$Co_2(CO)_6$, although unusually in low temperature glass the intensity of the observed broad emission is notably increased by approximately 75 %. As observed for the PyrCCTMS ligand, excitation of PyrCCTMS$Co_2(CO)_6$ in a low temperature glass also dramatically increases the lifetime (τ) of the excited state from 2.4 ns observed in room temperature solution to 42 ns in a 77 K glass. Thus at 77 K the lifetimes of both the ligand PyrCCTMS and its complex PyrCCTMS$Co_2(CO)_6$ are dramatically extended and are comparable to those observed at 77 K for the deprotected analogue PyrCCH.

The emission spectrum of PyrCCH in a 77 K 4:1 EtOH:MeOH glass following 342 nm excitation shows the continued presence of a number of sharp intense emission bands, which are similar in position and shape to those observed at room temperature. However, at room temperature the emission maximum of PyrCCH is located at 385 nm, while a weaker band is also located at 405 nm. Conversely, in a 77 K 4:1 EtOH:MeOH glass these emission bands appear to retain their intensity but also appear to be red-shifted by approximately 18 nm to 402 and 425 nm respectively. A number of weaker bands not previously observed are also observed at 382 and 393 nm. These may not have been previously observed in room temperature solution as they are very close to the low energy absorbances of this compound and any emission at this wavelength may be rapidly reabsorbed. This shift to lower energy at low temperature also has the effect of increasing the already longer lifetime of this system to 91.7 ns although a shorter lived species with a lifetime of 27 ns is also present at

much lower percentages. This latter lifetime may be due to the less intense emission at 425 nm. As can be seen in Figure 33 the emission spectrum of the complex $PyrCCHCo_2(CO)_6$ is too broad in both 298 K solution and 77 K glass to note any discerning features. As a result the lifetimes measured for this species at low temperatures, using the available instrumentation, are unreliable and may be too short lived to be accurately measured. An interesting point to note is that the complex $PyrCCHCo_2(CO)_6$ is brown in 4:1 EtOH/MeOH solution but quickly becomes red in colour on cooling to 77 K.

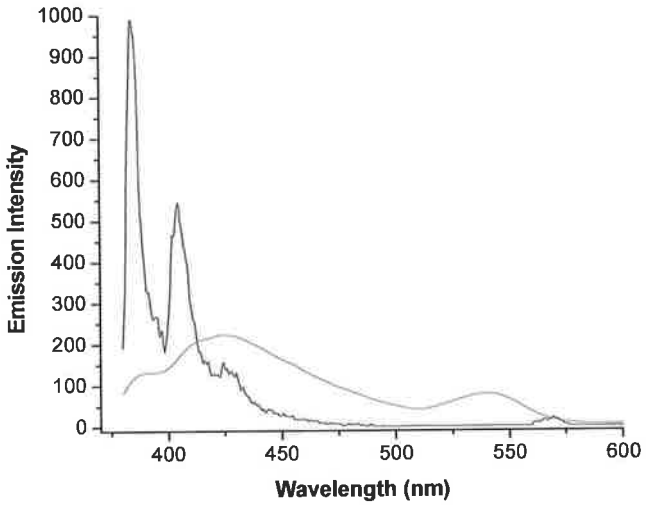

(A)

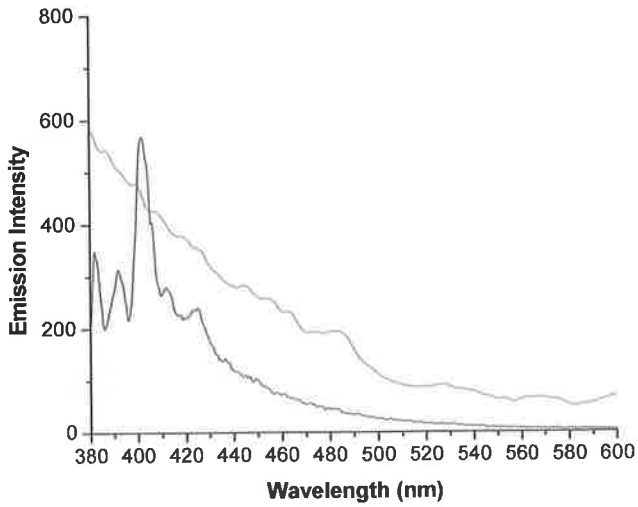

(B)

Figure 33 (A) Room temperature (298 K) emission spectra of PyrCCH (—) and $PyrCCHCo_2(CO)_6$ (—) in CH_2Cl_2 and (B) low temperature (77 K) emission spectra of PyrCCH (—) and $PyrCCHCo_2(CO)_6$ (—) following excitation at 280 nm

Unlike, the emission properties of PyrCCH and its $Co_2(CO)_6$ complex, the emission properties of PyrCCTh and its complex $PyrCCThCo_2(CO)_6$ do not appear to be greatly effected by excitation at low temperatures although in room temperature CH_2Cl_2 solution there is a notable decrease in emission intensity on complexation.

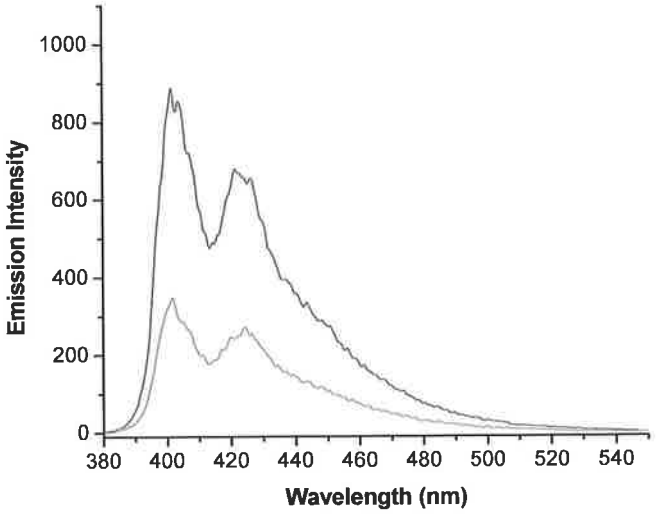

(A)

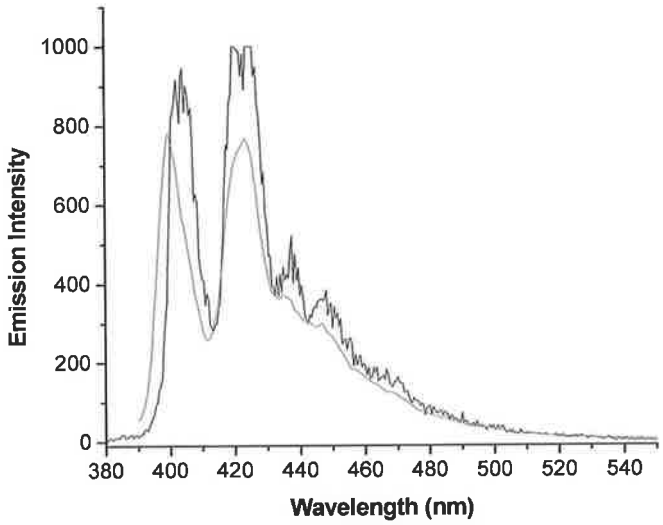

(B)

Figure 34 (A) Room temperature (298 K) emission spectra of PyrCCTh (—) and $PyrCCThCo_2(CO)_6$ (—) in CH_2Cl_2 and (B) low temperature (77 K) emission spectra of PyrCCTh (—) and $PyrCCThCo_2(CO)_6$ (—) following 370 nm excitation

As is evident in Figure 34 there is no discernable shift or change in shape of the dual emission bands observed at 400 and 424 nm following either complexation with $Co_2(CO)_6$ or excitation in a 77 K 4:1 EtOH: MeOH glass. This suggests that in all cases the observed emission is ligand based with negligible MLCT contributions. However, in contrast to room temperature solution, coordination of the complex in frozen 77 K glass does not appear to quench the emission and in fact results in very sharp well defined emission bands at 400 and 425 nm, as shown in Figure 34. Interestingly, there is nonetheless a marked difference in the excited state lifetimes observed for both the ligands and the $Co_2(CO)_6$ complexes at room temperature and at 77 K. In solution at room temperature both PyrCCTh and the complex $PyrCCThCo_2(CO)_6$ are short lived, possessing singlet lifetimes ($^1\tau$) in the range 0.14-0.16 ns. The dual emission spectrum observed for PyrCCTh at 77 K, when fitted with a bi-exponential function, results in two separate lifetimes of 1.77 ns and 4.91 ns, with relative percentage contributions of 95% and 5% respectively. This indicates that the dominant lifetime for this emission is 1.77 ns, which is somewhat longer than that observed for this species in room temperature solution. Similarly, in a low temperature 77 K glass the complex $PyrCCThCo_2(CO)_6$ is also slightly longer lived possessing a singlet lifetime of 0.88 ns. This lifetime possesses a percentage relative contribution towards the excited state of the complex of approximately 93 %, indicating that this excited state is the dominant one observed on excitation of $PyrCCThCo_2(CO)_6$.

Further to this the room temperature and low temperature luminescence properties of the extended π-system PyrCCThCCH were investigated. As previously described the emission spectrum of PyrCCThCCH at room temperature following 320 nm excitation exhibits two sharp and well defined emission bands at 420 and 440 nm (Figure 35). These are red-shifted by 15 nm compared to those observed at 405 and 425 nm for the monosubstituted thiophene system PyrCCTh. This shift to lower energies is the result of increased electronic coupling and delocalisation along the ligand following coordination of the second ethynyl unit. In a 77 K glass no shift in the position of the emission band is observed, suggesting that at both 298 K and 77 K the same excited state is responsible for the emission observed.

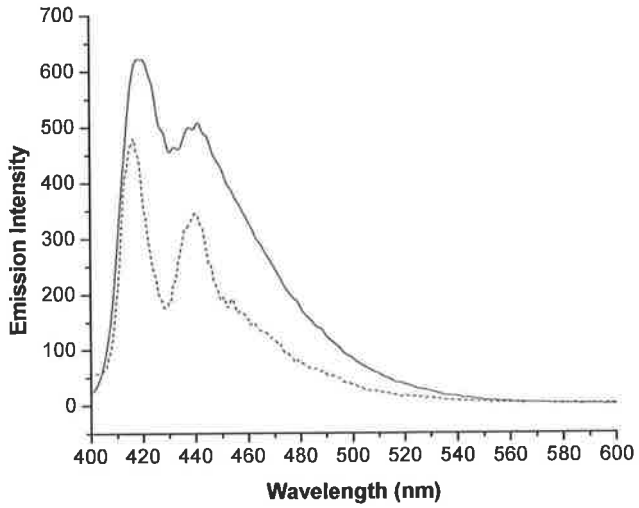

Figure 35 Emission spectra of PyrCCThCCH in room temperature CH_2Cl_2 (—) and low temperature (77 K) 4:1 EtOH:MeOH glass (---) following 320 nm excitation

However, at lower temperatures there is a noticeable decrease in the intensity of the emission band following 320 nm excitation. A comparison of the emission profile at both 298 K and 77 K with the electronic absorption spectrum shows a very small Stokes shift of approximately 20 nm and both the emission and absorption profiles do not show good mirror symmetry. This suggests that there may be substantial mixing between a $\pi \rightarrow \pi^*$ and intramolecular charge transfer (ICT) excited state. The observed dual emission was fitted with a bi-exponential function to give two lifetimes of 1.07 ns and 0.24 ns although the former value is the dominant lifetime for this emission. In low temperature glasses two excited state lifetimes are also observed, where $^1\tau = 1.49$ ns and $^2\tau = 3.72$ ns. However, again the former lifetime value of 1.49 ns is the dominant species at low temperature. However, overall the observation of dual emission and two excited state lifetimes in both room temperature solution and 77 K glass suggests that emission for this species is from an excited state with mixed $\pi \rightarrow \pi^*$ and ICT character.

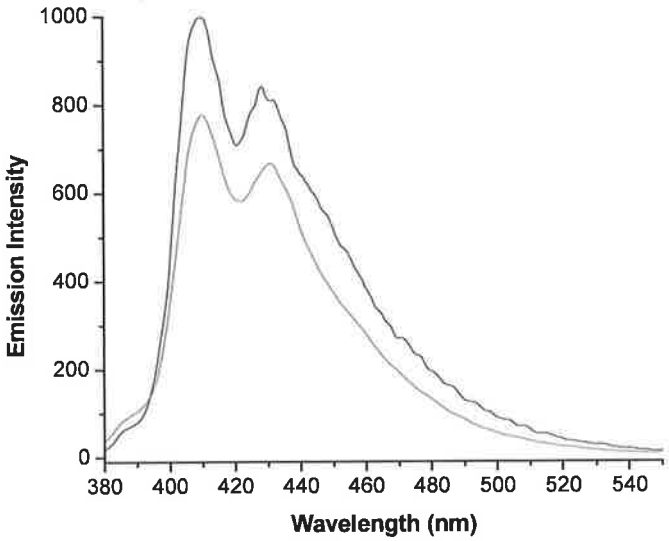

(A)

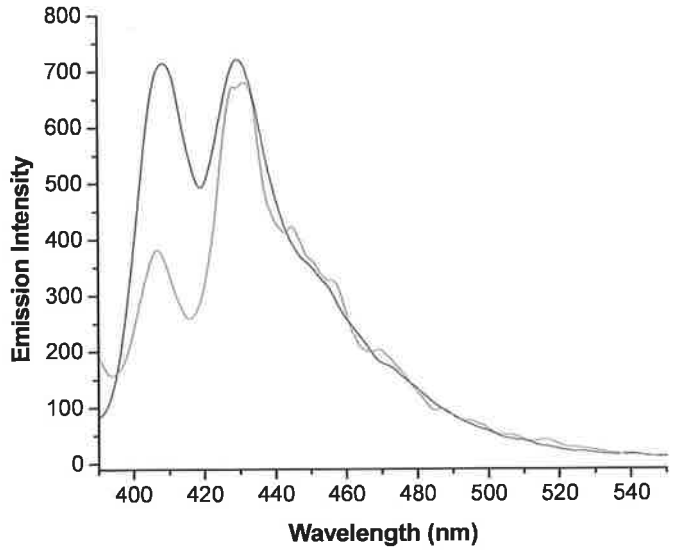

(B)

Figure 36 (A) Room temperature (298 K) emission spectra of PyrCCThBr (—) and $PyrCCThBrCo_2(CO)_6$ (—) in CH_2Cl_2 and (B) low temperature (77 K) emission spectra of PyrCCThBr (—) and $PyrCCThBrCo_2(CO)_6$ (—) following 286 nm excitation

As is evident in Figure 36 the emission spectrum of PyrCCThBr at room temperature following 286 nm excitation contains two emission bands at 410 and 430 nm, red-shifted by approximately 5 nm compared to the mono-substituted thiophene analogue PyrCCTh.

On complexation with $Co_2(CO)_6$ to form PyrCCThBr$Co_2(CO)_6$ no shift in the position of the emission bands is observed following excitation at 286 nm. Furthermore little decrease in the intensity of the emission bands is observed. This is in contrast to many of the other systems in this study, where complexation dramatically reduces the intensity of the emission bands. Single photon counting studies at room temperature of both the ligand and the complex indicate a very short lived excited state lifetime in the range 0.63-0.64 ns. In a low temperature 4:1 EtOH:MeOH glass no change in the position of the emission bands for PyrCCThBr were observed (Figure 36), although there is a reduction in the emission intensity of approximately 25 % at 77 K compared to room temperature.

The 77 K emission bands for both PyrCCThCHO and PyrCCThmal are notably blue-shifted by approximately 50 nm and 100 nm respectively compared to their room temperature spectra. These may be assigned to a thermally induced Stokes shift. For both compounds there is however a notable change in the shape and vibronic spacing of the emission bands observed at 77 K. The emission bands for the PyrCCThmal$Co_2(CO)_6$ complex are also shifted towards the red by approximately 100 nm compared to that observed for PyrCCThCHO$Co_2(CO)_6$. In contrast, to the room temperature spectra whereby coordination of $Co_2(CO)_6$ resulted in notable quenching of the emissive state, at 77 K complexation does not result in a significant reduction in emission intensity (Figure 37 B).

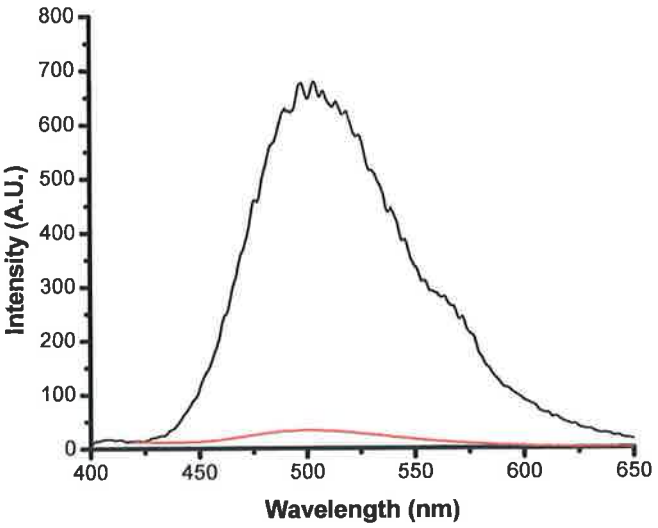

(A)

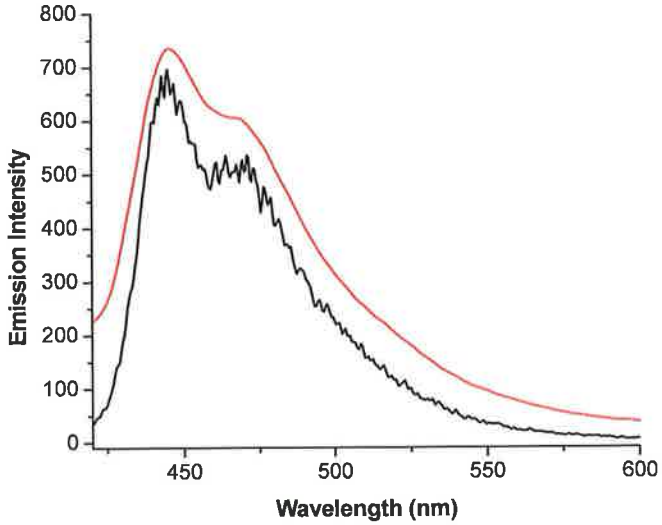

(B)

Figure 37 (A) Room temperature (293 K) emission spectra of PyrCCThCHO and its $Co_2(CO)_6$ complex in CH_2Cl_2. The emission spectra of the uncomplexed aldehyde is represented by (—) while that of the $Co_2(CO)_6$ complexed analogue is similarly indicated by (—). Also shown in (B) are the analogous 77 K emission spectra carried out in 4:1 EtOH:MeOH. PyrCCThCHO and $PyrCCThCHOCo_2(CO)_6$ are again indicated by (—) and (—) respectively.

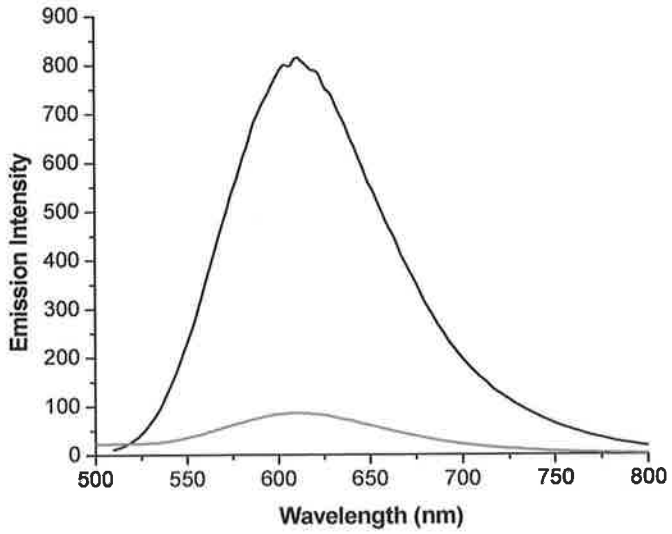

(A)

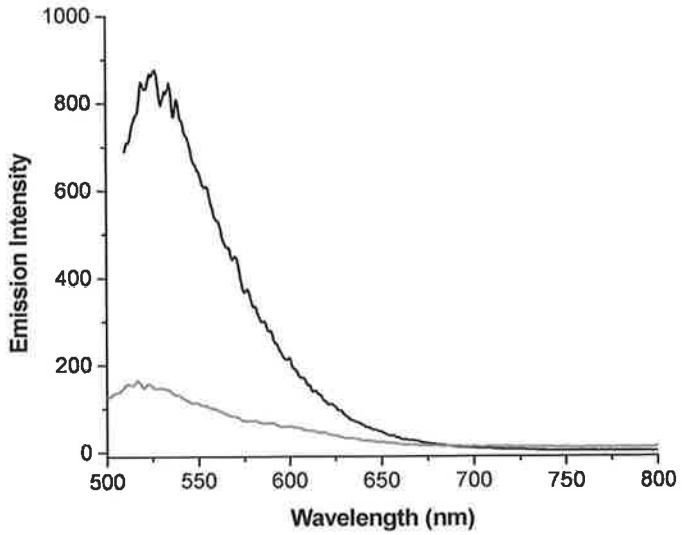

(B)

Figure 38 (A) Room temperature (298 K) emission spectra of PyrCCThmal (—) and $PyrCCThmalCo_2(CO)_6$ (—) in CH_2Cl_2 and (B) low temperature (77 K) emission spectra of PyrCCThmal (—) and $PyrCCThmalCo_2(CO)_6$ (—) following 478 and 450 nm excitation respectively.

Overall, both room temperature (298 K) and low temperature (77 K) emission studies suggest that for PyrCCThCHO, the dicyanovinyl derivative, PyrCCThmal and the corresponding $Co_2(CO)_6$ complexes, the lowest lying excited state is IL in nature. This phenomenon has been previously observed by other authors in studies of pyrenylacetylene bearing compounds[29]. For all of the systems studied lifetimes in the range 0.5-2.0 ns were observed.

5.5.3. Electrochemistry

For the uncomplexed organic ligands (PyrCC-/-TMS, -H, -Th, -ThBr, -ThCHO, -Thmal, ThCCH) the first oxidation observed on cyclic voltammetry occurs at potentials of 1.0-1.1 V vs. Ag/Ag^{+}. Based on previous reports in the literature[27,28, 32] this can be assigned as the irreversible oxidation of the pyrene chromophore. It is suggested that this process is irreversible due to generation of a dimer π-radical cationic species by association of the oxidised pyrene with a second pyrene subunit.[27] Oxidation at higher potentials (+1.6 V) leads to a gradual loss of all characteristic oxidation and reduction potentials. This phenomenon has been previously observed[29] and assigned to decomposition of similar complexes. We have however observed that in each case oxidation at high positive potentials results in "polymerisation" or deposition of a film onto the working and counter electrode surfaces, which perturbs further electrochemical measurements. This may explain loss of characteristic potentials following oxidation at high potentials. Displayed in Figure 39 are the oxidation waves of $PyrCCThCHOCo_2(CO)_6$ at high oxidation potentials. A gradual decrease in the current in the oxidation peak at 0.75 V vs. Ag/Ag+ is observed while concomitantly the oxidation peak at 1.0 V vs. Ag/Ag^{+} increases. This is due to destruction of the $Co_2(CO)_6$ based oxidation and continued oxidation of the pyrene unit, respectively. Subsequent oxidation and reduction scans indicate complete loss of the characteristic peak potentials.

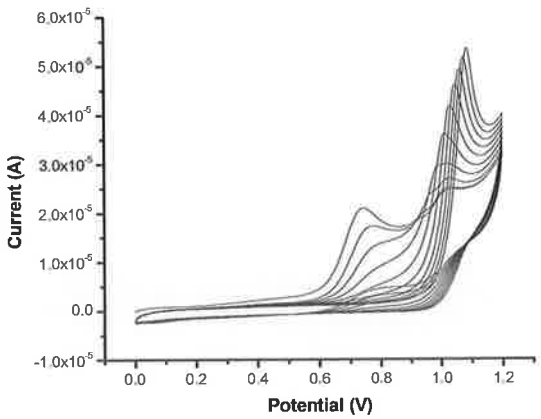

Figure 39 Cyclic Voltammogram of $PyrCCThCHOCo_2(CO)_6$ showing oxidation only at high oxidation potentials (+1.6 V)

The deposited film is insoluble in acetonitrile and is removed by cleaning with alumina. The remaining complex solution retains its characteristic peak potentials. This suggests that overall complex destruction does not occur but deposition of a film onto the electrode surface hinders the working of the electrode. In BrThmal$[W(CO)_5]_2$, where the pyrene substituent is absent, this effect is not observed.

The cyclic voltammogram of PyrCCTMS contains the previously mentioned irreversible oxidation of the pyrene unit at approximately 1.0 V vs Ag/Ag^+. However, a quasi-reversible oxidation wave at 0.41 V and a quasi-reversible reduction wave at -1.60 V vs. Ag/Ag^+ were also observed. The energy band gap (ΔEp) was calculated at 120 mV, while i_{pa}/i_{pc} = 1. This suggests that this process is a fully-reversible one-electron process. Based on similarities with observations by Harriman and co-workers[32] this reduction may be assigned to the reduction of the pyrene terminal unit. However, in PyrCCTMS$Co_2(CO)_6$, an irreversible oxidation is also observed at 0.51 V vs. Ag/Ag^+. This is assigned to oxidation of the cobalt metal centre. The previously mentioned quasi-reversible oxidation and reduction waves, occur at 0.21 V and -1.40 V vs. Ag/Ag^+, respectively. These are shown in the cyclic voltammogram of PyrCCTMS$Co_2(CO)_6$ (Figure 22).The energy band gap (ΔEp) was calculated at 120 mV, while i_{pa}/i_{pc} = 1.6. This suggests that coordination of the cobalt hexacarbonyl moiety reduces the reversibility of the redox system. This may be due to increased charge transfer from the pyrene unit to the metal centre.

The presence of the irreversible pyrene based oxidation is especially obvious in the cyclic voltammogram of PyrCCH, where this oxidation observed at 1.09 V vs. Ag/Ag^+, is the dominant feature (Figure 21). This irreversible oxidation occurring at a positive potential of 1.09 V and at a current of nearly 80 μA may also be due to overlap between the irreversible oxidation of the pyrene unit and the irreversible oxidation of the ethynyl unit, which according to Pappenfus and Mann[26] is also expected to occur at similar potentials. This overlap may explain the intensity of this positive potential oxidation. However, reduction of the 1-ethynylpyrene moiety, previously observed by Harriman et al.[32] at -1.78 V vs. SCE is absent. This may be due to rapid reduction of the previously oxidised species resulting in no net reduction being observed. A weak irreversible oxidation is also observed at 0.65 V vs. Ag/Ag^+.

This positive potential however disappears on successive positive scans, thereby suggesting that it may be due to a trace impurity in the solution. Following coordination of the $Co_2(CO)_6$ moiety to yield $PyrCCHCo_2(CO)_6$, the two positive oxidations assigned to the oxidation of the pyrene and ethynyl units are somewhat more separated from one another. The oxidation of the pyrene unit is observed at 0.95 V, while that of the ethynyl terminal unit is observed at slightly higher potentials of 1.09 V vs Ag/Ag^+. As would be expected for these complexes a broad irreversible oxidation assigned to oxidation of the cobalt metal centres is also observed at 0.64 V vs. Ag/Ag^+. This is assigned to the irreversible oxidation of the cobalt metal centre and are similar to the oxidation potentials for $Co_2(CO)_6$ complexes observed by Allen et al[60] and Dimbinski et al.[61] but lower, by approximately 300 mV, than those observed by Bruce and co-workers[62] for $Co_2(CO)_6$ coordinated $Fc(C{\equiv}C)_nW(CO)_3Cp$ type complexes. For all other $Co_2(CO)_6$ coordinated complexes this irreversible oxidation is observed at similar potentials (see Table 3). A quasi-reversible reduction at $E_{½}$ = -1.27 V vs. Ag/Ag^+ also present on complexation may be due to the reduction of the 1-ethynylpyrene unit, not previously observed for the free ligand. Coordination of the $Co_2(CO)_6$ moiety appears to lower the reduction potential of the 1-ethynylpyrene terminal unit by approximately 50 mV from -1.78 V to -1.27 V, although this value may be substantially less as both values were obtained using different reference electrodes – the SCE and Ag/Ag^+ electrodes respectively.

As observed for the previous systems, the cyclic voltamagramm of the thiophene bound ethynylpyrene system, PyrCCTh, as shown in Figure 21 possesses a positive potential at 0.90 V vs. Ag/Ag^+ due to oxidation of the pyrene unit. Furthermore, a fully reversible two electron reduction of the thiophene terminal unit is observed at a half wave potential ($E_{½}$) of -1.21 V vs. Ag/Ag^+. At more reductive potentials a quasi-reversible reductive process is observed at -1.81 V vs Ag/Ag^+. On the basis of comparison with the literature[27] this is tentatively assigned to the one-electron reduction of the pyrene moiety. Following coordination of $Co_2(CO)_6$, a reduction in the intensity of the oxidative and reductive potentials is observed, perhaps as a result of a reduction in the π-conjugation and thus reduced electronic coupling along the ligand backbone of the complex. As expected an irreversible oxidation is observed at 0.56 V vs. Ag/Ag^+ as a result of oxidation of the coordinated Co carbonyl unit. This

assignment is based on comparison with the band position of $Co_2(CO)_6$ coordinated complexes observed by Dembinski et al.[61] Coordination of the dicobalt unit again appears to lower the reduction potentials of the thiophene and pyrene based reductions from -1.21 V to -1.20 V and -1.81 V to -1.71 V vs. Ag/Ag^+, for the thiophene and pyrene units respectively.

The level of π-conjugation and thus delocalisation of electron density throughout the pyrenylacetylene ligand was increased by the addition of a further ethynyl unit in the 5-position of the substituted thiophene ring resulting in the generation of PyrCCThCCH. An apparent irreversible oxidation of the pyrene unit was observed at positive potentials of 1.0 V vs. Ag/Ag^+ with no further features evident in this region. In contrast however a number of features are evident at reductive potentials. The primary reductive process involves the apparent quasi-reversible reduction of the thiophene unit at -1.26 V followed by a secondary reductive process at -1.83 V vs. Ag/Ag^+ involving reduction of the pyrene unit. This observed reductive potential for the pyrene subunit is in very good agreement with that observed by Benniston et al.[27] at -1.88 V vs. Ag/AgCl for the one – electron reduction of the pyrene unit. Furthermore, a very weak reductive feature observed at -1.53 V vs. Ag/Ag^+ between the thiophene and pyrene based reductions may be tentatively assigned to the expected reduction of the ethynyl terminal unit, which according to Harriman et al.[32] should occur at approximately -1.78 V vs. SCE for 1-ethynylpyrene. However, due to its very low intensity and proximity to two very strong reductive potentials the assignment of this weak reductive feature must remain tentative.

As well as the pyrene based oxidation observed at 0.95 V vs. Ag/Ag^+, an irreversible reduction is observed at -1.88 V vs. Ag/Ag^+ in the cyclic voltammogram of PyrCCThBr. Based on comparison with observations made by Benniston et al.[27] in similar systems this is assigned to the one-electron reduction of the pyrene unit. However, a quasi-reversible reductive feature is also observed at -2.08 V vs. Ag/Ag^+. This is assigned to the one electron reduction, where ΔEp = 49 mV, of the thiophene unit. This low reduction potential for the thiophene unit may be attributed to the electron withdrawing effect of the appended Br atom. effect. Following coordination of the $Co_2(CO)_6$ subunit an irreversible oxidation due to oxidation of the cobalt metal centre is observed at 0.67 V while that due to the pyrene unit remains at

approximately 0.9 V vs. Ag/Ag^+. Although the one-electron reduction of the pyrene unit remains at approximately -1.8 V, going from -1.84 V for PyrCCThBr to -1.88 V for $PyrCCThBrCo_2(CO)_6$, the band at -2.08 V previously assigned to the quasi–reversible reduction of the thiophene is unit shifted to lower reduction potentials on complexation. This lowering of the thiophene reduction potential to -1.19 V is a result of a cation induced charge shift[27,28] and results in a thiophene based reduction potential, which is more in line to those observed in the literature[28].

Aside from the irreversible pyrene oxidation, PyrCCThCHO exhibits a fully reversible one–electron reduction peak with a half-wave potential ($E_{½}$) of -1.67 V vs. Ag/Ag^+, which is similar to literature values observed for the reduction of the thiophene group[28]. A quasi reversible reductive process is also observed at $E_{½}$ = -1.88 V vs. Ag/Ag^+. This is assigned to the one-electron reduction of the pyrene moiety on the basis of similarities with literature data[63]. On complexation with $Co_2(CO)_6$ an irreversible oxidation is also observed at 0.67 V vs. Ag/Ag^+. Coordination of the cobalt metal centre also appears to lower the reduction potential for the thiophene unit by ~ 500 mV to -1.18 V vs. Ag/Ag^+. This has been previously explained in terms of a cation-induced charge shift reaction following Zn^{2+} coordination to a similar pyrene-thiophene dyad system[27,28]. Furthermore, the thiophene based reduction now appears to be poorly reversible. As observed for PyrCCThCHO, its complexed analogue also displays a quasi-reversible reduction due to reduction of the pyrene unit at a half-wave potential ($E_{½}$) of -1.86 V vs. Ag/Ag^+. The cyclic voltammograms of both ethynylpyrenethiophene carboxaldeyde and its $Co_2(CO)_6$ complexed analogue are shown below. However, the proximity of both reduction potentials to one another makes definite assignment difficult.

Conversely, the dicyanovinyl derivative, PyrCCThmal and its complexed analogue $PyrCCThmalCo_2(CO)_6$ while both possessing an irreversible pyrene based oxidation at ~ 1.1 V also possess an apparently irreversible reduction of the thiophene unit at -1.16 V vs. Ag/Ag^+, similar to that observed for the aldehyde complex. However, an irreversible reduction of the dicyanovinyl unit is also observed at -1.36 V vs Ag/Ag^+ for both PyrCCThmal and its cobalt complex. These reduction potentials are in good

agreement with those observed by Roncali and co-workers for dicyanovinyl units in triphenylamine-thienylenevinylene systems[9].

For comparison, electrochemical studies were also carried out on BrThmal$(W(CO)_5)_2$, to investigate what effect the absence of the pyrene donor group might have on the system. In the cyclic voltammogram, there is, as expected, a marked absence of the irreversible oxidation at ~1.0 V due to the pyrene unit. However, an irreversible oxidation wave observed at 0.766 V vs. Ag/Ag^+ is assigned to oxidation of the two $W(CO)_5$ units. This oxidation potential is similar to values in the literature[64] for complexes containing two $W(CO)_5$ moieties. Both irreversible oxidation waves for the dicyanovinyl and thiophene moieties occur at similar positive potentials to those observed for these redox processes in PyrCCThmal and PyrCCThmal$Co_2(CO)_6$. The irreversible oxidation process assigned to oxidation of the dicyanovinyl unit and the thiophene unit occur at -1.30 V and -1.06 V vs Ag/Ag^+, respectively. These appear to occur at potentials *ca.* 20 mV less negative than those observed for the same irreversible oxidations in the free bromothiophenemalonitrile ligand.

5.5.4. Steady-State Photolysis

Extended broadband photolysis of PyrCCTMS$Co_2(CO)_6$ at λ_{exc} > 520 nm for 600 s (10 mins) resulted in bleaching of the parent absorption bands and generation of weak product bands at 2059, 2012 and 2001 cm^{-1}. Subsequent photolysis at λ_{exc} > 400 nm for 15 mins resulted in a notable increase in intensity of these bands, assigned to formation of the pentacarbonyl species PyrCCTMS$(Co_2(CO)_5)(PPh_3)$. Weak bands were also generated at 1984, 1968, and 1941 cm^{-1} on photolysis with λ_{exc} > 400 nm, which are tentatively assigned to generation of the tetracarbonyl species, PyrCCTMS$(Co_2(CO)_4)(PPh_3)_2$ based on similarities with those observed at 2028, 1982, 1965, 1948 cm^{-1} by Long et al.[47] following formation of $(\mu_2$-$C_2H_2)Co_2(CO)_4(PPh_3)$. Photochemically induced CO loss appears to be more efficient on higher energy irradiation, as suggested in Figure 40 where broadband irradiation at wavelengths > 520 nm are shown in red while those > 400 nm are shown in black.

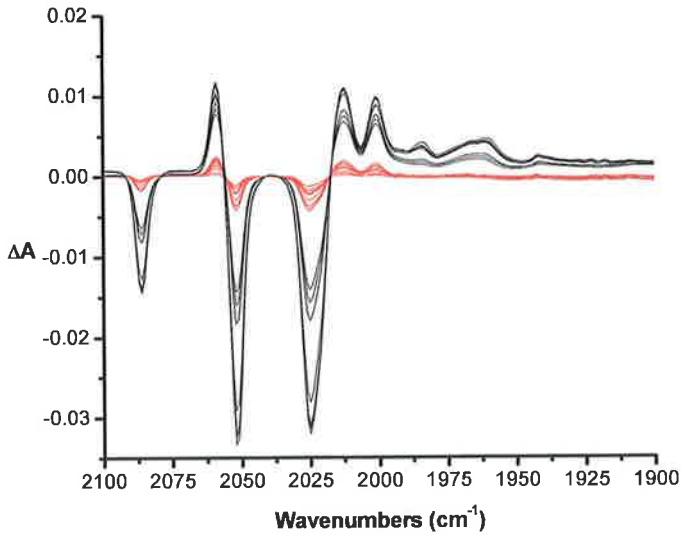

Figure 40 Difference IR spectrum following broad-band irradiation of PyrCCTMS$Co_2(CO)_6$ in pentane at λ_{exc} > 520 nm (red) and > 400 nm (black). Negative bands indicate bleaching of the parent bands while positive bands indicate generation of a pentacarbonyl and tetracarbonyl species.

Irradiation of ethynylpyrene dicobalt hexacarbonyl ($PyrCCHCo_2(CO)_6$) in pentane solution in the presence of triphenylphosphine at $\lambda_{exc} > 520$ nm for 10 mins resulted in the generation of product bands at 2064, 2016 and 2005 cm^{-1} (Figure 41 red bands). These bands are similar to those previously observed for the formation of a pentacarbonyl species and are thus assigned to formation of $PyrCCH(Co_2(CO)_5(PPh_3)$. Furthermore, these bands compare favourably with those observed by Long et al.[47] at 2065, 2016, 2006, 1997 and 1972 cm^{-1} for formation of $(\mu_2\text{-}C_2H_2)Co_2(CO)_5$(pyridine) following irradiation at $\lambda_{exc} > 320$ nm of $(\mu_2\text{-}C_2H_2)Co_2(CO)_6$ in cyclohexane solution in the presence of pyridine. Subsequent higher energy irradiation at > 400 nm for 20 mins resulted in further bleaching of the parent bands and further formation of the tetracarbonyl product, shown in black (Figure 41) as suggested by the generation of new product bands at 2023, 1979 and 1971 cm^{-1}.

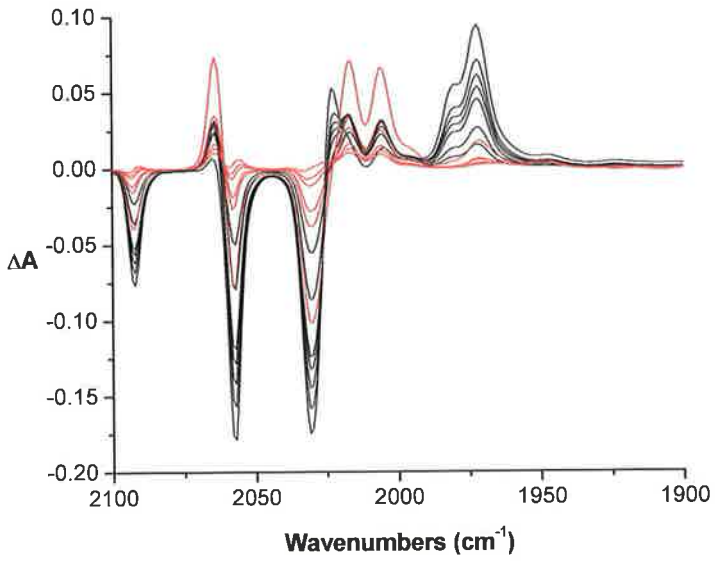

Figure 41 Difference IR spectrum following broad-band irradiation of $PyrCCHCo_2(CO)_6$ in pentane at $\lambda_{exc} > 520$ nm (red) and > 400 nm (black). Negative bands indicate bleaching of the parent bands while positive bands indicate generation of a pentacarbonyl and tetracarbonyl species.

In contrast to $PyrCCTMSCo_2(CO)_6$, the photoinduced CO loss following irradiation of $PyrCCHCo_2(CO)_6$ at > 520 nm appears to be reasonably efficient resulting in formation of the pentacarbonyl species $PyrCCHCo_2(CO)_5PPh_3$. Higher energy irradiation at > 400 nm produces bands at 2023, 1979 and 1971 cm^{-1} assigned to

$PyrCCHCo_2(CO)_4(PPh_3)_2$, which suggests preferential formation of $PyrCCHCo_2(CO)_4(PPh_3)_2$ over the previously observed pentacarbonyl product at this irradiation wavelength.

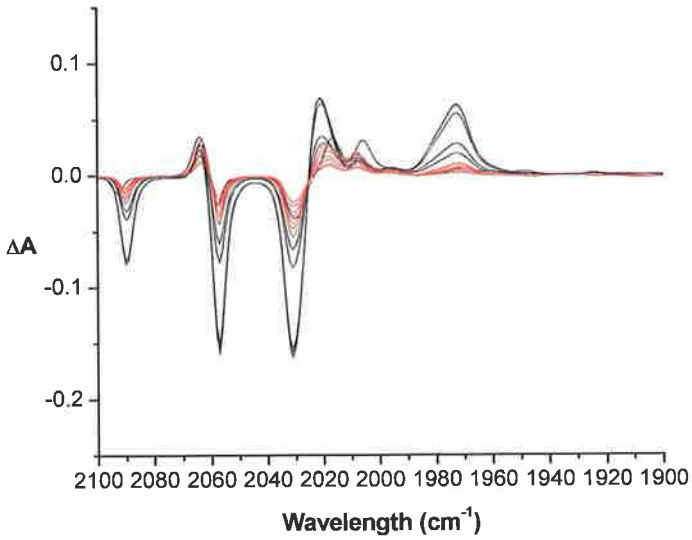

Figure 42 Difference IR spectrum following broad-band irradiation of $PyrCCThCo_2(CO)_6$ in pentane at λ_{exc} > 520 nm (red) and > 400 nm (black). Negative bands indicate bleaching of the parent bands while positive bands indicate generation of a pentacarbonyl and tetracarbonyl species.

Irradiation (λ_{exc} > 520 nm, 10 mins) of $PyrCCThCo_2(CO)_6$ in pentane solution in the presence of the trapping ligand PPh_3 resulted in bleaching of the parent bands with concomitant generation of weak bands at 2064, 2021 and 2007 cm^{-1}, assigned to the generation of $PyrCCThCo_2(CO)_5PPh_3$. However, this process as shown in red in Figure 42 does not appear to be efficient thus resulting in little product formation. Subsequent irradiation at λ_{exc} > 400 nm resulted in further bleaching of the parent bands and an increase in intensity of the product bands at 2064, 2021 and 2007 cm^{-1} indicating further formation of $PyrCCThCo_2(CO)_5PPh_3$ (Figure 42). Irradiation at this wavelength also produced intense bands at 1973 and 1924 cm^{-1} assigned to generation of the tetracarbonyl species, $PyrCCTh\ Co_2(CO)_4(PPh_3)_2$ based on similarities with those observed by Long and co-workers.[47]

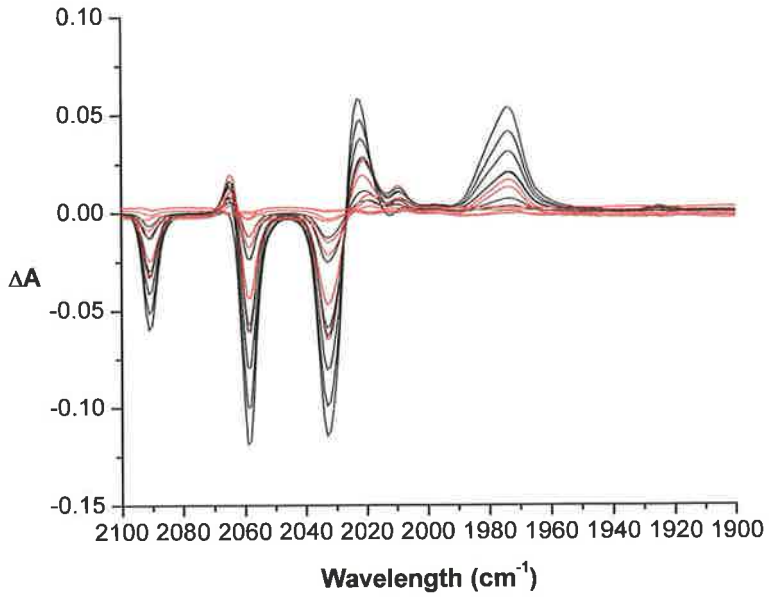

Figure 43 Difference IR spectrum following broad-band irradiation of $PyrCCThBrCo_2(CO)_6$ in pentane at λ_{exc} > 520 nm (red) and > 400 nm (black). Negative bands indicate bleaching of the parent bands while positive bands indicate generation of a pentacarbonyl and tetracarbonyl species.

Broadband photolysis of $PyrCCThBrCo_2(CO)_6$ with λ_{exc} > 520 nm for 10 mins in the presence of the trapping ligand PPh_3 produced the monosubstituted species $PyrCCThBrCo_2(CO)_5PPh_3$ as suggested by generation of bands at 2064, 2022, 2008 and 1974 cm^{-1}. However, as can be seen in Figure 43 this process does not appear to be very efficient as the product bands produced are quite weak. In contrast, following irradiation at λ > 400 nm for a total of 20 mins, further bleaching of the parent bands were observed with little change in the previously produced pentacarbonyl bands[-1]. However, as is evident in Figure 43 the product bands at 2022 and 1974 cm^{-1}, dramatically increase in intensity. Furthermore, a weak band is generated at 1925 cm^{-1} with concomitant depletion of the weak product band previously generated at 2008 cm^{-1}. Overall, this suggests formation of the tetracarbonyl species $PyrCCThBrCo_2(CO)_4(PPh_3)_2$, on higher energy irradiation.

Broadband photolysis of $PyrCCThCHOCo_2(CO)_6$ with λ_{exc} > 520 nm resulted in very little change in the spectrum. However, subsequent irradiation at > 400 nm resulted in the predominant formation of the pentacarbonyl species $PyrCCThCHO(Co_2(CO)_5)(PPh_3)$ (Figure 44) with bands at 2067, 2022, 2013, 2001

and 1975 cm^{-1}. Little evidence for the formation of the tetracarbonyl PyrCCThCHO$(Co_2(CO)_4)(PPh_3)_2$ was observed.

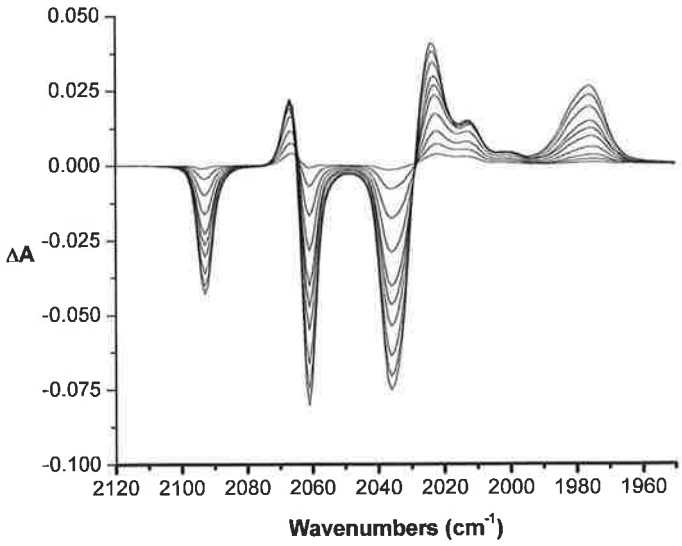

Figure 44 Difference IR spectrum following broad-band irradiation of PyrCCThCHO$Co_2(CO)_6$ in pentane at λ_{exc} > 400 nm. Negative bands indicate bleaching of the parent bands while positive bands indicate generation of a pentacarbonyl and tetracarbonyl species.

Under similar conditions, broadband irradiation of PyrCCThmal$Co_2(CO)_6$ at > 400 nm resulted in bleaching of the parent absorption bands and generation of bands at 2067, 2025, 2014, 2001 and 1977 cm^{-1} assigned to formation of the pentacarbonyl species PyrCCThmal$(Co_2(CO)_5)(PPh_3)$. Little evidence is observed for formation of the tetracarbonyl species, PyrCCThmal$(Co_2(CO)_4)(PPh_3)_2$.

5.6. Conclusion

In this chapter the syntheses, characterisation, electrochemistry, photophysics, and photochemistry of a number of pyrene-thiophene dyads linked by an ethynyl bridge and their dicobalt hexacarbonyl complexes, are described. All of the synthesised compounds exhibit UV-Vis spectra in the visible region , although the dicyanovinyl analogue PyrCCThmal absorbs further into this region due to a intramolecular charge transfer based electronic transition. Furthermore, the $Co_2(CO)_6$ complex absorb further towards the red due to the presence of low energy MLCT transitions although these transitions do not appear to be involved in the photophysics of these complexes.

Both room temperature (298 K) and low temperature (77 K) fluorescence spectroscopy studies of these systems indicates that the excited state chemistry is ligand based in both the organic ligand and their $Co_2(CO)_6$ complexes, with negligible MLCT involvement in the excited state. In the majority of cases this excited state results in intraligand charge transfer (IL) based emission. This has been previously observed in similar systems by a number of authors. It is suggested[27] that this charge transfer involves the formation of a photoexcited pyrene$^+$-thiophene$^-$ state. This is further suggested in electrochemical studies of these systems in acetonitrile solution. Cyclic voltammetry demonstrates the apparent irreversible one-electron oxidation of the pyrene terminal unit with concomitant quasi-reversible reduction of the thiophene unit. In the case of the complexes, the coordinated $Co_2(CO)_6$ units are also irreversibly oxidised at high oxidation potentials.

In addition, steady-state photolysis studies in pentane solution in the presence of the trapping ligand triphenylphosphine indicated the formation of the pentacarbonyl and tetracarbonyl CO loss species. Low energy broadband irradiation ($\lambda_{exc} > 520$ nm) was observed to result in weak production of the pentacarbonyl species. However, following higher energy irradiation at > 320 nm, CO loss appears to be a more facile process with efficient production of both the pentacarbobnyl and tetracarbonyl CO loss products observed.

5.7. Bibliography

1 E.O. Danilov, I.E. Pomestchenko, S. Kinayyigit, P.L Gentili, M. Hissler, R. Ziessel, F.N. Castellano, *J. Phys. Chem. A*, **2005**, 109, 2465-2471

2 A. Khatyr, R. Ziessel, *Org. Lett.* **2001**, 3, 12, 1857-1860

3 R.A Evangelista, A. Pollak, B. Allore, E.F. Templeton, R.C. Morton, E.P. Diamandis, *Clin. Biochem.* **1988**, 21, 173-178

4 A. Okamoto, Y. Ochi, I. Saito, *Chem. Comm.* **2005**, 1128-1130

5 D. Gust, T.A. Moore, *Science*, **1989**, 244, 35-41

6 S. Charaborty, T.J. Wadas, H. Hester, R. Schmehl, R. Eisenberg, *Inorg. Chem.*, **2005**, 44, 6865-6878

7 E.H. Van Dijk, D.J.T. Myles, M.H. van der Veen, J.C. Hummelen, *Org. Lett.* **2006**, 8, 11, 2333-2336

8 V. Grosshenny, F.M. Romero, R. Ziessel, *J. Org. Chem.* **1997**, 62, 1491-1500

9 S. Roquet, A. Cravino, P. Leriche, O. Alévêque, P. Frère, J. Roncalli, *J. Am. Chem. Soc.* **2006**, 128, 3459-3466

10 C.E. Whittle, J.A. Weinstein, M.W. George, K.S. Schanze, *Inorg. Chem.* **2001**, 40, 4053-4062

11 C. Goze, D.V. Kozlov, D.S. Tyson, R. Ziessel, F.N. Castellano, *New. J. Chem.* **2003**, 27, 1679-1683

12 I.E. Pomestchenko, F.N. Castellano, *J. Phys. Chem. A* **2004**, 108, 3485-3492

13 S. Leroy-Lhez, F. Fages, *C.R. Chimie*, **2005**, 8, 1204-1212

14 A.P. De Silva, H.Q.N. Gunaratne, T. Gunnlauggsson, A.J.M. Huxley, C.P. McCoy, J.T. Rademacher, T.E. Rice, *Chem. Rev.*, **1997**, 97, 1515

15 B. Valeur, I. Leray, *Coord. Chem. Rev.*, **2000**, 205, 3

16 A. Khatyr, R. Ziessel, *Tetrahedron Lett.*, **2002**, 43, 7431-7434

17 E.C. Constable, C.H. Housecroft, M. Neuburger, S. Schaffner, E.J. Shardlow, *J. Chem. Soc. Dalton Trans.*, **2005**, 234-235

18 M. Schmittel, V. Kalsani, F. Jäckel, J.P. Rabe, J.W. Bats, D. Fenske, *Eur. J. Org. Chem.*, **2006**, 3079-3086

19 S.S. Sun, A.J. Lees, *Coord. Chem. Rev.*, **2002**, 230, 171-192

20 E. Antonelli, P. Rosi, C. Lo Sterzo, E. Viola, *J. Organomet. Chem.*, **1999**, 578, 210-222

21 A. Orita, F. Ge, G. Babu, T. Ikemoto, J. Otera, *Can. J. Chem.*, **2005**, 83, 716-727

22 S. Goeb, A. De Nicola, R. Ziessel, C. Sabatini, A. Barbieri, F. Barigelletti, *Inorg. Chem.*, **2006**, 45, 1173-1183

23 M. Manuele, M. Raposo, A.M.R.C. Sousa, G. Kirsch, P. Cardoso, M. Belsley, E. de Matos Gomes, A. M.C Fonseca, *Org. Lett.*, **2006**, 8, 17, 2681-2684

24 J-M. Raimundo, P. Blanchard, N. Gallego-Planas, N. Mercier, I. Ledoux-Rak, R. Hierle, J. Roncali, *J. Org. Chem.*, **2002**, 67, 205-218

25 A. Cravino, S. Roquet, P. Leriche, O. Alévêque, P. Frère, J. Roncalli, *Chem. Commun.*, **2006**, 1416-1418

26 T.M. Pappenfus, K.R. Mann, *Org. Lett.*, **2002**, 4, 18, 3043-3046

27 A.C. Benniston, A. Harriman, D.J. Lawrie, A. Mayeux, K. Rafferty, O.D. Russell, *Dalton Trans.*, **2003**, 4762-4769

28 A.C. Benniston, A. Harriman, D.J. Lawrie, S.A. Rostron, *Tetrahedron Lett.*, **2004**, 45, 2503-2506

29 D.V. Kozlov, D.S. Tyson, G. Goze, R. Ziessel, F.N. Castellano, *Inorg. Chem.* **2004**, 43, 6083-6092

30 C. Goze, D.V. Kozlov, F.N. Castellano, J. Suffert, R. Ziessel, *Tetrahedron Lett.*, **2003**, 44, 8713-8716

31 D.S. Tyson, K.B. Henbest, J. Bialecke, F.N. Castellano, *J. Phys. Chem. A.*, **2001**, 105, 8154-8161

32 A. Harriman, M. Hissler, R. Ziessel, *Phys. Chem. Chem. Phys.*, **1999**, 1, 4203-4211

33 A. Harriman, G. Izzet, R. Ziessel, *J. Am. Chem. Soc.*, **2006**, 128, 10868-10875 and references therein

34 F. Hua, S. Kinayyigit, J.R. Cable, F.N. Castellano, *Inorg. Chem.*, **2005**, 44, 471-473

35 I.E. Pomestchenko, C.R. Luman, M. Hissler, R. Ziessel, F.N. Castellano, *Inorg. Chem.*, **2003**, 42, 1394-1396

36 I.E. Pomestchenko, F.N. Castellano, *J. Phys. Chem. A.*, **2004**, 108, 3485-3492

37 E.O. Danilov, I.E. Pomestchenko, S. Kinayyigit, P.L. Gentili, M. Hissler, R. Ziessel, F.N. Castellano, *J. Phys. Chem. A*, **2005**, 109, 2465-2471

38 R. Cabot, A. Lledó, M. Revés, A. Riera, X. Verdaguer, *Organometallics*, **2007**, 26, 1134-1142 and references therein

39 F. Robert, A. Milet, Y. Gimbert, D. Konya, A.E. Greene, *J. Am. Chem. Soc.*, **2001**, 13, 5396-5400

40 V. Rautenstrauch, P. Megard, J. Conesa, W. Kuester, Angew. *Chem., Int. Ed. Engl.*, **1990**, 29, 1413-1416

41 J. Gair-Ford, W.J. Kerr, G.G. Kirk, D.M. Lindsay, D. Midlemiss, *Synlett*, **2000**, 1415-1418

42 P.L. Pagenkopf, T. Livinghouse, *J. Am. Chem Soc.*, **1996**, 118, 2285-2286

43 A. Coleman, N. Boyle, W.R. Browne, M.T. Pryce, K.L. Ronayne, *Organometallics*, **2007**, in preparation

44 M. Iqbal, N. Vysem J. Dauvergne, P. Evans, *Tetrahedron Lett.*, **2002**, 43, 7859-7862

45 (a) I.S. Chia, W.R. Cullen, M. Franklin, A.R. Manning, *Inorg. Chem.*, **1975**, 14, 2521-2526;
(b) R.F. Heck, *J. Am. Chem. Soc.*, **1963**, 85, 657-661;
(c) M. Arewgoda, B.H. Robinson, J. Simpson, *J. Am. Chem. Soc.*, **1983**, 105, 1893-1903

46 C.M. Gordon, M. Kiszka, I.R. Dunkin, W.J. Kerr, J.S. Scott, J. Gebicki, *J. Organomet. Chem.*, **1998**, 554, 147-154

47 S.M. Draper, C. Long, B.M. Myers, *J. Organomet. Chem.*, **1999**, 588, 195-199

48 J. Marhenke, S.M. Massick, P.C. Ford, *Inorg. Chim. Acta*, **2007**, 360, 825-836 and references therein

49 M.F. Desrosiers, D.A. Wink, R. Trautman, A.E. Friedman, P.C. Ford, *J. Am. Chem. Soc.*, **1986**, 108, 1917-1927

50 J. DiBenedetto, D.W. Ryba, P.C. Ford, *Inorg. Chem.*, **1989**, 28, 3503-3507

51 M. Hissler, A. Harriman, A. Khatyr, R. Ziessel, *Chem. Eur. J.*, **1999**, 5, 11, 3366-3381

52 W.R. Browne, C.M. O'Connor, C. Villani, J.G. Vos, *Inorg. Chem.*, **2001**, 40, 5461-5464

53 J. Ruiz, N. Cutillas, F. López, G. López, D. Bautista, *Organometallics*, **2006**, 25, 5768-5773

54 N. Miyaura, A. Suzuki, *Chem. Rev.*, **1995**, 95, 2457-2483

55 E. Negishi, L. Anastasia, *Chem. Rev.*, **2003**, 103, 1979-2017

56 Y.-Q. Fang, M.I.J. Polson, G.S. Hanan, *Inorg. Chem.*, **2003**, 42, 5-7

57 S. Schröter, C. Stock, T. Bach, *Tetrahedron*, **2005**, 61, 706, 2245-2267

58 K. Sonogashira, Y. Tohda, N. Hagihara, *Tetrahedron Lett.* **1975**, 16,50, 4467-4470

59 W.B. Austin, N. Bilow, W.J. Kelleghan, K.S.Y. Lau, *J. Org. Chem.***1981**, 46, 11, 2280-2286

60 M. Bahadur, C.W. Allen, W.E. Geiger, A. Bridges, *Can. J. Chem.*, **2002**, 80, 1393-1397

61 N. Esho, B. Davies, J. Lee, R. Dembinski, *Chem. Commun.*, **2002**, 332-333

62 M.I. Bruce, M.E. Smith, B.W. Skelton, A.H. White, *J. Organomet. Chem.*, **2001**, 637, 484-499

63 A. Harriman, M. Hissler, R. Ziessel, *Phys. Chem. Chem. Phys.*, **1999**, 1, 4203-4211

64 J.T. Lin, S.S. Sun, J.J. Wu, L. Lee, K.-J. Lin, Y.F. Huang, *Inorg. Chem.*, **1995**, 34, 2323-2333

Chapter 6

The synthesis, photochemistry, photophysics and electro-chemistry of a series of Pyrene-pyridine and Pyrene-Ferrocene dyads and the corresponding metal carbonyl complexes

Chapter six involves the study of organometallic pyrenyl-ferrocenyl dyads. This chapter begins with a brief review of the literature of organometallic ferrocene compound (luminescent pyrenyl dyad systems were previously discussed in detail in chapter five). The effect of the ferrocenyl moiety on the excited state in organometallic systems and the level of conjugation present is examined using fluorescence spectroscopy and electrochemistry. The results of photoinduced CO loss of the $Co_2(CO)_6$ complexes in the presence of the trapping ligand triphenylphosphine and are also discussed.

6.1. Literature Survey

Supramolecular systems incorporating metallocenes, in particular ferrocene, are of great interest in industry, particularly in the area of opto-electronic devices and materials science. This is due to the unique redox properties of ferrocene and the stability of ferrocene in both the Fe^{2+} and Fe^{3+} oxidation states. This allows for the development of systems possessing opto-electronic or ferromagnetic properties, which may be tuned.

Bhadbhade and co-workers.[1] have synthesised a number of ferrocene derivatives bound via an olefinic bond to a 4-pyridyl linker. Attachment of this 4-styrylpyrdine linker allows for isomerisation about the styryl double bond. The molybdenum complexes of these ligands were synthesised via coordination of a [Mo(tris(3,5-dimethylpyrazolyl)hydroborate)(NO)Cl] fragment to the vacant pyridyl site. Tucker and co-workers[2] have synthesised a number of ferrocene derivatives containing pyridyl units linked to the ferrocene donor group by either an olefinic or amide linkage. The properties of these systems were then investigated using electrochemical and spectroscopic techniques. Interestingly, addition of a Zn or Cu triflate salt solution in acetonitrile to a solution of the bispyridyl system, shown in Figure 1, resulted in formation of a dimeric Zn(II) or Cu(I) complex respectively.

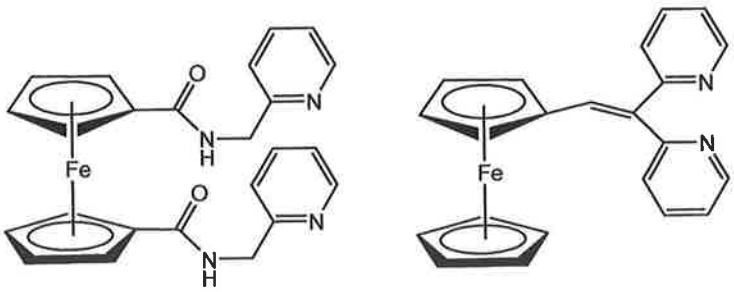

Figure 1 Bis-pyridyl ferrocene derivatives synthesised[2]

Perepichka and co-workers[3] have also synthesised a number of unusual ferrocenyl nitrofluorene derivatives and have extensively studied their properties using both electrochemical and spectroscopic techniques. It was observed that intramolecular charge transfer resulted in an overall lowering of the rotational barrier about the CH=fluorene bond resulting in isomerisation. Solvatochromic effects were also observed in a number of solvents. Furthermore, varying the length of the linkage between the nitrofluorene and ferrocene moieties resulted in bathocrmoic shifts and an increase in intensity of the intramolecular charge transfer (ICT) bands in the electronic absorption spectrum.

More recently, Hamon et al.[4] have expanded on this idea by linking a ferrocene unit and a $[CpFe(\eta^6\text{-arene})]^+$ unit together via a hydrazine type linkage to form a series of substituted ferrocenyl hydrazones. Both electrochemical and spectroscopic studies demonstrated that the presence of the elongated unsaturated chain resulted in a shift of both the redox potentials and MLCT bands compared to the shorter chain analogues. The polarised nature of these systems further suggests possible applications in the development of non-linear optical materials. Similarly, Schottenberger et al.[5] have also synthesised a number of ferrocenylethenylcobaltocenium cations (fec-ene-coc$^+$) (as those shown in Figure 2).

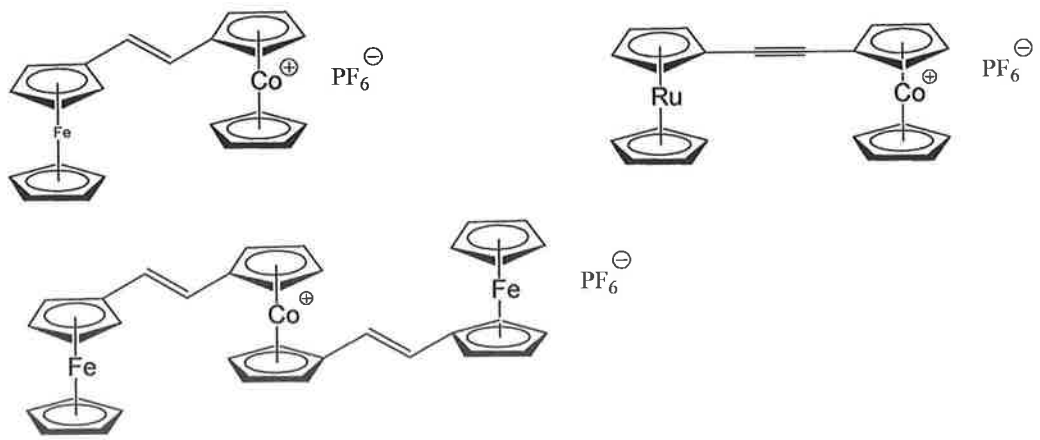

Figure 2 Ferrocenium-cobaltocenium cationic systems

These systems were analysed using cyclic voltammetry and the solvatochromic properties in a range of solvents were investigated. The systems depicted in Figure 2 exhibited negative solvatochromism in a range of solvents. However, the solvatochromic properties are quite irregular and thus difficult to quantify, in terms of a polarity scale. Similarly, Jiang et al.[6] synthesised a number of ferrocene derivatives, containing a number of electron withdrawing substituents such as aldehyde or dicyanovinyl functionalities. Again the electrochemical and spectroscopic properties of these systems were investigated. More recently, Pannell and co-workers[7] have synthesised and investigated the electrochemical and spectroscopic properties of a number of bis-silyl substituted ferrocenylenes similarly containing Br, aldehyde and dicyanovinyl electron withdrawing groups. These systems have been synthesised with the aim of developing new non-linear optical materials. The properties of these ferrocenylene systems containing varied electron-withdrawing substituents were investigated using electrochemistry, X-ray diffraction and Mössbauer spectroscopy.

Within the last decade many groups have become interested in the incorporation of ferrocene units into homo- and hetero-metallic transition metal complexes with an acetylene linkage connecting the two. Previously, Inouye and co-workers[8] synthesised a number of artificial biological receptors inspired by naturally abundant bio-molecules. These systems based on a diamidopyridine substituted ferrocene unit allowed for H-bonding interactions with the nucelobase of interest, in this case thymine. Furthermore, the receptor unit was provided by addition of a highly emissive chromophore such as anthracene, pyrene, or perylene, which was bound to the lower cyclopentadienyl ring of the ferrocene group via an ethynyl linkage. Noticeable π-stacking between the upper diamidopyridine unit and the lower polycyclic hydrocarbon was observed although due to the pivot character of the ferrocene group any great level of π-interaction between the upper and lower units was avoided, with stacking energies of only 0.5 kcal/mol observed.

Lin and co-workers[9] have also developed conjugated pyridine based systems with terminal ferrocene units, which act as strong electron donating groups. As indicated in Figure 3 these systems consist of pyridyl and ferrocenyl terminal units bridged by 1,4-diethynybenzene linkages. Interestingly, the use of these π-conjugated bridges also

allows for the possibility of polymerisation, whereby the pyrdinyl and ferrocenyl terminal units are bridged by a long chain consisting of alternating phenyl and acetylene units. Furthermore, coordination of a metal carbonyl group to the nitrogen donor atom of the pyridine unit also enables possible MLCT interactions as well as σ-donation to the metal centre from the nitrogen atom. These properties open the door for the use of such systems in non-linear optical materials.

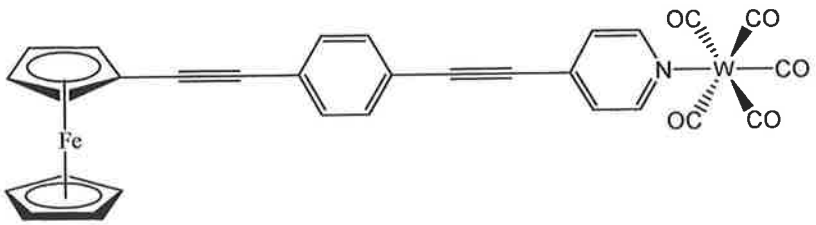

Figure 3 Conjugated pyridyl system with a ferrocenyl terminal unit and diethynylbenzene linkage[9]

The electronic absorption spectra of these systems contained the expected $\pi \rightarrow \pi^*$ and MLCT transitions although a shift in position of the alkynyl bridge based $\pi \rightarrow \pi^*$ transition of ethynylferrocene was observed on coordination to the conjugated diethynylbenzene system, presumably a result of a reduction in energy of the π^* orbital following elongation of the conjugated bridge. Electrochemical analysis of these systems indicated the typically observed tungsten and iron based oxidation chemistry although the typically observed Fc/Fc^+ redox potential was observed at somewhat higher positive potentials, which the authors[9] ascribe to the electron-withdrawing effect of the alkynyl unit on the ferrocene systems following coordination.

Further to these initial studies by Lin and co-workers[9] the photochemical and photophysical properties of the pyridyl-ferrocenyl systems and their tungsten carbonyl complexes have been investigated by Lees and co-workers.[10] Room temperature emission studies of the system shown in Figure 3 and a number of similar systems containing chains of alkyl linkages up to three units long (Figure 4) have been investigated in deoxygenated acetonitrile solution. Overall, these systems show no room temperature emission, while only very weak broad structureless emission, with fluorescence quantum yields (ϕ_F) in the order 10^{-4}, was observed in 77 K EPA glass.

This low temperature emission is assigned to emission from a ^{3}MLCT state and with these systems possessing a triplet lifetime of 27 - 35 ns.

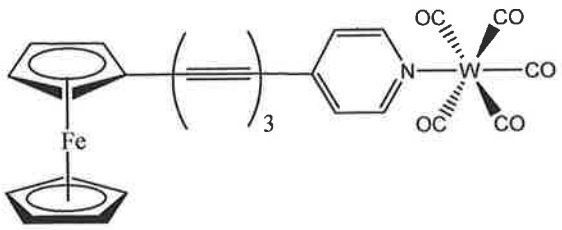

Figure 4 Pyridyl-ferrocenyl complex containing multiple alkyl bridging units[10]

Notably, addition of the 1,4-diethynylbenzene unit into the bridging system between the ferrocenyl and pyridyl terminal units has the effect of red-shifting the emission maximum by approximately 20 nm. It is suggested that this may be due to distortion of the benzene ring in the excited state resulting in improved π-conjugation thereby reducing the energy of the π* orbital. The rate constant for the decay process is in the range 3.0 - 3.7 x 10^3 s^{-1} for these systems. This slow decay process coupled with the relatively short lifetimes suggests that in all cases the observed intramolecular charge transfer system from the ^{3}MLCT state to the ferrocene unit is highly efficient at low temperatures. In contrast, the emissive properties of a $Re(CO)_3$bpy complex were also investigated. This complex exhibited an intense structureless emission band at 562 nm in acetonitrile at 293 K with a lifetime of 132 ns, which is significantly longer to that previously observed. This emission is assigned to a $^3\pi\rightarrow\pi^*$ excited state transition. This low fluorescence quantum yield (Φ_F = 1.8 x 10^{-3}) and lifetime (132 ns) in comparison to other rhenium carbonyl systems is attributed to a ferrocene centred non-emissive LF excited state as well as possible ferrocene to bpy charge transfer states. Furthermore, the photochemistry of these systems was investigated following irradiation in the presence of PPh_3. Irradiation between 405 nm and 514 nm resulted in dissociative loss of the carbonyl moiety to varying degrees with ensuing generation of the PPh_3 trapped species.

Recently, Fischer and co-workers[11] have also developed novel systems containing a chromium pentacarbonyl unit, which is bound via an olefinic linkage to the pyridine ring as opposed to via the nitrogen donor atom, thus affording an allenylidene. As shown in Figure 5 analogues have also been synthesised whereby the allenylidene-

$Cr(CO)_5$ terminus is linked to the ferrocene terminal unit by one or more diethynylbenzene bridging units.

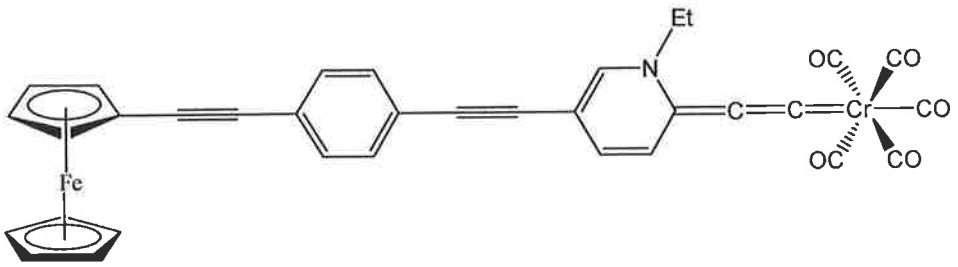

Figure 5 Chromium allenylidene carbon wire with ferrocene terminal unit[11]

The electrochemistry of these systems was investigated in CH_2Cl_2/[NBu4]PF_6 electrolyte solution with a saturated calomel electrode (SCE). In each case with zero, one or two diethnylbenzene linkages present between the allenylidene-$Cr(CO)_5$ and ferrocene termini, the ferrocene unit is readily oxidised, with the Fc/Fc^+ redox wave shifting to less positive potentials. Notably the electron withdrawing allenylidene-$Cr(CO)_5$ terminal unit significantly shifts the reversible ferrocene based oxidation to high potentials. This increase in the potential of the Fc/Fc^+ redox process of approximately 150 mV, where the termini are bridged by an ethynyl unit and approximately 130 mV where the termini are bridged by two diethynylbenzene units (Figure 5) is due to the electron-withdrawing nature of the allenylidene-$Cr(CO)_5$ unit. The negative shift in oxidation potential of the ferrocene unit induced by the electron-withdrawing allenylidene-$Cr(CO)_5$ unit is partially offset by the diethynylbenzene linkages which shift the Fc/Fc^+ to more oxidative potentials. Spectroelectrochemical studies with IR and UV-Vis monitoring suggest that in each case, following oxidation of the ferrocene unit, the IR bands of the pentacarbonyl unit are shifted to higher energy by up to 100 cm^{-1}. This is due to a decrease in back bonding or back-donation from the Cr atom to the CO ligands as a result of reduced electron density on the metal centre. This suggests significant charge delocalisation between the two termini following oxidation. In contrast the ν_{ccc} bands are shifted to lower energy. Oxidation also results in a large blue shift, of approximately 100 nm, of the MLCT absorption bands of the pentacarbonyl moiety. Again the extent of this blue shift of the MLCT band is slightly reduced on increasing the diethynylbenzene chain length. As previously noted following a shift to higher energy of the IR bands, these large shifts

to higher energy indicate delocalisation of the positive charge onto the Cr atom thus reducing the back-donation between the Cr atom and the allenylidene unit.

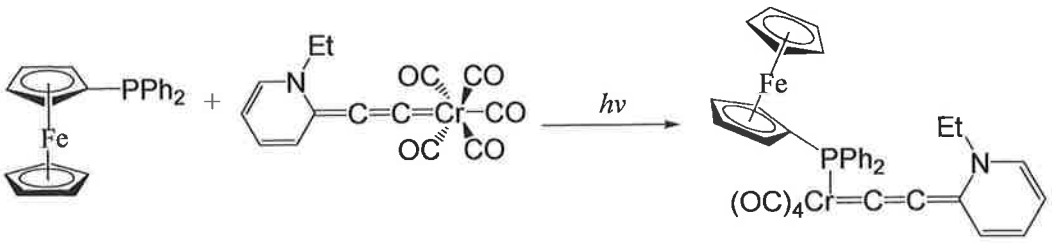

Figure 6 Photochemically induced substitution of PPh_2 into an allenylidene system[11]

Photochemically induced introduction of a PPh_2 unit between the ferrocene terminus and Cr atom via CO loss (Figure 6) resulted in a number of notable electrochemical changes. Two reversible oxidations are observed. The oxidation of the chromium atom and the ferrocene unit. The Fc/Fc^+ redox potential is negatively shifted by approximately 290 mV to lower oxidation potentials compared to that of ferrocene. This suggests that addition of the phosphine bridging unit makes oxidation of the ferrocene unit easier. These electrochemical changes were also monitored spectroelectrochemically using IR and UV-Vis spectroscopy. As previously observed, oxidation results in a shift to higher energy of the ν_{ccc} bands due to reduced back-donation from Cr to the allenylidene unit. There is also a significant blue shift of 130 nm of the $Cr(CO)_5$ based MLCT band in the phosphine bound system. This blue shift is somewhat larger compared those observed where the PPh_2 unit is absent.

In a similar fashion, Bruce and co-workers[12] have dispensed with the pyridyl donor unit and coordinated a Cp-tungsten tricarbonyl unit directly to the alkynyl bridge (Figure 7). Electrochemical studies by Bruce et al.[12] on the uncomplexed ferrocene ligand show a shift towards more positive potentials of the redox process of the ferrocene unit. This is due to an increase in the chain length. The oxidation of the tungsten centre however, does not appear to be affected by the chain length. In all cases reaction of the alkynyl systems with $Co_2(CO)_8$ resulted in the expected $Co_2(CO)_6$ complex. Where a single ethynyl linkage was present the presence of the large $CpW(CO)_3$ terminal unit appears to have partially precluded formation of the $Co_2(CO)_6$ substituted complex, with a yield of only 14 % observed.

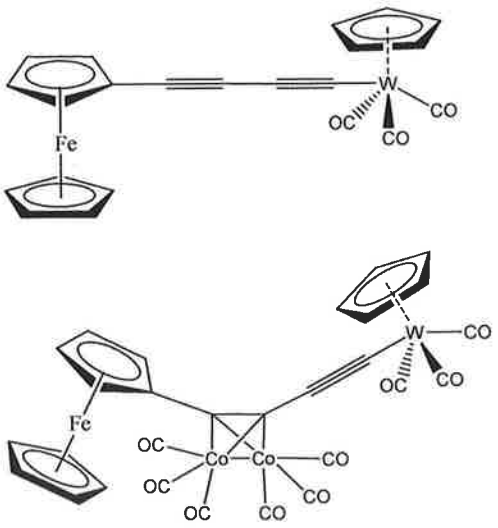

Figure 7 Ferrocenylacetylene-$W(CO)_3Cp$ complex and the dicobalt hexacarbonyl complex $FcCCCo_2(CO)_6W(CO)_3Cp$

In the case where two or more ethynyl linkages were present the $Co_2(CO)_6$ coordinated to the ethynyl linkages furthest away from the sterically bulky $CpW(CO)_3$ moiety, resulting in mono and disubstituted $Co_2(CO)_6$ complexes with yields of 40-60%. More recently, the same group in conjunction with Low and co-workers have developed a novel series of iron and ruthenium complexes of ethynylferrocene and diethynylferrocene groups bound to phosphine based ligands[13]. In addition the tetracyanoethane (tcne) derivatives have also been synthesised.

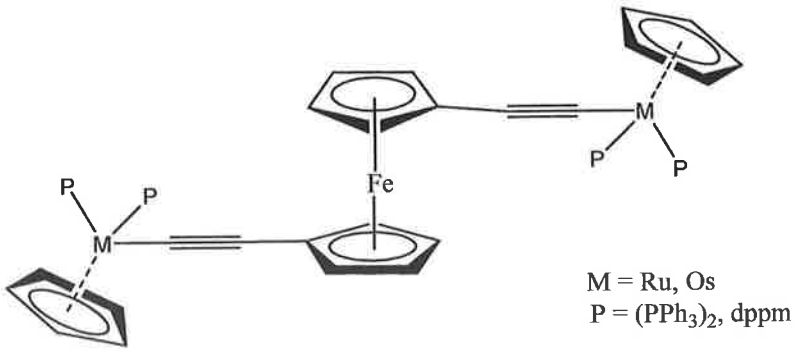

Figure 8 Novel diethynylferrocene CpMPP systems[13]

The electrochemistry of both the monosubstituted binuclear ferrocene systems (Fe and Ru) and trinuclear ferrocene systems (2 x Ru and Fe) were examined using cyclic voltammetry. In the case of the dinuclear species two chemically reversible redox processes were observed while for the trinuclear systems, three redox processes were

observed suggesting that the presence of the central Fe atom significantly decouples the otherwise identical Ru centres. The presence of the phosphine electron-withdrawing group has the effect of lowering the oxidation potential of the first oxidation in the dinuclear systems. This is even more clearly evident in the trinuclear systems where shifts to more reductive potentials, by approximately -170 mV, of the first oxidation are observed compared to those observed for the dinuclear systems. Furthermore, spectroelectrochemical studies at -20 °C in a $CH_2Cl_2/[NBu_4]PF_6$ solution suggest that the first oxidation of the dinuclear Ru systems involves the C=C centred molecular orbitals while the second oxidation appears to be localised on the terminal ferrocene unit. Attempts to undertake spectroelectrochemical studies on the trinuclear systems proved unsuccessful due to rapid decomposition of the dication species formed on oxidation. Overall, absorption and spectroelectrochemical studies of the dinuclear and trinuclear systems suggests that there is significant delocalisation of electron density between the ferrocene and Ru centre in the dinuclear systems. In contrast however, no evidence of photoinduced Ru-Ru interactions via the Fe centre are observed in the trinuclear systems suggesting that in these cases ferrocene acts as a buffer between the two terminal metal centres.

Recently, Baumgartner and co-workers[14] have developed a number of multinuclear ferrocenylethynyl phosphane systems as shown in Figure 9. Furthermore, the $PdCl_2$ and $PtCl_2$ complexes of these systems have also been synthesised (Figure 10). These systems have been synthesised towards the development of materials with specific opto-electronic properties.

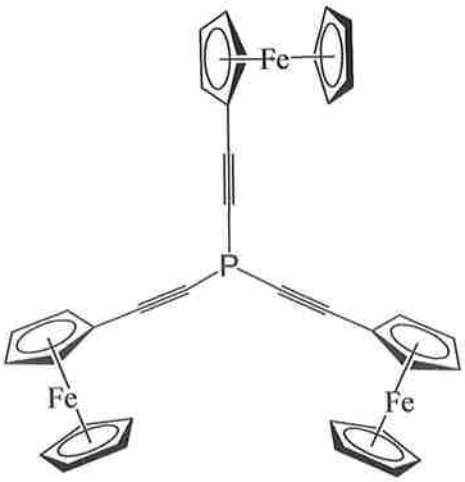

Figure 9 Tris (ferrocenylethynyl) phosphane ligand[14]

In this study the authors have incorporated both the ferrocene unit and phosphane unit as "smart" redox active linkers, which impart unique properties into the overall conjugated system. The electrochemical properties of the tris (ferrocenylethynyl) phosphane system shown in Figure 9 were investigated in a $CH_2Cl_2/[NBu_4]PF_6$ solution. The cyclic voltammograms of these systems displayed a single reversible redox wave although three separate ferrocenyl units were present. However, the presence of the central phosphorus atom does have a marked influence on the redox potential of the ferrocene unit, which is shifted to higher potentials by approximately 150 mV compared to the typical Fc/Fc^+ couple. This shift to higher oxidation potentials of the Fc/Fc^+ couple in this system is attributed to the electron-withdrawing effect of the phosphorus centre making oxidation of the ferrocene more difficult. The lack of any further irreversible processes, associated with formation of a phosphane radical on oxidation suggests that only the Fc/Fc^+ redox process occurs for these systems and that no coupling between the ferrocenyl units is observed.

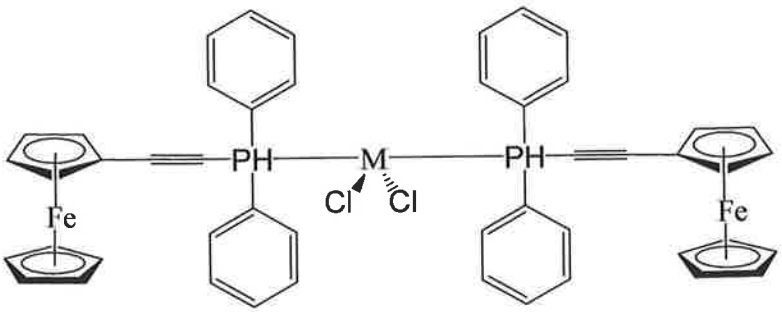

M = Pt, Pd

Figure 10 $PdCl_2/PtCl_2$ complex of ferrocenylethynyl phosphane system[14]

The $PtCl_2$ and $PdCl_2$ complexes shown in Figure 10 also exhibit similar behaviour, with a shift of the Fc/Fc^+ redox couple to higher potentials (~ 100 mV). However, in the case of these $PtCl_2$ and $PdCl_2$ complexes these shifts to higher potential is due to decreased electron density on the iron centre following complexation. This occurs as a result of delocalisation of electron density from the Fe centre towards the phosphorus centre. This is similar to observations by Fischer[11] and Bruce[12] where the Fc/Fc^+ redox couple was found to be shifted to higher oxidation potentials as a result of delocalisation of electron density away from the ferrocene unit to the terminal metal carbonyl units.

Robinson and co-workers [15] have developed a number of ethynyl and ethenyl ferrocenyl dyads containing polycyclic *N*-heteroaromatic donor moieties such as acradine, acridone and anthraquinone (Figure 11). These were chosen as they allow for functionalisation with ethynylferrocene via the N donor atom or the π-aromatic ring system. Typically, in ferrocenyl dyads the ethynylferrocene and ethenylferrocene units act as electron donors, while following oxidation their cations $[FcC{=}C]^+$ and $[FcC{\equiv}C]^+$, act as electron acceptors.

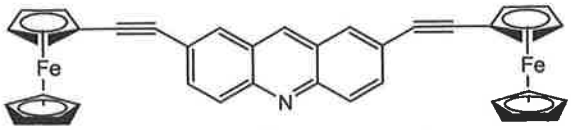

2,7-diethynylferroceneacridine

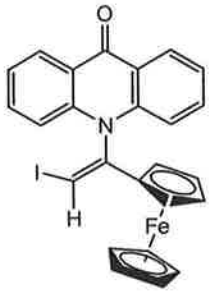

(*Z*)-10-(2-iodo-1-ethenylferrocene)-9(10*H*)-acrinone

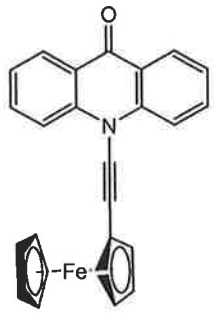

10-(Ethynylferrocene)-9(10*H*)-acrinone

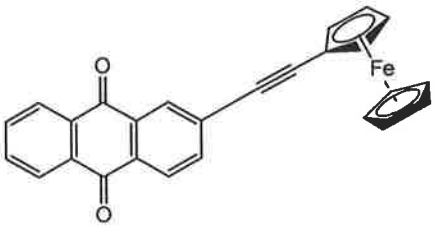

2-Ethynylferroceneanthraquinone

Figure 11 Structures of ferrocenyl acridine, acridinone and anthraquinone dyads[15]

The UV-Vis absorption spectra of these systems exhibit $\pi \rightarrow \pi^*$ and $n \rightarrow \pi^*$ bands between 315 - 380 nm, which are somewhat red-shifted compared to the free parent fluorophore. In the case of the ethynyl linked systems these transitions are also significantly more intense. For both the acridine and acridone systems the ferrocenyl d-d transition band occurs at approximately 450 nm, and partially overlaps with the higher energy $\pi \rightarrow \pi^*$ fluorophore transitions. However, in the case of the anthraquione systems these ferrocene based d-d transitions are red-shifted by 50-80 nm compared to the acridine and acridone analogues. This suggests that over all for the acridine and adridone systems, poor π-conjugation exists between the ferrocenyl and polycyclic units, while in the anthraquinone analogues the fluorophore is significantly perturbed by the ferrocene redox centre, indicating increased π-conjugation and thus electronic communication between the two units.

The spectroelectrochemical properties of these dyad systems were also investigated. In all cases a fully reversible Fc/Fc^+ redox couple was observed. Where the two dyad components were linked by an ethynyl group, an $E^{\circ\prime}$ = 0.68 - 0.71 V vs. decamethylferrocene was observed. This is similar to the reversible redox potential observed at 0.71 V observed for ethynylferrocene.[15] This suggests that overall in the neutral dyads, the π-conjugated link (ethenyl or ethynyl) acts as a buffer between the ferrocenyl couple and the electron acceptor, preventing an effective dyad system from being formed. This is assigned by the authors to a symmetry mismatch between the fluorophore and the ethenyl or ethynylferrocene unit, regardless of the point of coordination of the ferrocenyl moiety onto the polycyclic system.

Room temperature emission studies showed that for both the acridone and anthraquinone dyad systems the emission was quenched to varying degrees. In contrast, significant emission was observed from the neutral acridine compounds. Significant Stoke's shifts and solvent induced shifts are observed for these systems. This suggests that these dyads possess considerably different ground state and excited state geometries. Furthermore, following oxidation of the ferrocenyl unit a significant enhancement of the emission is observed while a red shift in the emission bands of a number of acridine, acridone and anthraquinone dyad systems were also observed. Overall, it was suggested that in the acridine systems significant perturbation of the

excited state of the oxidised dyads exists, while in the case of the oxidised acridone and anthraquinone systems, emission occurs predominantly from the polycyclic fluorophore.

Recently Lang and co-workers[16,17] have developed a novel series of heterobimetallic and heterotrimetallic systems based on a 2,2′-bipyridine-5-yl ethynyl linkage with a terminal ferrocene unit. In these systems the metal atoms are connected by carbon rich π-conjugated linkages. These type of systems allow for extensive electronic communication between terminal ends, which may themselves exhibit unique redox behaviour and optical properties. Furthermore, an alkynlated bpy ligand acts as a building block for addition of further organometallic fragments. Lang et al.[16] have successfully synthesised a number of derivatives of 2,2′-bipyridine-5-ylethynylferrocene ligands, to yield the $Mo(CO)_4$, $Mn(CO)_3Br$, $PtCl_2$, and $Ru(bpy)_2(PF_6)_2$, complexes (Figure 12).

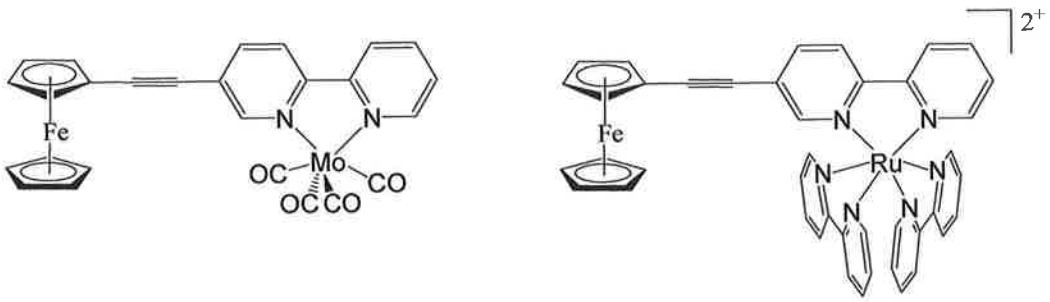

Figure 12 Reaction of 2,2′-bipyridine-5-ylethynylferrocene complex to yield $Mo(CO)_4$ or $Ru(bpy)_2(PF_6)_2$ heteronuclear bimetallic complexes[16]

Cyclic voltammetry studies of the precursor complex 2,2′-bipyridine-5-yl ethynylferrocene in a THF/$(NBu_4)PF_6$ electrolyte solution reveal two reductions at -2.36 V and -2.76 V assigned to the irreversible reduction of the bpy unit. A Fc^{2+}/Fc^{3+} redox couple is also observed for the ferrocene unit although this is shifted to more positive oxidation potentials by approximately 100 mV compared to the free Fc/Fc^+ couple. This was explained in terms of the electron-withdrawing properties of the appended bpy unit. The cyclic voltammogram observed for the Pt chelate complex, as shown in Figure 13, is somewhat similar with two bpy centred reductions observed -1.59 and -2.24 V. These are however shifted to higher potentials by 77 mV and 52 mV respectively compared to the 2,2′-bipyridine-5-yl ethynylferrocene complex.

Additionally, the redox potential for oxidation of the ferrocene unit is also shifted to higher oxidation potentials in the Pt chelate complex. Complexation of the Pt chelate with $CuFBF_3$ does not appear to affect the redox potentials of the Pt chelate complex although the Cu(I) ion exhibits an irreversible oxidation at -1.82 V.

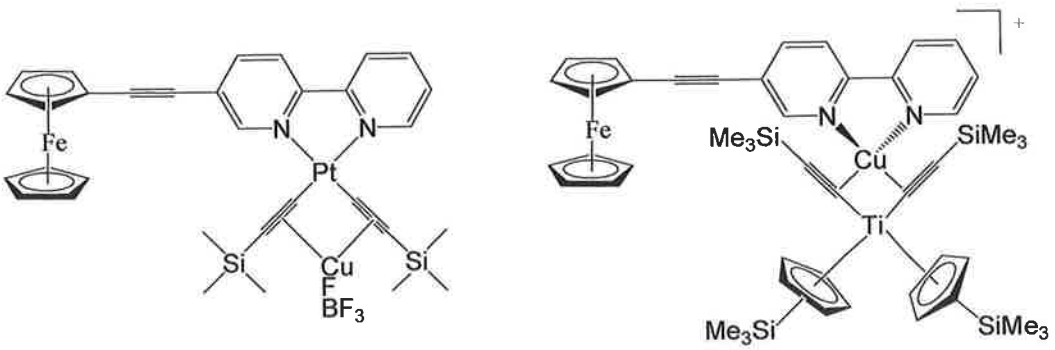

Figure 13 Pt chelate complexes with complexed bpy ligand[16]

The heterotrimetallic systems shown in Figure 13 exhibit interesting electrochemical properties. The $Fe^{2+/}Fe^{3+}$ ferrocene redox potential is observed at 0.12 V, the reduction of the copper unit at -1.45 V and the reduction of the bpy unit at -2.67 V. Interestingly, in this heterotrimetallic system the oxidation potential of the observed ferrocene based redox couple is significantly less than that for the other complexes and much more similar to that observed for the free Fc/Fc^+ redox couple. Reduction of the Cu(I) unit to Cu(0) suggests that reduction of copper is the initial redox process with subsequent fragmentation of the remaining systems occurring following reduction.

A number of groups have incorporated ferrocene and pyrene units into fluorescent molecular architectures towards the generation of molecular switches and other optoelectronic devices. However, few examples exist with direct linkage of the oxidisable ferrocene unit to the pyrene chromophore. Recently Veciana and co-workers[18] have published work regarding the synthesis and photophysical properties of a range of redox-active 1,4-disubstituted azine systems with terminal ferrocene and pyrene units (Figure 14). The electrochemical properties of this systems were studied in a NBu_4PF_6/CH_3CN electrolyte solution. This revealed a single reversible redox process at 0.770 V, assigned to oxidation of the ferrocene terminal unit. An

irreversible oxidation observed at the higher potential of 1.49 V is assigned to the irreversible oxidation of the pyrene unit.

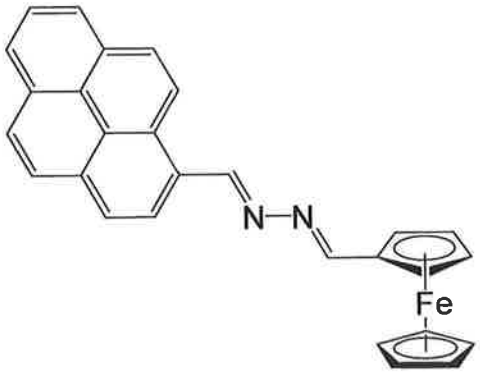

Figure 14 Structure of 1-ferrocenyl-4-pyrenyl-2,3-diaza-1,3-butadiene

The UV-Vis absorption spectrum of the dyad system depicted in Figure 14 in acetonitrile solution exhibits $\pi \rightarrow \pi^*$ based transitions between 320 - 430 nm, with a λ_{max} at 382 nm. The dyad system was also found to be weakly fluorescent (Φ = 0.0035) with weak emission bands centred at 385, 405 and 425 nm following 350 nm excitation. However oxidation with copper triflate, $[Cu(OSO_2CF_3)_2]$, resulted in a bathochromic shift in the UV-Vis absorption spectrum, with a decrease in intensity of the 382 nm centred band and generation of a new absorption band at 457 nm assigned to a Cp $\rightarrow$ Fe^{3+} LMCT transition. Following, oxidation to Fe^{3+} the fluorescence quantum yield and fluorescence intensity were increased. This is further suggested by spectroelectrochemical studies whereby oxidation of the dyad system in an electrolyte solution resulted in a decrease in the efficiency of the quenching ability of the ferrocene unit on the pyrene based emission, resulting in a net increase in emission intensity. However, following subsequent reduction results similar to those exhibited by the neutral dyad system were observed, suggesting overall that oxidation results in formation of the ferrocenium ion, which has the effect of decreasing electron transfer process from the ferrocene unit to the pyrene donor unit.

Similarly, Manning and co-workers[19] have synthesised a number of ethenyl and ethynyl polyaromatic dyad systems containing ferrocenyl and phenyl, naphthyl, phenanthryl, anthryl, pyrenyl or perylenyl termini (Figure 15).

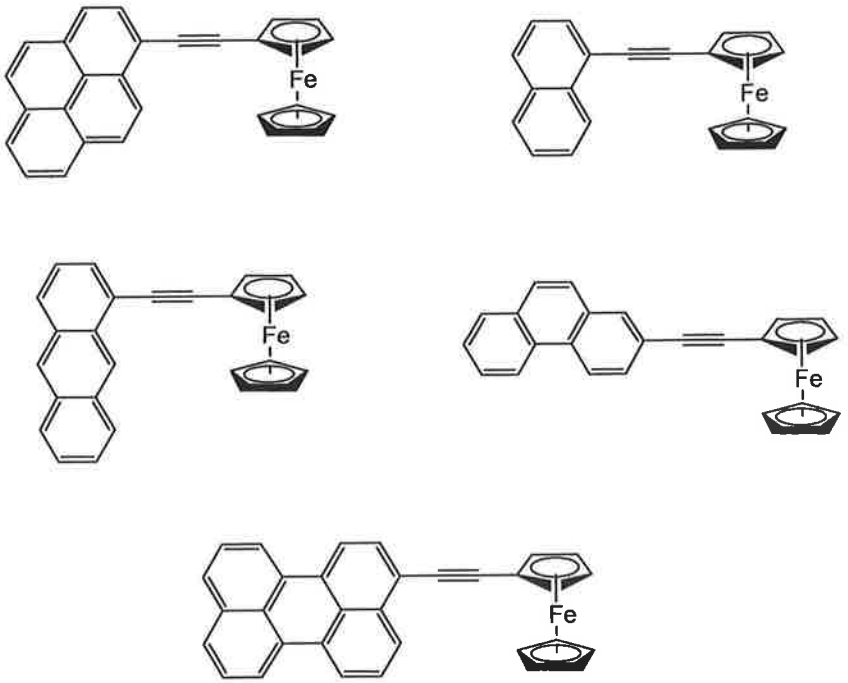

Figure 15 Series of polyaromatic – ferrocene dyad systems with an ethynyl bridge[19]

The UV-Vis spectra of each of the polyaromatic – ferrocene dyads shown in Figure 15 contain two sets of bands, which lie between 300 - 350 nm and 440 - 460 nm. The former group of bands are the most intense are red-shifted on increasing the level of annelation in the polyaromatic substituent[19]. The red-shift on increased annelation is due to the ethynylferrocene unit acting as an electron donor, which results in a lowering of the energy of the $\pi \rightarrow \pi^*$ transitions. As the vibrationally fine structure of the polyaromatic terminal unit is retained to an extent on coordination to the ferrocenyl unit it may be assumed that a high level of π-conjugation does not occur in these systems as that would be expected to result in loss of these vibrationally fine structures. However, in contrast, where there is an ethenyl linkage between both terminal units, this vibrationally fine structure is lost and is replaced by a broad band at lower energies than observed for the ethynyl analogues. This suggests an improved level of π-conjugation in the systems containing an ethenyl bridge. In addition, the bands observed between 440 - 460 nm are assigned to low energy ferrocene d-d transitions. These systems were also investigated using spectroelectrochemical techniques. As expected all dyads contained a fully reversible one-electron redox couple due to the ferrocene terminus. For all systems possessing an ethynyl bridging

unit this occurred ~ 0.67 V in CH_2Cl_2 solution, while it was observed at somewhat lower oxidation potentials for the ethenyl analogues. Furthermore, significant changes were also observed in the electronic absorption spectrum following oxidation. The high energy $\pi \rightarrow \pi^*$ bands between 300 - 350 nm were blue shifted due to the weakened ferrocene-π-conjugated link following formation of the ferrocenium cation. In addition the ferrocene based d-d transition bands between 440 - 460 nm, were blue shifted on oxidation and more structured than those observed for the neutral dyads. However, in contrast to the neutral dyads this band observed for the cationic species is sensitive to the both the polyaromatic ring system used and the solvent used. Raman studies show that there is an enhancement of the Fc-based breathing modes on oxidation, thereby suggesting that unlike in the neutral dyads, these bands involve an excited state possessing both ferrocenyl and polyaromatic character. However, interestingly oxidation also appears to produce new low energy, low-intensity charge transfer bands between 820 - 900 nm. The CT bands are assigned to LMCT transitions involving charge transfer from the ethynyl arene ligand terminus to the ferrocenium cation, $Fc^+ \leftarrow \{C{\equiv}C\text{-}Ar\}$ based on the observation that the energy of this LMCT band was dependent of the polyaromatic substituent present and that a large blue solvatochromic shift was observed in going from dichloromethane to acetonitrile solution. More recently, Robinson and co-workers[20] have examined the electronic structure and NIR transitions of these ferrocene-polyaromatic systems in more detail using DFT quantum chemical calculations. These have shown that coordination of a polyaromatic unit to a Cp ring of the ferrocene terminus via an ethynyl bond results in destabilisation of the ferrocenyl π orbitals such that a change in the frontier orbital configuration is observed, whereby the dyad π-orbitals for the neutral and oxidised species are in the HOMO-2 and HOMO respectively. The level of contribution of the polyaromatic unit to this π-orbital varies with the level of annelation in the polyaromatic ring systems. Formation of the cationic species, while not significantly changing the orbital configuration does lower the orbital energy. This is as a result of the Fc centred positive charge following oxidation.

Incorporation of ferrocene units into thiophene containing systems is also of interest due to possible charge transfer interactions of the ferrocene unit with the thiophene

unit on oxidation. Furthermore, the addition of a thiophene unit provides an alternative pathway for electron delocalisation, at a more efficient rate than that observed when phenyl units are present. Recently, Mollina and co-workers[21] have developed a number of ferrocene-dyads linked with 2-aza-1,3-butadiene spacer units (Figure 16) similar to those synthesised by Veciana et al.[18]

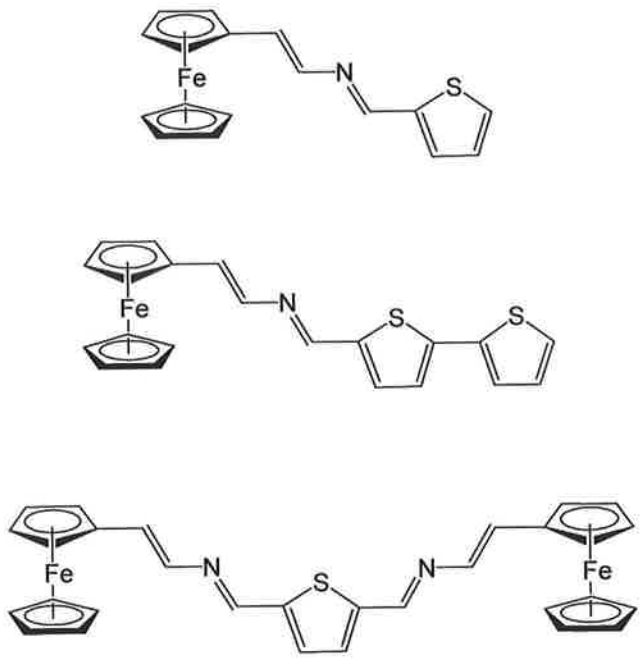

Figure 16 Ferrocene-thiophene dyad systems with 2-aza-1,3-butadiene bridges[21]

Electrochemical studies of the systems shown in Figure 16 in $CH_2Cl_2/(NBu_4)ClO_4$ electrolyte solution indicate electroactivity due to the ferrocene and thiophene units as well as the organic azadiene bridge. For all ferrocene-thiophene dyads a reversible redox process is observed at positive potentials between 0.52-0.65 V. Increasing the number of thiophene units does not appear to affect the Fe^{2+}/Fe^{3+} redox potential. Furthermore, a shift of approximately 20 mV is observed on coordination of a second ferrocene unit (Figure 17).

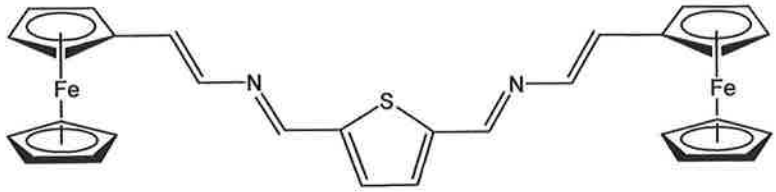

Figure 17 Structure of 4,4′-diferrocenyl-1,1′-(2,5-thiophenediyl)-bis(2-aza-1,3-butadiene)[21]

However, where the ferrocene units are coordinated to the azadiene bridge in the 1,1′ position (Figure 18), noticeable changes were observed. The Fc^{2+}/Fc^{3+} redox process previously observed at 0.54 V shifts to higher oxidation potentials by 110 mV to 0.65 V. Ligand based irreversible oxidation processes are also observed from 1.05 – 1.68 V and are assigned to oxidation of the thiophene ring. Differences observed according to the location of the N atom in the azadiene ring are also observed, with oxidation of the thiophene unit occurring at a higher oxidation potential of 1.68 V where N is closer to the thiophene unit compared to a more reductive potential of 1.05 V where N is closer to the ferrocene unit. Thus it is evident that the electron withdrawing effects of the imine unit of the azadiene bridge are stronger where N is closer to the thiophene unit.

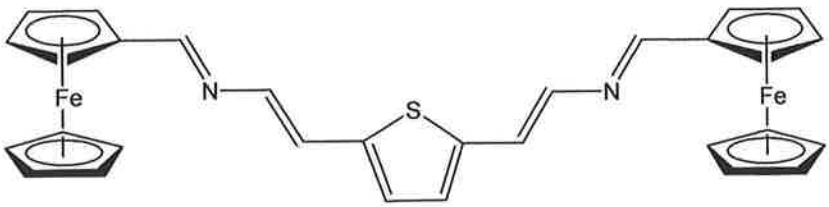

Figure 18 Structure of 1,1′-diferrocenyl-4,4′-(2,5-thiophenediyl)-bis(2-aza-1,3-butadiene)

In addition a broad oxidation is also observed for the systems shown in Figure 17 and Figure 18. This is assigned by the authors[21] as possibly arising from electrochemically generated products. Spectroelectrochemical studies were also undertaken on the ferrocene-thiophene dyad systems. The UV-Vis-NIR spectra of the systems, possessing one or more azadiene bridges where the N atom is closest to the thiophene unit, exhibit a strong band between 353 - 424 nm assigned to azadiene based $\pi \rightarrow \pi^*$ transitions. A weaker band observed between 588 - 665 nm is assigned to a Cp $\rightarrow$ Fe^{3+} ligand to metal charge transfer transition, based on previous observations.[21,22]

Furthermore, this absorption band is more intense in the system where N is closer to the thiophene unit compared to those where it is closest to the ferrocene unit. Absorption bands are also generated in the NIR region between 876 - 1069 nm. These are not present in the neutral molecule and are generated following electron loss from the HOMO. These bands are assigned to a ligand (azadiene) $\rightarrow$ metal (Fe^{3+}) charge transfer transitions based on the fact that these NIR absorptions reached their highest intensity on completion of the oxidation process and were observed to increase during this process. Furthermore, these low energy CT transitions are similar to those previously observed in oligothiophene systems containing a Ru^{3+} or Fe^{3+} metal centre[21]. On oxidation of the first diferrocenyl system shown in Figure 17 the absorbance band situated at 534 nm is quenched with concomitant generation of a band at 720 nm assigned to the ferrocenium ion. Conversely, this band continues to grow, reaching maximum intensity following oxidation. Overall, these provide evidence for the gradual formation of the ferrocenium ion on oxidation of neutral ferrocene. Similarly, it was observed for the species shown in Figure 18 that oxidation produced a decrease in the intensity of the 491 nm absorbance band, which is eventually lost following oxidation.

Due to the presence of the cation-binding N atom in the azadiene bridge, titration experiments with a number of perchlorate salts of metal ions were carried out in CH_2Cl_2 solution and monitored by UV-Vis spectroscopy. Compounds of the type shown in Figure 17, where the N atom is closest to the thiophene unit showed no sensitivity towards alkali metals, while increasing concentrations of the ClO_4^- salt of Ni^{2+}, Cd^{2+}, Hg^{2+} ions resulted in a red-shift of 100-200 nm of the low energy absorption bands characteristic of the ferrocene unit producing a characteristic colour change from orange to purple. In contrast, the analogous compounds of the type shown in Figure 18, where the N atom is closest to the ferrocene unit not only showed sensitivity to Ni^{2+}, Cd^{2+}, Hg^{2+} ions but also Mg^{2+} ions producing a red-shift of approximately 100 nm of the low energy bands.

The following section describes the synthesis of a number of pyrene-pyridine and pyrene-ferrocene dyad systems and their associated dicobalt hexacarbonyl complexes. The photophysical and electrochemical properties are then examined for both the ligands and their complexes. In addition the photochemistry of the dicobalt hexacarbonyl complexes is also examined using steady-state photolysis.

6.2. Aims and Objectives

The aim of this study was to synthesise a number of novel pyrene-pyridine and pyrene-ferrocene dyads linked by an ethynyl bridge and to investigate their photochemical, photophysical and electrochemical properties. The associated dicobalt hexacarbonyl complexes of these dyads were also synthesised and their properties investigated in a similar manner to those of the dyads.

6.3. Experimental

6.3.1. Materials

All manipulations were carried out under an atmosphere of argon or nitrogen using standard schlenk techniques. All solvents were supplied by the Aldrich Chemicals Co. Dichloromethane, chloroform, diethyl ether, pentane and cyclohexane were dried over $MgSO_4$ prior to use. Ethanol and methanol were distilled over magnesium turnings and iodine before use. Tetrahydrofuran (THF) was distilled from sodium/ benzophenone ketyl solution and used immediately. Diisopropylamine was distilled over potassium hydroxide prior to use. All solvents used in emission and lifetime experiments were of spectroscopic grade and were used without further purification. Silica Gel (Merck) was used as received. All mobile phases for column chromatography were dried over $MgSO_4$ before use. 5-bromo-2-thiophene carboxaldehyde was purified by distillation using a Büchi Kügelrohr apparatus. The starting materials 1-Trimethylsilylethynylpyrene and 1-ethynylpyrene were synthesised according to literature methods[23]. All other chemicals were obtained commercially and were used without further purification. All solutions were deoxygenated by purging with argon or nitrogen for ~10 mins. Column chromatography was carried out using neutral silica gel pH 6.5 – 7.5 or neutral Aluminium oxide.

6.3.2. Equipment

IR spectra were recorded on a Perkin-Elmer 2000 FT-IR spectrophotometer (2 cm^{-1} resolution) in a 0.1 mm sodium chloride liquid solution cell using spectroscopic grade pentane, cyclohexane, dichloromethane. ^{1}H-NMR and ^{13}C-NMR were recorded on a Bruker AC 400 spectrophotometer in $CDCl_3$ or d_6-acetone and were calibrated according to the deuterated solvent peak. All UV spectra were measured in spectroscopic grade solvents on a Hewlett-Packard 8452A-photodiode-array spectrometer using a 1cm quartz cell. Elemental analysis of C, H, & N were carried out by the Chemical services Unit, University College Dublin using an Exeter Analytical CE-440 elemental analyser. All syntheses were performed using conventional laboratory glassware under an inert argon or nitrogen atmosphere. All melting points were determined on a Gallenkamp melting point apparatus. ESI mass spectra were obtained using a Bruker-Esquire LC_00050 electrospray ionization at positive polarity with cap-exit voltage of 77.2 V. Spectra were recorded in the scan range 100-1000 m/z with an acquisition time of 300-3000 μs and a potential of 30-70 V. Recorded spectra were the summation of 10 scans. Emission spectra (accuracy±5 nm) were recorded at 298 K using a LS50B luminescence spectrophotometer, equipped with a red sensitive Hamamatsu R928 PMT detector, interfaced with an Elonex PC466 employing Perkin–Elmer FL WinLab custom built software. Luminescence lifetime measurements were made using an Edinburgh Analytical Instruments (EAI) Time-Correlated Single-Photon Counting apparatus (TCSPC) as described by Browne et al.[24] Emission lifetimes were calculated using a single exponential fitting function, involving a Levenberg-Marquardt algorithm with iterative reconvolution (Edinburgh Instruments F900 software) and are ±10%. The χ^2 and residual plots were used to judge the quality of the fits. Cyclic voltammetry experiments were carried out using a CH instruments Model 600a electrochemical workstation at a scan rate of 0.1 VS^{-1}. Electrochemical studies were conducted using a three-electrode system with a 0.1 M solution of $TBAPF_6$ in anhydrous acetonitrile or CH_2Cl_2 as the supporting electrolyte. The working electrode was either a 3 mm diameter Teflon shrouded glassy carbon or platinum electrode, which were polished before each use. The counter electrode was a platinum wire and the reference electrode was a non-aqueous Ag/Ag^{+} electrode. Deoxygenation of the solutions was achieved by bubbling through with argon for approximately 10 mins and a blanket of

argon was maintained over the solution during all experiments. The filling solution for the non-aqueous Ag/Ag^+ reference electrode was 0.1 M $TBAPF_6$ and 0.1 mM $AgNO_3$ in anhydrous acetonitrile. All potentials are quoted with respect to the potentials of the ferrocene/ferrocenium couple ($E^{0'} = 0.31$ V vs. Ag/Ag^+).

6.3.3. Synthesis

All ligands synthesised in this study were prepared using a Sonogashira cross-coupling reaction[25] with 1-ethynylpyrene in each case providing the pyrenyl group. This was initially prepared from 1-bromopyrene via a trimethylsilyl protected derivative.[23,26] The dicobalt hexacarbonyl ($Co_2(CO)_6$) substituted complexes were prepared by stirring the appropriate ligand and $Co_2(CO)_8$ in pentane at room temperature overnight under inert conditions. The Sonogashira cross coupling reactions were catalysed by $PdCl_2(PPh_3)$, CuI, and PPh_3 in the presence of *i*-Pr_2NH to remove the nascent acid formed.

6.3.3.1. Pyrenylacetylenepyridine {PyrCCPy}

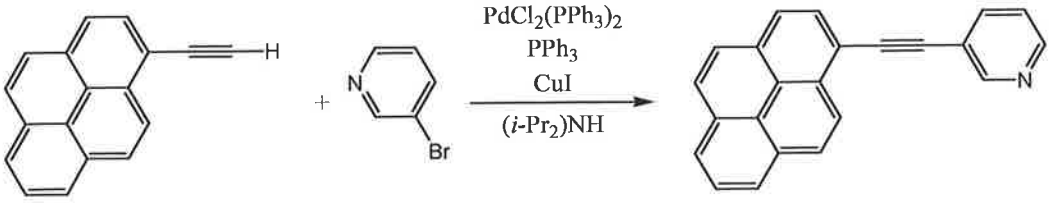

To freshly distilled and argon purged diisopropylamine (25 mL) was added 1-ethynylpyrene (0.400 g, 1.76 mmol), $PdCl_2(PPh_3)_2$ (0.073 g, 0.105 mmol, 6%), CuI (0.019 g, 0.105 mmol, 6%), PPh_3 (0.055 g, 0.211 mmol, 12 %). This solution was purged with argon for a further 5 mins. To this was then added 3-bromopyridine (0.169 mL, 1.76 mmol). This solution was then allowed to stir overnight under inert conditions resulting in the formation of a yellow precipitate in solution. Solvent was removed under reduced pressure. The yellow residue was purified by column chromatography on silica gel with a 9:1 CH_2Cl_2: Pentane mobile phase. The desired product eluted off the column as the first intense yellow band. Solvent was removed by rotary evaporation yielding a brightly coloured yellow solid.

Yield : 0.200g, 38 %

IR (CH_2Cl_2) : ($\nu_{C\equiv C}$) 2307 cm^{-1}; UV-Vis (CH_2Cl_2) : 238, 248, 272, 284, 326, 342, 360, 384 nm; ^{1}H-NMR (400 MHz, $CDCl_3$) : 8.60 ppm (d, 1H), 8.25 ppm (m, 12H); ^{13}C-NMR (100 MHz, $CDCl_3$) : δ 132.80, 131.45, 130.55, 130.13, 129.94, 129.12, 127.60, 127.53, 127.42, 127.38, 126.15, 126.15, 125.25, 124.71, 124.65, 124.60, 124.27, 125.35, 123.30, 123.15, 115.76, 115.47, 81.87, 81.78; M.P. = 95-100 ° C; Mass Spec. ESI m/z 303.1;

6.3.3.2. Pyrenylacetylenepyridine $Co_2(CO)_6$ {PyrCCPy$Co_2(CO)_6$}

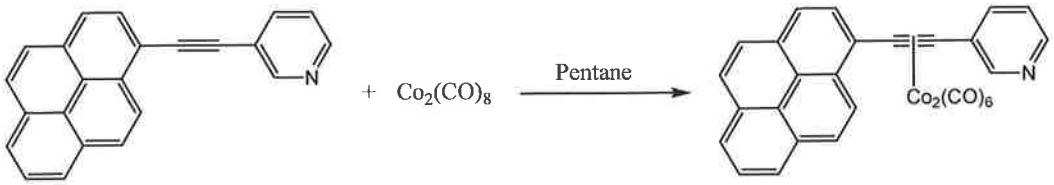

To 20 mL pentane was added pyrenylacetylenepyridine (0.100 g, 0.33 mmol) and $Co_2(CO)_8$ (0.113 g, 0.33 mmol). This solution was then stirred overnight under inert conditions to yield a dark green-brown coloured solution. Solvent was removed by rotary evaporation. The crude product was purified by column chromatography on silica gel with a 20:80 CH_2Cl_2: Pet. ether 40-60 mobile phase. The desired product eluted off the column as a dark green band. The solvent was removed by rotary evaporation yielding a dark green solid.

Yield : 0.180g, 90 %

IR (pentane) : 2092, 2057, 2031 cm^{-1}, UV-Vis (pentane) : 234, 270, 386, 560 nm; ^{1}H-NMR (400 MHz, $CDCl_3$) : 8.55 ppm (d,1H), 8.29 ppm (d, 1H), 8.16 ppm (m, 10H) ; ^{13}C-NMR (100 MHz, $CDCl_3$) : δ 130.55, 130.33, 130.19, 129.85, 127.01, 126.96, 126.45, 125.33, 124.74, 124.57, 123.80, 123.61, 123.14;

6.3.3.3. Pyrenylacetyleneferrocene {PyrCCFc}

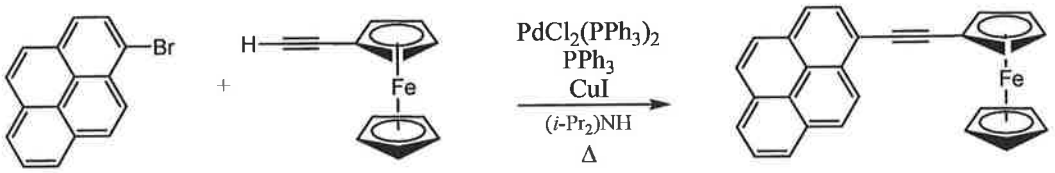

To freshly distilled and argon purged diisopropylamine (15 mL) was added 1-bromopyrene (0.200 g, 0.71 mmol), $PdCl_2(PPh_3)_2$ (0.029 g, 0.042 mmol, 6%), CuI (0.079 g, 0.042 mmol, 6%), PPh_3 (0.022 g, 0.085 mmol, 12 %). This solution was purged with argon for a further 5 mins. To this was then added ethynylferrocene (0.150 g, 0.71 mmol). This orange-brown coloured solution was then allowed to stir overnight under inert conditions. However, no colour change was observed and TLC analysis showed no reaction had taken place. The reaction mixture was then refluxed under inert conditions for 6 hours to yield an orange coloured precipitate. Solvent was removed under reduced pressure. The orange residue was purified by column chromatography on silica gel with a 9:1 Pet. ether : CH_2Cl_2 mobile phase. The desired product eluted off the column as the first coloured band. Solvent was removed by rotary evaporation yielding an orange solid.

Yield : 0.110g, 38 %

IR (CH_2Cl_2) : ($\nu_{C\equiv C}$) 2201, 2221 cm^{-1}; UV-Vis (CH_2Cl_2) : 238, 284, 350, 364, 378 nm; ^{1}H-NMR (400 MHz, $CDCl_3$) : 8.66 ppm (d, 1H), 8.13 ppm (m, 8H), 4.68 ppm (t, 2H), 4.45 ppm (t, 2H), 4.32 ppm (s, 5H); ^{13}C-NMR (100 MHz, $CDCl_3$) : δ 128.39, 127.12, 126.80, 126.30, 125.18, 124.62, 124.40, 123.42, 70.57, 69.05, 68.04, 28.68 ; M.P. = 205-209 ° C; Mass Spec. ESI m/z 410.4

6.3.3.4. Pyrenylacetyleneferrocene $Co_2(CO)_6$ {PyrCCFcCo$_2$(CO)$_6$}

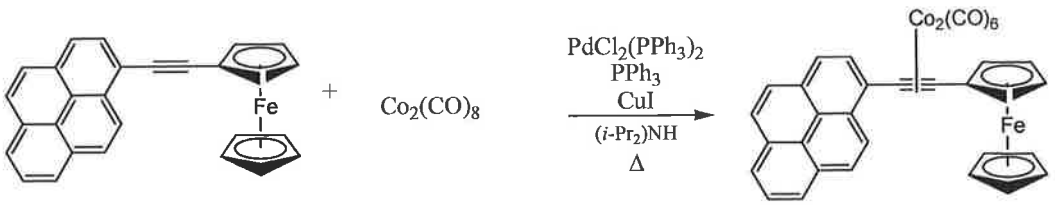

To 20 mL pentane was added pyrenylacetyleneferrocene (0.100 g, 0.243 mmol) and $Co_2(CO)_8$ (0.083 g, 0.243 mmol). This solution was then stirred overnight under inert conditions to yield a dark green-brown coloured solution. Solvent was removed by rotary evaporation. The crude product was purified by column chromatography on silica gel with a Pet. ether 40-60 mobile phase. The desired product eluted off the column as a dark green band. The solvent was removed by rotary evaporation yielding a dark green solid.

Yield : 0.118g, 69 %

IR (pentane): 2085, 2051, 2024 cm^{-1}; UV-Vis (pentane) : 236, 278, 328, 386, & 564 nm; ^{1}H-NMR (400 MHz, $CDCl_3$) : 8.70ppm (d, 1H), 8.13 ppm (m, 8H), 4.60ppm (d, 2H), 4.48 ppm (d, 2H), 4.33 ppm (s, 5H); ^{13}C-NMR (100 MHz, d^6-acetone) : δ 167.1, 155.5, 153.9, 147.7, 146.7, 143.7, 139.4, 138.7, 135.9, 133.5, 134.1, 132.7, 129.2, 128.0, 127.0, 126.2, 125.4, 124.6, 113.9, 108.0, 104.9, 103.8, 84.4, 79.6, 79.3, 70.3, 69.5, 69.2

6.3.3.5. 2-pyrenylacetylene, 5-ferrocenylacetylene-thiophene {PyrCCThCCFc}

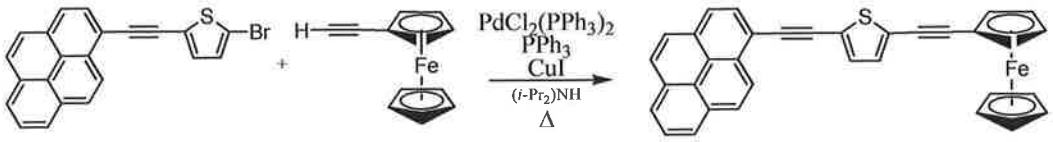

To freshly distilled and argon purged diisopropylamine (10 mL) was added 2-bromo, 5-ethynylpyrene thiophene (0.100 g, 0.26 mmol), $PdCl_2(PPh_3)_2$ (0.011 g, 0.015 mmol, 6%), CuI (0.0029 g, 0.015 mmol, 6%), PPh_3 (0.0081 g, 0.031 mmol, 12 %). This solution was purged with argon for a further 5 mins. To this was then added ethynylferrocene (0.054 g, 0.258 mmol). This solution was then stirred at relux temperature for 3 hrs yielding a bright orange coloured solution. Solvent was removed under reduced pressure. The crude product was purified by column chromatography on neutral aluminium oxide by initially eluting with 100 % petroleum ether followed by a 90:10 petroleum ether:diethyl ether mix. Solvent was removed by roary evaporation yielding the desired bright orange product.

Yield : 0.095 g, 71 %

IR (CH_2Cl_2) : 2054, 2127, 2156, 1738, 1603 cm^{-1}; UV-Vis (CH_2Cl_2) : 240, 276, 286, 322, 334, 394, 416 nm; ^{1}H-NMR (400 MHz, $CDCl_3$) : 8.59 ppm (d, 1H), 8.17 ppm (m, 8H), 7.30 ppm (d, 1H, ^2J = 4 Hz), 7.16 ppm (d,1H, ^2J = 4 Hz), 4.53 ppm (t, 2H), 4.28 (t, 2H), 4.27 ppm (s, 5H); ^{13}C-NMR (100 MHz, $CDCl_3$) : δ 130.79, 130.44, 130.19, 128.41, 127.51, 127.34, 126.23, 125.31, 124.75, 124.70, 124.37, 123.55, 126.45, 123.26, 122.78, 116.10, 92.10, 70.49, 69.07, 68.19 ; M.P. = 205-209 ° C;

6.3.3.6. 2-pyrenylacetylene, 5-ferrocenylacetylene bis $Co_2(CO)_6$ {PyrCCThCCFc[$Co_2(CO)_6$]$_2$}

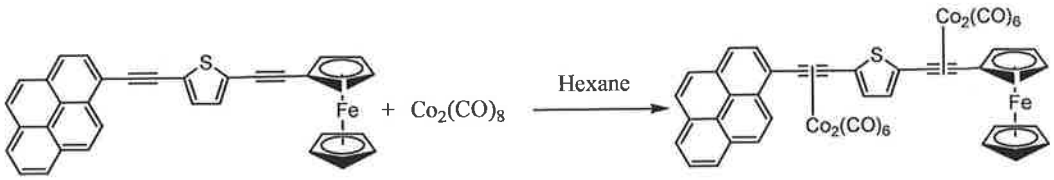

To 15 mL hexane was added 2-pyrenylacetylene, 5-ferrocenylacetylene thiophene (0.050 g, 0.097 mmol) and $Co_2(CO)_8$ (0.066 g, 0.194 mmol). This solution was then stirred overnight under inert conditions to yield a dark green-brown coloured solution. Solvent was removed by rotary evaporation. The crude product was purified by column chromatography on silica gel with a 100 % hexane mobile phase. The desired product eluted off the column as the second dark green band. The solvent was removed by rotary evaporation yielding a dark green solid.

Yield : 0.100g, 93.8 %

IR (pentane): 2090, 2083, 2058, 2028, 2015 cm^{-1}; UV-Vis (pentane) : 226, 278, 378, & 576 nm; ^{1}H-NMR (400 MHz, $CDCl_3$); ^{13}C-NMR (100 MHz, $CDCl_3$) : δ 8.36 ppm (d,1H), 8.08 ppm (m, 8H), 7.40 ppm (d, 1H, ^2J=3.84 Hz), 7.39 ppm (d, 1H, ^2J=3.84 Hz), 4.26 ppm (m, 2H), 4.23 ppm (d, 1H), 4.03 ppm (m, 2H), 3.71 ppm (s, 5H)

6.4. Results

6.4.1. UV-vis absorption spectra

Table 1 lists the absorption maxima (λ_{max}) and extinction coefficients (ε) for all compounds in this study. All compounds exhibit strong absorption bands in the UV region of the spectrum normally associated with ligand localised $\pi \rightarrow \pi^*$ transitions[27]. All UV-Vis spectra were recorded in spectrophotometric grade CH_2Cl_2. All contain UV bands in the electronic absorption spectrum between 240 - 280 nm, which may be assigned to ligand based transitions on both the pyrene and thiophene groups. The lower energy absorbances from 300 - 400 nm are due to the presence of the ferrocene unit. For the $Co_2(CO)_6$ complexes a weak low energy band is also observed between 580 - 600 nm. This is assigned to a weak Co ($d\pi$) $\rightarrow$ ligand (π) charge-transfer (MLCT) transition.

Table 1 Absorption properties and extinction coefficients (ε) for compounds in this study[#]

	λ_{max} (nm), ε (x 10^7 $M^{-1}cm^{-1}$)
PyrCCPy	248 (1.92), 272 (1.03), 284 (1.56), 328 (6.06)*, 342 (1.47), 360 (1.89), 384 (1.67)*
$PyrCCPyCo_2(CO)_6$	236 (6.39), 268 (3.37), 384 (3.17), 560 (2.43)*
PyrCCFc	280 (2.58), 294 (1.83), 350 (2.27), 364 (2.91), 380 (2.37)
$PyrCCFcCo_2(CO)_6$	234 (3.59), 276 (1.98), 328 (1.05), 388 (1.21), 564 (1.88)*
PyrCCThCCFc	274 (6.85), 286 (8.20), 312 (5.51), 324 (7.26), 334 (7.50), 394 (1.30)†, 412 (1.25)†
$PyrCCThCCFcCo_2(CO)_6$	230 (3.66)†, 278 (2.04)†, 388 (1.35)†, 580 (1.96)

*ε = x 10^6 M^{-1} cm^{-1}; † = x 10^8 M^{-1} cm^{-1}
All spectra were recorded in CH_2Cl_2

6.4.2. Fluorescence studies

Room temperature emission studies of all compounds in this series were carried out in CH_2Cl_2 and the lifetimes of the emissive excited state species measured using the single photon counting (SPC) technique. For all organic ligands in this series, irradiation of each of the different absorption bands resulted in the same emission band. Complexation with $Co_2(CO)_6$ strongly quenches the strong emission observed for the uncomplexed ligands. No notable shift is observed in the λ_{max} in the emission spectra, which suggests the emission observed is ligand based. Visible excitation led to structured luminescence in all pyrenyl-acetylide compounds in this study. Room temperature (298 K), low temperature (77 K) emission bands, and their lifetimes (τ) are shown below in Table 2. Low temperature emission and lifetime studies could only be obtained for the PyrCCPy system and its complex $PyrCCPyCo_2(CO)_6$, due to the insolubility of the ferrocenyl systems.

Table 2 Luminescence properties (298 K and 77 K) of the ligands and the complexes

	298 K[a]		77 K[b]	
	λ_{em} (nm)	τ (ns)	λ_{em} (nm)	τ (ns)
PyrCCPy	384, 404, 425(sh.)	17.6, 6.49	383, 401, 448, 473, 493, 665	23.5
$PyrCCPyCo_2(CO)_6$	386, 406,	18.8, 6.15	345, 407, 448, 488, 528, 663	4.52, 58.1
PyrCCFc	395, 407 (sh.)	15.61, 0.38	-	-
$PyrCCFcCo_2(CO)_6$	397, 418	3.38, 6.93	-	-
PyrCCThCCFc	406, 465, 486	1.46, 17.67	-	-
$PyrCCThCCFcCo_2(CO)_6$	405, 427, 445	1.70, 11.07	-	-

Room temperature (298 K) luminescence spectra and excited state lifetimes recorded in spectrophotometric grade dichloromethane.[b] Low-temperature (77 K) luminescence spectra and excited state lifetimes (τ) recorded in 4:1 EtOH:MeOH. Low–temperature (77 K) luminescence spectra and lifetimes could not be obtained for the pyrene-ferrocene dyad systems or their dicobalt hexacarbonyl complexes due to insolubility in 4:1 EtOH:MeOH

6.4.3. Cyclic voltammetry studies

Cyclic voltammetry studies were carried out on PyrCCPy and $PyrCCPyCo_2(CO)_6$ in a 0.1 M $TBAPF_6/CH_3CN$ electrolyte solution with a Teflon shrouded platinum working electrode (3 mm diameter), a platinum wire counter electrode and a non-aqueous Ag/Ag^+ reference electrode. The filling solution for the non-aqueous Ag/Ag^+ reference electrode was 0.1 M $TBAPF_6$ and 0.1 mM $AgNO_3$ in anhydrous acetonitrile In the case of the ferrocenyl systems and their dicobalt hexacarbonyl complexes, due to insolubility in acetonitrile solution, cyclic voltammetry studies were carried out in a 0.1 M $TBAPF_6/CH_2Cl_2$ electrolyte solution. All potentials are quoted in volts vs. Ag/Ag^+ reference electrode with respect to the Fc^+/Fc redox pair. Scan rate is 100 mV S^{-1} unless otherwise stated. E_{ap} corresponds to an irreversible anodic process. E_{cp} corresponds to an reversible cathodic process. $E_{½}$ corresponds to a reversible electrode process, it is assumed that $E_{½} \approx E^{o\prime}$. The half-wave potential $E_{½} = (E_{ap}-E_{cp})/2$ and $\Delta E_p = E_{ap}-E_{cp}$. Table 3 indicates the electrochemical data obtained for all ligands and complexes in this study

Table 3 Electrochemical properties at room temperature

Complex	E_{ap} or $E_{½}$ (V) [ΔE_p (mV)]	E_{cp} or $E_{½}$ (V) [ΔE_p (mV)]
PyrCCPy	1.2,	-0.37, -1.17, -1.41
$PyrCCPyCo_2(CO)_6$	0.49, 0.82, 1.2	-0.54, -1.38, -1.82
PyrCCFc	0.33 (101), 0.72, 1.2	-1.17, -1.40
$PyrCCFcCo_2(CO)_6$	0.33 (65), 0.92, 1.2	-1.11, -1.35
PyrCCThCCFc	0.34 (57), 1.1, 1.2	-1.21, -1.46
$PyrCCThCCFc[Co_2(CO)_6]_2$	0.34 (68), 0.92, 1.2	-1.14, -1.36

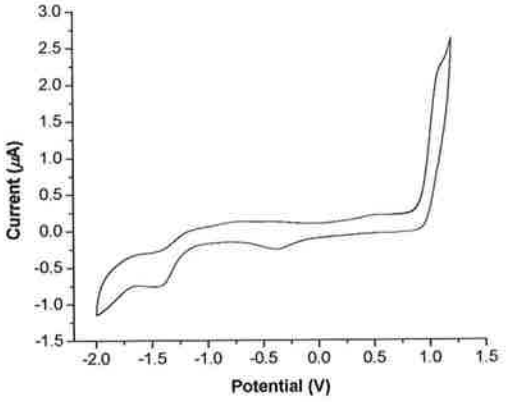

PyrCCPy

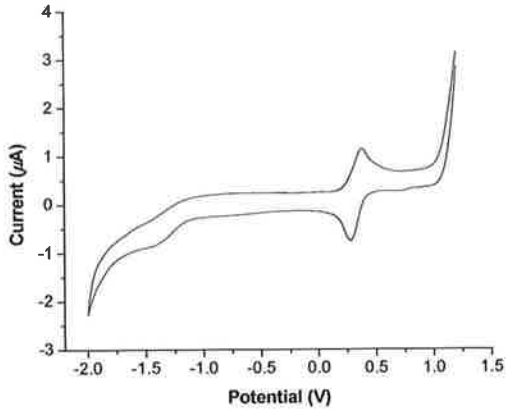

PyrCCFc

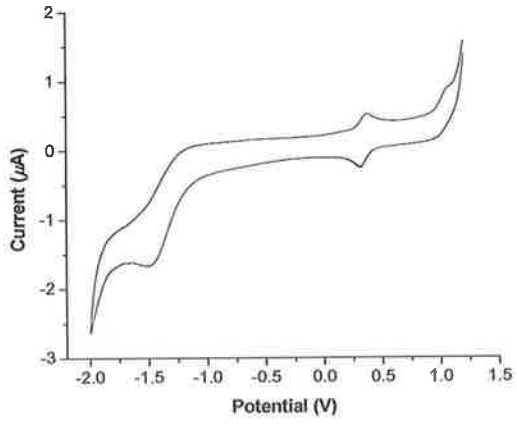

PyrCCThCCFc

Figure 19 Cyclic voltammograms of the uncoordinated ligands PyrCCPy, PyrCCFc, and PyrCCThCCFc

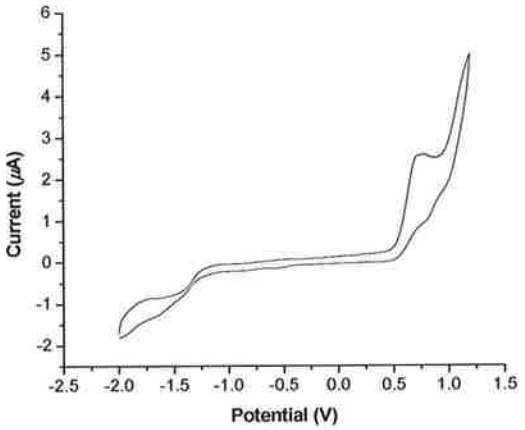

PyrCCPyCo$_2$(CO)$_6$

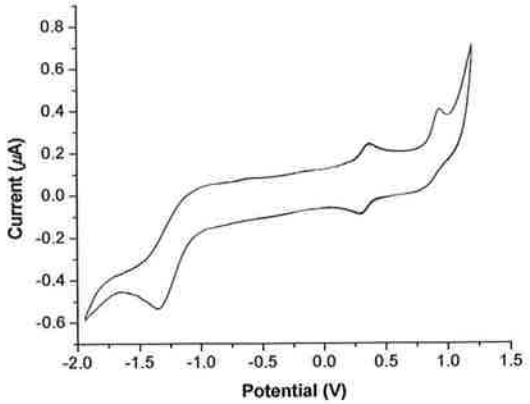

PyrCCFcCo$_2$(CO)$_6$

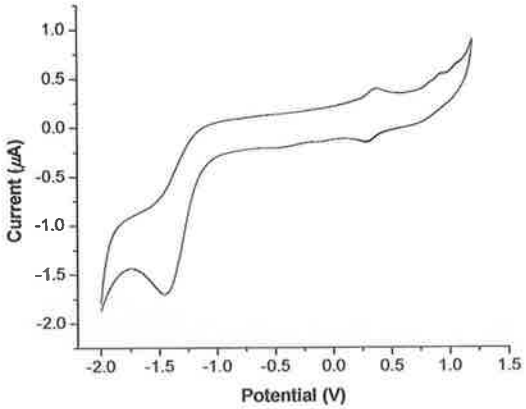

PyrCCThCCFc[Co$_2$(CO)$_6$]$_2$

Figure 20 Cyclic voltammograms of PyrCCPyCo$_2$(CO)$_6$, PyrCCFcCo$_2$(CO)$_6$, PyrCCThCCFc[Co$_2$(CO)$_6$]$_2$

6.4.4. Steady-State Photolysis

Broadband photolysis of the dicobalt hexacarbonyl complexes in this study with visible light ($\lambda_{exc} > 520$ nm and $\lambda_{exc} > 400$ nm) in the presence of the trapping ligand PPh_3 showed formation of both pentacarbonyl and tetracarbonyl species. (Table 4). In each case, product bands were assigned by comparison with similar species described in the literature.

Table 4 The carbonyl band positions in pentane for the parent dicobalt hexacarbonyl complexes and the photoproducts in this study

Complex	ν_{co} ($cm^{-1} \pm 2\ cm^{-1}$)
$PyrCCPyCo_2(CO)_6$	2092, 2057, 2031
$PyrCCPyCo_2(CO)_5PPh_3$	2064, 2016, 2006, 1980
$PyrCCPyCo_2(CO)_4(PPh_3)_2$	2021, 1980, 1971
$PyrCCFcCo_2(CO)_6$	2085, 2051, 2024
$PyrCCFcCo_2(CO)_5PPh_3$	2058, 2012, 2001, 1992
$PyrCCFcCo_2(CO)_4(PPh_3)_2$	1980, 1970, 1959
$PyrCCThCCFc[Co_2(CO)_6]_2$	2091, 2086, 2058, 2030
$PyrCCThCCFc[Co_2(CO)_{6-n}]_2(PPh_3)_n$	2064, 2048, 2014, 2002, 1981, 1973

6.5. Discussion

6.5.1. Room temperature emission studies and lifetime measurements

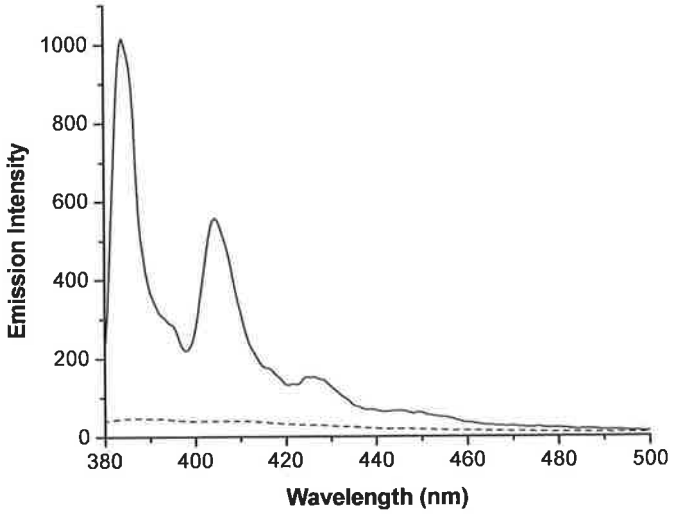

Figure 21 Room temperature emission spectrum of PyrCCPy (—) and the corresponding hexacarbonyl complex $PyrCCPyCo_2(CO)_6$ (----) following 360 nm excitation (iso-absorptive CH_2Cl_2 solutions at 360 nm)

As is evident in Figure 21 excitation of PyrCCPy at 360 nm leads to dual emission, with bands at 384 and 404 nm and a weak shoulder at 425 nm. This dual emission is very similar in both appearance and position to that observed in chapter 5 for the PyrCCTMS and PyrCCH systems, where two sharp and well-defined emission bands were observed at 385 and 405 nm following excitation at 345 nm. This suggests that as observed for both PyrCCTMS and PyrCCH the 298 K emission observed for PyrCCPy is pyrene based. On complexation with dicobalt hexacarbonyl to yield $PyrCCPyCo_2(CO)_6$ the emission intensity is significantly reduced, by approximately 95 % when compared to PyrCCPy. Although significant quenching of the emission is observed no shift in band position or generation of new bands is observed on complexation. This suggests that in both PyrCCPy and its hexacarbonyl complex in room temperature CH_2Cl_2 solution the observed emission is entirely ligand based with no significant MLCT contributions observed following complexation.

Little change in the singlet excited state lifetime ($^1\tau$) is observed on going from PyrCCPy which possesses a lifetime, $^1\tau$, of 17.6 ns to the hexacarbonyl complex $PyrCCPyCo_2(CO)_6$ with a lifetime of 18.8 ns. In both cases the observed dual emission was fitted with a bi-exponential function, resulting in singlet lifetimes of 17.6 and 6.49 ns for the PyrCCPy ligand and 18.8 and 6.15 ns for the complex $PyrCCPyCo_2(CO)_6$. For both systems however, the longer lifetimes of 17.6 and 18.8 accounted for the major relative contribution (approximately 95 %) for PyrCCPy and $PyrCCPyCo_2(CO)_6$, respectively while the shorter lived species possessing singlet lifetimes in the range 6.0-6.5 ns accounted for only 5-7 % of the relative contribution. The observed singlet lifetimes ($^1\tau$) for these systems are very similar to those observed for the analogous systems PyrCCH and $PyrCCHCo_2(CO)_6$ discussed in Chapter 5, where lifetimes of 17 and 18 ns were observed for the ligand and complex, respectively. This coupled with the similar emission profile suggests that both systems share a common excited state photochemistry resulting in similar photophysical properties. Furthermore, this also suggests that the appended pyridine unit does not significantly partake in the excited state dynamics of this system.

The room temperature emission properties and excited state lifetime of PyrCCFc were also investigated in CH_2Cl_2 solution. Excitation at 384 nm of a weak solution of PyrCCFc in CH_2Cl_2 (where the O.D at the excitation wavelength was ~ 0.3 A.U.) resulted in a single intense broad featureless emission band centred at 395 nm (Figure 22). This band position is similar to one of the emission bands observed by Veciana and co-workers[18] for a similar Pyrene-Ferrocene dyad where emission bands were observed at 385, 405 and 425 nm following 350 nm excitation. The weak emission discussed by this group was assigned to quenching of the pyrene based emission by the ferrocene unit. Addition of the oxidising agent copper (II) triflate resulted in a large increase in the emission band intensity. However, the emission band observed for PyrCCFc is significantly broader, and as such may overlap with possible emission bands at 405 and 425 nm. Furthermore, the emission band observed following excitation of PyrCCFc is very intense, suggesting that in this system the ligand based emission is not quenched by the ferrocene unit as is often observed[10,18,28].

As is suggested in Figure 22 complexation with dicobalt hexacarbonyl to yield $PyrCCFcCo_2(CO)_6$ significantly reduced the intensity of the PyrCCFc based emission band by approximately 98 % resulting in almost complete quenching of the pyrene based emission. However, little change in the emission band profile or position is observed on complexation with $Co_2(CO)_6$. Furthermore, no new emission bands are observed for the complexed species compared to PyrCCFc. This suggests that PyrCCFc too appears to follow the trend described in the previous chapter, whereby the emission for both ligand and hexacarbonyl complex is ligand based and as such predominantly due to the pyrene chromophore.

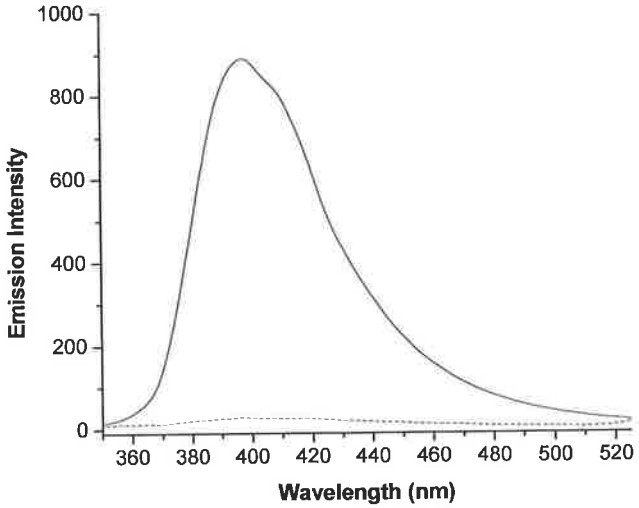

Figure 22 Room temperature emission spectrum of PyrCCFc following 280 nm excitation (—) and the hexacarbonyl complex $PyrCCFcCo_2(CO)_6$ (----) following 280 nm excitation in CH_2Cl_2 solution, respectively.

However, the singlet excited state lifetime ($^1\tau$) of 15.6 ns is significantly longer lived than that of 3.38 ns observed under similar conditions for the $PyrCCFcCo_2(CO)_6$ complex. However, in both cases these lifetimes are predominant lifetimes observed for PyrCCFc and $PyrCCFcCo_2(CO)_6$, respectively following analysis of the observed emission with a bi-exponential function. In the case of PyrCCFc the shorter lived species has a lifetime of approximately 0.38 ns and comprises a percentage relative contribution towards the emission of 38.62 %. Similarly, $PyrCCFcCo_2(CO)_6$ when fit with a bi-exponential produces two lifetimes of 3.38 ns and 6.93 ns, contributing 71.94 and 28.06 %, respectively.

The room temperature emission properties of the more conjugated system PyrCCThCCFc were also investigated. This system contains a central 2-5-diethynylthiophene unit between the pyrenyl and ferrocenyl terminal ends. The addition of a thiophene bridge increases the π-conjugation between the donor and acceptor terminal ends. Furthermore, it has been observed that the thiophene linker is more effective in improving electronic coupling between these terminal units compared to other aromatic linkers such as diethynylbenzene. Thus it has been suggested that these α-disubstituted oligoethynylthiophene units show good potential in improving metal-metal charge transfer and in promoting electron transfer along the carbon rich backbone of these linear systems[29]. The emission spectrum observed following excitation of PyrCCThCCFc in a room temperature CH_2Cl_2 solution at 394 nm is shown in Figure 23. As is evident from Figure 23, excitation at 294 nm results in the generation of a single intense broad emission band centred at 465 nm. However, a shoulder is also observed at ~ 493 nm. This may be due to a second emission band, which is partially masked by the broad intense emission observed at 465 nm.

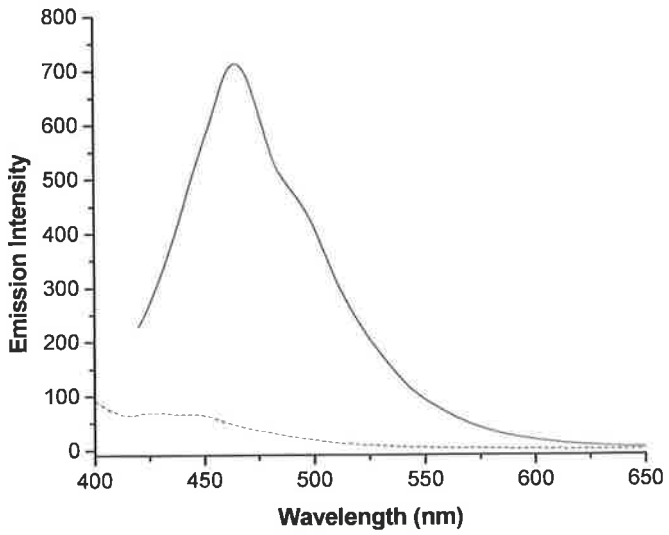

Figure 23 Room temperature emission spectrum of PyrCCThCCFc following 394 nm excitation (—) and the hexacarbonyl complex PyrCCThCCFc[$Co_2(CO)_6$]$_2$ (----) following 388 nm excitation in CH_2Cl_2 solution, respectively.

The observed emission was best fitted with a bi-exponential function, where χ^2 = 1.032. This gave two excited state lifetimes of 1.46 ns and 17.67 ns, possessing percentage relative contributions towards the excited state of 79.75 % and 20.25 % respectively. This suggests that the dominant excited state species observed on excitation of PyrCCThCCFc possesses a singlet excited state lifetimes ($^1\tau$) of 1.46 ns. This is similar to those observed by Benniston and co-workers.[31,37] for similar pyrene-thiophene systems. However, this singlet excited state lifetime is significantly lower than those observed for PyrCCPy and PyrCCFc, where the central thiophene unit is absent and for a number of ferrocene-pyridine and metal carbonyl substituted pyridine dyad systems studied by Lees and co-workers[10] where lifetimes of 27-32 ns were observed.

Addition of the dicobalt hexacarbonyl units to both ethynyl bridges present in PyrCCThCCFc resulted in the production of the PyrCCThCCFc$[Co_2(CO)_6]_2$. As previously observed for other hexacarbonyl complexes in this series complexation resulted in a significant reduction (~ 90 %) in the intensity of the emission band. Furthermore, on complexation the emission maximum is blue shifted by 40 nm from 465 nm to 425 nm. This suggests that complexation with two $Co_2(CO)_6$ units may result in some weak MLCT contributions from the carbonyl units. However, as for the ligand PyrCCThCCFc the observed emission is predominantly ligand based and is significantly reduced in intensity on complexation. However, little change is observed in the singlet exited state lifetime. For PyrCCThCCFc$[Co_2(CO)_6]_2$, fitting with a bi-exponential function resulted in two lifetimes, $^1\tau$ = 11.07 ns and $^2\tau$ = 1.70. As observed for PyrCCThCCFc, the shorter singlet lifetime of 1.70 ns was again the dominant excited state lifetime (86.52 % relative contribution) for this complex.

6.5.2. Low temperature emission studies and lifetime measurements

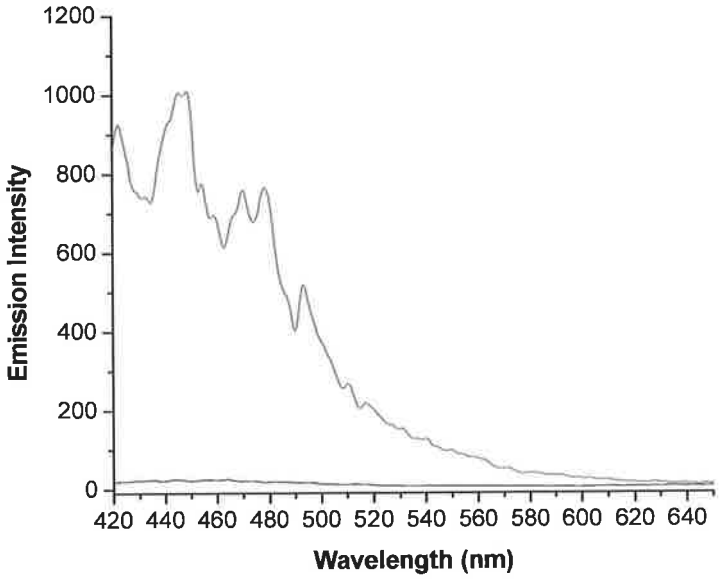

Figure 24 Low temperature (77 K) emission spectra of PyrCCPy (—) and the hexacarbonyl complex PyrCCPy$Co_2(CO)_6$ (—) in frozen 4:1 EtOH:MeOH glasses following 384 nm excitation

Excitation of a 77 K glass of PyrCCPy at 384 nm resulted in a emission profile similar to that previously observed at room temperature in CH_2Cl_2 solution. However, the previously observed easily defined emission bands are not as well defined due to significant splitting, which may be as a result of scattering of light from the 77 K glass. However, as observed in room temperature CH_2Cl_2 solution, the emission spectrum of PyrCCPy in 4:1 EtOH:MeOH glass contains emission bands at 447, 469, 479 and 493 nm respectively, which are red-shifted by approximately 65 nm compared to those observed at room temperature. In addition, complexation with dicobalt hexacarbonyl resulted in significant bleaching of the emission profile by approximately 98 % compared to that of the PyrCCPy at 77 K. This suggests that overall, the same processes are responsible for emission in both room temperature solution and 77 K glasses.

Significant changes are also observed in the singlet excited state lifetimes ($^1\tau$) between the ligand PyrCCPy and the complex $PyrCCPyCo_2(CO)_6$ in low temperature glasses. Low temperature excited state lifetimes studies of PyrCCPy produced two excited state lifetimes of 2.48 and 23.52 ns respectively, with the latter supplying the major relative percentage contribution of 73.16 % to the excited state. However, a shorter lived species (2.24 ns) was also observed at a lower percentage relative contribution (26.84 %). This is notably higher than that of 17 ns observed for PyrCCPy in room temperature solution. An increase in the excited state lifetime on cooling to 77 K is often observed for such systems due to improved ISC and reduced non-radiative decay resulting in an increase in possible triplet emission. Furthermore, the lifetime observed for the complex $PyrCCPyCo_2(CO)_6$ is significantly decreased from 17 ns to 5 ns, in going from a 298 K solution to a 77 K 4:1 EtOH:MeOH glass.

Low temperature (77 K) emission spectra and low temperature lifetimes could not be obtained for either ferrocene ligands, PyrCCFc or PyrCCThCCFc or the corresponding dicobalt hexacarbonyl complexes due to insolubility in the EtOH:MeOH mixture which is used to obtain the 77 K glass.

6.5.3. Electrochemistry

In both the pyrene-pyridine and pyrene-ferrocene dyads an oxidation is observed at positive potentials of 1.0 - 1.1 V *vs.* Ag/Ag^+. This apparently irreversible oxidation is assigned to oxidation of the pyrene unit based on comparison with values in the literature[30,35,37] for this oxidation process. No reduction potential is observed for this species. This may be due to the combination of the initially formed oxidised pyrene unit combing with a second pyrene to form a dimeric cationic species.[31] Furthermore, oxidation at high potentials (+1.4 - +1.8 V) results in pacification of the electrode surface and a concomitant loss of all characteristic redox potentials. This has been previously observed and is due to deposition or electropolymerisation of the compound onto the electrode surface preventing further measurement.[32]

The cyclic voltammograms of PyrCCPy and its dicobalt hexacarbonyl complex were measured in $TBAPF_6/CH_3CN$ electrolyte solution. In both systems an irreversible oxidation process, assigned to oxidation of the pyrene unit, was observed at approximately 1.1 V *vs.* Ag/Ag^+. The cyclic voltammogram of PyrCCPy also exhibits two irreversible reduction processes at -0.37 and -1.17 V *vs.* Ag/Ag^+. The former reduction potential may be due to an impurity present on successive scanning as it was absent on initial scanning. The latter reduction potential at -1.17 V *vs.* Ag/Ag^+ is tentatively assigned to reduction of the pyridine unit. On complexation to form $PyrCCPyCo_2(CO)_6$, the previously mentioned irreversible pyrene oxidation is observed at approximately 1.2 V. Furthermore, a broad irreversible oxidation is also observed at 0.768 V *vs.* Ag/Ag^+. This oxidation assigned to oxidation of the cobalt carbonyl unit is at somewhat higher (100 mV) oxidation potentials than that typically observed.[33] This shift towards higher oxidation potentials may be due to the electron withdrawing effect of the pyridine unit making it more difficult to oxidise the Co metal centre. No redox processes are observed in the region of -0.37 V, which further suggests the -0.37 V irreversible reduction wave observed for PyrCCPy, is due to an impurity present in solution. Although a weak irreversible reduction wave is initially observed in the cyclic voltammogram of $PyrCCPyCo_2(CO)_6$ at -1.37 V *vs.* Ag/Ag^+ this quickly disappears suggesting an irreversible electrochemical process which results in decomposition at the electrode surface. This was further confirmed by

examination of the electrode surface where deposition of a thin yellow layer was evident. This resulted in the previously described pacification of the electrode.

The electrochemical properties of the pyrene-ferrocene dyad system, PyrCCFc, were also investigated. However, due to issues of poor solubility these studies were undertaken in a $TBAPF_6/CH_2Cl_2$ electrolyte solution. As previously described an irreversible oxidation of the pyrene unit was observed at potentials of +1.2 V *vs.* Ag/Ag^+. Furthermore, as would be expected a reversible redox process was observed at $E_{½}$ = 0.33 V *vs.* Ag/Ag^+. The energy band gap (ΔEp) was calculated as 101 mV while i_{pa}/i_{pc} was calculated to be 1.1. This reversible redox potential is due to the oxidation and reduction (Fe^{2+}/Fe^{3+}) of the terminal ferrocene unit. This ferrocene based Fe^{2+}/Fe^{3+} redox couple is observed at higher potentials, by approximately 100 mV, compared to Fc/Fc^+ under similar experimental conditions. This shift of the redox potential to more reductive potentials may be due to the electron-donating properties of the appended pyrene unit. This Fe^{2+}/Fe^{3+} redox process for PyrCCFc, was observed at the significantly more oxidative potential of 0.67 V vs. decamethylferrocene by Robinson and co-workers[19] in CH_2Cl_2 solution. This significant difference in the Fc/Fc^+ redox potential may be due to different reference electrodes being employed. This redox process also occurs at significantly more reductive potentials than those observed at 0.77 V vs. decamethylferrocene by Veciana and co-workers[18] for similar pyrene-ferrocene dyad systems, where the ethynyl bridge is substituted for an azine bridge (Figure 14). This significant difference is due to a number of factors. The less electronegative azine bridge increases the potentials required to oxidise the ferrocene unit. Furthermore, different solvents and different reference electrode (Ag/AgCl) were employed. However, the observed potential at 0.33 V *vs.* Ag/Ag^+ is similar to that observed at 0.48 V *vs.* SCE by Baumgartner and co-workers[14] for diphenylphoshine-ethynylferrocene systems in a $TBAPF_6/CH_2Cl_2$ solution. This value is also in the range of that observed by Connelly and Geiger[34] for the Fc/Fc^+ redox couple at 0.46 V *vs.* SCE in CH_2Cl_2 solution.

The cyclic voltammogram of the dicobalt hexacarbonyl complex $PyrCCFcCo_2(CO)_6$ also exhibits the characteristic irreversible pyrene based oxidation at approximately 1.2 V *vs.* Ag/Ag^+. As previously observed for the dicobalt hexacarbonyl complexes an

irreversible oxidation of the cobalt centre is also observed at 0.92 V vs. Ag/Ag^+. This oxidation is observed at similar potentials to those observed by Dembinski and co-workers[33] at 0.99 V *vs.* Ag pseudo-reference electrode in $(NBu_4)BF_4/CH_2Cl_2$ electrolyte solution for a dicobalt hexacarbonyl 5-*p*-tolylethynyl-2'-deoxyuridine system. Furthermore, the oxidation of the cobalt centre is shifted to higher potentials due to the electron withdrawing effects of the ferrocenyl units. This accounts for the ~ 300 mV difference in oxidation potential of the cobalt centre in system containing a ferrocene unit (0.9 V) compared to those discussed in chapter 5 where the ferrocene unit is absent (0.6 - 0.7 V). Additionally, an irreversible oxidation process is also observed at 0.33 V *vs.* Ag/Ag^+. As previously discussed this reversible redox process is based on the Fe^{2+}/Fe^{3+} redox chemistry of the ferrocene terminal unit. Comparison of this potential with that observed for the uncomplexed dyad, PyrCCFc, indicates that coordination of the dicobalt hexacarbonyl unit has no effect on the redox properties of the ferrocene unit. The energy band gap (ΔEp) for this process was calculated as 65 mV, while $i_{pa}/i_{pc} = 0.76$. Overall, this suggests that this process is a fully reversible redox process involving the one-electron oxidation and subsequent reduction of the iron (Fe^{2+}) centre of the ferrocene unit. Moreover, a reduction wave is also observed at strongly reductive potentials of -1.4 V *vs.* Ag/Ag^+. This reduction process is tentatively assigned to the quasi-reversible reduction of the previously oxidised pyrene unit. This assignment is based on comparison of these quasi-reversible process with reduction potentials of -2.07 V and -1.78 V *vs.* SCE reported by Harriman and co-workers [35] for reduction of pyrene and 1-ethynylpyrene respectively. The reported PyrCCFc dyad is structurally more similar to the latter ethynylpyrene species and would as such be expected to have pyrene reduction potential closer to the value observed for that species. Furthermore, the presence of the electron donating ferrocene unit further shifts the observed reduction potential to more positive (oxidative) potentials.

The electrochemical properties of the system PyrCCThCCFc, containing a pyrene, thiophene and ferrocene linked by ethynyl linkages, were also investigated. The first oxidation observed for this system is the expected oxidation of the pyrene unit at approximately 1.05 V *vs.* Ag/Ag^+. A ferrocene based reversible Fe^{2+}/Fe^{3+} redox process is also exhibited at 0.34 V *vs.* Ag/Ag^+. This redox couple possesses an energy band gap (ΔEp) of 57 mV with an i_{pa}/i_{pc} value of 1.33. This energy band gap

corresponds to that expected for a fully reversible one – electron redox process, and is based on the Fc/Fc^+ redox couple. Furthermore the low i_{pa}/i_{pc} value of 1.33 further suggests that this is a one-electron redox process. This redox potential occurs at slightly higher potentials than that of the shorter PyrCCFc dyad. Bruce and co-workers[36] have previously observed that increasing the carbon chain length results in a shift of the ferrocene redox process to higher potentials. In addition to this an intense reduction wave is also observed at reductive potentials of -1.21 V *vs.* Ag/Ag^+. This assignment is based on the similarity of this reductive process, in terms of reduction potential, with that observed by Benniston and co-workers[37] at -1.40 V *vs.* Ag/AgCl for the reduction of the thiophene unit in a pyrene-thiophene-anthracene-terpyridine array. Furthermore, this potential is also similar to that observed for the analogous system PyrCCThCCH at -1.26 V *vs.* Ag/Ag^+, which was discussed in Chapter 5. Overall, coordination of the ferrocene unit appears to have little effect on the reductive potentials of the central thiophene unit. Coordination of two dicobalt hexacarbonyl units to this ligand, resulting in the formation of $PyrCCThCCFc[Co_2(CO)_6]_2$ does not appear to significantly alter the electrochemical properties of the previously discussed PyrCCThCCFc unit. A weak irreversible oxidation process due to oxidation of pyrene is observed at 1.2 V *vs.* Ag/Ag^+, while at slightly lower oxidation potentials a weak irreversible process at 0.92 V *vs.* Ag/Ag^+ is assigned to the irreversible oxidation of cobalt. This oxidation potential is in good agreement with the oxidation of cobalt observed by Dembinski and co-workers[33] in a dicobalt hexacarbonyl complex. A reversible ferrocene based redox couple is observed at 0.34 V *vs.* Ag/Ag^+, indicating no shift in the redox potential of this unit on complexation with the two dicobalt hexacarbonyl units. An increase in the energy band gap (ΔEp) from 57 mV to 68 mV is observed while the i_{pa}/i_{pc} value also increase from 1.33 to 1.44 between the PyrCCThCCFc ligand the $Co_2(CO)_6$ complex respectively. While coordination of the dicobalt hexacarbonyl units does appear to very slightly reduce the oxidation potential of Fe^{2+}, it also appears to more significantly reduce the reduction potential by approximately 15 mV, thus making reduction of Fe^{3+} to Fe^{2+} more difficult. This accounts for the slightly higher ΔEp and i_{pa}/i_{pc} values. As previously observed for PyrCCThCCFc, the corresponding bis dicobalt hexacarbonyl complex also exhibits an irreversible reduction at -1.14 V vs. Ag/Ag^+ assigned to the irreversible reduction of the central thiophene unit. Unusually this appears at a reductive potential approximately 10 mV more positive than that

observed for the same reduction process in PyrCCThCCFc. This trend had been previously observed and is ascribed to the increased electron density present at the Co_2C_2 core.[36,38]

6.5.4. Steady-State photolysis

Steady-state photolysis of $PyrCCPyCo_2(CO)_6$ with $\lambda_{exc} > 520$ nm in pentane solution in the presence of the trapping ligand PPh_3, resulted in bleaching of the parent hexacarbonyl bands at 2092, 2057 and 2031 cm^{-1} and predominant formation of the pentacarbonyl photoproduct $PyrCCPyCo_2(CO)_5PPh_3$ with carbonyl bands at 2064, 2016, 2006, 1980 and 1971 cm^{-1} (Figure 25). The assignment of these bands as belonging to a PPh_3-trapped pentacarbonyl species is based on favourable comparison with those observed by Long et al.[39] for $(\mu_2\text{-}C_6H_5C_2H)Co_2(CO)_5(PPh_3)$ in cyclohexane solution and by Gordon et al[40] following formation of $(PhCCH)Co_2(CO)_5Ar$ in a frozen argon matrix.

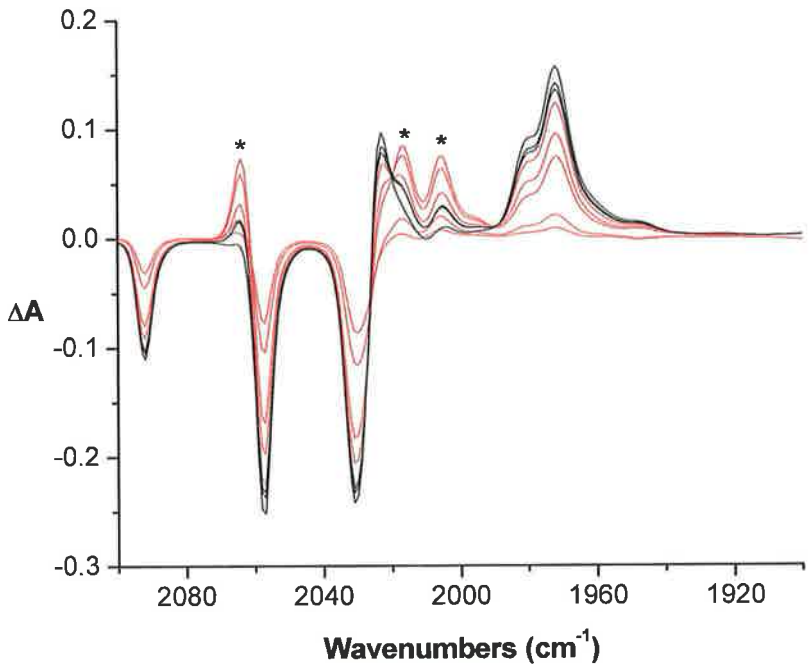

Figure 25 Difference spectrum following steady-state photolysis with $\lambda_{exc} > 500$ nm of $PyrCCPyCo_2(CO)_6$ in pentane solution in the presence of excess PPh_3. Photolysis during the first 10 mins is shown in red, while the subsequent 5 mins are shown in black. Formation of the pentacarbonyl species is denoted by *.

However, as can be seen in Figure 25 extended irradiation ($\lambda_{exc} > 500$ nm) over 15 mins results in the preferential formation of the tetracarbonyl species

$PyrCCPyCo_2(CO)_4(PPh_3)_2$ with bands at 2021, 1980 and 1971 cm^{-1}. Although the latter two product bands are also observed for the pentacarbonyl species, it is evident from Figure 25, that on extended irradiation, these bands continue to increase in intensity along with the newly generated product band at 2021 cm^{-1}, while those previously assigned to the pentacarbonyl species do not change in intensity indicating the formation of a steady-state.

During the initial 5 mins irradiation at > 400 nm, further bleaching of the parent absorption bands is observed, with little concomitant generation of the pentacarbonyl bands previously observed. Conversely, during the subsequent 5 mins photolysis, notable depletion of the previously generated pentacarbonyl bands at 2064, 2016, 2006, 1980 and 1971 cm^{-1} and tetracarbonyl bands at 2021, 1980 and 1971 cm^{-1} was observed. This occurred with concomitant generation of product bands at 2080, 2044 and 2037 cm^{-1} due to the generation of an unknown tertiary photoproduct. This may be as a result of orthometallation similar to that observed by Hong and co-workers[41] in a bulky cobalt containing phosphine ligand system.

Steady state photolysis was also carried out on the ferrocenyl bound dicobalt carbonyl complex, $PyrCCFcCo_2(CO)_6$ in pentane solution in the presence of the trapping ligand triphenylphosphine. As is evident in Figure 26 initial irradiation with λ_{exc} > 520 nm for 10 mins in pentane solution in the presence of PPh_3 resulted in bleaching of the parent hexacarbonyl bands at 2085, 2051 and 2025 cm^{-1} with concomitant generation of product carbonyl bands at 2058, 2012, 2001 and 1992 cm^{-1}. These bands are of similar intensity and are as such assigned to generation of the CO loss pentacarbonyl species $PyrCCFcCo_2(CO)_5PPh_3$[39].

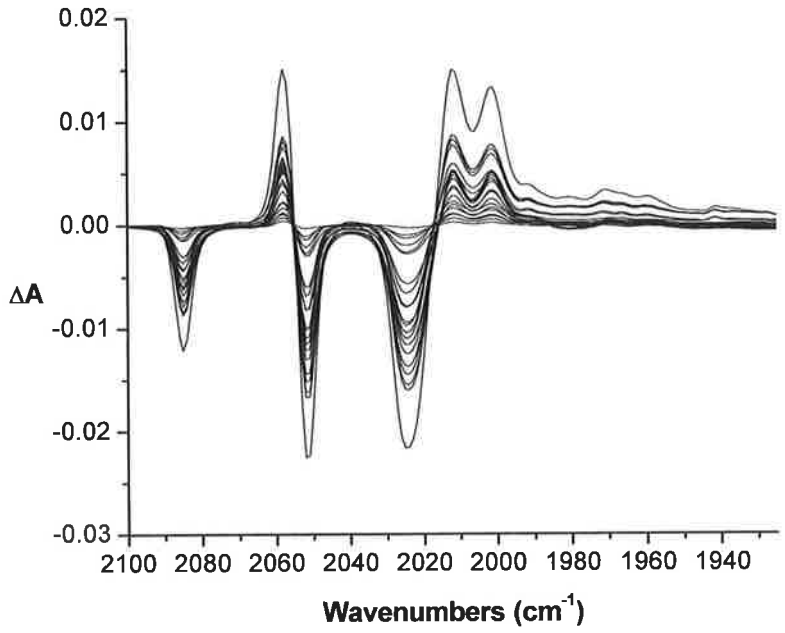

Figure 26 Difference spectrum following steady-state photolysis at > 520 nm and > 400 nm of $PyrCCFcCo_2(CO)_6$ in pentane solution in the presence of PPh_3.

Significantly weaker product bands are also generated at 1980, 1970 and 1959 cm^{-1} and are tentatively assigned to formation of a tetracarbonyl product based on comparison with the ν_{co} absorptions observed for $(\mu_2\text{-}C_6H_5C_2H)Co_2(CO)_4(Pyridine)_2$ and $(\mu_2\text{-}C_2H_2)Co_2(CO)_5(PPh_3)_2$.

Subsequent higher energy irradiation at λ_{exc} > 400 nm of $PyrCCFcCo_2(CO)_6$ in pentane solution in the presence of excess PPh_3 resulted in further bleaching of the parent carbonyl bands as well as a continued increase in intensity of the product bands at 2058, 2012, 2001 and 1992 cm^{-1} and 1980, 1970 and 1959 cm^{-1}, which suggests overall that higher energy irradiation continues to form both the pentacarbonyl and tetracarbonyl CO loss products, $PyrCCFcCo_2(CO)_5PPh_3$ and $PyrCCFcCo_2(CO)_4(PPh_3)_2$, respectively (Figure 26).

CO loss was also observed from the disubstituted dicobalt hexacarbonyl complex, PyrCCThCCFc $[Co_2(CO)_6]_2$ in pentane solution in the presence of PPh_3 following broadband irradiation with both λ_{exc} > 520 nm and λ_{exc} > 400 nm. The overall IR differences spectrum are shown in Figure 27.

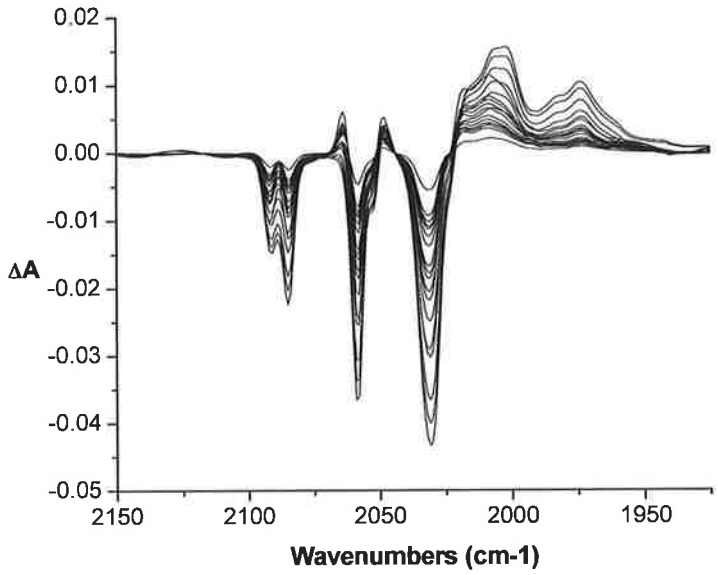

Figure 27 IR differences spectrum of PyrCCThCCFc[$Co_2(CO)_6$]$_2$ in pentane solution in the presence of PPh_3 following broadband irradiation at $\lambda > 520$ nm and > 400 nm.

Steady-state irradiation of PyrCCThCCFc[$Co_2(CO)_6$]$_2$ with $\lambda_{exc} > 520$ nm for 10 mins in pentane solution in the presence of the trapping ligand PPh_3 resulted in bleaching of the parent bands at 2031, 2059, 2084 and 2091 cm^{-1}. It should be noted that in this bis[$Co_2(CO)_6$] substituted complex, two high energy carbonyl bands are observed. This splitting of the IR active bands may be due to the asymmetry of the systems containing both pyrene and ferrocene terminal units. Following irradiation product bands were generated at 2064, 2048, 2014, 2001, 1981, and 1973 cm^{-1}. Again these results suggest that both the PPh_3 trapped pentacarbonyl and tetracarbonyl products are formed. Bleaching of the parent bands including both high energy bands at 2084 and 2091 cm^{-1} suggests that photoinduced CO loss occurs for both coordinated hexacarbonyl units. However, as previously stated a product band is also generated at 2048 cm^{-1}. Based on comparison with observations by Long and co-workers[39] and Ford and co-workers[42] this band does not appear to be concurrent with a product band indicative of either a pentacarbonyl or tetracarbonyl product and may in fact suggest formation of a cobalt cluster system as described by Ford and co-workers[42] or orthometallation as suggested by Gan and co-workers.[41] However, due to the presence of a single band this assignment is purely tentative.

On switching the irradiation wavelength to $\lambda_{exc} > 400$ nm more significant bleaching of the parent bands is observed with a concomitant increase in intensity of the product bands at 2064, 2048, 2014, 2001, 1981, and 1973 cm^{-1}, thus indicating further formation of the pentacarbonyl and tetracarbonyl products. As observed following irradiation with $\lambda_{exc} > 520$ nm, irradiation at $\lambda_{exc} > 400$ nm results in generation of PyrCCThCCFc$[Co_2(CO)_6]_5(PPh_3)$ and PyrCCThCCFc$[Co_2(CO)_6]_4(PPh_3)_2$.

6.6. Conclusions

This chapter involves the synthesis, characterisation, electrochemistry, photophysics and photochemistry of a pyrene-pyridine dyad and a number of pyrene-ferrocenyl dyads. In addition, the properties of the corresponding dicobalt hexacarbonyl complexes are also investigated using the aforementioned techniques. All of the dyads studied display high energy absorption bands due to pyrene and pyridine based $\pi \rightarrow \pi^*$ transitions. Furthermore, a number of bands in the visible region may be ascribed to the ferrocene unit. Following complexation with $Co_2(CO)_6$, the resulting complexes absorb much further into the red due to low energy MLCT transitions between 560 - 600 nm.

Room temperature (298 K) emission studies and emission lifetimes were obtained for all compounds in CH_2Cl_2 solution. Generally, it was observed that the observed emission was pyrene based with no quenching effects observed in spite of the appended ferrocene unit. This is in contrast to many observations where ferrocene has been observed to quench the ligand based emission. Complexation with $Co_2(CO)_6$ significantly reduces the emission by approximately 90 % but retains the same overall emission profile. This suggests that in both cases the observed emission is ligand centred and is IL ($\pi \rightarrow \pi^*$) in nature. Electrochemical studies indicate in all cases the presence of the irreversible pyrene based oxidation and in the case of the hexacarbonyl complexes, a cobalt centred irreversible oxidation. For the ferrocene systems the typically observed ferrocene redox couple is observed. Notably this appears to shift to slightly higher oxidation potentials on increasing the molecular chain length. For PyrCCThCCFc and the corresponding hexacarbonyl cobalt complex a quasi-reversible thiophene based reduction wave is also evident.

Steady-state photolysis studies have also shown that following irradiation of the hexacarbonyl complexes in pentane solution in the presence of PPh_3 the "trapped" CO loss pentacarbonyl and/or tetracarbonyl products are generated with concomitant bleaching of the parent absorptions.

6.7. Bibliography

1 M.M. Bhadbhade, A. Das, J.C. Jeffery, J.A. McCleverty, J.A. Navas Badiola, M.D. Ward, *J. Chem. Soc. Dalton Trans.*, **1995**, 2769-2777

2 J.D. Carr, S.J. Coles, M.B. Hursthouse, J.H.R. Tucker, *J. Organomet. Chem.*, **2001**, 637-639, 304-310

3 D. F. Perepichka, I.F. Perepichka, A.F. Popov, M.R. Bryce, A.S. Batsanov, A. Chesney, J.A.K. Howard, N.I. Sokolov, *J. Organomet. Chem.*, **2001**, 637-639, 445-462

4 A. Trujillo, M. Fuentealba, C. Manzur, D. Carrillo, J.-R. Hamon, *J. Organomet. Chem.*, **2003**, 681, 150-157

5 G. Laus, C.E. Strasser, M. Holzer, K. Wurst, G. Pürstinger, K.-H. Ongania, M. Rauch, G. Bonn, H. Schottenberger, *Organometallics*, **2005**, 24, 6085-6093

6 Y. Jiang, X. Chai, W. Tang, D. Zhang, Y. Cao, Z. Zhu, T. Li, J.-M. Lehn, *Science in China (Series B)*, **1997**, 40, 3, 236-244

7 X. Zhao, H.K. Sharma, F.Cervantes-Lee, K.H. Pannell, G.J. Long, A.M. Shahin, *J. Organomet. Chem.*, **2003**, 686, 235-241

8 M. Inouye, Y. Hyodo, H. Nakazumi, *J. Org. Chem.*, **1999**, 64, 2704-2710

9 J.T. Lin, J.J. Wu, C.-S. Li, Y.S. Wen, K.-J. Lin, *Organometallics*, **1996**, 15, 5028-5034

10 S.-S. Sun, D.T. Tran, O.S. Odongo, A.J. Lees, *Inorg. Chem.*, **2002**, 41, 132-135

11 N. Szesni, M. Drexler, J. Maurer, R.F. Winter, F. de Montigny, C. Lapinte, S. Steffens, J. Heck, B. Weibert, H. Fischer, *Organometallics*, **2006**, 25, 5774-5787

12 M.I. Bruce, M.E. Smith, B.W. Skelton, A.H. White, *J. Organomet. Chem.*, **2001**, 637-639, 484-499

13 M.I. Bruce, P.J. Low, F. Hartl, P.A. Humphrey, F. de Montigny, M. Jevric, C. Lapinte, G.J. Perkins, R.L. Roberts, B.W. Skelton, A.H. White, *Organometallics*, **2005**, 24, 5421-5255

14 T. Baumgartner, M. Fiege, F. Pontzen, R. Arteaga-Müller, *Organometallics*, **2006**, 25, 5657-5664

15 E.M. McGale, B.H. Robinson, J. Simpson, *Organometallics*, **2003**, 22, 931-939 and references therein

16 R. Packheiser, B. Walfort, H. Lang, *Organometallics*, **2006**, 25, 4579-4587

17 H. Lang, R. Packheiser, B. Walfort, *Organometallics*, **2006**, 25, 1836-1850

18 R. Martínez, I. Ratera, A. Tárraga, P. Molina, J. Veciana, *Chem. Commun.*, **2006**, 3809-3811

19 L. Cuffe, R.D.A. Hudson, J.F. Gallagher, S. Jennings, C.J, McAdam, R.B.T. Connelly, A.R. Manning, B.H. Robinson, J. Simpson, *Organometallics*, **2005**, 24, 2051-2060 and references therein

20 A.H. Flood, C.J. McAdam, K.C. Gordon, H.G. Kjaergaard, A.M. Manning, B.H. Robinson, J. Simpson, *Polyhedron*, **2007**, 26, 448-455

21 A. Caballero, A. Tárraga, M.D. Velasco, P. Molina, *J. Chem. Soc., Dalton Trans.*, **2006**, 1390-1398 and references therein

22 Y.S. Sohn, D.N. Hendrickson, H.B. Grey, *J. Am. Chem. Soc.*, **1971**, 93, 3603

23 M. Hissler, A. Harriman, A. Khatyr, R. Ziessel, *Chem. Eur. J.*, **1999**, 5, 11, 3366-3381

24 W.R. Browne, C.M. O'Connor, C. Villani, J.G. Vos, *Inorg. Chem.*, **2001**, 40, 5461-5464

25 K. Sonogashira, Y. Tohda, N. Hagihara, *Tetrahedron Lett.* **1975**, 16,50, 4467-4470

26 W.B. Austin, N. Bilow, W.J. Kelleghan, K.S.Y. Lau, *J. Org. Chem.***1981**, 46, 11, 2280-2286

27 D.V. Kozlov, D.S. Tyson, G. Goze, R. Ziessel, F.N. Castellano, *Inorg. Chem.* **2004**, 43, 6083-6092

28 Jonathen Rochford, Ph.D Thesis, Dublin City University, **2004**

29 L.-B. Gao, J. Kan, Y. Fan, L. –Y Zhang, S.-H. Liu, Z.-N. Chen, *Inorg. Chem.*, **2007**,Online

30 J.L. Sessler, Y. Kubo, A. Harriman, *J. Phys. Org. Chem.*, **1992**, 5, 644-648

31 A.C. Benniston, A. Harriman, D.J. Lawrie, A. Mayeux, K. Rafferty, O.D. Russell, *Dalton Trans.*, **2003**, 4762-4769

32 D.V. Kozlov, D.S. Tyson, C. Goze, R. Ziessel, F.N. Castellano, *Inorg. Chem.*, **2004**, 43, 6083-6092

33 N. Esho, B. Davies, J. Lee, R. Dembinski, *Chem. Commun*, **2002**, 4, 332 - 333

34 N.G. Connelly, W.E. Geiger, *Chem. Rev.*, **1996**, 96, 877-910

35 A. Harriman, M. Hissler, R. Ziessel, *Phys. Chem. Chem. Phys.*, **1999**, 1, 4203-4211

36 M.I. Bruce, M.E. Smith, B.W. Skelton, A.H. White, *J. Organomet. Chem.*, **2001**, 637-639, 484-499

37 A.C. Benniston, A. Harriman, D.J. Lawrie, S.A. Rostron, *Tetrahedron Lett.*, **2004**, 45, 2503-2506

38 C.J. McAdam, N.W. Duffy, B.H. Robinson, J. Simpson, *Organometallics*, **1996**, 15, 3935

39 S.M. Draper, C. Long, B.M. Myers, *J. Organomet. Chem.*, **1999**, 588, 195-199

40 C.M. Gordon, M. Kiszka, I.R. Dunkin, W.J. Kerr, J.S. Scott, J. Gebicki, *J. Organomet. Chem.*, **1998**, 554, 147-154

41 Y.-H. Gan, J.-C. Lee, F.E. Hong, *Polyhedron*, **2006**, 25, 3555-3561

42 J. Marhenke, S.M. Massick, P.C. Ford, *Inorg. Chim. Acta*, **2007**, 360, 825-836

Appendix

A Matrix Isolation – Sample Preparation

The sample is transferred to either a linear or "L-shaped" pyrex side arm which is then attached to the lower part of the matrix shroud. The system is brought to the required vacuum (approximately 10^{-6} Torr.) and deposition temperature (20 K). A specific volume of the required matrix gas is allowed into the gas handling line. This is then co-condensed onto the cold window with the sample. A gauge on the gas handling controls the rate of deposition of the matrix gas. Varying the temperature of the sample in the side arm controls the rate of sample deposition. The amount of sample deposition is periodically monitored using IR spectroscopy, until the maximum absorbance of the sample is 0.8 and 1.0 AU in the carbonyl region.
For matrix isolation studies equipment essential for construction of a system are as follows:

- Refrigeration system

The refrigerator consists of a compressor unit connected to a compact expander unit or head module by high pressure (feed) and low-pressure (return) helium. The helium is compressed and then allowed to expand within the head module. The expansion of the helium causes the cooling effect. The choice of both coolant gas and host gas controls the temperature allowed in the matrix system. A cryostat from APD Cryogenics Inc. was used in the experiments described in this study.

- Vacuum system

The shroud enclosing the head module of the refrigerator must be evacuated to insulate the cold sample from warming by convection and conduction (Dewar vacuum). Pressures of around 10^{-3} millibarr are sufficient to provide an efficient vacuum, however to minimise contamination, the highest achievable vacuum is required. A vacuum system of about 10^{-7} Torr inside the sample chamber, when the cold window is at its experimental temperature (12 K) is required in all experiments. This vacuum was achieved by using an oil diffusion pump backed by a 5 stage rotary pump from Edwards High Vacuum International.

- Gas handling system

The gases used were of very high purity from standard metal cylinders, supplied by Cryoservice Ltd. These were connected to regulators suitable for high purity gases, fitted with a flow control valve on the outlet, also supplied by Cryoservice Ltd. This allowed deposition of the matrix host at a controlled rate. Gas mixtures may be made up using a subsidiary gas handling line, increasing the risk of error, but greatly reducing the preparation time.

- Method for generation of transient species

The most common methods of generating reactive species are photolysis and pyrolysis. Photolysis was the chosen method in this study. A variety of light sources have been reported from tungsten filament bulbs to lasers The most versatile light sources are probably high or medium pressure mercury arc lamps, with outputs in the range 200-1000 W and 150-200 W respectively. The monitoring light source used was an air-cooled Oriel Instruments medium pressure xenon arc lamp (300 W), similar to that used in the laser flash photolysis experiments.

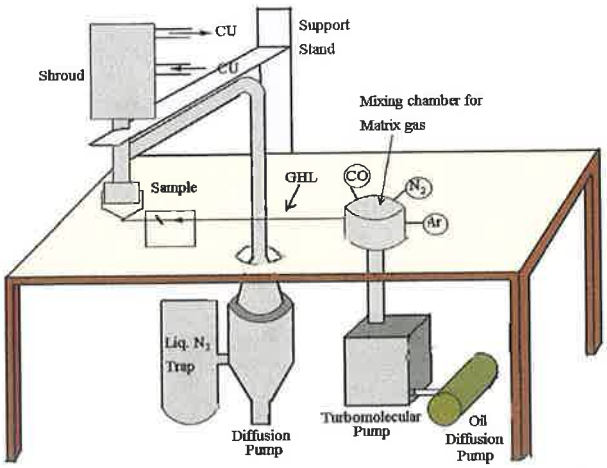

Figure 1 Schematic diagram of Matrix instrumentation.
[CU is the compressor unit. GHL is the gas handling line.][1]

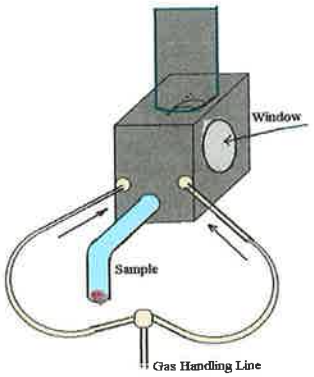

Figure 2 Schematic diagram of matrix isolation cold cell[1]

B Matrix Isolation studies of (η^6-allylbenzene)$Cr(CO)_3$

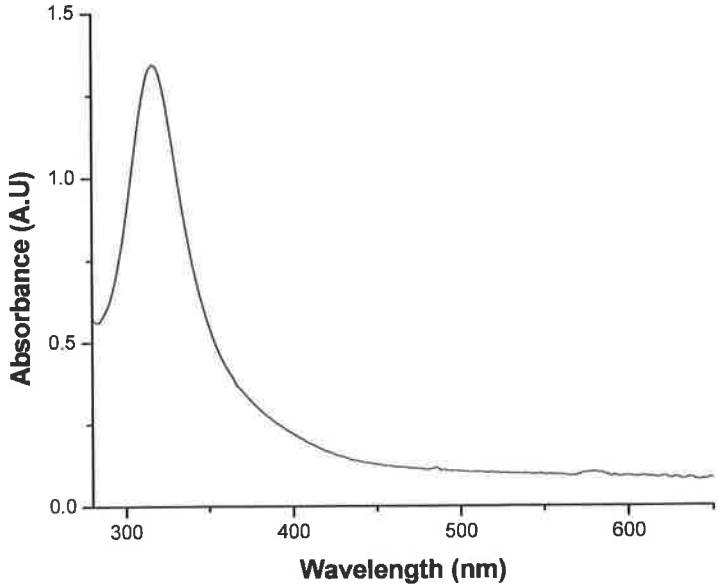

Figure 3 Electronic absorption spectrum of η^6-(allylbenzene)$Cr(CO)_3$ in pentane

B1 Photolysis of (η^6-allylbenzene)$Cr(CO)_3$ in a methane matrix

On deposition of (η^6-allylbenzene)$Cr(CO)_3$ in a methane matrix two strong ν_{co} bands were observed at 1980 and 1907 cm^{-1}. UV irradiation at 365 nm for 95 mins resulted in a small decrease in intensity of the parent bands with concomitant generation of a free CO band at 2137cm^{-1} indicating possible decomposition of the parent species. Subsequent irradiation at 334 nm for 50 mins and 313 nm for 60 mins resulted in further depletion of the parent bands with concomitant generation of weak bands at 1918 and 1864 cm^{-1}. However, no change is observed in the free CO band at 2137 cm^{-1}. Broadband irradiation at > 400 nm for 60mins produced a decrease in intensity of the generated bands at 1918 and 1864 cm^{-1} with concomitant regeneration of the parent bands.

B2 Photolysis of (η^6-allylbenzene)$Cr(CO)_3$ in a dinitrogen matrix

On deposition of (η^6-allylbenzene)$Cr(CO)_3$ in a dinitrogen matrix two ν_{co} bands were observed at 1979 and 1907 cm^{-1}. UV irradiation at 365 nm for 50 mins resulted in a decrease in intensity of the parent bands with concomitant generation of two weak ν_{co} bands at 1935 and 1886 cm^{-1}, a ν_{NN} band at 2150 cm^{-1} and a band at 2140 cm^{-1} due to free CO. Irradiation with 334 nm for 90 mins produced a further decrease in intensity of the parent bands with continued growth of carbonyl bands at 1886, 1935, 2140, 2150 cm^{-1}.

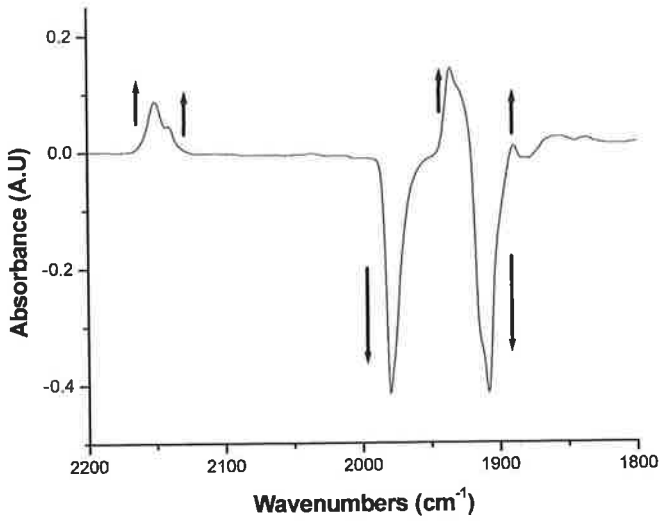

Figure 4 IR difference spectrum of (η^6-allylbenzene)$Cr(CO)_3$ in a dinitrogen matrix following 313 nm irradiation

Subsequent irradiation at 313 nm (Figure 2) produced a very noticeable decrease in the intensity of the parent carbonyl bands with a concomitant sharp increase in the intensity of the product bands at 1935, 1886, 2140 and 2150 cm^{-1} suggesting favourable formation of the N_2 substituted product (η^6-allylbenzene)$Cr(CO)_2N_2$.

B3 Photolysis of (η^6-allylbenzene)$Cr(CO)_3$ in a 10% CO doped methane matrix

On deposition of (η^6-allylbenzene)$Cr(CO)_3$ in a 10% CO doped methane matrix two carbonyl bands were observed at 1979 and 1907 cm^{-1}. Broadband irradiation at $\lambda >$ 320 nm for 80 mins resulted in a very weak decrease in intensity of the parent carbonyl bands and generation of weak bands at 2014, 2036, 2066 and 2110 cm^{-1}. Subsequent broadband irradiation at > 300 nm produced very little change in the intensity of the parent bands or the free CO band at 2137 cm^{-1}.

C Matrix Isolation studies of (η^6-phenanthrene)$Cr(CO)_3$

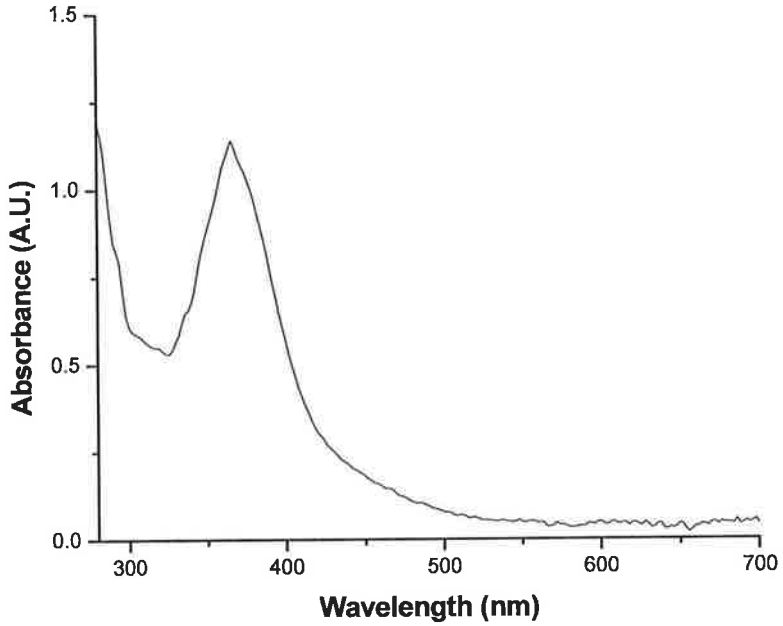

Figure 5 Electronic absorption spectrum of (η^6-phenanthrene)$Cr(CO)_3$ in cyclohexane

C1 Photolysis of (η^6-phenanthrene)$Cr(CO)_3$ in a methane matrix

On deposition of (η^6-phenanthrene)$Cr(CO)_3$ in a methane matrix at 20 K, carbonyl bands were observed at 1973, 1913 and 1901 cm^{-1}. Broadband visible irradiation at λ > 400 nm for 120 nm produced little change in the IR spectrum. On changing the irradiation wavelength to >320 nm and irradiating for 105 mins no change was again observed. This suggests that no CO loss species is generated and in fact a rotamer form of (η^6-phenanthrene)$Cr(CO)_3$ may be generated. Such an isomeric form would involve rotation of the $Cr(CO)_3$ moiety with no net change observed in the ground state spectrum of the complex.

D Quantum Chemical Calculations

D1 Geometry optimisation of 2,6- and 3,5-difluoropyridineW(CO)$_5$

The structures of both 2,6-difluoropyridineW(CO)$_5$ and 3,5 difluoropyridineW(CO)$_5$ were optimised using the B3LYP/LANL2DZ level of theory. Geometry optimisation was initiated at the RHF/STO-3G theory level with the size of the basis set increased incrementally to LANL2DZ followed by further optimisation with this basis set and B3LYP model chemistry.

(a) (b)

Figure 6 Geometry optimised structures of (a) 2,6-difluoropyridineW(CO)$_5$ and (b) 3,5-difluoropyridineW(CO)$_5$ attained using the B3LYP/LANL2DZ level of theory

The calculated bond lengths (Å) and bond angles (°) for the geometry optimised structures of **(a)** 2,6-difluoropyridineW(CO)$_5$ and **(b)** 3,5-difluoropyridineW(CO)$_5$ shown in Figure 6 are outlined in Table 1. The geometrical parameters following geometry optimisation at the B3LYP/LANL2DZ level of theory are compared for each compound.

$2,6\text{-}F_2PyW(CO)_5$		$3,5\text{-}F_2PyW(CO)_5$	
Bond lengths		**Bond lengths**	
N4-W21	2.323	N4-W18	2.288
W21-C1	2.040	W18-C1	2.038
C1-O9	1.181	C1-O9	1.182
W21-C5	2.040	W18-C5	2.038
C5-11O	1.181	C5-O11	1.182
W21-C3	2.040	W18-C3	2.038
C3-O7	1.181	C3-O7	1.182
W21-C6	2.040	W18-C6	2.038
C6-O8	1.181	C6-O8	1.182
W21-C2	1.982	W18-C2	1.992
C2-O10	1.187	C2-O10	1.186
N4-C16	1.356	N4-C16	1.365
C15-C16	1.393	C15-C16	1.397
C15-C14	1.405	C15-C14	1.397
C14-C13	1.405	C14-C13	1.397
C13-C12	1.393	C13-C12	1.397
C12-N4	1.356	C12-N4	1.365
C12-F20	1.375	C13-F21	1.386
C16-F22	1.375	C15-F22	1.386
Bond angles		**Bond angles**	
C2-W21-C1	88.90	C2-W18-C1	89.31
C2-W21-C5	88.90	C2-W18-C5	89.31
C2-W21-C3	88.90	C2-W18-C3	89.31
C2-W21-C6	88.90	C2-W18-C6	89.31
W21-C1-O9	177.56	W18-C1-O9	178.61
W21-C5-O11	177.56	W18-C5-O11	178.61
W21-C3-O7	177.56	W18-C3-O7	178.61
W21-C6-O8	177.56	W18-C6-O8	178.61
W21-C2-O10	180.00	W18-C2-O10	180.00
W21-N4-C16	122.71	W18-N4-C16	120.81
W21-N4-C12	122.71	W18-N4-C12	120.81
N4-C16-C15	125.62	N4-C16-C15	121.05
C16-C15-C14	117.54	C16-C15-C14	122.25
C15-C14-C13	119.07	C15-C14-C13	115.00
C14-C13-C12	117.54	C14-C13-C12	122.25
C13-C12-N4	125.62	C13-C12-N4	121.05

Table 1 Comparison of selected bond lengths (Å) and bond angles (°) for $2,6\text{-}F_2PyW(CO)_5$ and 3,5-F2PyW(CO)5 following geometry optimisation at the B3LYP/LANL2DZ level of theory

Following geometry optimisation of the above structures a vibrational analysis of the ground state electronic structure was undertaken. The frequency calculation was carried out on the B3LYP/LANL2DZ optimised structures to investigate whether any negative frequencies were present, which would indicate that the geometry-optimised structure was not a minimum on the potential energy surface.

For each complex (a) 2,6-F_2PyW(CO)$_5$ and (b) 3,5-F_2PyW(CO)$_5$ no negative frequencies were found indicating that the geometry optimised structures obtained were at an energy minimum. Each complex which is of the type W(CO)$_5$L, has C_{4v} symmetry and as such is predicted to have 3 IR active carbonyl bands – $2A_1$ and E. The E mode is expected to be very strong while both A_1^1 and A_1^2 are expected to be weak bands. In the predicted IR active bands of the two complexes optimised at the B3LYP/LANL2DZ level of theory are compared. For both 2-FPyW(CO)$_5$ and 3-FPyW(CO)$_5$ the calculated IR stretching frequencies are scaled with respect to the experimental values obtained.

2,6-F_2PyW(CO)$_5$	3,5-F_2PyW(CO)$_5$	Assignment
1893[a]	1895	asymmetric CO stretch (E mode)
1894	1898[b]	asymmetric CO stretch (A_1)
	1899	
1929	1932	asymmetric CO stretch (B_1 – not observed)
2021	2023	Symmetric CO stretch (A_1)

Table 2 Comparison of IR active frequencies of 2,6-difluoropyridineW(CO)$_5$ and 3,5-difluoropyridineW(CO)$_5$ calculated at the B3LYP/LANL2DZ theory level. [a]For 2,6-F_2PyW(CO)$_5$ splitting of the E vibrational mode is predicted. [b]For 3,5-F_2PyW(CO)$_5$ splitting of the asymmetric A_1 vibrational mode is predicted.

D2 Calculation of the ground state electronic structures of 2,6- and 3,5-difluoropyridineW(CO)$_5$

Following ground state geometry optimisations at the B3LYP/LANL2DZ level of theory the ground state electronic structures for each of the complexes were calculated and the highest occupied (HOMO) and lowest virtual (LUMO) molecular orbitals were examined in order to provide a framework for the subsequent Time dependent DFT (TDDFT) excited state calculations. For each complex the valence orbitals are plotted according to their energies. Such valence orbitals are very important in that they play an active role in the determination of the electronic excitations and electronic character of the particular complex. The assignment of the type of molecular orbital was made on the basis of its relative composition and by inspection of the three dimensional representation. In each case the compositional assignment is relative in that the majority are of mixed character with a particular MO giving the major compositional contribution. Table 3 lists the most important molecular orbitals

for each of the studied complexes. Five occupied MO's (HOMO to H-4) and nine unoccupied or virtual MO's (LUMO to L+8).

MO	2,6-F_2PyW(CO)$_5$	3,5-F_2PyW(CO)$_5$
L+8	-0.19	-0.56
L+7	-0.38	-0.71
L+6	-0.41	-0.73
L+5	-1.32	-1.56
L+4	-1.65	-2.06
L+3	-1.71	-2.09
L+2	-2.27	-2.39
L+1	-2.29	-2.71
LUMO	-3.04	-3.22
HOMO	-6.28	-6.55
H-1	-6.29	-6.60
H-2	-6.62	-6.99
H-3	-8.92	-8.96
H-4	-10.17	-9.88

Table 3 The molecular orbitals of 2,6-F_2PyW(CO)$_5$ and 3,5-F_2PyW(CO)$_5$ and their energies (eV). HOMO: Highest occupies molecular orbital. LUMO: Lowest unoccupied molecular orbital.H-1 is HOMO-1 and L+1 is LUMO+1

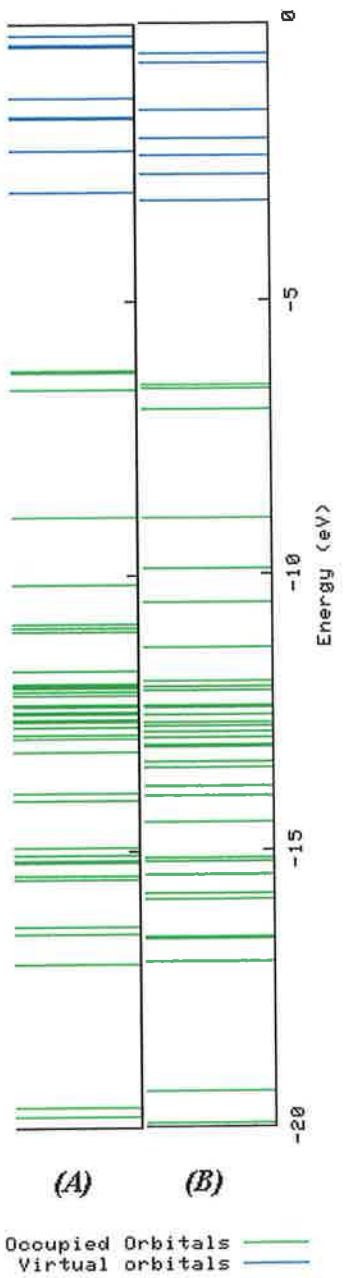

Figure 7 Energy level diagram of (A) 2,6-F_2PyW(CO)$_5$ and (B) 3,5-F_2PyW(CO)$_5$. Extracted from Density of states (DOS) diagram generated by the GaussSum 2.0 programme[2]

MO no.	Assignment	Energy (eV)	W %	CO_{cis} %	CO_{trans} %	2,6-F2Py %
71	L+4	-1.65	11	88	1	0
70	L+3	-1.71	10	88	1	1
69	L+2	-2.27	23	80	0	0
68	L+1	-2.29	0	0	0	98
67	LUMO	-3.04	2	0	2	95
66	HOMO	-6.28	64	24	13	0
65	H-1	-6.29	61	24	13	5
64	H-2	-6.62	62	40	0	0
63	H-3	-8.92	0	0	0	100
62	H-4	-10.17	1	4	1	95

Table 4 The contribution of manganese, each of the four *cis* CO orbitals, the single *trans* CO orbital and the 2,6-difluoropyrdine orbital in 2,6-F_2PyW(CO)$_5$ for each of the selected molecular orbitals

MO no.	Assignment	Energy (eV)	W %	CO_{cis} %	CO_{trans} %	3,5-F2Py %
76	L+4	-2.06	9	88	0	2
75	L+3	-2.09	11	88	2	0
74	L+2	-2.39	1	16	0	83
73	L+1	-2.71	22	80	1	1
72	LUMO	-3.22	1	4	2	94
71	HOMO	-6.55	61	24	12	5
70	H-1	-6.60	64	24	13	0
69	H-2	-6.99	61	40	0	0
68	H-3	-8.96	0	0	0	100
67	H-4	-9.88	1	0	0	97

Table 5 The contribution of manganese, each of the four *cis* CO orbitals, the single *trans* CO orbital and the 3,5-difluoropyrdine orbital in 3,5-F_2PyW(CO)$_5$ for each of the selected molecular orbitals

D3 Time –dependent Density Functional Theory (TDDFT) calculations

State	E (eV) [λ (nm)[a]]	f [b]	$\psi_o \rightarrow \psi_v$ [c]	Character [d]
1	2.4948 (496.98)	0.00	HOMO → LUMO (99 %)	d_{xy}, π-CO → π* Py ligand
2	2.7893 (444.49)	0.1626	H-1 → LUMO (89 %)	d_{xz}, π-CO → π* Py ligand
3	2.8434 (436.05)	0.00	H-2 → LUMO (89 %)	d_{yz}, π-CO_{cis} → π* Py ligand
4	3.1270 (396.49)	0.0113	HOMO → L+2 (81 %) H-2 → L+4 (15 %)	dxy, π-CO → 4 x π*-CO_{cis} d_{yz}, π-CO_{cis} → 4 x π*-CO_{cis}
5	3.1374 (395.18)	0.0114	H-1 → L+2 (80 %) H-2 → L+3 (15 %)	d_{xz}, π-CO → 4 x π*-CO_{cis} d_{yz}, π-CO_{cis} → 4 x π*-CO_{cis}
6	3.1877 (388.94)	0.0008	H-2 → L+2 (80 %) HOMO → L+4 (2 %)	d_{yz}, π-CO_{cis} → 4 x π*-CO_{cis} dxy, π-CO → 4 x π*-CO_{cis}

Table 6 Selected calculated singlet excited states for 2,6-difluoropyridine $W(CO)_5$

State	E (eV) [λ (nm)[a]]	f [b]	$\psi_o \rightarrow \psi_v$ [c]	Character [d]
1	2.6084 (475.33)	0.00	H-1 → LUMO (99 %)	d_{xy}, π-CO → π* Py ligand
2	2.8095 (441.30)	0.1506	HOMO → LUMO (89 %)	d_{xz}, π-CO → π* Py ligand
3	2.9505 (420.21)	0.0075	HOMO → L+1 (61 %) H-2 → LUMO (29 %)	d_{xz}, π-CO → 4 x π*-CO_{cis} d_{yz}, π-CO_{cis} → π* Py ligand
4	3.0162 (411.07)	0.0114	H-1 → L+1 (81 %) H-2 → L+3 (13 %)	d_{xy}, π-CO → 4 x π*-CO_{cis} d_{yz}, π-CO_{cis} → 4 x π*-CO_{cis}
5	3.0506 (406.43)	0.0063	H-2 → LUMO (71 %) HOMO → L+1 (21 %)	d_{yz}, π-CO_{cis} → π* Py ligand d_{xz}, π-CO →4 x π*-CO_{cis}
6	3.1273 (396.46)	0.0016	H-2 → L+1 (88 %) H-1 → L+3 (3 %)	d_{yz}, π-CO_{cis} → 4 x π*-CO_{cis} d_{xy}, π-CO → 4 x π*-CO_{cis}

Table 7 Selected calculated singlet excited states for 3,5-difluoropyridine $W(CO)_5$

[a] Energy of vertical excitation from ground state, [b] Oscillator strength, [c] Occupied to unoccupied (virtual) orbital excitation, [d] Character of excited state

E Synthesis

E1 (*trans, trans*-1,4-diphenyl-1,3-butadiene)Cr(CO)3

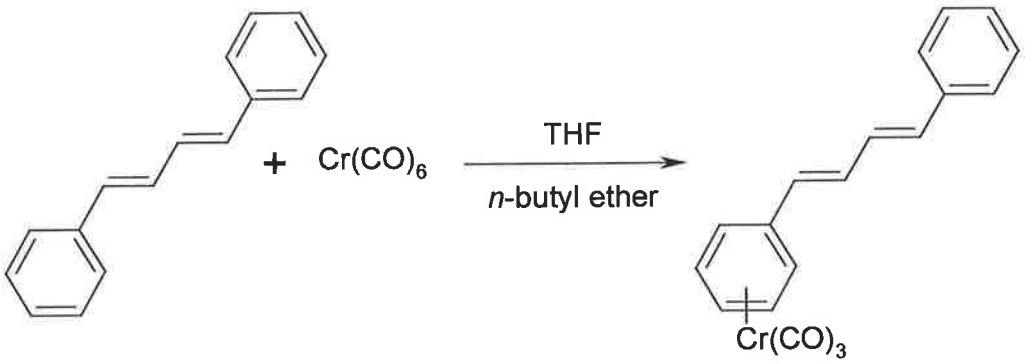

Synthesised according to a method outlined by Pryce[3] with some minor alterations.

To a clean round bottom flask was added *n*-butyl ether (15 mL), which was purged with argon for 10 mins. To this was added 3 mL dry THF, *trans,trans*-1,4-dipehnyl-1,3-butadiene (0.300 g, 1.45 mmol) and $Cr(CO)_6$ (0.319 g, 1.45 mmol). This solution was refluxed overnight under inert conditions to yield a red-orange solution. The solvent and excess $Cr(CO)_6$ were removed under reduced pressure to yield an orange coloured precipitate. TLC analysis on silica with both $CHCl_3$ and pentane showed the presence of an orange and a yellow band. Washing the crude residue with pentane separated the two bands as the orange product was insoluble, while the yellow residue easily went into solution. ^{1}H-NMR analysis showed the orange residue to be the desired product.

Yield: 70%, 0.345 g; IR ($CHCl_3$): $\nu_{(CO)}$ 1972 and 1903 cm^{-1}, UV-Vis (cyclohexane): 206, 316, 332 and 432 nm, ^{1}H-NMR (400 MHz, $CDCl_3$): 7.40pm (d, 2H), 7.22ppm (t, 2H), 7.13ppm (t, 1H), 6.97ppm (m, 2H), 6.67ppm (d, 1H), 6.28ppm (d, 1H), 5.77 ppm (d, 2H), 5.61ppm (t, 2H), 5.47ppm (t, 1H)

E2 (η^6-allylbenzene)$Cr(CO)_3$

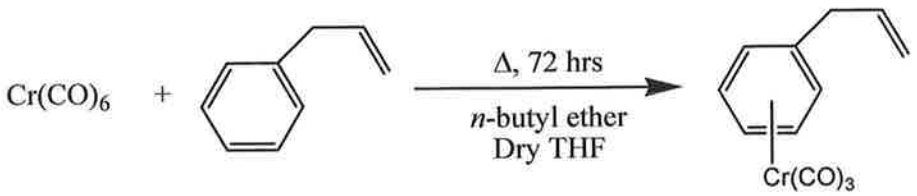

Synthesised according to a method outlined by Pryce[3] with some minor alterations.

To 15 mL argon purged *n*-butyl ether was added 3 mL of freshly distilled THF.To this purged solution was then added $Cr(CO)_6$ (0.300 g, 1.36 mmol) and allylbenzene (0.72 mL, 5.44 mmol, 4 x excess).This solution was then stirred under reflux conditions and under an inert argon atmosphere for 72 hours resulting the formation of a yellow precipitate. The solution was allowed cool to room temperature and the solvent removed under reduced pressure. The resulting crude oil was then washed with hexane yielding an oily yellow residue.

E3 (η^6-phenanthrene)$Cr(CO)_3$

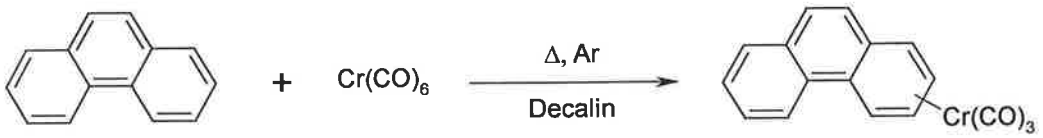

Synthesised according to the method outlined by Hrnviar et al.[4] and Pryce et al.[3] with minor alterations.

To a round bottom flask was added decalin (10 mL), which was purged with argon for 1 hr. To this was then added Cr(CO)6 (0.300 g, 1.35 mmol) and phenanthrene (0.240 g, 1.35 mmol). This solution was then refluxed for 3 hrs under inert conditions to yield a yellow coloured solution. The solution was allowed to cool to room temperature and placed at -20 °C to precipitate out the product. The resulting precipitate was filtered and dried over vacuum. The precipitate was then recrystallised from petroleum ether/benzene.

Yield: 0.085 g, 20%; IR (cyclohexane): $\nu_{(CO)}$ 1905, 1916 and 1975 cm^{-1}, UV-Vis (cyclohexane): 370, 246 nm; ^{1}H-NMR (400 MHz, $CDCl_3$): 8.64 ppm (d, 1H), 8.30 ppm (d, 2H), 7.84 ppm (d, 1H), 7.30 ppm (d, 2H), 6.61 ppm (d, 2H), 5.99 ppm (d, 2H)

E4 1,6 and 1,8 dibromopyrene

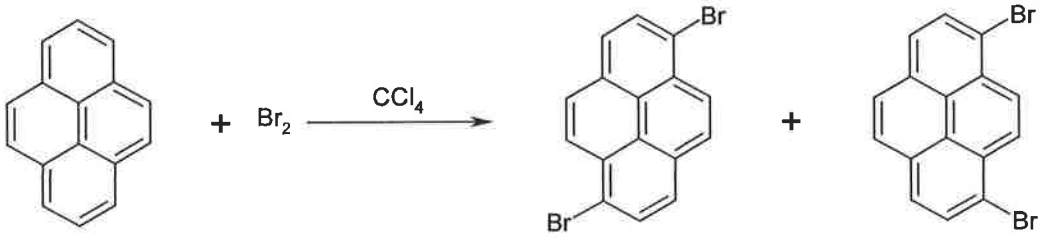

Synthesised according to the method outlined by Grimshaw and Trocha-Grimshaw[5] with minor alterations.

To 25 mL carbon tetrachloride was added pyrene (1.00 g, 4.94 mmol). This was stirred under inert conditions until the pyrene had dissolved. To this solution was then added dropwise over 3 hours Bromine (0.50 mL, 9.88 mmol) in 25 mL carbon tetrachloride. This rust coloured solution was then stirred overnight under inert conditions to yield a pale cream coloured precipitate. This solution was then filtered to yield 1.65 g of crude product, presumably a mixture of both 1,6- and 1,8-dibromopyrene. This crude product was dissolved in a minimum amount of hot tomuene, resulting in a pale yellow solution and an insoluble precipitate. This was then vacuum filtered yielding a pale cream solid and a pale yellow filtrate. On cooling, a solid precipitated from the filtrate, which was subsequently filtered.

E5 Ethynylferrocene dicobalt hexacarbonyl

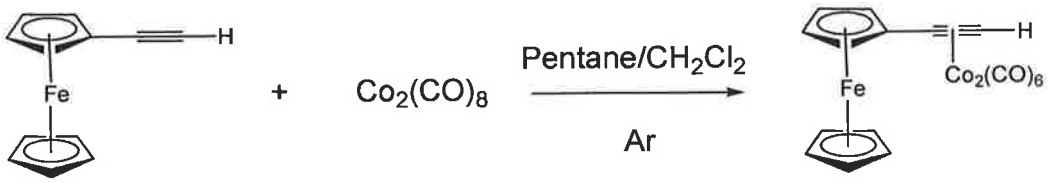

To 20 mL pentane was added ethynylferrocene (0.200 g, 0.952 mmol) and dicobalt octacarbonyl (0.325 g, 0.952 mmol). This solution was then stirred overnight at room temperature under inert conditions to yield a dark green coloured solution. Solvent was removed by rotary evaporation and the resulting green-brown residue purified by column chromatography on silica gel with a 70 % pentane: 30 % CH_2Cl_2 mobile phase. The dark green band due to the desired product was collected and the solvent removed by rotary evaporation to yield a dark green solid.

Yield: 0.209 g, 44 %; IR (CH_2Cl_2): (ν_{cc}) 2210 cm^{-1}, (ν_{co}) 2090, 2051, 2024 cm^{-1}; UV-Vis (CH_2Cl_2): 234, 292, 416, 600 nm; ^{1}H-NMR (400 MHz, $CDCl_3$) : 4.28 ppm (d, 2H), 4.08 ppm (s, 2H), 1.49 ppm (s, 5H), 1.18 ppm (s, 1H),

E6 Trimethylsilylacetylene dicobalt hexacarbonyl

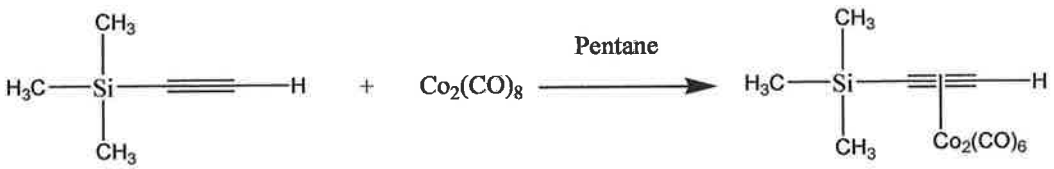

To 25 mL pentane was added trimethylsilylacetylene (0.40 mL, 2.8 mmol) and dicobalt octacarbonyl (0.478 g, 1.4 mmol). This solution was then stirred overnight under inert conditions to yield a dark red coloured solution. Solvent was removed by rotary evaporation and the resulting red residue was dissolved in pentane and placed on a neutral alumina column. This was then subject to elution with pentane. The desired fraction was collected and the solvent removed by rotary evaporation to yield a dark red solid.

Yield: 0.440 g, 81 %; IR (pentane): 2092, 2054, 2029, and 2022 cm^{-1} ; UV-Vis (pentane): 346, 354, 418 and 532 nm; ^{1}H-NMR (400 MHz, $CDCl_3$): 0.3 ppm (s, 9H), 6.4 ppm (s, 1H); ^{13}C-NMR (100 MHz, $CDCl_3$): δ 84.30, 0.84 ppm

E7 Ferrocenylcyclopentenone

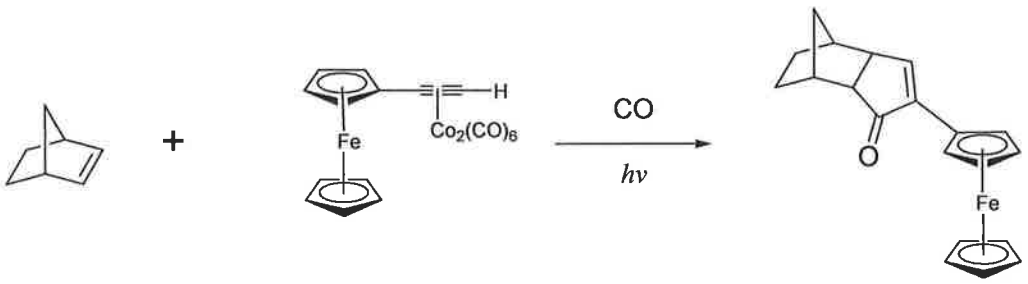

Two photochemical methods were employed to synthesise this ferrocene bound cyclopentenone via a Pauson-Khand type reaction. Method 1 employed the use of natural "white" light for this photochemically driven Pauson-Khand reaction. The second employed the use of a photographic projector for the photochemically driven Pauson-Khand reaction. The differences in yield and mechanism are discussed in The Photochemical Pauson-Khand reaction, A. Coleman, N. Boyle, W. R. Browne, B.L. Feringa, M.T. Pryce, *J. Phys. Chem.*, **2007**, in preparation

Method 1

To 25 mL hexane was added ferrocenylacetylene$Co_2(CO)_6$ (0.050 g, 0.10 mmol).This solution was then purged with CO for 10 mins. To this solution was then added norbornene (0.035 g, 0.37 mmol). This reaction flask was then quickly sealed and placed on a south facing window in natural light. This solution was initially dark green in colour but following 2 months in natural light the green coloured solution had become much paler in colour and a brown-red precipitate had formed. Solvent was removed by rotary evaporation to yield a dark brown residue. This was the purified by column chromatography on a neutral alumina column with an *n*-hexane mobile phase. The desired cyclopentenone product was collected as a rust brown coloured fraction and the solvent removed by rotary evaporation.

Yield: 0.032 g, 23%

Method 2

To 30 mL hexane was added ferrocenylacetylene$Co_2(CO)_6$ (0.210 g, 0.422 mmol). This solution was then purged with CO for 10 mins. To this solution was then added norbornene (0.148 g, 1.58 mmol). Te reaction flask was quickly sealed and placed in front of a Kodak Ektapro 3000 slide projector at a sufficient distance so as to minimise thermal effects. After 45 hrs irradiation the reaction solution had gone from dark green in colour to a dark brown coloured solution containing a rust brown coloured precipitate. Solvent was removed by rotary evaporation to yield a rust brown coloured residue. This was purified by column chromatography on neutral alumina with an *n*-hexane mobile phase. The desired cyclopentenone product was collected as a rust brown coloured fraction and the solvent removed by rotary evaporation.

Yield: 0.110 g, 78 %; IR ($CHCl_3$): 1737 and 1695 cm^{-1}; UV-Vis (pentane):212, 254, 264, 280, 382, 444 nm; ^{1}H-NMR (400 MHz, $CDCl_3$): 7.33 ppm (s, 1H), 4.78 ppm (s, 2H), 4.72 ppm (s, 1H), 4.26 ppm (s, 1H), 4.06 ppm (s, 5H), 2.55 ppm (s, 1H), 2.45 ppm (s, 1H), 2.25 ppm (d, 1H), 2.20 pm (d, 1H), 0.9-1.7 ppm (number of overlapping signals); ^{13}C-NMR (100 MHz, $CDCl_3$): δ 208.8, 155.9, 145.7, 69.5, 54.7, 48.21, 39.27, 38.19, 31.36, 29.08, 28.45; Mass Spec. ESI m/z 332; Anal. Calcd. for $C_{20}H_{20}OFe$ (332.23 $gmol^{-1}$) C 72.31 %, H6.07 %, Found C 72.0 %, H 6.10 %

E8 Trimethylsilylcyclopentenone

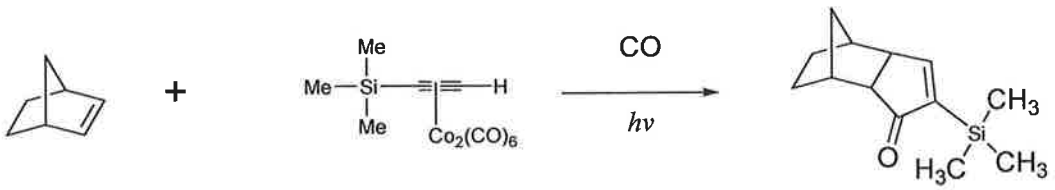

Two photochemical methods were employed to synthesise this trimethylsilyl bound cyclopentenone via a Pauson-Khand type reaction. Method 1 employed the use of natural "white" light for this photochemically driven Pauson-Khand reaction. The second employed the use of a photographic projector for the photochemically driven Pauson-Khand reaction The differences in yield and mechanism are discussed in Photochemical Pauson-Khand reaction, A. Coleman, N. Boyle, W. R. Browne, B.L. Feringa, M.T. Pryce, *J. Phys. Chem.*, **2007**, in preparation.

Method 1

To 30 mL toluene was added Trimethylsilylacetylene$Co_2(CO)_6$ (0.050 g, 0.13 mmol). This solution was then purged with CO for 10 mins. To this solution was then added norbornene (0.025 g, 0.28 mmol). This reaction flask was then quickly sealed and placed on a south facing window in natural light. This solution was initially dark red in colour but following 1 month in natural light the red coloured solution had become much paler in colour and an off white-cream coloured precipitate had formed. Solvent was removed by rotary evaporation to yield a pale red residue. This was then dissolved in pentane and placed on a neutral alumina column. This was then subject to elution with pentane followed by diethyl ether. The desired cyclopentenone product eluted with diethyl ether, was collected and the solvent removed by rotary evaporation.

Yield: 0.050 g, 59 %

Method 2

To 30 mL toluene was added trimethylsilylacetylene$Co_2(CO)_6$ (0.200 g, 0.520 mmol). This solution was then purged with CO for 10 mins. To this solution was then added norbornene (0.097 g, 1.04 mmol). The reaction flask was quickly sealed and placed in front of a Kodak Ektapro 3000 slide projector at a sufficient distance so as to minimise thermal effects. After 45 hrs irradiation the reaction solution had gone from dark red in colour to a pale red coloured solution containing off white-cream coloured precipitate. Solvent was removed by rotary evaporation to yield a cream-yellow coloured residue. This was then dissolved in pentane and placed on a neutral alumina column. This was then subject to elution with pentane followed by diethyl ether. The desired cyclopentenone product eluted with diethyl ether, was collected and the solvent removed by rotary evaporation

Yield: 0.090 g, 78 %; IR ($CDCl_3$): 1735, 1686 cm^{-1}; UV-Vis (pentane):244, 276, 346 nm; ^{1}H-NMR (400 MHz, $CDCl_3$): 7.54 ppm (d, 1H); 2.62 ppm (m, 1H), 2.35 ppm (d, 1H), 2.14 ppm (d, 1H), 2.09 ppm (d, 1H), 1.54 ppm (s, 2H), 1.25 ppm (m, 4H), 0.5 ppm (s, 9H); ^{13}C-NMR (100 MHz, $CDCl_3$): δ 173.12, 150.12, 54.33, 51.91, 39.10, 37.97, 31.05, 29.03, 28.31, -0.2

F UV-Vis spectra of Pyrene-Thiophene dyads

F1 UV-Vis spectrum of $PyrCCTMSCo_2(CO)_6$

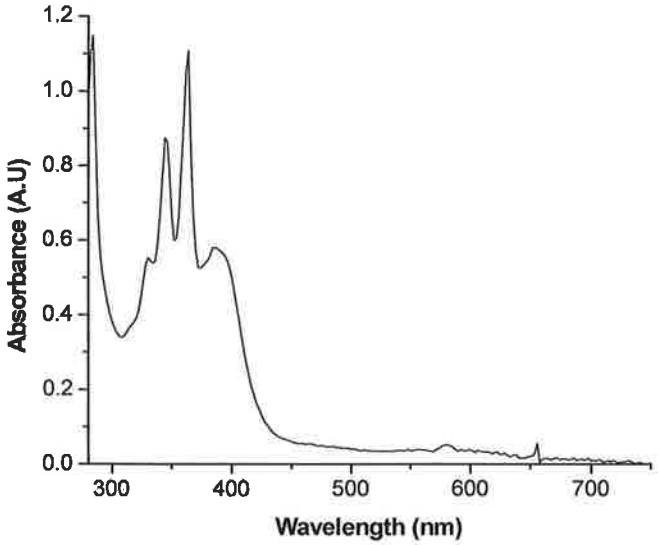

Electronic absorption spectrum of $PyrCCTMSCo_2(CO)_6$ in pentane solution

F2 UV-Vis spectrum of $PyrCCHCo_2(CO)_6$

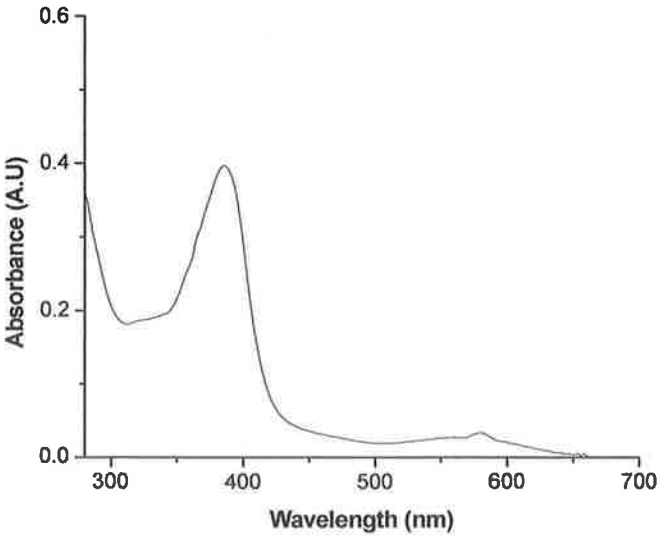

Electronic absorption spectrum of $PyrCCHCo_2(CO)_6$ in pentane solution

F3 UV-Vis spectrum of PyrCCTh

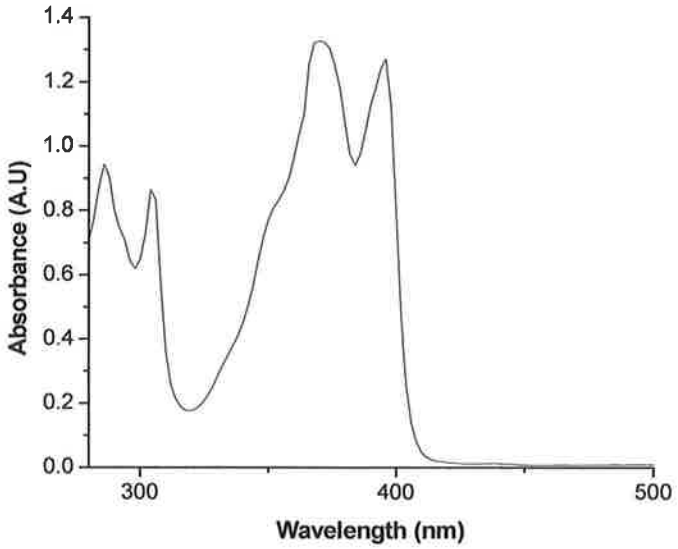

Electronic absorption spectrum of PyrCCTh in CH_2Cl_2 solution

F4 UV-Vis spectrum of PyrCCTh$Co_2(CO)_6$

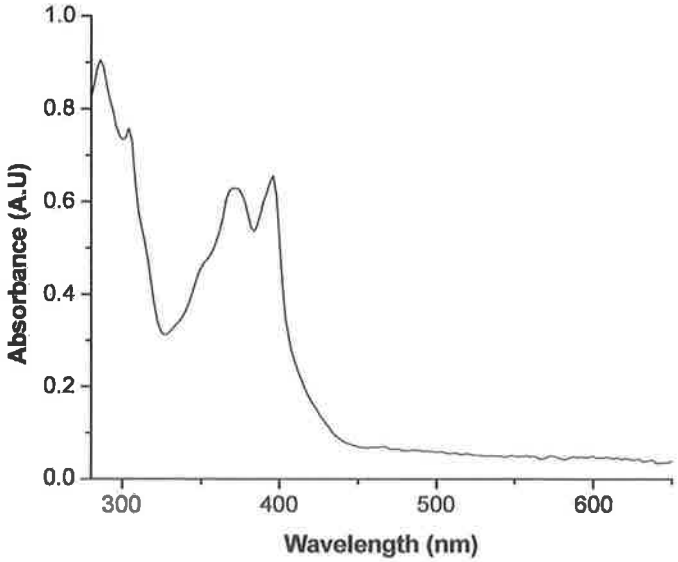

Electronic absorption spectrum of PyrCCTh$Co_2(CO)_6$ in CH_2Cl_2 solution

F5 UV-Vis spectrum of PyrCCThBr

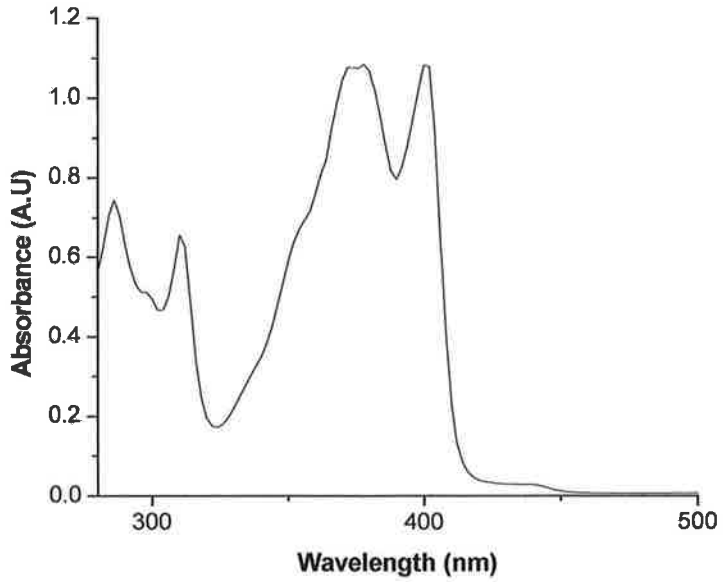

Electronic absorption spectrum of PyrCCThBr in CH_2Cl_2 solution

F6 UV-Vis spectrum of PyrCCThBr$Co_2(CO)_6$

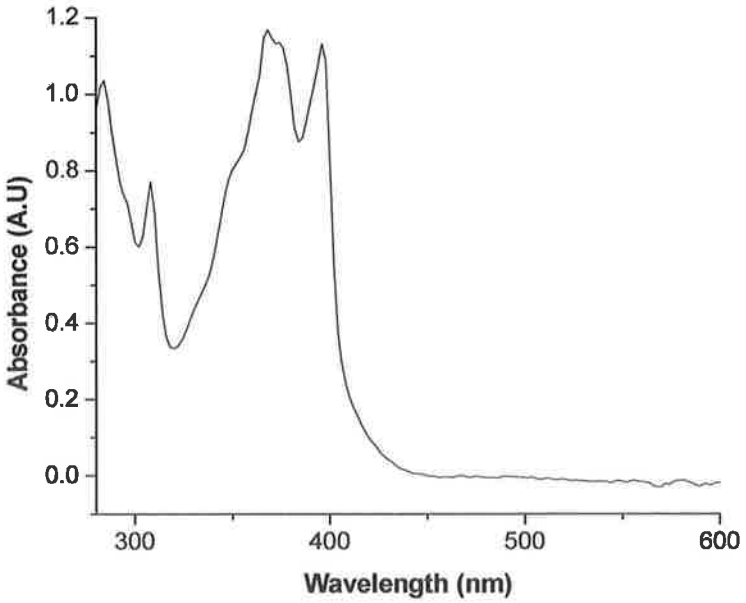

Electronic absorption spectrum of PyrCCThBr$Co_2(CO)_6$ in CH_2Cl_2 solution

F7 UV-Vis spectrum of PyrCCThmal

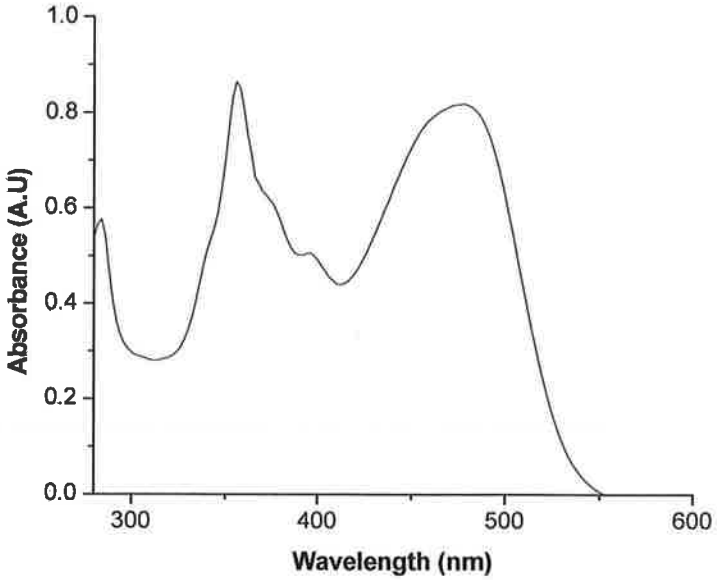

Electronic absorption spectrum of PyrCCThmal in CH_2Cl_2 solution

F8 UV-Vis spectrum of PyrCCThmal$Co_2(CO)_6$

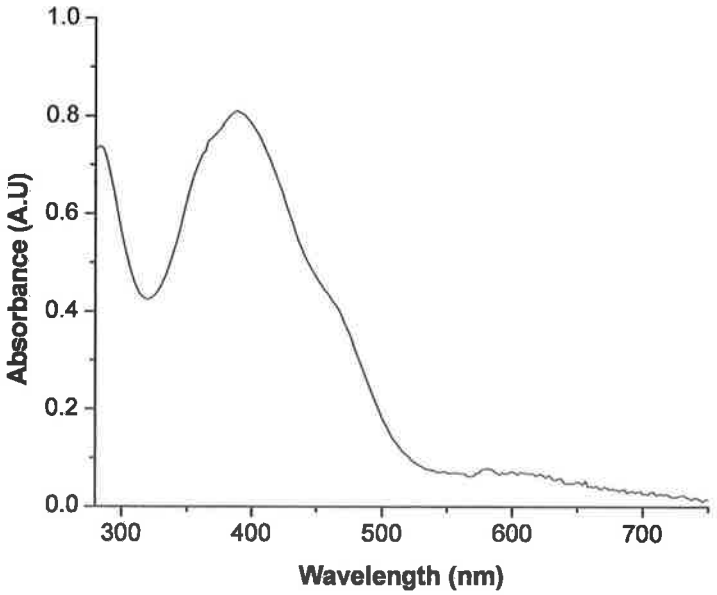

Electronic absorption spectrum of PyrCCThmal$Co_2(CO)_6$ in CH_2Cl_2 solution

F9 UV-Vis spectrum of PyrCCThCCTMS

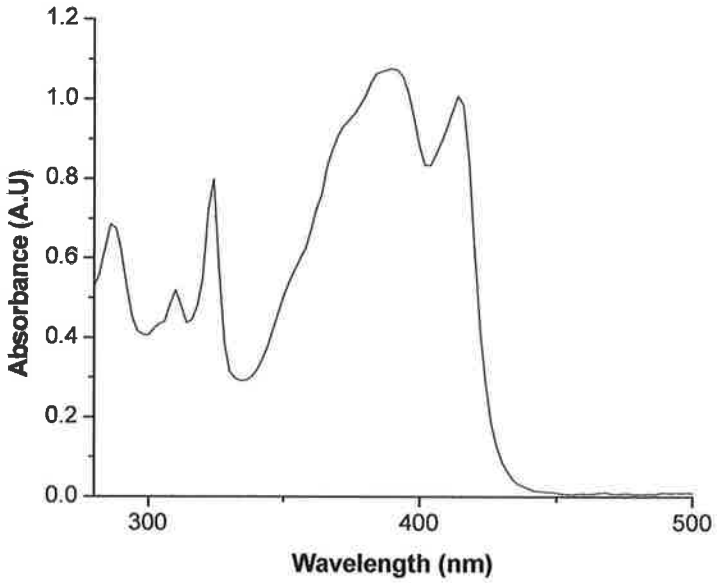

Electronic absorption spectrum of PyrCCThCCTMS in CH_2Cl_2 solution

F9 UV-Vis spectrum of PyrCCThCCH

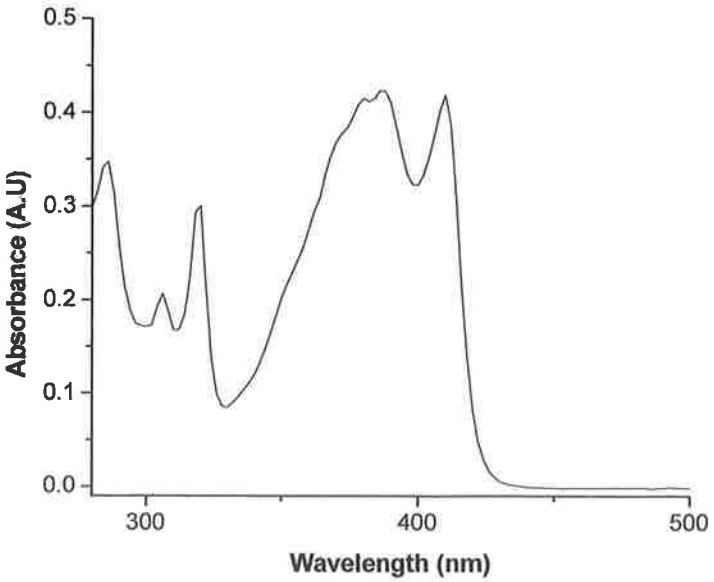

Electronic absorption spectrum of PyrCCThCCH in CH_2Cl_2 solution

G UV-Vis spectra of Pyrene-Pyridine and Pyrene-Ferrocene dyads

G1 UV-Vis spectrum of PyrCCpy

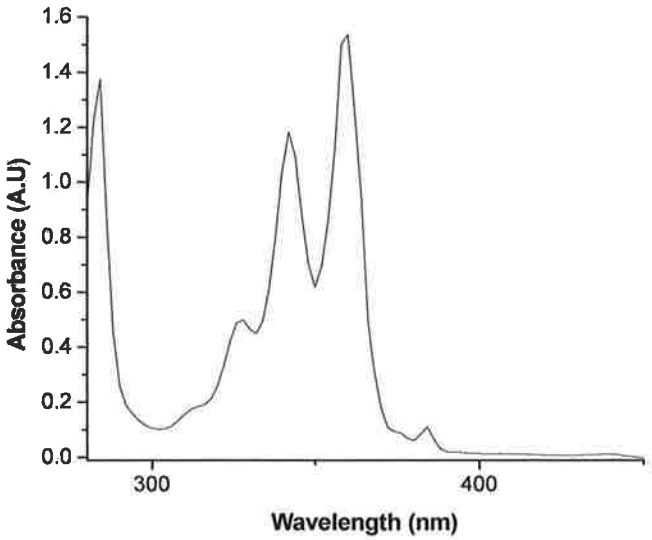

Electronic absorption spectrum of PyrCCpy in CH_2Cl_2 solution

G2 UV-Vis spectrum of $PyrCCpyCo_2(CO)_6$

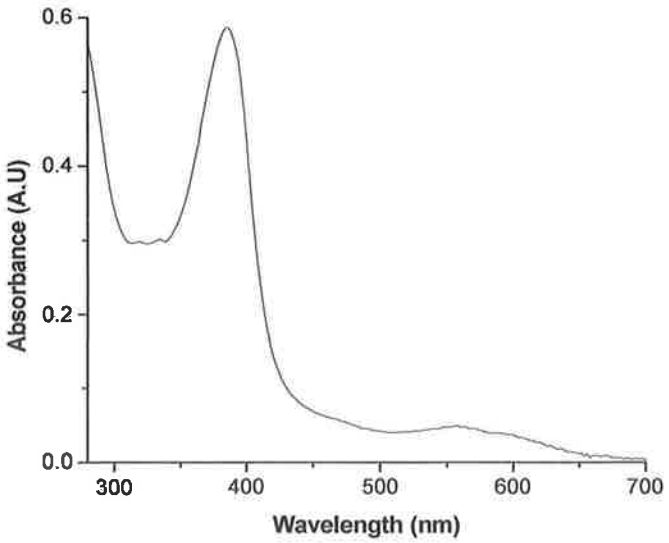

Electronic absorption spectrum of $PyrCCpyCo_2(CO)_6$ in CH_2Cl_2 solution

G3 UV-Vis spectrum of PyrCCFc

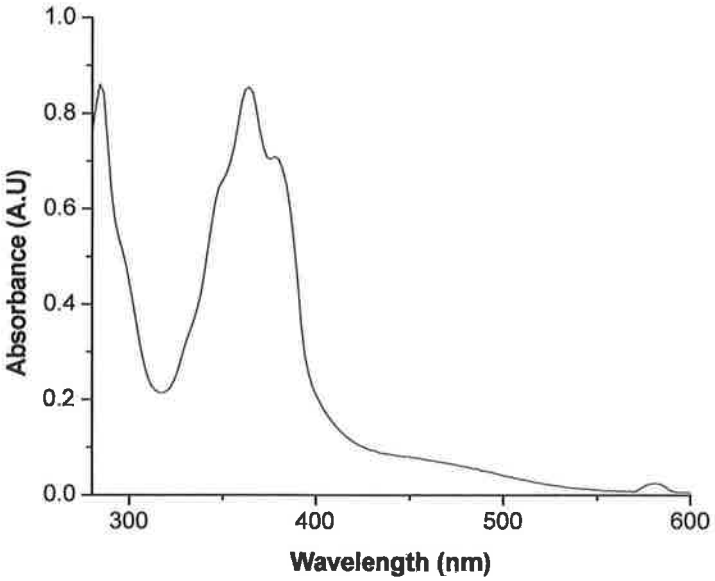

Electronic absorption spectrum of PyrCCFc in CH_2Cl_2 solution

G4 UV-Vis spectrum of PyrCCFc

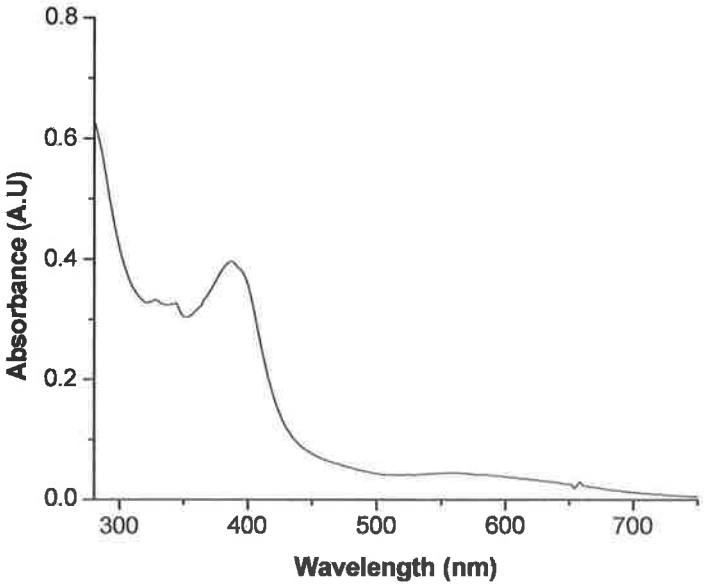

Electronic absorption spectrum of $PyrCCFcCo_2(CO)_6$ in CH_2Cl_2 solution

G5 UV-Vis spectrum of PyrCCThCCFc

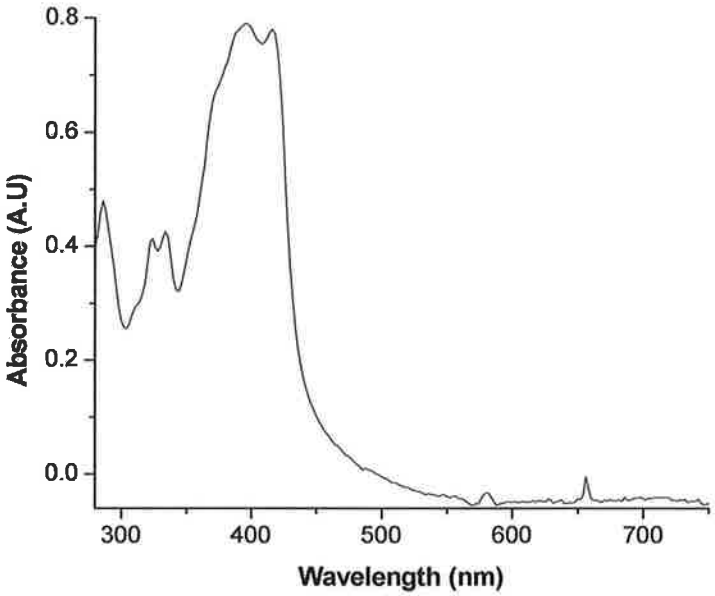

Electronic absorption spectrum of PyrCCThCCFc in CH_2Cl_2 solution

G6 UV-Vis spectrum of PyrCCThCCFc$[Co_2(CO)_6]_2$

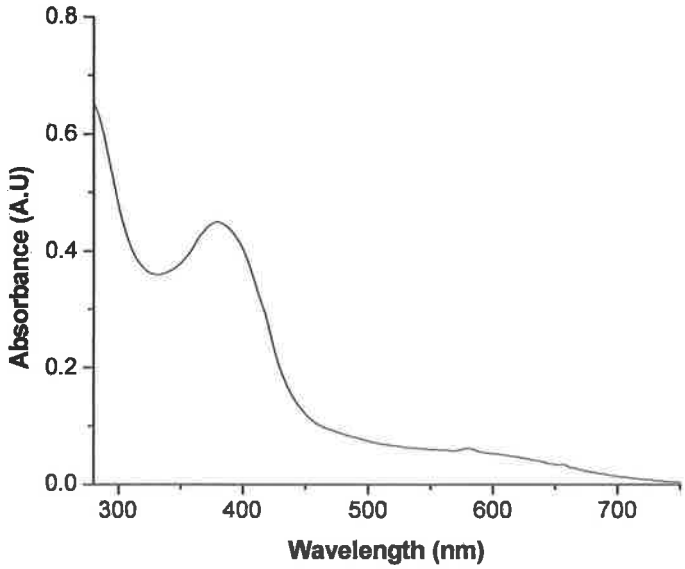

Electronic absorption spectrum of PyrCCThCCF$[Co_2(CO)_6]_2$ in CH_2Cl_2 solution

H Bibliography

1 Mohammed Abid Hassan Alamiry, Ph.D Thesis, Dublin City University, 2005

2 Noel M. O'Boyle, Johannes G. Vos, GaussSum 0.9, Dublin City University, 2005. Available at http://gausssum.sourceforge.net

3 Mary Pryce, Ph.D Thesis, Dublin City University, 1994

4 Hrnviar, P., Hudeck, M., Magomedov, G.K.I., Toma, S.; *Collect. Czech. Comm.*;**1991**, 56, 1477

5 Grimshaw, J.; Trocha-Grimshaw, J.; *J. Chem. Soc. Perkin 1*, **1972**, 1622-1623